UNIVERSITY OF SOUTHAMPTON

FACULTY OF NATURAL AND ENVIRONMENTAL SCIENCES

Chemistry

Volume 1 of 1

EXPLOITATION OF NONCOVALENT/DYNAMIC COVALENT INTERACTIONS IN SENSING, SELF-ASSEMBLY AND MEMBRANE TRANSPORT

by

Xin Wu

Thesis for the degree of Doctor of Philosophy

May 2016

UNIVERSITY OF SOUTHAMPTON

ABSTRACT

FACULTY OF NATURAL AND ENVIRONMENTAL SCIENCES

Chemistry

Thesis for the degree of Doctor of Philosophy

EXPLOITATION OF NONCOVALENT/DYNAMIC COVALENT INTERACTIONS IN SENSING, SELF-ASSEMBLY AND MEMBRANE TRANSPORT

Xin Wu

This thesis reports the development of several novel chemical sensing systems, self-assembled aggregates, and membrane transporters in which noncovalent and/or dynamic covalent interactions operate.

Perylenebisimide dyes functionalized with boronic acid groups were designed as effective chirality sensors for α-hydroxy carboxylates. Binding of chiral α-hydroxy carboxylate guests via boronate ester linkage leads to formation of optically active helical stacks of perylenebisimide dyes in water, giving diagnostic induced circular dichroism signals in the perylene absorption region.

A boronic acid-functionalized pyrene fluorophore forms excimer-emissive stacks upon cooperative binding of fluoride ion and catechol to the boron centre, allowing sensitive sensing of fluoride at ppm levels in aqueous solution which was unprecedented for boronic acids. The stabilization of boron-fluoride adduct in the aggregate and increase of Lewis acidity via catechol binding were proposed responsible for the unprecedented affinity, as supported by control experiments.

A dynamic covalent amphiphile comprised of 4-formylphenylboronic acid and octylamine forms vesicular aggregates selectively with glucose which can bind two boronic acids thus forming "Gemini-type" amphiphiles. The aggregates feature stabilization of imine bond and boronate ester linkage, with the two dynamic covalent bonds working in synergy promoting the formation of each other despite the spatial separation. The system allows selective sensing of glucose against the interference of fructose, for the first time without resorting to any synthesis.

A dynamic covalent approach was employed to transmembrane transport of amino acids by the formation of a three-component assembly. A mixture of a squaramide and a lipophilic and electrophilic aldehyde is shown to synergistically transport glycine across phospholipid vesicle membranes. The transport is proposed to occur via a hydrogen-bonded anionic glycine hemiaminal/imine, with control experiments supporting the role of hemiaminal/imine in the observed facilitated glycine transport

Finally, the issue of electrogenic/electroneutral transport mechanisms and potential proton or hydroxide transport for synthetic anionophores were examined. It is shown that depending on acidity, many synthetic anionophores can facilitate electrogenic proton or hydroxide transport. However, two newly-developed small molecules are shown to promote chloride transport without significant proton/hydroxide transport (pH gradient dissipation) at low concentrations, essentially mimicking the electrogenic cationophore valinomycin. The chloride > proton/hydroxide selective anionophores feature encapsulation of chloride ion via weak hydrogen or halogen bonds.

Table of Contents

DECLARATION OF AUTHORSHIP

I, Xin Wu, declare that this thesis and the work presented in it are my own and has been generated by me as the result of my own original research.

Exploitation of Noncovalent/Dynamic Covalent Interactions in Sensing, Self-assembly and Membrane Transport

I confirm that:

1. This work was done wholly or mainly while in candidature for a research degree at this University;
2. Where any part of this thesis has previously been submitted for a degree or any other qualification at this University or any other institution, this has been clearly stated;
3. Where I have consulted the published work of others, this is always clearly attributed;
4. Where I have quoted from the work of others, the source is always given. With the exception of such quotations, this thesis is entirely my own work;
5. I have acknowledged all main sources of help;
6. Where the thesis is based on work done by myself jointly with others, I have made clear exactly what was done by others and what I have contributed myself;
7. Parts of this work have been published as:

X. Wu, X.-X. Chen, B.-N. Song, Y.-J. Huang, Z. Li, Z. Chen, T. D. James, Y.-B. Jiang, *Chem. Eur. J.,* **2014**, *20*, 11793-11799. (Chapter 2)
Z. Chen, Q. Wang, X. Wu, Z. Li, Y.-B. Jiang, *Chem. Soc. Rev.,* **2015**, *44*, 4249-4263. (Chapter 2)
X. Wu, X.-X. Chen, B.-N. Song, Y.-J. Huang, W.-J. Ouyang, Z. Li, T. D. James, Y.-B. Jiang, *Chem. Commun.,* **2014**, *50*, 13987-13989. (Chapter 3)
X. Wu, Z. Li, X.-X. Chen, J. S. Fossey, T. D. James, Y.-B. Jiang, *Chem. Soc. Rev.,* **2013**, *42*, 8032-8048. (Chapter 4)
X. Wu, X.-X. Chen, M. Zhang, Z. Li, P. A. Gale and Y.-B. Jiang, *Chem. Commun.*, **2016**, *52*, 6981-6984. (Chapter 4)
X. Wu, N. Busschaert, N. J. Wells, Y.-B. Jiang, P. A. Gale, *J. Am. Chem. Soc.,* **2015**, *137*, 1476-1484. (Chapter 5)
X. Wu, L. W. Judd, E. N. W. Howe, A. M. Withecombe, V. Soto-Cerrato, H. Li, N. Busschaert, H. Valkenier, R. Pérez-Tomás, D. N. Sheppard, Y. Jiang, A. P. Davis and P. A. Gale, Chem, **2016**, DOI: 10.1016/j.chempr.2016.04.002. (Chapter 6)

Signed:

Date:

Acknowledgements

I would like to thank my supervisors Prof. Philip A. Gale and Prof. Yun-Bao Jiang for their guidance and support throughout my PhD in Southampton and in Xiamen. Thanks to Dr Lirong Lin for guiding me to start an undergraduate project, my first step in the exploration of supramolecular chemistry. I would also like to thank Yanjun Huang for sharing his expertise in boronic acid chemistry, Nathalie for advice in membrane transport experiments and Ethan for guidance in crystallographic and computational studies. My gratitude to all members of the Jiang group (Dr Jianbin Lin, Dr Zhao Li, Ms Daiping Guo, Jinhe Wang, Jinsong Zhao, Fu Cai, Wenbin He, Fang Wang, Na Chen, Wenjuan Ouyang, Zhan Chen, Ying Zhan, Yuchen Liu, Keyi Wei, Rong Zhou, Xiaosheng Yan, Shan Ma, Kun Wu, Meiling Wu, Yuan Yuan, Wenlu Wu, Qian Wang, Qian Zhang and Bingnan Song), and the Gale group (Jenny, Issy, Louise, Wim, Vanessa, Inés, Franci, Stu, Mike, Harriet and Laura) for their help and enlightening discussions on research. I acknowledge project student Annie for her great contributions to the selectivity projects.

I would like to thank Dr. Neil Wells, Dr. Philip Wiliamson and Dr. Stuart Findlow for their help in NMR experiments, Ms Julie Herniman for performing HRMS experiments, and Dr. Xiaodong Yang for assistance in TEM experiments.

I'm grateful to Prof. Tony James for manuscript revision, to Prof. Antony P. Davis, Dr. Hennie Valkenier and Dr. Luke W. Judd for collaborations on the selectivity project. To Dr Vanessa Soto-Cerrato, Dr. Hongyu Li, Prof. Ricardo Pérez-Tomás, Prof. David N. Sheppard for performing biological studies for the selectivity project.

I thank the University of Southampton and China Scholarship Council for the financial support for my PhD, and EPSRC for funding the research.

I wish to thank my family for support, without which the thesis would not have been possible. I thank Xuanxuan for her continuous encouragement.

Abbreviations

2ClMan	2-Chloromandelic acid
4FBA	4-Formylphenylboronic acid
a.u.	Arbitrary unit
BINOL	1,1'-Bi-2-naphthol
BODIPY	Boron dipyrromethene
C8AM	1-Octylamine
CB	Cucurbituril
CCCP	Carbonyl cyanide *m*-chlorophenyl hydrazine
CD	Circular dichroism;
CTAB	Cetyltrimethyl ammonium bromide
DCM	Dichloromethane
DFT	Density function theory
DLS	Dynamic light scattering
DMG	*N*,*N*-dimethylglycine
DMSO	Dimethyl sulfoxide
DPPC	Dipalmitoylphosphatidylcholine
EPN	Electrostatic potential at nitrogen nucleus
EtOAc	Ethyl acetate
EtOH	Ethanol
FCCP	Carbonyl cyanide-4 (trifluoromethoxy)phenylhydrazone
FRT	Fischer rat thyroid
Glu	Gluconate
Gly	Glycine
Gra	Gramicidin
HEPES	4-(2-Hydroxyethyl)-1-piperazineethanesulfonic acid

HHMan	Hexahydromandelic acid
HPTS	8-Hydroxypyrene-1,3,6-trisulfonic acid
HRMS	High-resolution mass spectrometry
Lac	Lactic acid
ISE	Ion-selective electrode
LDA	Linear discriminant analysis
LUV	Large unilamellar vesicles
Mal	Malic acid
Man	Mandelic acid
MnTPPCl	meso-Tetraphenylporphyrin manganese(III) chloride
Mon	Monensin
NDI	Naphthalene diimide
NMDG	*N*-methyl-D-glucamine
NMR	Nuclear magnetic resonance
PBI	Perylene Bismide
PCA	Protocatechuic acid
PhLac	3-Phenyllactic acid
POPC	1-Palmitoyl-2-oleoylphosphatidylcholine
POPG	1-Palmitoyl-2-oleoyl-*sn*-glycero-3-phosphoglycerol
ppm	Parts per million
Prod	Prodigiosin
Sar	Sarcosine
SD	Standard deviation
Tar	Tartaric acid
TBA	Tetrabutylammonium
TEA	Tetraethylammonium

TEM:	Transmission electron microscopy
UV-Vis	Ultraviolet-visible
Val	Valinomycin
YFP	Yellow fluorescent protein

Contributions from other researchers

All of the work presented in this thesis was completed by the author (XW) unless otherwise stated. On these occasions, the work is attributed to the contributing researchers by the initials as abbreviated below:

ALS	Adam L. Sisson
ENWH	Ethan N.W. Howe
ILK	Isabelle L. Kirby
LWJ	Luke W. Judd
MW	Marco Wenzel
NB	Nathalie Busschaert
TNL	Timothy N. Lambert
WJOY	Ouyang Wenjuan
XXC	Xuanxuan Chen

Chapter 1: General Introduction

Modern supramolecular chemistry has gradually evolved from studying purely non-covalent interactions to the inclusion of dynamic covalent bonds[1] as well into the construction of host-guest complexes or more complicated molecular assemblies. With the extensive exploitation of well-known interactions including hydrogen bond, ion pair, solvophobic interactions, aromatic π stacking, and cation-π interactions, recently the noncovalent toolbox has been enriched by halogen bond,[2] and anion-π interactions,[3] the distinct selectivity or applicability profiles of which have added to the diversity of supramolecular systems. These noncovalent interactions associate and dissociate instantly (*e.g.* half-life of hydrogen bonds typically less than 1 ns), allowing for rapid response to changes in environment and component concentrations. This however, implies low stability of the assembly. Dynamic covalent interactions are covalent bonds that are reversible (under certain conditions), as opposed to "permanent" covalent bonds used in organic synthesis. Examples include boronate ester,[4] disulfide bond,[5] imine bond,[6] hemiaminal,[7] (hemi)acetal,[8] and thioester[9] etc. The metal-ligand coordination may be regarded as a "borderline" case. The rates of bond formation and breaking vary among different dynamic covalent bonds. For example, boronate esters can form and break within a few seconds or minutes, representing arguably the most labile dynamic covalent bond (excluding metal coordination). Slightly less labile are some nucleophilic addition reactions of carbonyl compounds, including hemiaminal and imine formations. Some dynamic covalent bonds allow controllable switch of reversibility. For example, hydrazones are stable under neutral and basic conditions, but become labile under acidic conditions. Compared with noncovalent interactions that are generally weak, dynamic covalent bonds can operate effectively in highly competitive media and lead to more stable assemblies that may be "permanantly" stablized (such as by reducing an imine bond[10]). Compared with irreversible covalent bonds, dynamic covalent bonds offer the possibility of component exchange, self-sorting and adaptability to environments. These are crucial to achieving important functions and applications that are otherwise inaccessible, such as optimizing receptor structure via evolution from a library of components,[11] template-assisted assembly into highly complex architectures[12], designing triggerable drug delivery vehicles,[13] and achieving controllable mechanical movement in molecular scale.[14]

The thesis focuses on three areas of research within supramolecular chemistry, namely, chemical sensing, self-assembly, and membrane transport, which feature the use of either (or both) noncovalent and dynamic covalent interactions. Chemical sensors are molecules or ensembles that generate an optical, electrochemical or other types of responses upon interacting with the analytical species of interest (analyte).[15] Note that in this thesis, a broader definition of chemical

sensors is adopted to include systems that are less reversible. They have found a wide range of biomedical and environmental applications. As rapid analysis and reversibility are desired, noncovalent or dynamic covalent interactions are often employed for binding of the analytical target to the chemical sensor. All sensing projects in this thesis involve the use of dynamic boronate ester formation for analyte binding. The sensors developed here are not conventional small molecules. In all cases, the analyte binding triggers (or enhances) a supramolecular polymerization event, accompanied by dramatic changes of properties such as circular dichroism, UV-Vis absorption, fluorescence emission and solution turbidity. The benefit of the self-assembly approach to selectivity and sensitivity, compared with the formation of a simple small molecule host-guest complex is demonstrated in the examples in this thesis. In particular, weak dynamic covalent bonds can be strengthened by forming supramolecular aggregates. Another important topic in this thesis is facilitation of membrane transport, in which both conventional non-covalent approach and underexploited dynamic covalent interactions were exploited in the design of novel small molecule transporters for amino acids and anions. Please refer to the following chapters for more detailed introductions to different topics covered.

Chapter 2 reported generation of optically active supramolecular π-stacks of perylenebisimide dyes, employing the dynamic boronate ester linkage for guest binding and chirality induction.[16] This leads to development of structurally simple yet rather effective sensors for rapid determination of enantiomeric excess of α-hydroxy acids, which may have applications in asymmetric synthesis. In Chapter 3, cooperative binding of fluoride ion and a catechol to a pyreneboronic acid resulted in formation of excimer-emissive supramolecular aggregates in water, achieving the challenging goal of fluoride sensing at ppm levels in water.[17] Chapter 4 reported aggregation of an in situ-formed amphiphile featuring two spatially separated dynamic covalent bonds (imine and boronate ester) promoting the formation of each other as a result of stabilization of both bonds within aggregates. This allows selective sensing of glucose simply by mixing commercially available reagents in water. In Chapter 5, it is demonstrated for the first time that lipophilic and electrophilic aldehydes can facilitate transport of amino acids across phospholipid bilayers via reversible formation of hemiaminal or imine intermediates.[18] Chapter 5 examined the $Cl^- > OH^-$ selectivity of a wide range of anionophores functioning via hydrogen bond, ion pair, halogen bond or metal coordination. It is shown that encapsulation of chloride via weak hydrogen or halogen bonds confers high $Cl^- > OH^-$ selectivity which is important for biological applications where pH gradient disruption is undesired, whereas binding chloride via dative covalent bonds to metal centre or strong hydrogen bonds is not favourable for selectivity against hydroxide transport presumably due to strong interaction with hydroxide.

Chapter 2: Chirality Sensing of α-Hydroxy Carboxylates by Induced Helical Chirality of Perylenebisimide Stacks

2.1 Introduction

2.1.1 Chirality sensing

Within the area of chemical sensing, there has been considerable interest in designing synthetic optical sensors that effectively discriminate between enantiomers of a certain class of chiral organic compounds.[19-21] Those sensors, here referred to as chirality sensors, are designed to interact with chiral analytes via covalent or noncovalent interactions, giving spectroscopic responses that depend on the enantiomeric excess of the tested chiral analytes. These sensors have shown their potentials in many fields where chirality is an important parameter, for instance, absolute configuration assignment and promoting the development of asymmetric syntheses by offering an effective means of determining enantiomeric excess (*ee*) of reaction products. In the case of optical sensors, given that the sensor-analyte interactions take place fast enough, which is usually not a problem for supramolecular sensors, the rapidness and relatively low cost of spectroscopic assays will confer great advantages over prevailing methods for determining enantiomeric excess such as chromatographic techniques especially when hundreds of reaction products need to be analysed to optimize the reaction conditions.

Chirality sensing is to distinguish right-handed and left-handed chirality and/or determine the optical purity of chiral samples. There are two major approaches to discriminate between enantiomers, chiral discrimination and chirality induction. In the chiral discrimination approach[19] a chiral sensor is designed to form diastereomeric host-guest complexes with chiral analytes, producing responses in the UV-Vis absorption, fluorescence or NMR spectra that are different between a pair of analyte enantiomers. In the chirality induction approach[21], achiral or dynamically racemic sensors are designed, which show induced molecular or supramolecular chirality upon sensor-analyte interactions giving responses detectable by a chiral discriminating spectroscopy such as circular dichroism (CD) or circularly polarized luminescence (CPL). A third, less common approach also exists, which does not involve the use of any chiral auxiliary or chiral discriminating spectroscopy, but is based on assembly of the sensor with (*R*)- and (*S*)-analytes that generates an *ee*-dependent response in a spectroscopic instrument that possesses no intrinsic chiral discriminating capacity.[22-24]

In the case of chiral sensors, (i) the differences in association constants of the diastereomeric sensor-analyte complexes should be sufficiently large, if the resulting diastereomeric complexes possess identical UV-Vis absorption or fluorescence spectra; or (ii) alternatively, the spectroscopic properties of the diastereomeric complexes should be different to allow discrimination by UV-Vis absorption, fluorescence or NMR methods. In the case of achiral sensors, they may have flexible conformations or exist as a racemic mixture of rapidly inter-converting enantiomeric conformers. Upon chiral analyte binding, the conformation of the sensor molecule should be effectively restricted that results in chirality induction, or the energy difference between the diastereomeric conformers should be sufficiently large to bias the formation of either conformer, resulting in nonracemic composition of the conformers and thus CD responses.

There are several criteria to evaluate the usefulness of a chirality sensor as an analytical tool in asymmetric synthesis. These include sensitivity to enantiomeric composition (*e.g.* large induced CD signals for the chirality induction approach), sensitivity to low sample concentration (thereby reducing sample consumption), whether prior knowledge of sample concentration is required, rapidness of chirality induction, selectivity (minimising interaction with impurities), long operating wavelength (minimising interference from impurities that absorb at short wavelengths), and reproducibility.

Most chirality sensors so far designed, by any of the three approaches described above, are small molecules. In spite of the great success achieved with small-molecule based sensors, often, an elaborately designed sensor structure is required. Recently, conceptually new chirality sensors based on macrocycles, synthetic polymers and supramolecular polymers have been developed. They may have distinct advantages compared with small molecules, such as ease of sensor design, broadening of substrate scope and amplified response to a small enantiomeric difference.[25] A few representative examples of different classes of chirality sensors are presented in this chapter.

2.1.2 Small molecule-based chirality sensors

As a classical approach to chirality sensing, the development of small molecular sensors that show optical responses to sample enantiopurity has boosted during the last two decades. In a broader sense, this can include early examples of covalent derivatization of chiral organic compounds with chromophores, enabling electronic circular dichroism (ECD) analysis of chiral compounds that do not have UV-Vis absorption.[26] In general, covalent derivatization requires a tedious and lengthy synthesis and purification procedure. Instead, recent examples have mostly employed noncovalent or dynamic covalent interactions to attach a chiral analyte to a sensor, the rapidness of analysis making possible high throughput screening (HTS) of asymmetric reaction products.

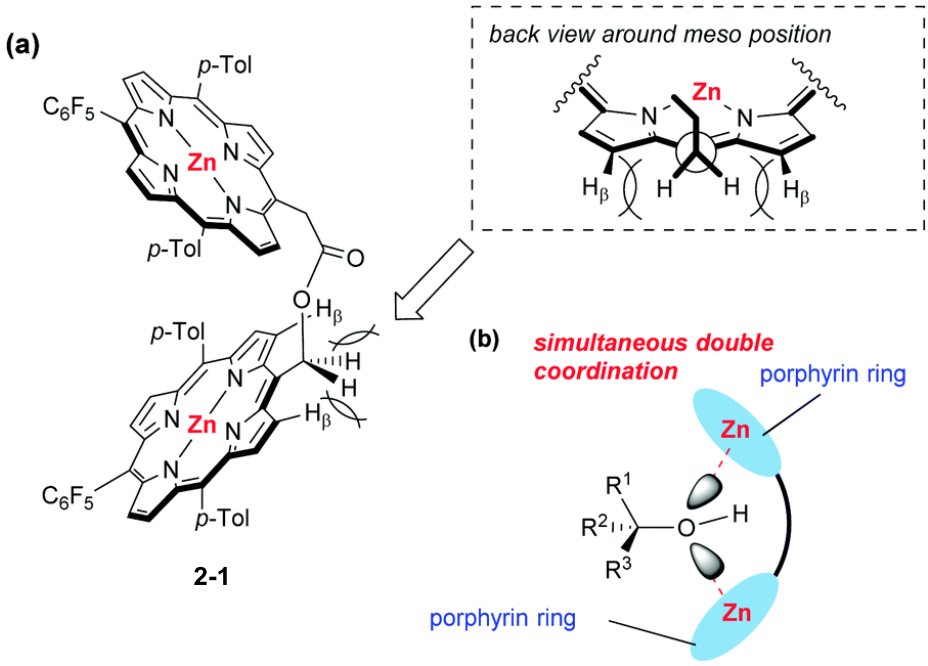

Figure 2.1 Structure of bis(Zn-porphyrin) sensor **2-1** and its interaction with chiral mono-alchohols. Reproduced with permission from *Chem. Commun.* **2015**, *51*, 11068-11071. Copyright 2015 Royal Society of Chemistry.

The "porphyrin tweezers" – dimeric metalloporphyrins are classical examples of chirality sensors that have been designed for successful chirality induction and sensing of a wide range of chiral organic compounds.[27] In general, two metalloporphryin units are linked by a flexible spacer. The porphyrin tweezers are conformationally flexible in the absence of chiral analytes. Binding of a chiral analyte (which needs to contain two metal binding sites,[28] or can be attached to a "carrier" which contains an additional binding site to satisfy this condition[29]) simultaneously with two metal centres "closes" the tweezer leading to helical arrangement of the two metalloporphyrin units with the handedness determined by the chirality of the analyte. Alternatively to using metal centre for analyte binding, the porphyrin tweezer can be functionalized with analyte binding sites to target a specific group of analytes.[30] The intense absorption bands (Soret bands and Q-bands) of porphyrins in the visible region allow high sensitivity to μM concentrations, while the large size of porphyrin units ensure efficient chirality induction (preference to form one helicity) as a result of steric interactions with the chiral analyte. Recently, the challenging goal of sensing chirality of weakly interacting mono-alcohols without covalent derivatization has been achieved by Takanami and coworkers using bis(Zn-porphyrin) sensor **2-1** (Figure 2.1).[31] The elegant structure design that involves pre-organising the porphyrin units in a splayed cofacial arrangement by steric repulsion between the hydrogen atoms at the methylene spacer and those at porphyrin β-positions (H_β) allows the two Lewis acidic metal centres to bind simultaneously with the two lone pairs of alcohol oxygen atom in non-polar solvents. Induction of strong excition-coupled circular dichroism (ECCD) signals in the Soret band of **2-1** was observed with several chiral mono-alcohol analytes,

and a working model has been proposed for non-empirical absolute configuration assignment of the analytes.

As exemplified by the porphyrin tweezers, using metal complexes has been a popular strategy for developing chirality sensors partly due to effective interactions of metal centres with chiral analytes. Other examples include several tripodal ligand-based chirality sensing systems developed by Anslyn and coworkers. Cu(II) complex **2-2** serves as a CD-based chirality sensor for mono-carboxylates (Figure 2.2a),[32] which exits as equal amount of enantiomers in equilibrium in the absence of chiral analytes, but preferably forms a diastereomer upon binding of a chiral carboxylate due to steric interactions between the tripodal ligand and the groups present in the chiral carboxylate. This protocol allows not only *ee* determination of chiral carboxylates, but also identification of different chiral carboxylates guests by linear discriminant analysis (LDA) due to different shapes and magnitudes of the CD signals induced by different carboxylate analytes. This system was later applied for chirality sensing and differentiation of *N*-Boc amino acids.[33]

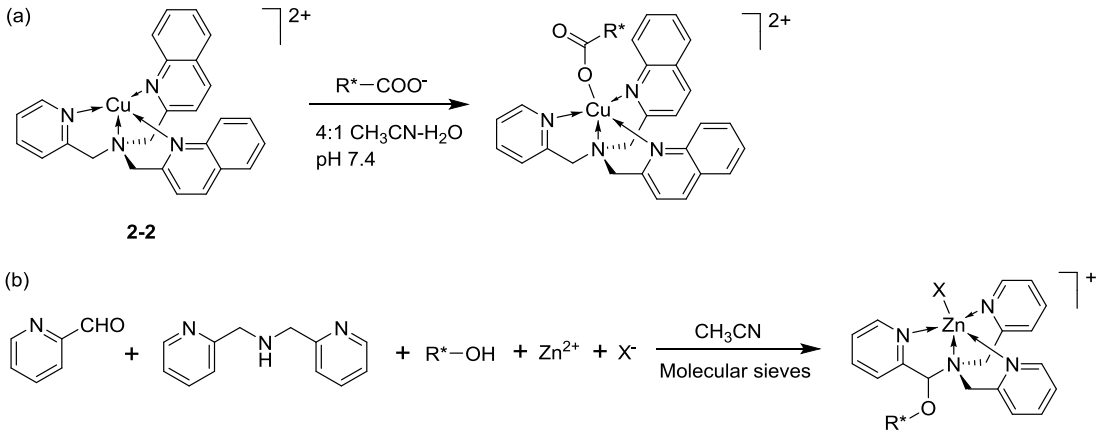

Figure 2.2 (a) Chirality sensing of chiral carboxylates by Cu(II) complex **2-2**. (b) Chirality sensing of chiral alcohols by a multicomponent dynamic covalent assembly leading to the formation of a hemiaminal ether-Zn(II) complex.

In 2011, the Anslyn group reported a new chirality sensing system for chiral alcohols based on helical metal complexes of in situ generated tripodal ligands.[34-35] While binding of alcohols is possible by direct coordination to a highly Lewis acidic metal centre as is the case of **2-1**, it is remarkable that Anslyn *el al.* have achieved reversible binding of alcohols via a C–O covalent bond. A multicomponent assembly was formed between 2-pyridinecarboxaldehyde, bis(2-pyridylmethyl)amine, Zn^{2+} and a chiral alcohol (Figure 2.2b), leading to diastereoselective formation of helical Zn(II) complexes with the major diastereomer determined by the chirality of the chiral alcohol used. The formation of the assembly was shown to occur via binding of the alcohol to a iminium ion formed between 2-pyridinecarboxaldehyde and bis(2-pyridylmethyl)amine, and the resulting hemiaminal ether was stabilized by chelation to a Zn^{2+} ion. This system allows absolute configuration assignment, identification and accurate ee

determination of chiral alcohols, but has the drawback of requiring a long reaction time (overnight) in the presence of molecular sieves for the assembly to complete.

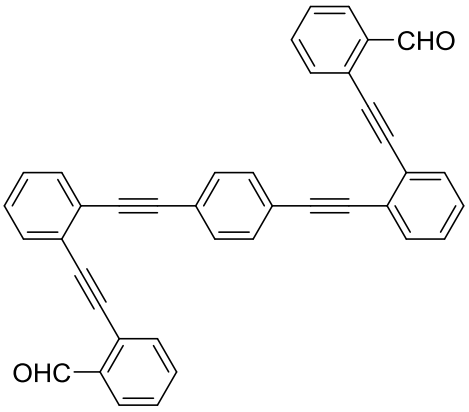

2-3

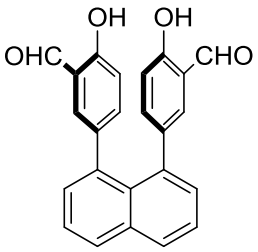

2-4

The arylacetylene framework is one of the metal-free scaffolds based on which effective chirality sensors have been designed. Bis-aldehyde **2-3**, developed by Wolf and coworkers, serves as a chirality sensor for *ee* determination of chiral primary amines.[36-37] **2-3** is conformationally flexible due to free rotation of the single bonds joining the aryl and acetylene groups. Binding of a chiral diamine simultaneously with two aldehyde groups in **2-3** gives a cyclic addition product with a restricted conformation and induced axial chirality. Interestingly, chirality induction of **2-3** was also observed with chiral monoamines that form acyclic diimine adducts with **2-3**. This is surprising since in acyclic diimine adducts the conformation restriction is not expected to be as effective as in cyclic adducts. The exact reason for the chirality induction by chiral monoamines was not examined by the authors. **2-4** is another chirality sensor based on imine bond formation developed by the same group.[38-39] Upon addition of two molecules of chiral amino alcohols or amino acids to **2-4**, an intramolecular hydrogen bond network bridges the two aryl units and favours the formation of a single diastereomer.

All of the abovementioned examples belong to the "chirality induction" approach that use achiral or dynamically racemic sensors. Chiral sensors that respond to enantiomeric excess of chiral analytes in UV-Vis absorption, fluorescence or NMR spectra have been widely developed as well. Similarly to "chirality-induction" systems, discrimination between a pair of guest enantiomers by a chiral host generally relies upon effective steric interactions within the complex to favour the formation of one diastereomer and/or lead to diastereomers that have different optical properties. The axial chiral 1,1'-bi-2-naphthol (BINOL) moiety[40] is one of the most popular scaffolds for the design of chiral sensors as functionalization of the motion-restricted and helically arranged naphthalene plains allows "multipoint" interactions with a chiral analyte – a prerequisite for effective chiral discrimination. An example of BINOL-based chiral sensor is **2-5** which shows a highly enantioselective fluorescence response to α-hydroxy carboxylic acids that interact with **2-5**

via multiple hydrogen bonds.[41] Interestingly, only one enantiomer of an α-hydroxy carboxylic acid leads to enhancement of monomer fluorescence emission of **2-5**, which was ascribed to guest-binding induced protonation of both nitrogen atoms in **2-5**, thus inhibiting fluorescence quenching by photo-induced electron transfer from the nitrogen atoms to the fluorophore. The structural origin of the high enantioselective fluorescence response remains unclear.

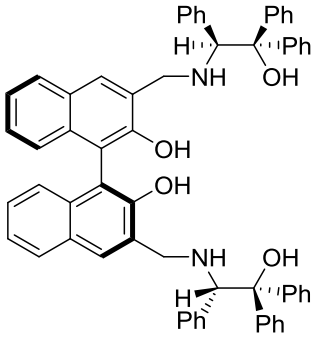

2-5

The cooperative dynamic covalent binding of an axial-chiral aromatic diol and a chiral primary amine to 2-formylphenylboronic acid gives diastereomeric ternary assemblies. This reaction has been utilized for the development of several chirality sensing systems for chiral primary amines based on different spectroscopic techniques (Figure 2.3). The earliest protocol that involves the use of BINOL, developed by Bull and coworkers, uses NMR spectroscopy to distinguish between the diastereomers, in which integration of the diastereotopic proton resonances from the respective diastereomers allows quantitative ee determination of the amine precursor.[42] Anslyn and coworkers later developed a CD-based protocol based on the same assembly.[43] Although BINOL is already chiral and CD active before the assembly, assembly formation alters the CD signal from the BINOL moiety, with two amine enantiomers giving changes in opposite directions (increase or decrease). This was attributed to the chiral amine changing the dihedral angle of the BINOL moiety in opposite directions. The CD responses were employed for ee determination and identification of chiral amines. Very recently, a fluorescence sensing ensemble for chiral amines was developed by Anzenbacher and coworkers.[44] More sterically hindered axial-chiral ligands **2-6** and **2-7** were used in place of BINOL, and it was anticipated that the different dihedral angels of the aromatic diols induced by different chiral amine enantiomers would lead to different fluorescence properties of two diastereomers. Fluorescence titration studies indeed demonstrated that the assemblies formed by 2-formylphenylboronic acid, a chiral amine and **2-6** or **2-7** have formation equilibrium constants and fluorescence emission intensities that are different between a pair of diastereomers. With the less bulky BINOL ligand, there is no significant difference between diastereomers in the complex stability and fluorescence property. This system

allows measurement of enantiomeric excess by fluorescence spectroscopy with low errors (1%-2%).

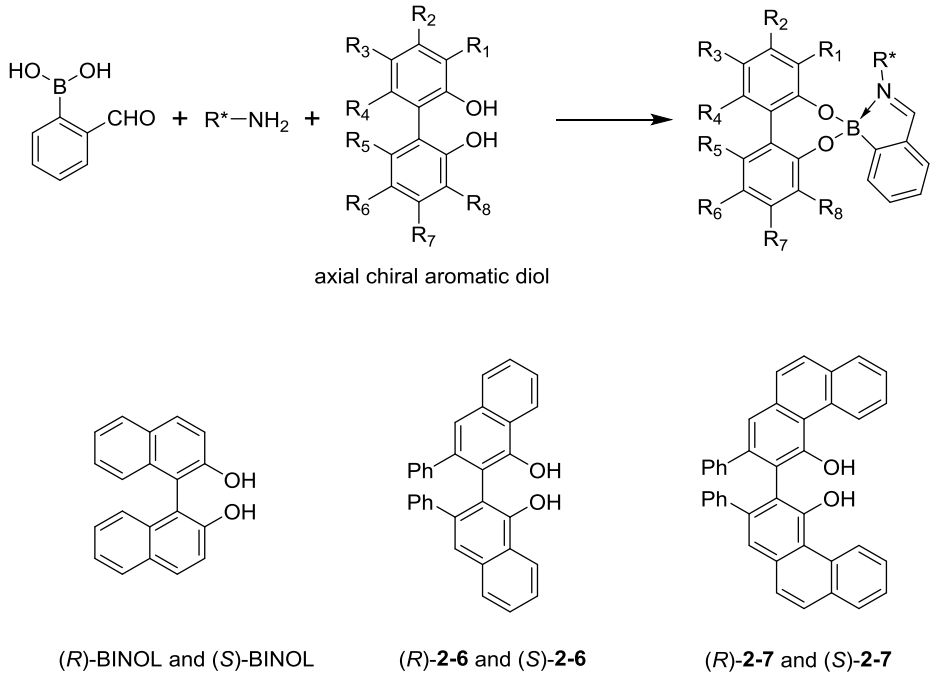

Figure 2.3 Chirality sensing systems for chiral primary amine based on three component assemblies between 2-formylphenylboronic acid, an axial-chiral aromatic diol, and a chiral primary amine.

The abovementioned examples either use achiral sensors with a chirality-discriminating spectroscopic technique (*e.g.* CD spectroscopy) or use chiral sensors. It may seem counterintuitive being able to achieve chirality sensing with achiral sensors using NMR which possesses no intrinsic chiral discriminating capacity. This is in theory possible, however, if a system can generate *ee*-dependent optical response. With porphyrin-based macrocycles, Hill and coworkers successfully developed several chirality sensing systems with achiral sensors generating NMR outputs (Figure 2.4). The earliest example[45] **2-8** forms 1:2 (host to guest) complex with mandelic acid guests. NMR signal of quinonoid (H_a) peaks, as well as that of β-pyrrolic (H_b) was found to undergo splitting at 100% guest *ee* but converged at 0% *ee*; the distance between separated peaks depending linearly on guest *ee*. Tautomerization of the protonated porphodimethene was found to occur upon addition of mandelic acids, which complicates the mechanistic study of the origin of *ee*-dependent peak splitting. It was not yet clear whether the formation of diastereomers plays a role in the *ee* sensing.

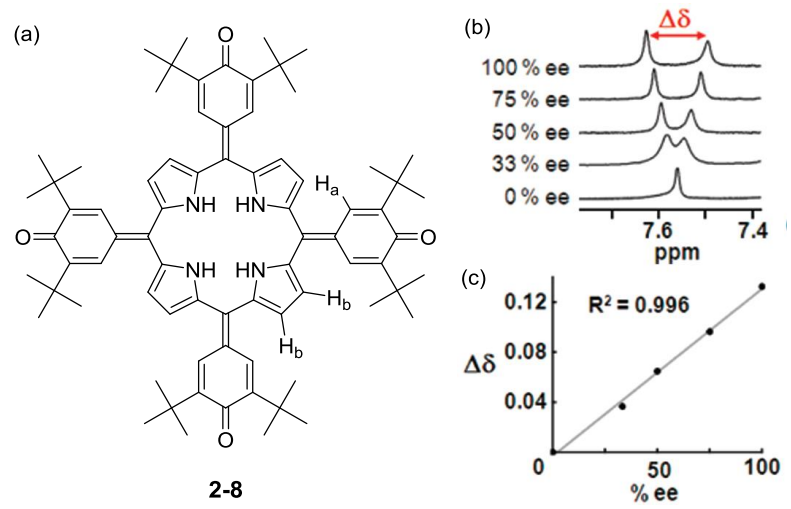

2-8

Figure 2.4 Structure of **2-8** (a) and separation of pyrrolic β-H resonances with *ee* of mandelic acid guest (b, c). Adapted with permission from *J. Am. Chem. Soc.*, **2009**, *131*, 9494-9495. Copyright 2009 American Chemical Society.

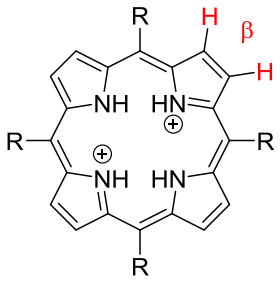

2-9: R = Ph
2-10: R = *t*Bu

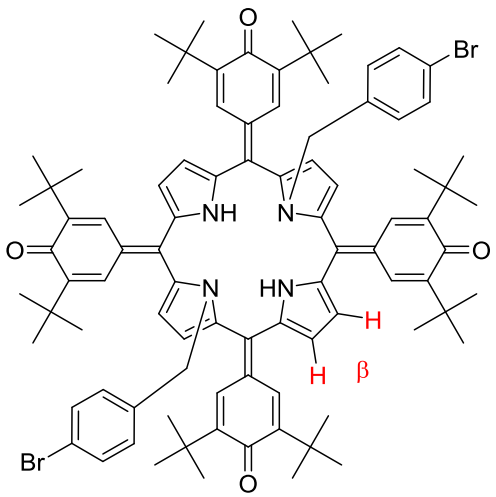

2-11

Later Hill and coworkers reported that a similar guest *ee*-dependent splitting of the β-pyrrolic proton resonances can also be observed even with simple achiral porphyrins **2-9** and **2-10**, although low temperature (-32.5 °C) was required.[46] A model accounting for the linear dependence of peak splitting distance on *ee* was proposed, which assumed the formation of enantiomers instead of diastereomers. The β-pyrrolic protons H_a and H_b which are enantiotopic before guest binding become diastereotopic upon formation of a 1:2 (host to chiral guest) complex, due to the chiral environment imposed by the chiral guest. With enantiopure guests (100% *ee*), different chemical shifts from the diastereotopic H_a and H_b were clearly observed, while the relative positions of the H_a and H_b peaks are opposite for the enantiomeric porphyrin complexes formed with (*R*)- and (*S*)-guests. With racemic guests, however, the host-(*R*)-guest complex rapidly exchanges with the host-(*S*)-guest complex, the H_a peaks from the (*R*)- and the (*S*)-complex therefore emerges as an averaged resonance, at the same chemical shift as the

emerged H_b peaks from the (*R*)- and (*S*)-complexes. This results in an apparent single peak from the H_a and H_b protons with 0% *ee*. The system was applied for determining *ee* of the chiral drug ibuprofen. The same group recently reported another porphyrin-based sensor[22] **2-11** with two pyrrole nitrogens substituted by bulky benzyl group, which leads to the formation of only 1:1 complexes and thus excludes the possibility of diastereomer formation. **2-11** shows similar splitting of β-pyrrolic proton resonances that depends linearly on guest *ee* at room temperature, enabling *ee* determination of various carboxylic acids/esters and some terpenoids. All those NMR-based porphyrin sensors also allow empirical absolute configuration assignment for the guest molecules, which can be realized by spiking the unknown sample with a pure enantiomer with known configuration.

2.1.3 Non-small-molecule chirality sensors

Using macrocyclic hosts represents an attractive approach for designing efficient chirality sensors. The possibility of accommodating multiple guest molecules within cavity of macrocyclic hosts is intriguing for chirality sensing in several ways. These guest molecules may be chiral analytes, chiral molecule responsible for enantioselective binding with chiral analyte, and / or chromophore responsible for generating spectroscopic outputs. By assembling those species within a macrocyclic host, synthetic efforts to covalently conjugate them are not needed yet more flexible and versatile sensing schemes can be designed.

Nau and coworkers have recently developed two different chirality sensing assays based on the inclusion complexes of cucurbituril (CB) hosts and dye molecules that act as spectroscopic reporters. One of them employed the stereospecific enzymatic reactions (Figure 2.5).[47] Enzymes able to convert specifically the L-enantiomers of amino acids to amines were chosen, following the fact that the amines show significantly higher affinities towards the CB[7] host than the amino acid substrates. Therefore, at suitable substrate concentrations, the amine produced by the enzymatic reactions, but not the amino acid substrate, displaces the fluorescent dye Dapoxyl previously included within the CB[7] cavity, leading to quenching of Dapoxyl fluorescence. When a mixture of enantiomers was subject to the analysis, the extent of fluorescence quenching depends on *ee* of the analytes. Because of the stereospecificity of enzymatic reactions and the sensitivity of the fluorescent assay, an accurate measurement of *ee* higher than 99% is made possible by using a high analyte concentration. Such assays for the high end of *ee* are not achieved with traditional small-molecule based sensors.

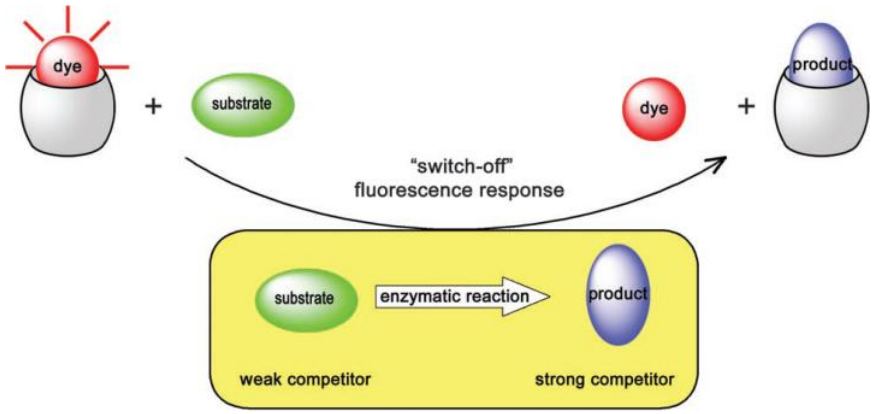

Figure 2.5 Chirality sensing by using an indicator displacement system involving a cucurbituril-dye complex coupled to an enzymatic reaction. Reproduced with permission from *Chem. Eur. J.*, **2008**, *14*, 6069-6077. Copyright 2008 Wiley-VCH.

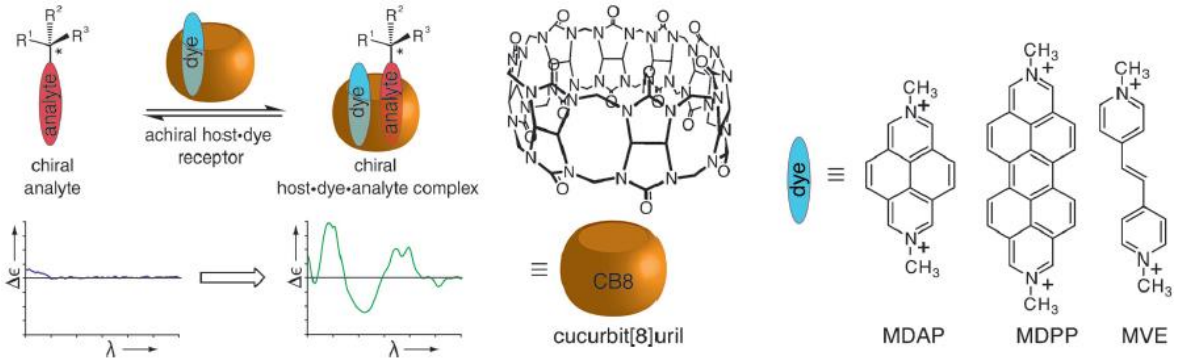

Figure 2.6 Chirality sensing based on circular dichroism (ICD) signal induced by co-inclusion of a dye and a chiral analyte inside an achiral cucurbituril cavity. Reproduced with permission from *Angew. Chem. Int. Ed.*, **2014**, *53*, 5694-5699. Copyright 2014 Wiley-VCH.

Another elegant example that demonstrates the advantage of using macrycycles is the CD-based chirality sensing assay relying on ternary complex formation between a cucurbituril host (CB[8]), a double-cationic achiral dye and a chiral analyte (Figure 2.6).[48] The CB[8]-dye complex remains achiral and thus is CD silent, while the co-inclusion of a chiral aromatic analyte inside the CB[8] cavity effectively induces strong CD signal in the dye absorption region. The CD signal depends linearly on the *ee* of the chiral analyte. This assay applied for a broad scope of analytes since it relies on non-covalent interaction between the CB host and the aromatic moieties of the guest molecules. This is a significant breakthrough compared to that based on small-molecule based sensors that require certain reactive functional groups to be present in the analyte. The assay is operable for micromolar concentrations of analytes and can be used for real time monitoring of chemical reactions, for example, the racemization of (*S*)-1-phenylethanol catalyzed by an amberlyst.

Macromolecular helicity can also result from synthetic polymers possessing bulky side chains thus create higher rotation energy barriers.[49] These helical oligomers / polymers are dynamically

racemic in the absence of any external influence, and simple sensor design can allow single-helicity induction by analyte binding. Compared with small molecules that generally show linear relationships between the optical response and the *ee*, sometimes non-linear *ee* response can be observed in polymeric systems, i.e. the "majority rules"[50-52] that offer the possibility of amplifying chiroptical response to a small region of *ee*. In "majority-rules" operative systems,[52] a small *ee* produces a non-proportionally large CD signal, and thus the CD-*ee* curve shows a steeper slope around 0% *ee*. Within a "heterochiral" polymer, repeating units with opposite chirality coexist which prefer opposite handedness of the polymer backbone. When the energy penalty for a helix reversal is larger than the energy penalty required for a "mismatch", the minority enantiomer unit will obey the handedness preference imposed by the majority, resulting in the "majority-rules" effect.

The "majority-rules" has been proposed by Yashima *et al.*[53] to be applicable to determination of a small enantiomeric imbalance. The working system is a stereoregular *cis*-transoidal poly(phenlyacetylene) **2-12** consisting of a polyacetylene backbone as the chromophore and bulky crown ether as the pendant binding unit for amino acid (Figure 2.7). Upon binding to L- and D-alanine (Ala), **2-12** exhibits strong chiral amplification which was apparent even with 0.01 equiv of L-Ala (Figure 2.7). An extremely strong "majority-rules" effect was observed and 5% *ee* of Ala was able to generate full induced CD signal. Detection of extremely small enantiomeric excess of 0.005% of Ala is possible. This system has been successfully applied to 19 L-amino acids as well as 5 chiral amino alcohols. Determining small *ee* values, is, however, of little value for optimising asymmetric synthetic methods that are aimed at achieving enantioselectivity close to 100% *ee*. Recently, Anslyn and coworkers proposed a clever way of utilising "majority-rules" active systems for this purpose.[54] By adding an equal amount of the dominant guest enantiomer, the *ee* of an unknown sample which is close to 100% will be shifted to an *ee* close to 0%, within the *ee* region where the CD intensity is the most sensitive to *ee* differences for "majority-rules" systems. The **2-12**-amino acid system was employed for a proof-of-the-principle investigation. Although promising results have been obtained, further improvement on the stability and reproducibility of a working system is required for implementation of this strategy.

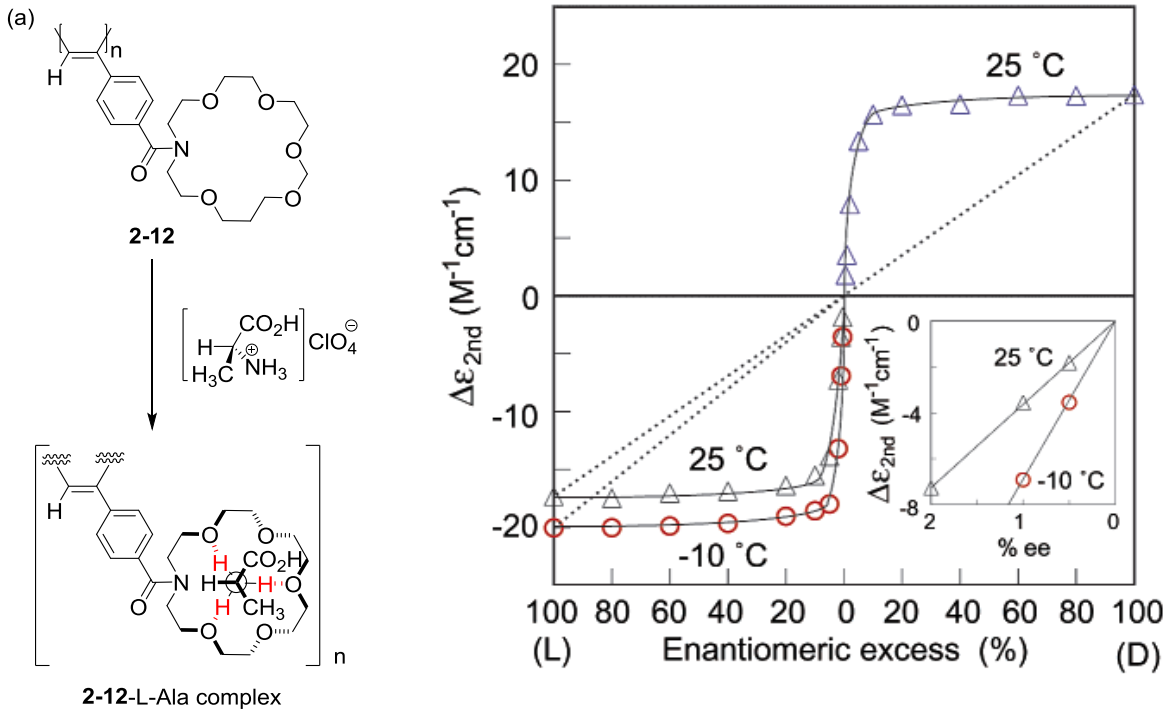

Figure 2.7 (A) Polymer **2-12** and its interaction with L-Alanine. (B) Titration curves of poly-**5** vs molar ratio of L-Ala·HClO4 in acetonitrile. (C) Changes of ICD intensity of poly-**5** vs *ee* of L-Ala·HClO4. Reprinted with permission from *J. Am. Chem. Soc.*, **2002**, *125*, 1278-1283. Copyright 2003 American Chemical Society.

Interaction of a chiral guest molecule can induce not only molecular chirality in small molecules and synthetic polymers, but also supramolecular chirality in molecular assemblies. The term "supramolecular chirality" differs from "molecular chirality" in that the chirality is not the property of a stereogenic centre or an asymmetric conformation within a single molecule, but arises from asymmetric spatial arrangement of molecular building blocks within a noncovalent assembly. Differing from synthetic oligomers/polymers, the building blocks of supramolecular polymers are held together by noncovalent interactions such as hydrogen bonding, aromatic π-stacking, and metal coordination. While achiral building blocks are expected to yield intrinsically achiral assemblies or racemic mixtures of left-handed (P) and right-handed (M) helices in the absence of any chiral influence, the formation of helical aggregates with preferred handedness has been achieved either by using building blocks bearing stereocenters,[55-56] or by using achiral building blocks in the presence of chiral polymers[57-59] or small molecules[60-64] as chemical chirality inducers, or under physical forces such as a vortex flow[65-66] or a magnetic force.[67] The phenomena of supramolecular chirality induction from small molecule chirality inducers may provide an attractive strategy for developing chirality sensors for the small molecular chirality inducers, but this has not been extensively explored. Before publication of the current work, the only example of this approach is the system reported by Amabilino and coworkers that uses supramolecular polymers formed by intermolecular hydrogen bonding of **2-13** to determine the enantiomeric excess of chiral acids.[68] In apolar solvents, **2-13** undergoes dimerization held by four

intermolecular hydrogen bonds and subsequent polymerisation to form long fibrillar stacks. In the presence of chiral acids that interact with the dimer of **2-13** via double hydrogen bonds, optically active chiral aggregates were formed that show CD signals in the absorption of the oligo(p-phenylenevinylene) chromophore. This system has the novelty of chirality sensing using supramolecular polymers and the advantage of requiring a low amount of chiral acid analytes. However, lengthy and tedious preparations that involves heating and cooling steps are required to prepare the aggregates, and the magnitude of induced CD is modest. More easily operative and sensitive systems are required for real applications in determining ee of asymmetric reaction products.

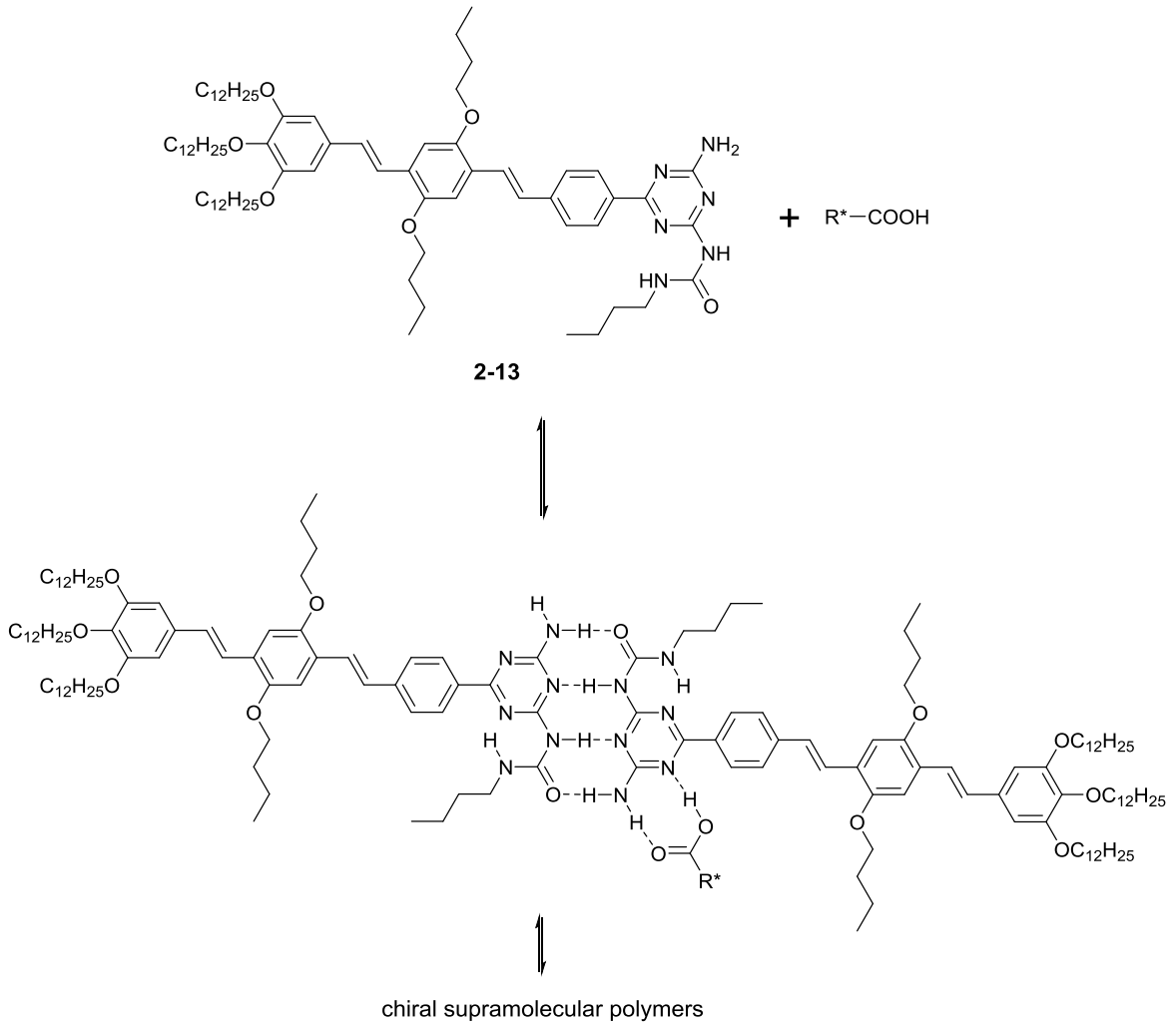

Figure 2.8 Formation of chiral supramolecular polymers by achiral precursor **2-13** and a chiral acid.

2.1.4 Scope and objectives of this chapter

To develop simple chirality sensing protocols for sensitive and interference-free *ee* determination, this chapter reported the use of the supramolecular chirality of helical stacks generated from aggregation of π-conjugated dyes in solution rather than using conformational chirality from a small molecule host-guest complex.[55-56] The phenomena of nonracemic chiral guest-directed

formation of optically active aggregates from achiral building blocks[58-60, 63, 69] have been well documented, but their potential analytical applications remain largely unexplored,[68] most likely due to the time-consuming and cumbersome process of preparing aggregates. Reported here is a simple and effective chirality sensing protocol by helical aggregates formed instantly after mixing achiral sensors and chiral analytes. It was envisioned that helical chirality from dye aggregates would allow chirality sensors to be designed as simply as attaching an analyte-binding site to an achiral dye capable of supramolecular polymerization. Perylenebismide dyes appear well suited as the dye component, by virtue of their capacity for efficient π-stacking and formation of columnar aggregates with a rotational offset,[70] allowing easy generation of supramolecular chirality.[71-72] As a proof of principle investigation, the boronic acid group[4] was chosen that rapidly and reversibly binds α-hydroxy carboxylates[73-75] (Figure 2.9) which are of biomedical interest.[76-78] The chirality sensors designed herein, **C1** and **C2** feature a perylenebismide (PBI) core and boronic acid moieties to attached to its periphery. The self-assembly involving aggregation of the PBI core and the binding of nonracemic α-hydroxy carboxylate guests to the periphery of the aggregates is expected to produce nonracemic helical PBI aggregates as a result of steric interactions due to compact intermolecular packing of the dyes (Figure 2.10), showing induced CD signals in the PBI absorption. The chapter reports the use of **C1** and **C2** for *ee* determination and differentiation of structurally diverse α-hydroxy carboxylates (Figure 2.11). The protocol uses simple sensor molecules to achieve *in situ* CD measurements of the chiral analyte, and could be potentially applied to other classes of compounds by attaching other binding sites to the PBI framework.

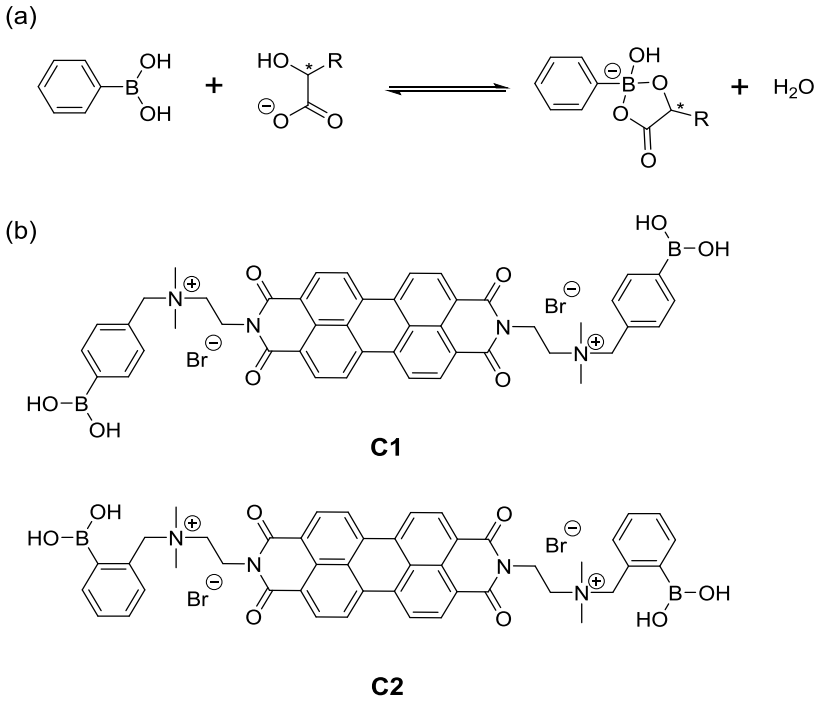

Figure 2.9 (a) Interaction of boronic acid with α-hydroxy carboxylate at pH below p*K*a of boronic acid. (b) Structures of chirality sensors **C1** and **C2**.

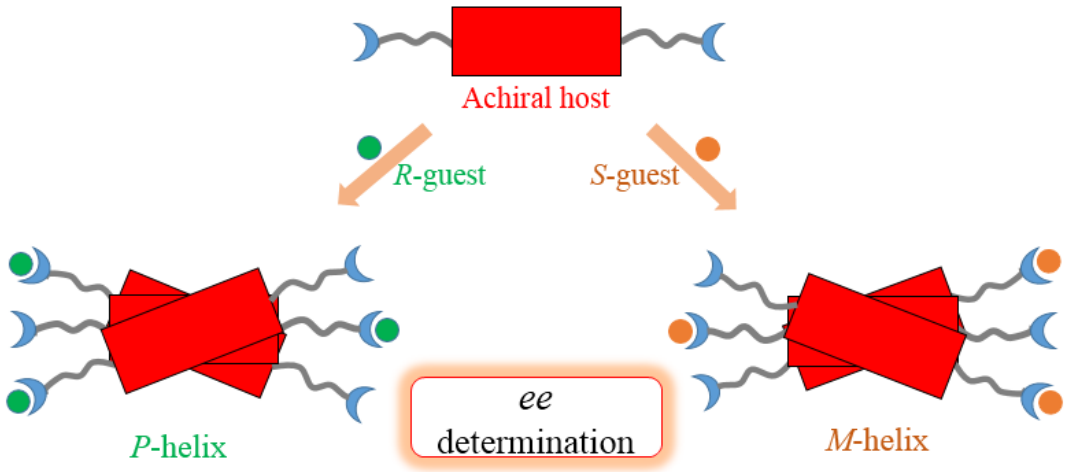

Figure 2.10 Cartoon representation of chirality sensing of chiral guests by an achiral host that forms chiral aggregates with chiral guests.

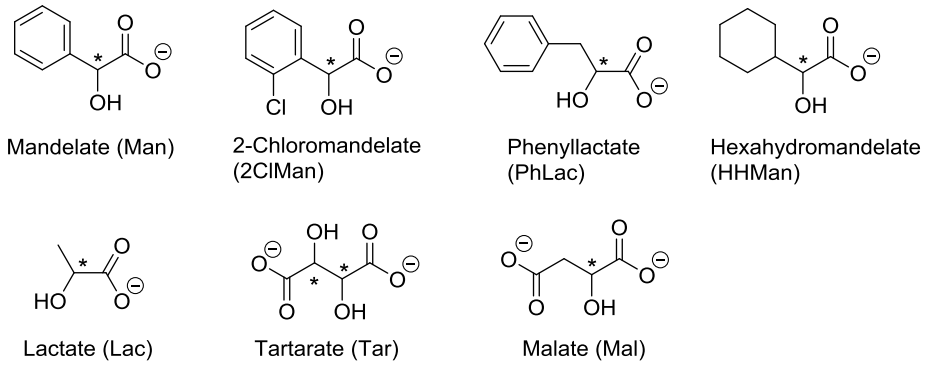

Figure 2.11 Structures of the tested α-hydroxy carboxylate analytes.

2.2 Results and discussion

2.2.1 Interaction with mandelic acids

Achiral sensors **C1** and **C2** are structurally related compounds differing only at the position of boronic acid group substituted at the terminal phenyl group (Figure 2.9). They were readily obtained via imide coupling of *N*,*N*-dimethylethylenediamine with perylene tetracarboxylic dianhydride followed by treating with bromomethylphenylboronic acids (Section 7.1.2, Chapter 7). Sensors **C1** and **C2** were found to exist dominantly as *H*-aggregates at 50 μM in water, as judged from the higher intensity of the 0-1 band (500 nm, $\varepsilon = 3.7 \times 10^4$ M^{-1} cm^{-2}) compared to that of the 0-0 band (542 nm, $\varepsilon = 1.9 \times 10^4$ M^{-1} cm^{-2}) (Figure 2.12b).[71-72] The dominant species are dimers or oligomers because (i) the shapes and molecular extinction coefficients of the absorption spectra were similar to the reported PBI dimers[79-82]; (2) the aggregates are too small for size determination by dynamic light scattering (DLS) techniques. The aggregates were CD silent as expected due to the achiral character of the building blocks **C1** and **C2**. For a rapid chirality induction by chiral analyte, the sensor-analyte aggregates were prepared by injecting a small volume of methanol solutions of the sensor to an aqueous solution of chiral analyte. In the presence of Man, a typical α-hydroxy carboxylate (Figure 2.11), the solution of **C1** now exhibits a bisignate Cotton effect crossing zero at 500 nm, the maximum absorption wavelength of the aggregated perylene chromophore (Figure 2.12a), clearly indicating exciton coupling of the rotationally displaced perylene chromophores.[83] These observations indicate a preferred helical arrangement of the aggregates of **C1**. Mirror-image CD spectra were observed from solutions of **1** with *R*- and *S*-Man (Figure 2.12a). The CD signal reaches its maximum value at Man concentration of 1.0 mM and decreases at higher Man concentration (Figure 2.13a), which is likely the result of variations in the size of the aggregates since the shape of the CD spectrum remains unchanged.

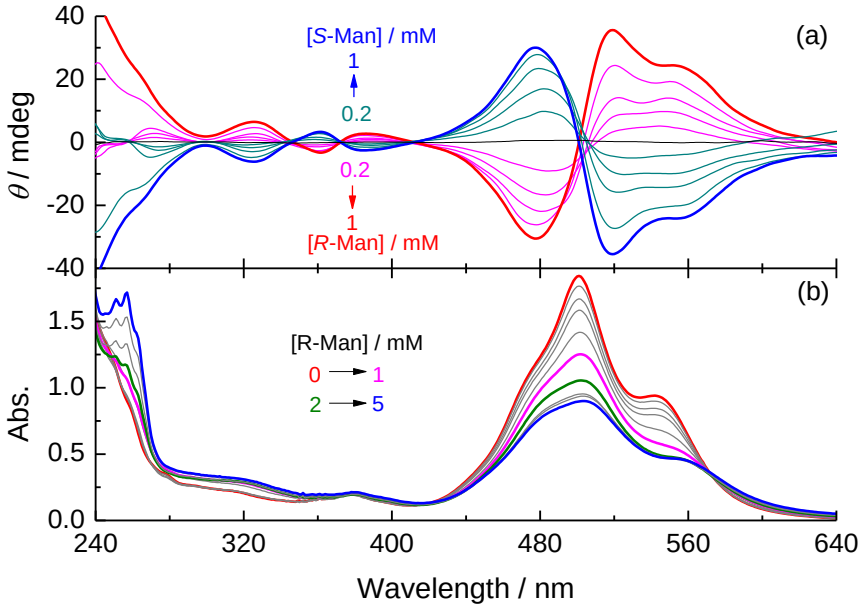

Figure 2.12 Absorption (a) and CD (b) spectra of **C1** (50 μM) in the presence of *R*-Man (solid line) or *S*-Man (dash line) of increasing concentration in 50 mM pH 5.0 acetate buffer containing 2.5% (vol %) MeOH.

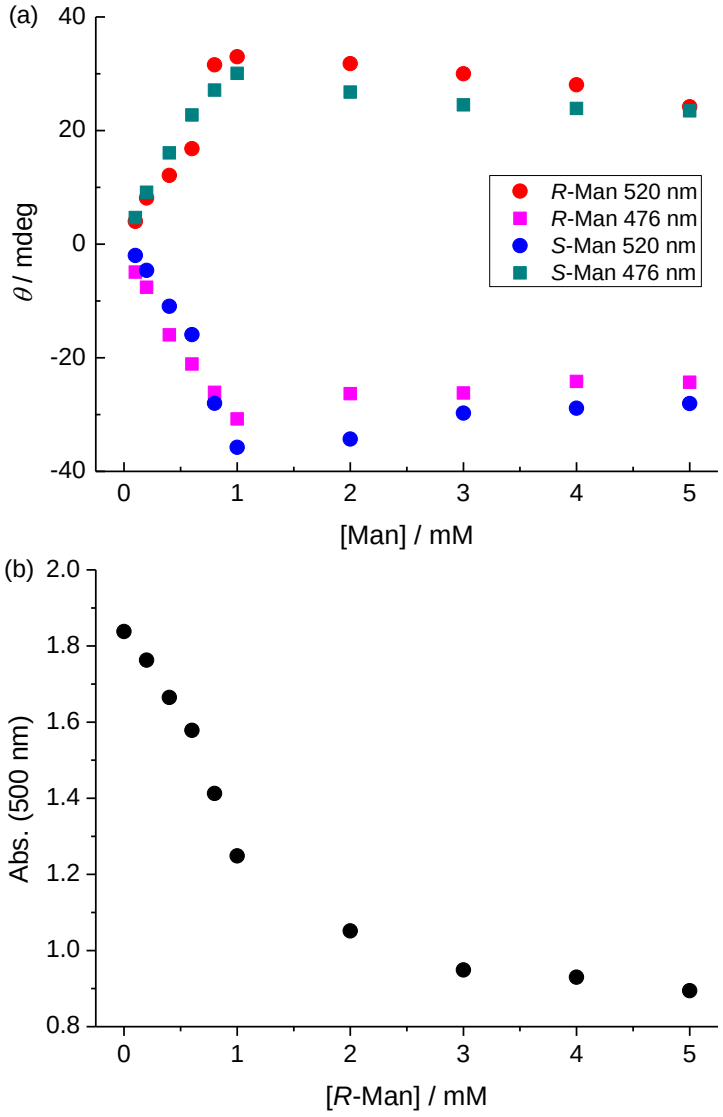

Figure 2.13 CD intensities at 520 nm and 476 nm (a) and absorbance at 500 nm (b) of **C1** (50 μM) against concentration of *R*- or *S*-Man in pH 5.0 acetate buffer containing 2.5% (vol%) MeOH.

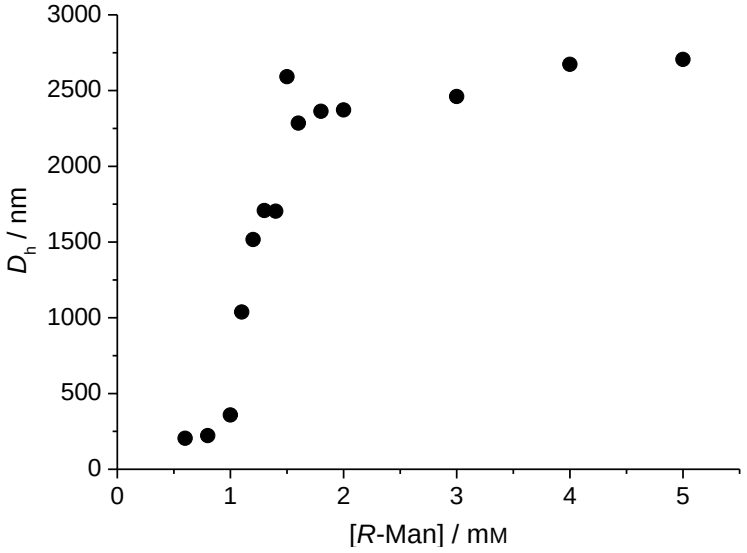

Figure 2.14 Average hydrodynamic diameter (D_h) of aggregates of **C1** (50 μM) versus concentration of *R*-Man in pH 5.0 acetate buffer containing 2.5% (vol%) MeOH. D_h was measured by dynamic light scattering.

The hypothesis was confirmed by the absorption spectra and dynamic light scattering (DLS) data. Addition of Man led to a decrease in the absorption of **C1**, suggesting a higher degree of aggregation.[84] In agreement with the absorption spectra, DLS data show an increase of the average hydrodynamic diameter (D_h) from 204 nm to 2706 nm with [Man] from 0.6 mM to 5 mM (Figure 2.14), while the aggregate size with lower Man concentrations was too small to be accurately determined by DLS methods. The sigmoidal profile of the D_h dependence on [Man] is likely due to the stepwise binding of Man, forming 1 : 1 and 1 : 2 (**C1** to Man) complexes. The observed aggregation of **C1** by Man can be rationalized as free bis-cationic **C1** becoming mono-cationic and mono-zwitterionic (1 : 1 **C1**-Man complex), or bis-zwitterionic (1 : 2 **C1**-Man complex) upon binding of Man, reducing intermolecular repulsions. It should be pointed out that the chiral induction process is indeed rapid. Injection of a methanol solution of **C1** into an aqueous solution of Man produces a stable CD spectrum instantly and remains unchanged for over a 1 h time period, except for a minor increase in the 1st Cotton effect (Figure 7.5, Chapter 7). The fact that 2-phenylpropionic acid, a structural analogue to Man with the hydroxy group replaced by a methyl group, failed in chirality induction and led to much weaker changes in the absorption spectra (Figure 7.6, Chapter 7) indicated that the successful chirality induction by Man is due to the boronic acid binding instead of binding of the quaternary ammonium group by ionic interactions. With the **C2**-Man complex, similar absorption and CD titration profiles were observed (Figure 7.7, Chapter 7) and interestingly, an opposite helical sense was observed in the presence of the same Man enantiomer when the position of the boronic acid substitution in the building block is changed.

2.2.2 Chirality induction by other α-hydroxy carboxylates

To test the scope for chirality sensing of α-hydroxy carboxylates, the CD responses of **C1** and **C2** toward six other analytes covering a wide structural diversity (Figure 2.11) were examined. In all cases, mirror-imaged CD spectra were observed for the *R*- and *S*-enantiomers (Section 7.1.7, Chapter 7), indicating the reliability of the CD signals. As shown in Figure 3, exciton coupled CD spectra were observed for all analytes, with the exception of Mal-**C1** where only weak monosignate CD was observed at high Mal concentrations (Figure 7.19, Chapter 7). Although in some cases (*e.g.* **C1** with Lac and Mal) the CD signal is not strong enough for accurate *ee* determination, by employing two sensors **C1** and **C2**, all the analytes generate CD signals of sufficient strength with one of the two sensors (the weakest being 2-chloroMan with a Δε value of ~15 mdeg). Small guest molecules have traditionally presented a challenge to both chiral discrimination and induction approaches; this protocol operates well with both large and small analytes.

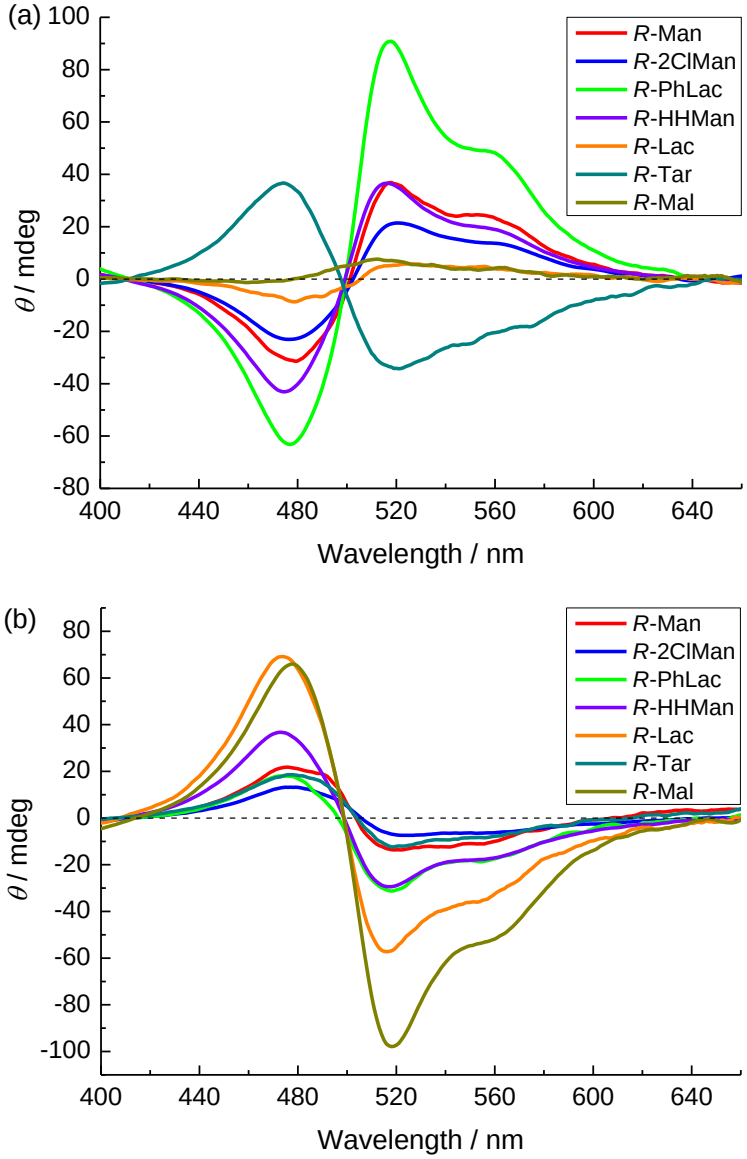

Figure 2.15 CD spectra of **C1** (50 μM, a) and **C2** (50 μM, b) in the presence of *R*-Man, *R*-2ClMan, *R*-PhLac, *R*-HHMan, *R*-Lac, *R*-Tar and *R*-Mal in pH 5.0 acetate buffer containing 2.5% (vol%) MeOH. Analyte concentrations are shown in Table 2.1.

Table 2.1 Concentration of α-hydroxy carboxylate unit that gives the largest excition-coupled CD (CD) signals for **C1** or **C2**.

Sensor	Concentration at maximum CD						
	Man	2-ClMan	PhLac	HHMan	Lac	Tar	Mal
C1	1.0 mM	1.0 mM	1.0 mM	2.0 mM	20 mM	60 μM	20 mM [a]
C2	2.0 mM	2.0 mM	1.0 mM	2.0 mM	20 mM	60 μM	0.3 mM

[a] **C1**-Mal aggregate shows only monosignate CD signal. This value cannot be compared to other values obtained when bisignate exciton-coupled CD signals were observed.

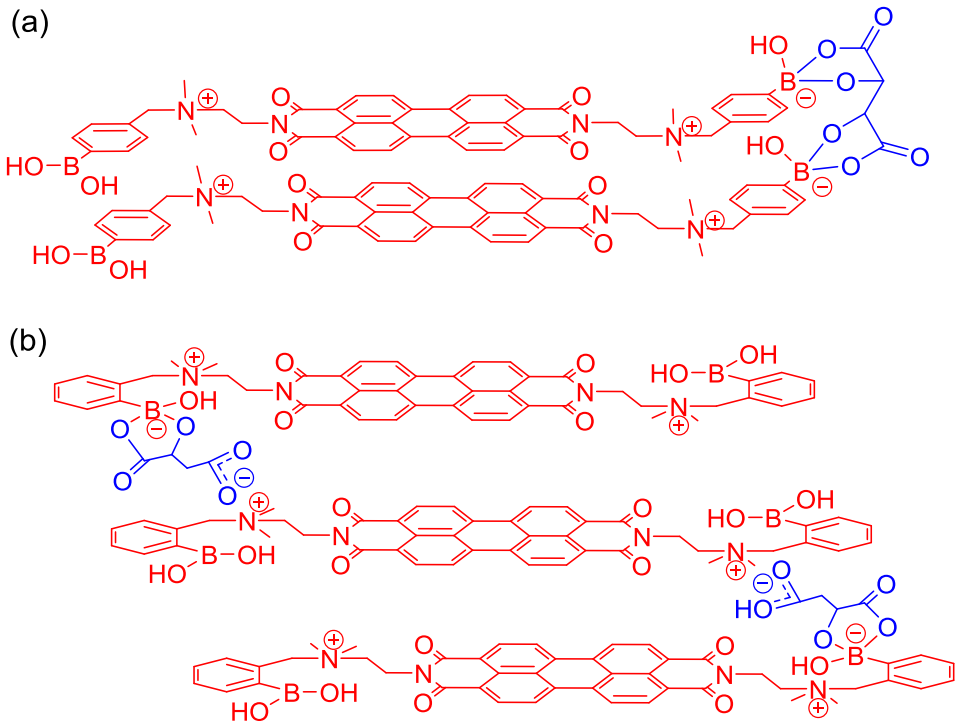

Figure 2.16 Proposed structures for the 2 : 1 **C1**-Tar (a) and the 3 : 2 **C2**-Mal complex (b)

Different α-hydroxyl carboxylate analytes were found to display different affinity for boronic acid sensors **C1** and **C2**, depending on the analyte lipophilicity and whether additional interactions are present. The affinity was evaluated by the concentration of α-hydroxyl carboxylate unit at which the CD signal reaches a maximum value (Table 2.1). Tar which contains two α-hydroxyl carboxylate units shows the highest affinity for both sensors, which allows for the stoichiometry to be determined using a Job plot (Figures 7.21 and 7.22, Chapter 7), giving a sensor (**C1** or **C2**) to tartrate stoichiometry of 2 : 1, or a sensor to α-hydroxyl carboxylate unit stoichiometry of 1 : 1 (Figure 2.16a). The highest affinity for Tar is the result of multivalent binding[85] between the divalent tartarate and the aggregate that can be regarded as a multivalent receptor for divalent tartarate.[86], An interesting inversion of the sign of the CD signal was observed for **C1** with higher concentration of Tar (Figure 7.17, Chapter 7). Since the 2 : 1 **C1**-Tar complex shows the opposite CD sign to that observed at high tartrate concentrations, as evidenced by the Job plot, the switch of the CD sign can be unambiguously ascribed to the binding of the other boronic acid group in **C1** to Tar.

Mal which contains a carboxylate group in addition to the α-hydroxy carboxylate unit shows a substantially higher affinity than other mono-α-hydroxy carboxylate analytes for **C2**, which can be ascribed to additional stabilization of the complex by the electrostatic interaction between the anionic carboxylate group and the cationic perylene sensor (Figure 2.16b). This has been supported by the 3 : 2 stoichiometry revealed by a Job plot study (Figure 7.23). For other monovalent analytes, while Man, 2-ClMan, PhLac and HHMan show similar affinity for the sensors, with maximum CD observed at a guest concentration of 1 – 2 mM, much weaker binding was observed for lactate which gave a maximum in the CD at 20 mM. It is likely that the binding of Man, 2-ClMan, PhLac and HHMan is also driven by hydrophobic interactions between the large hydrocarbon units of the two bound analyte molecules within the same aggregate.

2.2.3 Applicability to ee determination

CD-*ee* curves were prepared for each analyte from the optimal sensor at the optimal analyte concentration (see Figure 2.17 for the **C1**-Man complex as an example, for other analytes see Section 7.1.9 in Chapter 7). Since different analytes show different affinities for the sensors, the analyte concentrations reported for the CD-*ee* curves are therefore not the same for different analytes. The "majority-rules" have been observed in supramolecular polymers,[50-52] in which a small *ee* produces a non-proportionally large CD signal. This effect was absent in the current system. In most cases reported here, a linear CD response to *ee* was observed (*e.g.* Figure 2.17 for Man).

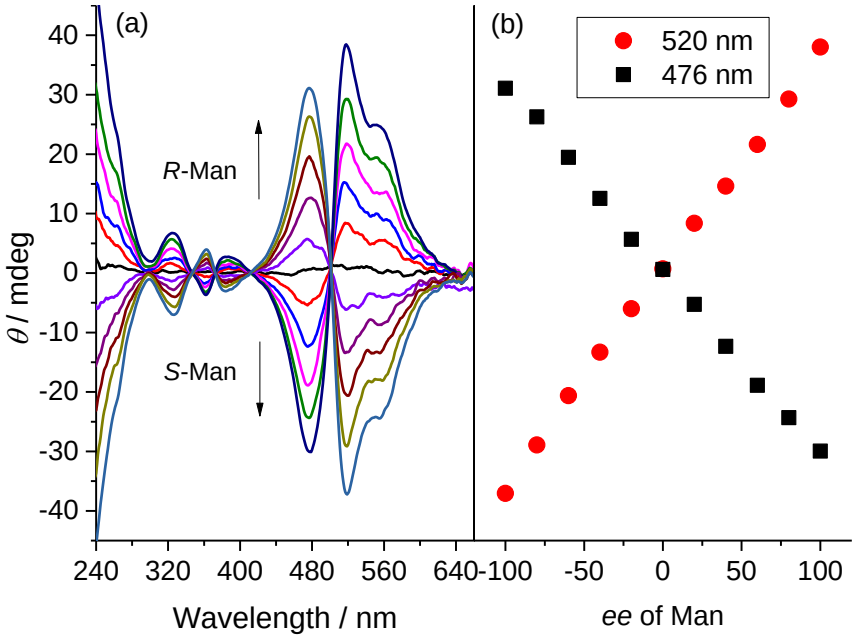

Figure 2.17 (a) CD spectra of **C1** (50 μM) in the presence of Man with different *ee*'s and (b) CD intensity of **C1** at 520 nm and 477 nm versus *ee* in pH 5.0 acetate buffer containing 2.5% (vol%) MeOH. [*R*-Man] + [*S*-Man] = 1.0 mM.

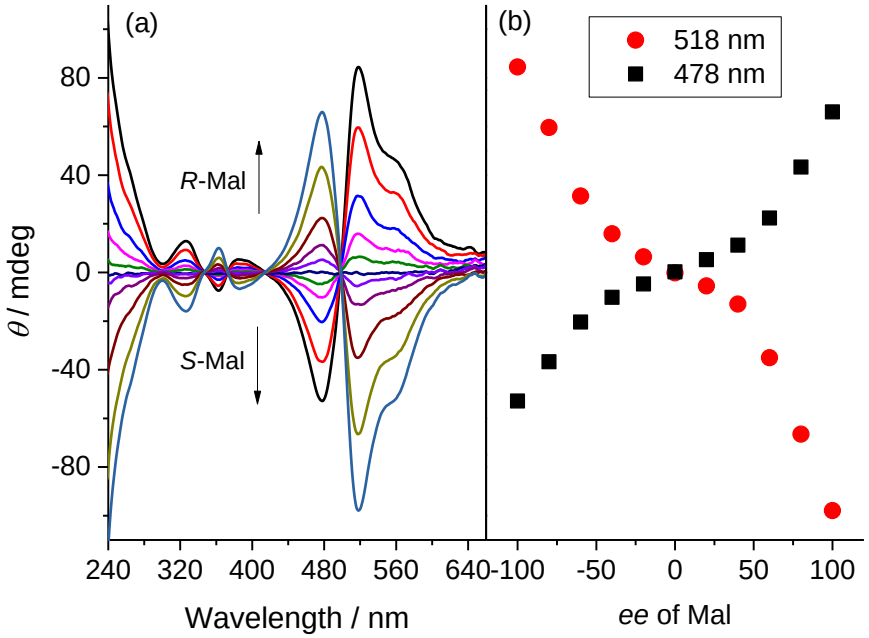

Figure 2.18 (a) CD spectra of **2** (50 μM) in the presence of Mal with different *ee*'s and (b) CD intensity of **C2** at 518 nm and 478 nm versus *ee* in pH 5.0 acetate buffer containing 2.5% (vol%) MeOH. [*R*-Mal] + [*S*-Mal] = 0.30 mM.

However, an interesting CD-*ee* profile was observed, which displays a steeper slope with high *ee* with the **C2**-Man assembly (Figure 2.18) and to a lesser extent the **C1**-PhLac assembly (Figure 7.25, Chapter 7). This means that a small *ee* produces an even weaker CD signal than a linear response, which is opposite to the "majority-rules". To the best of my knowledge, this is the first time that such an "anti-majority rules" effect has been observed in supramolecular polymers. To account for this unusual observation, the absorption spectra of sensors in the presence of analytes of the same concentration yet at varying *ee* for these two cases were examined. No significant *ee* dependence was observed (see Figure 7.29 for the **C1**-PhLac assembly and Figure 7.30 for the **C2**-Man assembly in Chapter 7), which precludes the possibility that the observed nonlinear relationship results from destabilization of the aggregates at low *ee*. Noticably in these two cases, the dependence of CD intensity on analyte concentration displays sigmoidal characteristics (see Figure 7.11 for the **C1**-PhLac assembly and Figure 7.20 for the **C2**-Man assembly in Chapter 7). Although the packing of two chiral-analyte bound dye monomers is sufficient to generate an exciton-coupled CD spectra, the non-linearly higher CD signal at higher analyte concentrations could possibly suggest that the consecutive packing of many enantiopure analyte-bound dye monomers produces a higher averaged CD signal than the packing of fewer chiral-analyte bound dye monomers alone. Thus, random insertion of a dye monomer bound to the minor enantiomer would disrupt the consecutive packing of several dye monomers bound to the dominant enantiomer, weakening the CD signal in a non-linear manner, which would account for the observed anti-majority-rules. To provide further support for this hypothesis, the CD-*ee* relationship at lower analyte concentrations were examined. Since at lower analyte

concentrations, there is less chance for consecutive packing of chiral analyte-bound dye monomers, the "anti-majority-rules" effect should disappear or be weakened, according to this hypothesis. In both cases where "counter majority-rules" were observed, decreasing the analyte concentration did restore the normal linear CD-*ee* relationship (Figures 7.31 and 7.32, Chapter 7). Although the "counter majority-rules" effect has not yet been well understood, the nonlinear CD dependence on *ee* which displays a larger change in the high *ee* region is, however, preferred for sensing *ee* close to 100% which is of greater practical importance in asymmetric synthesis.

To examine the applicability of this system for the screening of organic reactions, when various species coexist with the product and may interfere with the CD measurements, CD spectra of **C1**-Man were recorded in the presence of a variety of common chiral compounds, including a chiral amine, a chiral amino alcohol, a chiral carboxylate and a chiral amino acid. The results indicate that, even when the potential interfering species is present at the same concentration as Man, the interference with the CD response is rather small (< 5.6%) (Figure 7.33, Chapter 7). Therefore, this protocol is selective for α-hydroxy carboxylates and any impurities present are unlikely to interfere with *ee* sensing of α-hydroxy carboxylate products. However, when these interfering species coexist with the chiral compound of interest even in trace amounts, *ee* determination by optical rotation is not possible. Conventional optical rotation measurements require a large amount of sample and are highly susceptible to impurities,[87] and therefore are not suitable for screening reaction products. It was also shown that the chirality induction is operational in methanol as well (Figure 7.34), rendering the current protocol suitable for water-insoluble chiral analytes.

Table 2.2 *ee* determination of seven α-hydroxy carboxylate anaytes of known concentration and comparison of the calculated *ee*'s with actual values

Entry	Guest	Concentration	Sensor used	Actual *ee* / %	Cal.*ee* / %	Absolute Error / %
1	Tar	30 μM	**C1**	10.0	11.6	1.6
2	Lac	20 mM	**C2**	-30.0	-33.7	-3.7
3	Man	1.0 mM	**C1**	50.0	46.5	-3.5
4	2ClMan	1.0 mM	**C1**	-70.0	-67.1	2.9
5	PhLac	1.0 mM	**C1**	80.0	79.4	0.6
6	Mal	0.3 mM	**C2**	-90.0	-90.6	-0.6
7	HHMan	2.0 mM	**C1**	96.0	95.0	-1.0

A series of samples of "unknown" *ee* and known concentration were prepared and subject to analysis by the present protocol. In the cases of linear CD-*ee* relationship, the *ee* of the "unknown" sample was calculated by comparing its CD intensity with that of a sample with 100% *ee*. In the cases where the CD signal varies non-linearly with *ee*, the "unknown" *ee* was calculated by linear

interpolation from the CD-*ee* plot. The calculated *ee*'s were compared to the actual values (Table 2.2), and an average absolute error of ±2.0% was found, which is within the range of acceptable error for HTS in asymmetric synthesis.[88]

Table 2.3 Comparison of actual concentration and *ee* of four Man samples with the concentrations and *ee* values calculated from respective absorption and CD spectral responses of **C1** to Man.

Entry	Actual Conc. / mM	Actual *ee* / %	Cal. Conc. / mM	Cal. *ee* / %	Absolute Error (*ee*) / %
1	0.55	63.6	0.50	63.9	0.3
2	0.65	-69.2	0.61	-67.8	1.4
3	0.75	-84.6	0.73	-80.6	4.0
4	0.85	94.1	0.85	91.2	-2.9

The decrease of the CD signals at high analyte concentrations appears a limitation, making the knowledge of analyte concentration necessary, since saturation of the CD spectra may not be reached (Figure 2.13a). However, the analyte-induced absorption quenching of the peryleneboronic acid sensor due to increased extents of aggregation (Figure 2.12b) allows the determination of the analyte concentration, overcoming that limitation (Figure. 2.13b). The results for simultaneous determination of concentration and *ee* are presented in Table 2, showing a satisfactory average absolute error of ±2.1% for *ee* determination.

2.2.4 Linear discriminant analysis

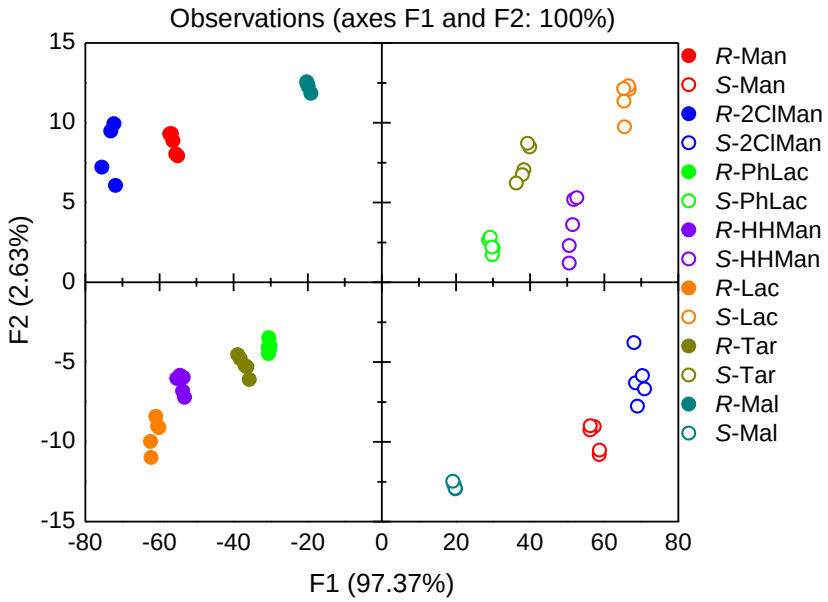

Figure 2.19 LDA plot created from CD responses of **C1** and **C2** to 14 α-hydroxy carboxylates.

Besides *ee* and concentration determination, this protocol is also suitable for chemo-differentiation of α-hydroxy carboxylates using linear discriminant analysis (LDA)[22], as different analytes generate different CD shapes (Figure 2.15). The ratio of the CD intensity at 475 nm to the

absolute value of CD intensity at 520 nm was analyzed for a total of 14 analytes, with each analyte tested at five concentrations (1 mM, 2 mM, 3 mM, 4 mM and 5 mM). The two-dimensional LDA plot is shown in Figure 2.19. Similar to reported assignments,[32, 34] the greatest axis of differentiation F1 indicates the chirality of the analyte while the second axis F2 arises from the shape of the CD spectrum. Figure 2.19 confirms that the data points for different analytes are well-separated. Jackknife analysis that classifies a data point based on functions created from the other four data points gives a 100% correct assignment, justifying the reliability of the current protocol in chemo-differentiation of α-hydroxy carboxylates.

2.3 Conclusions

In summary, a novel CD protocol has been established for chirality sensing of chiral analytes bearing no chromophore, and which does not require the creation of conformational chirality in a single host-guest complex. This approach employs analyte-directed chiral aggregation of achiral PBI dyes which contain binding sites for the analyte. The analyte-sensor interaction can in principle be covalent or non-covalent. A proof-of-principle assay was demonstrated with two structurally related boronic acid-conjugated achiral PBI sensors, capable of the *ee* determination of α-hydroxy carboxylates. Sufficiently strong CD signals can be observed at the perylene absorption region of around 500 nm, immediately after mixing the sensor with solutions of seven structurally diverse α-hydroxy carboxylates. Diastereoselective aggregation of the sensor-analyte complex was shown to be responsible. Determination of a series of "unknown" *ee* produces average absolute errors of ±2.0% and ±2.1% for samples of known and unknown concentrations, respectively. The different shapes of the CD spectra of the sensor molecules observed in the presence of different analytes allows the identification of the α-hydroxy carboxylates using linear discriminant analysis. Compared with currently available chirality sensors, the protocol exhibits many advantages such as: not requiring analyte derivatization, simplicity of host design and synthesis, and applicability to structurally diverse analytes. The system is also environmentally benign by using water as a "green" solvent. It was expectd that this protocol will be generally applicable to chiral analytes that bear a stereocenter either close or remote to the binding site.

Chapter 3: Aqueous Fluoride Sensing by Induced Aggregation of a Boronic Acid-Catechol Ensemble

3.1 Introduction

3.1.1 Development of molecular receptors and sensors for fluoride ion

The development of supramolecular optical sensors capable of rapidly detecting aqueous fluoride ions[89] has received considerable attention due to the toxicity of fluoride ions, which can cause dental and skeletal fluorosis. Binding of aqueous fluoride, however, has always been challenging because of the high hydration enthalpy of fluoride ion.[90] Therefore, very few examples have been developed for sensing aqueous fluoride at ppm levels which is required for drinking water quality control. Sensors selective for binding or reacting with fluoride[91] have been designed *via* several types of non-covalent, dynamic covalent or irreversible covalent interactions as outlined below.

Hydrogen bonding

Fluoride is a strong hydrogen bond accepter due to its high charge density. It is therefore not surprising that hydrogen bond donors make up the majority of fluoride receptors and sensors in the literature. However, most of the hydrogen bond receptors function only in organic solvents. Very few receptors are capable of fluoride binding in the highly competitive water medium via relatively weak (compared to metal coordination) hydrogen bonds. To achieve this challenging goal, Steed and coworkers have resorted to using multi-cationic receptors to strengthen fluoride binding by additional Coulombic attraction, which is a common strategy in general to achieve anion binding in water.[92] Macrobicyclic cage **3-1** in its hexa-protonated state shows a very strong affinity for fluoride in water with a 1:1 binding constant as high as $10^{9.54}$ M^{-1}, while the fluoride affinity is still remarkable in its tri-protonated form ($10^{4.89}$ M^{-1}). A significant F^-/Cl^- selectivity was found. The higher fluoride affinity was attributed to the highly preorganised structure enabling fluoride binding via three N–H and three C–H hydrogen bonds.

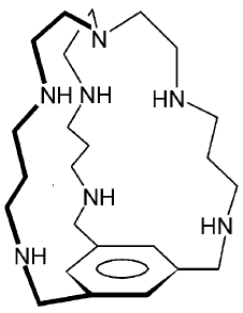

3-1

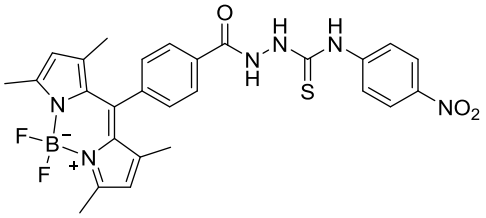

3-2

Recently, Rurack and coworkers reported a rare example of hydrogen bond receptors that allows optical sensing of fluoride in an organic aqueous media with 50% water content.[93] **3-2** contains a amidothiourea anion binding motif attached to a BODIPY dye as a spectroscopic reporter. A nitro group was attached to enhance the anion affinity. In 1:1 DMSO/H_2O, **3-2** displays a selective fluorescence quenching response to fluoride with a binding constant of 5.35×10^4 M^{-1}. The high fluoride affinity in such a highly competitive media is quite surprising, considering the simplicity of the receptor structure. This can be explained by the extreme electron deficiency of the thiourea moiety of **3-2** compared with other structurally related literature examples, as revealed by computational analysis. The fluorescence quenching was attributed to photo-induced electron transfer from the F^- bound receptor to the BODIPY fluorophore. Detection of fluoride in 100% water can be achieved by a test-strip assay, with sensitivity down to 0.2 ppm. This work highlights the possibility that without designing structural complicated preorganised receptors, noncovalent binding of fluoride in water can be achieved by using highly electron deficient hydrogen bond donors.

Anion–π interaction

Guha and Saha have demonstrated sensitive colourimetric fluoride sensing in aqueous organic solvents by employing anion−π interactions.[94] Electron-deficient naphthalene diimide (NDI)-based receptors **3-3**, **3-4**, and **3-5** were found to bind fluoride via anion-π interactions and underwent subsequent F^-→NDI charge transfer to generate orange coloured $NDI^{\bullet-}$ radical anions, evidenced by UV-Vis absorption and electron paramagnetic resonance (EPR) spectroscopic studies. With higher concentration of fluoride, the $NDI^{\bullet-}$ anions further reduced to NDI^{2-} dianions giving a pink colour. Other halides and oxoanions tested were unable to induce the colour change, which was ascribed to weak binding, larger size or orbital mismatch. These NDI receptors can form NDI/F^-/NDI sandwich complexes, with preorganised receptors **3-4** and **3-5** showing nanomolar fluoride sensitivity in 85:15 DMSO/H_2O.

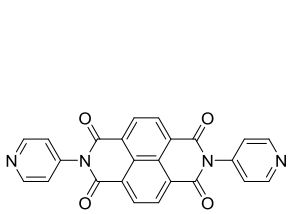

3-3

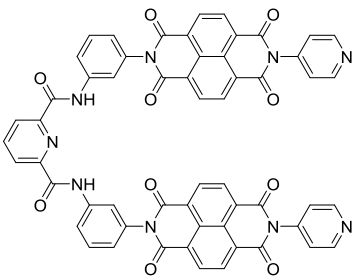

3-4

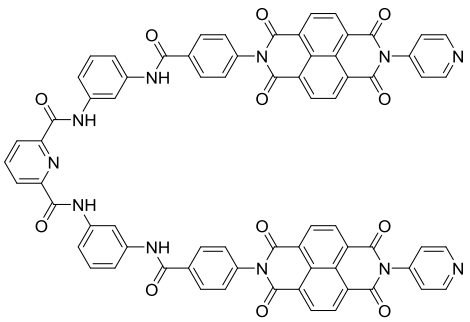

3-5

Metal coordination

The use of strongly Lewis acidic metal centres has been the most frequently employed approach to fluoride binding and sensing in water. Alternatively, organoboron compounds can be used as Lewis acids, which is discussed in Section 3.1.2. For example, cationic antimony(V) receptor **3-6** has a high fluoride binding constant of 1.2 x 10^4 M^{-1} in 9:1 H_2O-DMSO at pH 4.8 (with 10 mM CTAB to solubilize the **3-6**·F^- complex).[95] The formation of the **3-6**·F^- complex generates a fluorescence "turn-on" response as a result of decrease of nonradiative decay rate of the anthracene fluorophore. For Lewis acid-based receptors, hydroxide binding is a competing process in water. **3-6** has a pK_a of 7.1, allowing fluoride sensing under acidic conditions. Binding aqueous fluoride using neutral metal-based receptors is more challenging than using cationic metal complexes such as **3-6**. This was recently achieved by Hirai and Gabbai. Neutral distiborane **3-7** binds fluoride with a binding constant of 700 M^{-1} in 19:1 H_2O-THF at pH 4.34. Crystal structure of the [**3-7**-μ_2-F]$^-$ complex was obtained, confirming binding of a fluoride ion to both Sb(V) centres. A monodentate control compound shows no fluoride binding in aqueous solutions, underscoring the importance of bidentate chelation in capturing aqueous fluoride using neutral Lewis acid receptors.

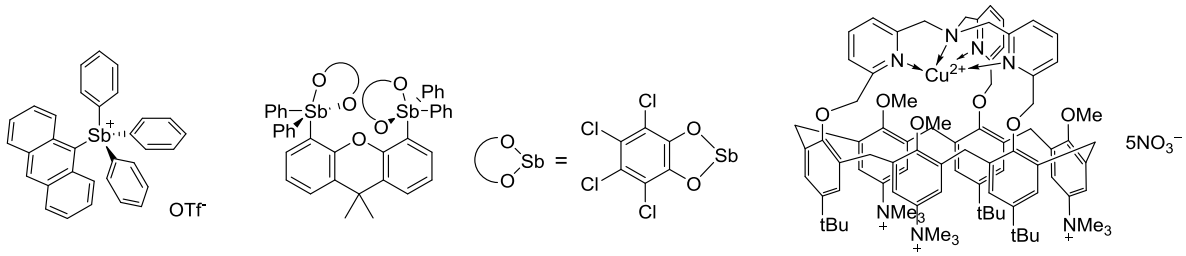

3-6 **3-7** **3-8**

Creating a hydrophobic microenvironment around the receptor binding site has been proved to be an effective strategy of enhancing anion binding affinity in water in several examples.[96] Recently, Brugnara and coworkers reported a Cu(II)-based fluoride receptor **3-8** that features embedding of the metal centre inside a hydrophobic calixarene cavity. In water at pH 5.9, **3-8** exhibits a strong fluoride affinity of 8.5 x 10^4 M^{-1}, with chloride binding 1000 times less efficient. Under the same condition, no fluoride binding was observed using the Cu^{2+}-free ligand in **3-8** or the Cu(II)-complex without the calixarene cavity or, highlighting the importance of a Lewis acid metal centre and a hydrophobic cavity. The crystal structure of **3-8**-F^- complex revealed that ability of the complex to accommodate a $CHCl_3$ molecule in the cavity, stabilised by a strong C–H···F^- hydrogen bond. It was proposed based on molecular modelling studies that a [F·H_2O·H_2O]$^-$ cluster was the actual guest species inside the cavity, which would be less energetically demanding than binding of a "naked" fluoride due to additional stabilisation by partial fluoride hydration and possible O–H···π between the entrapped water molecules and the aromatic walls.

Cleavage of organosilicon compounds

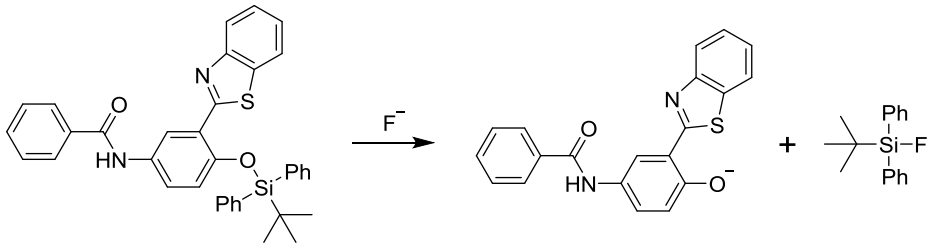

3-9

Figure 3.1 Fluoride-induced cleavage of silyl ether **3-9**.

As it remains challenging to develop fluoride receptors functioning via noncovalent interactions in aqueous solutions, sensors (or more accurately, "chemodosimeters") based on the fluoride-triggered cleavage of organosilicon have been developed that can well tolerate aqueous environments.[97] The reaction is fluoride-specific, allowing excellent fluoride selectivity without designing elaborated receptor structures. Major drawbacks are irreversibility and the long reaction times (typically 1-2 h) usually required. In 2010, Yang and coworkers developed organosilicon **3-9** (Figure 3.1) that shows UV-Vis absorption and fluorescence responses to fluoride at ppm concentrations in aqueous cetyltrimethylammonium bromide (CTAB) micellar solutions.[98] The response time was only ~200 s, a significant improvement compared to other fluoride sensors based on this reaction.

3.1.2 Organoboron compounds as fluoride receptors and sensors

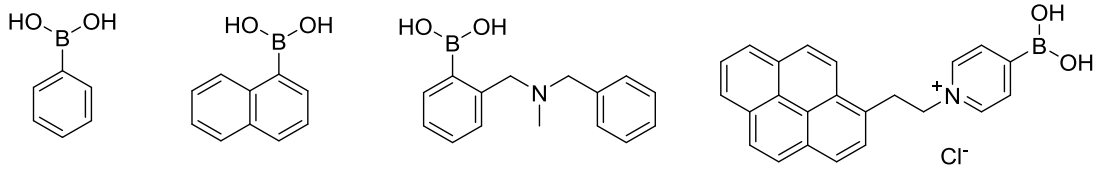

3-9 **3-10** **3-11** **3-12**

The selective and reversible binding of fluoride by boron centers renders organoboron compounds good candidates for developing fluoride sensors.[99] In a seminal work, James and coworkers studied fluoride sensing capacity of simple arylboronic acids **3-9**, **3-10** and **3-11**.[100] In 1:1 MeOH/H_2O at pH 5.5, these receptors show fluorescence quenching response upon binding of fluoride to convert the neutral trigonal boron centres to the tetrahedral, anionic forms. However, the fluoride affinity is too low for real applications. The strongest fluoride binder **3-11** in which the boron-fluoride adduct was assumed to be additionally stablized by hydrogen bonding and an ion pair, has a fluoride binding constant of 101 M^{-1}, allowing fluoride sensing only at millimolar concentrations. Later many boronic acids have developed for fluoride sensing, but there was no significant improvement in the sensitivity of aqueous fluoride sensing until in 2013 when **3-12** was

developed.[101] **3-12** binds fluoride via a 2:1 (**3-12** to fluoride) stoichiometry as confirmed by Job plots and mass spectrometry, the complex giving excimer emission from the stacked pyrene units. It was assumed that a B–F–B bridge in the complex induced the pyrene stacking. Sensing of aqueous fluoride at ppm concentrations was realised by a biphasic extraction, in which **3-12** partitions in a CH_2Cl_2 phase and captures fluoride from the aqueous phase. The high sensitivity likely benefits from the high acidity of the pyridiniumboronic acid moiety. However, before publication of the current work, no boronic acid-based fluoride sensor was developed that allows direct operation in the aqueous phase with ppm-sensitivity, which would not require the use of toxic organic solvents.

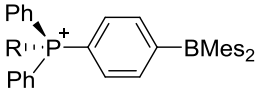

R = Me **3-13**
Et **3-14**
*n*Pr **3-15**
Ph **3-16**

Gabbai and coworkers have developed organoboranes fluoride receptors that are intrinsically more Lewis acidic than boronic acids.[102] Compounds **3-13**-**3-16** can bind fluoride in water, with Lewis acidity (affinity for hydroxide) and fluoride affinity following the order of **3-13** < **3-14** < **3-15** < **3-16**. The thermodynamic origin for this trend was unclear and the authors proposed that less favourable solvation of more hydrophobic boranes may be responsible. The strongest borane in the series **3-16** has a fluoride binding constant of 10^4 M^{-1}, allowing binding of aqueous fluoride at environmentally significant levels. Despite the high fluoride affinity of these organoboranes, they have not yet been functionalised with a spectroscopic reporter for sensing applications, possibly due to the instability of the borane moiety making sensor design challenging.

3.1.3 Scope and objectives of this chapter

Boronic acid receptors are attractive candidates for developing optical fluoride sensors as they are readily available, can be easily functionalised and offer the possibility of binding fluoride in aqueous solutions. However the sensitivity of sensing aqueous fluoride achieved in previously reported boronic acid-based sensors cannot meet the requirement for real applications. It was envisioned that the affinity of boronic acids for fluoride in aqueous solutions can be enhanced by (i) presence of a diol component to increase the Lewis acidity of the boron centre and (ii) stabilisation of the boronic acid-fluoride complex in supramolecular aggregates that can potentially provide a hydrophobic microenvironment. The chapter here reports a boronic acid based sensor for direct aqueous fluoride detection at ppm levels, employing fluoride binding induced diol binding and aggregation of an amphiphilic boronic acid. It has been reported that

formation of supramolecular aggregates could stabilize originally weak and water susceptible interactions such as imine-bond[103-104] and hydrogen bonding,[105] presumably due to a lower local concentration of water and a higher local concentration of the binding sites. It was therefore hypothesized that a boronic acid sensor that form aggregates upon binding fluoride ion could potentially enhance fluoride affinity and therefore the sensitivity for fluoride sensing. Combining this with cooperative fluoride and diol binding by a boronic acid, a highly sensitive boronic acid-based fluoride functioning in aqueous solutions may be expected. Amphiphilic boronic acid **F1**[106] (Figure 3.2) appears a suitable candidate as a fluoride sensor to test this hypothesis. **F1** is known to form excimer emissive supramolecular aggregates in its zwitterionic form, while exhibiting a low tendency to aggregate and only monomer fluorescence in its cationic form.[106] It was also envisioned that the presence of a diol component would further enhance the fluoride affinity, given the higher acidity of boronate esters than boronic acids.[107-108] In this context, an increase in the affinity towards hydroxide was expected, a common interference to fluoride sensing with boronic acid based receptors. It was therefore decided to carry out fluoride sensing under acidic conditions, under such conditions binding of hydroxide ion is not significant, while fluoride remains effective to form a boronic acid-diol-Lewis base ternary complex. Indeed, **F1** in combination with a carboxy-substituted catechol, protocatechuic acid (PCA), forms a highly selective and sensitive sensing ensemble for the direct sensing of fluoride at ppm levels in acidic aqueous solutions (Figure 3.2).

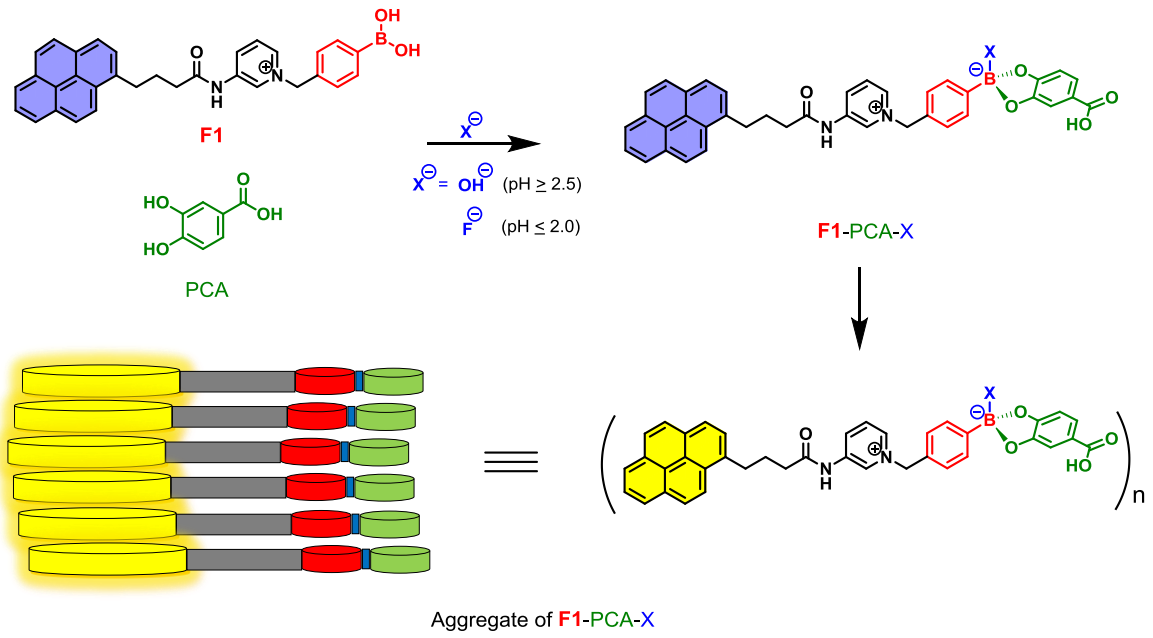

Figure 3.2 Schematic representation of fluoride sensing by **F1**-PCA ensemble.

3.2 Results and discussion

3.2.1 Binding and sensing of fluoride by the F1-PCA ensemble

In the absence of any diol at pH 2, **F1** is cationic and at 0.1 mM it exists dominantly in its monomeric form, since the absorbance of pyrene chromophore at 344 nm depends linearly on the concentration of **F1** up to 0.1 mM (Figure 7.35, Chapter 7). Indeed, at 0.1 mM **F1** only exhibits a very weak excimer emission at 500 – 600 nm along with the monomer fluorescence (Figure 3.3b). The presence of 5 mM PCA leads to a slight decrease in the absorbance of **F1** at 344 nm (0–0 vibronic band of S_0–S_1 transition) and a slightly elevated baseline (Figure 3.3a), indicating a slightly increased extent of aggregation.[109-110] Meanwhile, a more intense excimer emission was observed (Figure 3.3b), showing a positive correlation between excimer emission and the extent of aggregation of **F1**. Upon addition of fluoride ion, the excimer emission of **F1** in the presence of 5 mM PCA undergoes a dramatic enhancement, allowing sensing of fluoride in aqueous solutions at ppm concentrations (Figure 3.4). It was noted that the enhancement of the excimer emission was accompanied by an increase in solution turbidity (Figure 3.5), suggesting the formation of large colloidal particles. Hence, it was shown that fluoride ion binding to **F1**-PCA ensemble promotes the aggregation of **F1** as a zwitterionic complex.

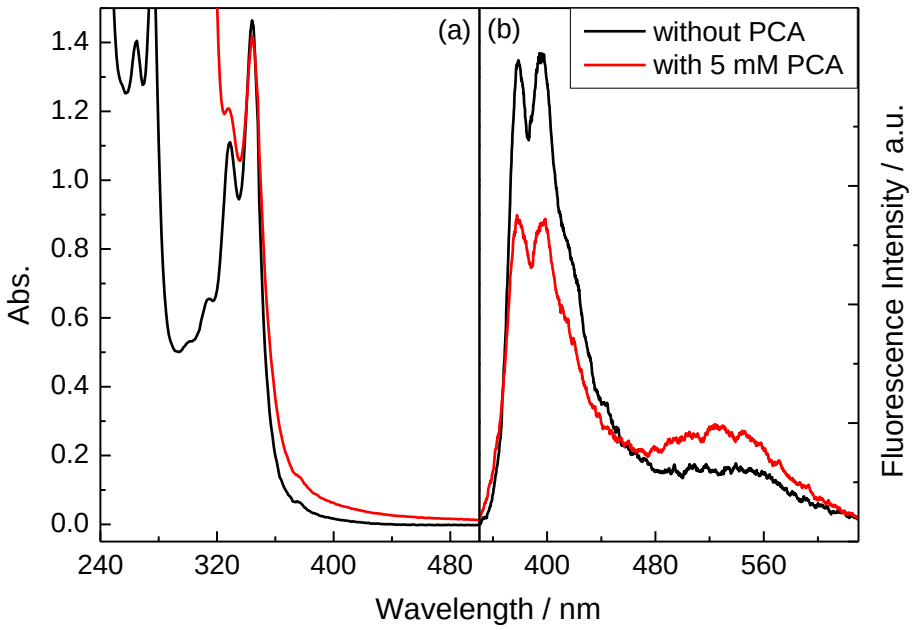

Figure 3.3 Absorption (a) and fluorescence spectra (b) of **F1** (0.1 mM) in the absence and presence of 5 mM PCA in default buffer. λ_{ex} = 328 nm.

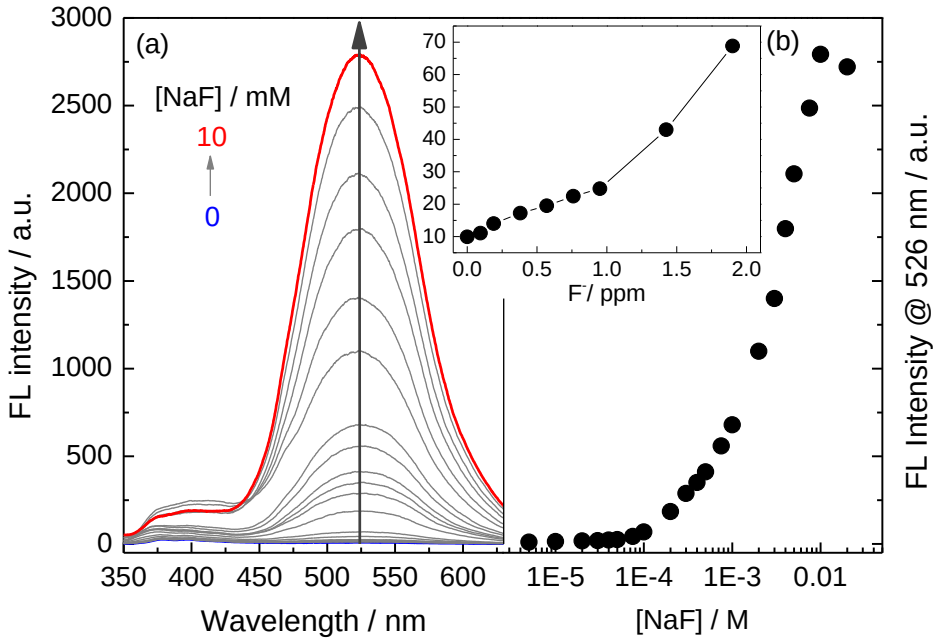

Figure 3.4 (a) Fluorescence spectra of **F1** (0.1 mM) in the presence of 5 mM PCA and NaF (0 – 10 mM) in pH 2.0 phosphate buffer containing 50 mM NaCl and 1.5% (vol%) methanol. (b) Fluorescence intensity at 526 nm vs NaF concentration. λ_{ex} = 328 nm.

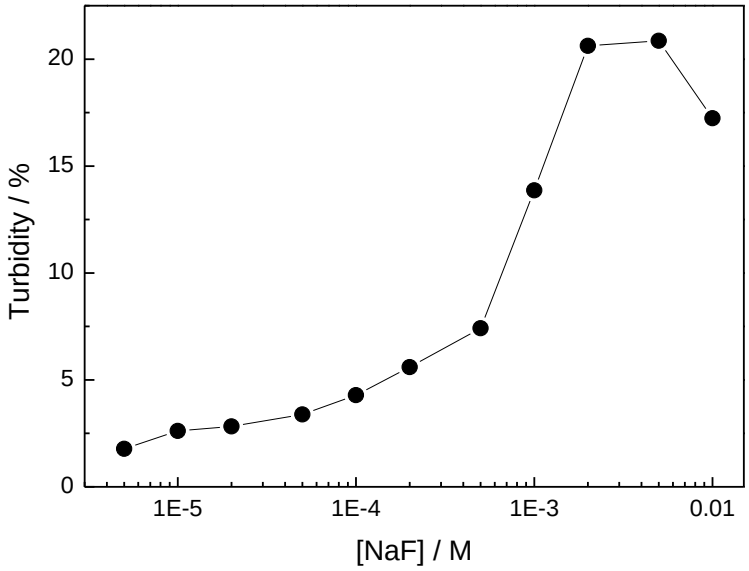

Figure 3.5 Turbidty of solution of **F1** (0.1 mM) and PCA (5 mM) with increasing concentration of NaF (0 – 10 mM) in default buffer.

3.2.2 Evidence of cooperative binding of fluoride and PCA

In the absence of PCA, strong excimer emission was also observed from **F1** upon fluoride binding. The titration plot shows a sigmoidal profile, and can be well fitted under a 1:3 stoichiometry (**F1** to fluoride), indicating formation of trifluoroboronate species (Figure 7.36, Chapter 7).[7c, 7e] The calculated fluoride binding constant of (3.0 ± 0.3) × 10^7 M^{-3} is more than three orders of magnitude higher than that of the phenylboronic acid determined in 50% MeOH/water buffered at pH 5.5.[7e] The fluoride affinity of **F1** was found to drop dramatically in the presence of

cetyltrimethylammonium bromide (CTAB) micelles that suppress aggregation of **F1** (Table 1). It's noticeable that with CTAB micelles, the fluoride affinity of **F1** increased in the presence of PCA, consistent with an increase of the Lewis acidity of the boron center. These results demonstrate that the formation of the PCA boronate ester and supramolecular aggregates strengthens the boron-fluoride interaction in aqueous solution.

Table 1 Apparent binding constants (K) of **F1** with fluoride under different conditions

	without CTAB			with 2mM CTAB	
[PCA] / mM	0	5	10	0	10
K / M^{-1}	310[a]	418	1363	36	192[b]

[a] The cubic root of the binding constant for the 1:3 **F1**-fluoride complex.
[b] Value of K_1 from a 1:2 (**F1** : fluoride) binding model (Figure 7.38, Chapter 7).

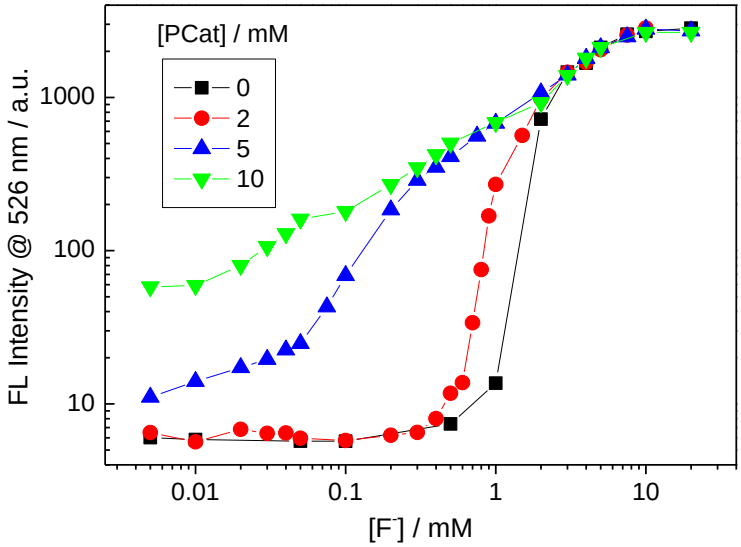

Figure 3.6 (a) Excimer fluorescence of **F1** (0.1 mM) at 526 nm versus fluoride concentration in the presence of PCA at different concentrations in default buffer. λ_{ex} = 328 nm. Note that both the horizontal and vertical axes are shown in logarithmic scale for a better view of the low NaF concentration region.

The presence of PCA leads to less sigmoidal response profiles. While the effect of PCA is more pronounced at low fluoride concentration, the excimer emission of **F1** displays no PCA dependence at fluoride concentrations higher than 3 mM (Figure 3.6). Attempts to fit the fluoride titration curves in the presence of PCA gave poor fitting for the data (Figures 7.39 and 7.40). Therefore, it was assumed that at high fluoride concentrations, the excess fluoride replaces PCA in the **F1**-PCA ensemble to form trifluoroboronate species. The apparent binding constants of **F1** for fluoride in the presence of PCA were then calculated using the data obtained at [F^-] < 1 mM (Figures 7.41 and 7.42), where fluoride alone is unable to induce excimer emission of **F1** in the absence of PCA, therefore, the excimer signal originates from the **F1**-PCA-fluoride ternary complex. The apparent binding constants obtained (Table 1) show dramatic increase with

increasing PCA concentration, confirming the role of PCA in enhancing the fluoride affinity of **F1** by formation of a boronate ester which is more Lewis acidic than the boronic acid.

The cooperative binding of PCA and fluoride to **F1** was additionally confirmed by the enhanced profile of excimer emission of **F1** with 1 mM NaF compared with just **F1** with increasing concentrations of PCA (Figure 3.7). Without NaF there is negligible interaction between **F1** and PCA with [PCA] ≤ 5 mM. In contrast, in the presence of fluoride, the titration curve almost levels off at PCA concentration of 5 mM, demonstrating that the **F1**-PCA interaction is significantly enhanced by fluoride.[111] Similar positive cooperativity was also observed for catechol (Figure 7.44, Chapter 7), but not for D-fructose and D-glucose (Figures 7.45 and 7.46, Chapter 7) which are also known to form boronate esters. This is likely due to hydrophilicity of fructose and glucose that inhibits supramolecular aggregation of the assembly. Note that PCA is a better diol component than catechol in promoting the assembly formation, likely due to stabilization of the aggregate by intermolecular hydrogen bonds between the adjacent carboxylic acid groups.

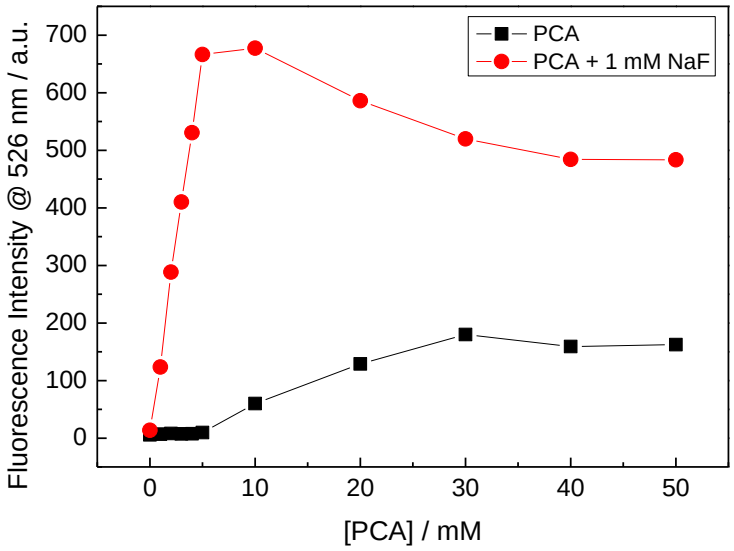

Figure 3.7 Fluorescence intensity of **F1** (0.1 mM) at 526 nm vs PCA concentration in the absence (black line) and presence (red line) of 1 mM NaF in default buffer.

3.2.3 pH dependence and interference of hydroxide

The pH dependence of the fluoride sensing of the **F1**-PCA ensemble was examined at PCA concentrations of 5 mM (Figure 3.8). The pH profile in the absence of fluoride shows significant binding of OH^- even at pH 2.5. An abrupt drop of excimer emission is observed within the pH region of 3.5-5, which likely results from the deprotonation of carboxylic group in PCA (pK_a 4.48[112]) leading to electrostatic repulsion and thereby disfavours pyrene aggregation. pH 2 was therefore chosen so that no appreciable hydroxide binding occurs, while further decreasing pH is not desired because of protonation of fluoride ion.

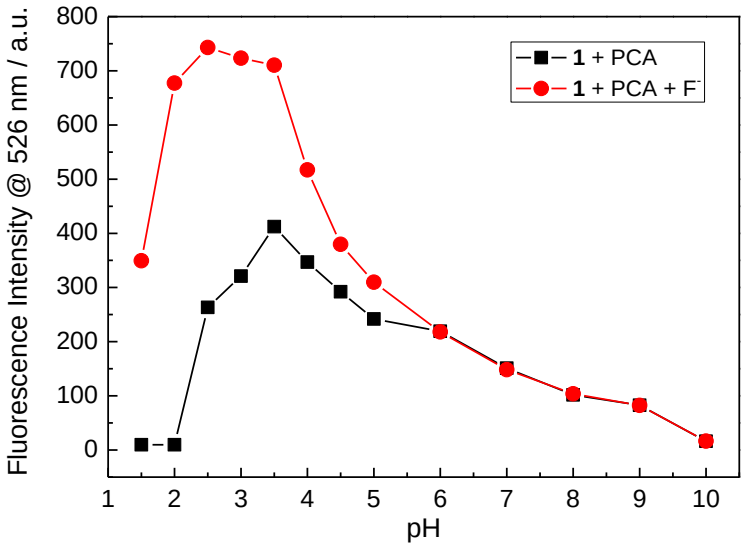

Figure 3.8 Fluorescence intensity of **F1** (0.1 mM) at 526 nm vs pH with 5 mM PCA in the absence and presence of 1 mM NaF in buffered aqueous solutions. λ_{ex} = 328 nm.

3.2.4 Anion selectivity

Selectivity of the **F1**-PCA ensemble among other common anions was tested (Figure 3.9), among which Cl^-, Br^-, AcO^-, $H_2PO_4^-$ and NO_3^- do not interfere even at concentrations 10-fold that of fluoride. However, for SO_4^{2-} at high concentration, significant aggregation and excimer emission is observed, which can be ascribed to its bis-charged nature promoting aggregation of positively charged **F1** by electrostatic interactions. However, no interference was found at [SO_4^{2-}] < 0.6 mM and the sulfate interference at high concentrations can be masked by using $BaCl_2$.

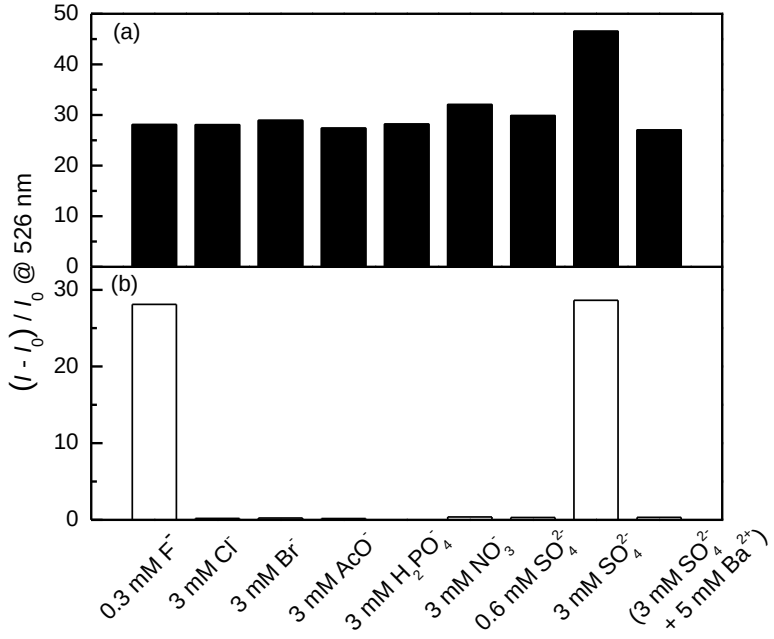

Figure 3.9 Enhancement of fluorescence of **F1** (0.1 mM) at 526 nm in response to fluoride and other anions alone (b) or in the presence of fluoride coexisting with other anions (a) in the presence of 5 mM PCA in default buffer. λ_{ex} = 328 nm.

3.3 Conclusions

In summary, a boronic acid-based sensing ensemble has been developed capable of directly sensing aqueous fluoride at ppm levels. The unprecedented sub-mM fluoride affinity of simple phenylboronic acid derivatives was found to arise from two factors: (i) the presence of PCA increases the Lewis acidity and therefore fluoride affinity of the boronic acid at highly acidic conditions; (ii) supramolecular aggregation of **F1**-PCA-fluoride adduct enhances the apparent fluoride affinity by shielding the boronate-fluoride complex from bulk water. Although higher binding affinity has been reported with intrinsically more Lewis acidic sensors, the current system shows large modulation of the excimer emission allowing fluoride ion to be determined over a large concentration range and a capacity of sensing at ppm levels. It is believe that the analyte-induced aggregation strategy can be used to enhance analyte affinity with other weak binders in the design of highly sensitive chemosensors for biologically important species.

Chapter 4: Self-assembly of a Glucose-Binding Amphiphile Featuring Two Dynamic Covalent Bonds

4.1 Introduction

4.1.1 Boronic acid as glucose sensors

The development of synthetic chemical sensors for saccharides has been driven by the clinical need to monitor saccharide concentrations in body fluids for disease diagnosis and management. While most chemical sensors developed use noncovalent interactions to bind the analytical target of interest, there is a huge challenge in binding saccharides in water. These neutral polyhydroxyl guests have high solvation enthalpies in aqueous solutions that are difficult for synthetic chemosensors to overcome as efficiently as naturally occurring saccharide-binding proteins (lectins) that operate solely by noncovalent interactions.[113] Another challenge is to achieve binding selectivity, as many saccharides show no structural difference except configuration of certain stereocentres. In this context, sensors utilizing biological recognition elements, including those based on enzymes or lections, have been developed and are widely used. Synthetic chemosensors, however, are more desired in terms of the stability, low cost, and oxygen independence. Boronic acid-based synthetic chemosensors therefore represent promising alternatives for saccharide sensing.[114]

To effective bind saccharides in water, researchers have mostly resorted to boronate ester formation, a dynamic covalent bond. The pH-dependent[107] reversible binding between boronic acids and *cis*-1,2- or 1,3- diols to form five- or six- membered cyclic esters respectively (Figure 4.1) has proved sufficiently strong enabling binding of saccharides at mM or sub-mM levels, rendering possible boronic-acid based saccharide sensing in biologically relevant scenarios. The strength of boronic acid binding to saccharides is determined by the orientation and relative position of hydroxyl groups, thus boronic acids can differentiate structurally similar saccharide molecules.

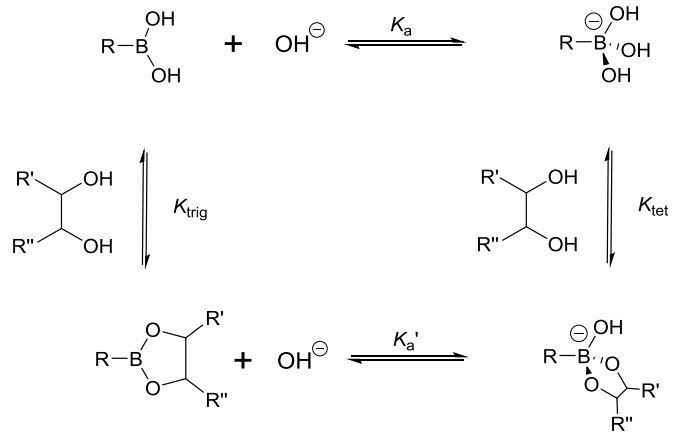

Figure 4.1 Thermodynamic cycle of boronic acid ionisation and interaction with *cis*-1,2-diols. K_a and K_a' represent ionisation constants of boronic acids and boronate esters, respectively. K_{trig} and K_{tet} represent formation constants of trigonal and tetrahedral boronate esters formed from boronic acid and boronate anion, respectively.

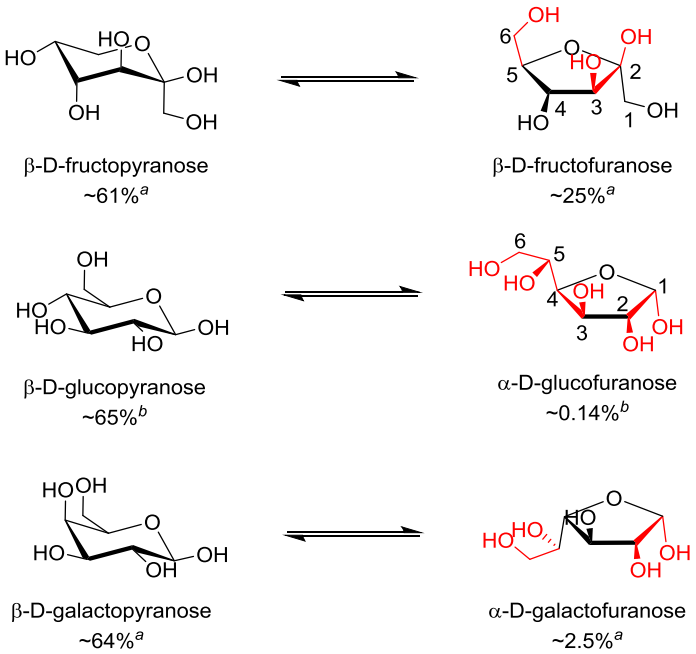

Figure 4.2 Equilibria between the dominant form (left) and the form that contains a *syn*-periplanar anomeric hydroxyl pair (right) of D-fructose (top), D-glucose (middle) and D-galactose (bottom).[114-116] Potential boronic acid binding sites are shown in red. Positions for hydroxyl groups are numbered in β-D-fructofuranose and α-D-glucofuranose.

It is now known that monoboronic acids exhibit inherent fructose selectivity among common monosaccharides.[117] This is because of the high abundance in solution of the form of fructose that contains a *syn*-periplanar pair of hydroxyl groups available for boronic acid binding, *i.e.* the β-d-fructofuranose form whose relative percentage of total fructose is 25% in D_2O at 31 °C.[115] In contrast, with glucose that is the more clinically relevant target, the available α-D-glucofuranose form makes up only 0.14% of the total composition in D_2O at 27 °C (Figure 4.2).[116] In line with

these facts the binding constant of phenylboronic acid with fructose is 4370 M^{-1} while that with glucose is 110 M^{-1}.[117] The generally observed binding affinity of phenylboronic acids with monosaccharides follows the order of fructose > galactose > mannose > glucose.[117] In general both the saccharide affinity and selectivity of the simple monoboronic acid based sensors are poor. This can be substantially improved using properly positioned multiboronic acids, utilizing different numbers of cis-diol moieties available in different saccharides. The α-glucofuranose form of glucose has two boronic acid binding sites, at its 1,2- and 3,5,6-positions, respectively (Figure 4.2). The β-D-fructofuranose, which is the fructose isomer that participates in boronic acid binding, in contrast, can only interact with one boronic acid moiety. This makes possible the design of glucose-selective receptors by enhancing the glucose selectivity via chelation (or multivalent binding[85]). It is of interest to develop boronic acid sensors that are selectivity for glucose over fructose, as fructose is also present in blood serum and can thus interfere with glucose sensing.

Glucose selective boronic acid-based sensors are typically diboronic acids that are able to form 1:1 cyclic boronate esters with glucose (*e.g.* Figure 4.3). The multivalent diboronic acid-glucose interaction leads to a higher affinity for glucose than for fructose, in contrast to the higher affinity for fructose observed with monoboronic acids. The successful design of a glucose-selective diboronic acid lies in a structural arrangement of two boronic acid moieties in the same covalent framework that fits both the distance between two potential binding sites (1,2- or 1,3-*cis* diol, Figure 4.2) of glucose and the orientation of the hydroxyl groups. Typically, a glucose-selective diboronic acid interacts with α-glucofuranose by binding the pair of hydroxyl groups at the 1,2-position and two or three hydroxyl groups at the 3,5,6-position. To this end, experiment-driven modular approaches by systematically varying the length of spacer or positions of the boronic acid groups and by referring to computer modeling have been effective.

The first breakthrough in this area was by Shinkai and co-workers in 1994[118], when a glucose selective fluorescence sensor **4-1** was designed. Compound **4-1** showed a high glucose binding constant of 3981 M^{-1} in 33.3% MeOH-H_2O, compared to that with fructose (316 M^{-1}) and galactose (158 M^{-1}). The **4-1**/glucose complex was initially assigned to the 1,2:4,6-α-glucopyranose diboronate complex (Figure 4.3b) and was later shown by Norrild *et al.*[119] to be the 1,2:3,5,6-α-glucofuranose diboronate complex (Figure 4.3c) formed in aqueous solutions. The initially-deduced product was found to form only under completely anhydrous conditions. It was proposed in later studies that the C–H···π interactions between the hydrocarbon skeleton of glucose and the extended aromatic surface of the anthracene core in **4-1** might also contribute to the high affinity to glucose.[120] **4-1** displays fluorescence enhancement responses to saccharides, and the high glucose affinity allows glucose sensing at sub-mM levels.

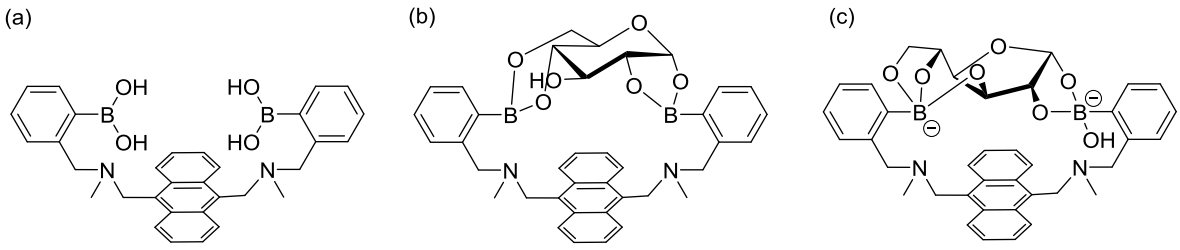

Figure 4.3 Structures of 4-1 (a), initially-deduced 4-1/α-glucopyranose complex formed in MeOD (b) and the latter assigned 4-1/α-glucofuranose complex formed under aqueous conditions (c).

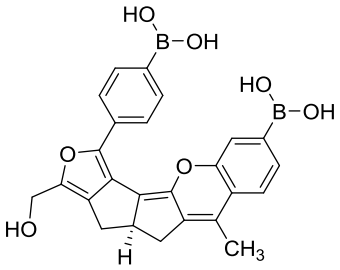

4-2

Other diboronic acid-based glucose sensors have been developed after the pioneering work by Shinkai and coworkers. One of the most noticeable examples is diboronic acid **4-2**[121] designed by Drueckhammer and coworkers. **4-2** binds to α-glucopyranose form instead of the α-glucofuranose form of glucose. Computer-guided design followed by an eight-step synthesis afforded **4-2** that contains a pair of almost parallelly-oriented boronic acid moieties attached to a highly rigid covalent framework. Compound **4-2** exhibits a much higher affinity for glucose 400-fold greater than those of other saccharides, with a glucose binding constant of 4.0×10^4 M^{-1}. The 400-fold binding selectivity for glucose over fructose and galactose remains the highest reported to date. Compound **4-2** represents an "extreme" example in which a highly rigid diboronic acid scaffold matches perfectly the structure of glucose, but requires an elaborate design and formidable synthetic efforts.

While the abovementioned strategy of *covalently* organizing two boronic acids to chelate glucose heavily relies on elaborate structural design, recently it has been envisioned that *noncovalent* aggregation of simple boronic acids would lead to supramolecular assemblies containing multiple boronic acid moieties, which could confer glucose selectivity by chelation. In this respect, attention has been paid to the employment of π-conjugated molecules that can form oligomeric or polymeric stacks in water via aromatic π-interactions and hydrophobic interactions. Most notably, aggregation of dye molecules may lead to dramatic changes in its fluorescence emission, either quenching or enhancement, such as the phenomena of "aggregation-induced emission".[122] Due to its ability to bind two boronic acids, glucose binding can induce the transition of a boronic

acid-functionalized dye from monomeric species to aggregates, accompanied by dramatic spectroscopic responses favorable for optical sensing of glucose.

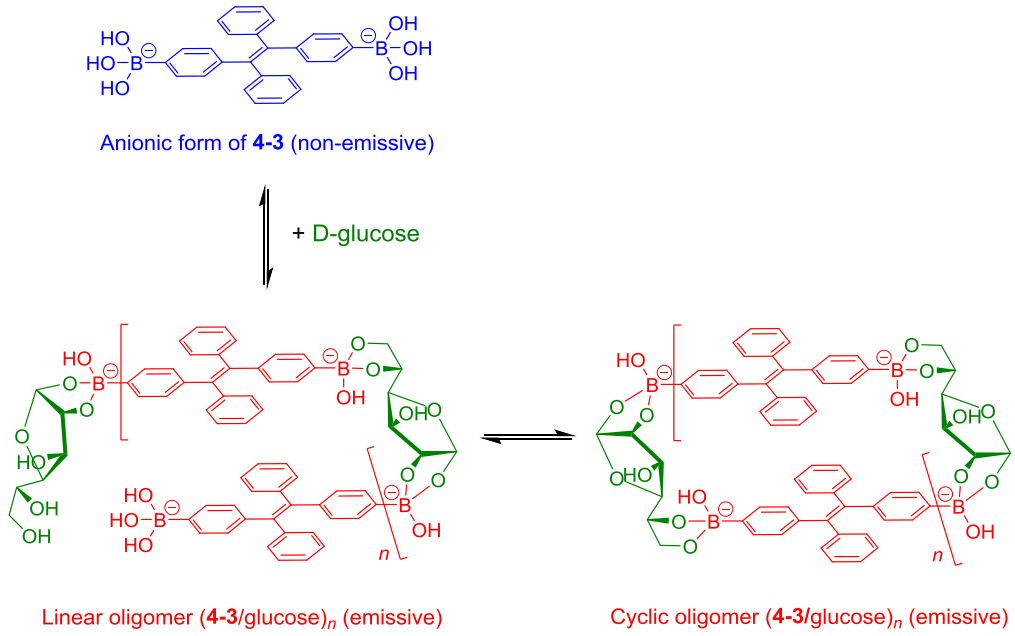

Figure 4.4 Proposed glucose-induced oligomerization mechanism of **4-3** sensing of glucose.

Using the aggregation approach, Tang and coworkers reported a tetraphenylethene (TPE)-cored diboronic acid **4-3**[123] that serves a specific "light-up" sensor for glucose. In the absence of saccharides in alkaline conditions, **4-3** in its dianionic form is weakly emissive. Fluorescence enhancement up to ~5.4 fold was observed upon addition of glucose, while that induced by fructose, galactose and mannose is much lower. It was proposed that it is the oligomers formed between bifunctional **4-3** and divalent glucose (Figure 4.4) that restricts the intramolecular rotations of the phenyl rotors that leads to the fluorescence enhancement. Other monosaccharides are unable to induce such oligomerisation of **4-3**, resulting in only minor fluorescence enhancements. The oligomerisation mechanism is supported by the observation of an emission drop at high glucose concentration and the negligible fluorescence change produced by glucose with the monoboronic acid counterpart of **4-3**. Thermodynamically it is not possible that only the interactions of the two boronic acid moieties in **4-3** with the two binding sites of glucose could lead to appreciable oligomerisation of **4-3** at a low concentration of 50 μM.[124] It is thus inferred that other interactions such as hydrophobic and π-π interactions between TPE moieties within the oligomer may operate and stabilize the assembly. While the fluorescence enhancement response is highly glucose-selective, the system shows no "binding selectivity" for glucose. Although no binding constant was determined, competitive experiments showed that the fluorescence enhancement produced by 4 mM glucose decreased by 60% when 0.1 mM of fructose co-exists, which reveals the much higher affinity of **4-3** towards fructose than glucose.

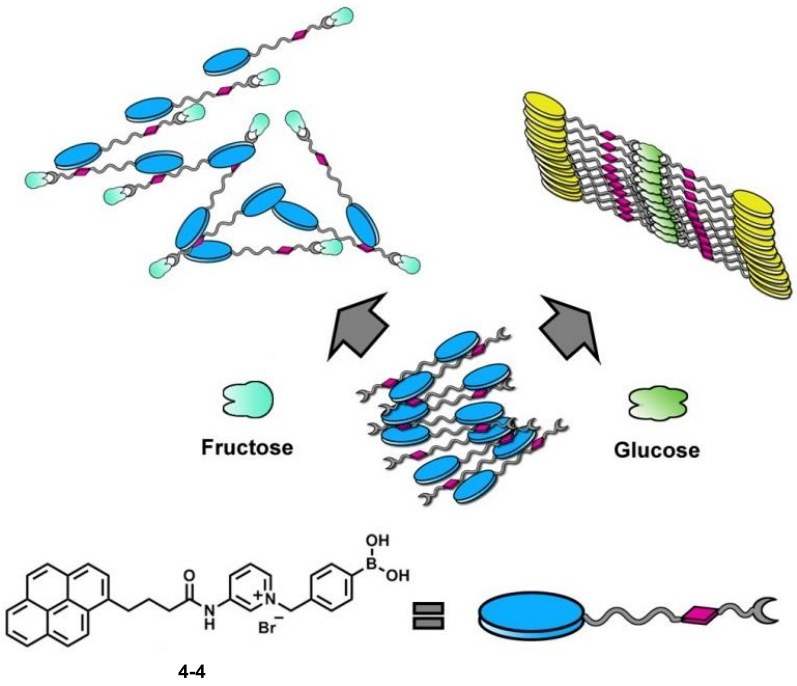

Figure 4.5 Cartoon representation of different aggregation behavior of 1:1 **4-4**/fructose and 1:2 **4-4**/glucose complexes. Adapted with permission from *J. Am. Chem. Soc.*, 2013, ***135***, 1700-1703. Copyright 2013 American Chemical Society.

While glucose binding selectivity is absent in **4-3**, pyrene-containing glucose sensor **4-4**[106] (compound **F1** used in Chapter 3) demonstrates that this is achievable by the aggregation approach as **4-4** shows a higher apparent affinity for glucose than for fructose. The amphiphilicity of the **4-4** and its-saccharide complex establishes the basis for its supramolecular aggregation in aqueous solution. In alkaline (pH 10) aqueous solution **4-4** at 0.1 mM exists in small aggregates that exhibit only pyrene monomer fluorescence at *ca.* 390 nm. Glucose binding to **4-4** leads to formation of large aggregates concomitant with development of pyrene excimer emission at 510 nm together with a minor increase in monomer emission. Fructose binding, on the contrary, results in aggregate size reduction and a modest enhancement of the monomer fluorescence. The fact that excimer emission was only observed upon glucose binding thus indicates that glucose binding leads to not only a higher extent of aggregation but also a well-ordered aggregate structure suitable for excimer emission. The 1:2 glucose/**4-4** complex was assumed responsible for the formation of larger aggregates and the strong excimer emission. An apparent binding constant of **4-4** with glucose of 1.9×10^6 M^{-2} (with an apparent 1:2 stoichiometry) was found whose square root being 1378 M^{-1} is higher than the binding constant with fructose 353 M^{-1} (1:1 stoichiometry). Self-association of the 1:2 glucose/**4-4** complex driven by aromatic π-stacking between two pyrene moieties from neighbouring complexes was assumed responsible for the higher tendency to form assembly of the 1:2 glucose/**4-4** complex than the unbound **4-4** and the 1:1 **4-4**/fructose complex. Aggregation of the 1:2 glucose/**4-4** complex facilitates the glucose binding that results in a higher apparent glucose affinity than that of fructose, allowing glucose to

be detected at 10 μM which has not been possible with any synthetic mono- or diboronic acid-based sensor reported to date. A high glucose affinity is crucial for the reduction of interference from fructose, *cf* **4-4** when compared with **4-3**.

4.1.2 Scope and objectives of this chapter

As demonstrated in **4-3** and **4-4**, by exploiting aggregation of π-conjugated molecules, selective sensing of glucose is possible by using structurally simple boronic acids, without the need of tedious multistep synthesis (*e.g.* **4-2**). The goal here is to develop glucose-selective sensing ensembles that requires precisely no synthetic efforts. This appears unlikely considering that simple monoboronic acids that are commercially available have intrinsic preference for binding fructose over glucose (Figure 4.2). The reported examples of utilizing dynamic covalent chemistry to create complicated molecular assemblies, however, have implied that the structurally complexity required for glucose sensing may be introduced via a dynamic covalent linkage. While the success of **4-4** implies that an effective glucose sensor can be as simple as an amphiphilic boronic acid, it was envisioned that attaching a hydrophobic group to a hydrophilic boronic acid via a dynamic covalent bond can lead to selective glucose sensing without synthesis, as glucose binding may be favored in the amphiphile aggregate that contains multiple copies of boronic acids. As a proof of the concept investigation, it was decided simply to attach a linear hydrophobic chain dynamic covalently to a boronic acid. Regarding the dynamic covalent linkage, the imine bond was chosen as it is arguably the most rapidly-forming dynamic covalent interaction that can be exploited (apart from the boronate ester bond, which clearly cannot be exploited here as orthogonality with respect to glucose binding is required).

The working sensing system is extremely simple, consisting of 4-formylphenylboronic acid (4FBA) and 1-octylamine (C8AM). It was found that upon mixing of 4FBA, C8AM and glucose in basic aqueous solutions, large aggregates were formed leading to solution turbidity which was ascribed to supramolecular aggregation of a “Gemini-type” surfactant formed via imine bonds linking 4FBA and C8AM, and binding of glucose simultaneously to two boronic acids (Figure 4.6). The aggregate morphology was revealed to be vesicles by transmission electron microscopy (TEM). The aggregate formation can be followed by appearance of solution turbidity or fluorescence enhancement of added Nile red. Fructose, in contrast, cannot induce aggregate formation. The system therefore serves as a highly selective sensing ensemble for glucose, simply by mixing commercial available reagents. Interestingly, the imine bond formation equilibrium was pushed forward by binding of glucose but not fructose. The system thus represents a rare example of cooperative formation of two orthogonal dynamic covalent bonds, even though there is a large spatial separation between these two bonds.

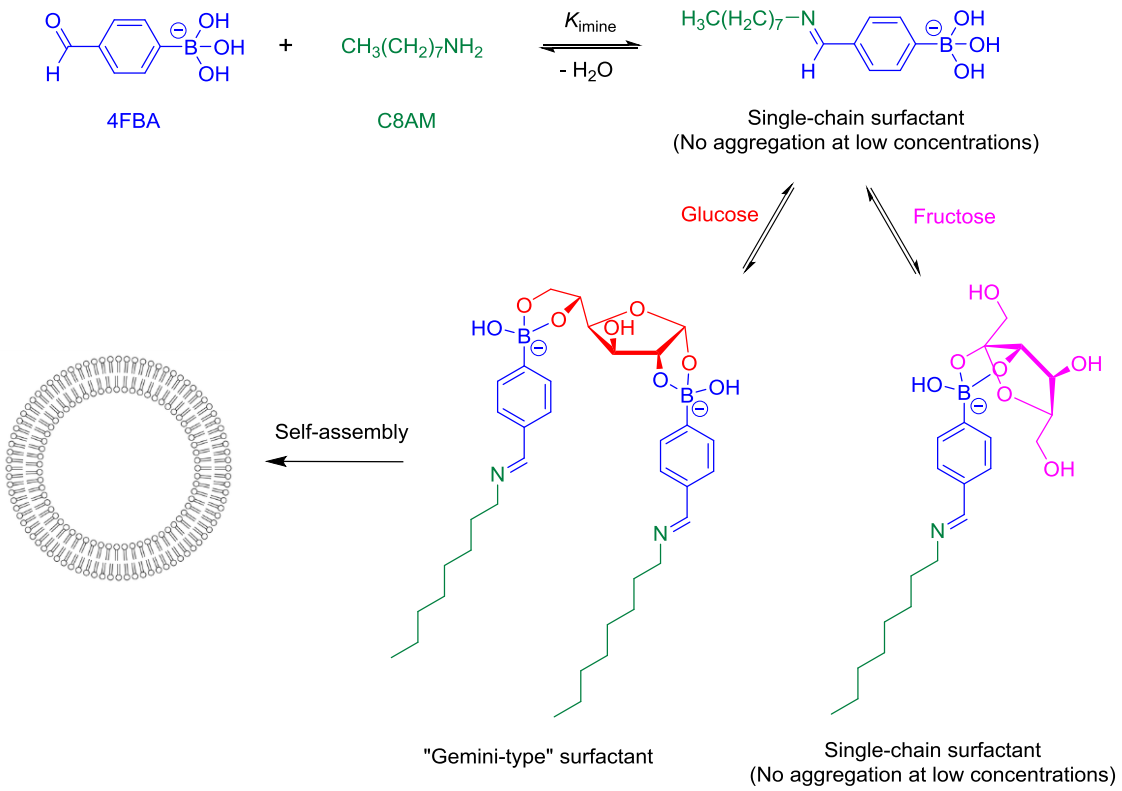

Figure 4.6 Schematic representation of selective glucose sensing via aggregation of an in situ formed amphiphile that involves formation of two orthogonal dynamic covalent bonds.

4.2 Results and discussions

To allow efficient imine bond formation while ensuring water-solubility of all components, the self-assembly studies was carried out at pH 10.5 (with 100 mM sodium carbonate buffer). Under this condition, C8AM (pK_a 10.65[125]) is partially protonated and remains soluble at 3 mM. 4FBA (pK_a 7.4[126]) exits fully in its anionic form which maximizes its saccharide binding affinity. When 4FBA (3 mM) and C8AM (3 mM) were mixed, the solution remained clear and transparent at 3 mM. In the presence of glucose (5 mM), however, the solution becomes increasingly turbid over the course of 30 min, indicating amphiphile aggregation taking place (Figure 4.7). With galactose (5 mM) used as the saccharide component, solution turbidity was also observed (5 mM), whereas the solution remained transparent with fructose (5 mM).

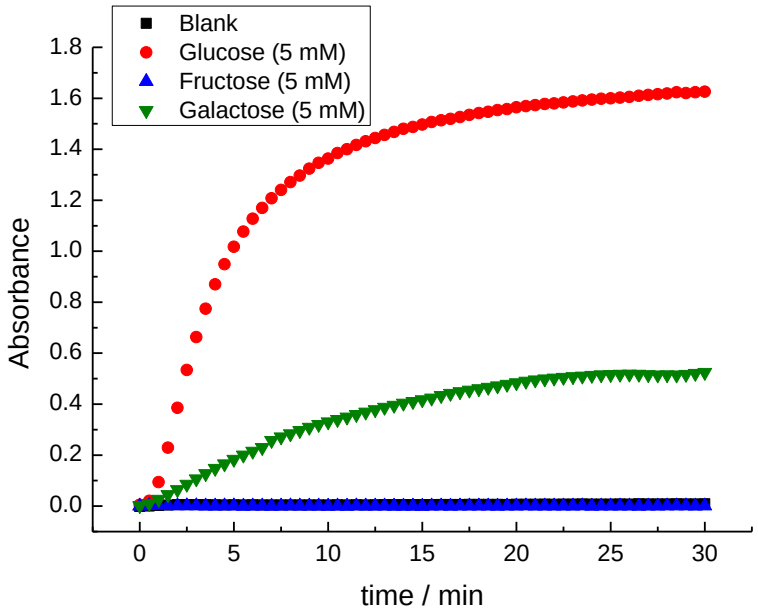

Figure 4.7 Turbidity of a mixture of 4FBA (3 mM) and C8AM (3 mM) over 30 min in the absence and presence of different saccharides in pH 10.5 100 mM $NaHCO_3$–Na_2CO_3 buffer. Turbidity is shown as absorbance at 450 nm (measured by a UV-Vis absorption spectrometer) due to light scattering.

Aggregate formation cannot be ruled out with no saccharide or with fructose even though transparent solutions were observed, since micelle formation is possible as previously reported with C8AM and a hydrophilic cationic aldehyde.[127] Nile red, an environment-sensitive fluorescence dye, was employed to investigate the amphiphile aggregation. In aqueous solutions, Nile red is non-fluorescent in aqueous, but in the presence of amphiphile aggregates (*e.g.* micelles and vesicles), Nile red can partition into the hydrophobic region of the aggregates and emits strong fluorescence. A mixture of 4FBA (3 mM) and C8AM (3 mM) in the absence and presence of varying concentrations of saccharides was incubated for 30 min, treated with a methanol solution of Nile red, and subject to fluorescence measurements. The results are shown in Figure 4.8. Very weak Nile red fluorescence was observed without saccharides or with fructose (0.1 – 10 mM),

confirming that little or no amphiphile aggregation occurred. In contrast, the presence of glucose and galactose (to a lesser extent) led to dramatic enhancement of Nile red fluorescence. These results agree well with those of the turbidity assay, confirming that under the described conditions no aggregates were formed without saccharides or with fructose, but glucose and to a lesser extent galactose induced self-assembly of the amphiphile formed between C8AM and 4FBA. Assembly of a control compound 4-formylbenzoic acid with C8AM was also examined using the Nile red assay, which showed no saccharide-dependence in the amphiphile aggregation (Figure 7.53, Chapter 7). It has been well established that among the three saccharides, fructose has the strongest intrinsic affinity towards monoboronic acids as its β-furanose form (the species available for boronic acid binding) has a much higher abundance compared to the boronic acid-acessible α-furanose forms of glucose and galactose (Figure 4.2). However, the α-furanose forms of glucose and galactose can simultaneously bind two boronic acid moieties whereas the β-fructofuranose can only bind a single boronic acid moiety (Figure 4.2). Therefore formation of "Gemini-type" amphiphiles is only possible for glucose and galactose. "Gemini-type" amphiphiles have a higher tendency to aggregate (i.e. a lower critical aggregation concentration)[128] compared with the single-chain amphiphile formed between fructose, 4FBA and C8AM (Figure 4.6). This explains that induction of aggregation was observed only with glucose and galactose. It should be noted that although the fluorescence intensity (which depends on the amount of Nile red) leveled off at 5 mM of glucose and galactose, the formation of amphiphile aggregates is still far from saturation, as will be demonstrated in the imine formation study below.

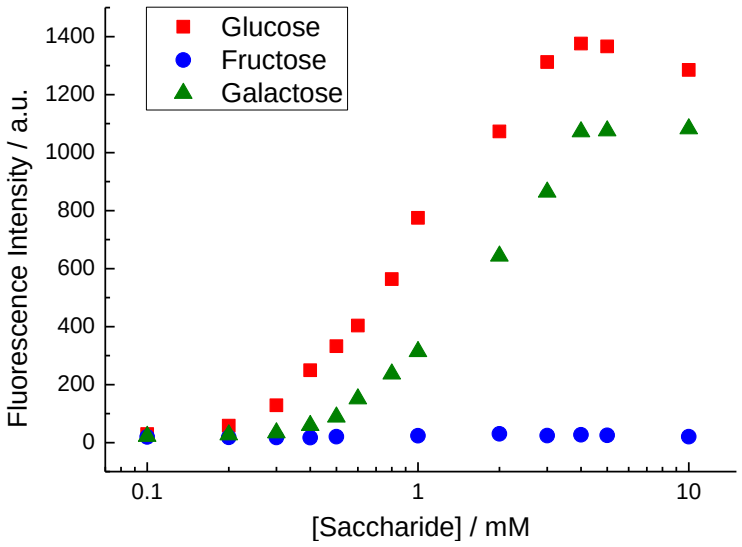

Figure 4.8 Amphiphile aggregation measured via Nile red fluorescence. A mixture of 4FBA (3 mM) and C8AM (3 mM) in the absence and presence of various concentrations of different saccharides were allowed to stand for 30 min and treated with Nile red (5 μM, added as a methanol solution). Fluorescence intensity of Nile red was shown (λ_{ex} = 500 nm, λ_{em} = 623 nm).

While glucose and galactose did induce aggregate formation, it is interestingly to investigate whether the equilibrium of imine bond could be influenced by saccharide binding and subsequent

self-assembly. It has been reported by van Esch and coworkers that amphiphile aggregation can drive imine bond formation by stabilizing it within the aggregate microenvironment that has a lower local concentration of water.[103-104, 127] ^{1}H NMR spectroscopy was employed to measure imine bond formation. Observable, albeit severely broadened imine proton NMR signals were observed, providing direct evidence of imine bond formation (Figure 7.54, Chapter 7). Although using conventional liquid-state NMR techniques, the NMR signals from aggregates cannot be quantified due to broadening, indirect measurement of imine formation percentage is feasible by calculation of 4FBA consumption by integration of its ^{1}H NMR signals. To enable this calculation, DMF was added as an internal reference. By comparing integrations of aldehyde (C*H*O) and DMF ^{1}H NMR signals, the imine formation percentage was calculated and summarized in Table 4.1.

Table 4.1 Percentage of imine formation in the absence and presence of different saccharides, determined with ^{1}H NMR spectroscopy. [4FBA] = [C8AM] = 3 mM, pD 10.5 with 100 mM $NaHCO_3$–Na_2CO_3 buffer.

Condition	Blank	Glucose (5 mM)	Fructose (5 mM)	Galactose (5 mM)
Imine formation	7%	38%	12%	26%

Indeed imine bond formation was found to be dramatically increased by glucose binding and to a lesser extent by galactose binding, whereas less significant with fructose that cannot promote amphiphile aggregation. These results can be explained by (i) amphiphile aggregation shifts the equilibrium of the imine bond formation in the forward direction, and (ii) binding of glucose and galactose promotes amphiphile aggregation due to the formation of "Gemini-type" amphiphiles. Notably, glucose binding *via* the boronate ester linkage exerted an influence on the imine bond despite the spatial separation between the two dynamic covalent bonds. This is possibly because of the supramolecular aggregation that requires and stabilises both the imine bond and the boronate ester linkages (with "divalent" binder glucose). This "indirect" interplay is conceptually distinct from the known synergistic binding of 2-formylphenylboronic acid (2FBA) to an amine and a *cis*-diol component, (*e.g.* the system shown in Figure 2.3), which is due to a boron-nitrogen interaction that directly enhances diol binding.[43]

The morphology of aggregates formed with glucose was examined by transmission electron microscopy (TEM) and the size by dynamic light scattering (DLS) techniques (Figure 4.9). TEM images revealed that the aggregates formed are vesicles. An average hydrodynamic diameter (D_h) of 678 nm was determined by DLS measurements for the glucose-induced aggregates, which is in good agreement with the TEM image.

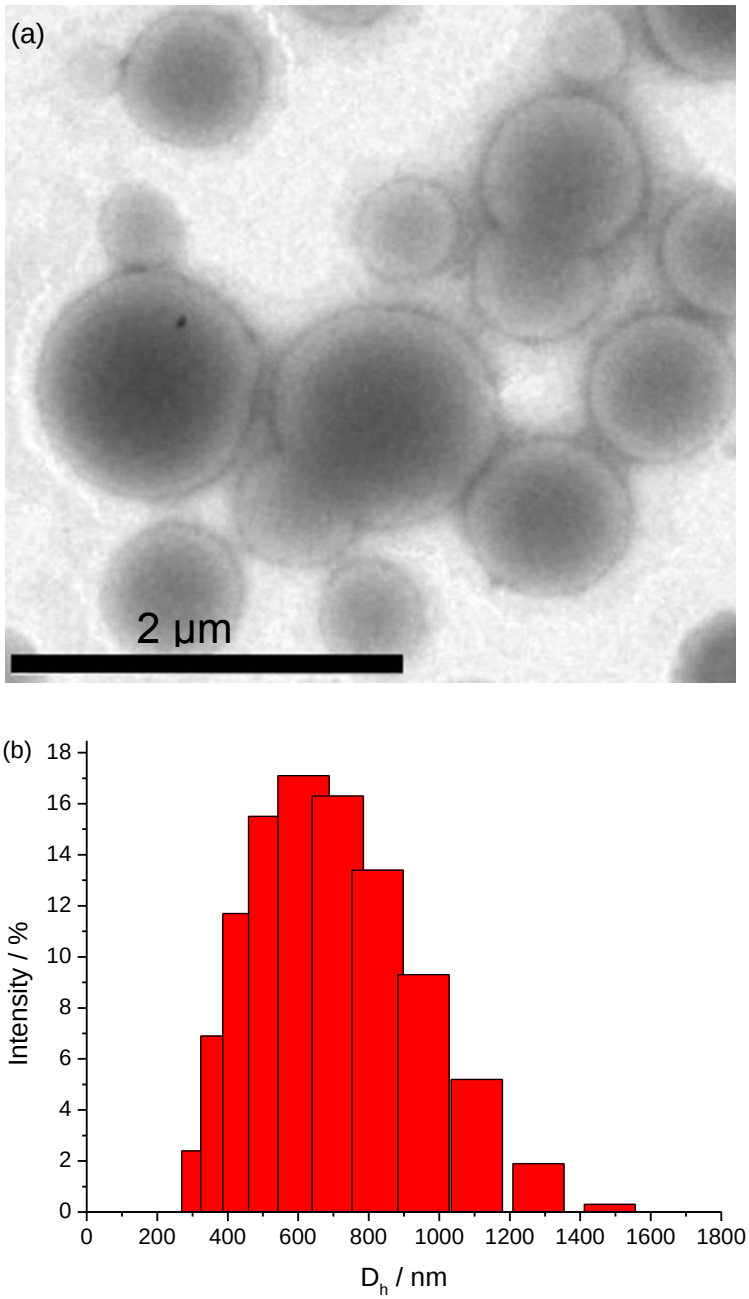

Figure 4.9 Transmission electron microscopy (TEM) (a) and dynamic light scattering (b) characterization of aggregates formed by 4FBA (3 mM), C8AM (3 mM), glucose (10 mM) in pH 10.5 in pH 10.5 100 mM $NaHCO_3$–Na_2CO_3 buffer. (b) was collected by XXC.

This system can be used for glucose sensing via appearance of solution turbidity which can be detected by naked eyes or quantified by measuring light scattering using a UV-Vis absorption or fluorescence spectrometer. Alternatively, the incorporation of Nile red allows sensitive sensing of glucose at sub-mM concentrations. It is of interest to test the ability of this glucose sensing ensemble to tolerate the coexistence of saccharide interferents. Promisingly, the coexistence of 0.2 mM of fructose or galactose resulted in little interference with sensing of 1 mM glucose, a significant improvement compared with other reported systems based on self-assembly.[106, 123]

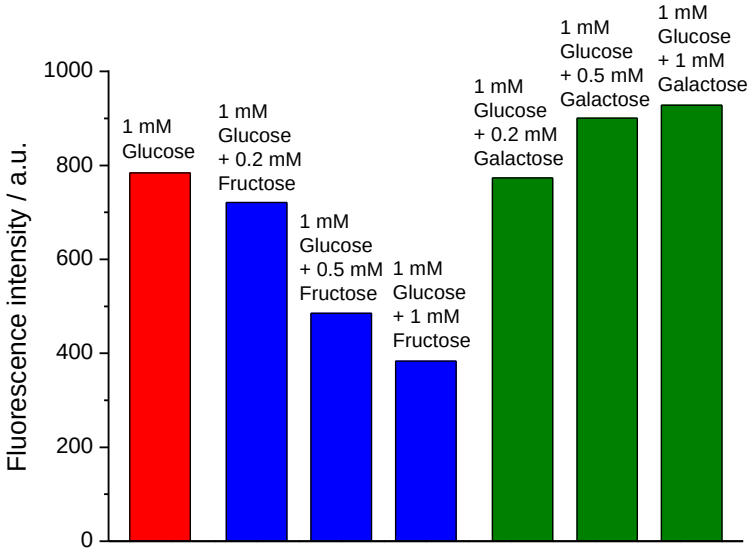

Figure 4.10 Fluorescence intensity of Nile red (5 μM) added to the assembly formed by 4FBA (3 mM), C8AM (3 mM) and glucose (1 mM) in the absence and presence of saccharide interferents in pH 10.5 100 mM $NaHCO_3$–Na_2CO_3 buffer.

4.3 Conclusions

In summary, we have demonstrated in a simple system that the equilibrium of a dynamic covalent bond that assembles a receptor can respond to a molecular recognition event *via* a different dynamic covalent bond, and such an assembly has been used for sensing applications. A mixture of 4FBA, C8AM and glucose formed a dynamic "Gemini-type" amphiphile that self-assembled to form vesicular aggregates which features simultaneous formation of an imine bond and boronate ester linkages with glucose. Interestingly, there is a large spatial separation between the two dynamic covalent bonds, and their mutual influence is made possible because of the amphiphile aggregation and multivalent binding with glucose. The reported system allows selective glucose sensing simply by mixing commercially available reagents, representing the first example that the intrinsic fructose over glucose selectivity of boronic acids can be overcome without resorting to synthesis. This suggests that the structural complexity required for creating selective synthetic receptors or other functional materials can be achieved by *in situ* dynamic covalent assembly of simple components.

Chapter 5: Dynamic Covalent Transport of Amino Acids across Lipid Bilayers

5.1 Introduction

There is currently considerable interest in developing synthetic systems[129-131] to mediate the transport of highly hydrophilic species, *e.g.*, cations, anions, sugars and amino acids across lipid bilayers, either functioning as a membrane-spanning channel[132-133] or a mobile carrier.[134-135] Such systems could perform the function of naturally occurring transmembrane proteins and could serve as important tools for biomedical research or have therapeutic potential.[136-138] For those functioning as mobile carriers, a dynamic interaction is responsible for reversibly binding and lipophilizing substrates, allowing the lipophilic complex to diffuse through the membrane and dissociate to release the transported substrate into the aqueous phase.[134-135] Non-covalent interactions including ion pairing,[139-141] hydrogen bond,[142-146] halogen bond,[147-148] metal-coordination[149-150] and cation[151-153]/anion[154-155]-π interactions are well exploited (See Section 6.1 for a more detailed introduction on ionophores). Dynamic covalent bonds,[4-6, 156-157] in contrast, have been rarely used as the interaction for reversible binding of the transported substrates.

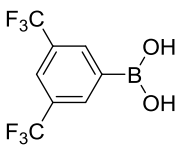

5-1

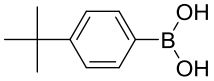

5-2

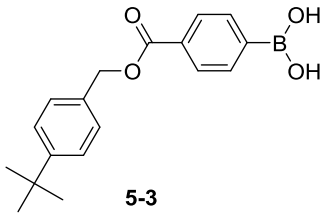

5-3

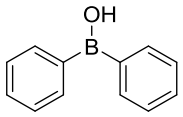

5-4

Westmark and Smith reported the ability of phenylboronic acids to facilitate the transport of saccharides across lipid bilayers via reversible boronate ester formation (See Section 4.1.1, Chapter 4 for an introduction to boronic acid-saccharide interactions). Efflux of saccharides from inside liposomes was measured using enzymatic assays. Millimolar concentrations of boronic acids were tested, and saccharide transport was monitored over the time scale of 100 min. The transport efficacy depends predominantly on the lipophilicity of boronic acid transporters, with **5-1** and **5-2** identified as two of the most active commercially available transporters, and the more lipophilic, synthetic transporter **5-3** being more active. The saccharide transport selectivity of simple monoboronic acids followed the order of sorbitol > fructose > glucose, which correlate with the order of binding affinity for these saccharides. The rate of saccharide transport showed bell-shaped pH dependence with transport acitivity peaking at a pH value just below the pK_a of boronic acids. The saccharide complex species responsible for membrane transport could be the

neutral form or the anionic form (see Figure 4.1). The authors proposed that it was the neutral form that actually diffused through the membrane, based on the observation that diphenylborinic acid **5-4**, which can only form anionic saccharide complexes, failed to facilitate glucose transport.[158-159] Boronic acids were later reported to facilitate ribonucleoside transport, and similarly, the transport mechanism was proposed to be via the formation of neutral complexes.[160]

Stillwell *et al.* studied facilitated diffusion of glycine and lysine across planar lipid bilayers using formaldehyde and pyridoxal that presumably form imines with amino acids.[161] This was the first report showing possible relevance of imine bond in membrane transport. Pyridoxal was found to give higher activity than formaldehyde, but the percentage of amino acid diffusion was less than 4% after 20 h. even with ~millimolar concentrations of aldehydes.

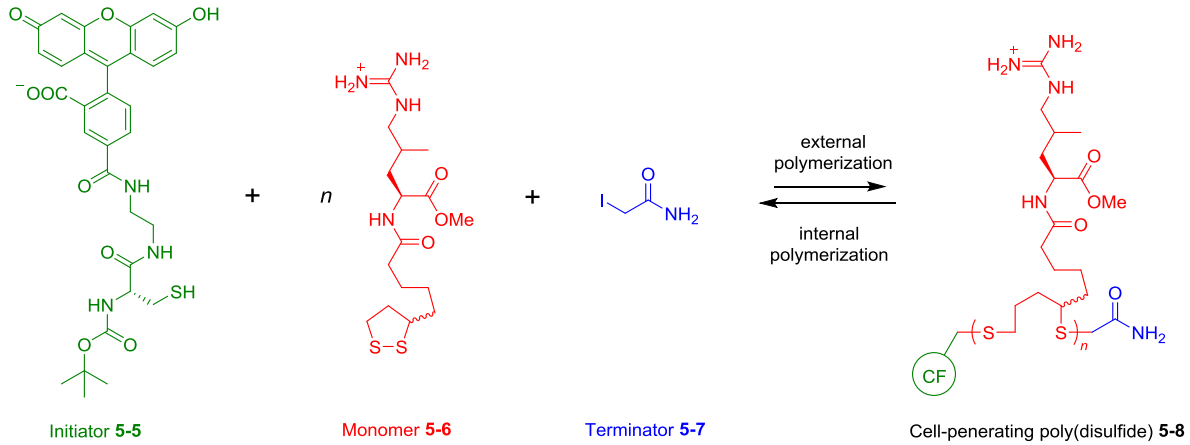

Figure 5.1 Cell uptake of a carboxyfluorescein (CF) substrate via formation and dissociation of a substrate-initiated poly(disulfide) (siCPD).

The cell-penetrating substrate-initiated poly(disulfide) (siCPD) cellular delivery system is an elegant example that demonstrates the utility of reversible disulfide bond in membrane transport. In a seminal study, Matile and coworkers grew siCPDs on fluorescent substrates and monitored their uptake into Hela cells using fluorescence techniques.[162] A polymerization reaction that involved an initiator (e.g. **5-5**), a monomer (e.g. **5-6**) and a terminator (**5-7**) occurred in neutral aqueous solutions at room temperature, to produce a siCPD (e.g. **5-8**, Figure 5.1). siCPDs could penetrate through lipid bilayers to enter cells in 5 min and subsequently depolymerize due to exchange with GSH in less than 1 min to release the free initiator. The membrane transport and cellular uptake was found to show be dependence on the presence of free thiols in the membrane. Based on this the authors proposed a thiol-mediated uptake mechanism that involved covalent binding to the lipid membrane by disulfide exchange with exofacial thiols. The siCPD systems are, however, conceptually different from the other abovementioned examples as they require intracellular glutathione (GSH) to break the disulfide bonds and release the substrate, whereas in the abovementioned examples the membrane transport process was only driven by a concentration gradient of the transported substrate.

In this chapter, dynamic covalent chemistry was exploited to facilitate membrane transport of amino acids. Although there have been many examples of amino acid transport through a liquid phase facilitated by synthetic molecules, to the best of my knowledge, few examples reported amino acid transport through phospholipid bilayer membranes. Of note are recently reported single molecule tubular channels that facilitated chiral selective amino acid transport. Here lipophilic and highly electrophilic aldehydes were studied, which could form imine and hemiaminal adducts with amino acids. Hemiaminals are labile adducts formed between carbonyl compounds and primary or secondary amines (Figure 5.2). Compared to imine chemistry, hemiaminals are less explored in the context of dynamic covalent chemistry due to their instability, while stabilization can be afforded by using highly electrophilic carbonyl compounds[8, 163-165] or a further binding event.[7, 35, 166] The biological relevance of hemiaminals is not limited to the involvement in imine formation. It has been reported that hemiaminal formation is used by *Escherichia Coli* dihydroxyacetone kinase for substrate binding.[167-168]

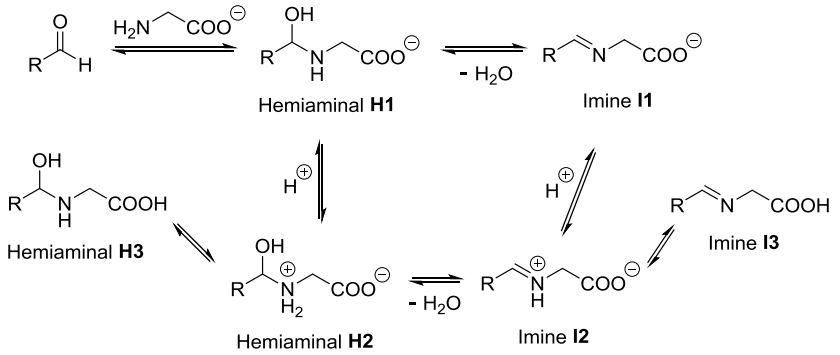

Figure 5.2 Formation of hemiaminals and imines between an aldehyde and glycine

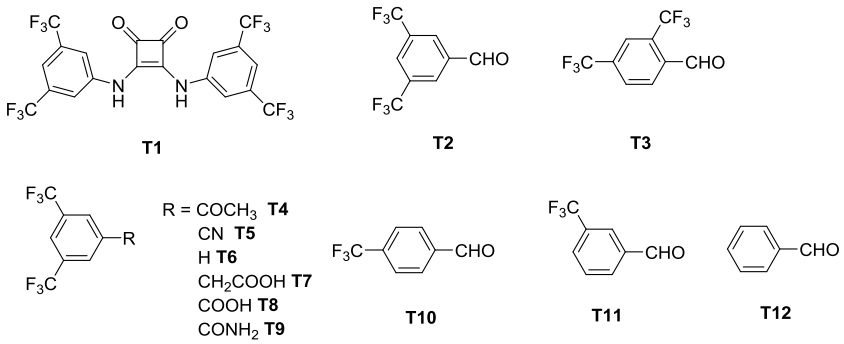

Figure 5.3 Structures of compounds tested for Gly transport

5.2 Results and discussion

5.2.1 ^{13}C NMR Assay

Evidence for glycine transport facilitated by a mixture of an aldehyde and a squaramide has been afforded by a ^{13}C NMR assay[169] (Figure 5.4). Gly-1-^{13}C was added externally to a suspension of giant multilamellar vesicles (GMLVs) of 1-palmitoyl-2-oleoyl-*sn*-glycero-3-phosphocholine (POPC) and DMSO solutions of an aldehyde and/or a squaramide (or DMSO as control) were added to start the Gly influx. After 2 h, paramagnetic Mn^{2+} was added to quench the ^{13}C NMR signal from extravesicular Gly, and then the ^{13}C NMR spectra of the vesicle suspension were measured. The results show that without any transporter, there is only very slow simple diffusion of Gly. An enhanced signal from the intact Gly-1-^{13}C was observed with only **T1** (1 mol% transporter to lipid) or **T2** (10 mol%) alone, but a mixture of **T1** and **T2** induced *c.a.* 50% more glycine transport than the sum of that induced by each component, as estimated by integration of the intravesicular Gly signal (Figure 7.59, Chapter 7). A similar synergistic effect in facilitating Gly transport by **T1** and **T3** was also observed (Figure 7.58, Chapter 7).

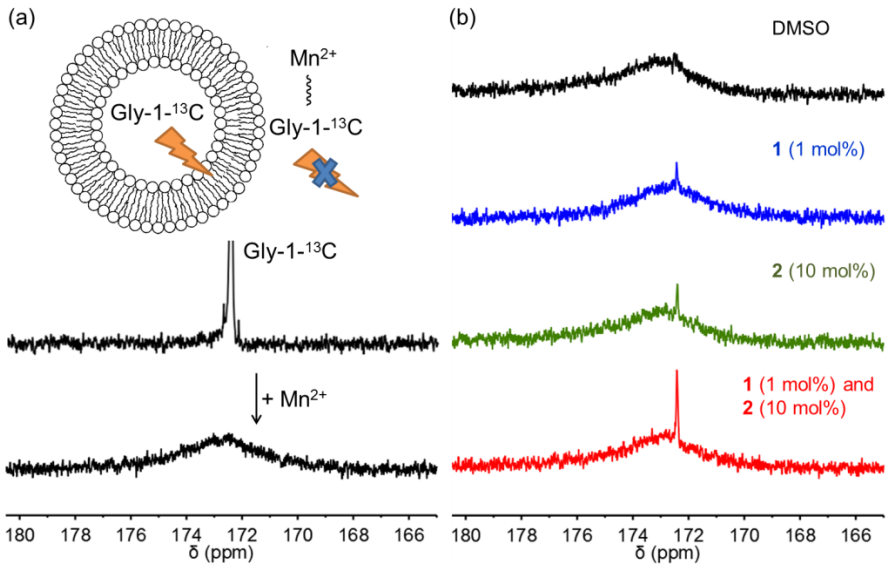

Figure 5.4 (a) Schematic representation of the ^{13}C NMR assay for Gly transport. POPC GMLVs were loaded with an internal solution of Na_2SO_4 (100 mM) and HEPES (20 mM) buffered at pH 7.4, and suspended in an external solution of Gly-1-^{13}C (50 mM), Na_2SO_4 (100 mM) and HEPES (20 mM) buffered at pH 7.4 in 9 : 1 (v : v) H_2O/D_2O. $MnSO_4$ was added to the external medium (0.5 mM), which led to broadening of ^{13}C NMR signal from Gly-1-^{13}C. (b) ^{13}C NMR spectra (100.6 MHz) of POPC vesicles solutions in 9 : 1 (v : v) H_2O/D_2O.with external Gly-1-^{13}C (50 mM) before and after addition of $MnSO_4$ (0.5 mM) (c) ^{13}C NMR spectra of POPC vesicles suspensions with 50 mM external Gly-1-^{13}C, obtained 2 h after the addition of DMSO or DMSO solutions of transporters. Transporter loadings are shown as transporter to lipid molar ratios.

5.2.2 Fluorescence assay

Due to the long acquisition time required, NMR assays are not suitable for quantitative kinetic studies. Previously amino acid transport kinetics has been measured using a radiometric assay[170] and a fluorescence labeling method.[171] However, both assays are expensive and time-consuming, and only allow collection of a limited number of data points which can be problematic when measuring very rapid transport. Here a novel fluorescence assay was developed and employed for amino acid influx using vesicles with an entrapped Cu^{2+}-Calcein complex. This is based on fluorescence quenching of Calcein by binding to Cu^{2+},[172] and the recovery of Calcein fluorescence by amino acids that rapidly compete with Calcein for Cu^{2+}.[173] The membrane impermeability, long-wavelength excitation and high fluorescence quantum yield of the Calcein dye are favorable for sensing of amino acids inside vesicles. Large unilamellar vesicles (LUVs, mean diameter 200 nm) of POPC entrapping Calcein (0.2 mM) and Cu^{2+} (0.2 mM) were prepared, and separated from the extravesicular markers by gel filtration. The vesicles were suspended in an external solution containing Gly (30 mM) and Cu^{2+} (0.2 mM) buffered at pH 7.4, and then DMSO solutions of transporters or DMSO were immediately added to the vesicle suspensions to start the transport. It was found that the presence of external Cu^{2+} is necessary to suppress Cu^{2+} efflux from inside vesicles, which would otherwise occur even without any transporter when high concentrations of external Gly is present (Figure 7.62, Chapter 7). Even with external Cu^{2+} when the simple diffusion or Gly-mediated diffusion of Cu^{2+} is suppressed, the addition of a transporter could still facilitate Cu^{2+} efflux (due to the difference between internal and external free Cu^{2+} concentrations when external Gly is present), leading to fluorescence enhancement that does not arise from Gly influx. Cu^{2+} transport, however, can be identified easily by doubling the concentration of extravesicular Cu^{2+}, and significant dependence of Calcein fluorescence on external Cu^{2+} concentration is an indication of Cu^{2+} transport. This effect is clearly observed (Figure 5.6a) with 8-hydroxyquinoline (**8HQ**), a known Cu^{2+} transporter.[174] In contrast, a mixture of **T1** and **T2** or **T3** induced enhancement of Calcein fluorescence (ΔI) that is practically independent of the external Cu^{2+} concentration (Figure 5.5b and 7.72c), indicating that Gly influx is responsible for the observed fluorescence enhancement, which is also supported by the results of the ^{13}C NMR assay (Figure 5.4). Similarly, without any transporter, a relatively small enhancement of Calcein fluorescence independent of external Cu^{2+} concentration is observed (Figures Figure **5.5** and 7.56), and is attributed to simple diffusion of Gly[171, 175171, 175171, 175171, 175171, 175171, 175] which is well-documented.[170, 174] The combination of 1 mol% (transporter to lipid) of **T1** and 50 mol% of **T3** leads to saturation of the fluorescence intensity within 20 min, and thus the maximum fluorescence intensity enhancement obtained under this condition (ΔI_{max}) is used for calibration. The use of a high loading of **T3** here is to ensure that completion of Gly transport is reached and

clearly shown, while the facilitated transport is observable at much lower loadings. Since the ΔI_{max} value shows a roughly linear relationship with the extravesicular Gly concentration (Figure 7.63, Chapter 7), the ΔI / ΔI_{max} value, here defined as the fractional fluorescence intensity I_f, can be approximated as the percentage of Gly transported relative to the maximum transport.

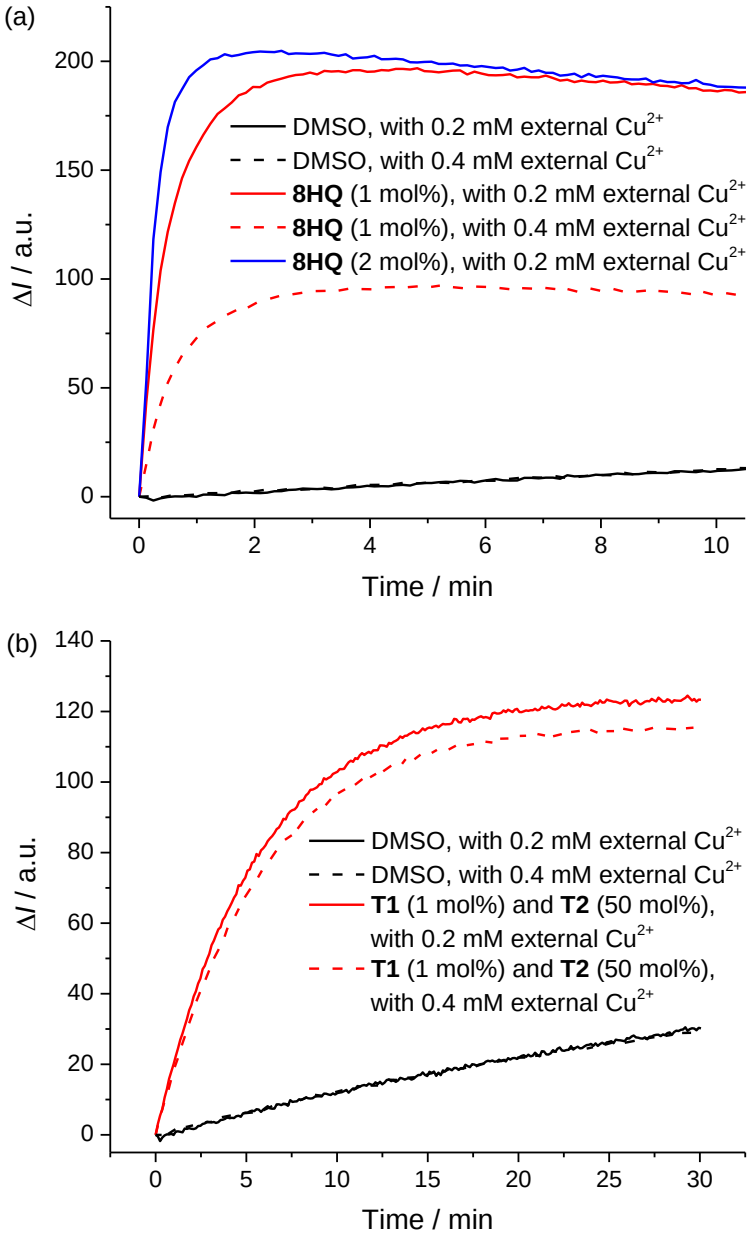

Figure 5.5 Evidence of Cu^{2+} transport in the case of **8HQ** (a) and Gly transport in the case of a mixture of **T1** and **T2** (b). POPC LUVs (mean diameter 200 nm) loaded with $CuSO_4$ (0.2 mM) and Calcein (0.2 mM) were suspended in an external solution containing Gly (30 mM) and $CuSO_4$ (0.2 mM or 0.4 mM). Both the internal and external solutions contained Na_2SO_4 (100 mM) and HEPES (20 mM) buffered at pH 7.4. At time 0, DMSO solutions of transporters or DMSO was added, and the fluorescence intensity (λ_{ex} = 495 nm, λ_{em} = 515 nm) was recorded. Transporter loadings are shown as transporter to lipid molar ratios. Note that in (a), doubling the **8HQ** loading (from 10 μM to 20 μM) did not significantly alter the maximum ΔI value, indicating that the fluorescence enhancement by **8HQ** is not due to competitive binding of **8HQ** to Cu^{2+}. The much higher saturated ΔI value in (a) compared to that in (b) indicates that Cu^{2+} efflux occurs in the presence of **8HQ**. Although it is possible that the Cu^{2+}-**8HQ** complex also transports Gly, the results in (a) show that the Cu^{2+}-Calcein assay is not suitable when a Cu^{2+} transporter is present.

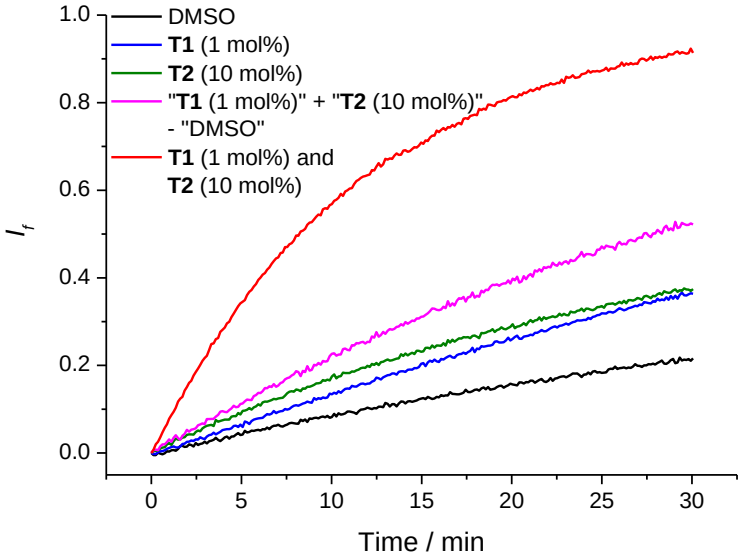

Figure 5.6 Gly transport kinetics measured by the Cu^{2+}-Calcein assay. POPC LUVs (mean diameter 200 nm) loaded with $CuSO_4$ (0.2 mM) and Calcein (0.2 mM) were suspended in an external solution containing Gly (30 mM) and $CuSO_4$ (0.2 mM). Both the internal and external solutions contained Na_2SO_4 (100 mM) and HEPES (20 mM) buffered at pH 7.4. At time 0, DMSO solutions of transporters or DMSO was added, and the fluorescence intensity (λ_{ex} = 495 nm, λ_{em} = 515 nm) was recorded. The fluorescence intensity was normalized by saturation using a mixture of **T1** (1 mol%) and **T3** (50 mol%). Transporter loadings are shown as transporter to lipid molar ratios.

Similarly to the results obtained with the ^{13}C NMR assay, the Cu^{2+}-Calcein assay demonstrates a synergistic effect between the squaramide **T1** and the aldehydes **T2** and **T3** (Figure 5.6 and Table 5.1). This is evidence in support of glycine transport by hemiaminal/imine formation with the amino group, and hydrogen bonding with the carboxylate group. Presumably, the observed synergistic effect results from the higher lipophilicity of a ternary squaramide-Gly-aldehyde complex compared to binary squaramide-Gly and aldehyde-Gly conjugates. Note that the relative rate of simple Gly diffusion measured in the ^{13}C NMR assay with GMLVs is slower than that measured in the Cu^{2+}-Calcein assay with LUVs, which is consistent with the lower permeability of MLVs.[176]

5.2.3 Osmotic response assay

It is possible that Cu^{2+} enhances Gly transport by binding to Gly, the hemiaminal, the imine or the squaramide **T1**, even though the kinetic profiles with different Cu^{2+} concentrations (Figure 5.5b) is evidence to suggest that this is unlikely. To examine the effect of Cu^{2+} on Gly transport, an independent osmotic response assay[177] was conducted. POPC LUVs (mean diameter 400 nm) loaded with 600 mM Gly were suspended in an isoosmotic external solution containing 195 mM Na_2SO_4 and 15 mM Gly. When Gly efflux occurs, the vesicles will become hyperosmotic, leading to water efflux and thus vesicle shrinkage, which results in an increase in 90° light scattering intensity. Thus Gly transport can be indirectly measured by monitoring the light scattering

intensity using a fluorimeter (Figure 5.7). Under the described experimental conditions, Gly transport by simple diffusion and facilitated by **T1** (1 mol%) is too slow to generate an osmotic response. A delay is observed in the osmotic response induced by **T2** (10 mol%), whereas the **T1**-**T2** mixture generates the osmotic response immediately after being loaded to the vesicle suspensions, showing the synergistic effect in Gly transport. Similar results have been obtained for **T1** and **T3** (Figure 7.60, Chapter 7). Importantly, the presence of Cu^{2+} has no observable effect on the rate of Gly transport (Figure 5.7) which confirms the validity of the Cu^{2+}-Calcein assay in studying the squaramide-aldehyde system. No change in light scattering intensity was found with vesicles with the same internal and external content, excluding aggregation or precipitation of the transporters as the cause for the observed increase in light scattering intensity (Figure 7.61, Chapter 7). The osmotic response assay appears, however, not sufficiently sensitive for accurate kinetic studies.

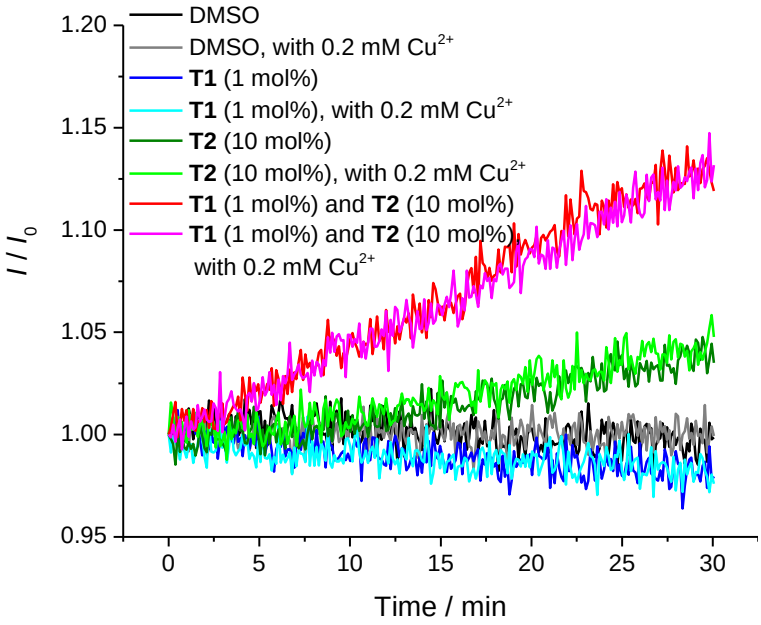

Figure 5.7 Gly transport measured by an osmotic response assay in the absence and presence of $CuSO_4$ (0.2 mM). POPC LUVs (mean diameter 400 nm) loaded with Gly (600 mM) were suspended in an external solution containing Na_2SO_4 (195 mM) and Gly (15 mM). Both the internal and external solutions were buffered at pH 7.4 with HEPES (20 mM). At time 0, DMSO solutions of transporters or DMSO was added, and the 90 ° light scattering intensity at 600 nm was recorded. Transporter loadings are shown as transporter to lipid molar ratios.

5.2.4 Gly transport studies

Using the new Cu^{2+}-Calcein assay, possible Gly transport by the non-aldehyde control compounds **T4**-**T9** were tested to provide more evidence for Gly transport by aldehyde carbonyl addition forming either hemiaminals or imines. First, the ketone analogue **T4** was tested to investigate the possible role of the carbonyl group of an aldehyde as a hydrogen bond acceptor for the

ammonium or amino group of Gly. Little activity was found with **T4** (Figure 7.65a, Chapter 7), ruling out this effect to be responsible for Gly transport. Second, **T5** with an electron-withdrawing cyano group was tested for possible anion-π interaction in the case of **T2** with the Gly carboxylate group. Compound **T5** shows far weaker transport activity (Figure 7.65b, Chapter 7), and therefore the observed glycine transport with aldehyde cannot be due to an anion-π interaction. Third, the synergistic transport of Gly by the lipophilic aldehydes with **T1** could arise from enhanced partition of **T1** in the lipid in the presence of **T2** or **T3**. The results with compound **T6** show this effect to be minor (Figure 7.65c, Chapter 7). Fourth, the aldehyde-Gly imine/hemiaminal formed in the lipid bilayer could serve as a Gly transporter by using its carboxylate group to ion pair with the ammonium group of the Gly substrate. Compound **T7**, which also contains an aliphatic carboxylate group, shows no facilitated Gly transport (Figure 7.65d, Chapter 7), thus ruling out that possibility. The facilitated Gly transport could also be due to aerobic oxidation of **T2** forming a trace amount of aromatic carboxylic acid **T8** that ion pairs with Gly, which is precluded as **T8** fails to transport Gly (Figure 7.65e, Chapter 7). A sixth, less likely possibility is the aldehyde proton serving as a hydrogen bond donor, which was also ruled out as the amide **T9** shows no Gly transport activity (Figure 7.65f, Chapter 7).

It is possible that **T1** facilitates Gly transport without binding to the carboxylate/carboxylic acid group and instead, only binds and transports OH^- while the anionic hemiaminal/imine with a carboxylate group crosses the membrane without binding to **T1**. In that case, **T1** would simply serve as a protonophore that cancelled the charge separation and pH imbalance due to the movement of anionic and basic $NH_2CH_2COO^-$. Carbonyl cyanide *m*-chlorophenyl hydrazine (CCCP),[178] which is an active protonophore but not a good hydrogen bond donor, was tested as a negative control. CCCP itself induced negligible Gly flux, and it was unable to enhance Gly transport in the presence of **T2** or **T3** (Figure 7.76, Chapter 7), indicating that **T1** needs to bind to the carboxylate/carboxylic acid group of Gly to facilitate Gly transport.

Less fluorinated aldehydes **T10**-**T12**, on the other hand, show appreciable transport activity. The aldehydes were tested at different loadings in the presence and absence of **T1**, and the fractional fluorescence intensity at 30 min was plotted against the transporter loading and subject to Hill analysis[179-180] to obtain the effective transporter loading needed to observe 50% transport at 30 min (EC_{50}) and a Hill coefficient (*n*) (Table 5.1). The *n* values close to 1 are consistent with the 1 : 1 stoichiometry for the hemiaminal or imine formed between glycine and an aldehyde, evidence in support of a mobile carrier mechanism. Similarily, the *n* value for **T1** in the presence of **T2** (10 mol%) is close to 1. The *n* values are consistent with the stoichiometry of the assumed three-component aldehyde-Gly-squaramide assembly. Without **T1**, the aldehydes, although significantly more active than the control compounds, are not particularly active. In the presence of **T1** loaded

at 1 mol% (transporter to lipid), **T2** and **T3** become reasonably active as mobile transporters with EC_{50} values at low percentage loadings. The significantly decreased activity with **T10** and little activity with **T11** are likely due to the lower electrophilicity (therefore slower rate for hemiaminal/imine formation) as well as the lower lipophilicity.

Table 5.1 Gly transport properties and calculated Log*P* values of **T1**-**T11**

Compound	EC50[a] / mol%	*n*	EC50[a] / mol%	*n*	cLogP[d]
	without **2**		with **2** (10 mol%)		
T1	~8[b]	~0.85[b]	0.1	0.96	6.94
	without **1**		with **1** (1 mol%)		
T2	56	0.94	1.9	1.1	3.58
T3	63	0.92	4.2	1.5	3.86
T4	> 100	nd[c]	> 100	nd[c]	4.06
T5	> 100	nd[c]	> 100	nd[c]	3.74
T6	> 100	nd[c]	> 100	nd[c]	3.64
T7	> 100	nd[c]	> 100	nd[c]	2.93
T8	> 100	nd[c]	> 100	nd[c]	4.28
T9	> 100	nd[c]	> 100	nd[c]	3.13
T10	47	0.88	23	1.1	2.61
T11	148	0.93	45	0.89	2.47
T12	> 100	nd[c]	> 100	nd[c]	1.64

[a] Transporter loading (transporter to lipid molar ratio) needed to observe 50% transport at 30 min.
[b] Small extent of Cu^{2+} transport found by **T1** (Figure 7.78a, Chapter 7), and therefore the values should be regarded as approximates.
[c] Not determined due to low activity.
[d] cLog*P* values calculated by ACD/Labs.

5.2.5 Transport of other substrates

The transport of other substrates, including sarcosine (Sar), *N*,*N*-dimethylglycine (DMG), oxalic acid/oxalate, and Calcein, was studied in an attempt to reveal the transport mechanism in the case of Gly transport. Sar can form hemiaminals but not imines with aldehydes. Interestingly, a mixture of **T1** (1 mol%) and **T2** or **T3** (10 mol%) promotes Sar transport synergistically (Figures 5.7a and 7.76), similarly to the results found with Gly transport. This suggests that formation of the hemiaminal is sufficient for facilitated transport of amino-containing substrates, without the

need for the dehydration step to form the imine, although it is still possible that transport by an imine intermediate is the dominant pathway in the case of Gly transport. It is also of interest to test the transport of DMG, which might form zwitterionic tetrahedral adducts[181] with aldehydes. The results (Figures 5.7b) show that DMG crosses the membrane by simple diffusion very quickly due to its lipophilicity. DMG diffusion is slightly enhanced by **T1** (1 mol%), whereas the aldehyde component does not affect the transport (Figure 5.8b and 7.77), which might be due to fast DMG simple diffusion making aldehyde-facilitated transport difficult to observe, or the inability of the aldehydes to promote the DMG transport due to the instability of the zwitterionic tetrahedral adduct.

To further confirm that the aldehyde-facilitated Gly/Sar transport is due to the aldehyde interaction with the amino group, instead of with the carboxylate/carboxylic acid group or with the squaramide **T1**, oxalic acid/oxalate transport was studied using a HPTS base pulse assay.[182-183] POPC LUVs (mean diameter 200 nm) were loaded with the pH sensitive dye 8-hydroxypyrene-1,3,6-trisulfonic acid (HPTS, 1 mM) and sodium oxalate (100 mM), suspended in an external solution containing sodium oxalate (100 mM). A pulse of NaOH (5 mM) was applied to generate a transmembrane pH gradient, and the dissipation of the pH gradient in the absence of presence of transporters was monitored. The dissipation of the pH gradient can be due to the transport of neutral oxalic acid, oxalate (or hydrogenoxalate) transport coupled to OH^- (or H^+) transport, Na^+ transport coupled to H^+ (or OH^-) transport, HEPES transport, HPTS transport or the detergent effect. As shown in Figure 5.9 and 7.80, **T1** (1 mol%) induces slow transport, while **T2** or **T3** (10 mol%) induces no transport and has little influence on the transport induced by **T1**. The HPTS response was found to be minor when the anion in both the internal and external solutions was changed from oxalate to the more hydrophilic SO_4^{2-} (Figure 7.87, Chapter 7), which proves that the HPTS response observed with the sodium oxalate system results, at least predominantly, from the transport of oxalic acid, hydrogenoxalate or oxalate. It is thus unlikely that the role of the aldehyde component in facilitating the transport of Gly/Sar is the interaction with the carboxylate/carboxylic group or “activating” the squaramide **T1**.

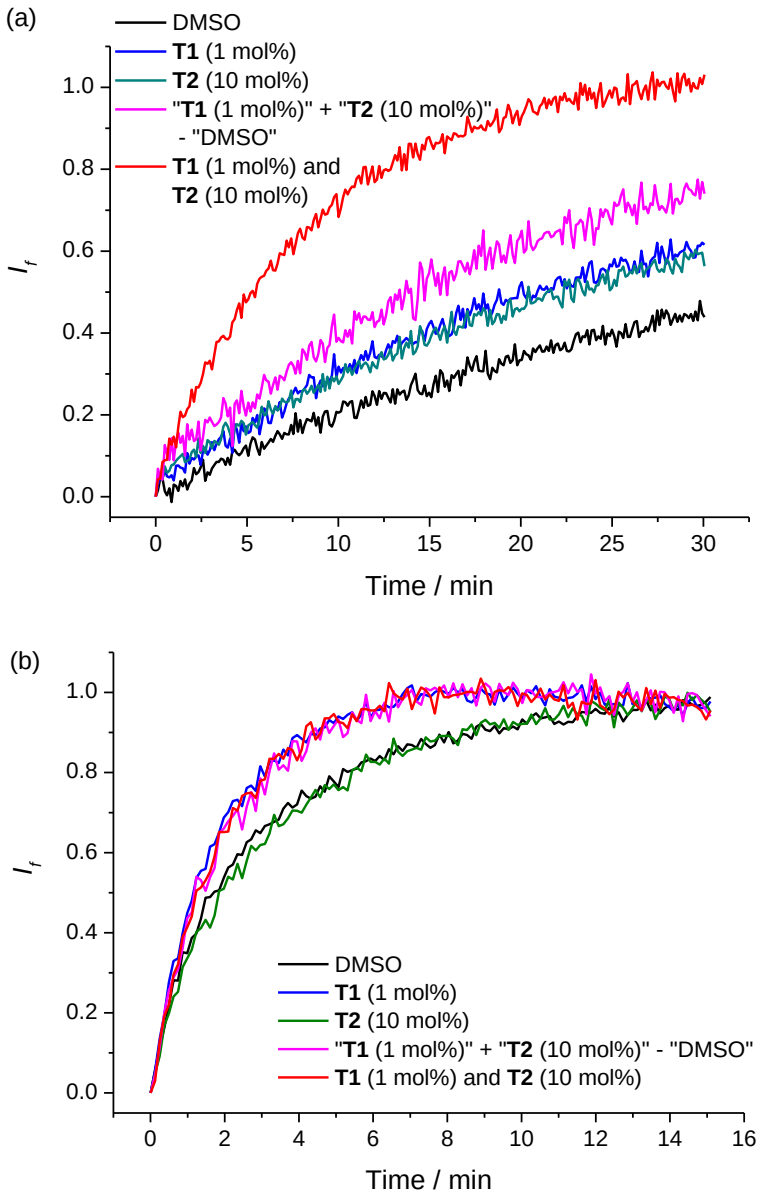

Figure 5.8 Transport kinetics of Sar (a) and DMG (b) measured by the Cu^{2+}-Calcein assay. POPC LUVs (mean diameter 200 nm) loaded with $CuSO_4$ (0.2 mM) and Calcein (0.2 mM) were suspended in an external solution containing Sar or DMG (30 mM) and $CuSO_4$ (0.2 mM). Both the internal and external solutions contained Na_2SO_4 (100 mM) and HEPES (20 mM) buffered at pH 7.4. At time 0, DMSO solutions of transporters or DMSO was added, and the fluorescence intensity (λ_{ex} = 495 nm, λ_{em} = 515 nm) was recorded. The fluorescence intensity was normalized by saturation using a mixture of **T1** (1 mol%) and **T3** (50 mol%) (a), or using the maximum fluorescence intensity over the course of the measurement (b). Transporter loadings are shown as transporter to lipid molar ratios. Note that in (b) there is a slight decrease of the fluorescence intensity after 10 min, due to the influx of Cu^{2+} ion when the DMG influx is close to completion. For a detailed discussion, see Section 7.4.6.

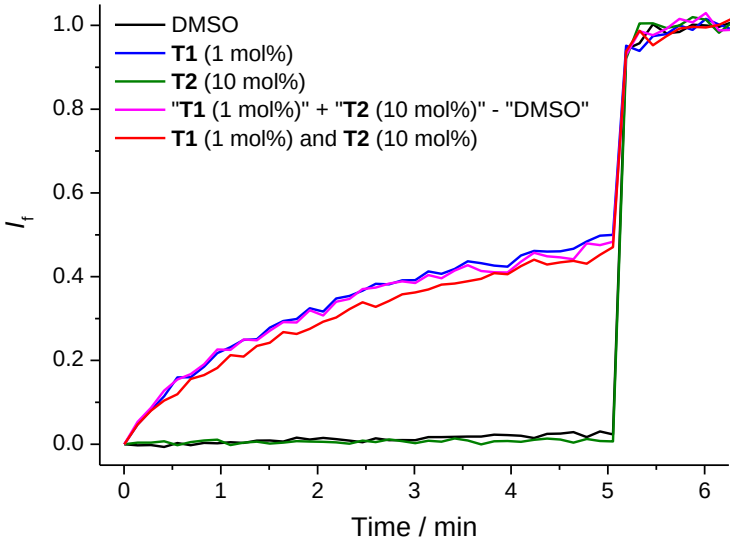

Figure 5.9 Oxalic acid/oxalate transport kinetics studied by a HPTS assay. POPC LUVs (mean diameter 200 nm) were loaded with HPTS (1 mM). Both the internal and external solutions contain sodium oxalate (100 mM) and HEPES (10 mM) buffered at pH 7.0. DMSO solutions of transporters or DMSO was added, followed by a pulse of NaOH (5 mM) at time 0, and the fluorescence ratio of HPTS (λ_{ex} = 460 nm, λ_{em} = 510 nm, base form vs λ_{ex} = 403 nm, λ_{em} = 510 nm, acid form) was recorded. The fluorescence ratio was normalized by calibration using a detergent to lyse the vesicles at 5 min.

A Calcein leakage assay[184] was also performed using POPC LUVs entrapping self-quenched Calcein dyes (100 mM), to test the integrity of the vesicle membrane. No leakage of Calcein dye was detected (Figure 7.90, Chapter 7), suggesting that Gly transport occurs with no disruption of the vesicle structure and no formation of large transmembrane pores.

A mixture of **T1** (1 mol%) and **T2** (10 mol%) was also tested to facilitate the transport of alanine (Ala) and serine (Ser). The synergistic effect between **T1** and **T2** was also observed (Figures 7.78 and 7.79). The rates of transport of the three tested amino acids with primary amino groups facilitated by the **T1**-**T2** mixture follow the order Ala ≈ Gly > Ser (Figure 5.10), which is consistent with the higher hydrophilicity of Ser.

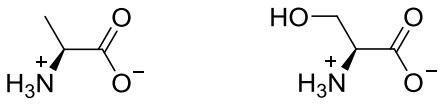

Ala Ser

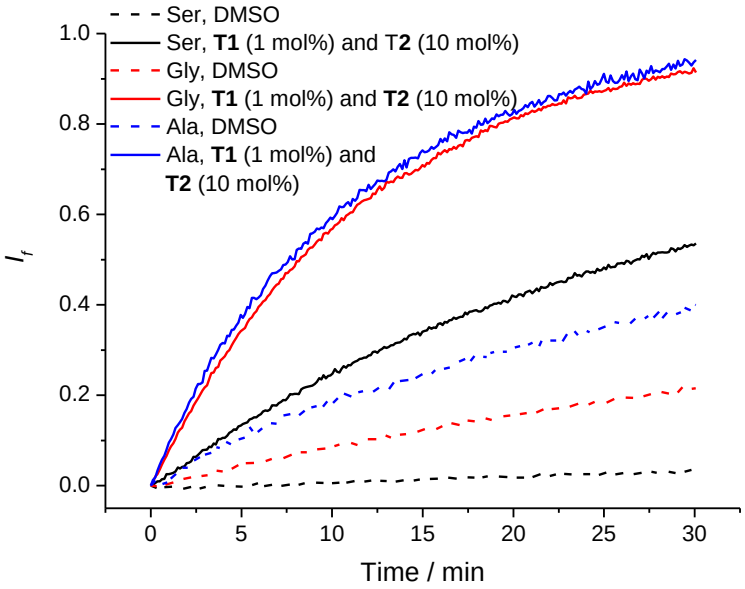

Figure 5.10 Transport kinetics of Ser, Gly and Ala measured by the Cu^{2+}-Calcein assay. POPC LUVs (mean diameter 200 nm) loaded with $CuSO_4$ (0.2 mM) and Calcein (0.2 mM) were suspended in an external solution containing the amino acid (30 mM) and $CuSO_4$ (0.2 mM). Both the internal and external solutions contained Na_2SO_4 (100 mM) and HEPES (20 mM) buffered at pH 7.4. At time 0, DMSO solutions of transporters or DMSO was added, and the fluorescence intensity (λ_{ex} = 495 nm, λ_{em} = 515 nm) was recorded. The fluorescence intensity was normalized by saturation using a mixture of **T1** (1 mol%) and **T3** (50 mol%). Transporter loadings are shown as transporter to lipid molar ratios.

5.2.6 ^{1}H NMR studies

The ability of the aldehyde component to form hemiaminals or imines was examined using a biphasic experiment. A $CDCl_3$ solution of **T2** (10 mM) was mixed with an aqueous solution of Gly (or Sar, 1 M) and tetrabutylammonium (TBA) salt of Gly (or Sar) anion (1 M). After vortexing of the mixture for 5 min, the $CDCl_3$ phase was subject to ^{1}H NMR measurements. The use of a Gly-TBAGly or Sac-TBASar mixture instead of TBAGly or TBASar alone is to prevent the aqueous solution from being too basic thus reducing undesired side reactions. With the Gly-TBAGly system (Figure 5.11, upper panel), both hemiaminals and imines can be observed in the ^{1}H NMR spectra of the $CDCl_3$ phase, along with the free aldehyde, the hydrate and the carboxylate that results from aldehyde oxidation under basic conditions. The Gly hemiaminal shows the CH proton resonance at δ = 5.45 ppm and two doublets for the methylene proton resonances between δ = 3.45 ppm and δ = 3.65 ppm which indicates the creation of a tetrahedral stereocenter. The Gly imine shows its CH proton resonance at 8.35 ppm which overlaps with the peak from one set of aldehyde aromatic protons, and a singlet peak for the methylene protons at δ = 4.37 ppm. With the Sar-TBASar system (Figure 5.11, lower panel), the hemiaminal is formed and shows also two doublets for the diastereotopic methylene protons. It is interesting to note that hemiaminals are normally not observed due to the instability. The presence of the hemiaminals observed in the current systems results from the high electrophilicity of the aldehyde carbonyl group due to the presence of two electron withdrawing trifluoromethyl groups. The coexistence of the hemiaminal and the imine in the case of Gly-TBAGly-**T1** system might suggest that Gly transport facilitated by aldehydes could occur by a mixture of hemiaminal and imine intermediates, although currently there has been no direct evidence for that hypothesis. When the aqueous phase contains only Gly

or Sar (2 M), no hemiaminal or imine is detectable in the $CDCl_3$ phase (Figure 7.91, Chapter 7), which is consistent with the reported low equilibrium constants for the formation of protonated hemiaminals[165] (**H2** and **H3** in the case of Gly) and protonated imines[185] (**I2** and **I3**) without stabilization by an intramolecular hydrogen bond.[186]

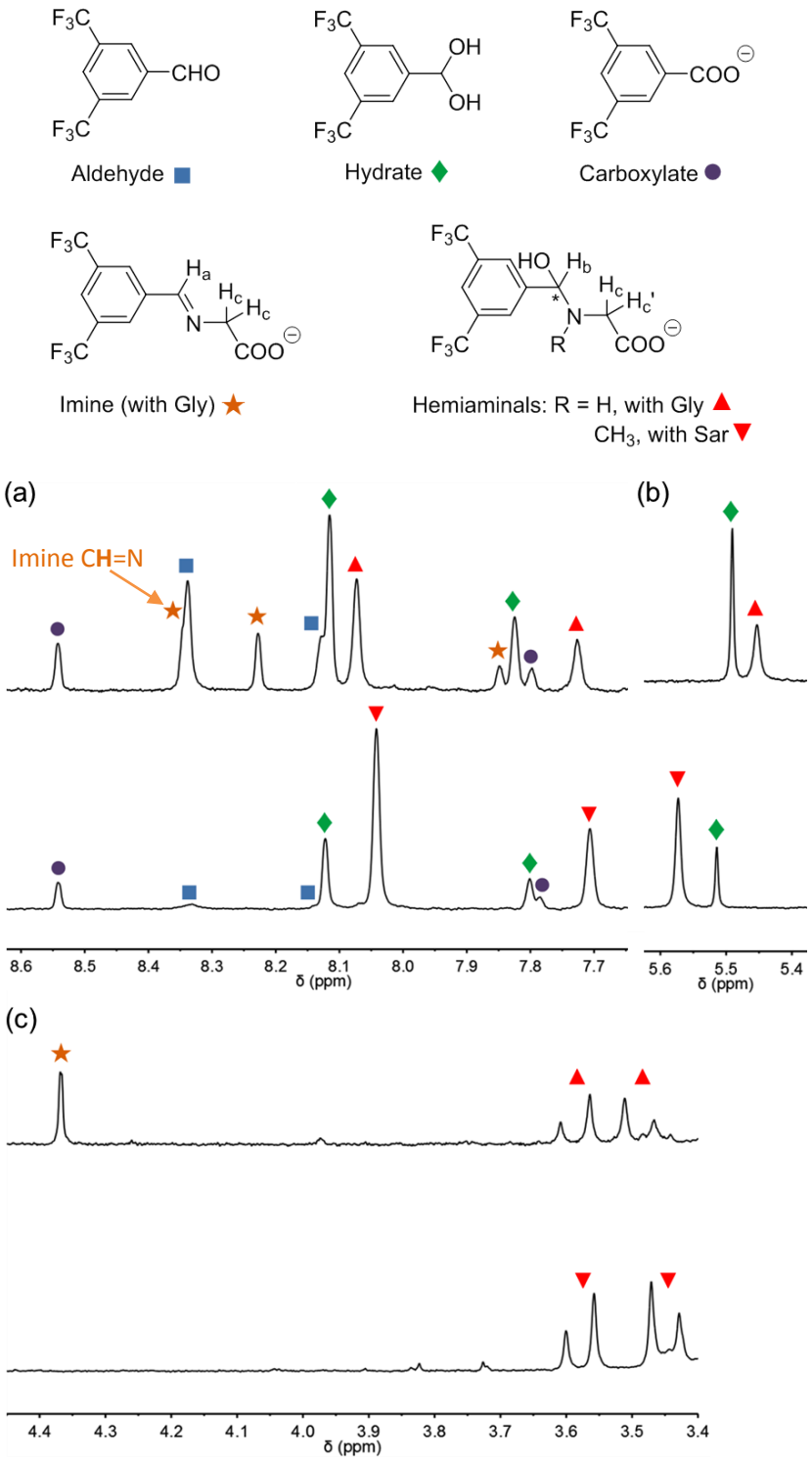

Figure 5.11 Partial ^{1}H NMR spectra (400 MHz) of $CDCl_3$ solutions of **T1** (10 mM) after treatment with an aqueous solution containing a mixture of Gly (1 M) and TBAGly (1 M) (upper panel), or Sar (1 M) and TBASar (1 M) (lower panel). (a) Downfield region showing aromatic protons and the imine CH proton H_a (labeled); (b) Midfield region showing CH protons (H_b) of the hemiaminals and the hydrate; (c) Upfield region showing methylene protons (H_c) of the hemiaminals and the Gly imine.

5.2.7 Transport mechanism

The Gly transport mechanism was examined using vesicles of different lipid compositions. The transport activity was found to decrease very slightly with POPC-cholesterol (7 : 3, molar ratio) LUVs (mean diameter 200 nm) compared to that with POPC LUVs (mean diameter 200 nm) (Figure 7.79, Chapter 7). Cholesterol is known to decrease the fluidity of the lipid membrane in the liquid phase, thus decreasing the activity of a mobile transporter.[187] However, enhanced partition of a lipophilic transporter by cholesterol[144] could also occur. The observed minor influence of cholesterol is possibly a result of both effects. With dipalmitoylphosphatidylcholine (DPPC) LUVs (mean diameter 200 nm) (Figure 7.80, Chapter 7), Gly transport was suppressed at 37 °C which is below the main phase transition temperature of 41 °C, while switched on at 45 °C, which might support a mobile carrier mechanism. The transport activity of the squaramide-aldehyde mixtures decreased markedly in LUVs (mean diameter 200 nm) of an anionic lipid 1-palmitoyl-2-oleoyl-sn-glycero-3-phosphoglycerol (POPG) as compared to POPC LUVs (mean diameter 200 nm) (Figure 7.81, Chapter 7), which is consistent with the transport of an anionic species that experiences electrostatic repulsion with the anionic lipid head group,[148] although binding of **T1** to anionic head group of POPG could also account for the decreased activity. These results, together with the Hill coefficients (Table 5.1), absence of nonspecific leakage and also the small size of the tested aldehydes support a mobile carrier mechanism for the observed facilitated Gly transport. Transport by a zwitterionic hemiaminal (**H2**) or imine (**I2**)is not favorable, because of the relative instability of the adducts when the hemiaminal nitrogen[165] or imine nitrogen[185-186] is protonated as compared to the deprotonated species (**H1** and **I1**), and also the hydrophilicity of the zwitterionic species. Therefore the transport facilitated by the squaramide-aldehyde mixtures is proposed to occur *via* the anionic aldehyde-glycine hemiaminal (**H1**) or imine (**I1**) with the negatively charged carboxylate group hydrogen bonded to **T1** (Figure 5.12 showing the hemiaminal pathway). Interestingly, the loss of activity in POPG vesicles is not observed with high concentration of aldehyde transporters without **T1** (Figures S24c and S24d), suggesting that in this case, the transported species is most likely the neutral aldehyde-glycine adduct (whether hemiaminal **H3** or imine **I3**), although it is less stable than the anionic adducts which might partly account for the lower transport activity of aldehydes when **T1** is absent. Similarly, the anionic vesicles did not decrease the rate of simple diffusion of Gly (Figure 7.81, Chapter 7), consistence with reported assignment of the simple diffusion to movement of the zwitterionic species through bilayer fluctuations and transient defects, or partitioning of the neutral H_2NCH_2COOH which is in equilibrium with the zwitterionic species.[188]

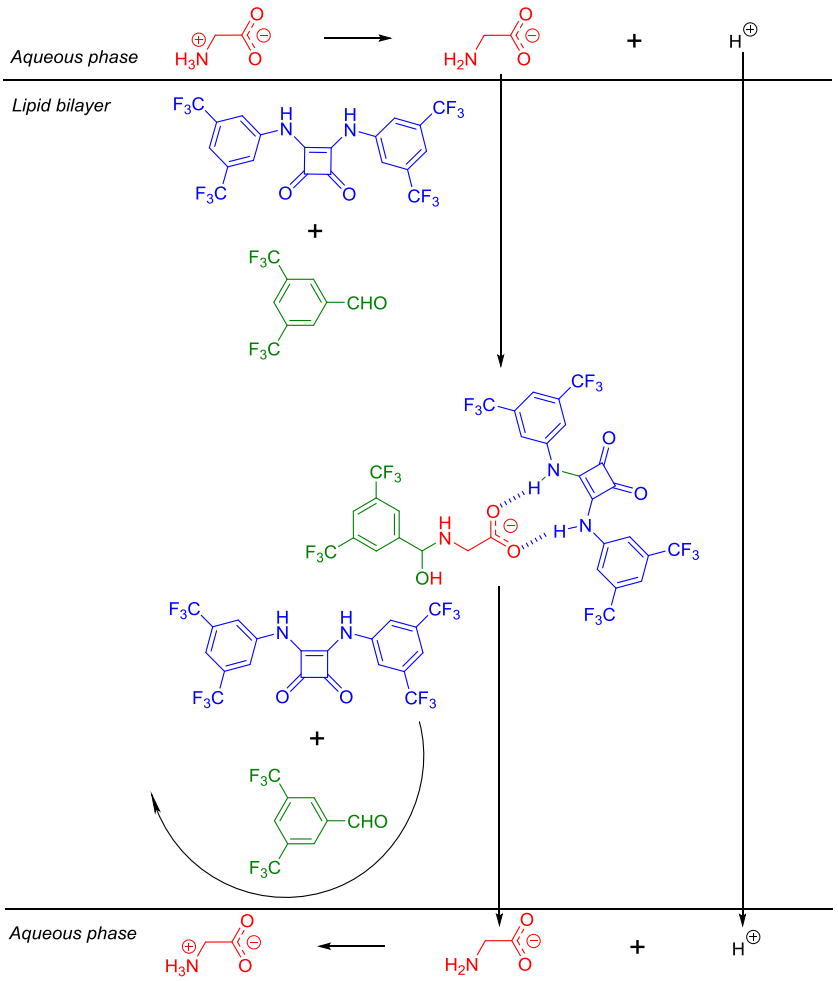

Figure 5.12 Proposed mechanism for Gly transport facilitated by **T1** and **T2** forming a three-component assay involving hemiaminal formation.[a] H^+ transport is facilitated by **T1**, which is not shown in details (refer to Figure 6.8a).

The movement of the anionic form of Gly facilitated by a squaramide-aldehyde mixture would need to be accompanied by co-transport with a cation or antiport with an anion. The dominant cation and anion present in the system are Na^+ and SO_4^{2-}, respectively. Because of the basicity of the Gly anion (pK_a of Gly ammonium group is 9.60), co-transport with Na^+ or antiport with SO_4^{2-} or HSO_4^- would lead to intravesicular basification. However, a HPTS assay (Figure 7.88, Chapter 7) shows that the internal pH change induced by 30 mM Gly is negligible (< 0.05 pH unit, with 5 mM HEPES buffer at pH 7.4) induced by Gly (30 mM), indicating $H^+/H_2NCH_2COO^-$ symport (Figure 5.11) or functionally equivalent $H_2NCH_2COO^-/OH^-$ antiport, the net result being transport of the overall neutral Gly. Given the ability of **T1** to function as a protonophore by deprotonation (pK_a = 8.4 in DMSO) seems more plausible to describe the transport as a $H^+/H_2NCH_2COO^-$ symport.

5.3 Conclusions

In summary, a dynamic covalent bond and a non-covalent interaction were combined in the design of transmembrane transport system for amino acids. A dynamic three-component assembly involving the squaramide hydrogen bonding to the Gly carboxylate group and an aldehyde forming a hemiaminal or a imine linkage with the Gly amino group is assumed responsible for reversibly binding and releasing Gly in the lipid bilayers. The transport process is proposed as $H_2NCH_2COO^-/OH^-$ antiport. Several negative control experiments and a biphasic ^1H NMR study support the role of aldehyde carbonyl group addition in the facilitated transport. Although it is currently not confirmed whether Gly transport facilitated by aldehydes proceeds *via* a hemiaminal or an imine intermediate, or *via* both pathways, the ability of hemiaminal formation to facilitate membrane transport has been revealed by the observation of Sar transport facilitated by a squaramide-aldehyde mixture working in a synergistic manner. Thus hemiaminal formation has been demonstrated as a new interaction for facilitated membrane transport. This might have implications for transmembrane delivery of larger cargos that contain primary or secondary amine groups. A rapid and easy fluorescence assay for amino acid transport has been developed that allows monitoring of fast transport kinetics. This assay is suitable for amino acid transporters that do not transport Cu^{2+}, which can be easily identified.

Chapter 6: Development of Valinomycin-like Chloride Ionophores Selective Against Proton/Hydroxide Transport

6.1 Introduction

6.1.1 Naturally occurring and synthetic ionophores

Biological membranes consist of lipid molecules whose hydrocarbon chains form a low-dielectric interior that prevents passage of small ionic species. In biological systems, the membrane-embedded protein channels and carriers are responsible for facilitating and regulating ion transport, either by actively pumping ions against their electrochemical gradient with energy provided by ATP hydrolysis, or facilitating passive ion diffusion. Ionophores represent an abiologcial means of overcoming the energy barrier for ions to cross the membrane. They are molecules capable of carrying ions across the membrane by reversibly forming lipid-soluble ion complexes. Alternatively, ion channels provide another mechanism to facilitate ion passage and conductance through lipid bilayers. This chapter only focuses on study and discussion of carrier-type ionophores. The first known examples of ionophores are small molecules secreted by microorganisms that can permeablise lipid bilayers towards biologically important cations.[189] They were first identified through their ability to modulate bioenergetic processes in mitochondria.[189] Synthetic, abiotic ionophores that facilitate the transport of cations,[190] anions[191-192], salts[139, 193] and protons[194] have been developed as well. In biological systems, ion transport processes, regulated by membrane-embedding protein channels or carriers, maintain important cellular and intracellular properties including electric potential, pH gradient and cell volumes.[195] Ionophores are important research tools due to the ability to modify these properties.[189] In addition, therapeutic applications of ionophores have been proposed.[134, 149] Here the functions of a few representative examples of well characterised ionophores are described. I emphasize important difference between electrogenic and electroneutral ionophores, exemplified by valinomycin and monensin respectively.

Valinomycin

Valinomycin (Val) is a naturally occurring cyclic oligopeptide that can facilitate membrane conductance of K^+, Rb^+ and Cs^+. These alkali ions can be encapsulated by valinomycin via coordination by six carbonyl groups, forming a lipophilic cationic complex that readily partitions into the lipid bilayer.[196] Na^+ ion, in contrast, cannot fit into the cavity of valinomycin, enabling the biologically relevant $K^+ > Na^+$ selective transport to be achieved. The ionophoric activity of valinomycin was first realised through its ability to uncouple oxidative phosphorylation[197] by dissipating the electric potential ($\Delta\Psi$) of the proton motive force (PMF) through K^+ transport, converting proton gradient (Δp) to a pH gradient (ΔpH).[189] The cycle of K^+ movement facilitated by valinomycin is shown in Table 6.1. This cycle consists of four steps: formation of the valinomycin·K^+ complex at the lipid-water interface, translocation of the complex through the lipid bilayer, dissociation of the complex at the lipid-water interface, and translocation of the free valinomycin backwards. Kinetic analysis revealed that the last three steps have comparable rates.[198] Note that the cycle results in the translocation of a net charge across the membrane, *i.e.*, an electrogenic process that leads to the diffusion of K^+ down its electrochemical gradient. Due to the electrogenic nature, valinomycin has been frequently used in K^+ containing media to modify the transmembrane electric potential. [189]

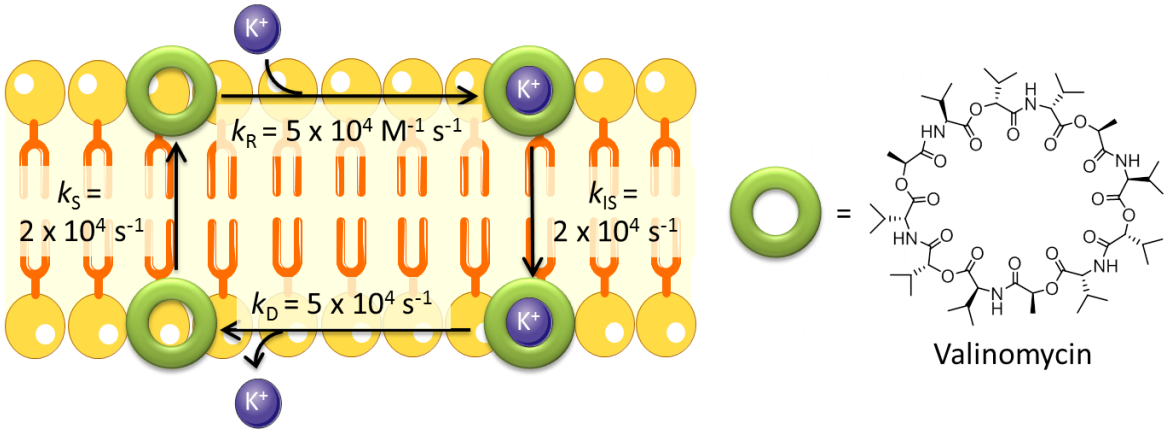

Figure 6.1 Electrogenic K^+ transport facilitated by valinomycin. The rate constants of association, complex translocation, dissociation, and free valinomycin translocation are denoted by k_R, k_{IS}, k_D, and k_S, respectively. The values shown were determined with a phosphatidylinositol membrane.[198]

In addition to its well-known $K^+ > Na^+$ selectivity, valinomycin exhibits another important selectivity, $K^+ > H^+$ selectivity. This was revealed in the membrane transport assays showing no occurrence of K^+/H^+ exchange in the presence of valinomycin alone, but rapid K^+/H^+ exchange in the presence of both valinomycin and a protonophore.[199] The inability to facilitate H^+ transport sets valinomycin apart from the channel forming molecule gramicidin which can facilitate K^+/H^+ exchange in addition to K^+ transport.[199] Other ionophores that facilitate alkali metal ion transport without proton transport include enniatin and actin homologues, but unlike valinomycin they are not particularly selective for K^+ over Na^+.[189]

Monensin

Compared with valinomycin, monensin (Mon) is a completely different class of cationophore that facilitates electroneutral exchange (antiport) of metal ion for proton or another metal ion, but with negligible activity in facilitating electrogenic metal ion transport.[200] Figure 6.2 shows the cycle of monensin facilitated M^+/H^+ exchange. The process is electroneutral in that no transfer of net charge occurs. With a deprotonated carboxylate group, the zwitterionic monensin-M^+ complex crosses the membrane as a charge-neutral species. After releasing M^+ at the lipid-water interface, the anionic species Mon^- cannot diffuse back and hence monensin cannot facilitate electrogenic transport of M^+. Instead, the protonated, neutral form MonH diffuses back to complete an M^+/H^+ antiport cycle. Due to the abovementioned transport mechanism, the final equilibrium of monensin-facilitated transport is pH-dependent whereas independent of the transmembrane electric potential.[189] Another example of electroneutral M^+/H^+ exchanger is nigericin, although nigericin can facilitate electrogenic processes at higher concentrations.[201]

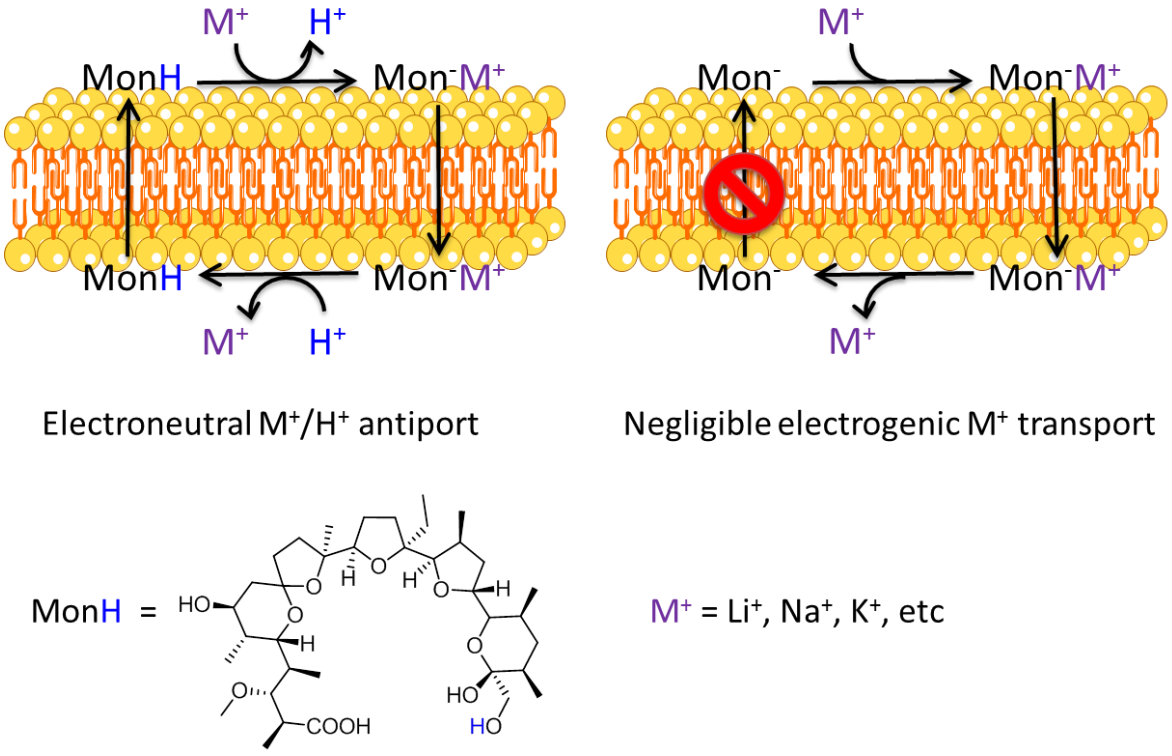

Figure 6.2 Electroneutral M^+/H^+ exchange facilitated by monensin and inability of monensin to facilitate electrogenic M^+ transport.

Protonophores

Protonophores are ionophores capable of facilitating electrogenic transport (i.e. conductance) of proton across the membrane (Figure 6.3). Most known protonophores are lipophilic weak acids whose deprotonated forms feature a delocalised negative charge enabling its lipid solubility.[194] Examples include carbonyl cyanide-*p*-trifluoromethoxyphenylhydrazone (FCCP),[178] carbonyl cyanide m-chlorophenyl hydrazine (CCCP),[178] and 2,4-dinitrophenol (DNP)[202]. Protonophores are known to be uncouplers of oxidative phosphorylation. In mitochondria, as protonophores increase the permeability of mitochondria inner membranes towards H^+, the energy from the proton motive force is dissipated into heat, instead of being used to drive ATP synthesis. [203]

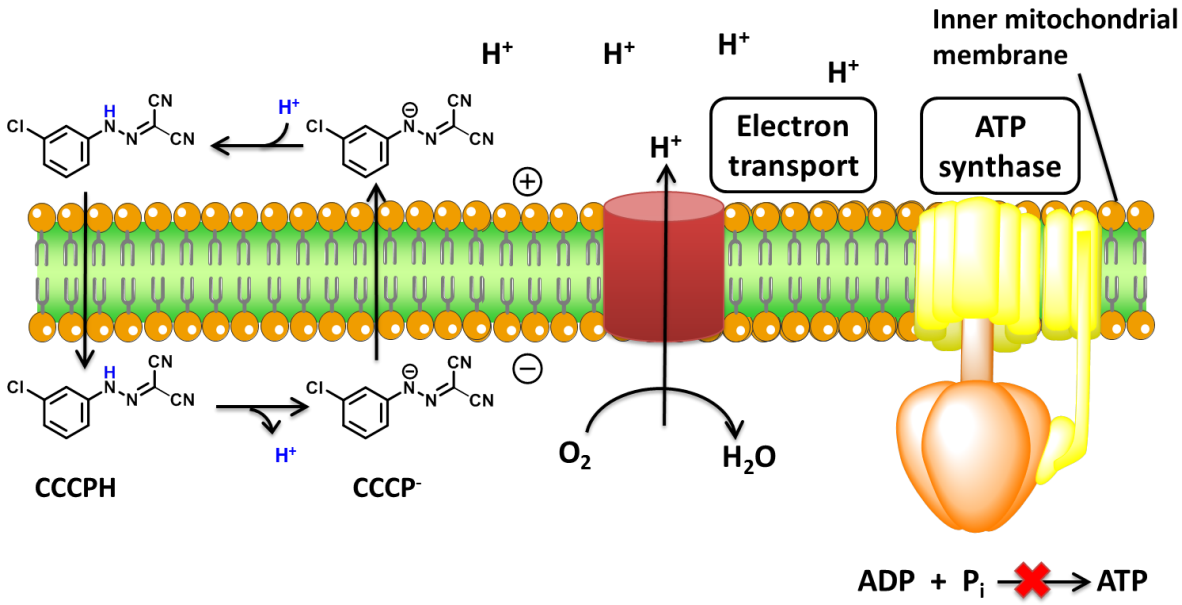

Figure 6.3 Electrogenic H^+ transport facilitated by protonophore CCCP, leading to uncoupling of oxidative phosphorylation.

Prodigiosin

While many naturally occurring cationophores are available for use in biological research, there are only a few known examples of naturally occurring anionophores. The best known anionophore is prodigiosin (Prod), a red pigment produced by Streptomyces and Serratia. Prodigiosin is able to uncouple the of vacuolar H^+-ATPase (V-APTase), inhibiting acidification of vacuolar organellesorganelles (including Golgi apparatus, lysosomes and endosomes) by promoting H^+/Cl^- cotransport (symport).[141, 204-205] Figure 6.4 shows its mechanism of action on lysosomes. In the lysosomal membrane, V-APTase actively pumps H^+ into the lysosome interior harnessing the energy from ATP hydrolysis. The electric potential from the H^+ gradient is dissipated by the ClC-7 H^+/Cl^- antiporter[206], leading to acidification (pH ~5) of the lysosome interior which is necessary for the functioning of the digestive enzymes.[207] Prodigiosin facilitates

electroneutral H^+/Cl^- symport and thereby dissipates the pH gradient. Similarly, monensin also neutralises acidic cellular compartments by promoting Na^+/H^+ exchange.[208] Sato *el al.* suggested that the effect of prodigiosin is electroneutral, as judged from the observation that the rate of pH gradient dissipation in liposome-based experiments is unaffected by the presence of an electric potential generated by valinomycin-K^+.[141] This is consistent with the inability of prodigiosin to disrupt the electric potential in lysosomes or alter cellular ATP levels,[204] suggesting that prodigiosin is unable to function as a protonophore (see Figure 6.5d and Section 6.2.1).

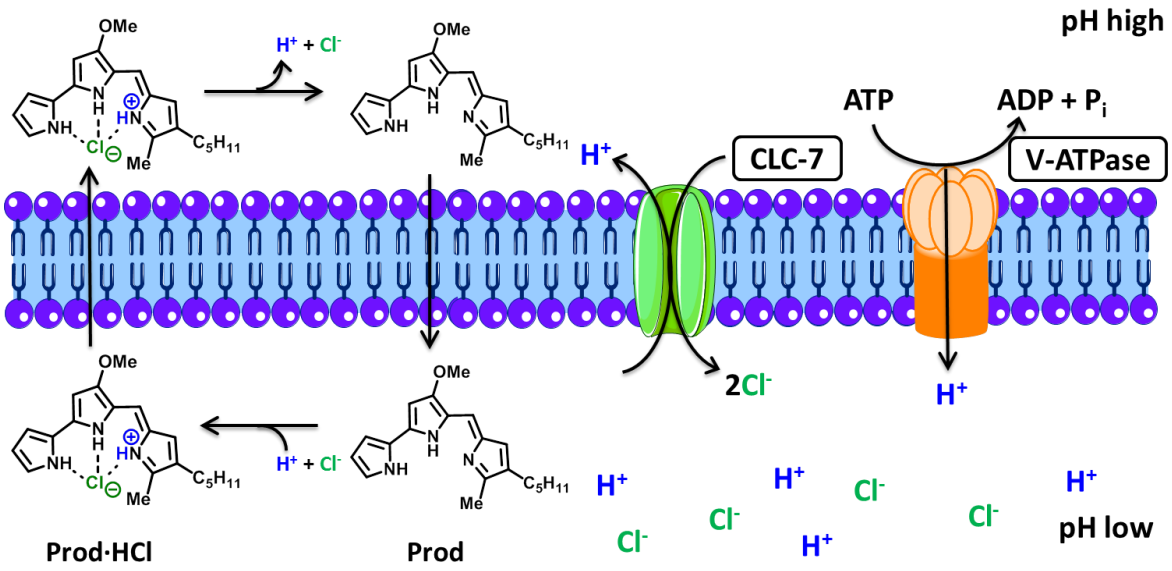

Figure 6.4 Mechanism of liposomal pH gradient dissipation induced by prodigiosin (Prod).

J. T. Davis and coworkers further studied the ionophoric properties of prodigiosin in liposome-based experiments, and reported that prodigiosin also functions as a Cl^-/NO_3^- exchanger.[209] Activity in Cl^-/NO_3^- exchange, however, does not indicate activity in electrogenic chloride transport, as Cl^-/NO_3^- exchange does not require dissociation of the complex into protonated prodigiosin and translocation of this species as required by an electrogenic mechanism (Figure 6.5). Recently, prodigiosin was employed in a biological study in which prodigiosin seems to be regarded as an electrogenic chloride transport,[210] so its mechanism needs to be clarified. Evidence is provided in this chapter that prodigiosin cannot facilitate electrogenic transport of chloride (see Figure 6.5d and Section 6.2.3) and therefore should not be regarded as a "valinomycin for chloride".

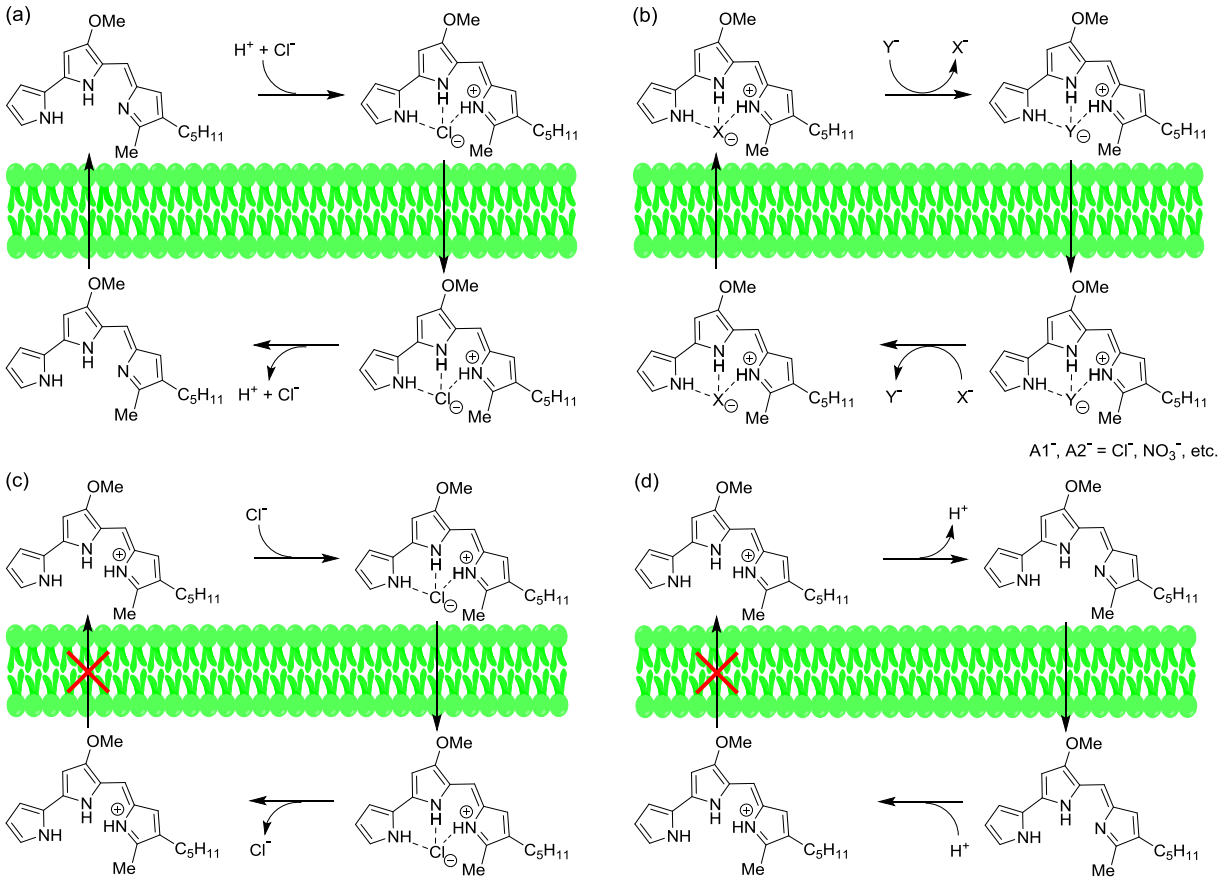

Figure 6.5 (a) Electroneutral H^+/Cl^- symport facilitated by prodigiosin; (b) Electroneutral anion exchange (*i.e.*, Cl^-/NO_3^- antiport) facilitated by prodigiosin; (c) Inability of prodigiosin to facilitate electrogenic Cl^- transport; (d) Inability of prodigiosin to facilitate electrogenic H^+ transport.

6.1.2 Ion transport assays

The activity, ion selectivity, ion transport mechanisms of ionophores are generally assessed by either liposome-based experiments or electrophysiology methods. This section describes several methods that can be used to study anionophores, and analyse their respective advantages and drawbacks.

Ion selective electrode (ISE)

Ion selective electrode (ISE) methods monitor ion transport process across liposome membranes by measuring the concentration of an ionic species that is transported from inside the vesicles to the external media. ISE methods allow easy calculation of the percentage of ion efflux as the ion concentration corresponding to 100% efflux can be measured after lysing the vesicles with detergents. In general, the ionic species measured needs to be removed from the external media. Most commonly, to evaluate anion transport activities of anionophores, assays using a chloride selective electrode are set up for Cl^-/NO_3^- exchange to occur.[138] Anionophores with $Cl^- > NO_3^-$ selectivity (*e.g.* metal complexes[150]), however, are underestimated for chloride transport activity

in this assay. Moreover, Cl^-/NO_3^- exchange experiments do not indicate whether an anionophore can facilitate electrogenic anion transport, as exemplified by prodigiosin (Figure 6.5) which is a very active Cl^-/NO_3^- exchanger but cannot facilitate electrogenic anion transport. Alternatively, Cl^-/cation cotransport can be studied, usually by using a combination of an anionophore and cationophore.[211]

Lucigenin assay

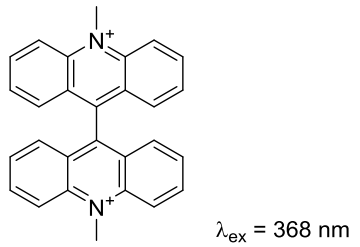

Figure 6.6 Structure and fluorescence emission property of lucigenin.

Lucigenin (Figure 6.6) is a membrane impermeable (over the time scale of several hours) fluorescence dye, whose fluorescence emission can be quenched by halide ions but is insensitive to oxoanions such as nitrate, sulfate, and phosphate.[212] Lucigenin assays have been devised for monitoring chloride transport across vesicle membranes.[213] Alternatively, 6-methoxy-*N*-(3-sulfopropyl)quinolinium (SPQ) can be used. In general, influx or efflux of chloride is monitored based on the fluorescence intensity of lucigenin loaded inside vesicles. An advantage of this assay is that the ionophore can be pre-incorporated into the lipid bilayer, and chloride flux can be triggered by adding chloride to the vesicle suspension. This allows studying of ionophores that cannot be delivered to the vesicle membrane by external addition to prepared vesicle suspensions. Most commonly, Cl^-/NO_3^- exchange study is performed, which has the same limitations as stated in the previous paragraph.

HPTS assays

8-Hydroxypyrene-1,3,6-trisulfonic acid (HPTS) is a membrane impermeable fluorescence dye that can monitor intravesicular or intracellular pH by ratiometric fluorescence emission (Figure 6.7a).[183] Matile and coworkers have developed liposome-based HPTS assays that indirectly measures cation or anion transport.[182] An obvious advantage of this assay is that the scope of ionic species that can be studied is not limited to those that can be detected by electrochemical or optical methods. Briefly, a transmembrane pH gradient is applied to vesicle suspensions prepared in lightly buffered solutions containing a salt component (MX). Ion transport is monitored as dissipation of the pH gradient, which requires (i) movement of H^+ or OH^- that is directly responsible for pH change (ii) counterion (M^+ or X^-) movement that accompanies H^+/OH^- transport to maintain electroneutrality of the bulk solutions. The net process can be any of the

following, induced by an ionophore: M^+/H^+ antiport, M^+/OH^- symport, X^-/OH^- antiport, and X^-/H^+ symport. Note that H^+ and OH^- transports are functionally equivalent and thus indistinguishable (*e.g.*, M^+/H^+ anitport cannot be distinguished from M^+/OH^- symport). However, it is easy to identify whether cation transport (including M^+/H^+ antiport and M^+/OH^- symport) or anion transport (including X^-/OH^- antiport and X^-/H^+ symport) is the "counterion pathway". A straightforward method is to use highly hydrophilic ions that are not likely to be transported by the tested ionophores as negative controls. Examples of highly hydrophilic ions include *N*-methyl-D-glucammonium ($NMDG^+$) as a control for cation transport, and gluconate or sulfate as a control for anion transport. For instance, dissipation of pH gradient observed when NaCl, but not Na-gluconate, is used as the medium identifies that Cl^-/OH^- antiport or Cl^-/H^+ symport, instead of Na^+/H^+ antiport or Na^+/OH^- symport, is responsible for the HPTS response. Other less likely processes that might lead to HPTS responses, such as HPTS transport, causing membrane defects, detergent effect and ionophore interference with HPTS fluorescence are easy to identify.

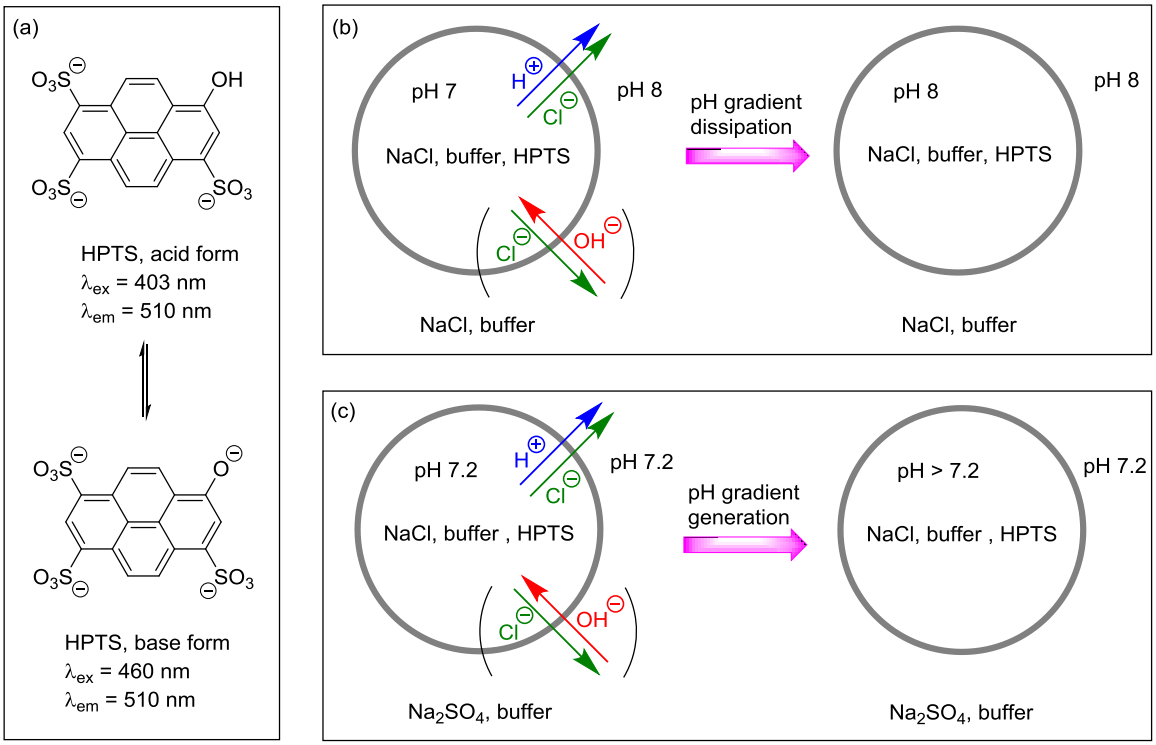

Figure 6.7 (a) Structures and fluorescence emission properties of acid and base forms of HPTS; (b) HPTS assay based on pH gradient dissipation. Initially a pH gradient is present and the internal and external NaCl concentrations are the same. Cl^-/OH^- antiport or H^+/Cl^- symport facilitated by the tested anionophore leads to dissipation of an existing pH gradient. (c) HPTS assay based on pH gradient generation. Initially, a Cl^- concentration gradient is present with no pH gradient. Cl^-/OH^- antiport or H^+/Cl^- symport facilitated by the tested anionophore leads to basicification of the internal solution, generating a pH gradient. Note that in both (b) and (c) the external pH does not change significantly as the volume of the external solution is much larger that the internal volume.

HPTS assays based on pH gradient dissipation (Figure 6.7b) have been routinely used to evaluate anion transport activity.[148, 150] However, as will be demonstrated by the present study, some anionophores show Cl^- > H^+/OH^- selectivity, in which cases the chloride transport activity is

underestimated by measuring the rate of Cl^-/OH^- antiport or Cl^-/H^+ symport. To overcome this drawback, it is suggested here to use a combination of the tested anionophore and a proton transporter (*e.g.* proton carrier CCCP or channel gramicidin. Note that gramicidin cannot be used in the presence of monovalent alkali metal ions such as Na^+ and K^+. $NMDG^+$ can be used as the cation component when gramicidin is used.) so that the rate of pH gradient dissipation will not be limited by H^+/OH^- transport.

As an alternative to measuring pH gradient dissipation, assays based on generation of a pH gradient from an ion concentration gradient (Figure 6.7c) have been employed to demonstrate the existence of Cl^-/OH^- antiport or Cl^-/H^+ symport.[138, 214] In these assays, a chloride concentration gradient (typically with chloride inside and sulfate outside, or the other way around) is applied to vesicles with the same internal and external pH. If an anionophore facilitates Cl^-/OH^- antiport or Cl^-/H^+ symport, a chloride concentration gradient will give rise to a pH gradient detectable via HPTS fluorescence.

NMR assays

NMR-based membrane transport assays distinguish between intra-vesicular and extra-vesicular species by employing a membrane impermeable paramagnetic shift reagent that is either loaded inside vesicles or added to the external medium. The shift reagent induces broadening and/or shifting of the NMR resonance of the species of interest in the same aqueous pool, but does not affect the species separated from the shift reagent by lipid bilayers. This allows transmembrane movement of the species of interest to be monitored using NMR. An example is using Co^{2+} to detect chloride transport with ^{35}Cl NMR spectroscopy.[146] However, NMR assays may not be suitable for measuring rapid membrane transport processes due to the requirement of a relatively long acquisition time for each spectrum.

Osmotic response assays

Though currently underexploited by supramolecular chemists, osmotic response assays are convenient methods that can be used to study membrane transport of any neutral or ionic species. These assays rely on the morphological changes of vesicles due to osmotic movement of water following membrane transport of solute molecules/ions. In a typical experimental setup, the species to be transported is encapsulated at a high concentration (*e.g.* 300 mM) in vesicles (usually with a mean diatemer of 400 nm). The vesicles are suspended in an external isoosmotic solution of an inert, membrane-impermeable solute. Initiation of efflux of solute inside vesicles results in water efflux to balance the osmotic pressure, leading to vesicle shrinkage and thereby increase of 90° light scattering that can be conveniently monitored by a fluorimeter. To study

anionophore-facilitated anion transport, a cationophore (*e.g.* valinomycin) can be used in combination with an anionophore to induce salt efflux.[177] Despite the wide applicability of osmotic response assays, they may not be sufficiently sensitive for accurately quantifying the rate of membrane transport. It requires attention that sometimes an increase of light scattering can result from aggregate or precipitate formation due to the addition of compounds.

Electrophysiology recordings

Electrophysiology methods, including planar lipid bilayer and patch clamp techniques, measure the rate of ion transport as an electric current across artificial lipid bilayer membranes painted on a hole (planar lipid bilayer) or intact cell membranes attached to the end of a pipette (patch clamp).[215] Unlike liposome-based transport assays that measure overall electroneutral processes (although electrogenic processes can be indirectly studied), electrophysiology recordings respond to electrogenic ion transport processes. Other advantages include enabling unproblematic measurement of ion selectivity[137] and distinguishability between channel and carrier mechanisms.[216]

6.1.3 Development of synthetic anionophores

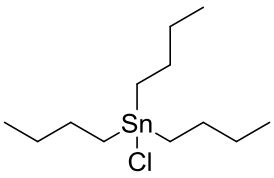

tributyltin chloride (TBT)

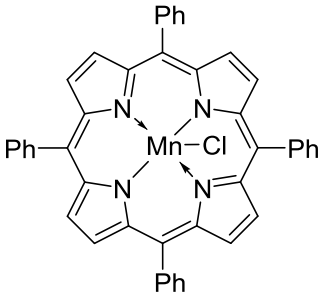

Mn(TPP)Cl

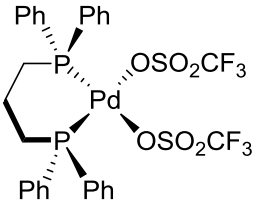

6-1

Although recent research efforts in developing synthetic anionophores have mostly focused on hydrogen bond receptors, quite surprising, the first generation of synthetic anionophores known to mediate anion transport in lipid bilayers are Lewis acidic organometallic compounds that form dative covalent bonds with anions. Those compounds were initially reported as ionophores used in potentiometric sensors for chloride[217] and their ability to facilitate anion across lipid bilayer membranes was later studied. Tributyltin chloride and other trialkyltin chlorides[218] were reported to dissipate pH gradient generated during active respiration in proteoliposomes, via electroneutral exchange of internal OH^- with external SCN^-, I^- or Cl^-. Tetraphenylporphyrin-Mn(III)-Cl complex (Mn(TPP)Cl) was found to induced anion conductance in mouse lung epithelial cells and anion transport in adenocarcinomic human lung epithelial (A549) cells.[149] Very recently, Pd(II) complex **6-1** was reported as a new metallo-anionophore.[150] **6-1** was able to facilitate anion/OH^- exchange, with significant selectivity for halide ions (Br^-, I^- and Cl^-) over oxoanions (NO_3^- and ClO_4^-) as shown in HPTS assays. The use of strong dative covalent bonds as shown in those examples is a working approach for designing anion transporters, as anion binding can occur effectively even in the aqueous phase. However, it is demonstrated experimentally in Section 6.2.2 that metallo-anionophores are not suitable for designing $Cl^- > OH^-$ selective transporters, as they interact favourably with hydroxide ion, as exampled by Mn(TPP)Cl which readily dissipates the pH gradient by Cl^-/OH^- exchange and shows no $Cl^- > OH^-$ selectivity.

Anion binding with sufficiently strong to allow operation in the aqueous phase is not a requirement for anion transport. Interfacial binding by weak hydrogen bond donors (compared with metal complexes) is sufficient for facilitating the movement of anions across lipid membranes. In fact, the use of hydrogen bond donors is arguably the most efficient approach in the design of anionophores, to which class the most active anionophores ever reported belong to. Lipophilic anion receptors featuring hydrogen bond donors such as ureas,[146] thioureas,[219] amides,[145] pyroles,[220] diols,[221] catechols[214] and squaramides[144] have been shown to function as anion carriers. It has been well established that anion transport activity depends on several

factors including receptor lipophilicity,[222] anion binding affinity,[223] and the extent of anion encapsulation.[224] A sufficient extent of lipophilicity is important to allow lipid solubility of both the free receptor and the receptor-anion complex. However, too lipophilic receptors can form aggregates or precipitate in the solution, hindering their partitioning into the lipid bilayer membrane.[214] In general high-affinity anion binding is favourable for anion transport, as the rate of anion-receptor association correlates positively with anion binding affinity. Too strong anion binding affinity, however, can be counterproductive for anion transport presumably due to anion dissociation becoming rate-limiting.[225] Increasing the degree of anion encapsulation by the receptor has been shown to improve anion transport affinity. This can be explained by the ease of interfacial translocation of a better desolvated, thus more lipophilic anion complex as a result of a higher degree of anion encapsulation. Examples of this effect include the higher anion transport activity of anionophores featuring cyclic, enclosed binding sites compared with acyclic analogues,[224] and the surprisingly high activity of flexible, tripodal anionophores in spite of their unimpressive anion binding affinity.[226] Here only a few examples of recently reported hydrogen bond-based anionophores are described.

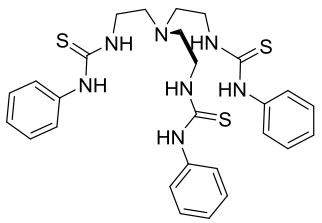

6-2

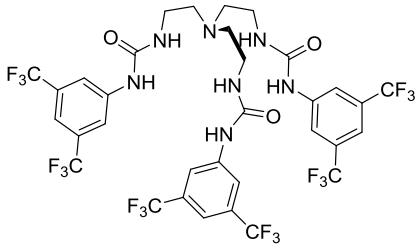

6-3

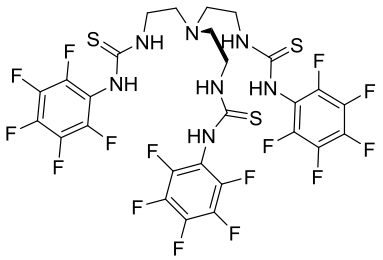

6-4

Tripodal urea/thiourea anionophores based on the tris-2-aminoethylamine (TREN) scaffold represent a class of easily accessible, yet highly active anionophores as shown by Gale and coworkers.[138, 227] Initially, a series of tripodal ureas and thioureas including **6-2** were reported to facilitate Cl^-/NO_3^- and Cl^-/HCO_3^- antiports, investigated by ISE assays with the anionophores added to the vesicle suspensions as DMSO solutions. In a subsequent study, fluorinated analogues were synthesized, leading to dramatic improvement in anion transport activity. The most active Cl^-/NO_3^- exchanger among the series, compound **6-3** could function at at concentrations as low as 1:250000 carrier-to-lipid ratio. Later some of this series of compounds were found to facilitate the transport of highly hydrophilic SO_4^{2-} (or HSO_4^-) ion (in exchange for chloride), with **6-4** being the most active sulfate transporter.[228]

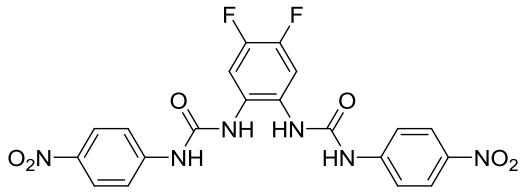

6-5

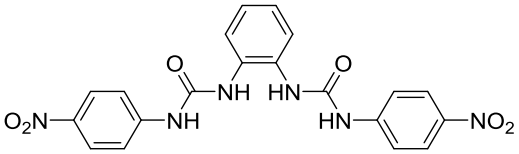

6-6

The TREN-based tripodal receptors are however, not the most active anionophores developed in the Gale group. Several anionophores from the simple ortho-phenylenediamine bisurea framework, such as **6-5**, outperform the most active TREN-based anionophore **6-3** in Cl^-/NO_3^- antiport, allowing anion transport to be observed at a 1:1000000 carrier-to-lipid ratio.[229-230] This is surprisingly considering the simplicity of the bisurea scaffold, and also the chloride binding constant of **6-5** (50 M^{-1} in DMSO-d_6/0.5% H_2O) that is an order of magnitude lower than that of **6-3** (517 M^{-1} in DMSO-d_6/0.5% H_2O). The exact reason for the high activity of bisureas is unclear at this moment. In the first publication of bisurea-based anionophores, several compounds including **6-6** were demonstrated to facilitate the transport of carboxylate anions including maleate and fumarate (in exchange for chloride).[230] While maleate (pK_a1 = 1.92, pK_a2 = 6.22) transport can be observed at both pH 4 and pH 7, fumarate (pK_a1 = 3.02, pK_a2 = 4.38) transport was only observed at pH 4. It was proposed that the mono-anionic forms of maleate and fumarate were the species transported.

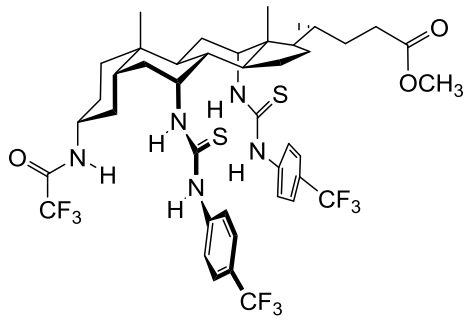

6-7

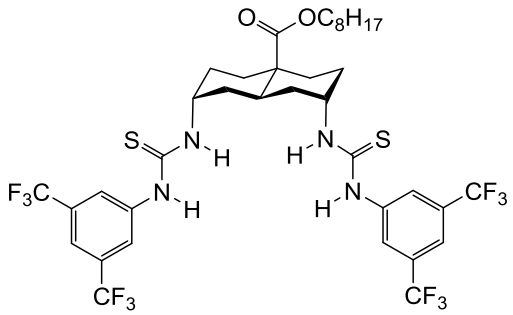

6-8

The A. P. Davis group have been dedicated to developing highly efficient anionophores based on rigid, pre-organised scaffolds including the steroid ("cholapods") [146, 231] and *trans*-decalin[223] scaffolds. In a very recent study, anionophores based on these scaffolds were optimised by introducing electro-withdrawing and lipophilic substitutes.[142] The Cl^-/NO_3^- antiport activity was investigated by the lucigenin assay, with the anionophores pre-incorporated into the lipid bilayer membrane at the stage of vesicle preparation. Anionophores **6-7** and **6-8** were highly active, allowing chloride transport at a 1:1000000 carrier-to-lipid ratio. The activity of the most active **6-8** per molecule in Cl^-/NO_3^- exchange in vesicle models can be translated to be ~1/250 the chloride transport activity of CFTR channel which is impressive considering that the molecular weight of **6-**

8 is ~1/200 that of the CFTR channel. Further improvements regarding the deliverability problem is required for real applications.

In 2012, Gale and coworkers reported anion binding and transport study of a series of simple squaramides such as **6-9**.[144] Those simple monopodal squaramides were found to exhibit superior anion binding affinity and anion transport (Cl^-/NO_3^- and Cl^-/HCO_3^- antiports) activity compared to simple monopodal urea or thiourea analogues. Although the anion transport activity of the squaramides cannot rival the best anionophores reported, the use of squaramides instead of urea/thioureas as the anion binding motif represents an attractive approach to improving anion transport activity without increasing anionophore lipophilicity, an advantage for developing anionophores that can be delivered to cells for real applications.

Later on, thiosquaramides such as **6-10** were reported to function as pH-switchable anion transporters.[143] The thiosquaramides have a lower pK_a of the N–H proton compared their squaramide analogues (*e.g.* pK_a = 5.3 for **6-10**, compared with pK_a = 9.8 for **6-9** in 9:1 acetonitrile/water). At pH 7.2, **6-10** exits as the mono-deprotonated form which is unable to facilitate anion transport. At pH 4.0, the anion transport activity is "switched on" as a result of **6-10** existing in its neutral form capable of anion binding and transport. The strategy of achieving pH switchable anion transport by utilizing deprotonation of hydrogen bond donors, as demonstrated in this example, is attractive for designing pH sensitive anionophores for selectively targeting cancer cells that have abnormal pH dynamics.

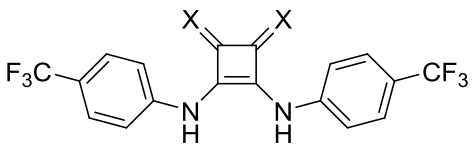

6-9 X = O
6-10 X = S

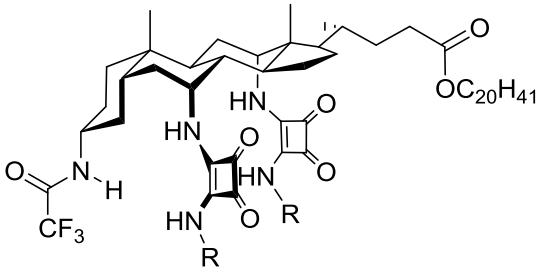

6-11 R = 3,5-BisCF_3Ar

The squaramide moiety has been incorporated into the steroid scaffold by Edwards and coworkers to give anion receptors with exceptionally high chloride affinity.[225] The strongest chloride binder, **6-11** shows a chloride affinity over 10^{14} M^{-1} in chloroform, the highest binding constant for chloride ever observed with a neutral anion receptor. It was found, however, that with the binding constant reaching a threshold value, the activity of Cl^-/NO_3^- exchange no longer benefits from high chloride binding affinity as was the normally observed trend. Presumably, this was due to unfavourable kinetics of anion release at the interface. Accordingly, the anion

transport activity of **6-11** is not impressive compared with best anionophores developed by the Davis group.

Most anionophores reported feature traditional hydrogen bond motifs containing acidic N–H protons, or less often, O–H protons. Recently, anionophores based on weaker C–H hydrogen bond donors have been reported. Hou and coworkers developed aryltriazole foldamer **6-12** that interacts with chloride via C–H hydrogen bonds.[232] X-ray crystallographic and 2D NMR studies have confirmed that free **6-12** is preorganised by a hydrogen-bonding network in the periphery, creating a cavity with five C–H hydrogen bond donors for anion binding. NMR titration of **6-12** with halide ions show downfield shift of the inner C–H protons upon addition of anions, confirming involvement of C–H hydrogen bonds in anion binding. The anion binding selectivity follows the sequence of $Cl^- > Br^- > I^-$ in CD_2Cl_2.**6-12** is able to facilitate Cl^- transport that couples with K^+ transport facilitated by valinomycin to give salt flux, as studied by the lucigenin assay. **6-12** is moderately active with chloride transport observable at a 1:2000 carrier-to-lipid ratio. This result should not be compared with the activity obtain by Cl^-/NO_3^- exchange experiment for most of reported anionophores, because the kinetic characteristics of K^+/Cl^- co-transport (in the presence of valinomycin) and anion exchange are different, as exemplified by the case of prodigiosin discussed in Sections 6.1.1 and 6.2.4.

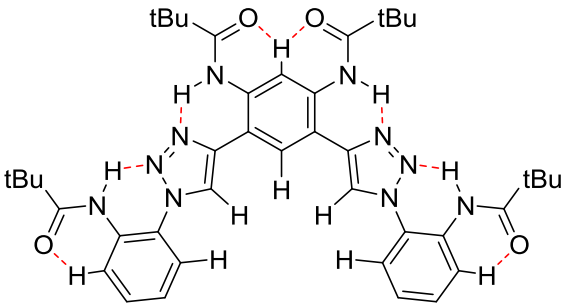

6-12

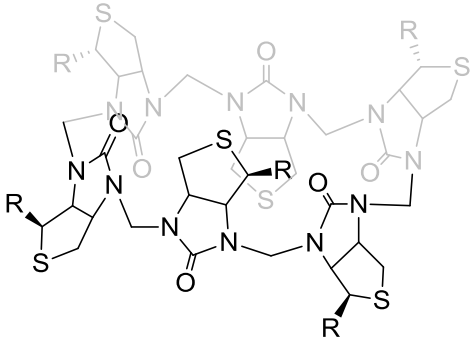

6-13 R = 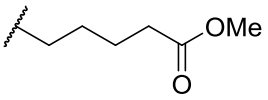

6-14 R = 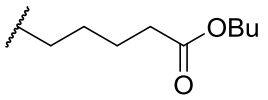

In a very recent study, Lisbjerg and coworkers demonstrated a potential advantage of C–H hydrogen bond-based anionophores, $Cl^- > HCO_3^-$ selectivity.[233] Molecular modelling shows that biotin[6]uril esters including **6-13** and **6-14** can bind chloride ion by 12 C–H hydrogen bond donors from the six biotin units. **6-13** displays a binding constant for Cl^- that is two orders of magnitude higher than those for NO_3^- and HCO_3^- in acetonitrile. The Cl^- vs. HCO_3^- selectivity study was conducted for the more active **6-14**. With **6-14** pre-incorporated into the vesicle membranes at a 1:1000 carrier-to-lipid molar ratio, chloride influx was observed for vesicles with internal-

NO_3^-/external-Cl^-, but not for vesicles with internal-HCO_3^-/external-Cl^-. In contrast, using a *trans*-decalin-bis-urea, chloride influx can be observed under both conditions mentioned above. These results demonstrate the selective anion transport of **6-14** for Cl^- and NO_3^-, over the more basic, charge dense anion HCO_3^-. The "soft" nature of C–H hydrogen bond donors was proposed responsible for the observed selectivity.

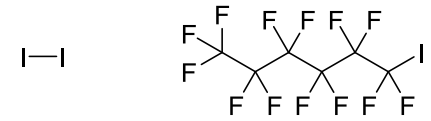

Iodine

6-15

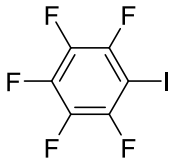

6-16

Halogen bonds are attractive interactions between covalently bonded electrophilic halogen atoms (donors) and nucleophilic species (acceptors, such as anions). With growing interest in the research of halogen bonding in recent years, halogen bond donors have been studied as anion transporters. I_2 was found to induce conductance of I^- and Br^- across lipid bilayer membranes by reversibly forming halogen-halide complexes. Klotz and Benz performed steady-state and kinetics studies of I_2-mediated halide transport, revealing that an interfacial complex mechanism operates instead of a solution-phase complexation mechanism.[234] It was not until 2012, however, that the more common organic halogen bond donors were used for anion transport. Matile and coworkers reported that halogen bond donors including perfluoroalkyl iodides (such as **6-15**) and fluorinated aryl iodides (such as **6-16**) function as anion transporters.[148] HPTS assays revealed that these compounds can dissipate pH gradients presumably by Cl^-/OH^- antiport. High Hill coefficients were found, indicating that the transport process involves several monodentate halogen bond donors forming a lipophilic shell around the transported anion (Cl^- or OH^-), which has been supported by DFT simulations. The halogen bond-based anionophores induce chloride conductance in planar lipid bilayer experiments, confirming the electrogenic nature of anion transport. Later, Matile and coworkers reported anion transport via hopping along transmembrane oligo(pentafluoroiodobenzene)-based halogen bonding cascades.[147] The halogen bond-based anionophores reported so far are probably too inactive for real applications, most likely due to their weak anion binding affinity. Promising, however, is the potential of achieving selectivity for halides over oxoanions,[235] if anion transport activity could be improved possibly by designing multidentate halogen bond receptors.

6.1.4 Biological applications of synthetic anionophores

Cystic fibrosis[236] is a genetic disease caused by mutations leading to under-functioning of the cystic fibrosis transmembrane conductance regulator (CFTR) protein. CFTR is an ATP-gated

electrodiffusive anion channel that provides the only pathway for chloride movement in the apical membrane of epithelial, functioning with the epithelial sodium channel to enable transepithelial salt absorption. Defective CFTR function as in cystic fibrosis patients leads to various pathological conditions, most notably lung infection and inflammation. There is currently no cure for cystic fibrosis. It has been proposed that synthetic anionophores may be useful for cystic fibrosis treatment by performing the function of CFTR channel. Another incentive for developing synthetic anionophores is for cancer treatment. Ideally, for a particular purpose, a careful choice from different class of anionophores that have different anion transport mechanisms is important. Research into biological activities of anionophores, is, however only at an early stage.

The investigation into anticancer activity of synthetic anionophores is most likely encouraged by the ability of the naturally occurring prodigiosins to selectively induce cancer cell apoptosis.[237] Its ability to facilitate H^+/Cl^- symport, thereby disrupting pH gradients across acidic cellular compartments, is one of the possible molecular mechanisms for its toxicity effects. Sessler and coworkers examined the anion binding, anion transport and in vitro anticancer activity of a series of prodigiosin analogues including **6-17**, **6-18** and **6-19**.[238] Single crystal of 1:1 **6-19**·HCl complex was obtained for X-ray crystallographic analysis. ITC binding studies revealed a strong affinity (10^5 – 10^6 M^{-1}) of monoprotonated form of these prodigiosin analogues for chloride, whereas their free bases displayed negligible chloride affinity. The ability of these compounds to facilitate H^+/Cl^- symport was confirmed by an HPTS assay showing their ability to dissipate a pH gradient across vesicles in a Cl^--containing medium. These compounds showed toxicity towards A549 human lung cancer and PC3 human prostate cell lines, with antiproliferative activity correlating with the anion transport activity but not anion binding affinity. These results support the hypothesis that the anticancer activity of prodigiosin is, at least in part, due to pH gradient disruption by H^+/Cl^- symport.

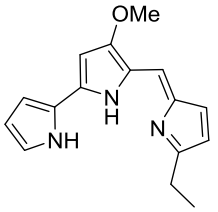

6-17

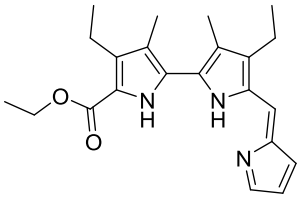

6-18

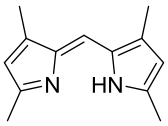

6-19

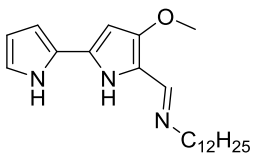

6-20

Tambjamine derivatives such as **6-20** represent another class of natural products which can bind chloride in their deprotonated form and their ionophoric ability was reported by Quesada and coworkers.[239] These compounds facilitated Cl^-/NO_3^- and Cl^-/HCO_3^- exchange in vesicles, and dissipated pH gradients in acidic cellular compartments such as lysosomes and endosomes, shown by fluorescence staining tests with acridine orange.

The prodigiosin and tambjamine derivatives and analogues contain protonatable nitrogen atoms and therefore pH gradient disruption by binding and transport of HCl is chemically plausible. Taking this into consideration, it may seem a surprise that the Gale group have observed similar behaviours by some bisureas (such as **6-6**)[230] and tripodal transporters (such as **6-3** and **6-4**).[138, 227] Note that the amine group in the tripodal transporters remains neutral in their active form responsible for anion transport (confirmed in Section 6.2.4) unlike prodigiosins and tambjamines. In vesicle-based experiments, these anionophores facilitate H^+/Cl^- symport or Cl^-/OH^- antiport confirmed by HPTS assays. In vitro acridine orange experiments demonstrate their ability to de-acidify acidic cellular compartments such as lysosomes. A plausible explanation is that these anionophores can transport OH^- by hydrogen bonding, or transport H^+ by deprotonation. This issue is the incentive for establishing the current project described in this chapter.

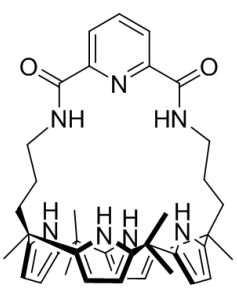

6-21

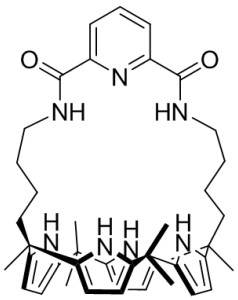

6-22

Apart from pH gradient disruption, another mechanism through which synthetic anionophores can display anticancer activity was recently reported by Sessler and coworkers.[136] A series of calixpyrrole-based anionophores were synthesized and their anion binding, anion transport and biological activities studied. Among the series, amide-strapped calixpyrroles **6-21** and **6-22** turned out to be much better anion binders and transporters compared to control compounds without the amide group or the calixpyrrole moiety. **6-21** and **6-22** can facilitate chloride transport that couples with valinomycin facilitated K^+ transport to generate salt flux, indicating that they can function as electrogenic chloride transporters. With monensin used in place of valinomycin as the cationophore component, the rate of salt flus is significantly slower. This observation was not interpreted in the publication, but based on the current study this can be attributed to Cl^- > H^+/OH^- selectivity of **6-21** and **6-22** (see Section 6.2.3 for explanations). The chloride transport activity of **6-21** and **6-22** is not very high compared to other literature examples as a 2 mol% (with respect to lipid) loading was used in the vesicle-based studies. However, they exhibit robust cytotoxicity in various cell lines with half maximum inhibitory concentration (IC_{50}) values ranging from 10 to 15 μM. They were found to increase intracellular chloride and sodium concentrations shown by intracellular fluorescence indicators. This was interpreted as Cl^- transport facilitated by **6-21** or **6-22** coupling with Na^+ transport facilitated by biological sodium channels. The NaCl flux

induced by **6-21** and **6-22** was proposed responsible for the observed apoptosis inducing effect, which was supported by the observations that the cell death was decreased by using Na^+-free or Cl^--free media, or with sodium channel blocker amiloride. This study demonstrates the ability of anionophores to induce apoptosis via disrupting the ion homeostasis within cells by electrogenic chloride transport. This may pave the way for developing new anticancer drugs based on a new mechanism, but also raises concern regarding potential toxicity when using anionophores for treating cystic fibrosis.

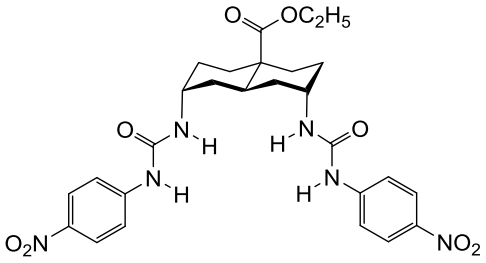

6-23

Very recently, to further investigate the potential of synthetic anionophores in performing the function of CFTR channel, Li and coworkers studied cellular anion transport activity of several synthetic anionophores based on the steroid, *trans*-decalin and cyclohexane-tripodal scaffolds.[240] Structural optimization on those previously reported scaffolds allows the anionophores to be delivered to phospholipid vesicles or cell membranes by an organic solvent or POPC. To assess anion transport activity in live cells, the authors devised a yellow fluorescent protein (YFP) assay, in which Cl^-/I^- exchange facilitated by the tested anionophore leads to fluorescence quenching of YFP inside Fischer rat thyroid (FRT) cells as a result of entry of externally added iodide ion. Trans-decaline-based bisurea **6-23** turned out to be the most active in facilitating Cl^-/I^- exchange in FRT cells, although its activity in Cl^-/NO_3^- exchange in vesicle-based experiments is only modest among the series. This was explained by good deliverability of **6-23**. In addition to the YFP tests, **6-23** was shown to induce conductance of apical membrane of epithelia using a Ussing chamber assay. Interestingly, **6-23** showed no toxicity to Hela cells up to 30 μM, in contrast to the potent toxicity displayed by calixpyrroles **6-21** and **6-22** (IC_{50} = 10 μM) towards the same cell line.[136] This is surprising because the calixpyrroles seem to be far less active chloride transporters compared with **6-23** in vesicle experiments (although direct comparison is not possible as the anionophores were subject to different assays employed by different authors), whereas the cytotoxicity of **6-21** and **6-22** has been attributed to chloride transport. Thus it remains an open question whether and under what conditions chloride transport itself can lead to toxicity. Another question may be whether and under what circumstances the activity in Cl^-/I^- exchange could indicate the activity of the tested anionophore in performing the function of CFTR channel, which does not simply function as an anion exchanger but facilitates electrogenic chloride transport that is central to its

role in inducing salt reabsorption across epithelia. This is an interesting question because of different kinetic steps involved in anion exchange and electrogenic anion transport (*e.g.* Figure 6.5).

6.1.5 Anion selectivity

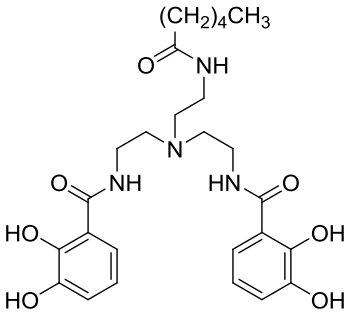

6-24

Anion selectivity (excluding selectivity over hydroxide ion) is probably not an important issue for application of an anionophore in cystic fibrosis treatment, since the CFTR channel is not particularly selective for chloride.[241] Anionophores selective for a particular biologically relevant anion, such as chloride, nitrate and fluoride may be useful for other purposes. However, a more intriguing question is the anion selectivity with regard to the hydrophilicity of anions (Hofmeister series[242]). It has been proposed in the context of anion extraction[243] and anion transport[244] that for relatively weakly-binding anionophores, the anion selectivity is governed by the energetic cost of anion hydration instead of hydrogen bond acceptor ability of different anions, leading to a "Hofmeister-selectivity", *i.e.* more lipophilic and weakly binding anions are transported at faster rates than more hydrophilic, strongly binding anions. A Hofmeister-selectivity of $ClO_4^- > I^- > NO_3^- > Br^- > Cl^-$ has been reported for a bis-catechol anionophore **6-24**.[214] Breaking the Hofmeister bias for lipophilic anions is possible by employing stronger interactions (such as metal coordination) or interactions that favour a particular class of anions (*e.g.*, halogen bonding for halides over oxoanions[235]), or by designing receptor structures that fit the size and geometry for particular ion(s).[245-246] An experimental investigation into anion selectivity is presented in Section 6.2.6

Planar lipid bilayer techniques represent a classical and reliable method to study anion selectivity of anionophores.[247] For this purpose, bi-ionic conditions are employed with each of two anions to be compared present on each side of the membrane. Reverse potential, the voltage corresponding to zero ionic current, was measured, and a permeability ratio between the two anions can be calculated using the Goldman-Hodgkin-Katz voltage equation. Alternatively the HPTS assay based on pH gradient dissipation may be used to investigate ion selectivity.[182] The HPTS assay is easier to perform for supramolecular chemists. However, its use in the investigation of anion selectivity requires precautions.[244, 248]

6.1.6 Proton/hydroxide transport and electroneutral/electrogenic transport mechanisms

Due to the essential role of transmembrane pH[249] and proton[203] gradients in cellular functions, it is important to know whether an ionophore facilitates proton transport or functionally equivalent hydroxide transport. It is also important to understand whether the proton or hydroxide transport facilitated by an ionophore can occur via an electrogenic mechanism (functioning as a protonophore) or an electroneutral mechanism (coupled with cation or anion transport, the overall process being electroneutral, *e.g.*, Na^+/H^+ exchange facilitated by monensin, Figure 6.2). With regard to this issue, many naturally occurring cationophores have been well studied. For example, valinomycin cannot facilitate proton or hydroxide transport.[199] Gramicidin can facilitate electrogenic proton transport.[250] Monensin can facilitate electroneutral M^+/H^+ exchange, but not electrogenic processes.[200]

Whereas the behaviours of many cationophores are well studied, little is known about the possibility and mechanism of proton or hydroxide transport facilitated by anionophores, despite intensive research efforts in the design of novel anionophores A few examples of anionophores have been assessed using the HPTS assays which demonstrate that they are able to facilitate electroneutral processes of H^+/Cl^- symport or Cl^-/OH^- antiport. But it remains unclear which process is actually responsible and whether they can also facilitate electrogenic H^+/OH^- transport which leads to the same outcome of protonophores. On the other hand, the possibility of proton or hydroxide transport was not tested for most of the reported anionophores that have been typically assessed for their ability to facilitate Cl^-/NO_3^- exchange. It should be noted that under typical experimental setups in which chloride efflux is measured by ISE or lucigenin assays (*e.g.*, with chloride inside vesicles and nitrate or sulfate outside vesicles), H^+/Cl^- symport or Cl^-/OH^- antiport can hardly be detected due to limited buffer capacity of the system.

As discussed in Section 6.1.4, some of the most powerful synthetic anionophores and prodigiosin can deacidify acidic cellular organelles presumably by H^+/Cl^- symport or Cl^-/OH^- antiport. Although they may be promising anticancer agents due to their ability to disrupt transmembrane pH gradients, chloride ionophores that do not facilitate H^+/OH^- transport are required for other applications when pH gradient dissipation and protonophoric effects are unwanted. These include (i) using chloride carriers for biological research[251] when other side effects beyond chloride transport will complicate the mechanism under study, and (ii) targeting cystic fibrosis when these side effects can lead to toxicity.[248]

To develop chloride ionophores that do not actively facilitate undesired proton or hydroxide transport, it is helpful to gain a structurally insight into how anionophores can facilitate proton or hydroxide transport. Most anionophores are hydrogen bond donors. It can be expected that some

high acidity hydrogen bond donors can undergo deprotonatation in water which would allow a proton transfer process like the weak acid protonophore CCCP (Figure 6.3, pK_a 6.0).[252] However, the pK_a values of hydrogen bond donors in most anionophores are higher than that of CCCP by several units.[253] Some should have pK_a values higher than 14 in which a proton transfer mechanism appears less unlikely. In addition, pH gradient dissipation has been observed even for halogen bond-based anionophores,[148] which do not contain acidic protons thus excluding a deprotonation mechanism. These suggest another possibility that can result in pH gradient dissipation: hydroxide transport (accompanied by movement of Cl^- in the opposite direction).

The fact that anionophores featuring a Lewis acid metal centre facilitate hydroxide transport is not surprising, as they readily form covalent complexes with hydroxide even in water. The question is whether anionophores operating by noncovalent interactions can transport hydroxide in a similar way as they transport chloride. A literature theoretical investigation suggests that hydroxide transport by noncovalent interactions is unlikely, based on the argument that equilibrium concentration of hydroxide is low (~10^{-7} M at pH 7, 298 K).[244] However, OH^- is an extremely strongly binding anion. This might explain efficient hydroxide transport observed despite its low equilibrium concentration. The chapter examines the possibility of OH^- transport and shows that the marked difference between the hydrophilicities of OH^- and Cl^- ($\Delta G_{hydration}(OH^-)$ = -430 kJ mol^{-1},$\Delta G_{hydration}(Cl^-)$ = -340 kJ mol^{-1})[254] may be key to designing a Cl^- > H^+/OH^- selective anionophore.

6.1.7 Scope and objectives of this chapter

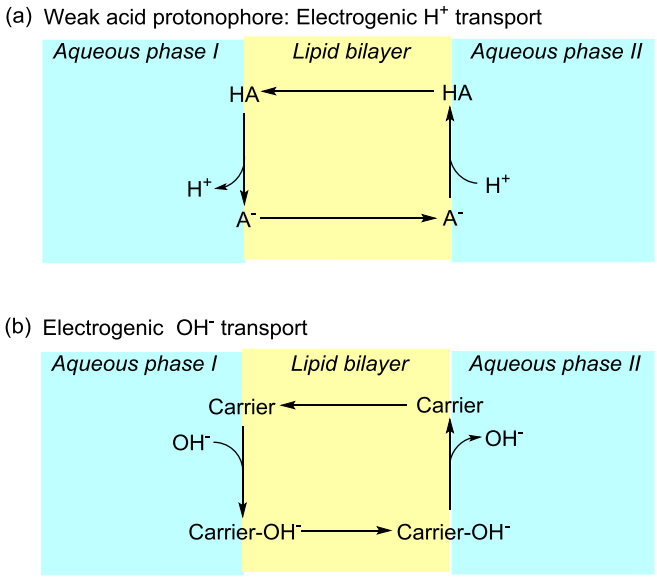

Figure 6.8 Two mechanism through which anionophores can display protonophoric activity.

As mentioned above, currently anionophores studied in the literature are either (i) not examined for their ability to facilitate proton or hydroxide transport, most of them only assessed for their ability to facilitate anion exchange (exchange of chloride for another anion such as nitrate, bicarbonate and iodide) or (ii) examined for potential H^+/Cl^- symport or Cl^-/OH^- antiport but without further mechanistic study. Assays that measure Cl^-/NO_3^- exchange are currently the most frequently used methods to study anionophores, but, as discussed previously, unable to distinguish between electrogenic/electroneutral transport mechanisms and unable to shed lights on Cl^- > H^+/OH^- selectivity. These are important issues for the potential application in cystic fibrosis treatment and for understanding the cytotoxic effects exhibited by some anionophores. In the present study, four fundamental questions are addressed regarding electrogenic/electroneutral transport mechanisms and the transport of proton or hydroxide:

(1) Can anionophores facilitate *electrogenic* proton (Figure 6.8a) or hydroxide (Figure 6.8b) transport, thus giving the same outcome as protonophores? (Section 6.2.1)

(2) Whether proton transport, or the functionally equivalent process of hydroxide transport, is responsible for the observations that some anionophores can dissipate a pH gradient? (Section 6.2.1)

(3) The electrogenic/electroneutral chloride transport mechanisms of prodigiosin and synthetic anionophores? (Sections 6.2.3 and 6.2.5)

(4) Can we design an anionophore that facilitates electrogenic chloride transport with weakened activity in dissipating a pH gradient, *i.e.*, a Cl^- > H^+/OH^- selective anionophore, which we can describe as a "valinomycin for chloride (Figure 6.9)"? (Section 6.2.2)

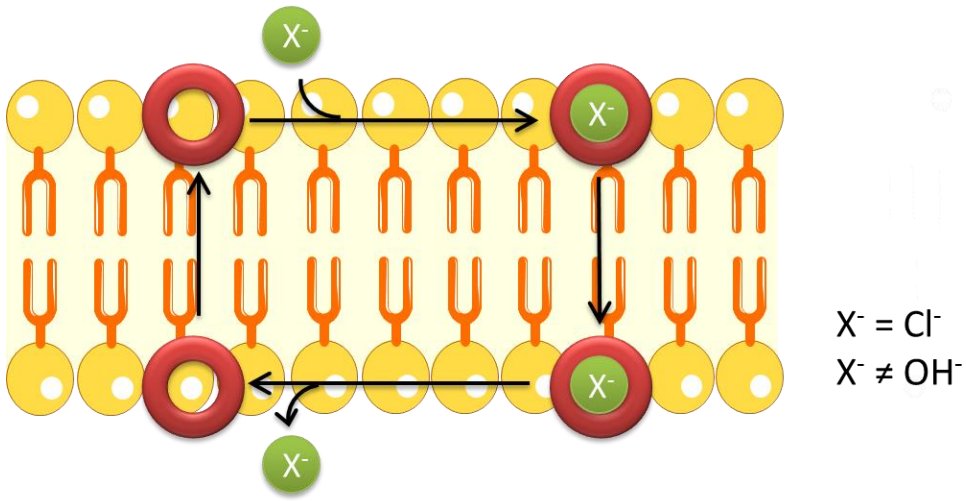

Figure 6.9 Cartoon presentation of a "valinomycin for chloride" – an electrogenic chloride carrier that does not facilitate proton or hydroxide transport.

To answer these questions, a library of 22 anionophores was studied, among them five novel compounds (marked with an asterisk). Unambiguous evidence is provided that (i) prodigiosin cannot facilitate electrogenic transport of Cl^-, H^+/OH^- and can be best described as a "monensin for anions"; (ii) many synthetic anionophores can facilitate electrogenic H^+/OH^- transport, giving the same outcome as protonophores. The functionally equivalent processes of proton transport and hydroxide transport were examined, and it is proposed that the actual transport process responsible for the observed protonophoric outcome likely depends on the acidity of hydrogen bond donors in the anionophore. Most importantly, for the first time two "valinomycin-like" anionophores have been developed that show outstanding selectivity for chloride over H^+/OH^- as confirmed by several independent vesicle-based experiments. In addition, the interesting issue of Cl^- vs NO_3^- selectivity was investigated (Section 6.2.6).

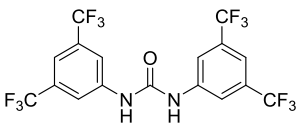

A1

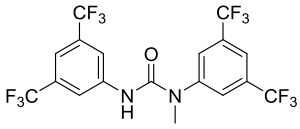

A2*

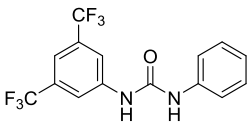

A3

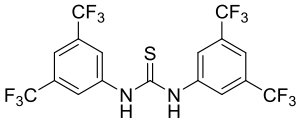

A4

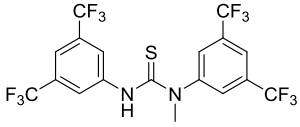

A5

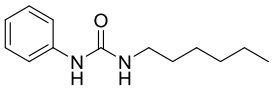

A6

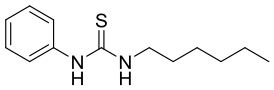

A7

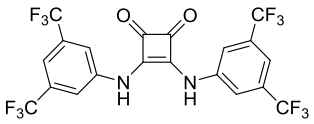

A8

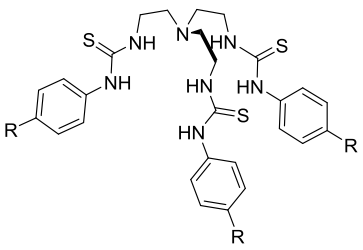

A9 R = H
A10 R = CN

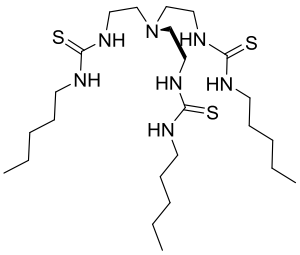

A11*

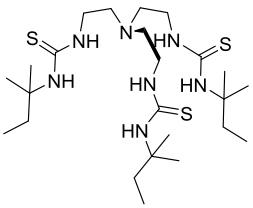

A12*

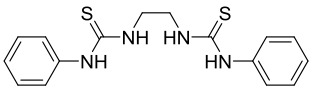

A13

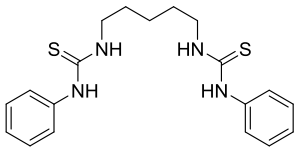

A14

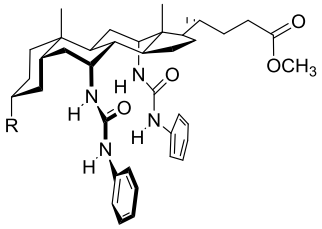

A15 R = OAc
A16 R = NHCOCF$_3$

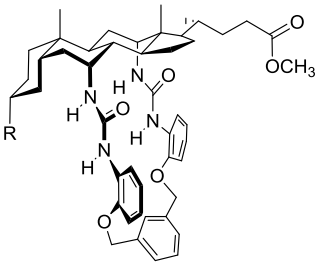

A17* R = OAc
A18* R = NHCOCF$_3$

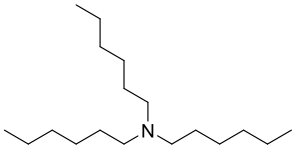

Trihexylamine

Iodine
(halogen bond donor)

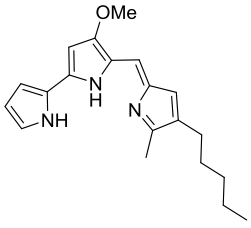

Prodigiosin (Prod)

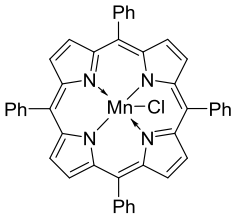

Mn(TPP)Cl
(functions by metal coordination)

*Novel anionophores

6.2 Results and discussion

6.2.1 Evidence of electrogenic proton or hydroxide transport

Previously, the Gale group[143] and others[148] have observed that anionophores can dissipate a transmembrane pH gradient whenever subject to vesicle-based experiments employing an intravesicular pH indicator 8-hydroxypyrene-1,3,6-trisolfonic acid (HPTS). Provided that the anionophores do not cause membrane defects or HPTS leakage, this implies the ability of anionophores to facilitate H^+/OH^- transport (accompanied by Cl^- transport to maintain the electroneutrality of the system), although an alternative mechanism of Cl^- transport coupled to simple (unassisted) diffusion of H^+ has been proposed[244] and in theory buffer agent transport is also possible. Assuming H^+/Cl^- symport or Cl^-/OH^- antiport, such a process may be a concerted, inseparable electroneutral process (*e.g.* Figure 6.5a). In this case, as H^+/OH^- transport cannot be separated from Cl^- transport, the anionophore is unable to facilitate electrogenic transport of H^+/OH^- like protonophores. Alternatively, H^+/Cl^- symport or Cl^-/OH^- antiport can be an electrically coupled process that consists of electrogenic H^+ (or OH^-) transport and electrogenic chloride transport. To the best of my knowledge, this issue is never examined experimentally in the literature.

To distinguish among these possible mechanisms, a new HPTS assay (here termed the TBAOH assay, Figure 6.10a) was devised for purely testing electrogenic H^+/OH^- transport (in other words, protonophoric activity), in which carrier-induced dissipation of a pH gradient across vesicle membranes (induced by adding 5 mM of tetrabutylammonium hydroxide (TBAOH) to a vesicle suspension) in a lightly-buffered sodium D-gluconate medium was monitored. Gluconate transport should be negligible due to its large size and hydrophilicity, and in this case electrogenic transport of H^+ or OH^-, facilitated by the tested carrier, couples to simple diffusion of membrane permeable TBA^+, leading to coupled TBA^+/OH^- symport or TBA^+/H^+ antiport. The results are compared with results from another HPTS assay (termed the NMDG-Cl assay, Figure 6.10b) set up for H^+/Cl^- symport or Cl^-/OH^- antiport, in which *N*-methyl-D-glucammonium chloride (NMDG-Cl) was used in place of sodium gluconate, and *N*-methyl-D-glucamine (NMDG, 5 mM) in place of TBAOH as the base pulse. The conditions for the NMDG-Cl assay are similar to the standard conditions employed by Matile and coworkers,[148] but NMDG-Cl is used instead of commonly used NaCl for the sake of another selectivity assay to be described below. Control experiments were conducted to ensure that the HPTS response did correspond to the transport process assumed to occur and not to other processes such as Na^+/H^+ exchange, gluconate/OH^- exchange and causing membrane defects. Dose-dependent experiments and Hill plot analyses were performed to obtain a Hill coefficient,[180] which indicates the stoichiometry of the unstable[179] active species involved in transport, and an effective concentration to reach 50% transport at 200s (EC_{50}) value to quantify the activity. Several simple ureas/thioureas **A1**-**A6**, prodigiosin, and a known protonophore

carbonyl cyanide *m*-chlorophenyl hydrazine (CCCP) were tested and the results are presented in Table 6.1.

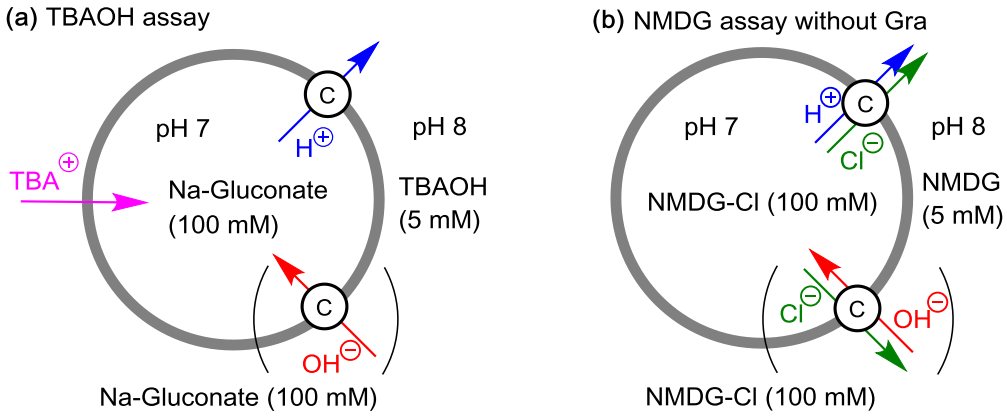

Figure 6.10 Schematic representation of (a) TBAOH assay devised for electrogenic H^+/OH^- transport and (b) NMDG-Cl assay devised for H^+/Cl^- symport or Cl^-/OH^- antiport.

Table 5.1 Summary of acidity and membrane transport data of ureas/thioureas 1-6, prodigiosin and CCCP.

Compound	pK_a	EPN[e] / E_h	TBAOH assay[f]		NMDG-Cl assay[h]	
			n	EC_{50} / %	*n*	EC_{50} / %
A1	13.8[a]	-18.2786	0.9	0.065	1.4	0.046
A2	nd[d]	-18.2798	1.9	0.83	2.4	0.61
A3	16.1[a]	-18.2947	1.5	0.26	2.3	0.16
A4	8.5[a], 8.9[b]	-18.2723	0.9	0.014	1.2	0.015
A5	10.7[b]	-18.2774	1.1	0.013	1.9	0.26
A6	nd[d]	-18.3453	2.9	12	3.2	20
Prod	nd[d]	nd[d]	-[g]	> 1[g]	1.3	0.000059
CCCP	6.0[c]	nd[d]	1.0	0.0054	-[i]	>100[i]

[a] In DMSO, reported by Schreiner et al.[32] [b] In acetonitrile/water (9:1, v:v, with 0.1 M $TBAPF_6$), determined using potentiometric titrations (Figures 7.101 and 7.102). [c] In water, reported by Šturdík et al.[34] [d] Not determined. [e] Electrostatic potential at nitrogen nucleus, expressed in atomic unit. The structures were optimized using PM6 semi-empirical method, assuming the *syn* conformer. The EPN values were calculated at the B3LYP/6-311++G(d,p) level of theory with the SMD water solvation model. [f] A fluorescence assay for electrogenic H^+/OH^- transport. Large unilamellar vesicles (LUVs) of POPC (mean diameter 200 nm) were loaded with HPTS (1 mM) and sodium gluconate (100 mM), buffered at pH 7.0 with 10 mM HEPES. The vesicles were suspended in an external solution of sodium gluconate (100 mM) buffered at pH 7.0 with 10 mM HEPES. At the beginning of the experiment, a base pulse of TBAOH (5 mM) was added to create a pH gradient, and the dissipation of the pH gradient induced by the compound tested (added as a DMSO solution) was monitored by HPTS fluorescence. Lipid concentration for fluorescence measurement is 0.10 mM. Dose-dependent Hill plot analysis was performed to obtain a Hill coefficient (*n*) and an effective concentration to reach 50% transport (EC_{50}) at 200s for each carrier. Carrier concentrations were shown as carrier to lipid molar ratios. [g] No transport at 1 mol% loading. Higher loadings not tested due to interference with HPTS fluorescence. [h] A fluorescence assay for H^+/Cl^- symport or Cl^-/OH^- antiport. The internal and external media used was NMDG-Cl (100 mM) buffered at 7.0 with 10 mM HEPES, and the base pulse used was NMDG (5 mM).

The other conditions are the same as in the TBAOH assay. [i] No transport even at 100 mol% concentration.

Although prodigiosin is extremely active in the NMDG-Cl assay that corresponds to H^+/Cl^- symport or Cl^-/OH^- antiport, consistent with its assumed electroneutral nature, it does not facilitate electrogenic H^+/OH^- transport and therefore cannot dissipate the pH gradient in the TBAOH assay. The conclusion is consistent with no protonophoric activity or alteration of cellular ATP levels reported for prodigiosin 25-C.[205] It is likely that in the protonated form of prodigiosin the positive charge is insufficiently delocalised to allow it to move across the membrane, which is a requirement for facilitating electrogenic processes. This is supported by the observation that prodigiosin is unable to facilitate electrogenic chloride transport as confirmed in Section 6.2.3.

CCCP can transport protons but not chloride, and is therefore active in the TBAOH assay and silent in the NMDG-Cl assay. The other hydrogen bond donors, in contrast, respond to both assays. The rates are essentially unaffected by switching the external buffer agent from HEPES to phosphate, indicating that buffer agent transport is unlikely. Further evidence for H^+/OH^- transport that completely rules out buffer agent transport is afforded by the observation of H^+/OH^- transport under buffer-free conditions (Section 7.5.9.1, Chapter 7). The results prove that these ureas and thioureas do facilitate electrogenic H^+/OH^- transport, leading to the same outcome as protonophore CCCP.

The molecular mechanism for proton conductance induced by weak acid protonophores such as CCCP is currently understood as movement of both neutral and deprotonated, anionic forms of protonophore across the membrane (Figure 6.8a).[194] Hydrogen bond donors may adopt a CCCP-like deprotonation mechanism. Alternatively, reversible binding and release of OH^- (Figure 6.8b) by the anionophore may be responsible for the apparent protonophoric outcome. In an attempt to investigate this issue, normal ureas/thioureas and their mono-*N*-methylated analogues were compared in both assays. *N*-methylation is expected to dramatically weaken anion (Cl^- or OH^-) binding and transport as only a single N–H hydrogen bond donor is present.[219]

Interestingly, while *N*-methylation dramatically decreased the activities of both urea **A2** and thiourea **A4** in the NMDG-Cl assay as expected from weakened chloride binding by *N*-methylation, the situation was found to be more complex in the TBAOH assay, in which urea **A1** is still far more active than *N*-methyl urea **A2**, but normal and *N*-methyl thioureas **A4** and **A5** show similar activities. To rationalize these effects, pK_a values of some compounds were determined by potentiometric titrations in acetonitrile/water (9:1, v:v) and literature pK_a values[253] (in DMSO) tabulated. Electrostatic potential values at the nitrogen nucleus (EPN)[255] obtained with DFT calculations were also used for acidity comparison when the pK_a values are too high for determination by potentiometric titrations.

Due to its high acidity, a significant proportion of compound **A4** is deprotonated under the experimental conditions (external pH ~8 after base pulse), likely allowing proton transport like CCCP. Despite its weaker acidity, compound **A5** can also deprotonate in water and it was assumed to transport protons by a CCCP-like mechanism on the basis of the following observations: (i) **A5** is a much better H^+/OH^- carrier than a chloride carrier (Table 1, compare EC_{50} values in the two assays); (ii) **A5** shows a Hill coefficient of ~2 in the NMDG-Cl assay, indicating chloride transport *via* a 2 : 1 **A5**-Cl^- complex. The different Hill coefficient of ~1 in the TBAOH assay, however, suggest a different process other than anion binding and this was attributed to a CCCP-like deprotonation mechanism. These observations for **A5** are in sharp contrast to other ureas/thioureas, which show EC_{50} values of the same order of magnitude, and similar Hill coefficients in the two assays. Regarding proton transport, the disadvantage of weaker acidity in the case of **A5** compared with **A4** is likely compensated by (i) **A4** binding to phosphate head group of lipids decreasing its activity (this effect is likely to be less pronounced for **A5** which is a poor anion binder) and (ii) the higher lipophilicity of **A5** which benefits membrane transport. These factors likely led to similar activities of **A4** and **A5** in H^+ transport.

Ureas **A1**-**A3** have pK_a values higher than 13, and therefore proton transport by a deprotonation mechanism is less likely at physiological pH compared to **A4** and **A5**. The higher activity of **A1** compared with *N*-methyl urea **A2** seems to support the hypothesis that **A2** and possibly also **A1** facilitate OH^- transport by hydrogen bonding to OH^-. However, as *N*-methylation weakens the acidity, comparison between **A2** and **A3** is more conclusive. When compared with **A3**, compound **A2** is more acidic based on its EPN values (Table 5.1) and it is also more lipophilic. Therefore if both **A2** and **A3** facilitated H^+ transport via deprotonation, then **A2** would be more active than **A3** in the TBAOH assay. However, the TBAOH assay revealed **A2** to have a lower activity than **A3**, highlighting the importance of two NH hydrogen bond donors, which supports the hypothesis of OH^- transport. This is also supported by the similar high Hill coefficients in the two assays, in the cases of **A2**, **A3** and **A6**, indicating similar anion (Cl^- and OH^-) binding processes. Although **A2** and **A6** contain two convergent N–H protons, they show high Hill coefficients presumably due to the weaker acidity of N–H protons (lower electrostatic potential energy at the anion binding site) compared to those in **A1** and **A4**, therefore needing more carrier molecules to sequester the negative charge of chloride. This is supported by the report that relatively weak halogen bond donors show high Hill coefficients in anion transport.[148] The abovementioned results demonstrate that hydroxide transport is the more likely pathway for less acidic anionophores to facilitate H^+/OH^- transport, while the more acidic **A5** can deprotonate in water and thereby transport H^+ in the same way as CCCP.

It should be noted that the hydroxide complex (1:1) and the hydrated deprotonated form of a urea/thiourea are structurally similar, differing only by small proton movements (Figure 6.11). This highlights the fact that, when deprotonation of the hydrogen bond donor cannot take place, hydroxide can nonetheless form a strong complex with a moderately acidic receptor. Taking into account solvation of the free anionophore, hydroxide transport can actually be viewed as a proton transfer process. The next section, however, show that with judicious design of the anionophore structure, we can diminish hydroxide or proton transport relative to chloride transport.

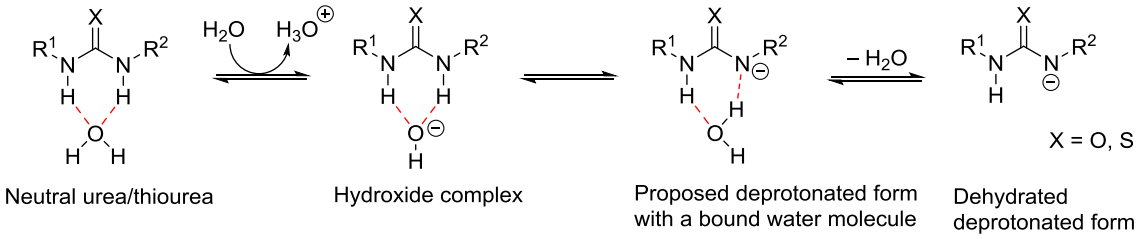

Figure 6.11 Equilibria involving hydrogen bonding to OH^- and deprotonation of ureas and thioureas. Hydrogen bonds are represented by red dashed lines.

6.2.2 Development of chloride > proton/hydroxide selective ionophores

In this section it is investigated whether it is possible for anionophores to possess Cl^- > H^+/OH^- selectivity. Due to the high K^+ > H^+/OH^- selectivity, valinomycin at low concentrations cannot facilitate K^+/H^+ exchange unless in the presence of a protonophore.[35] A HPTS assay for Cl^- > H^+/OH^- selectivity (Figure 6.12) was devised and employed based on the same rationale. The effect of proton channel gramicidin on the rate of pH gradient dissipation (indicating H^+/Cl^- symport or Cl^-/OH^- antiport) measured in the previously described NMDG-Cl assay was studied. The rationale is, if H^+/OH^- transport is rate-limiting, *i.e.*, the carrier shows Cl^- > H^+/OH^- selectivity, the pH gradient dissipation will be accelerated by gramidicin that facilities electrogenic H^+ transport (*e.g.* Figure 6.13). Conversely, if Cl^- transport is rate-limiting (or if the anionophore at the tested concentration does not facilitate electrogenic Cl^- transport), the rate of pH gradient dissipation will be unaffected by gramidicin. Here the use of proton channel gramicidin, instead of proton carriers such as carbonyl cyanide phenylhydrazones, is to prevent potential intermolecular interaction between carrier molecules, which is less likely for the neutral channel molecule gramicidin. The use of inert $NMDG^+$ as the counterion for chloride prevents gramicidin itself dissipating the pH gradient by facilitating M^+/H^+ exchange. The ratio between EC_{50} values obtained in the absence and presence of gramicidin (S-value shown in Table 6.2) is used to quantify the Cl^- > H^+/OH^- selectivity. Subject to the selectivity test are 22 anionophores shown in Section 6.1.7, the majority of them being hydrogen bond receptors.

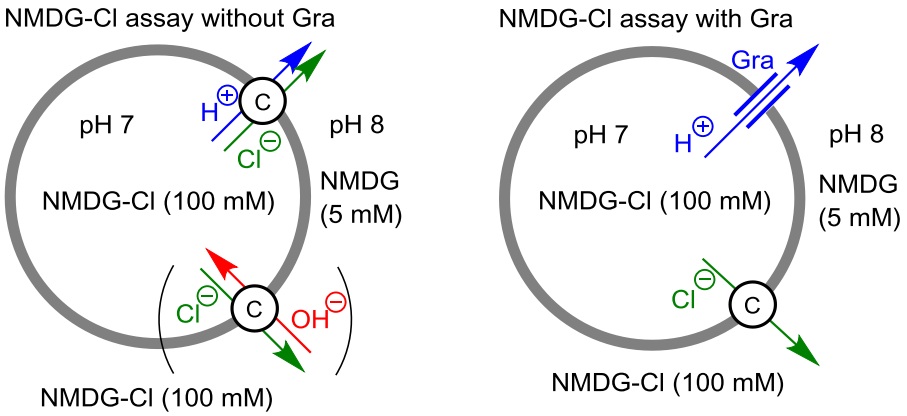

Figure 6.12 Schematic representation of using the NMDG-Cl assay in the absence and presence of proton channel gramicidin to determine Cl^- > H^+/OH^- selectivity.

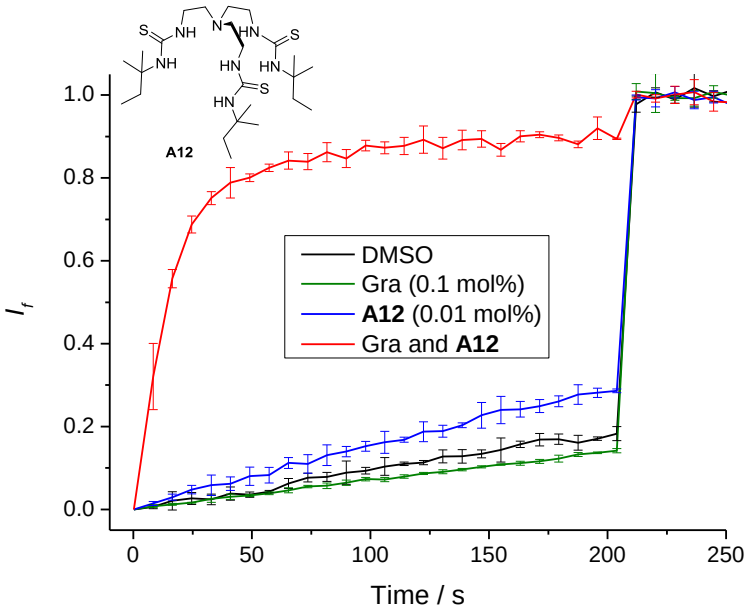

Figure 6.13 Cl^- > H^+/OH^- selectivity of **A12** demonstrated by a single-concentration comparison in NMDG-Cl assay. This is shown as the rate of pH gradient increased dramatically in the presence of proton channel gramicidin D (Gra). The progress of pH gradient dissipation was monitored by ratiometric fluorescence of HPTS (λ_{ex} = 460 nm, λ_{em} = 510 nm, base form divided by λ_{ex} = 403 nm, λ_{em} = 510 nm, acid form). The HPTS fluorescence response was normalized by addition of detergent at 200 s to completely destroy the pH gradient. Note that the background change in HPTS fluorescence is due to simple diffusion of neutral form of NMDG that slowly dissipates the pH gradient. Error bars represent SD from two or three repeats.

Table 6.2 Summary of chloride transport activity and $Cl^- > H^+/OH^-$ selectivity. Hill plot analysis of anionophores **A1**-**A18**, trihexylamine (Hex_3N), iodine (I_2), prodigiosin (Prod), and MnTPPCl in the NMDG-Cl assay[a] in the absence and presence of proton channel gramicidin D (Gra).

	without Gra		with Gra (0.1 mol%)		Selectivity
	n	EC_{50} / mol%	*n*	EC_{50} / mol%[b]	(S)[c]
A1	1.4	0.046	1.4	0.043	1.1
A2	2.4	0.61	1.9	0.29	2.1
A3	2.3	0.16	2.0	0.11	1.4
A4	1.2	0.015	1.2	0.015	1.0
A5	1.9	0.26	1.8	0.33	0.8
A6	3.2	20	3.1	13	1.5
A7	2.5	7.9	2.7	5.9	1.3
A8	1.3	0.00074	1.3	0.00085	0.9
A9	1.3	0.042	1.1	0.0030	14
A10	1.2	0.0011	1.2	0.0012	0.9
A11	1.3	0.11	1.3	0.0028	39
A12	1.2	0.067	1.4	0.00086	78
A13	-	too inactive	-	too inactive	-[d]
A14	1.2	9.5	1.0	1.3	7.4
A15	1.5	0.25	1.2	0.077	3.3
A16	1.3	0.016	1.4	0.017	0.9
A17	-	too inactive	0.9	0.089	-[e]
A18	1.4	0.18	1.2	0.0017	100
Hex_3N	1.1	0.026	1.1	0.023	1.1
I_2	1.6	6.9	1.5	6.1	1.1
Prod	1.4	0.000061	1.3	0.000059	1.0
MnTPPCl	1.1	0.0051	1.2	0.0045	1.1

[a] A fluorescence assay for H^+/Cl^- symport or Cl^-/OH^- antiport. Large unilamellar vesicles (LUVs) of POPC (mean diameter 200 nm) were loaded with HPTS (1 mM) and NMDG-Cl (100 mM), buffered at pH 7.0 with 10 mM HEPES. The vesicles were suspended in an external solution of NMDG-Cl (100 mM) buffered at pH 7.0 with 10 mM HEPES. At the beginning of the experiment, a base pulse of NMDG (5 mM) was added to create a pH gradient, and the dissipation of the pH gradient induced by the compound tested (added as a DMSO solution) was monitored by HPTS fluorescence. Lipid concentration for fluorescence measurement is 0.10 mM. Dose-dependent Hill plot analysis was performed to obtain a Hill coefficient (*n*) and an effective concentration to reach 50% transport (EC_{50}) at 200 s for each carrier. Carrier concentrations were shown as carrier to lipid molar ratios.

[b] EC_{50} in the presence of Gra, instead of EC_{50} in the absence of Gra, indicates chloride transport activity, since without Gra, H^+/OH^- transport may be rate-limiting. The activity here, however, refers to a "total" activity including electrogenic chloride transport and electroneutral H^+/Cl^- symport or Cl^-/OH^- antiport.

[c] $Cl^- > H^+/OH^-$ selectivity (S) is quantified by the EC_{50} in the absence of Gra divided by EC_{50} in the presence of Gra, an S-value of 1 indicating H^+/OH^- transport faster than Cl^- transport, *i.e.*, no selectivity.

[d] Too inactive for Hill plot analysis. A single-concentration comparison shows no selectivity.

[e] No S-value given because without gramicidin **A17** was too inactive for Hill plot analysis. This indicates a very high $Cl^- > H^+/OH^-$ selectivity that cannot be quantified by this method.

Prodigiosin shows no selectivity as consistent with its assumed electroneutr al nature. Commercially available chloride ionophore Mn(TPP)Cl is unselective as well, which is not unexpected as the Lewis acid metal centre binds hydroxide with appreciable affinity even in water. This implies that anionophores functioning via strong covalent interactions with anions are not suitable candidates for $Cl^- > OH^-$ selective transport.

Simple monopodal ureas/thioureas and a squaramide show rather weak to no selectivity. It is noticeable, however, that *N*-methyl urea **A2** shows the highest selectivity of 2-fold among **A1-A8**. An explanation for this is given below.

While screening the compounds developed in the Gale group, it was serendipitously identified that tripodal thiourea **A9**, but not other tripodal urea/thioureas containing electrowithdrawing –F or $–CF_3$ substients,[138] has a rather high selectivity of 14 fold while being comparatively active. New tripodal thioureas were synthesized in an attempt to gain further improvements in both activity and selectivity. Interestingly, adding electron-withdrawing cyano- substituents to **A9** leads to loss of selectivity (pK_a of **A10** was determined to be 10.5 in 9:1 acetonitrile/water, Figure 7.109, Chapter 7), while changing the phenyl group to an *n*-pentyl group, on the contrary, improved the selectivity to 39 fold, so it seems that the selectivity is sensitive to the acidity of the N–H groups. By changing the linear *n*-pentyl group to the bulky *tert*-pentyl group, surprisingly, both the activity and the selectivity further improved from **A11** to **A12**, with **A12** showing a remarkable selectivity up to 78 fold (refer to Figure 6.13 for a single-concentration comparison) while its chloride transport activity matches that of squaramide **A8**[37] that is among the most active anionophores in the Gale group reported to date. It is shown in the Section 6.2.4 that despite the presence of a protonatable nitrogen atom, the tripodal thioureas transport chloride in their neutral forms (forming anionic complexes) unlike prodigiosin and trihexylamine. The ability of the neutral form of **A12** to encapsulate chloride with six N–H···Cl^- hydrogen bonds was demonstrated by the crystal structure of **A12**·tetraethylammonium chloride (TEACl) complex (Figure 6.14a).

Two effects arising from the tripodal anionophores might be key to their superior $Cl^- > H^+/OH^-$ selectivity compared to monopodal ones: (i) enhanced affinity for chloride due to the chelate effect[256] (*e.g.* compare the chloride affinity of **A7** (K = 13.5 M^{-1})[39] and **A9** (K = 191 M^{-1})[36] in DMSO-d_6/0.5% H_2O); (ii) encapsulation of anion enforcing a high degree of anion desolvation. Although the Hill coefficient of ~2.6 in the case of **A7** (Supplementary Information) suggests that chloride was sequestered by three thioureas similarly to binding of chloride within a tripodal thiourea cage **A9**, the alkyl spacer in **A9** enforces a higher degree of desolvation. To rationalise these effects, the selectivity of bis-thioureas **A13** and **A14** was examined. Both compounds can bind chloride via four N–H···Cl^- hydrogen bonds but the long alkyl spacer in **A14** can enforce a higher degree of

anion desolvation (compare Figure 6.14b and 6.14c). Indeed, appending an additional thiourea moiety leads to enhancement of chloride affinities of both **A13** (K_1 = 151 M^{-1}, K_2 = 3.4 M^{-1}) and **A14** (K_1 = 535 M^{-1}, K_2 = 6.2 M^{-1}) in DMSO-d_6/0.5% H_2O relative to that of **A7** (K = 13.5 M^{-1}). But improvement of selectivity (relative to **A7**, 1.4 fold selectivity) was only observed for **A14** (7-fold selectivity) while **A13** shows precisely no selectivity, underscoring the importance of anion encapsulation. This was also supported by the higher selectivity of **A12** compared with **A11**, as the bulky alkyl substituents in **A12** makes the chloride ion less solvent-accessible compared with linear alkyl substituents in **A11**. The exact reason behind the benefit of anion encapsulation for selectivity is unclear at the moment. This could be related to the higher hydration enthalpy of hydroxide compared with that of chloride.[40] The anion-binding dehydration enthalpic cost for receptors that enforces a higher degree of dehydration (when the dehydration is caused by the part of the receptor that does not contribute enthalpically to binding anions, such as a spacer group) will be higher than for those enforcing a lower degree of dehydration. This may confer a greater selectivity on anionophores that encapsulate anions to a higher degree.

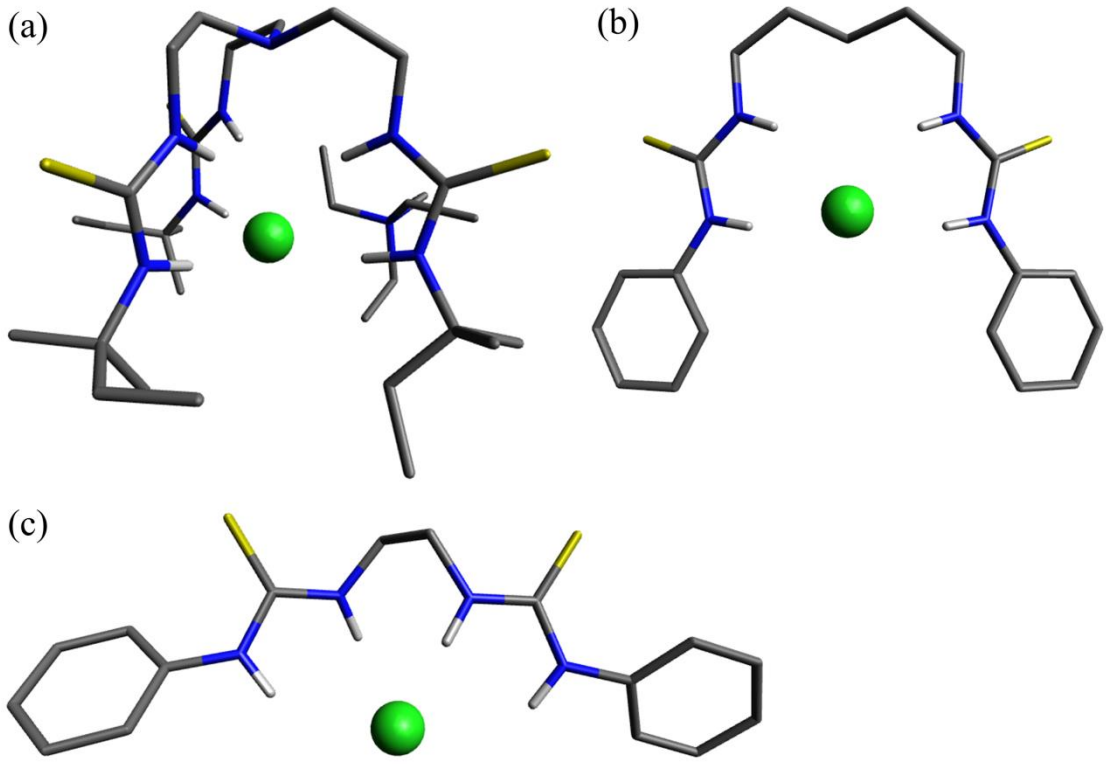

Figure 6.14 Crystallographic or optimized structures of chloride complexes. (a) X-ray crystal structure of **A12**·TEACl complex (ENWH performed the crystallographic studies); (b,c) Molecular models of chloride complexes of **A14** and **A13**, optimized using semi-empirical PM6 method. Non-hydrogen bonding hydrogen atoms are omitted for clarity. Atom colours: C (gray), H (white), N (blue), S (yellow), and Cl (green).

Although in general more acidic hydrogen bond donors are favorable for anion binding and transport (in terms of activity),[39,41] it seems that Cl^- > H^+/OH^- selectivity is severely compromised when more acidic protons are present. For example the selectivity sequence of **A11** > **A9** >> **A10** illustrates this effect. The negative correlation between selectivity and acidity is also supported by a comparison between **A2** (highest selectivity, binding anions with an N–H group and an N–CH_3 group as a C–H hydrogen bond donor as confirmed by downfield shift of CH_3 proton NMR signals upon addition of TBACl in $CDCl_3$, Figure 7.106, Chapter 7), **A3** (decreased, yet observable selectivity, two N–H groups), and **A1** (no selectivity, two N–H groups more acidic than those in **A3**). An obvious disadvantage of higher acidity anionophores is the possibility of proton transport by a deprotonation of a N–H proton. Deprotonation is, however, not the only reason for the observed negative correlation between selectivity and acidity, as even the halogen bonding-based carrier iodine shows no selectivity despite its inability to transport H^+ by deprotonation. Comparison of **A2** and **A3** which are assumed to transport OH^- but not H^+, suggest that this correlation might also in part arise from the more charge dense nature of OH^- compared to Cl^-. It seems that more acidic (thus more electron-deficient) anionophores favor the transport of the more charge dense OH^- over the less charge dense Cl^-. This idea is consistent with the previous report that the CH hydrogen bond-based anionophore **6-14**, which is much less acidic than NH hydrogen bond receptors, showed a high selectivity for Cl^- over the more charge dense anion HCO_3^-. In contrast, a highly acidic bis-urea anionophore lacked the Cl^- > HCO_3^- selectivity.[233]

The steroid scaffold is known to preorganise two anion binding motifs, resulting in powerful chloride carriers. Several reported and new cholapod-based urea carriers were also subject to the selectivity test. Compound **A15**[146] shows a modest selectivity of 3 fold, which completely vanished when a trifluoroacetamide group[231] as an additional hydrogen bond donor was introduced, likely due to its high acidity. However, remarkable selectivity was shown for **A17** and **A18**, which feature binding site enclosure.[224] Compound **A17** was extremely selective to the extent that H^+/OH^- transport is too inactive for performing Hill plot analysis, although this compound is not a very active chloride carrier. Despite containing an acidic trifluoroacetamide group, the more active **A18** shows a surprising 100-fold selectivity. Presumably, the advantages of binding site enclosure, possibly also from decrease of urea N–H acidity due to electron-donating alkoxy substituents, outweigh the disadvantage of having an acidic trifluoroacetamide group.

Further evidence for the Cl^- > H^+/OH^- selectivity of **A9**, **A12** and **A18** has been afforded by another independent assay that shows their coupling to proton carrier CCCP to facilitate H^+/Cl^- symport or Cl^-/OH^- antiport, which couples to simple diffusion of NH_3 leading to formal NH_4Cl flux that can be measured using ion selective electrode (ISE, Section 7.5.8.2, Chapter 7) and osmotic response (Section 7.5.9.2, Chapter 7) assays.

6.2.3 Anion transport mechanisms – three types of anionophores

As valinomycin (an electrogenic carrier) and monensin (an electroneutral carrier) function via fundamentally different mechanisms, these compounds were used to investigate the anion transport processes of representative anionophores. Carrier-induced chloride efflux was measured from vesicles entrapping KCl and suspended in an inert external K_2SO_4 solution. Valinomycin is able to dissipate the membrane potential from electrogenic chloride transport, allowing electrically coupled K^+/Cl^- flux in the presence of an electrogenic chloride transporter (Figure 6.15a).[211] Monensin, instead, dissipates the transmembrane pH gradient from Cl^-/OH^- antiport (or H^+/Cl^- symport) by allowing K^+/H^+ exchange, leading to formal KCl flux in the presence of a H^+/Cl^- symporter or Cl^-/OH^- exchanger (Figure 6.15b). The ability of an anionophore to couple with valinomycin to facilitate K^+/Cl^- flux, but not the ability to couple with monensin, is relevant to cystic fibrosis treatment, as the epithelial salt absorption process is the result of electric coupling between Cl^- flux through CFTR channel and Na^+ flux through epithelial sodium channels.[236]

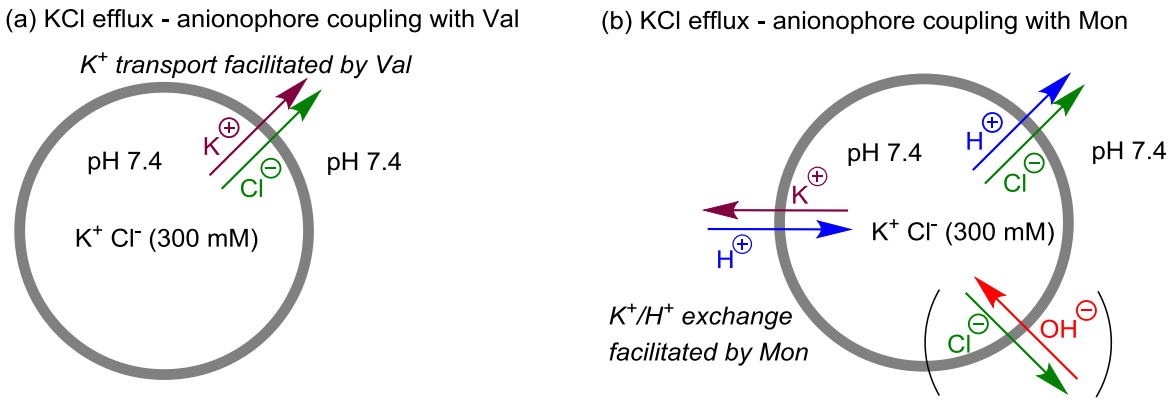

Figure 6.15 Schematic representation of (a) anionophore-facilitated electrogenic Cl^- transport coupling to valinomycin facilitated K^+ transport to give K^+/Cl^- co-transport and (b) anionophore-facilitated H^+/Cl^- symport or Cl^-/OH^- antiport coupling to monensin-facilitated K^+/H^+ antiport to give *formal* K^+/Cl^- co-transport. Buffer agent HEPES and K_2SO_4 used to balance the internal and external osmotic concentrations are omitted for clarity.

Indeed, prodigiosin couples to monensin but not valinomycin (Figure 6.16a), proving the "monensin-likeness", *i.e.*, electroneutral nature of prodigiosin facilitated anion transport. As expected, unselective anionophore **A1** couples to both valinomycin and monensin (Figure 6.16b), demonstrating that **A1** can facilitate both electrogenic chloride transport and electroneutral Cl^-/OH^- exchange (or H^+/Cl^- symport) at the same concentration. Importantly, selective anionophores **A12** and **A18** couple to valinomycin but not to monensin (Figure 6.16c and 6.16d), indicating that they can facilitate electrogenic chloride transport with negligible H^+/OH^- transport at the same loading. Notably the ionophore coupling behaviors of anionophores **A12** and **A18** are exactly the same as that of cationophore valinomycin which couples to "valinomycin-like"

anionophores **A12** and **A18** but not to the "monensin-like" anionophore prodigiosin. The "valinomycin-likeness" of selective anionophores **A12** and **A18**, but not of other unselective anionophores **A1** and prodigiosin, is thereby firmly established.

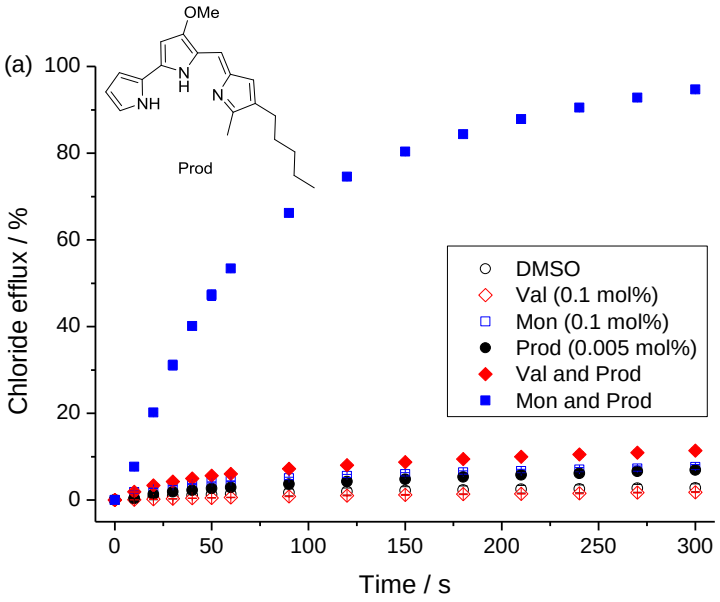

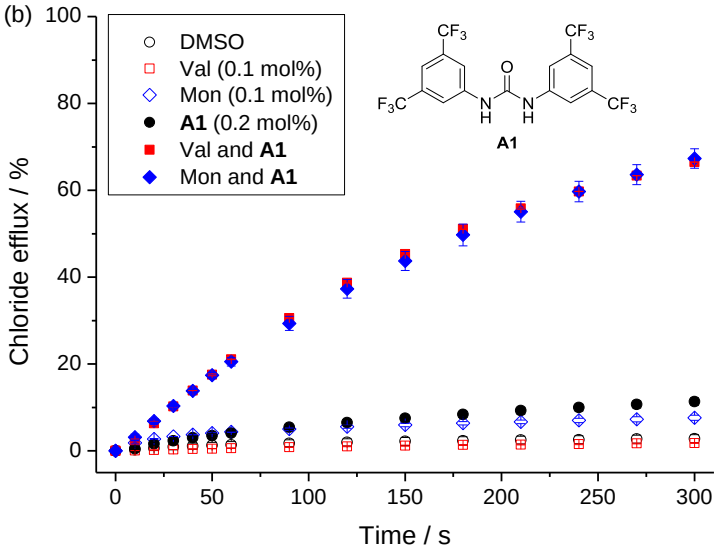

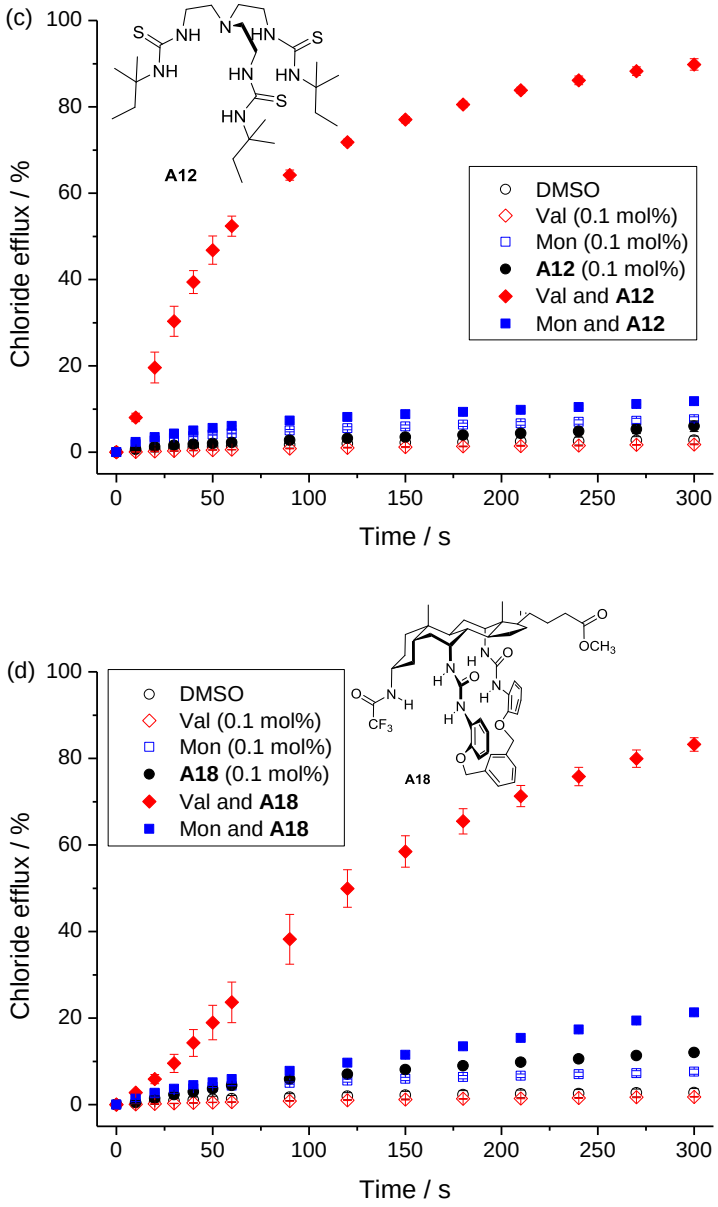

Figure 6.16 Coupling between cationophores and anionophores in facilitating net KCl flux. POPC LUVs (mean diameter 200 nm) were loaded with KCl (300 mM) and K_2SO_4 (200 mM), buffered at pH 7.4 with 5 mM HEPES. The vesicles were suspended in an external solution of K_2SO_4 (200 mM) buffered at pH 7.4 with 5 mM HEPES. Chloride efflux induced by prodigiosin (Prod), **A1**, **A12** or **A18** in the absence and presence of valinomycin (Val, 0.1 mol% with respect to lipid) or monensin (Mon, 0.1 mol%) was monitored by a chloride selective electrode. All compounds were added to the vesicle suspensions as DMSO solutions. Detergent was added at 5 min to release all chloride and calibrate to 100% chloride efflux. Lipid concentration is 1.0 mM. Error bars represent SD from two or three repeats.

The above results demonstrate that prodigosin, **A1**, and **A12**&**A18** are representative examples of three types of anionophores. The function of **A1** can be roughly described as a combination of **A12** (or **A18**) and a protonophore. To further demonstrate their characteristic behavior, the effects of K^+ carrier valinomycin and proton carrier CCCP on the rates of pH gradient dissipation induced by these anionophores in a KCl medium were examined. Previously, valinomycin and cyanide-4-(trifluoromethoxy)phenylhydrazone (FCCP, which is similar to CCCP) have been used by

Matile and coworkers in HPTS base-pulse assays to identify the selectivity of ion channels with respect to proton transport.[182] For ion channels that facilitate K^+/H^+ antiport, accelerated transport (dissipation of pH gradient) with valinomycin indicates the transport rates of $H^+ > K^+$ (K^+ transport rate-limiting, valinomycin improves the rate-limiting step)[257], while accelerated transport with FCCP, on the contrary, indicates the transport rates of $K^+ > H^+$ (H^+ transport rate-limiting, FCCP improves the rate-limiting step)[258]. The same rationale is likely also true for anion transporters that facilitate H^+/Cl^- symport or Cl^-/OH^- antiport: Accelerated transport with valinomycin indicates the transport rates of $H^+/OH^- > Cl^-$ (Cl^- transport rate-limiting, valinomycin-facilitated K^+ transport replaces slow Cl^- transport to accompany H^+/OH^- transport); accelerated transport with FCCP (or CCCP) indicates the transport rates of $Cl^- > H^+/OH^-$ (H^+/OH^- transport rate-limiting). For ionophores that only facilitate electroneutral processes, the transport rate should not be affected by either valinomycin or FCCP (CCCP).

Here HPTS tests were performed with valinomycin and CCCP (which is similar to FCCP but significantly cheaper) to support the conclusions regarding characteristic behaviour of different types of cationophores (Figure 6.17) and anionophores (Figure 6.18). The results are indeed as expected. Table 6.3 summarizes different behaviour of three types of ionophores in HPTS base-pulse assays. Valinomycin itself leads to no pH gradient dissipation at 0.005 mol%, but in the presence of CCCP coupled K^+/H^+ exchange leads to rapid pH gradient dissipation (Figure 6.17a). Monensin is an electroneutral cationophore and therefore insensitive to electrogenic ionophores valinomycin and CCCP in this assay (Figure 6.17b), the same behaviour observed with prodigiosin (Figure 6.18a) that is an anionophore counterpart of monensin. The rate of pH gradient dissipation induced by **A1** was accelerated by valinomycin and not by CCCP (Figure 6.18b), indicating $H^+/OH^- > Cl^-$ selectivity. Conversely, the sensitivity to CCCP and insensitivity to valinomycin observed with **A12** (Figure 6.18c) and **A18** (Figure 6.18d) in the HPTS assay is consistent with their $Cl^- > H^+/OH^-$ selectivity. Figure 6.19 showed that perfluorohexyl iodide (**5-15**), a halogen-bond based anionophore also has $Cl^- > OH^-$ selectivity. Figure 6.20 illustrates the function of the ionophores studied in this section.

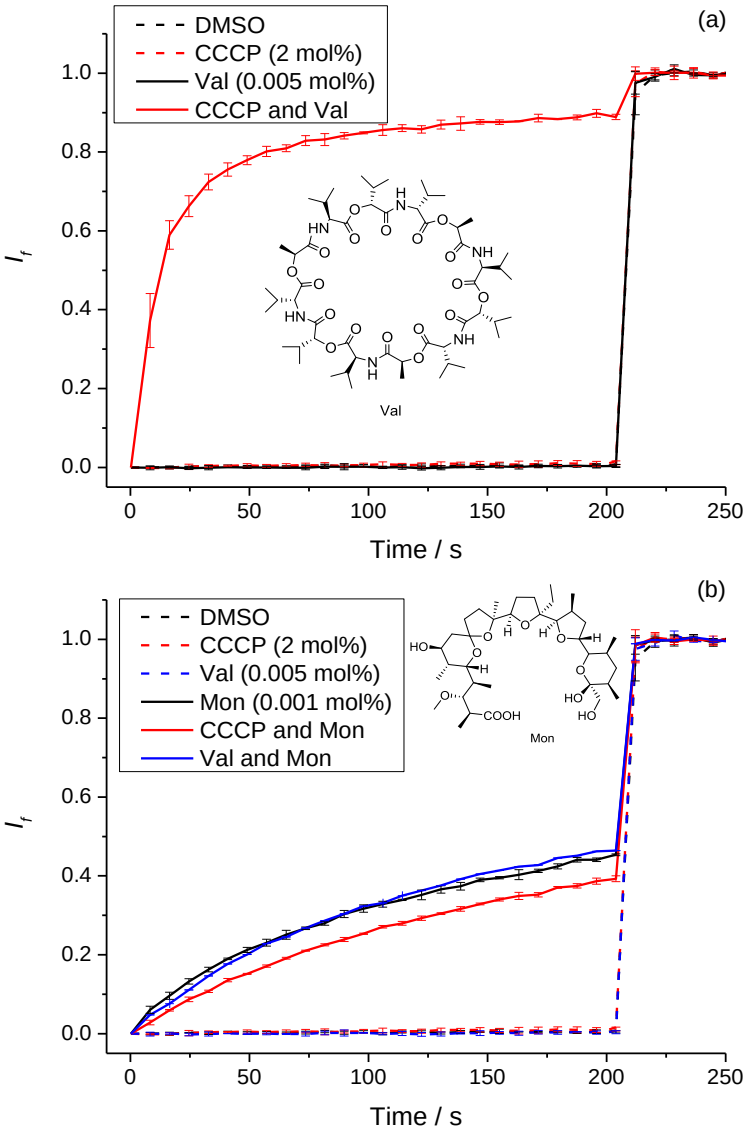

Figure 6.17 (a) Effect of CCCP (2 mol%) on the rate of pH gradient dissipation (measured by HPTS fluorescence) induced by valinomycin (Val, 0.005 mol%) in POPC LUVs (mean diameter 200 nm) loaded with and suspended in a HEPES-buffered potassium gluconate (100 mM) solution. (b) Effects of CCCP (2 mol%) and valinomycin (Val, 0.005 mol%) on the rate of pH gradient dissipation induced by monensin (Mon, 0.001 mol%) in LUVs suspended in a potassium gluconate (100 mM) containing media. Carrier concentrations are shown as carrier to lipid molar ratios. Error bars represent SD from two or three repeats.

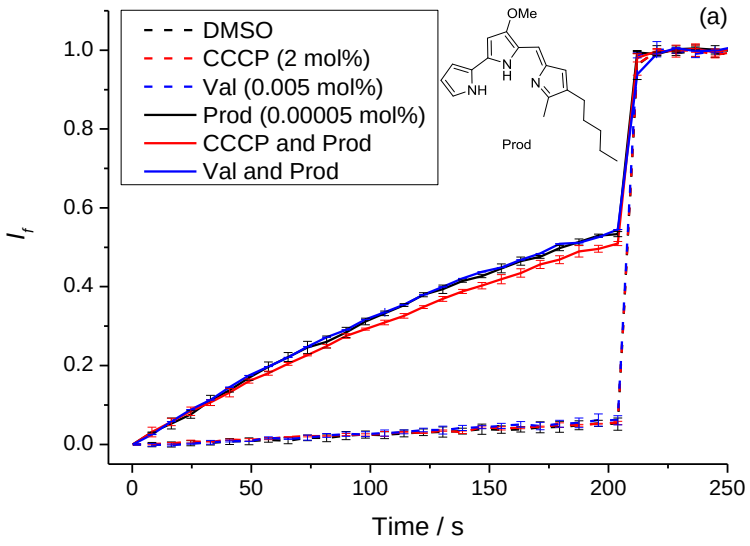
(a)
DMSO
CCCP (2 mol%)
Val (0.005 mol%)
Prod (0.00005 mol%)
CCCP and Prod
Val and Prod
OMe
NH
N
H
N
Prod
I_f
Time / s

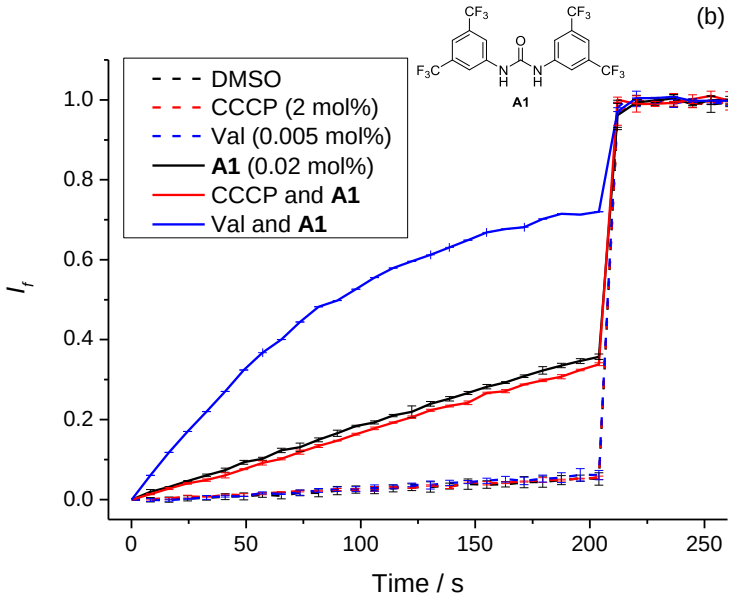
(b)
DMSO
CCCP (2 mol%)
Val (0.005 mol%)
A1 (0.02 mol%)
CCCP and A1
Val and A1
CF3
F3C
CF3
CF3
O
N
H
N
H
A1
I_f
Time / s

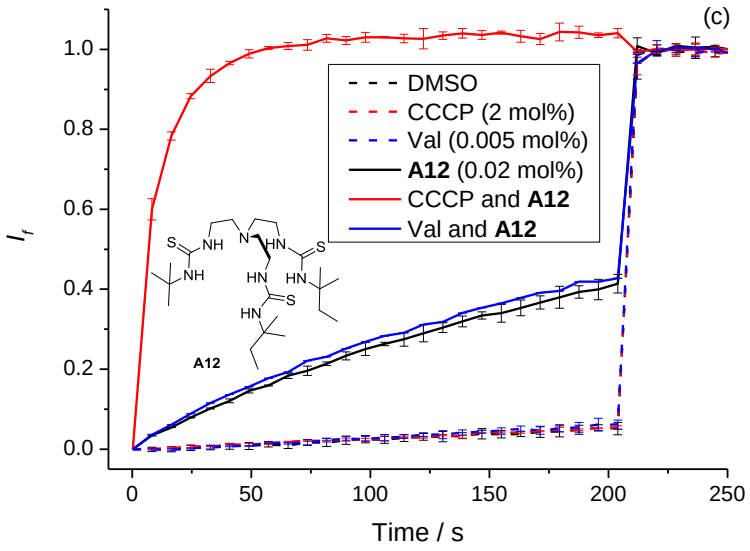
(c)
DMSO
CCCP (2 mol%)
Val (0.005 mol%)
A12 (0.02 mol%)
CCCP and A12
Val and A12
S
NH
NH
N
HN
S
HN
HN
HN
S
HN
A12
I_f
Time / s

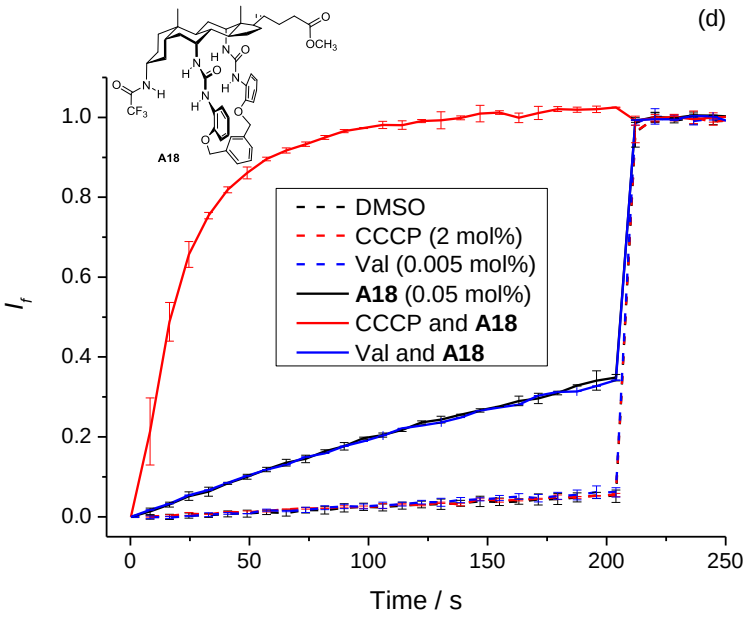

Figure 6.18 Effects of CCCP (2 mol%) and valinomycin (Val, 0.005 mol%) on the rate of pH gradient dissipation (measured by HPTS fluorescence) induced by prodigiosin (Prod, 0.00005 mol%), **A1** (0.02 mol%), **A12** (0.02 mol%) or **A18** (0.05 mol%) in POPC LUVs (mean diameter 200 nm) loaded with and suspended in a HEPES-buffered KCl (100 mM) solution. Carrier concentrations are shown as carrier to lipid molar ratios. Error bars represent SD from two or three repeats.

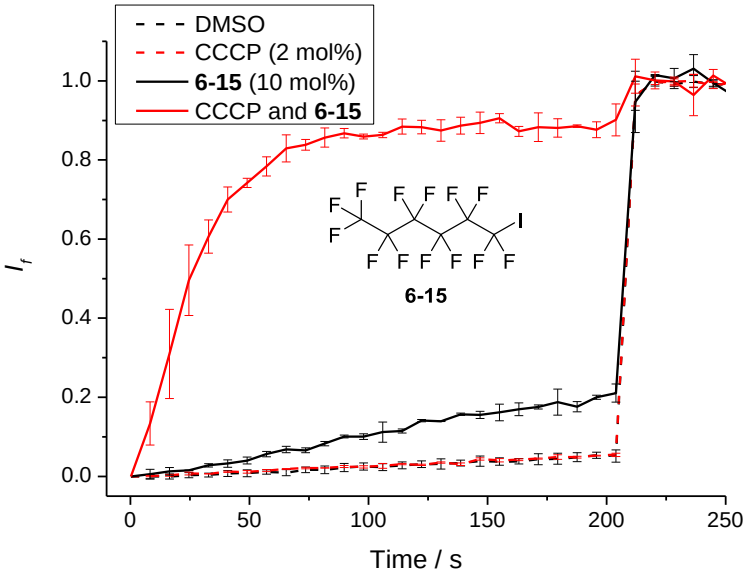

Figure 6.19 Effects of CCCP (2 mol%) on the rate of pH gradient dissipation (measured by HPTS fluorescence) induced by **6-15** (10 mol%) in POPC LUVs (mean diameter 200 nm) loaded with and suspended in a HEPES-buffered KCl (100 mM) solution. Carrier concentrations are shown as carrier to lipid molar ratios. Error bars represent SD from two or three repeats. The insensitivity of **6-15** to valinomycin in HPTS assays has been reported previously by Matile *et al.*[148]

Table 6.3 Different behaviour of three types of ionophores in HPTS base-pulse assays in response to the presence of a protonophore (*e.g.* FCCP, CCCP and gramidicin D[a]) and valinomycin.

Ionophore type	Electroneutral ionophores	Electrogenic ionophores	
		H^+/OH^- > K^+ (cationophores) H^+/OH^- > A^- (anionophores)	K^+ > H^+/OH^- (cationophores) A^- > H^+/OH^- (anionophores)
Accelerated transport with a protonophore?	No	No	Yes
Accelerated transport with valinomycin?	No	Yes	No
Examples (cationophores)	Monensin	-[b]	Valinomycin[c]
Examples (anionophores)	Prodigiosin	**A1**	**A12**, **A18** and **6-15**

[a] Gramicidin D cannot be used to study cationophores because it facilitates M^+ transport.
[b] No example available in this paper.
[c] "Enhanced transport with valinomycin?" not applicable because of self-referencing.

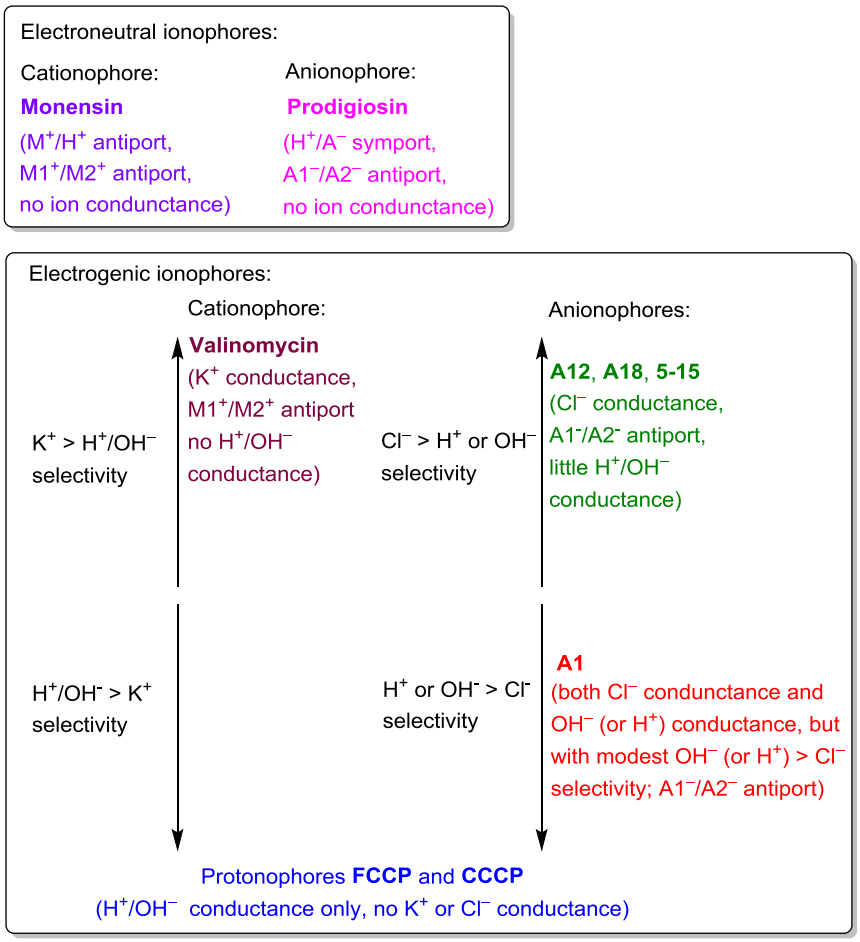

Figure 6.20 Schematic representation illustrating different functions of several cationophores and anionophores. $M1^+/M2^+$ antiport refers to exchange of two metal ions, *e.g.* K^+/Rb^+ antiport. $A1^-/A2^-$ antiport refers to exchange of two anions, *e.g.* Cl^-/NO_3^- antiport.

6.2.4 pH dependence of chloride/nitrate exchange

As the tripodal thioureas **A9**-**A12** contain a protonatable nitrogen atom, a concern exits whether they carry anions in their protonated form (Figure 6.22b) as is the case with prodigiosin, or they function as neutral carriers (Figure 6.22a). The pH dependence of Cl^-/NO_3^- exchange facilitated by **A9**, **A12**, trihexylamine and prodigiosin, all of which contain a protonatable nitrogen atom, was examined, with **7** tested as a negative control. The experiments were conducted under conditions of our standard ISE assay for investigating pH-dependent Cl^-/NO_3^- exchange.[143] Carrier-facilitated chloride efflux was measured from vesicles loaded with NaCl suspended in an external $NaNO_3$ solution. Both the internal and external solutions were buffered at the same pH (using sodium citrate salts for pH 4.5, sodium phosphate salts for pH 7.2, and NaOH for pH 11.5), and a constant ionic strength of 500 mM was used. Possible $Metal^+/Cl^-$ symport that may contribute to the observed chloride efflux has been previously confirmed to be non-existing or negligible for **A7**[259], **A9**[227], trihexylamine[227], and prodigiosin[209], as replacement of external $NaNO_3$ in the vesicle transport experiments by Na_2SO_4 (SO_4^{2-} transport is unlikely due to the hydrophilicity of SO_4^{2-}) leads to negligible chloride flux. This is also true for **A12** as can be seen from Figure 6.16c, in which **A12** itself induced negligible chloride efflux from vesicles loaded with KCl suspended in a K_2SO_4 solution.

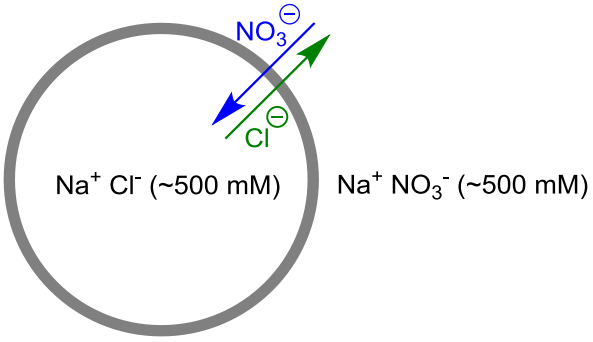

Figure 6.21 Schematic representation of ISE assay for Cl^-/NO_3^- exchange. Chloride efflux is measured by a chloride selective electrode. Buffer agent is omitted for clarity.

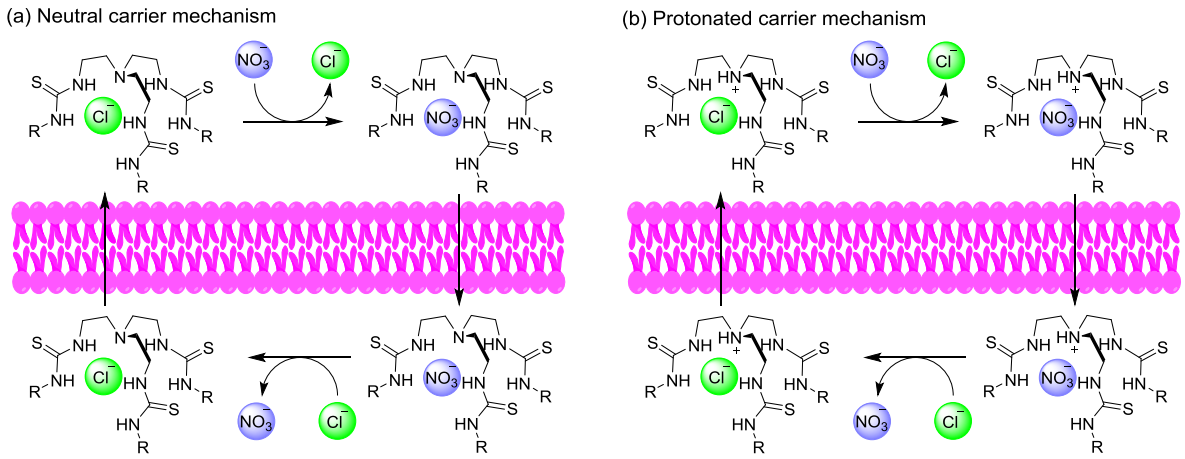

Figure 6.22 Two mechanisms for Cl^-/NO_3^- antiport facilitated by TREN-based tripodal thioureas: (a) Neutral carrier mechanism; (b) Protonated cationic carrier mechanism. pH-dependent studies have confirmed that (a) is the correct mechanism.

The results are shown in Figure 6.23. Control compound **A7** shows no appreciable pH dependence as expected (Figure 6.23a). The transport activity of tripodal thioureas **A9** (Figure 24b) and **A12** (Figure 6.23c) shows almost no pH dependence from pH 11.5 to pH 7.2, but chloride transport was almost completely quenched at pH 4.5. This confirms our previous hypothesis that the species responsible for chloride and nitrate transport are their neutral forms while their protonated forms are inactive in facilitating anion transport. Taking into account results from the NMDG-Cl-gramicidin assay which show that their chloride transport can be coupled to electrogenic proton transport facilitated by gramicidin, this means that they can facilitate electrogenic transport of chloride by (in their neutral form) forming an anionic complex with chloride from the aqueous phase, the anionic complex diffusing through the lipid bilayer membrane, release of chloride at the lipid bilayer-water interface, and the neutral, uncomplexed form diffusing back to the other side of the membrane.

Trihexylamine (Figure 6.23d) and prodigiosin (Figure 6.23e), on the contrary, show transport activity at neutral and acidic conditions (pH 4.5 and pH 7.2), whereas being inactive at pH 11.5. This confirms that they transport anions in their protonated forms, forming overall neutral chloride and nitrate complexes. The results with prodigosin support its assumed mechanism for facilitating Cl^-/NO_3^- exchange (Figure 6.5b), proposed by J. T. Davis *et al*.[209]

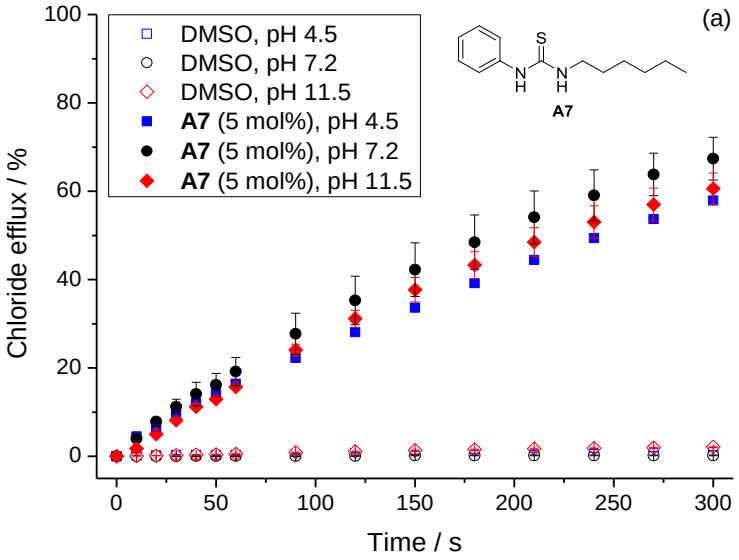
(a)
DMSO, pH 4.5
DMSO, pH 7.2
DMSO, pH 11.5
A7 (5 mol%), pH 4.5
A7 (5 mol%), pH 7.2
A7 (5 mol%), pH 11.5
A7
Chloride efflux / %
Time / s

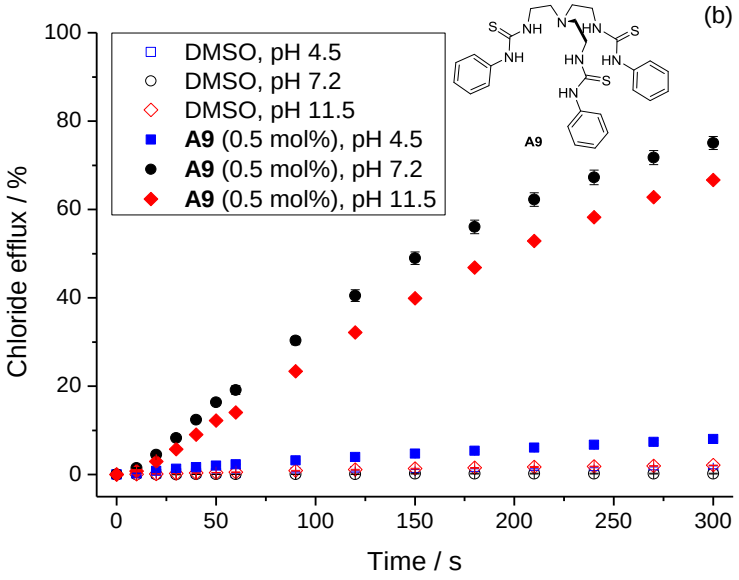
(b)
DMSO, pH 4.5
DMSO, pH 7.2
DMSO, pH 11.5
A9 (0.5 mol%), pH 4.5
A9 (0.5 mol%), pH 7.2
A9 (0.5 mol%), pH 11.5
A9
Chloride efflux / %
Time / s

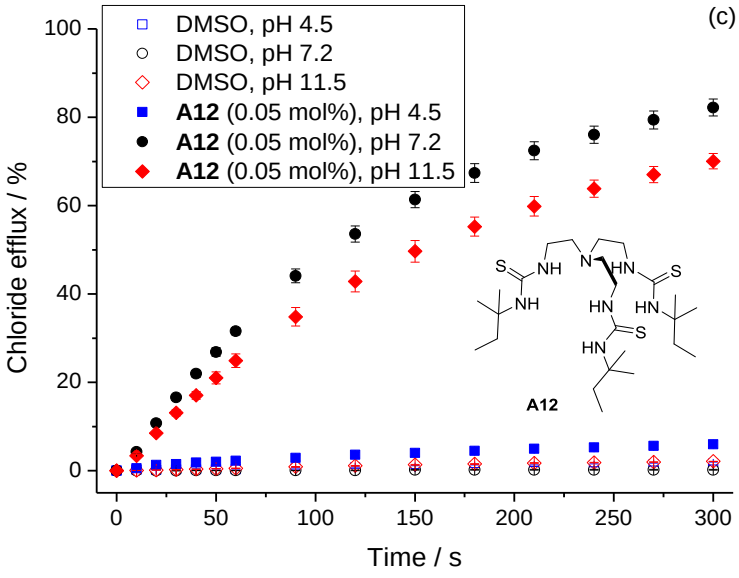
(c)
DMSO, pH 4.5
DMSO, pH 7.2
DMSO, pH 11.5
A12 (0.05 mol%), pH 4.5
A12 (0.05 mol%), pH 7.2
A12 (0.05 mol%), pH 11.5
A12
Chloride efflux / %
Time / s

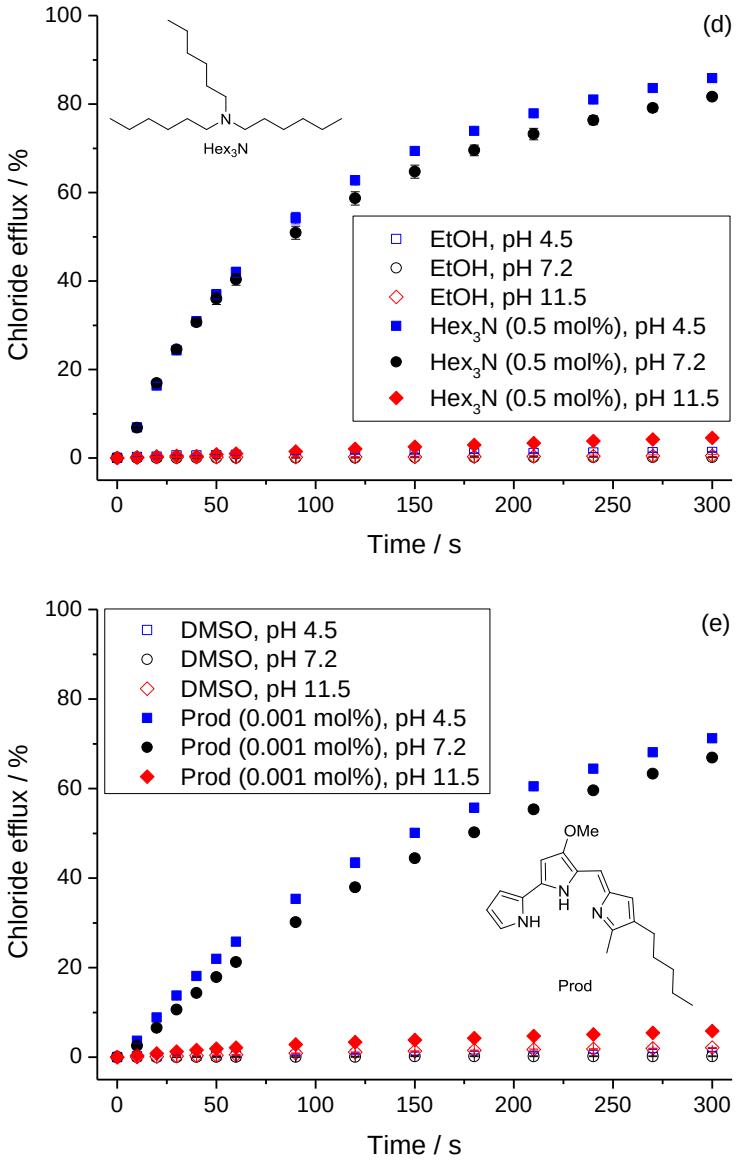

Figure 6.23 pH dependence of chloride efflux (measured using a chloride selective electrode) facilitated by **A7** (5 mol%), **A9** (0.5 mol%), **A12** (0.05 mol%), trihexylamine (Hex_3N, 0.5 mol%) and prodigiosin (Prod, 0.001 mol%) from POPC LUVs (mean diameter 200 nm) loaded with NaCl (~500 mM) and suspended in a $NaNO_3$ (~500 mM) solution buffered at different pH. Carrier concentrations are shown as carrier to lipid molar ratios. Error bars represent SD from two or three repeats.

6.2.5 Effect of anion binding affinity on electrogenic/electroneutral mechanisms

In Section 6.2.3, vesicle-based assays are presented that allow distinguishing between electrogenic (*e.g.* valinomycin, **A1**, **A12** and **A18**) and electroneutral (*e.g.* monensin and prodigiosin) ionophores. It can be seen that among these limited examples that electrogenic ionophores are neutral receptors that form charged complexes with the transported ionic species, whereas electroneutral ionophores contain a pH-sensitive groups that allows ion transport via formation of an overall neutral ion pair complex. Similarly, Pressman have categorized naturally occurring cationophores into "electrogenic" or "electrophoretic" carriers (usually neutral cationophores, *e.g.* valinomycin) and "exchange diffusion" carriers (carboxylate-containing cationophores, *e.g.* monensin, which belong to the class of electroneutral ionophores).[189] However, this rule is not always true for anionophores. Even without a pH-sensitive group, an anionophore can behave as an electroneutral anionophore that facilitates electroneutral processes including Cl^-/OH^-antiport (or H^+/Cl^- symport) and Cl^-/NO_3^- antiport, but is inactive in facilitating electrogenic Cl^- transport. **A10** (Figure 6.24a) and **A16** (Figure 6.24b) are found to behave in such manner, in which respect they appeared functionally similar to prodigiosin (Figure 6.5 and Figure 6.16a).

It is surprising that neutral anionophores **A10** and **A16** are inactive in facilitating electrogenic chloride transport, despite their high activity in facilitating electroneutral anion exchange of Cl^- for NO_3^- or OH^-. Interestingly, a similar statement was made by Edwards and coworkers that cholapod bis-squaramides are active in anion exchange but inactive in unidirectional anion transport (or in other words "electrogenic chloride transport"), although the data have not been published.[225] It was proposed by Edwards and coworkers that strong anion binders cannot decomplex (which is a requirement for electrogenic chloride transport, Figure 6.25b) and therefore are inactive in electrogenic transport. But they can undergo direct anion exchange at the lipid-water interface, effectivel facilitating electroneutral anion exchange and HCl cotransport which do not require back diffusion of the uncomplexed form (Figure 6.25c). Another likely cause for their low electrogenic activity is binding to the lipid phosphate head group which inhibits back diffusion of the uncomplexed form. The current results indeed support the hypothesis that too strong anion binders have poor electrogenic activities. Compared with their respective analogues **A12** and **A18**, **A10** and **A16** have higher affinity for anions due to more acidic N–H protons (also **A18** has electron-rich oxygen atoms which repulse anions and therefore binds anions more weakly than **A16**). Presumably due to the "too strong" anion binding affinity, **A10** and **A16** cannot facilitate electrogenic chloride transport, whereas weaker binders **A12** and **A18** are rather active electrogenic chloride carriers (Figure 6.25a).

The results imply that in some cases (*e.g.* **A10** and **A16**) the activity in facilitating Cl^-/NO_3^- exchange cannot indicate the usefulness of an anionophore in cystic fibrosis treatment which requires an electrogenic mechanism. To design active electrogenic chloride ionophores, the anion binding affinity cannot be too strong.

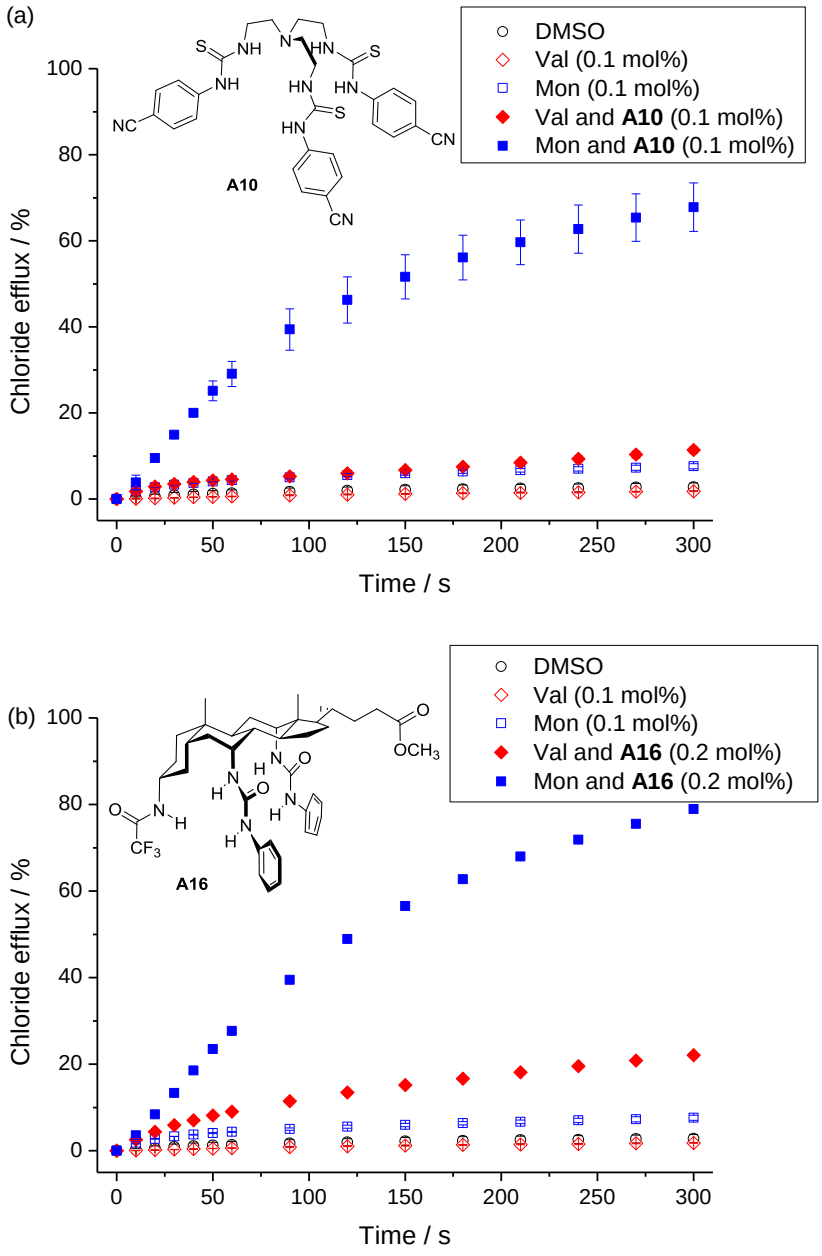

Figure 6.24 Coupling between cationophores and anionophores in facilitating net KCl flux. POPC LUVs (mean diameter 200 nm) were loaded with KCl (300 mM) and K_2SO_4 (200 mM), buffered at pH 7.4 with 5 mM HEPES. The vesicles were suspended in an external solution of K_2SO_4 (200 mM) buffered at pH 7.4 with 5 mM HEPES. Chloride efflux induced by **A10** or **A16** in the absence and presence of valinomycin (Val, 0.1 mol% with respect to lipid) or monensin (Mon, 0.1 mol%) was monitored by a chloride selective electrode. All compounds were added to the vesicle suspensions as DMSO solutions. Detergent was added at 5 min to release all chloride and calibrate to 100% chloride efflux. Lipid concentration is 1.0 mM. Error bars represent SD from two or three repeats. The behaviours of **A10** and **A16** in this test are similar to those of prodigiosin shown in Figure 6.16a.

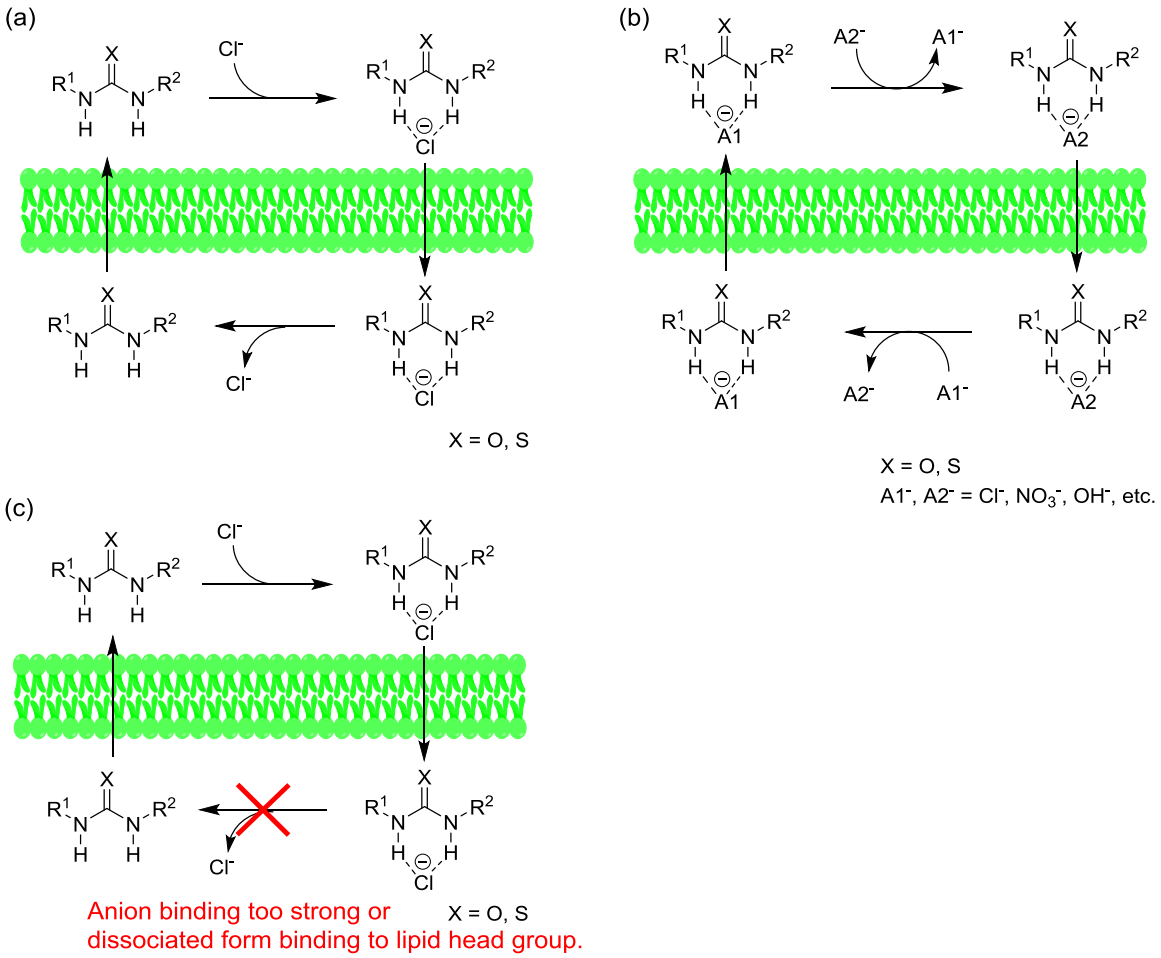

Figure 6.25 (a) Electrogenic Cl^- transport facilitated by a neutral urea or thiourea (*e.g.* **A1**, **A12**, and **A18**); (b) Electroneutral anion exchange (*i.e.*, Cl^-/NO_3^- antiport) facilitated by a neutral urea or thiourea (*e.g.* **A1**, **A12**, **A18**, **A10** and **A16**); (c) Inability of a neutral urea/thiourea that binds Cl^- or lipid head group too strongly to facilitate electrogenic Cl^- transport (*e.g.* **A10** and **A16**).

6.2.6 Chloride vs. nitrate selectivity

The interest in studying chloride vs. nitrate selectivity (in membrane transport) of synthetic anionophores is mainly motivated by the curiosity whether that the chloride transport activity can be underestimated for some $Cl^- > NO_3^-$ selective anionophores if they were only assessed in the Cl^-/NO_3^- exchange experiment, the most popular assay currently being used. In addition, chloride vs. nitrate selectivity provides insight into the relationship between anion transport selectivity and the Hofmeister series. Moreover, chloride or nitrate selective anionophores may be peculiarly useful for certain biological research.

Initially the observation that **A9** is very active in the NMDG-Cl HPTS assay (EC_{50} (200s) = 0.0030 mol% with gramicidin, Table 6.2) but comparably inactive in Cl^-/NO_3^- exchange (EC_{50} (270 s) = 0.31 mol%[227]) attracted my attention. Although the EC_{50} values in the two different assays are not directly comparable, for most anionophores tested the EC_{50} (270 s) value in the Cl^-/NO_3^- exchange ISE assay is around 10 times of the EC_{50} (200 s) value in the NMDG-Cl HPTS assay (with gramicidin).

For **A9** however, these two values differed by two orders of magnitude. To examine the possibility of slow NO_3^- transport that led to the modest activity of **A9** in Cl^-/NO_3^- exchange, EC_{50} values were determined in the HPTS assays with NMDG-NO_3 used as the internal and external salt component, while gramicidin was added to allow proton permeation thus making the transport process rate-limited by nitrate transport. The results were compared with those from the HPTS assays using NMDG-Cl as the salt component. Table 6.4 shows that **A9** indeed has a remarkable ~10-fold $Cl^- > NO_3^-$ selectivity, whereas **A12** is only weakly $Cl^- > NO_3^-$ selective and trihexylamine on the contrary shows a remarkable 20-fold $NO_3^- > Cl^-$ selectivity. This explains the relatively modest activity of **A9** in the Cl^-/NO_3^- exchange assay.

Table 6.4 Quantitative determination of Cl^- vs NO_3^- selectivity using HPTS assays.

	HPTS, NMDG-Cl [a]		HPTS, NMDG-NO_3 [b]	
	n	EC_{50} / %	*n*	EC_{50} / %
A9	1.3	0.0029	1.0	0.027
A12	1.4	0.000856	1.2	0.00146
Hex_3N	1.1	0.023	1.0	0.0012

[a] A fluorescence assay to determine chloride transport activity. Large unilamellar vesicles (LUVs) of POPC (mean diameter 200 nm) were loaded with HPTS (1 mM) and NMDG-Cl (100 mM), buffered at pH 7.0 with 10 mM HEPES. The vesicles were suspended in an external solution of NMDG-Cl (100 mM) buffered at pH 7.0 with 10 mM HEPES. At the beginning of the experiment, a base pulse of NMDG (5 mM) was added to create a pH gradient, gramicidin D (0.1 mol%) was added to allow proton permeation and the dissipation of the pH gradient induced by the compound tested (added as a DMSO solution) was monitored by HPTS fluorescence. Lipid concentration for fluorescence measurement is 0.10 mM. Dose-dependent Hill plot analysis was performed to obtain a Hill coefficient (*n*) and an effective concentration to reach 50% transport (EC_{50}) at 200s for each carrier. Carrier concentrations were shown as carrier to lipid molar ratios.

[b] A fluorescence assay to determine nitrate transport activity. The conditions are the same as the above assay for chloride transport, except that NMDG-NO_3 (100 mM, both inside and outside) was used in place of NMDG-Cl.

The $Cl^- > NO_3^-$ selectivity determined for **A9** and the inverted selectivity determined for trihexylamine are consistent with the previous hypothesis by Gale and coworkers regarding the observation of a HPTS experiment.[227] In that test, vesicle suspensions with internal NaCl and external $NaNO_3$, upon treatment with **A9** or other tripodal urea/thioureas, show an initial increase of the internal pH (pH_i) followed by a slow pH_i decrease. This was explained by faster Cl^-/OH^- antiport (or functionally equivalent H^+/Cl^- symport, Figure 6.26a) followed by slower NO_3^-/OH^- antiport (or H^+/NO_3^- symport), which corresponds to $Cl^- > NO_3^-$ selectivity as confirmed here. In

contrast, the NO_3^- > Cl^- selective anionophore trihexylamine was reported to induce initial pH_i decrease followed by a slow pH_i increase in this test (Figure 6.26b).

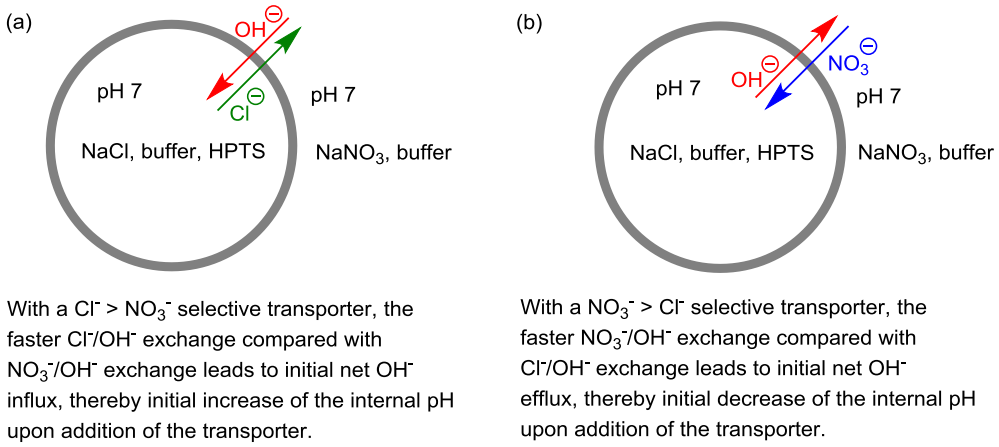

Figure 6.26 HPTS assay to identify Cl^- vs. NO_3^- selectivity. Note that the functionally equivalent processes of H^+/anion symport are not shown for clarity.

Based on this rationale, it was decided to screen several anionophores using this simple assay in Figure 6.26, determining whether they are Cl^- > NO_3^- selective or *vice versa* without quantitatively measuring the extent of selectivity. An advantage of this assay is the ability to detect a very weak selectivity. In contrast, the assay described in Table 6.4 required comparison of results obtained from two different batches of vesicle preparations, and thus has a high error not amenable to discerning a very small difference in transport rates. The results are summarized in Figure 6.27. Most mono- and di-podal ureas/thioureas and a monopodal squaramide show NO_3^- > Cl^- selectivity, which follows the relative lipophilicities of the two anions in the Hofemister series. This indicates that in these cases the transport selectivity was governed by the ease of dehydrating the transported anion.

Interestingly, as discussed previously, the two tripodal thioureas **A9** and **A11**, as well as other tripodal ureas/thioureas reported previously,[227] on the contrary, show Cl^- > NO_3^- selectivity. This may be attributed to different geometries of chloride and nitrate. Compared with the planar nitrate, the spherical geometry of chloride favours interactions with the 3D binding cavity of a tripodal receptor by forming six N–H···Cl^- hydrogen bond. This effect overcomes the Hofmeister bias favouring the transport of the more lipophilic nitrate. Note that a Cl^- > NO_3^- selectivity has been observed also for monopodal thiourea **A7**, in contrast to the behaviour of monopodal anionophores **A1** and **A8**. This apparent discrepancy can be explained by the Hill coefficient of ~3 of **A7** in chloride transport (Table 6.2), indicating that chloride is sequestered by three thiourea moieties in the membrane similarly to the situation with tripodal anionophores. The other hydrogen bond-based anionophores shown in Figure 6.27, in contrast to **A7**, show Hill coefficient values close to 1, implying chloride transport likely via 1:1 recepter-chloride complexes.

It is interesting also to note that halogen bond anionophore iodine shows $Cl^- > NO_3^-$ selectivity. This should not be interpreted as "anti-Hofmeister" selectivity, as iodine has been previously shown to transport iodide and bromide faster than it transports chloride.[234] Instead, the $Cl^- > NO_3^-$ selectivity can be attributed to the intrinsic selectivity of iodine for halides over oxoanions due to the charge-transfer character of iodine-halide interactions.[2]

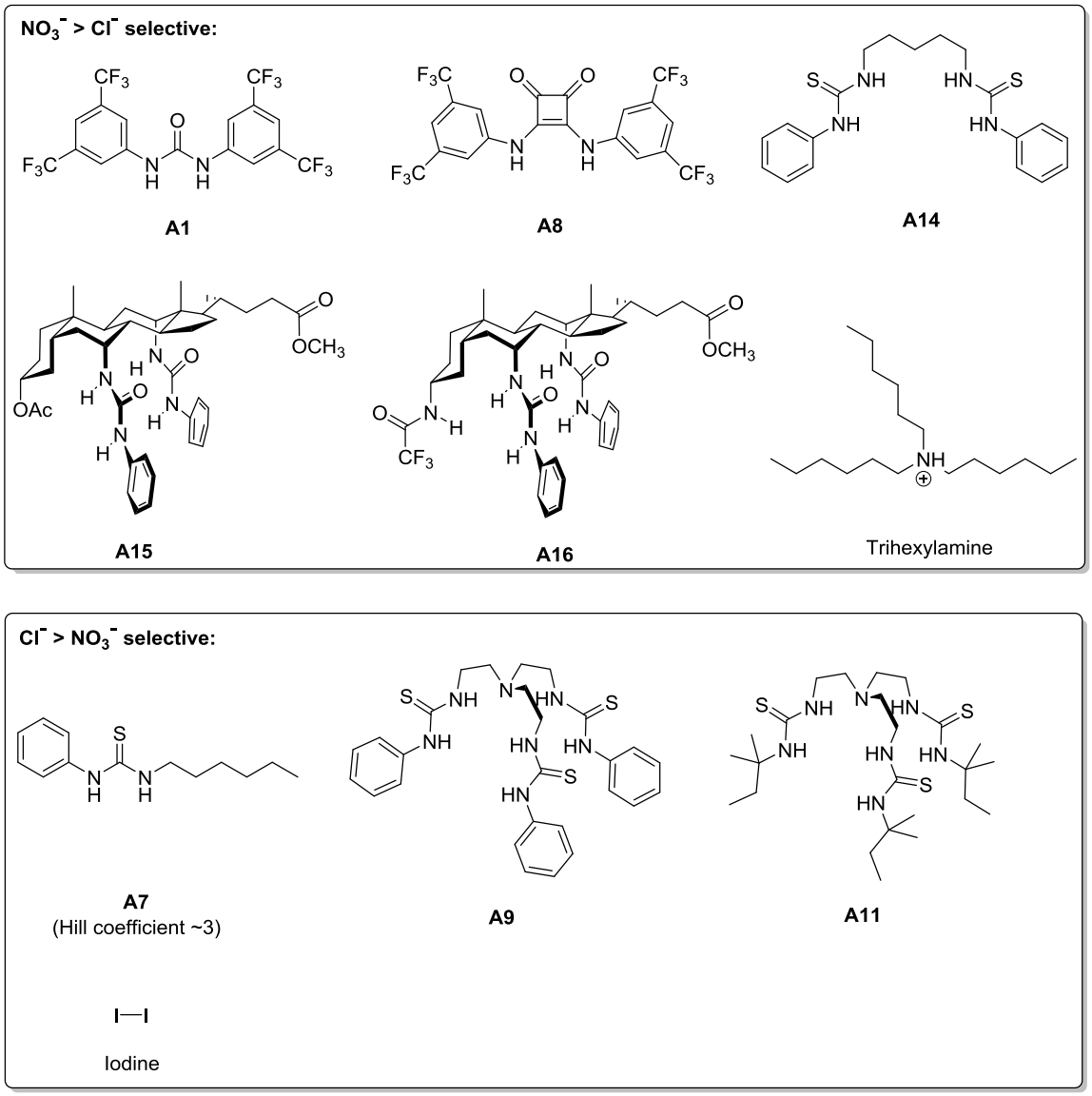

Figure 6.27 Cl^- vs. NO_3^- selectivity examined for several anionophores using the assay described in Figure 6.26.

6.3 Conclusions

(1) It is shown that prodigiosin is unable to facilitate electrogenic transport (conductance) of H^+, OH^- or Cl^- at low concentrations, despite its powerful activity in facilitating H^+/Cl^- symport and Cl^-/NO_3^- exchange which are electroneutral processes. Therefore prodigiosin cannot function as a

protonophore or an electrogenic anionophore, and should not be used to perform the function of CFTR channel.

(2) It is demonstrated for the first time the side-effect of electrogenic H^+/OH^- transport facilitated by many synthetic anionophores. By comparison between normal and mono-N-methylated ureas/thioureas evidence was provided that receptors acting through hydrogen bonding can transport protons by a CCCP-like deprotonation mechanism or hydroxide ions by hydrogen bonding, the latter pathway more likely for less acidic hydrogen bond donors.

(3) Synthetic small molecule chloride carriers **A12** and **A18** have been developed for which H^+/OH^- transport is suppressed, and thus act as counterparts to the highly-evolved electrogenic K^+ carrier valinomycin. The remarkable $Cl^- > H^+/OH^-$ selectivity of these systems is confirmed by (i) coupling to both proton channel gramicidin and proton carrier CCCP in facilitating H^+/Cl^- symport (or Cl^-/OH^- antiport) as shown by fluorescence, ISE and osmotic response assays; (ii) coupling to valinomycin but not to monensin to facilitate net KCl flux. **A12** and **A18** represent the first proven examples of chloride ionophores that facilitate "pure" electrogenic chloride transport. Compounds of this type can play a unique role in physiological research, and are potentially more suitable for treating "channelopathies" such as cystic fibrosis.

(4) The results provide guidelines in designing/choosing different types of anionophores (electroneutral or electrogenic, dissipate pH/proton gradient or not) for different biological applications: (i) The ability to encapsulate chloride with weakly acidic hydrogen bond donors seems to be crucial for the $Cl^- > H^+/OH^-$ selective electrogenic ionophores. (ii) Strong anion binders are active in facilitating electroneutral anion exchange, but can be inactive in facilitating electrogenic chloride transport due to slow decomplexation kinetics.

(5) Some literature anionophores show noticeable $Cl^- > H^+/OH^-$ selectivity. These include organic halogen bond donor **6-15**, strapped calixpyrroles **6-21** and **6-22**, which can be inferred from the data shown in the literature or obtained here. Such a merit was not noted in the original publications of these anionophores. Notably, all of these anionophores feature encapsulation of chloride with weakly acidic hydrogen or halogen bond donors, supporting the proposed structure-selectivity relationship.

(6) In general most neutral hydrogen bond-based anionophores show $NO_3^- > Cl^-$ selectivity following the Hofmeister bias favouring the transport of more lipophilic anions. Exceptions are found for tripodal urea/thiourea anionophores that show $Cl^- > NO_3^-$ selectivity, presumably due to better geometry fit of the 3D binding cavity for spherical anions than for planar anions.

Chapter 7: Supporting information

7.1 Supporting information for Chapter 2

7.1.1 General

All commercial reagents and solvents were used as received. 3,4,9,10-Perylenetetracarboxylic acid dianhydride, *R*-mandelic acid, *S*-mandelic acid, *S*-lactic acid, *S*-tartaric acid, *S*-1-phenylethylamine and *R*-1-phenylpropionic acid were purchased from Energy Chemicals. *N*,*N*-dimethylethylenediamine, *R*-2-chloromandelic acid, *S*-phenyllactic acid, *R*-malic acid, and *L*-phenylalanine were purchased from Aladdin Reagents. 1,8-Bis(dimethylamino)naphthalene, *S*-2-chloromandelic acid, *R*-hexahydromandelic acid and *S*-hexahydromandelic acid were purchased from Sigma-Aldrich. *R*-2-phenyllactic acid, *R*-lactic acid and *S*-malic acid were products of J&K Scientific. 4-Bromomethylphenylboronic acid was obtained from Frontier Scientific. *S*-1-phenylethanol was purchased from Alfa Aesar, (1*R*,2*S*)-1,2-diphenyl-2-aminoethanol was purchased from Shanghai Darui Fine Chemical Co. Ltd. 2-Bromomethylphenylboronic acid was purchased from Bepharm Limited. Other reagents such as *R*-tartaric acid and 2-butanol were products of Sinopharm Chemical Reagent Co. Ltd.

^{1}H NMR and ^{13}C NMR spectra were recorded on a Bruker AV500 NMR spectrometer. High-resolution mass spectra (HRMS) were taken on a Bruker En Apex ultra 7.0T FT-MS mass spectrometer. Absorption spectra were obtained on a Varian Cary 300 UV-Vis spectrophotometer. Circular dichroism (CD) spectra were recorded on a Jasco J-810 CD spectropolarimeter, using a 1 cm quartz cuvette. Dynamic light scattering measurements were performed on a Malvern Zetasizer Nano ZS. All spectroscopic and DLS measurements were carried out at the ambient temperature of 298 K. Linear discriminant analysis (LDA) was carried out using the software XLSTAT 2013.

7.1.2 Experimental

Synthesis of Sensors C1 and C2

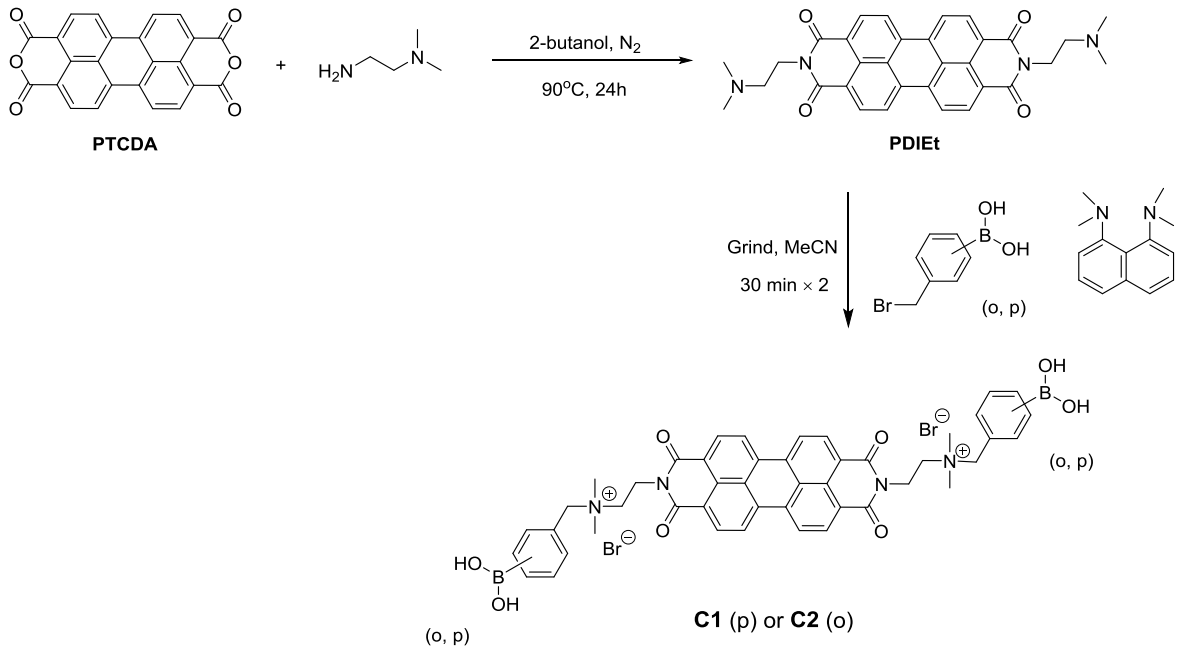

Synthesis of PDIEt

N,*N*'-Bis(ethylenedimethylamine)-3,4,9,10-perylenediimide (**PDIEt**) was synthesized according to a reported procedure[61]. 3,4,9,10-Perylenetetracarboxylic acid dianhydride (**PTCDA**, 1.18 g, 3 mmol) and N,N-dimethylethylenediamine (3 mL, 27.3 mmol) were added to 40 mL of isobutanol and stirred at 90 °C for 24 h under nitrogen atmosphere. The reaction mixture was allowed to cool to room temperature and the crude product was filtered and washed with deionized water and ethanol. The obtained residue was suspended in 5% aqueous NaOH solution and heated at 90°C for 30 min to remove the unreacted **PTCDA**. The suspension was filtered and washed with water and ethanol, dried under vacuum to give **PDIEt** as a black solid (1.55g, 97%). ^{1}H NMR (500 MHz, TFA) δ 9.15 (d, *J* = 8.2 Hz, 4H), 9.08 (d, *J* = 8.1 Hz, 4H), 5.07 (m, 4H), 4.04 (m, 4H), 3.48 (s, 12H). ^{13}C NMR (126 MHz, TFA) δ 166.39, 136.58, 133.33, 129.48, 126.57, 124.60, 121.60, 58.39, 44.04, 36.36.

General procedure for the synthesis of C1 and C2

PDIEt (0.107g, 0.2 mmol), bromomethylphenylboronic acid (0.108 g, 0.5 mmol), and 1,8-bis(dimethylamino)naphthalene (0.02 g, 0.1 mmol) was mixed and subject to grinding for 30 min, during which process several drops of MeCN was added to assist mixing. To the mixture was added bromomethylphenylboronic acid (0.108 g, 0.5 mmol) and 1,8-bis(dimethylamino)naphthalene (0.02 g, 0.1 mmol) again, and the mixture was subject to further grinding for 30 min with several drops of MeCN. The resultant mixture was dissolved in hot

methanol and the product was precipitated by adding Et_2O after cooling. The red product was collected and dried under vacuum.

Compound **C1**. 0.18 g, yield: 95%. ^{1}H NMR (500 MHz, 9.1% (vol%) D_2O-CF_3COOD) δ (ppm) 11.75 (d, *J* = 8.0 Hz, 4H), 11.68 (d, *J* = 8.0 Hz, 4H), 10.82 (d, *J* = 7.5 Hz, 4H), 10.47 (d, *J* = 7.6 Hz, 4H), 7.78 (t, *J* = 6.4 Hz, 4H), 7.54 (s, 4H), 6.70 (t, *J* = 6.4 Hz, 4H), 6.16 (s, 12H). ^{13}C NMR (126 MHz, 9.1% (vol%) D_2O-CF_3COOD) δ (ppm) 167.79, 138.89, 137.05, 135.54, 134.52, 131.89, 130.94, 128.99, 126.81, 124.03, 72.24, 63.41, 52.40, 36.73. HRMS (ESI-TOF) m/z: $[M + 2CH_3OH - 2H_2O]^{2+}$ Calcd for $C_{48}H_{48}B_2N_4O_8$ 415.1831; Found 415.1835.

Compound **C2**. 0.14 g, yield: 74%. ^{1}H NMR (500 MHz, 9.1% (vol%) D_2O-CF_3COOD) δ (ppm) 11.94 (d, *J* = 8.1 Hz, 4H), 11.87 (d, *J* = 8.1 Hz, 4H), 10.99 (d, *J* = 6.8 Hz, 2H), 10.74 – 10.59 (m, 6H), 8.18 (s, 4H), 7.98 (t, *J* = 7.1 Hz, 4H), 6.94 (t, *J* = 7.1 Hz, 4H), 6.32 (s, 12H). ^{13}C NMR (126 MHz, 9.1% (vol%) D_2O-CF_3COOD) δ (ppm) 168.18, 139.25, 138.86, 136.48, 135.90, 134.71, 133.86, 133.61, 132.33, 129.39, 127.23, 124.55, 71.14, 64.68, 52.68, 37.13. HRMS (ESI-TOF) m/z: $[M + 4CH_3OH - 4H_2O]^{2+}$ Calcd for $C_{50}H_{52}B_2N_4O_8$ 429.1980; Found 429.1977.

CD and UV-Vis titrations

Stock solutions of **1** and **2** (2.0 mM) were prepared in MeOH. Stock solutions of α-hydroxy carboxylic acids (1 mM, 0.1 mM or 0.01 mM) were prepared in water. In the cases of lactic acid and malic acid titrations where high guest concentrations were used, the guests were converted to the sodium salts using NaOH before use. The guest solutions were diluted using 100 mM acetate buffer and water to the desired concentrations. To 1.95 mL of the guest solutions in 50 mM pH 5.0 acetate buffer was added 50 μL 2.0 mM MeOH sensor stock solutions and the resultant samples were instantly subject to CD and absorption spectra measurements.

Determination of "unknown" ee with known guest concentration

The samples with different *ee*'s were prepared by adding stock solutions of each enantiomer to buffer. 2.0 mM MeOH stock solution of the sensor that gives the larger CD to the guest was added and the resultant solutions were subject to CD measurements. In the cases where the CD signal depends linearly on *ee*, the *ee* of the "unknown" samples was calculated by dividing the CD intensity of the 2nd Cotton effect of the sample with 100% *ee* by that of the "unknown" sample. In the cases where non-linear CD-*ee* relationship was found, the "unknown" *ee* was calculated by linear interpolation of the adjacent data points from the CD-*ee* plot, using the 2nd Cotton effect for calculation.

Determination of "unknown" ee with "unknown" guest concentration

Mandelic acid solutions with different concentrations and *ee* were prepared by adding stock solutions of each enantiomer to buffer. 2.0 mM MeOH stock solution of **C1** and the resultant solutions were subject to absorption measurements. The sample concentration was calculated by linear interpolation of the adjacent data points from the A_{500nm}-[Man] plot. Once the sample concentration was determined, a separate sample with the same sample concentration as the determined value and 100% *ee* was prepared, and the two samples with **C1** were subject to CD measurements. The *ee* of the "unknown" sample was calculated by dividing the CD intensity at 476 nm of the sample with 100% ee by that of the "unknown" sample.

7.1.3 NMR spectra of C1 and C2

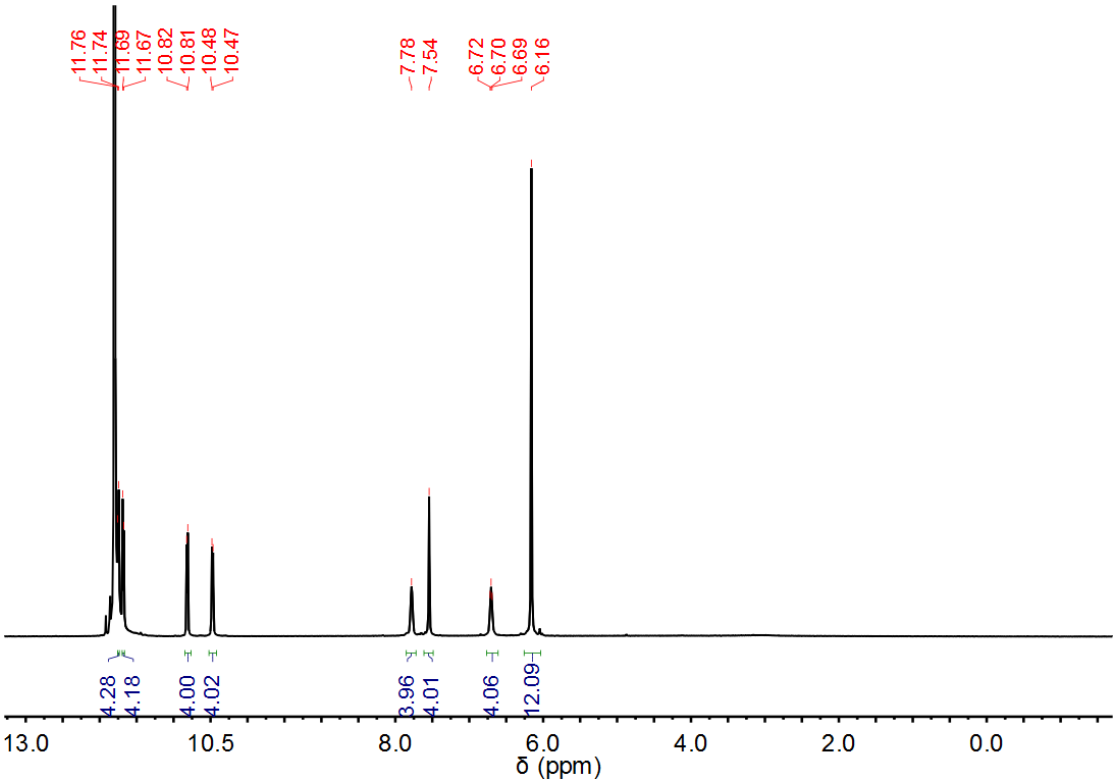

Figure 7.1 ^{1}H NMR (500 MHz) spectrum of **C1** in 9.1% (vol%) D_2O-CF_3COOD.

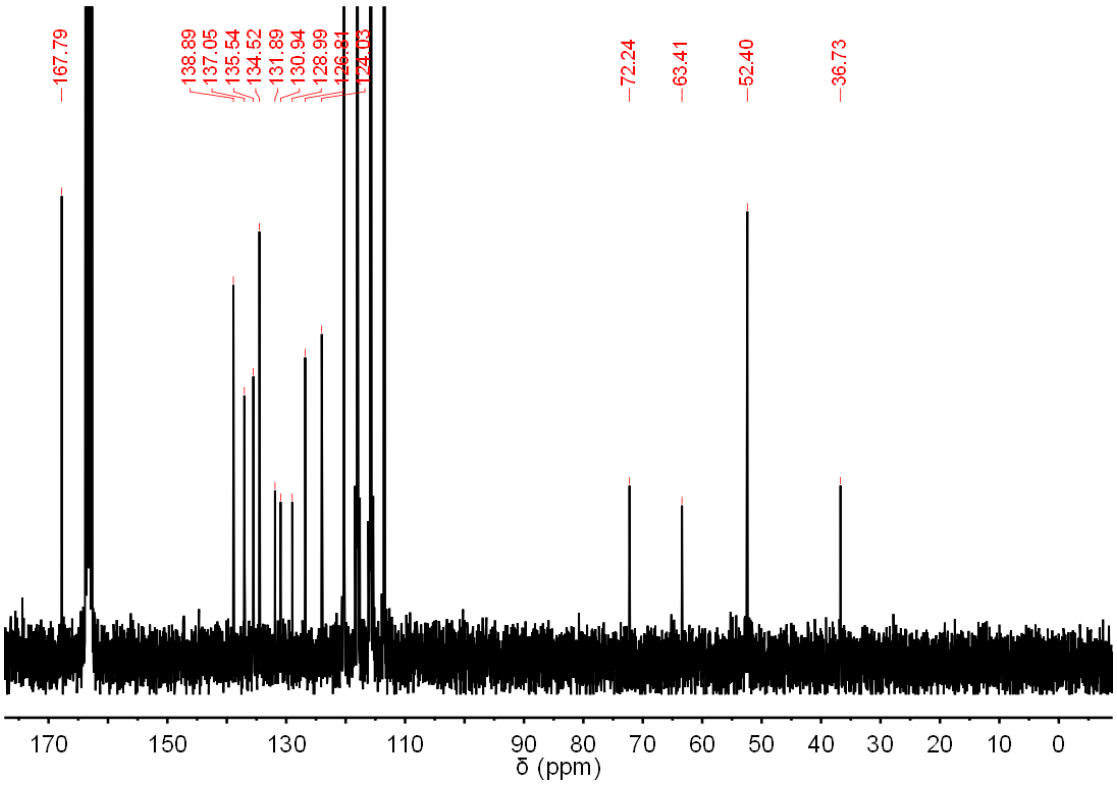

Figure 7.2 ^{13}C NMR (126 MHz) spectrum of **C1** in 9.1% (vol%) D_2O-CF_3COOD.

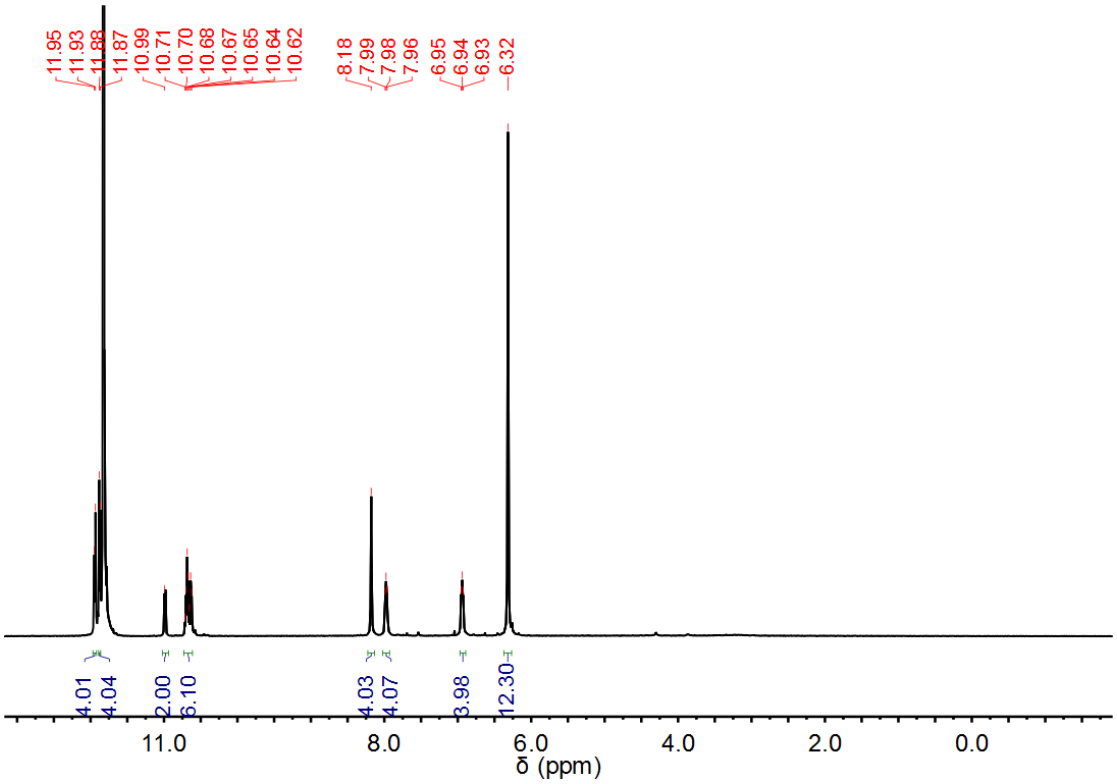

Figure 7.3 ^{1}H NMR (500 MHz) spectrum of **C2** in 9.1% (vol%) D_2O-CF_3COOD.

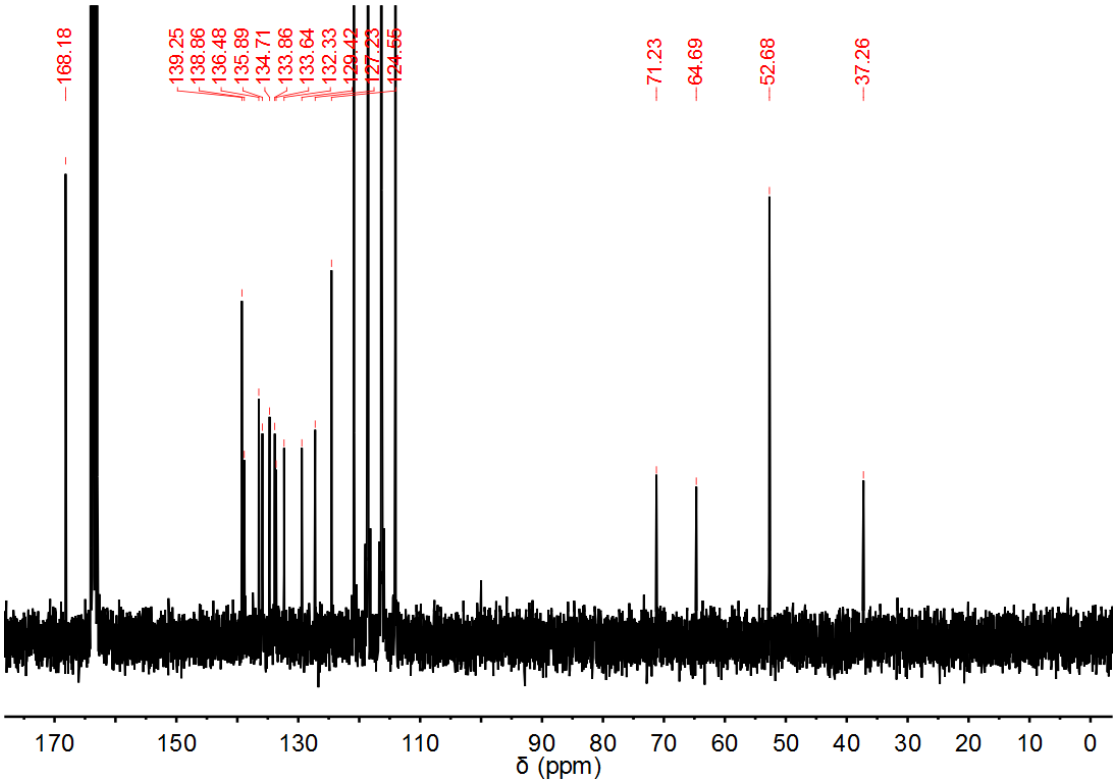

Figure 7.4 ^{13}C NMR (126 MHz) spectrum of **C2** in 9.1% (vol%) D_2O-CF_3COOD.

7.1.4 Time-dependent CD spectra of C1 with Man

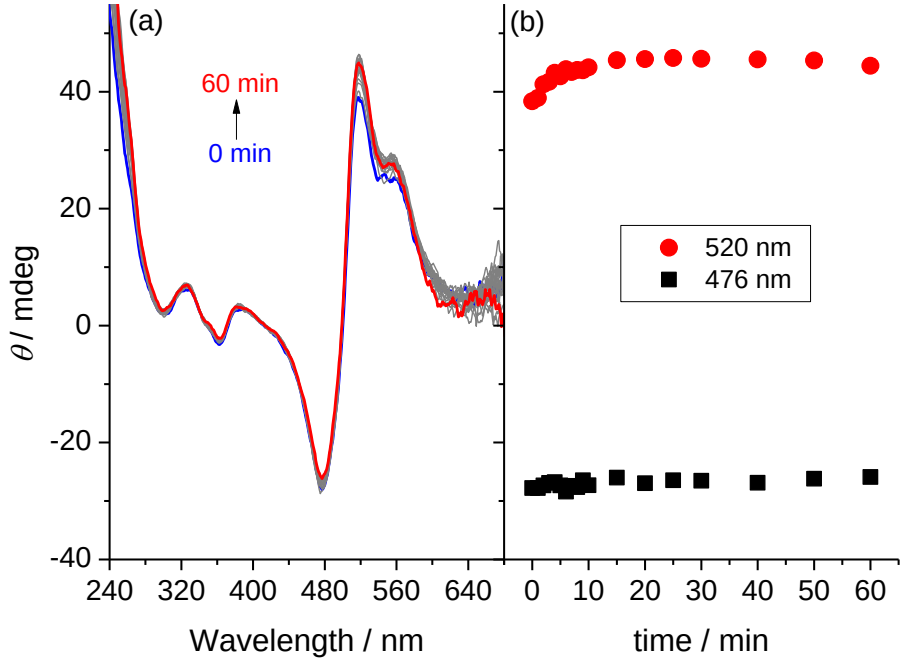

Figure 7.5 (a) Time-dependent CD spectra of **1** (50 μM) in the presence of 1.0 mM *R*-Man and (b) plots of CD intensity at 520 nm and 476 nm *versus* time in pH 5.0 acetate buffer containing 2.5% (vol%) MeOH.

7.1.5 Absorption and CD titrations of C1 with 2-phenylpropionate

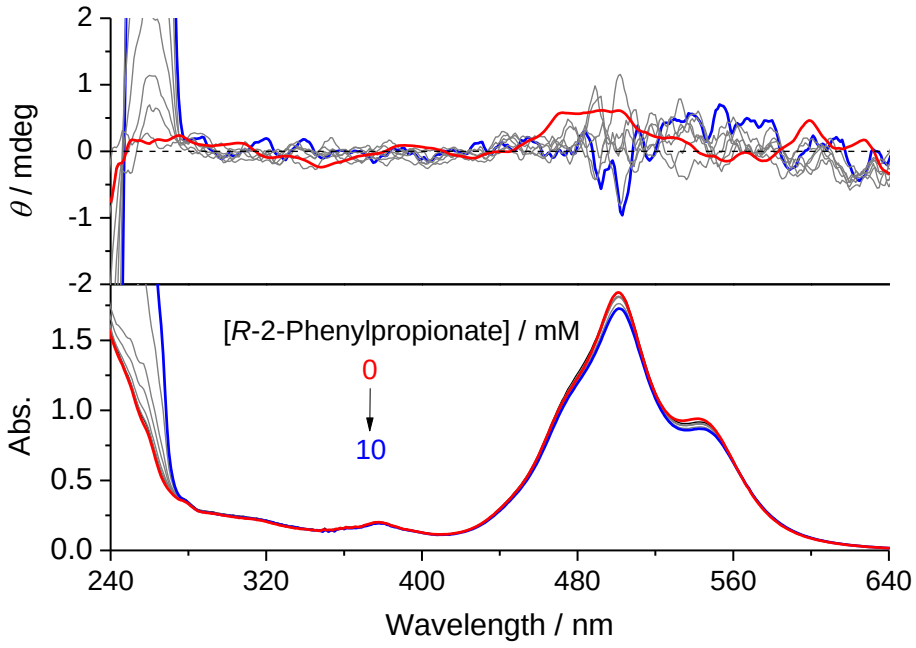

Figure 7.6 Absorption (a) and CD (b) spectra of **C1** (50 μM) in the presence of *R*-2-phenylpropionate of increasing concentration in pH 5.0 acetate buffer containing 2.5% (vol%) MeOH.

7.1.6 Absorption and CD titrations of C2 with Man

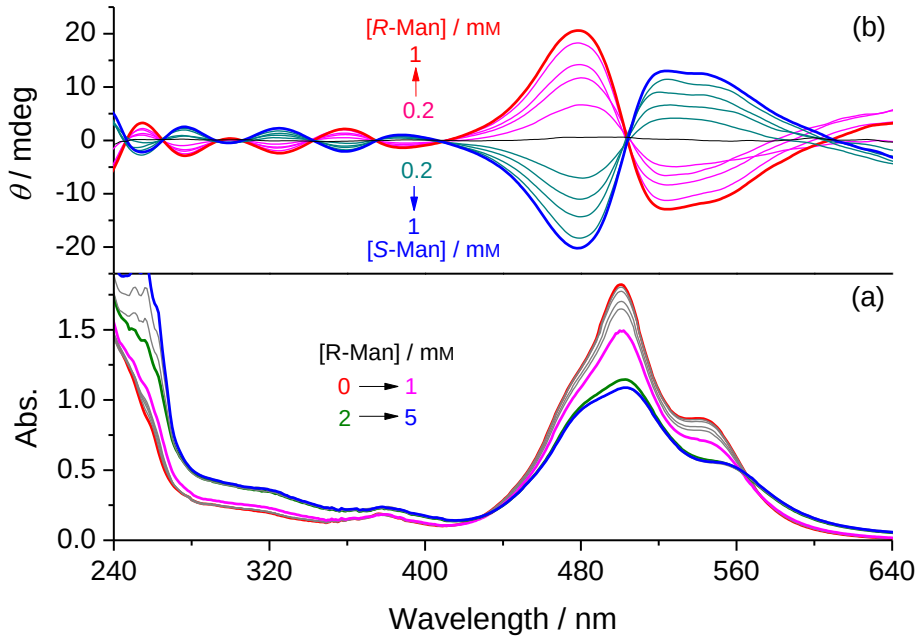

Figure 7.7 Absorption (a) and CD (b) spectra of **C2** (50 μM) in the presence of Man of increasing concentration in pH 5.0 acetate buffer containing 2.5% (vol%) MeOH.

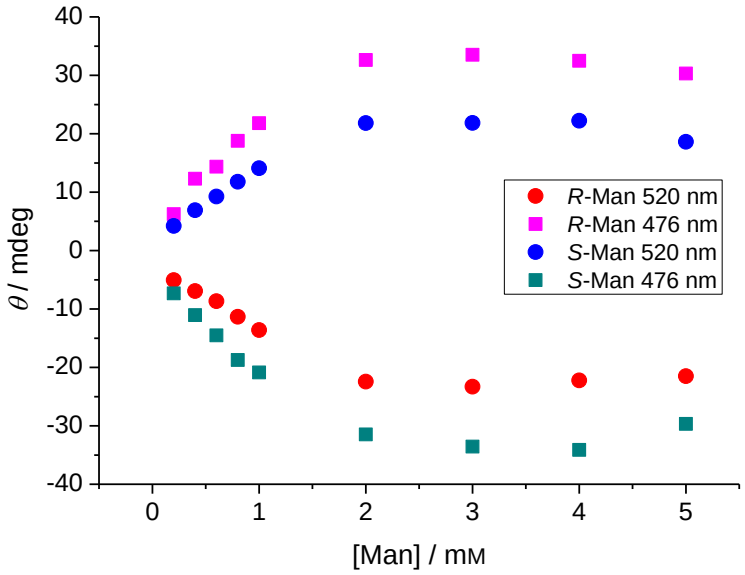

Figure 7.8 CD intensity of **C2** (50 μM) at 520 nm and 476 nm versus concentration of *R*- or *S*-Man in pH 5.0 acetate buffer containing 2.5% (vol%) MeOH.

7.1.7 CD titrations with other α-hydroxy carboxylates

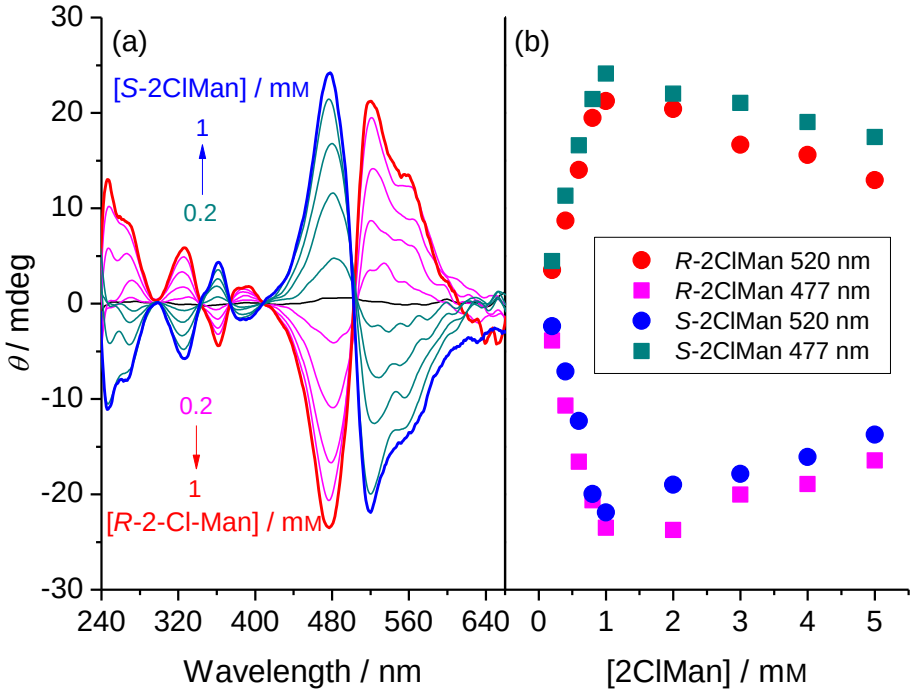

Figure 7.9 (a) CD spectra of **C1** (50 μM) in the presence of *R*- or *S*-2-ClMan of increasing concentration and (b) CD intensity of **C1** at 520 nm and 477 nm versus concentration of *R*- and *S*-2-ClMan in pH 5.0 acetate buffer containing 2.5% (vol%) MeOH.

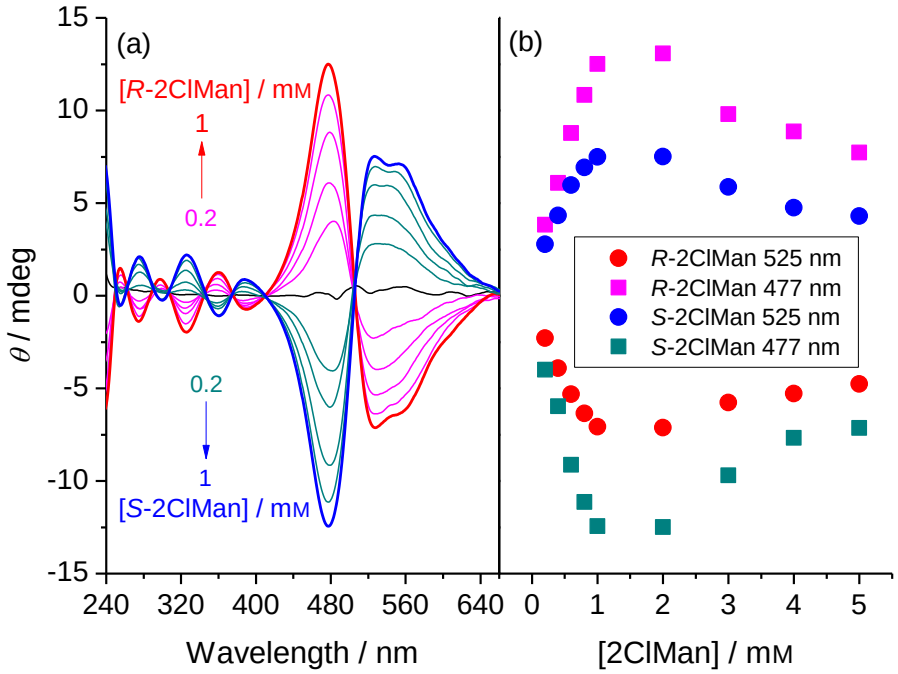

Figure 7.10 (a) CD spectra of **C2** (50 μM) in the presence of *R*- or *S*-2-ClMan of increasing concentration and (b) CD intensity of **C2** at 525 nm and 477 nm versus concentration of *R*- and *S*-2ClMan in pH 5.0 acetate buffer containing 2.5% (vol%) MeOH.

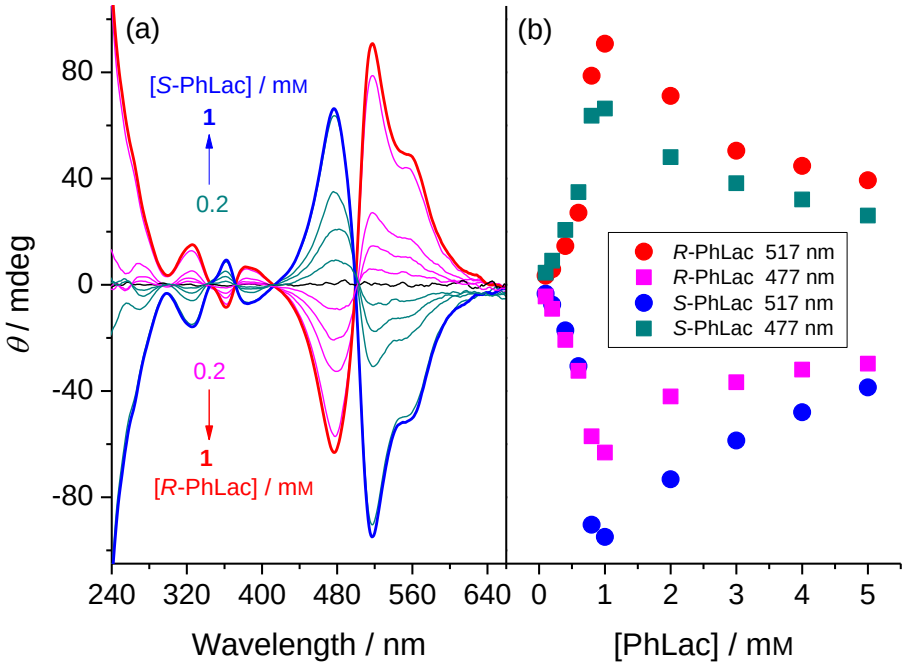

Figure 7.11 (a) CD spectra of **C1** (50 μM) in the presence of *R*- or *S*-PhLac of increasing concentration and (b) CD intensity of **C1** at 517 nm and 477 nm versus concentration of *R*- and *S*-PhLac in pH 5.0 acetate buffer containing 2.5% (vol%) MeOH.

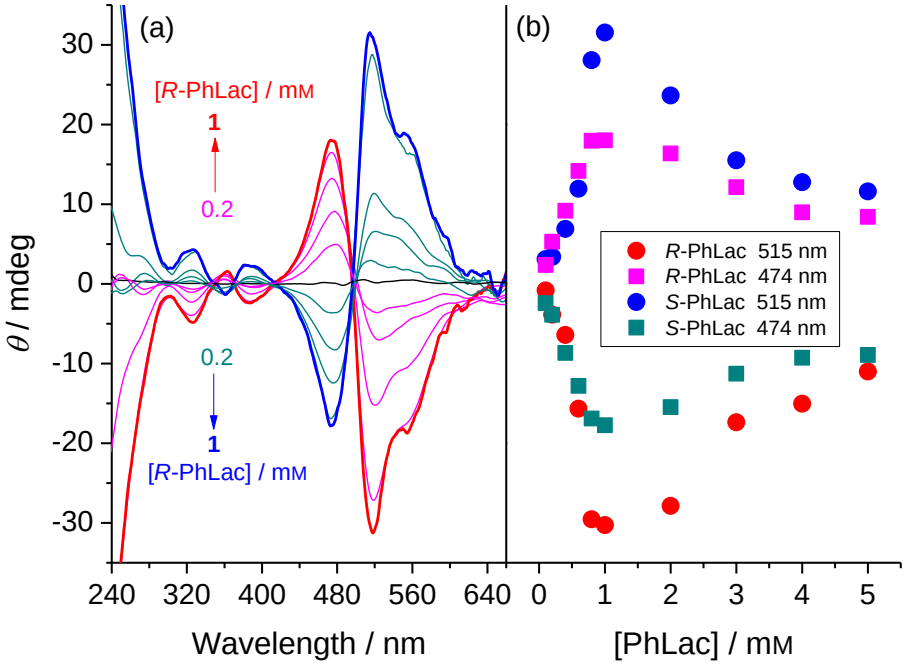

Figure 7.12 (a) CD spectra of **2** (50 μM) in the presence of *R*- or *S*-PhLac of increasing concentration and (b) CD intensity of **2** at 515 nm and 474 nm versus concentration of *R*- and *S*-PhLac in pH 5.0 acetate buffer containing 2.5% (vol%) MeOH.

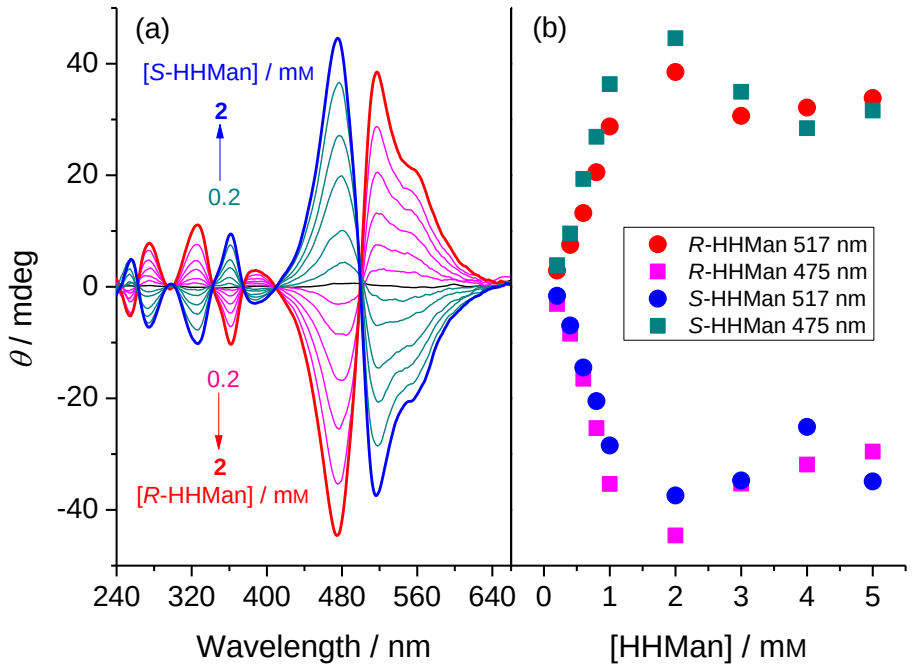

Figure 7.13 (a) CD spectra of **C1** (50 μM) in the presence of *R*- or *S*-HHMan of increasing concentration and (b) CD intensity of **C1** at 517 nm and 475 nm versus concentration of *R*- and *S*-HHMan in pH 5.0 acetate buffer containing 2.5% (vol%) MeOH.

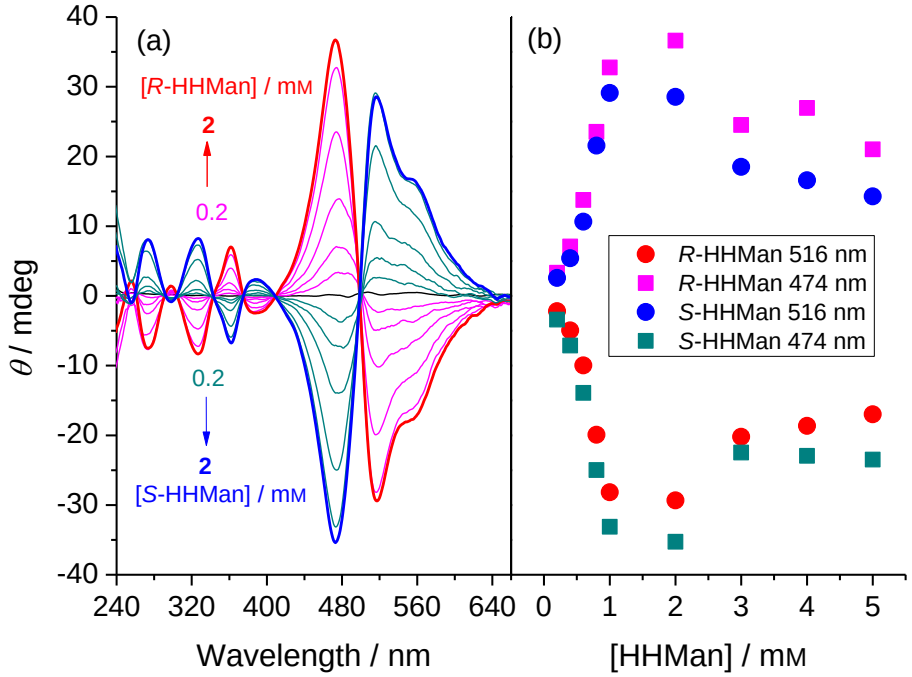

Figure 7.14 (a) CD spectra of **C2** (50 μM) in the presence of *R*- or *S*-HHMan of increasing concentration and (b) CD intensity of **C2** at 516 nm and 474 nm versus concentration of *R*- and *S*-HHMan in pH 5.0 acetate buffer containing 2.5% (vol%) MeOH.

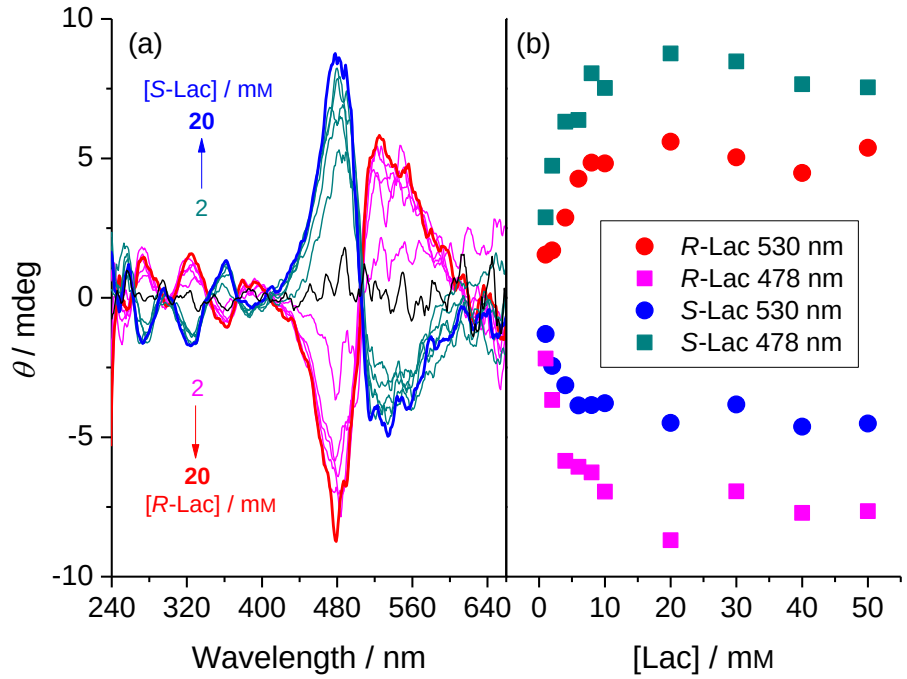

Figure 7.15 (a) CD spectra of **C1** (50 μM) in the presence of *R*- or *S*-Lac of increasing concentration and (b) CD intensity of **C1** at 530 nm and 478 nm versus concentration of *R*- and *S*-Lac in pH 5.0 acetate buffer containing 2.5% (vol%) MeOH.

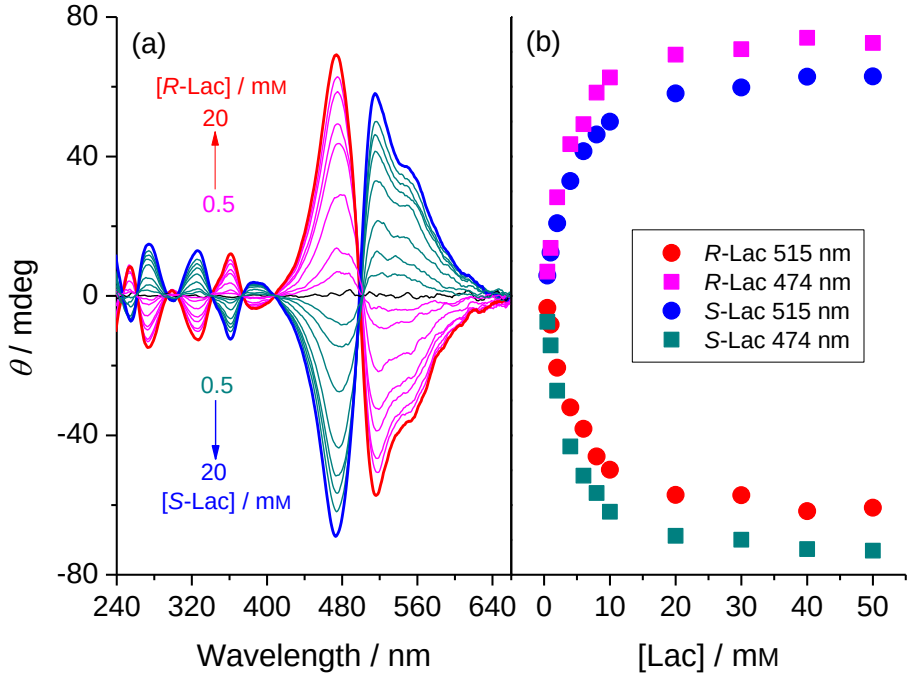

Figure 7.16 (a) CD spectra of **C2** (50 μM) in the presence of *R*- or *S*-Lac of increasing concentration and (b) CD intensity of **C2** at 515 nm and 474 nm versus concentration of *R*- and *S*-Lac in pH 5.0 acetate buffer containing 2.5% (vol%) MeOH.

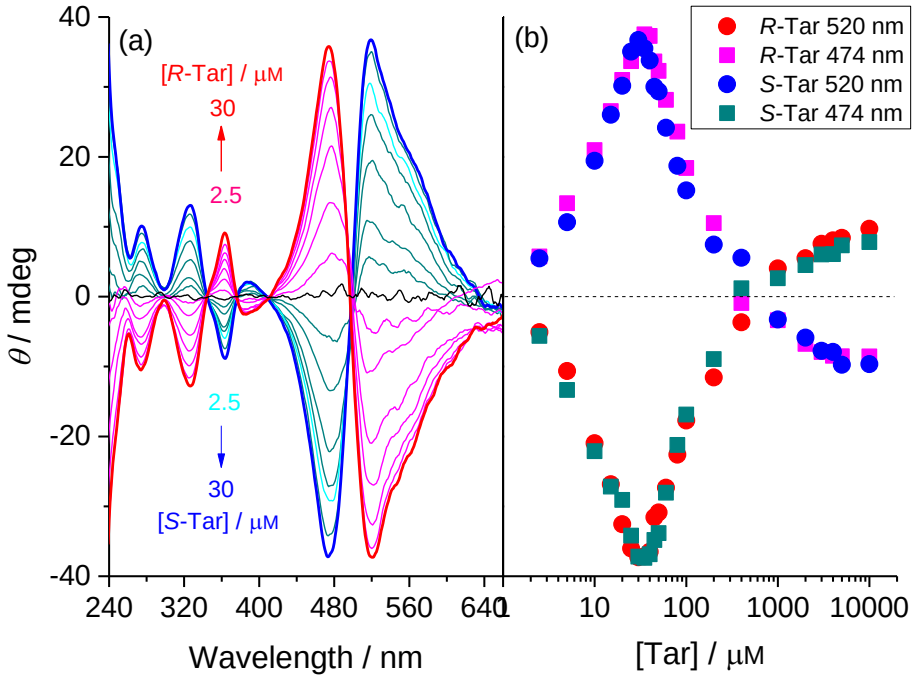

Figure 7.17 (a) CD spectra of **C1** (50 μM) in the presence of *R*- or *S*-Tar of increasing concentration and (b) CD intensity of **C1** at 520 nm and 474 nm versus concentration of *R*- and *S*-Tar in pH 5.0 acetate buffer containing 2.5% (vol%) MeOH.

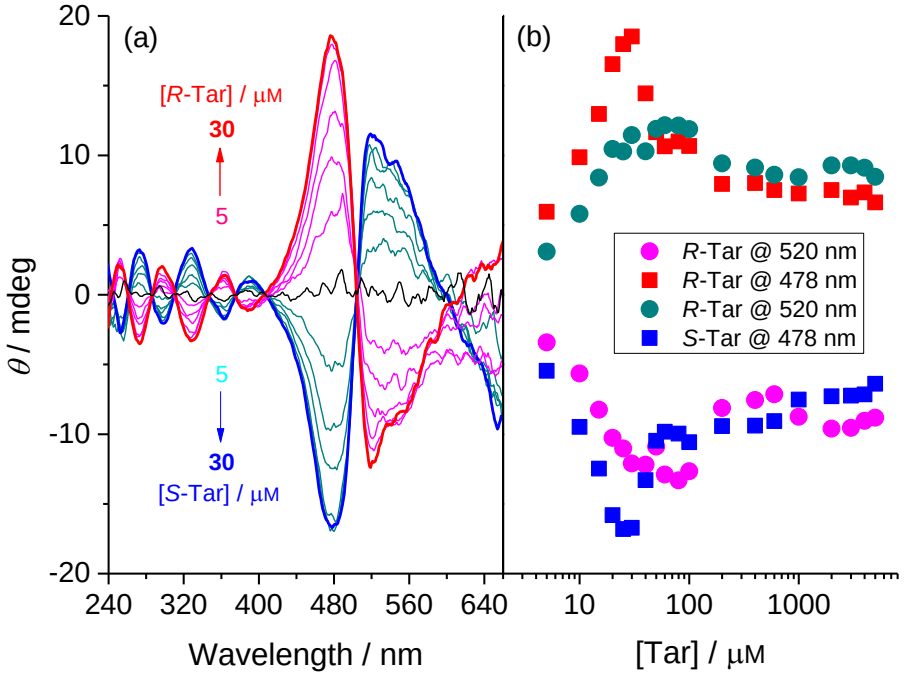

Figure 7.18 (a) CD spectra of **C2** (50 μM) in the presence of *R*- or *S*-Tar of increasing concentration and (b) CD intensity of **C2** at 520 nm and 478 nm versus concentration of *R*- and *S*-Tar in pH 5.0 acetate buffer containing 2.5% (vol%) MeOH.

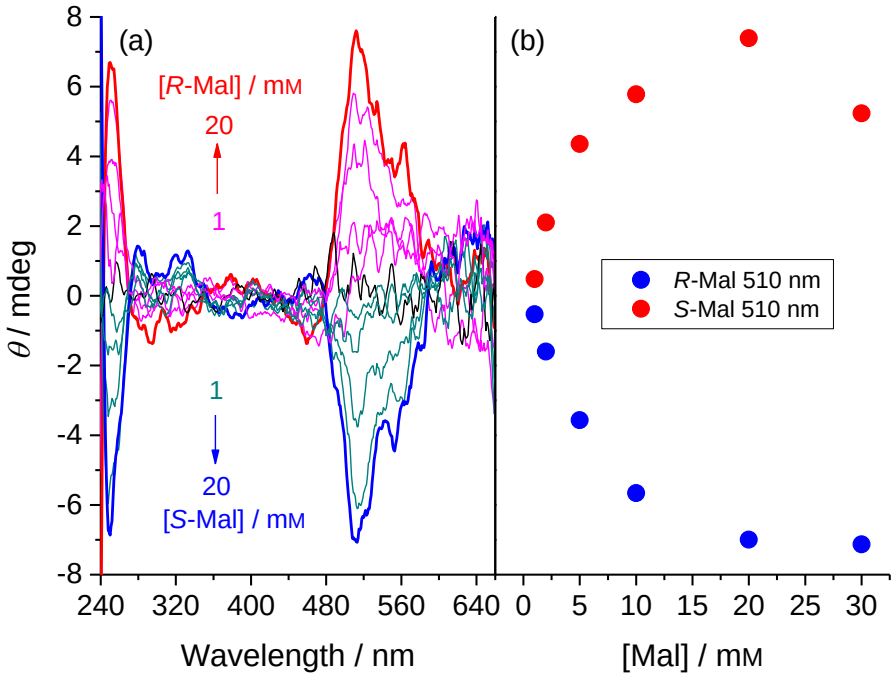

Figure 7.19 (a) CD spectra of **C1** (50 μM) in the presence of *R*- or *S*-Mal of increasing concentration and (b) CD intensity of **C1** at 510 nm versus concentration of *R*- and *S*-Mal in pH 5.0 acetate buffer containing 2.5% (vol%) MeOH.

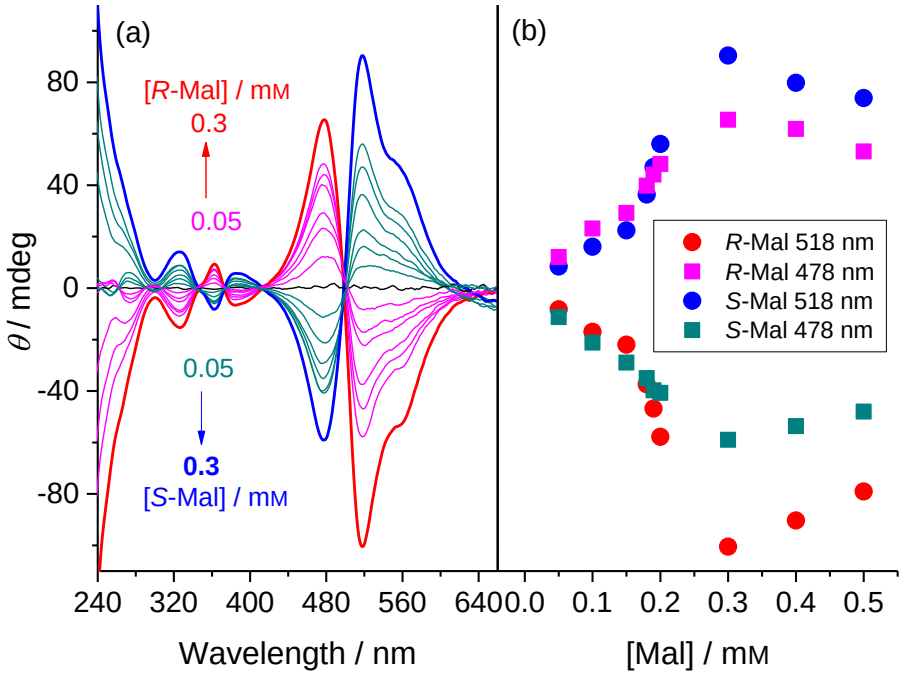

Figure 7.20 (a) CD spectra of **C2** (50 μM) in the presence of *R*- or *S*-Mal of increasing concentration and (b) CD intensity of **C2** at 518 nm and 478 nm versus concentration of *R*- and *S*-Mal in pH 5.0 acetate buffer containing 2.5% (vol%) MeOH.

7.1.8 Job plots

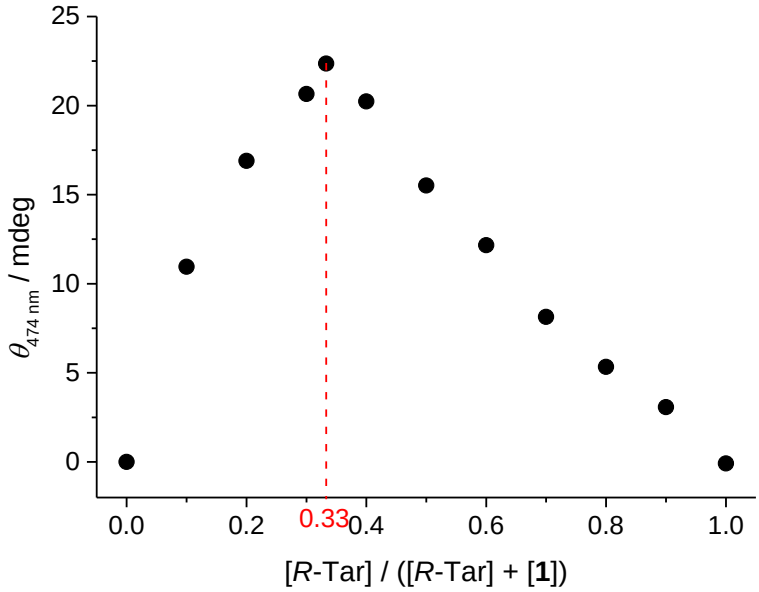

Figure 7.21 Job plot for the **C1**-*R*-Tar complex created from the CD intensity at 474 nm. [**C1**] + [*R*-Tar] = 50 μM.

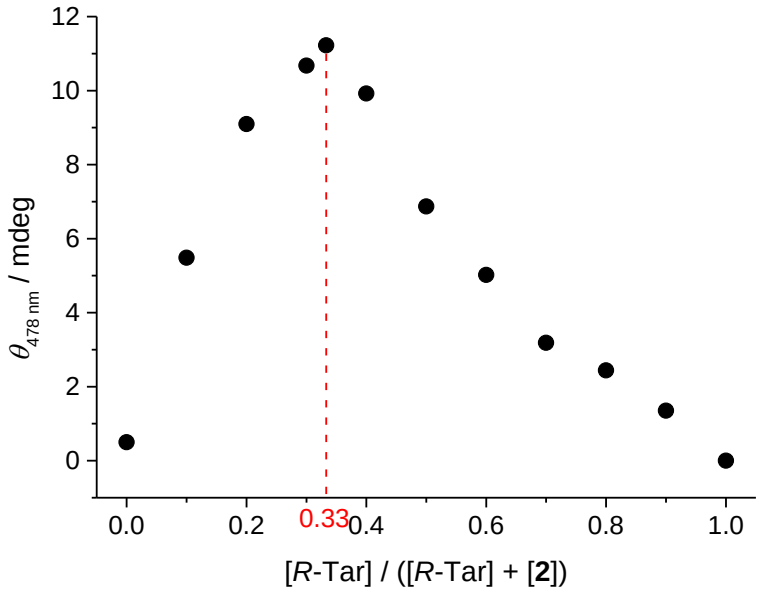

Figure 7.22 Job plot for the **C2**-*R*-Tar complex created from the CD intensity at 478 nm. [**C2**] + [*R*-Tar] = 50 μM.

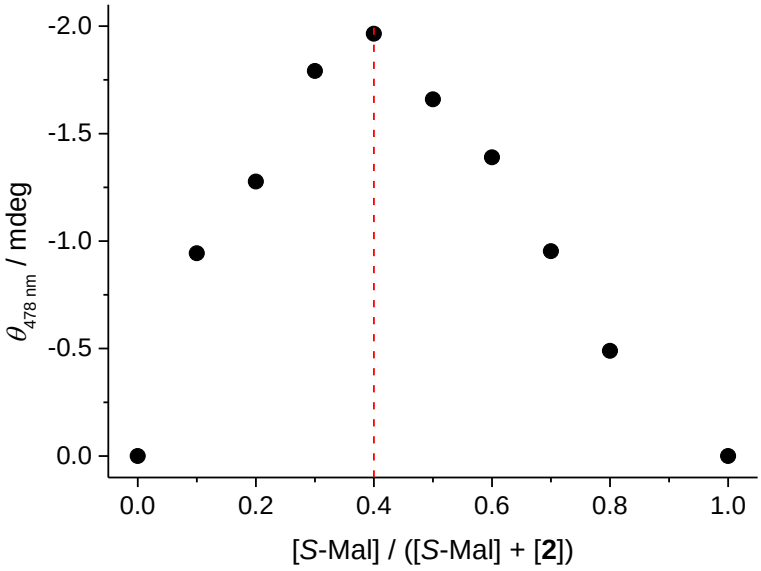

Figure 7.23 Job plot for the **C2**-*S*-Mal complex created from the CD intensity at 478 nm. [**C2**] + [*S*-Mal] = 50 μM.

7.1.9 CD spectra with different *ee*

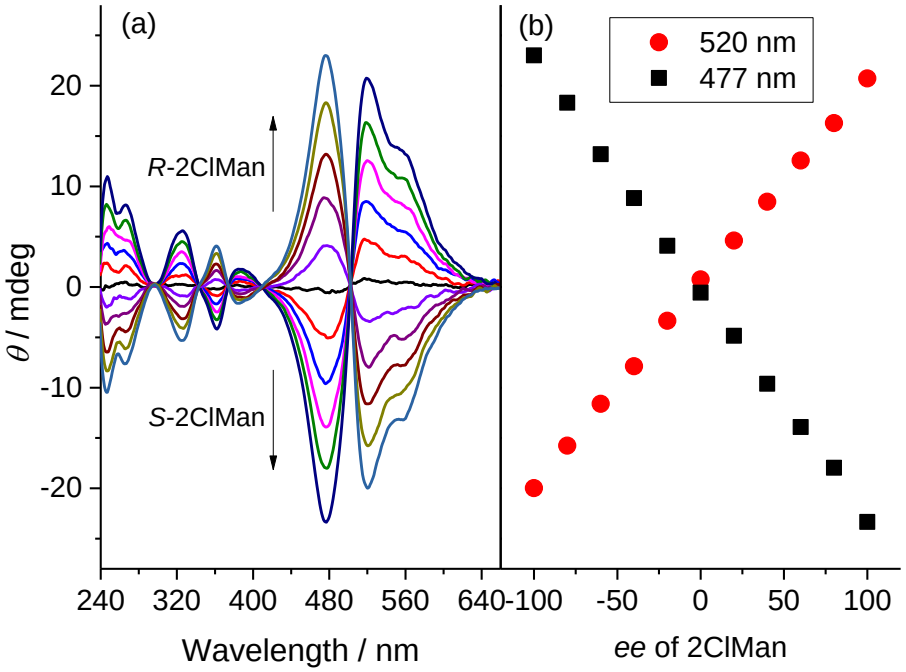

Figure 7.24 (a) CD spectra of **C1** (50 μM) in the presence of 2-ClMan with different *ee*'s and (b) CD intensity of **C1** at 520 nm and 477 nm versus *ee* in pH 5.0 acetate buffer containing 2.5% (vol%) MeOH. [*R*-2ClMan] + [*S*-2ClMan] = 1.0 mM.

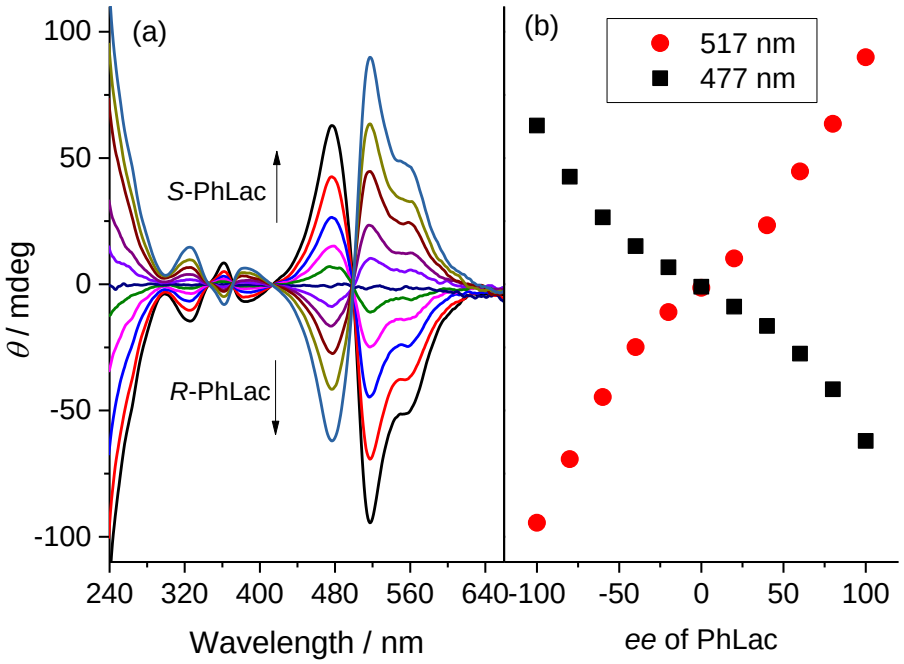

Figure 7.25 (a) CD spectra of **C1** (50 μM) in the presence of PhLac with different *ee*'s and (b) CD intensity of **C1** at 517 nm and 477 nm versus *ee* in pH 5.0 acetate buffer containing 2.5% (vol%) MeOH. [*R*-PhLac] + [*S*-PhLac] = 1.0 mM.

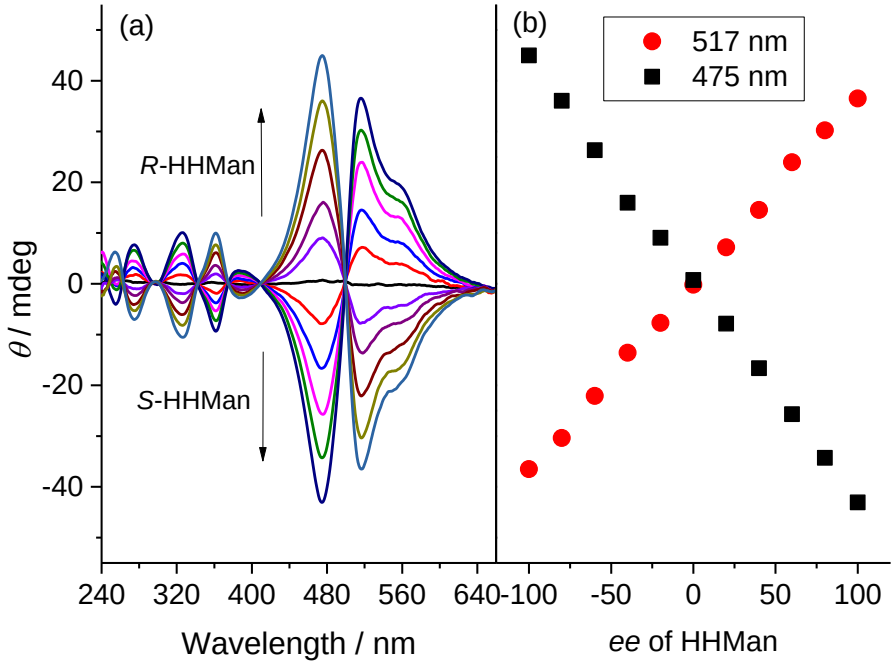

Figure 7.26 (a) CD spectra of **C1** (50 μM) in the presence of HHMan with different *ee*'s and (b) CD intensity of **C1** at 517 nm and 475 nm versus *ee* in pH 5.0 acetate buffer containing 2.5% (vol%) MeOH. [*R*-HHMan] + [*S*-HHMan] = 2.0 mM.

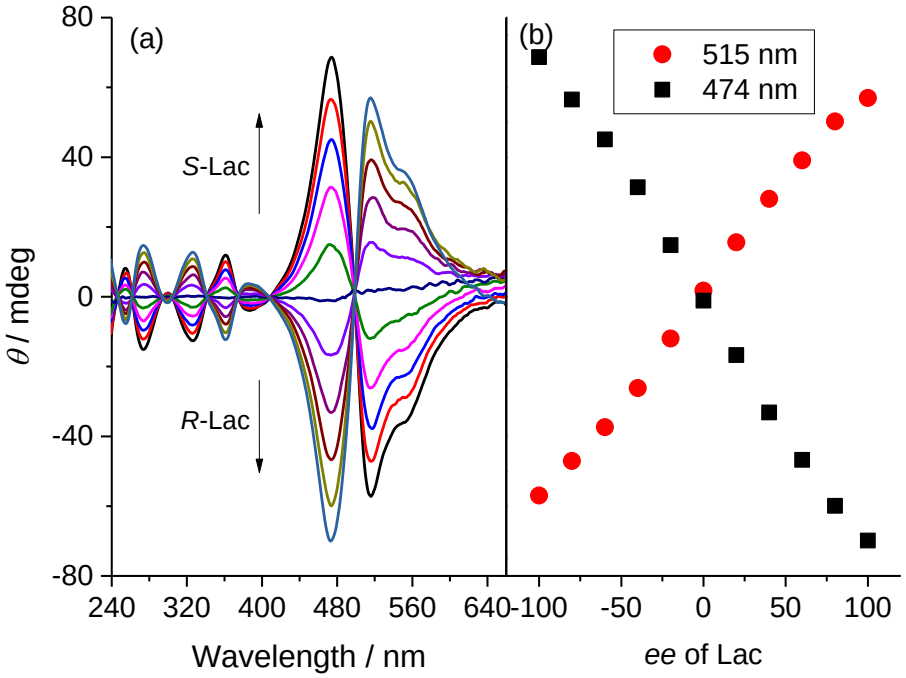

Figure 7.27 (a) CD spectra of **C2** (50 μM) in the presence of Lac with different *ee*'s and (b) CD intensity of **C2** at 515 nm and 474 nm versus *ee* in pH 5.0 acetate buffer containing 2.5% (vol%) MeOH. [*R*-Lac] + [*S*-Lac] = 1.0 mM.

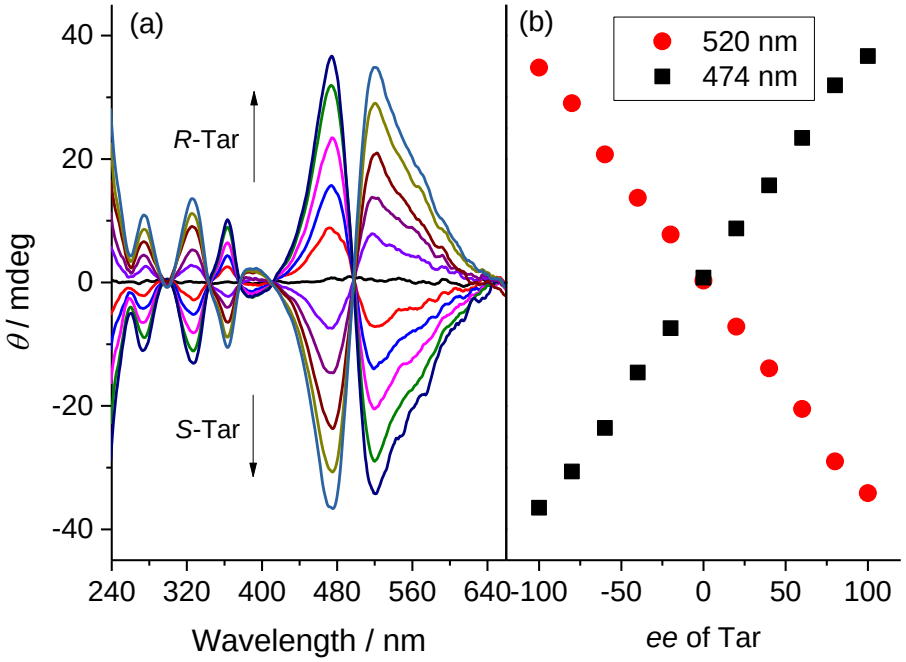

Figure 7.28 (a) CD spectra of **C1** (50 μM) in the presence of Tar with different *ee*'s and (b) CD intensity of **C1** at 520 nm and 474 nm versus *ee* in pH 5.0 acetate buffer containing 2.5% (vol%) MeOH. [*R*-Tar] + [*S*-Tar] = 30 μM.

7.1.10 Absorption spectra with different *ee*

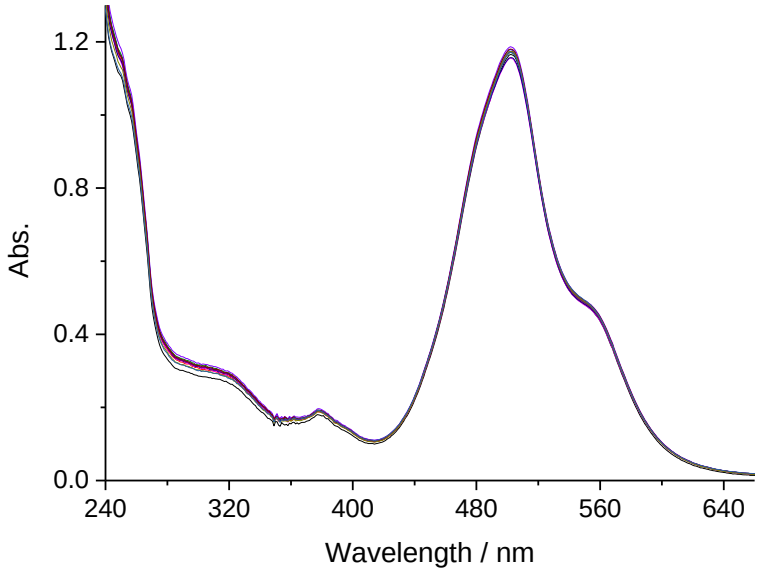

Figure 7.29 Absorption spectra of **C1** (50 μM) in the presence of PhLac with different *ee* (-100% to 100%) in pH 5.0 acetate buffer containing 2.5% (vol%) MeOH. [*R*-PhLac] + [*S*-PhLac] = 1.0 mM.

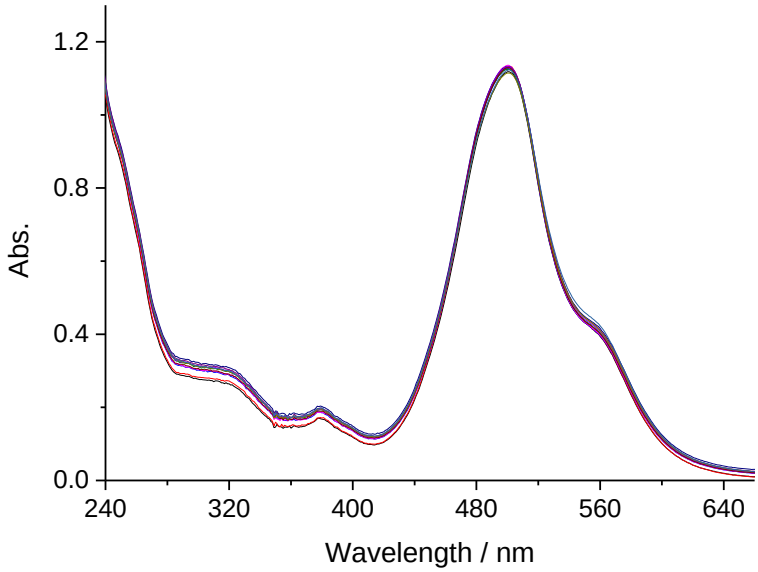

Figure 7.30 Absorption spectra of **C2** (50 μM) in the presence of Mal with different *ee* (-100% to 100%) in pH 5.0 acetate buffer containing 2.5% (vol%) MeOH. [*R*-Mal] + [*S*-Mal] = 0.3 mM.

7.1.11 CD-*ee* relationship at different analyte concentrations

(Experimental work in this section was performed by XXC)

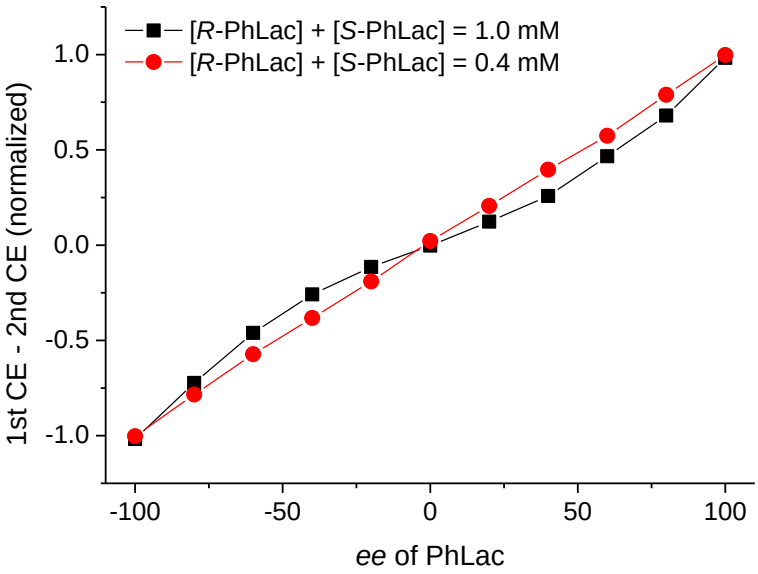

Figure 7.31 Normalized CD intensity (normalized value of 1st Cotton effect minus 2nd Cotton effect) of **C1** versus *ee* of PhLac with total PhLac concentration of 1.0 mM (black line) and 0.4 mM (red line) in pH 5.0 acetate buffer containing 2.5% (vol%) MeOH.

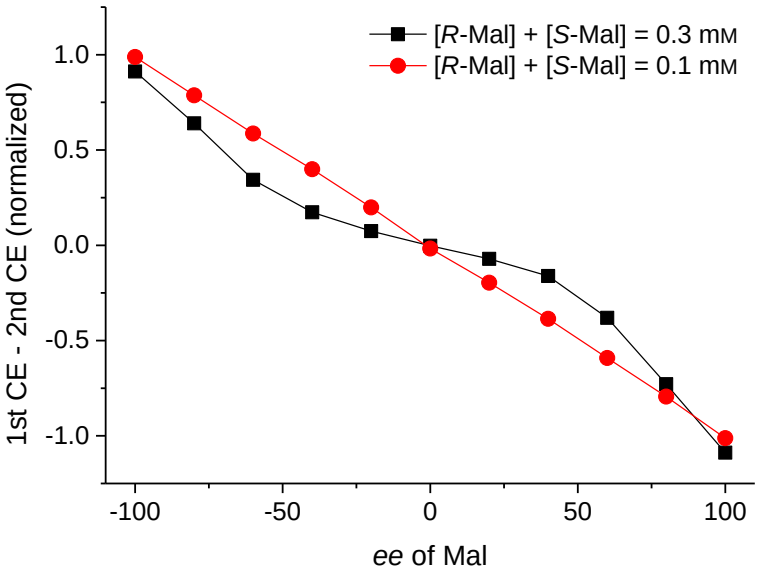

Figure 7.32 Normalized CD intensity (normalized value of 1st Cotton effect minus 2nd Cotton effect) of **C2** versus *ee* of Mal with total Mal concentration of 0.3 mM (black line) and 0.1 mM (red line) in pH 5.0 acetate buffer containing 2.5% (vol%) MeOH.

7.1.12 CD response of C1 to *R*-Man in the presence of various chiral compounds

(Experimental work in this section was performed by XXC)

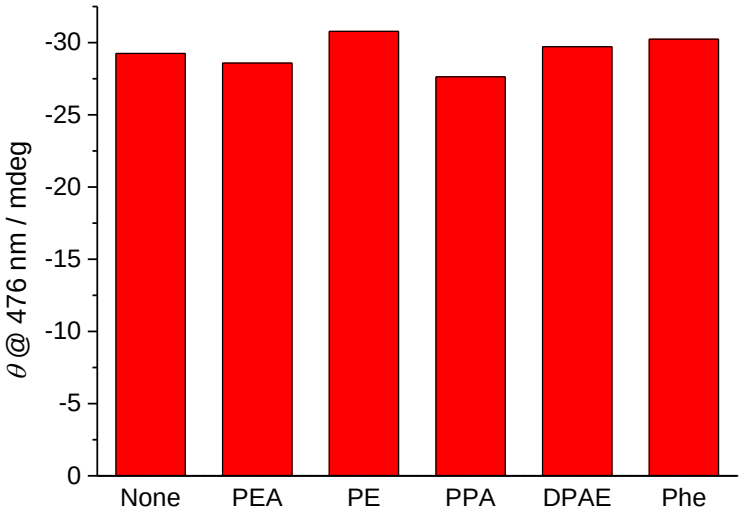

Figure 7.33 Histogram showing CD responses of **C1** to *R*-Man (1.0 mM) in the absence and presence of various coexisting chiral compounds (1.0 mM) including *S*-1-phenylethylamine (PEA), *S*-1-phenylethanol (PE), *R*-2-phenylpropionic acid (PPA), (1*R*,2*S*)-1,2-diphenyl-2-aminoethanol (DPAE) and L-phenylalanine (Phe).

7.1.13 Absorption and CD spectra of C1-Man complex in MeOH

(Experimental work in this section was performed by XXC)

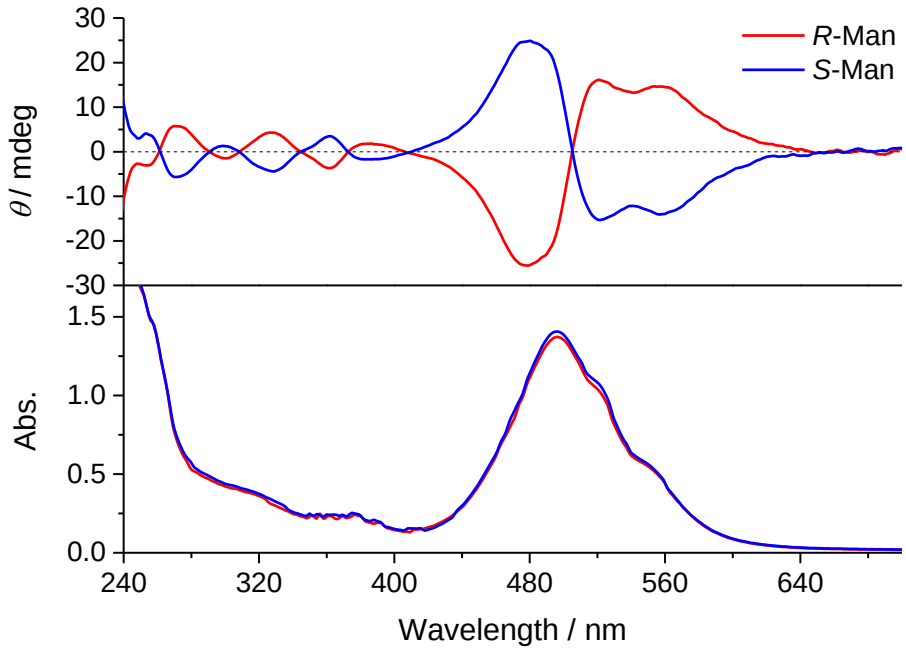

Figure 7.34 Absorption (a) and CD (b) spectra of **C1** (50 μM) in the presence of sodium *R*-mandelate or sodium *S*-mandelate (1 mM) in MeOH.

7.2 Supporting information for Chapter 3

7.2.1 General

All commercial reagents and solvents were used as received. Protocatechuic acid (PCA) was purchased from Energy Chemicals. D-glucose was purchased from Acros. D-fructose was purchased from TCI. 4-(2-hydroxyethyl)-1-piperazineethanesulfonic acid (HEPES) was purchased from Aladdin Industrial Inc. Other chemicals were products of Sinopharm Chemical Reagent Co. Ltd. **F1** was synthesized by WJOY.[106] Absorption spectra and turbidity measurements were performed on a Varian Cary 300 UV-Vis spectrophotometer. Fluorescence spectra were recorded on Hitachi F-4500 fluorescence spectrophotometer. All spectroscopic measurements were carried out at ambient temperature of 298 K.

7.2.2 Experimental

Procedure for sample preparation for spectroscopic measurements

Stock solutions of **F1** (10 mM), PCA (1 M, 2 M or 4 M) and catechol (1 M, 2 M, or 4 M) were prepared in MeOH. Stock solutions of NaF (10 mM, 0.1 M or 0.5 M), glucose (1 M) and fructose (1 M) were prepared in water. The NaF solutions were diluted by buffer and water to the desired concentrations. Spectroscopic measurements were carried out in default buffer (pH 2.0 50 mM sodium phosphate buffer with 50 mM NaCl). To 2 mL of the NaF solutions in default buffer was added 20 µL 10 mM MeOH stock solution of **F1**, followed by a stock solution of the diol component if a diol was used. The samples were incubated for 20 min and then subject to spectroscopic measurements.

*pH dependence of fluoride sensing by the **F1**-PCA ensemble*

The samples for fluorescence measurements were prepared following the general procedure described above, except that different buffering agents (50 mM) were used in place of the sodium phosphate buffer for pH above 2.5. The buffering agents used are H_3PO_4-NaH_2PO4 (pH 1.5-2.5), HCOOH-HCOONa (pH 3.0-3.5), HOAc-NaOAc (pH 4.0-5.0), 4-morpholineethanesulfonic acid (MES, pH 6.0), NaH_2PO_4-Na_2HPO_4 (7.0), HEPES (8.0), $NaHCO_3$-Na_2CO_3 (9.0-10.0).

7.2.3 Data analysis

Binding constants (*K*) for 1:3 (host to guest) stoichiometry were calculated by fitting the fluorescence titration data to the following eq 1, where *x* denotes the fluoride concentration, *y* is

the fluorescence intensity, y_0 is the fluorescence intensity in the absence of fluoride and y_∞ is the saturated value.

$$y = \frac{y_0 + y_\infty K x^3}{1 + K x^3} \tag{1}$$

Binding constants (K) for 1:1 stoichiometry were calculated by fitting the data to eq 2, where the denotations of x, y and y_0 are the same as in eq 1, c is the concentration of the host, and a is the proportionality efficient of fluorescence intensity change versus fraction of guest-bound host.

$$y = y_0 + \frac{a}{2c}(c + x + 1/K - \sqrt{(c + x + 1/K)^2 - 4cx}) \tag{2}$$

Bindingconstants K_1 and K_2 for 1:2 (host:guest) stoichiometry were calculated by fitting the data to eq 3, where the where the denotations of x, y and y_0 are the same as in eq 1, and a and b are proportionality efficients of fluorescence intensity change versus fraction of guest-bound host for the 1:1 host-guest complex and 1:2 host-guest complex, respectively.

$$y = y_0 + \frac{acK_1 x + bcK_1K_2 x^2}{1 + K_1 x + K_1K_2 x^2} \tag{3}$$

Stepwise acid dissociation constants (pK_{a1} and pK_{a2}) for a "diprotic acid (H_2A)" were calculated by fitting the fluorescence-pH titration data to eq 4, where $I_{\text{subscript}}$ is the relative fluorescence intensity of the respective species.

$$y = \frac{I_{H_2A} 10^{pK_{a1} + pK_{a2} - 2pH} + I_{HA} 10^{pK_{a2} - pH} + I_A}{10^{pK_{a1} + pK_{a2} - 2pH} + 10^{pK_{a2} - pH} + 1} \tag{4}$$

7.2.4 Spectral traces

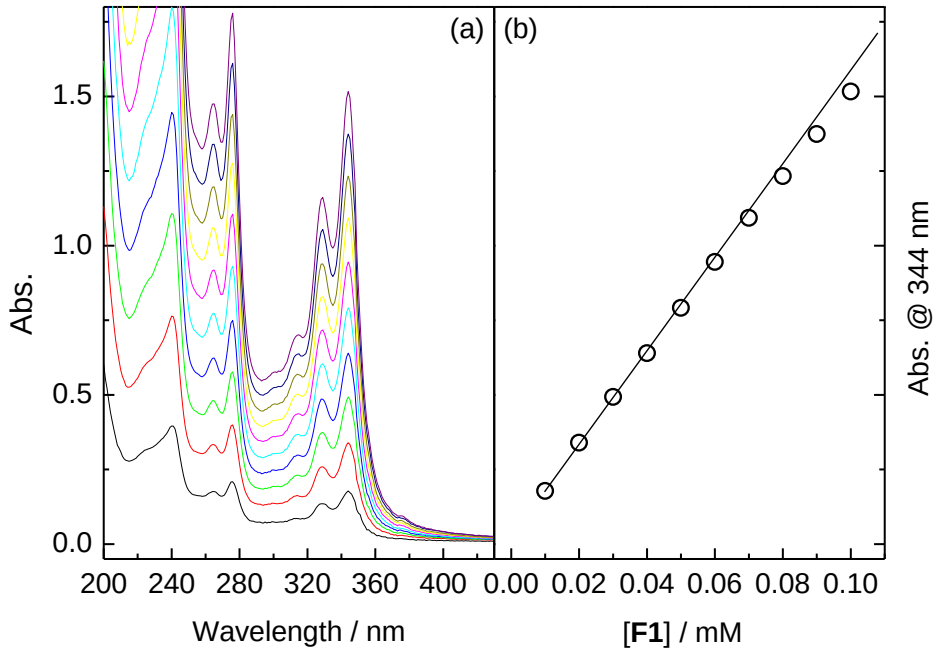

Figure 7.35 (a) Absorption spectra of **F1** at varying concentrations (10 μM – 0.1 mM) in default buffer. (b) Absorbance of **F1** at 344 nm vs concentration of **F1**.

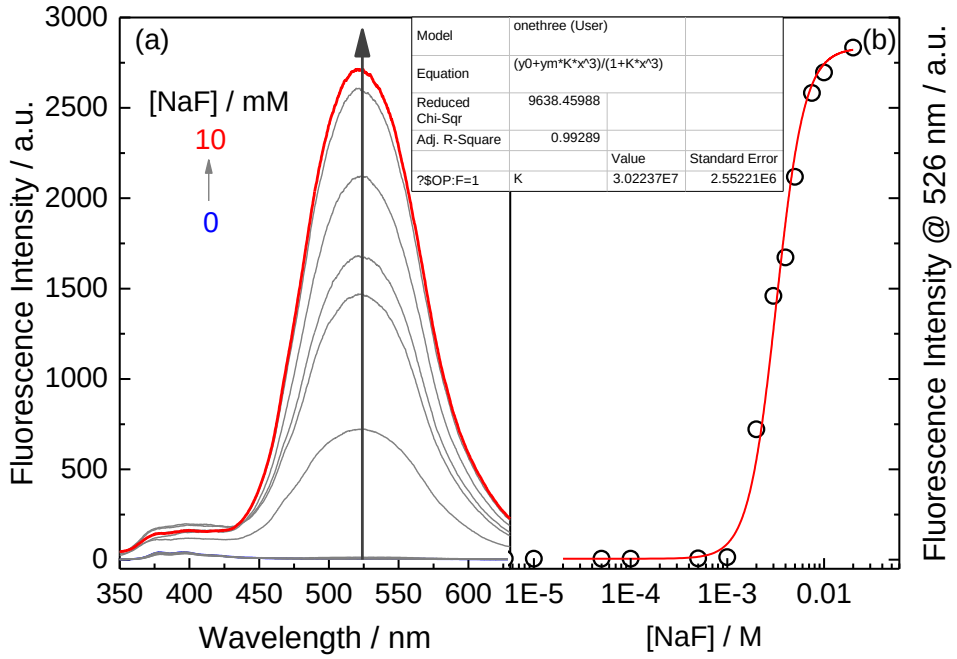

Figure 7.36 (a) Fluorescence spectra of **F1** (0.1 mM) in the presence of NaF over 0 – 10 mM in default buffer. (b) Fluorescence intensity of **F1** at 526 nm vs NaF concentration and the curve fit (line) using eq 1. λ_{ex} = 328 nm.

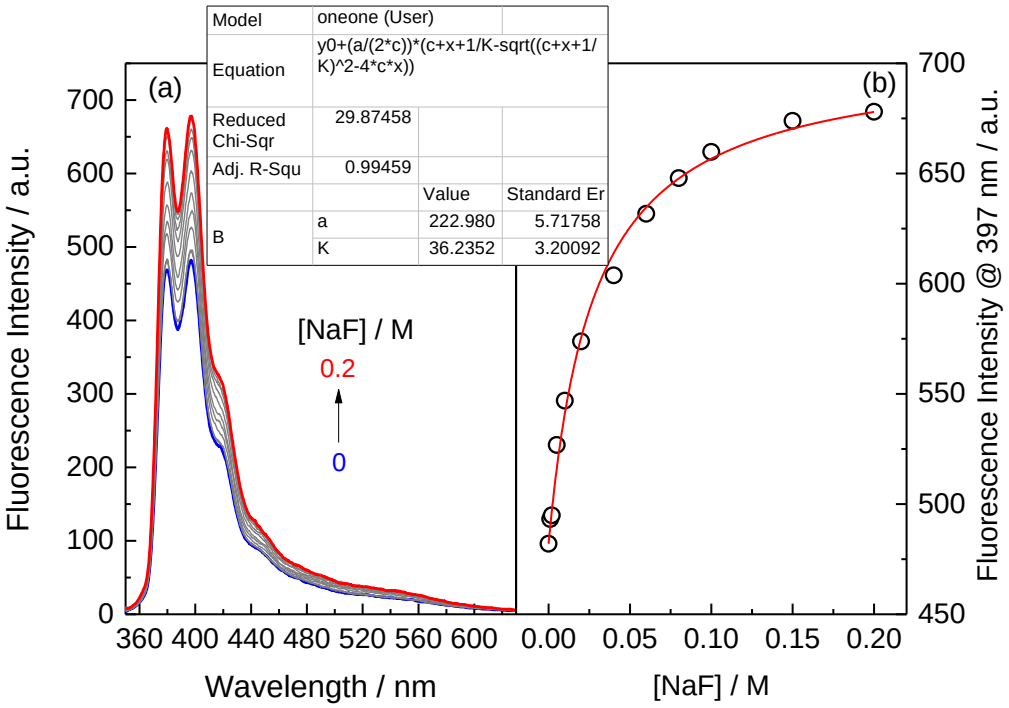

Figure 7.37 (a) Fluorescence spectra of **F1** (0.1 mM) in the presence of NaF (0 – 0.2 M) in default buffer with 2 mM CTAB. Note that CTAB micelles solubilize **F1** and prevent its aggregation, as no excimer emission is observed and **F1** shows enhancement of the pyrene monomer fluorescence with addition of fluoride. (b) Fluorescence intensity of **1** at 526 nm vs NaF concentration and the curve fit (line) using eq 2. λ_{ex} = 328 nm.

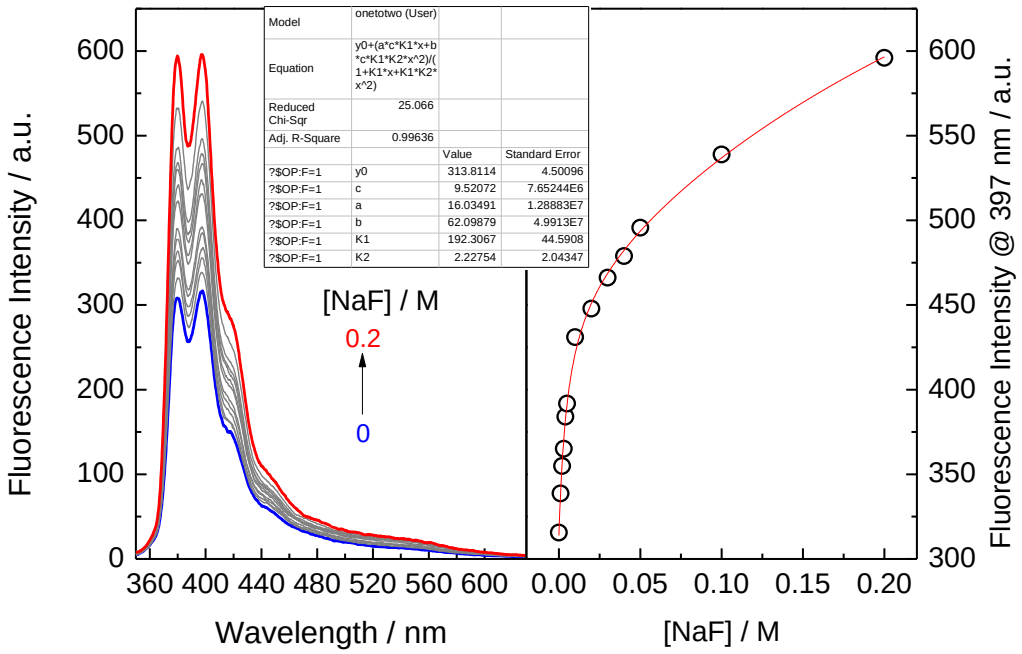

Figure 7.38 (a) Fluorescence spectra of **F1** (0.1 mM) in the presence of PCA (10 mM) and NaF (0 – 0.2 M) in default buffer with 2 mM CTAB. (b) Fluorescence intensity of **F1** at 526 nm vs NaF concentration. λ_{ex} = 328 nm. Fluorescence intensity of **F1** at 526 nm vs NaF concentration and the curve fit (line) using a 1:2 (host:guest) binding model. This is because the fluoride titration curve shows two distinct regions, likely due to the formation of both ternary **F1**-PCA-fluoride complex and binary **F1**-fluoride complex. Using a 1:1 model gave a poor fitting of the data. λ_{ex} = 328 nm.

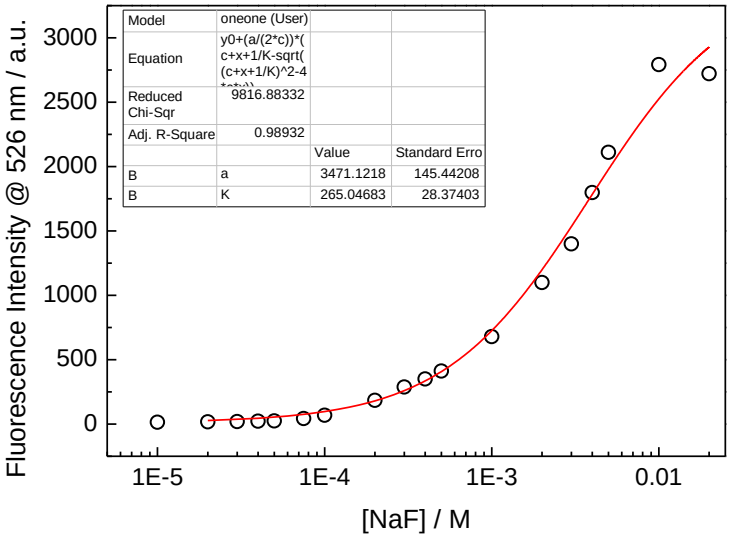

Figure 7.39 Fluorescence intensity of **F1** (0.1 mM) at 526 nm vs NaF concentration over 0 – 20 mM in the presence of 5 mM PCA in default buffer and curve fit (line) using eq 2, which gives a poor fitting of the data. λ_{ex} = 328 nm.

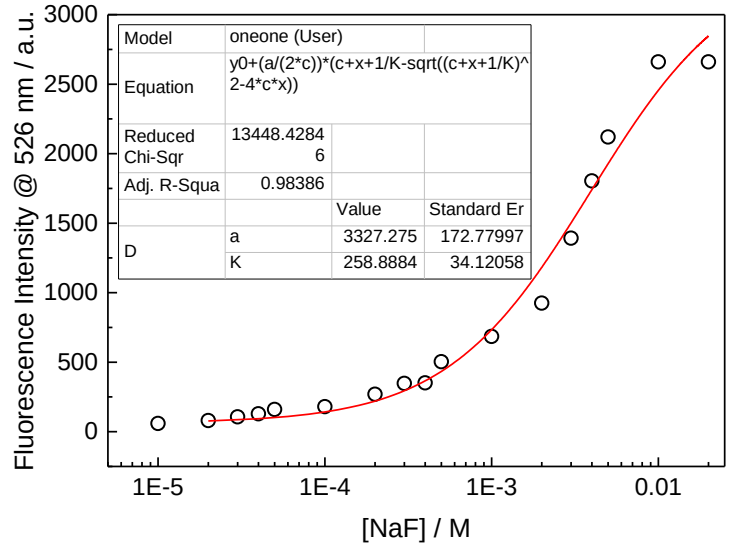

Figure 7.40 Fluorescence intensity of **F1** (0.1 mM) at 526 nm vs NaF concentration over 0 – 20 mM in the presence of 10 mM PCA in default buffer and curve fit (line) using eq 2, which gives a poor fitting of the data. λ_{ex} = 328 nm.

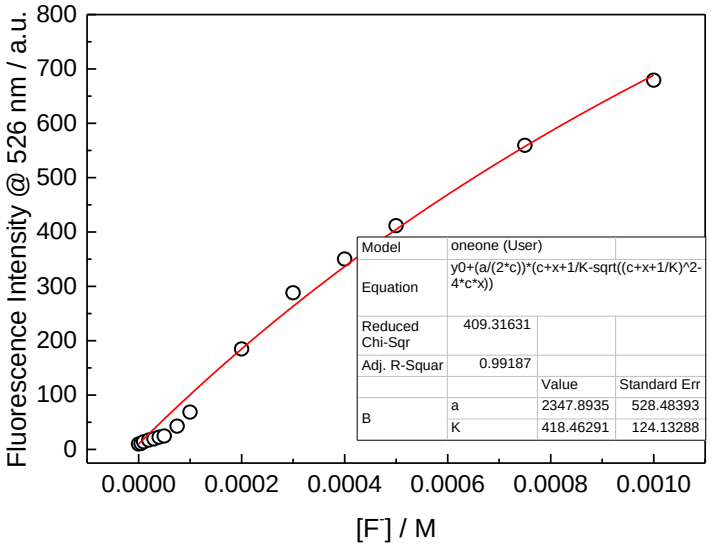

Figure 7.41 Fluorescence intensity of **F1** (0.1 mM) at 526 nm vs NaF concentration over 0 – 1 mM in the presence of 5 mM PCA in default buffer and the curve fit (line) using eq 2. λ_{ex} = 328 nm.

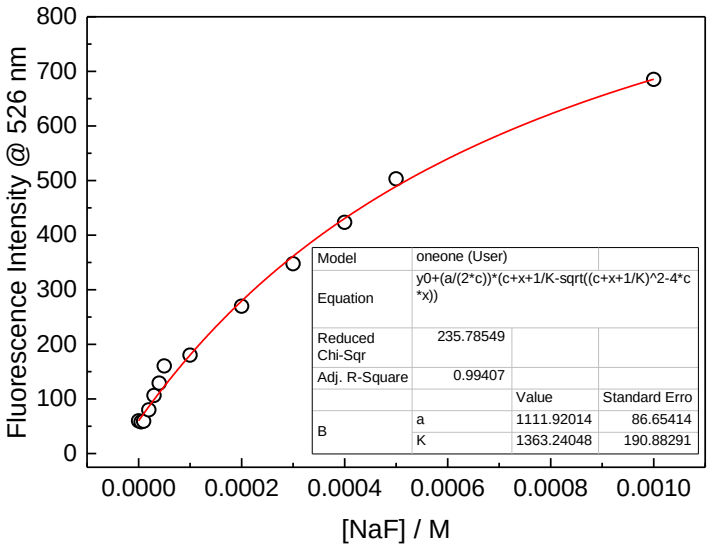

Figure 7.42 Fluorescence intensity of **F1** (0.1 mM) at 526 nm vs NaF concentration over 0 – 1 mM in the presence of 10 mM PCA in default buffer and curve fit (line) using eq 2. λ_{ex} = 328 nm.

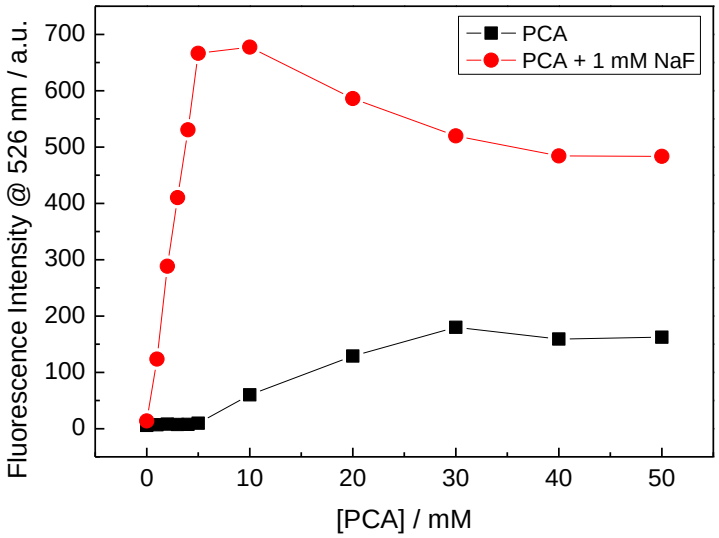

Figure 7.43 Fluorescence intensity of **F1** (0.1 mM) at 526 nm vs PCA concentration in the absence (black line) and presence (red line) of 1 mM NaF in default buffer. Note that without NaF there is negligible interaction between **F1** and PCA with [PCA] ≤ 5 mM. In contrast, in the absence of fluoride, the titration curve almost levels off at PCA concentration of 5 mM, suggesting that binding of PCA and fluoride to **F1** occurred in a cooperative manner to form a tetrahedral boronate ester of **F1**-PCA-fluoride.

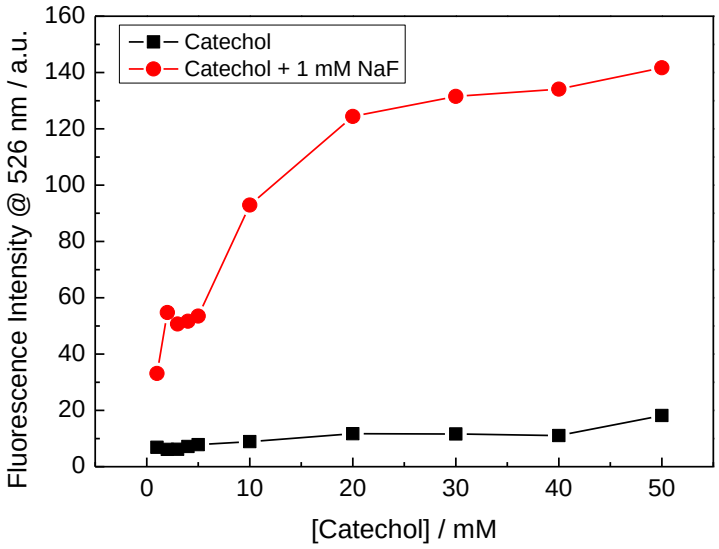

Figure 7.44 Fluorescence intensity of **F1** (0.1 mM) at 526 nm vs catechol concentration in the absence (black line) and presence (red line) of 1 mM NaF in default buffer.

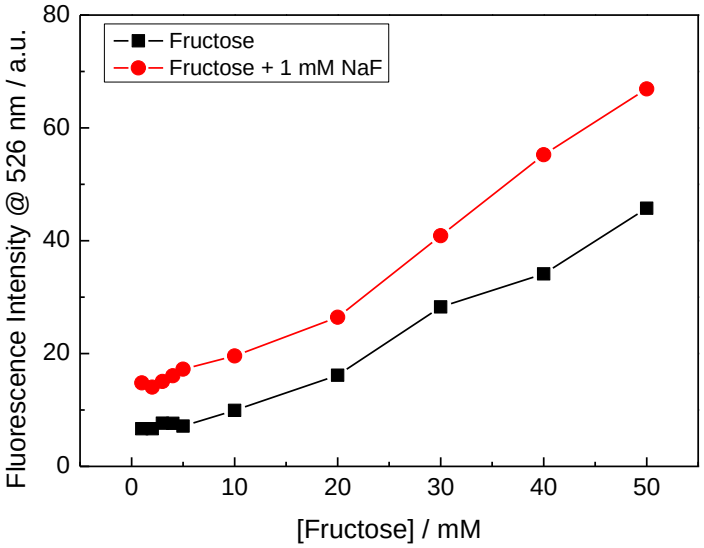

Figure 7.45 Fluorescence intensity of **F1** (0.1 mM) at 526 nm vs D-fructose concentration in the absence (black line) and presence (red line) of 1 mM NaF in default buffer.

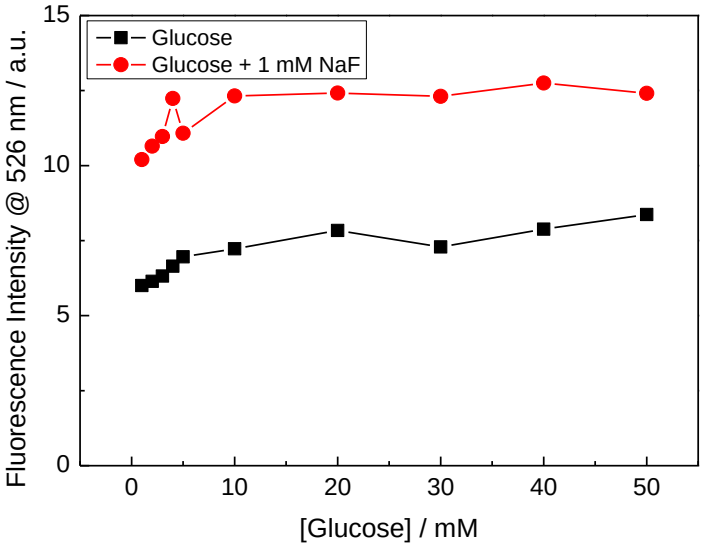

Figure 7.46 Fluorescence intensity of **F1** (0.1 mM) at 526 nm vs D-glucose concentration in the absence (black line) and presence (red line) of 1 mM NaF in default buffer. Note that the difference between the two curves hardly changes with increasing glucose concentration, indicating that fluoride ion did not enhance the aggregation of the **F1**-glucose complex.

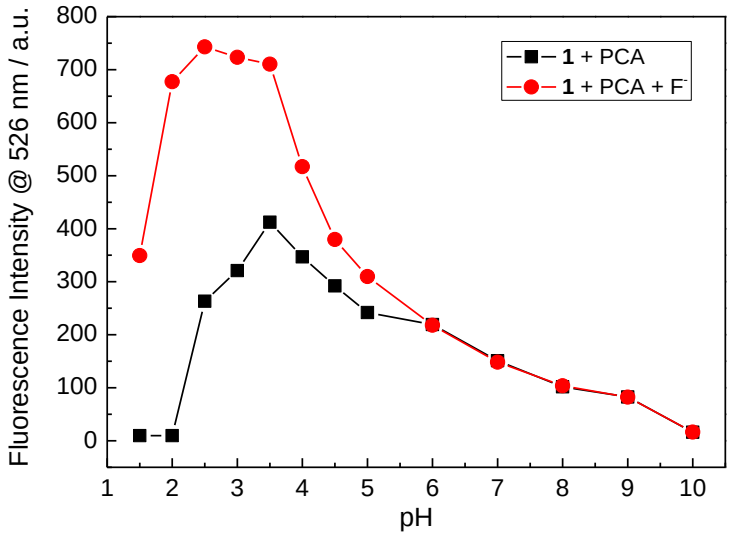

Figure 7.47 Fluorescence intensity of **F1** (0.1 mM) at 526 nm vs pH with 5 mM PCA in the absence and presence of 1 mM NaF in buffered aqueous solutions. λ_{ex} = 328 nm.

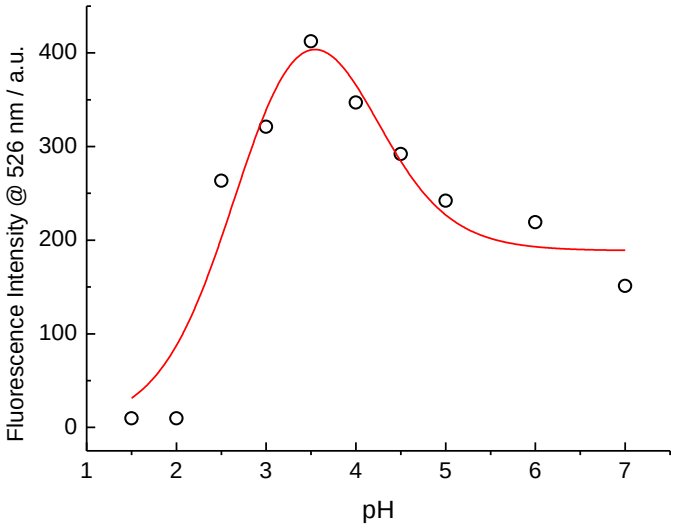

Model	twopKas (User)		
Equation	(H2A*10^(pKa1+pKa2-2*x)+HA*10^(pKa2-x)+A)/(10^(pKa1+pKa2-2*x)+10^(pKa2-x)+1)		
Reduced Chi-Sqr	2683.15751		
Adj. R-Square	0.85239		
		Value	Standard Error
B	H2A	0	61.8278
B	HA	517.22286	141.98542
B	A	188.71315	35.21332
B	pKa1	2.69188	0.38221
B	pKa2	4.12196	0.4923

Figure 7.48 Curve fit for Figure 7.47 (F1 + PCA) using eq 4. The data obtained with higher pH were not used for fitting since appreciable deprotonation of the phenol group of PCA occurs (pKa 8.83).

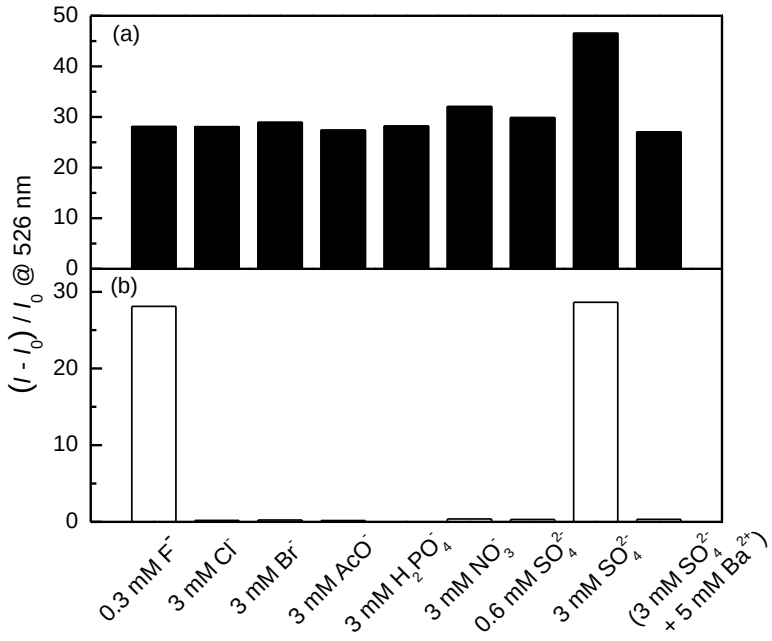

Figure 7.49 Enhancement of fluorescence of **F1** (0.1 mM) at 526 nm in response to fluoride and other anions alone (b) or in the presence of fluoride coexisting with other anions (a) in the presence of 5 mM PCA in default buffer. λ_{ex} = 328 nm.

7.3 Supporting information for Chapter 4

7.3.1 General

All commercial reagents and solvents were used as received. Turbidity measurements were performed on a Varian Cary 300 UV-Vis spectrophotometer. Fluorescence spectra were obtained on Hitachi F-4500 fluorescence spectrophotometer. ^{1}H NMR spectra were recorded on a Bruker AV500 NMR spectrometer. Dynamic light scattering (DLS) measurements were performed on a Malvern Zetasizer Nano ZS. Transmission electron microscope (TEM) images were taken on a JEOL JEM-1400 transmission electron microscope. All sample preparation and spectroscopic measurements were carried out at ambient temperature of 298 K.

7.3.2 Experimental

A stock solution of 50 mM 4-formylphenylboronic acid (4FBA) was prepared in 100 mM sodium carbonate buffer of pH 10.5, with 2 eqv of NaOH (*i.e.* 100 mM) added (to ionize the boronic acid and neutralize octylamine-HCl for the self-assembly study). A stock solution of 500 mM octylamine-HCl (C8AM-HCl) was prepared in water. Stock solutions of D-glucose (1 M), D-fructose (1 M) and D-galactose (0.5 M) were prepared in water and diluted with buffer prior to use. For 1H NMR determination of imine formation, the solutions were prepared in D2O.

In the self-assembly study, stock solutions of a saccharide (if used), C8AM-HCl, 4FBA-2NaOH were added to 100 mM sodium carbonate buffer of pH 10.5 to obtain the final solution with desired component concentrations. For NMR and DLS studies, the solution was incubated for 30 min and then subject to the measurements. For the fluorescence experiments, the solution (2 mL) was incubated for 30 min, treated with Nile red (10 μL of 1 mM methanol solution), and then immediately subject to fluorescence measurements. For TEM imaging, the solution was incubated for 30 min, pipetted onto a copper grid, dried under vacuum for 30 min and subject to TEM imaging.

7.3.3 NMR evidence of imine and boronate ester formation

To confirm the ability of 4FBA to form an imine with C8AM and bind saccharides via boronate ester linkages, NMR binding studies were conducted. 4FBA (10 mM) was mixed with a large excess of C8AM (100 mM), in the presence of the non-ionic detergent octaethylene glycol monododecyl ether (C12E8, 200 mM, to solubilize all components and prevent vesicle formation). ^{1}H NMR spectrum in the absence of saccharides (Figure 7.50 black) showed that the boronic acid existed predominantly as the imine. The presence of saccharides led to appearance of new signals in the ^{1}H NMR spectra of the imine, confirming saccharide binding to the imine. ^{11}B NMR was attempted on those micelle samples; however, the ^{11}B NMR signals of the imine broadened to baseline, likely due to restricted molecule motion as a result of the imine aligning with the C12E8 surfactant molecules in micelles. Therefore ^{11}B NMR saccharide binding study was only performed for 4FBA (Figure 7.51).

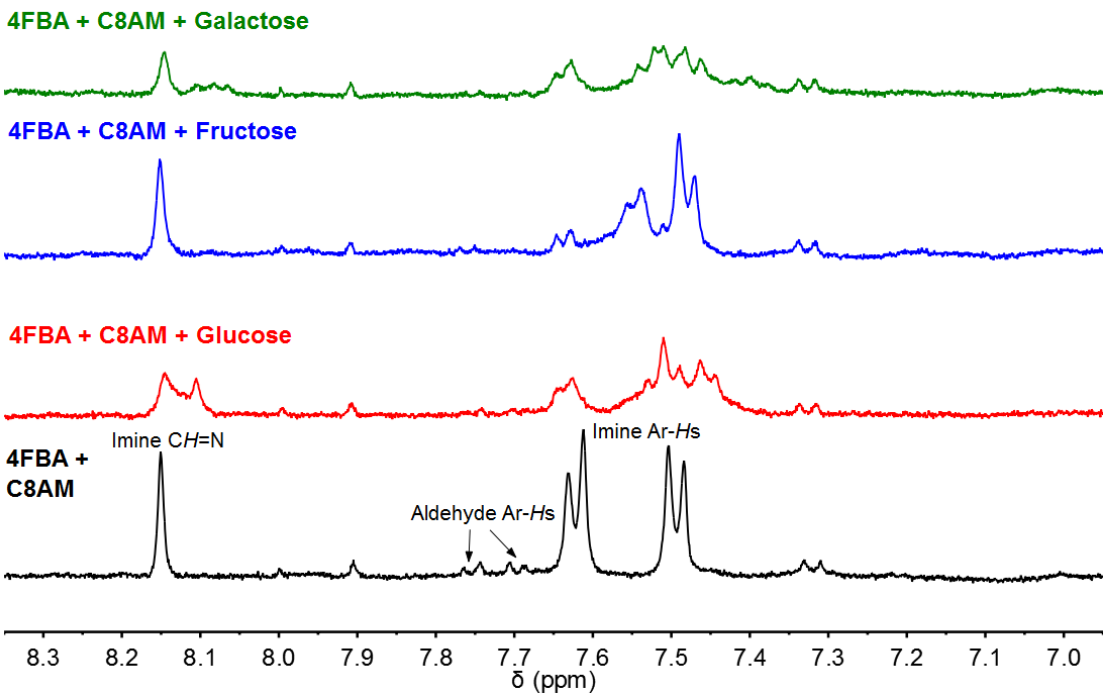

Figure 7.50 1H NMR spectra (400 MHz) of a mixture of 4FBA (10 mM, sodium salt used), C8AM (100 mM) and C12E8 (200 mM) in the absence and presence of saccharides (10 mM) in 9:1 H_2O/D_2O. The imine product was solubilized in C12E8 micelles.

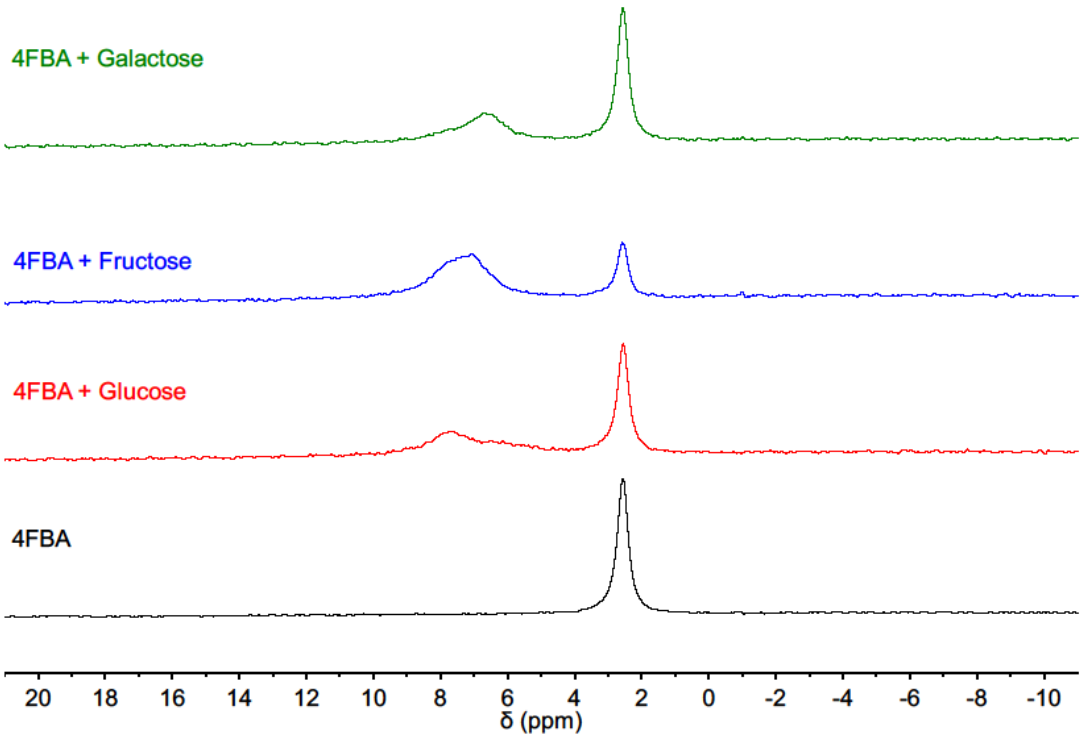

Figure 7.51 ^{11}B NMR spectra (160 MHz, without decoupling, referenced to $BF_3 \cdot Et_2O$ in $CDCl_3$) of 4FBA (10 mM) in the absence and presence of saccharides (10 mM) in 9:1 H_2O/D_2O buffered at pH 10.5 with 100 mM $NaHCO_3$–Na_2CO_3.

7.3.4 Fluorescence spectra

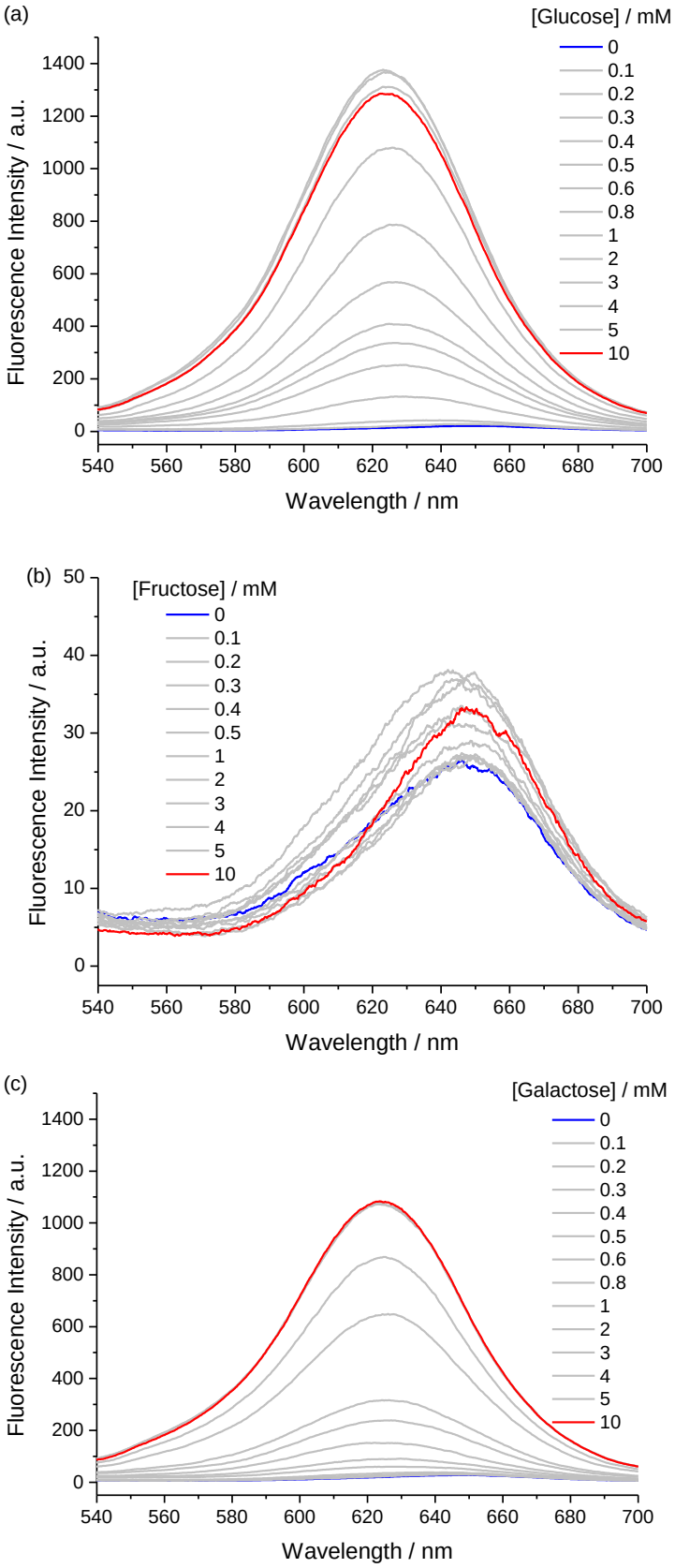

Figure 7.52 Fluorescence spectra of Nile red (5 μM) added to a mixture of 4FBA (3 mM), C8AM (3 mM) and increasing concentration of D-glucose (a), D-fructose (b) and D-galactose (c) in pH 10.5 100 mM $NaHCO_3$–Na_2CO_3 buffer. 4FBA, C8AM and the saccharide component (if used) were mixed in the buffer for 30 min before the addition of Nile red.

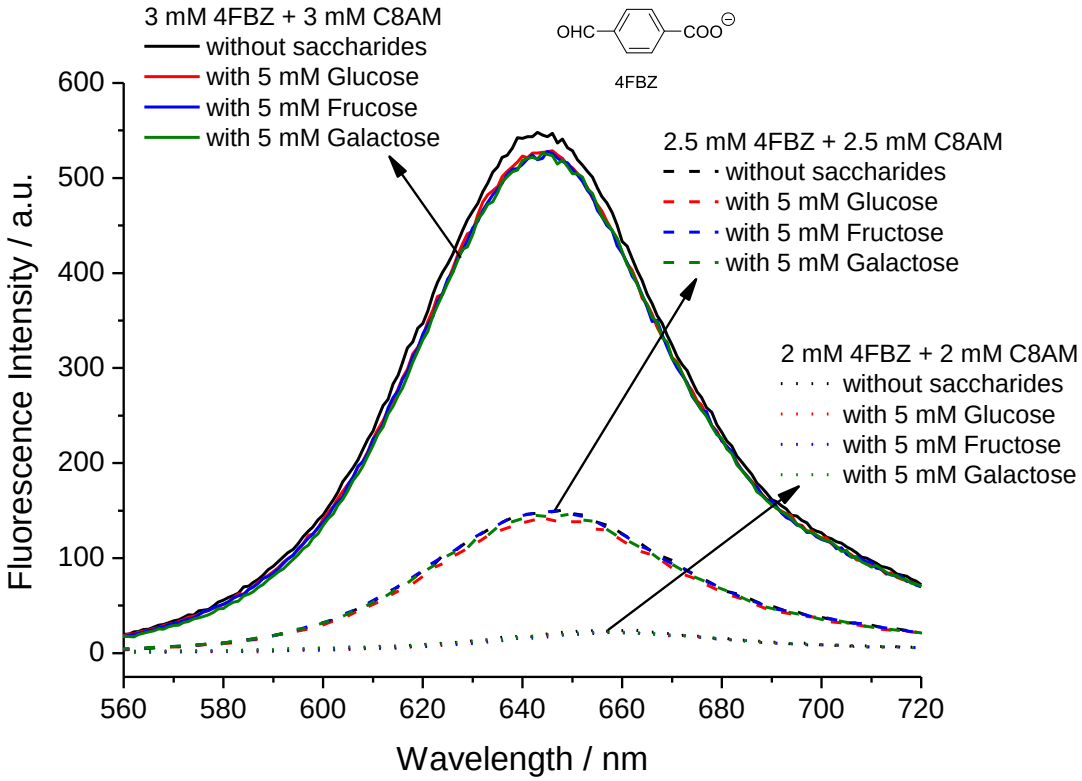

Figure 7.53 Fluorescence spectra of Nile red (5 μM) added to a mixture of 4-formylbenzoate (4FBZ, 2 mM, 2.5 mM or 3 mM) and C8AM (2 mM, 2.5 mM or 3 mM) in the absence and presence of saccharides (5 mM) in pH 10.5 100 mM $NaHCO_3$–Na_2CO_3 buffer. 4FBZ, C8AM and the saccharide component (if used) were mixed in the buffer for 30 min before the addition of Nile red. Inset shows the structure of 4FBZ.

7.3.5 NMR determination of imine formation

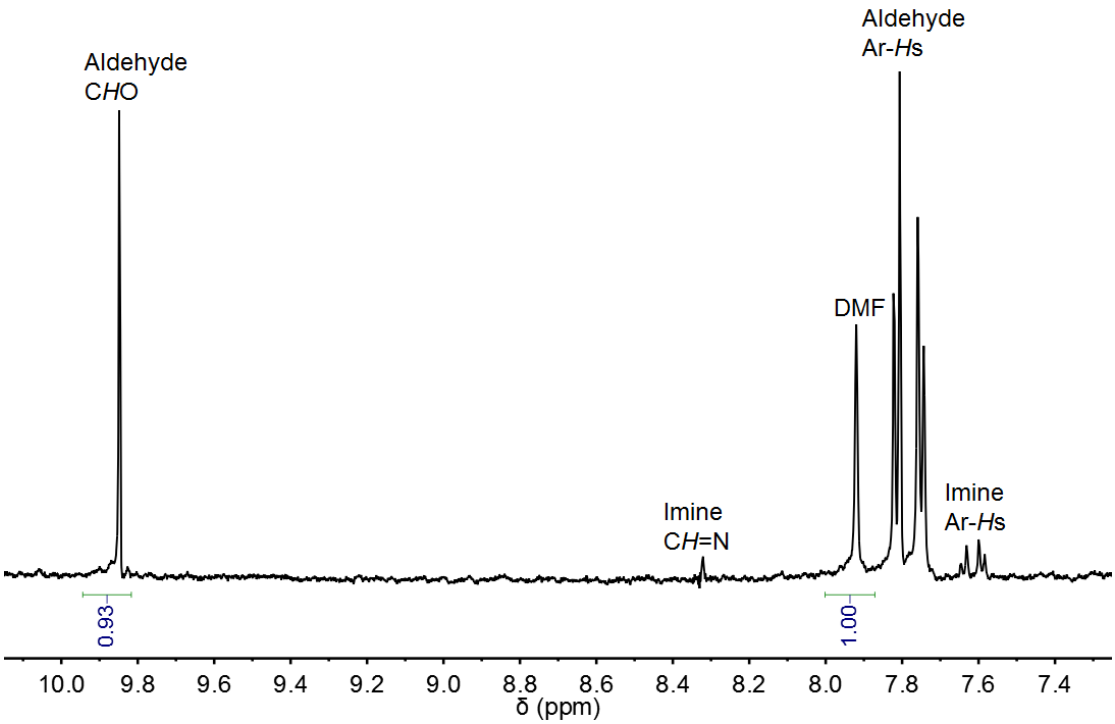

Figure 7.54 ^{1}H NMR (500 MHz) spectrum of a mixture of 4FBA (3 mM) and C8AM (3 mM) in D_2O buffered at pD 10.5 with 100 mM $NaHCO_3$–Na_2CO_3. DMF (3 mM) was added as an internal reference for determination of imine formation.

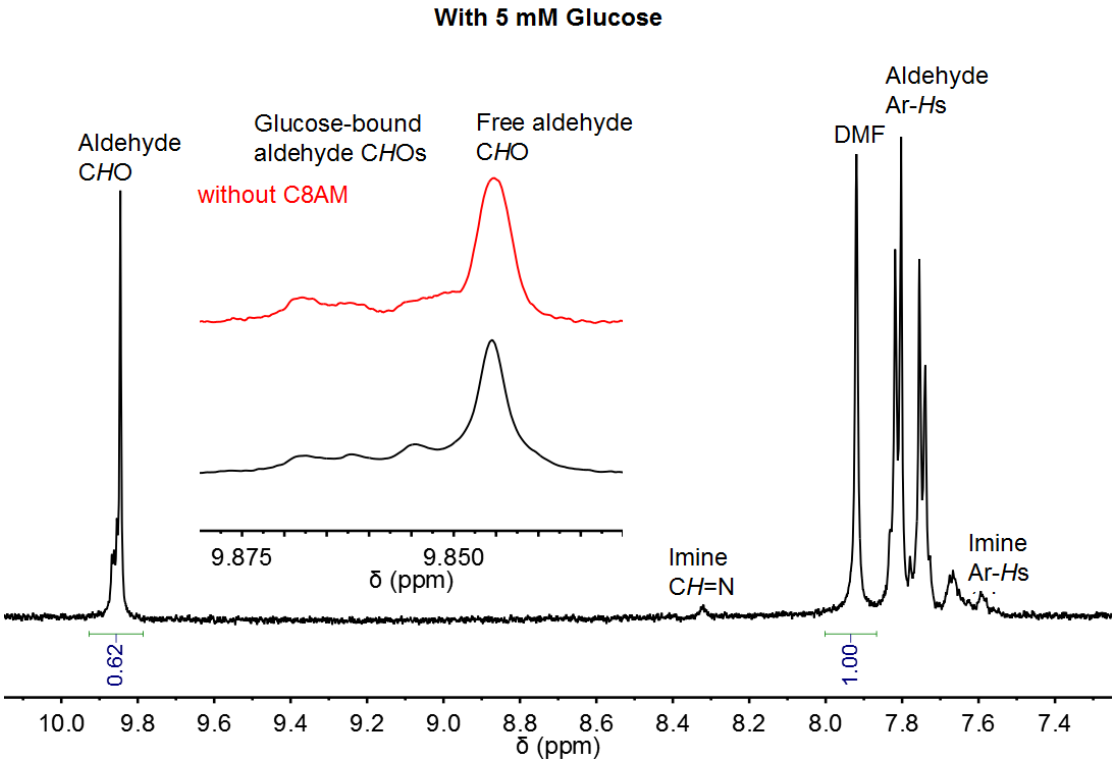

Figure 7.55 ^{1}H NMR (500 MHz) spectrum of a mixture of 4FBA (3 mM), C8AM (3 mM) and glucose (5 mM) in D_2O buffered at pD 10.5 with 100 mM $NaHCO_3$–Na_2CO_3. DMF (3 mM) was added as an internal reference for determination of imine formation. Note that multiple sets of signals were observed in the aldehyde CHO region and the aromatic regions of aldehydes and imines. This is due to the coexistence of the free aldehyde, glucose-bound aldehydes, free imine, and glucose-bound imines. The aldehyde region was zoomed and compared with the control sample without the amine component C8AM (red spectrum). Similar multiple signals were observed without C8AM, indicating that the multiple signals are due to coexistence of the free aldehyde and glucose-bound aldehydes (a mixture of complexes[260]).

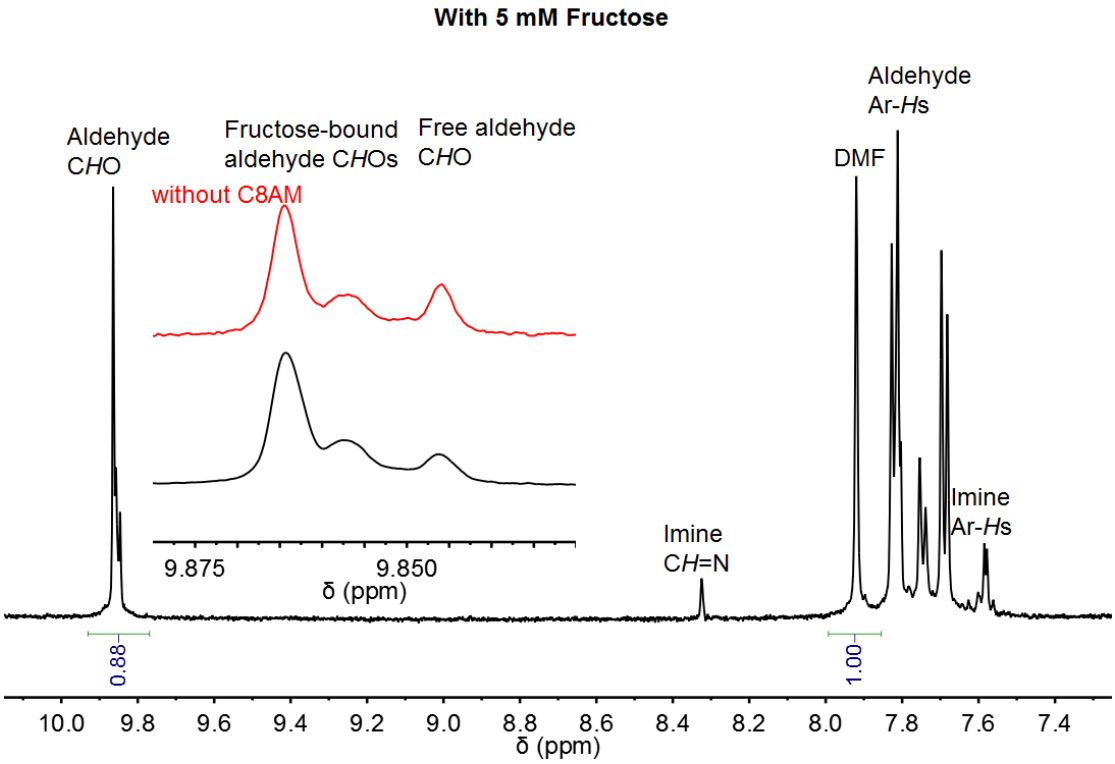

Figure 7.56 ^{1}H NMR (500 MHz) spectra of a mixture of 4FBA (3 mM), C8AM (3 mM) and fructose (5 mM) in D_2O buffered at pD 10.5 with 100 mM $NaHCO_3$–Na_2CO_3. DMF (3 mM) was added as an internal reference for determination of imine formation. Note that multiple sets of signals were observed in the aldehyde CHO region and the aromatic regions of aldehydes and imines. This is due to the coexistence of the free aldehyde, fructose-bound aldehydes, free imine, and fructose-bound imines. The aldehyde region was zoomed and compared with the control sample without the amine component C8AM. Similar multiple signals were observed without C8AM, indicating that the multiple signals are due to coexistence of the free aldehyde and fructose-bound aldehydes (a mixture of complexes[261]). Note that comparison of Figure 7.55 and Figure 7.56 reveals that in the bulk solution most of 4FBA was bound to fructose whereas glucose binding only occurred to a low extent. This is consistent with the much higher affinity of monoboronic acid for fructose than for glucose.[117, 126]

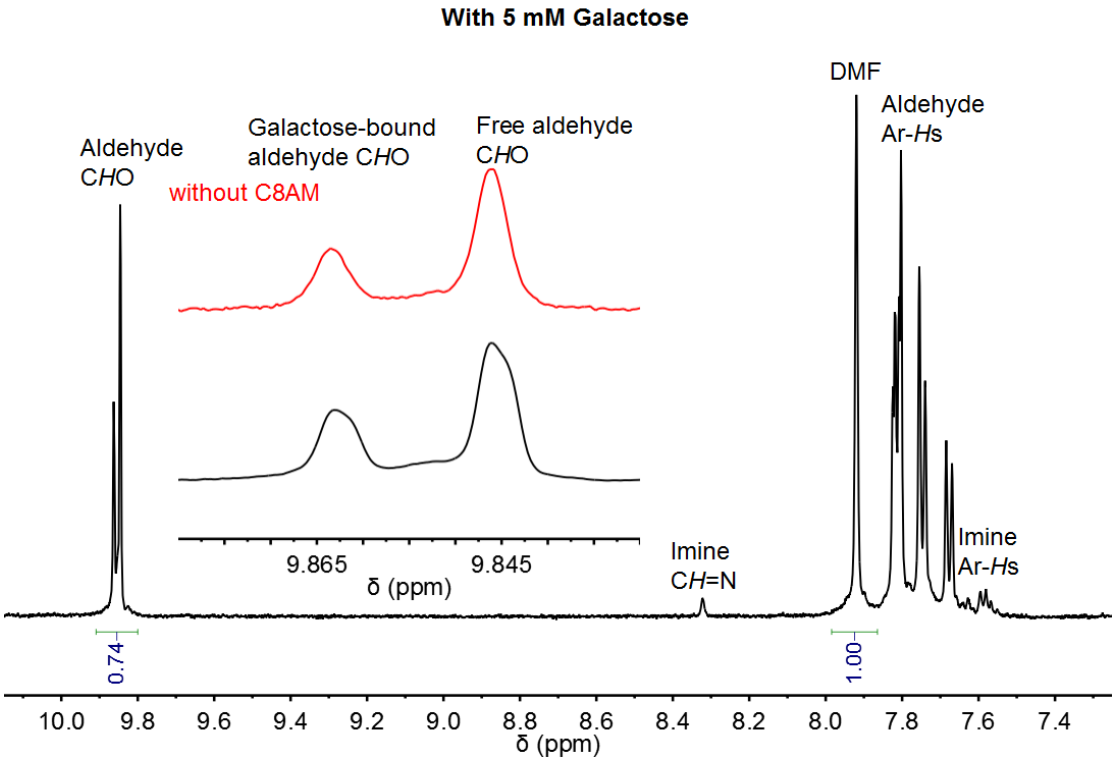

Figure 7.57 ^{1}H NMR (500 MHz) spectra of a mixture of 4FBA (3 mM), C8AM (3 mM) and galactose (5 mM) in D2O buffered at pD 10.5 with 100 mM NaHCO3–Na2CO3. DMF (3 mM) was added as an internal reference for determination of imine formation. Note that multiple signals were observed in the aldehyde CHO region and the aromatic regions of aldehydes and imines. This is due to the coexistence of the free aldehyde, galactose-bound aldehydes, free imine, and galactose-bound imines. The aldehyde region was zoomed and compared with the control sample without the amine component C8AM. Similar double signals were observed without C8AM, indicating that the multiple signals are due to coexistence of the free aldehyde and the galactose-bound aldehydes.

7.4 Supporting information for Chapter 5

7.4.1 General

T1 was synthesized by NB.[144] The lipids POPC, DPPC and POPG were purchased from Avanti Lipids. Other chemicals were purchased from Sigma-Aldrich, Alfa-Aesar, Apollo Scientific or Tokyo Chemical Industry, and used as received. ^{1}H NMR and ^{13}C NMR spectra were obtained on a Bruker AVIII HD400 FT–NMR Spectrometer. Fluorescence measurements were performed using a Varian Cary Eclipse Fluorescence Spectrophotometer equipped with a stirrer plate and a temperature controller.

7.4.2 ^{13}C NMR assay for Gly transport

Giant multilamellar vesicles of POPC were prepared as follows. A chloroform solution of POPC was evaporated in a round-bottle flask and the lipid film formed was dried under vacuum for at least 6 h. The lipid film was hydrated by vortexing with a buffered aqueous solution (pH 7.4, 20 mM HEPES, 100 mM Na_2SO_4) to a lipid concentration of 40 mM. The lipid solution was subjected to 6 freeze/thaw cycles, and vortexed after every 3 cycles for 30 s to facilitate hydration. The lipid solution was then extruded 35 times through a 5.0 μm polycarbonate membrane to obtain a concentrated lipid stock solution.

For each ^{13}C NMR transport experiment, the lipid stock solution prepared as stated above (300 μL) was added to an external Gly-1-^{13}C solution (300 μL, pH 7.4, 20 mM HEPES, 100 mM Na_2SO_4, 100 mM Gly-1-^{13}C). To this solution was added DMSO solutions of **T1**(8 mM) or an aldehyde (**T2** or **T3**, 80 mM), or both of them, or DMSO as control. The total volume of DMSO added for each sample was fixed at 30 μL. The resulting solution was stirred at room temperature for 2 h. An aqueous solution of $MnSO_4$ (30 μL, 10 mM) and D_2O (67 μL) were then added, and the sample was subject to ^{13}C NMR measurement. Acquisition parameters: frequency, 100.6 MHz; acquisition time, 1.36 s; spectrum width, 24038 Hz; 90° pulse width, 7.91 μs; relaxation delay, 2 s; number of scans, 512; temperature, 298 K.

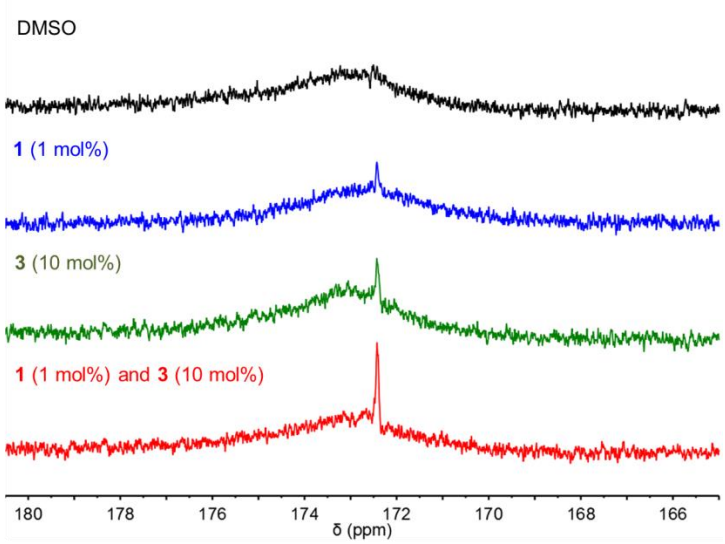

Figure 7.58 ^{13}C NMR spectra (100.6 MHz) of POPC vesicles suspensions with external Gly-1-^{13}C (50 mM), obtained 2 h after the addition of DMSO or DMSO solutions of transporters, with Mn^{2+} added externally (0.5 mM) to quench the signal from external Gly-1-^{13}C. Both the internal and external solutions contained Na_2SO_4 (100 mM) and HEPES (20 mM) buffered at pH 7.4. Transporter loadings are shown as transporter to lipid molar ratios.

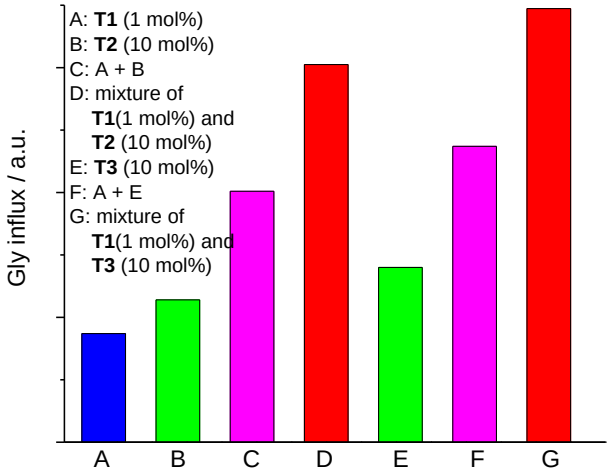

Figure 7.59 Comparison of Gly influx into POPC giant multilamellar vesicles facilitated by **T1** (1 mol%), **T2** (10 mol%), **T3** (10 mol%), or their mixtures, measured by the ^{13}C NMR assay. Transporter loadings are shown as transporter to lipid molar ratios.

7.4.3 Osmotic response assay for Gly transport

POPC LUVs (mean diameter 400 nm) were prepared as follows. A chloroform solution of lipids was evaporated in a round-bottle flask and the lipid film formed was dried under vacuum for at least 6 h. The lipid film was hydrated by vortexing with an aqueous solution of Gly (pH 7.4, 20 mM HEPES, 600 mM Gly) to a lipid concentration of 40 mM. The lipid solution was subjected to nine freeze/thaw cycles and then extruded 25 times through a 400 nm polycarbonate membrane to obtain a lipid stock solution. For each measurement, the lipid stock solution (50 µL) was added to an isosmotic external solution of Na_2SO_4 (1950 µL, pH 7.4, 20 mM HEPES, 200 mM Na_2SO_4) in the absence or presence of $CuSO_4$ (0.2 mM). The lipid solution was stirred and thermostated in a polystyrene cuvette at 25 °C. The 90° light scattering intensity at 600 nm was monitored using a fluorimeter. After 3 min when the light scattering intensity stabilized, DMSO solutions of transporters (20 µL, in the cases of mixed transporters, the DMSO solutions of different transporters were added separately instead of being pre-mixed in DMSO) or DMSO (20 µL) was added to the lipid solution to start the measurement of Gly transport, and the light scattering intensity was recorded over 30 min. Each experiment was run in triplicate and the data were averaged over three runs.

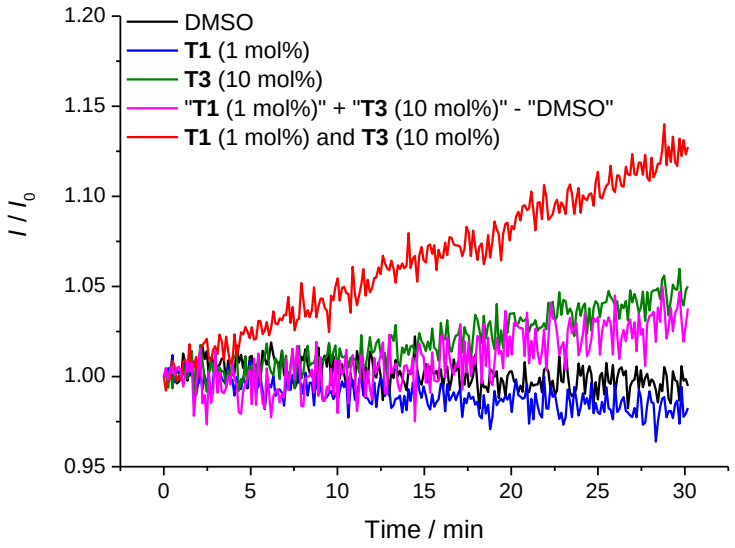

Figure 7.60 Gly transport measured by an osmotic response assay in the absence and presence of $CuSO_4$ (0.2 mM). POPC LUVs (mean diameter 400 nm) loaded with Gly (600 mM) were suspended in an external solution containing Na_2SO_4 (195 mM) and Gly (15 mM). Both the internal and external solutions were buffered at pH 7.4 with HEPES (20 mM). At time 0, DMSO solutions of transporters or DMSO was added, and the 90 ° light scattering intensity at 600 nm was recorded. Transporter loadings are shown as transporter to lipid molar ratios.

The control experiment was conducted to exclude the possibility that the increase of light scattering observed was due to aggregation or precipitation of the added transporters. POPC LUVs (mean diameter 400 nm) were prepared as follows. A chloroform solution of lipids was

evaporated in a round-bottle flask and the lipid film formed was dried under vacuum for at least 6 h. The lipid film was hydrated by vortexing with an aqueous solution of Gly (pH 7.4, 20 mM HEPES, 195 mM Na_2SO_4, 15 mM Gly) to a lipid concentration of 40 mM. The lipid solution was subjected to 25 freeze/thaw cycles and then extruded 25 times through a 400 nm polycarbonate membrane to obtain a lipid stock solution. The lipid solution was diluted with an external solution (pH 7.4, 20 mM HEPES, 195 mM Na_2SO_4, 15 mM Gly) to a final lipid concentration of 1 mM. The lipid solution (2 mL) was stirred and thermostated in a polystyrene cuvette at 25 °C. The 90° light scattering intensity at 600 nm was monitored using a fluorimeter. After 3 min when the light scattering intensity stabilized, DMSO solutions of **T1** (10 µL, 2 mM) and **T2** or **T3** (10 µL, 20 mM), or DMSO (20 µL) was added, and the light scattering intensity was recorded over 30 min. Each experiment was run in triplicate and the data were averaged over three runs. The results show no change in light scattering intensity after the addition of the transporters, excluding aggregation or precipitation of the transporters as the cause of the light scattering change.

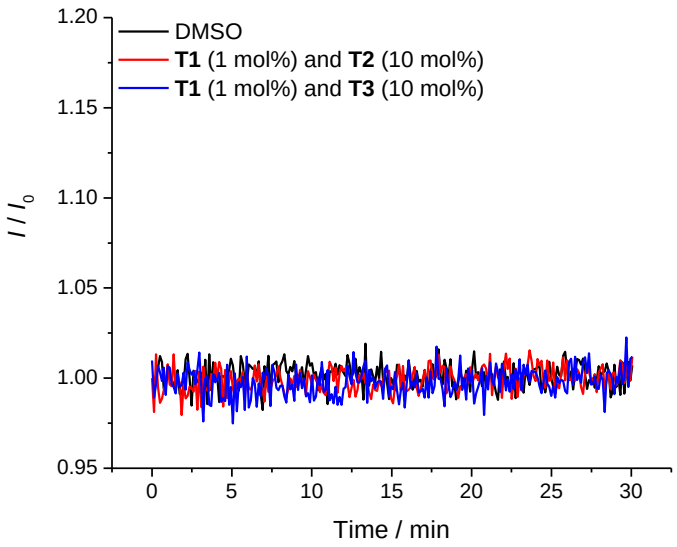

Figure 7.61 Intensity of 90 ° light scattering intensity at 600 nm with time of POPC LUV (mean diameter 400 nm) solutions with the same internal and external content (pH 7.4, 20 mM HEPES, 195 mM Na_2SO_4, 15 mM Gly). At time 0, DMSO solutions of transporters or DMSO was added. Transporter loadings are shown as transporter to lipid molar ratios.

7.4.4 Cu(II)-Calcein assay for Gly transport

7.4.4.1 Method

LUVs (mean diameter 200 nm) of POPC, POPC-cholesterol (7 : 3, molar ratio), or POPG were prepared as follows. A chloroform solution of lipids was evaporated in a round-bottle flask and the lipid film formed was dried under vacuum for at least 6 h. The lipid film was hydrated by vortexing with a buffered aqueous solution containing Cu^{2+} and Calcein (pH 7.4, 20 mM HEPES, 100 mM Na_2SO_4, 0.2 mM $CuSO_4$, 0.2 mM Calcein). The lipid solution was subjected to 25 freeze/thaw cycles and then extruded 25 times through a 200 nm polycarbonate membrane. The unentrapped Cu^{2+} and Calcein were removed by size exclusion chromatography on a Sephadex G-25 column using a buffer solution as the eluent (pH 7.4, 20 mM HEPES, 100 mM Na_2SO_4).

For each run, the LUV stock solution prepared as stated above was added to an external solution containing Cu^{2+} and Gly (pH 7.4, 20 mM HEPES, 100 mM Na_2SO_4, 0.2 mM $CuSO_4$, 30 mM Gly) to a final lipid concentration of 1 mM and a final volume of 2 mL. The lipid solution was stirred and thermostated in a polystyrene cuvette at 25 °C. DMSO solutions of the transporters (DMSO volume ≤ 20 μL, in the cases of mixed transporters, the DMSO solutions of different transporters were added separately instead of being pre-mixed in DMSO) or DMSO (20 μL) was added to the lipid solution to start the measurement of Gly transport, and the fluorescence emission (λ_{ex} = 495 nm, λ_{em} = 515 nm) was recorded over 30 min. Each experiment was run in triplicate and the data were averaged over three runs. For each vesicle preparation, using a mixture of **T1** (1 mol%) and **T3** (50 mol%), a maximum change of fluorescence intensity ($\Delta I_{max} = I_{max} - I_0$, where I_{max} is the maximum fluorescence intensity reached and I_0 is the fluorescence intensity before the addition of transporters) was obtained for calibration. The fractional fluorescence intensity, which is an approximate of the percentage of Gly influx compared to the maximum transport, is calculated using the following equation.

$$I_f = \frac{I_t - I_0}{\Delta I_{\max}}$$

where I_t is the fluorescence intensity at time t, and I_0 is the fluorescence intensity at time 0.

7.4.4.2 Effect of external Cu^{2+} on measurement of simple diffusion

The purpose of this experiment is to examine if Cu^{2+} diffusion can be observed without any transporter. POPC LUVs prepared according to the general method were suspended in external solutions (pH 7.4, 20 mM HEPES, 100 mM Na_2SO_4) with different concentrations of Gly and Cu^{2+}. DMSO (20 µL) was added to the samples and the fluorescence emission (λ_{ex} = 495 nm, λ_{em} = 515 nm) was recorded. By comparing the changes of Calcein fluorescence of samples with the same external Gly concentration (30 mM) but different external Cu^{2+} concentrations (0 mM, 0.2 mM, or 0.4 mM), it can be seen that without external Cu^{2+}, simple diffusion or Gly-mediated efflux of Cu^{2+} occurs significantly, as the presence of high concentration of external Gly has an overwhelming tendency to bind Cu^{2+} from inside whose overall concentration is in the submicromolar range. The presence of external Cu^{2+} up to 0.2 mM effectively suppresses Cu^{2+} transport, and the relatively small enhancement of Calcein fluorescence is ascribed to simple diffusion of Gly, since doubling the concentration of external Cu^{2+} has precisely no effect on the fluorescence intensity change (ΔI), while doubling the concentration of external Gly (60 mM) increased the ΔI value by 63%. The sensitivity to the external Gly concentration and insensitivity to the external Cu^{2+} concentration proves Gly diffusion, instead of Cu^{2+} diffusion to be the cause of the observed fluorescence enhancement in the presence of external Cu^{2+}.

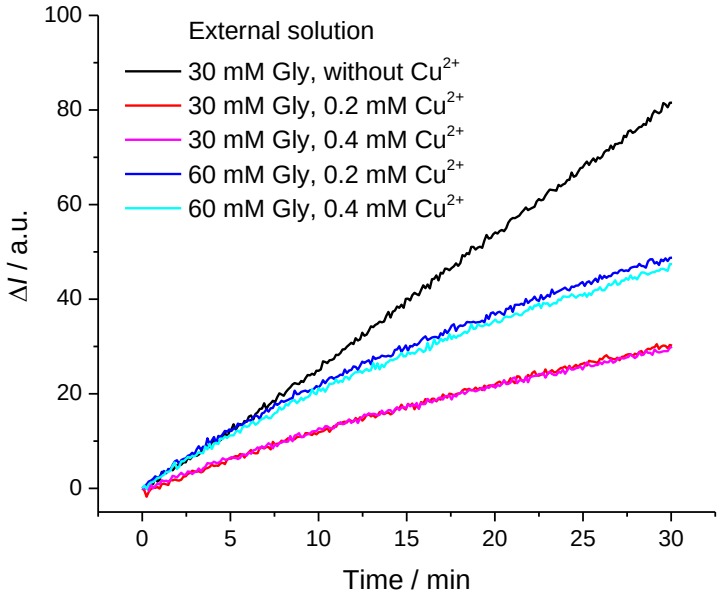

Figure 7.62 Change of fluorescence intensity (λ_{ex} = 495 nm, λ_{em} = 515 nm) vs time of POPC LUVs (mean diameter 200 nm) loaded with $CuSO_4$ (0.2 mM) and Calcein (0.2 mM), suspended in an external solution containing Gly (30 mM or 60 mM) and $CuSO_4$ (0, 0.2 mM or 0.4 mM). Both the internal and external solutions contained Na_2SO_4 (100 mM) and HEPES (20 mM) buffered at pH 7.4.

7.4.4.3 Dependence of maximum fluorescence intensity change on Gly concentration

Dependence of maximum fluorescence intensity change (ΔI_{max}) on the concentration of externally added Gly was examined to check in what concentration range of Gly the fluorescence intensity shows a linear relationship with the internal Gly concentration. POPC LUVs prepared according to the general method were suspended in external solutions (pH 7.4, 20 mM HEPES, 100 mM Na_2SO_4, 0.2 mM $CuSO_4$) with different Gly concentrations, and after the addition of a mixture of **T1** (1 mol%) and **T3** (50 mol%), the maximum change of fluorescence intensity ($\Delta I_{max} = I_{max} - I_0$, where I_{max} is the maximum fluorescence intensity reached and I_0 is the fluorescence intensity before the addition of transporters) was obtained. The results show that ΔI_{max} is reasonably linear with the concentration of externally added Gly up to 30 mM, while significant deviation from linearity is observed with higher concentration of Gly (Figure 7.63).

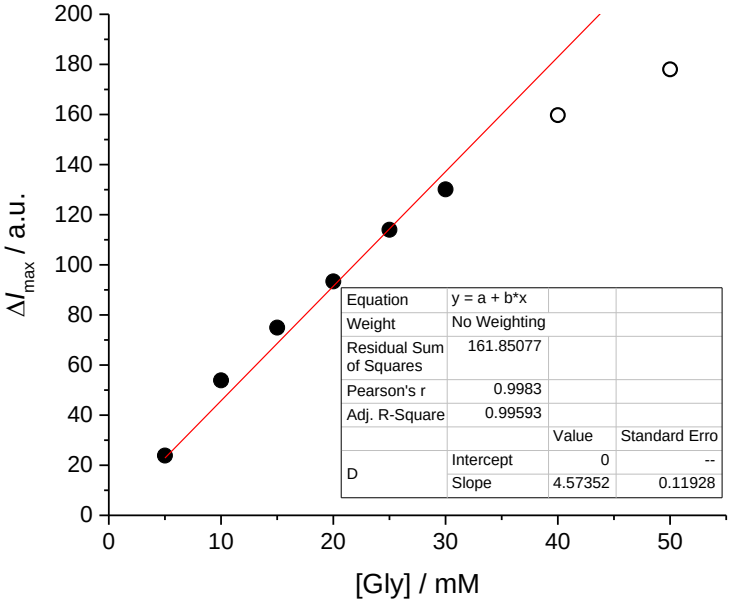

Figure 7.63 Maximum change of fluorescence intensity ΔI_{max} (λ_{ex} = 495 nm, λ_{em} = 515 nm) vs concentration of external Gly of POPC LUVs loaded with $CuSO_4$ (0.2 mM) and Calcein (0.2 mM), treated with **T1** (1 mol%, transporter to lipid) and **T3** (50 mol%). Both the internal and external solutions contained Na_2SO_4 (100 mM) and HEPES (20 mM) buffered at pH 7.4. Only data with [Gly] ≤ 30 mM were subject to the linear fit shown in the inset.

7.4.4.4 Interference of transporters with the fluorescence assay

The purpose of this set of experiments is to examine if the transporters or the imines formed between the transporters and Gly interfere with the Cu^{2+}-Calcein assay by competing with Calcein to bind Cu^{2+}. POPC LUVs prepared according to the general method were suspended in an external solution containing Cu^{2+} and Gly (pH 7.4, 20 mM HEPES, 100 mM Na_2SO_4, 0.2 mM $CuSO_4$, 30 mM Gly). A detergent (20 µl of 0.232 mM octaethylene glycol monododecyl ether in 7 : 1 (v / v) H_2O-DMSO) was added to lyse the vesicles. The fluorescence emission (λ_{ex} = 495 nm, λ_{em} = 515 nm) was recorded. At 5 min, DMSO solutions of transporters were added to the solutions. The results show little interference (Figure 7.64).

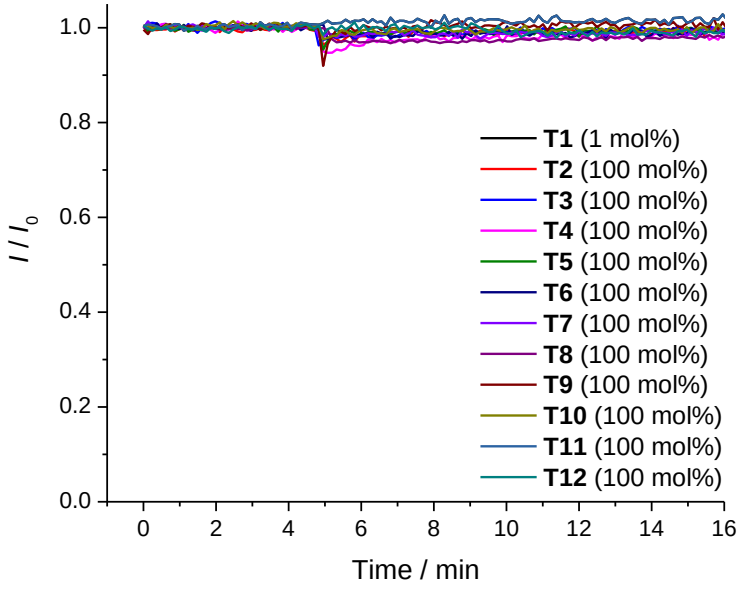

Figure 7.64 Relative fluorescence intensity I / I_0 (λ_{ex} = 495 nm, λ_{em} = 515 nm) vs time of detergent-treated POPC LUV solutions. Vesicles were originally loaded with $CuSO_4$ (0.2 mM) and Calcein (0.2 mM) and suspended in an external solution containing $CuSO_4$ (0.2 mM) and Gly (30 mM). Both the internal and external solutions contained Na_2SO_4 (100 mM) and HEPES (20 mM) buffered at pH 7.4. At 5 min, DMSO solutions of transporters were added to the detergent-treated solutions. Transporter loadings are shown as transporter to lipid molar ratios.

7.4.4.5 Gly transport by non-aldehyde analogues

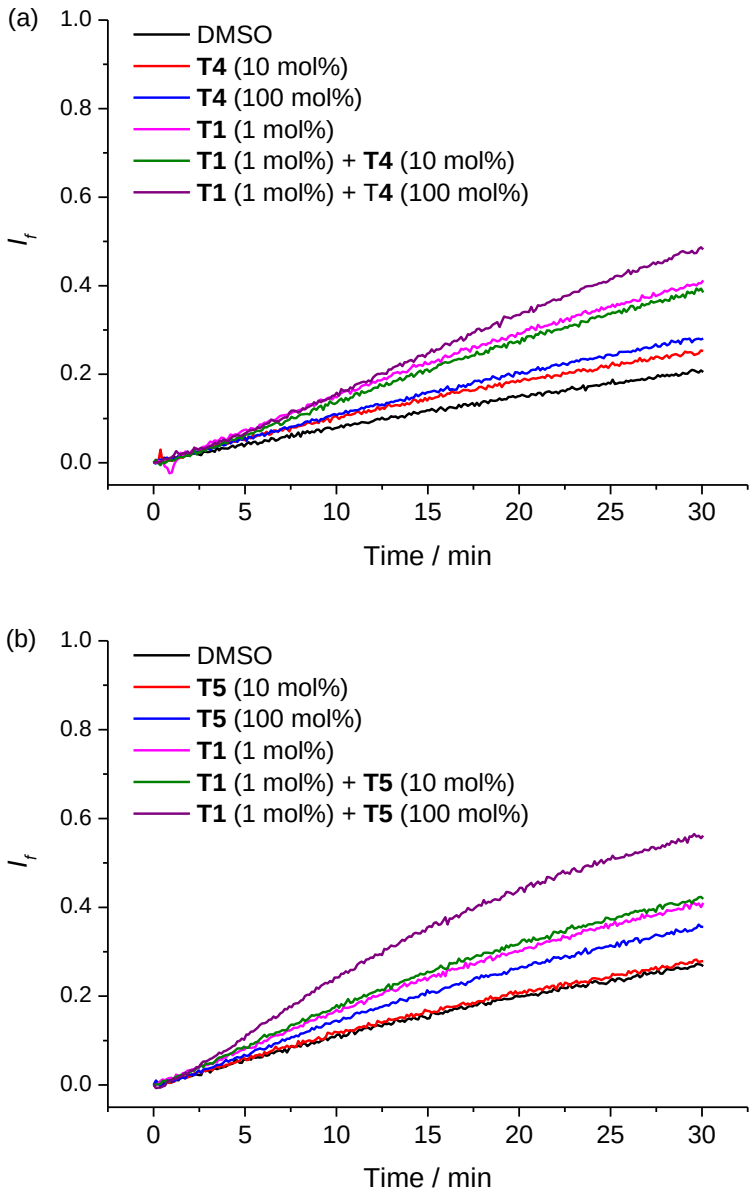

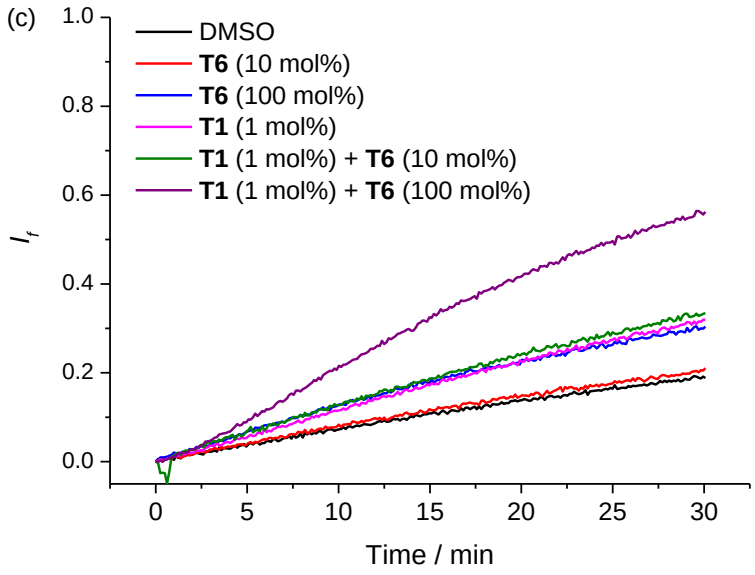
(c)
DMSO
T6 (10 mol%)
T6 (100 mol%)
T1 (1 mol%)
T1 (1 mol%) + T6 (10 mol%)
T1 (1 mol%) + T6 (100 mol%)
I_f
Time / min

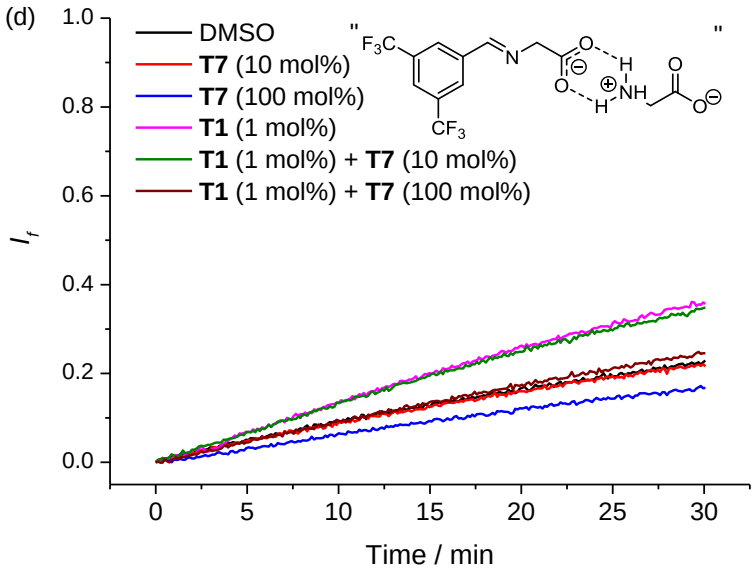
(d)
DMSO
T7 (10 mol%)
T7 (100 mol%)
T1 (1 mol%)
T1 (1 mol%) + T7 (10 mol%)
T1 (1 mol%) + T7 (100 mol%)
I_f
Time / min

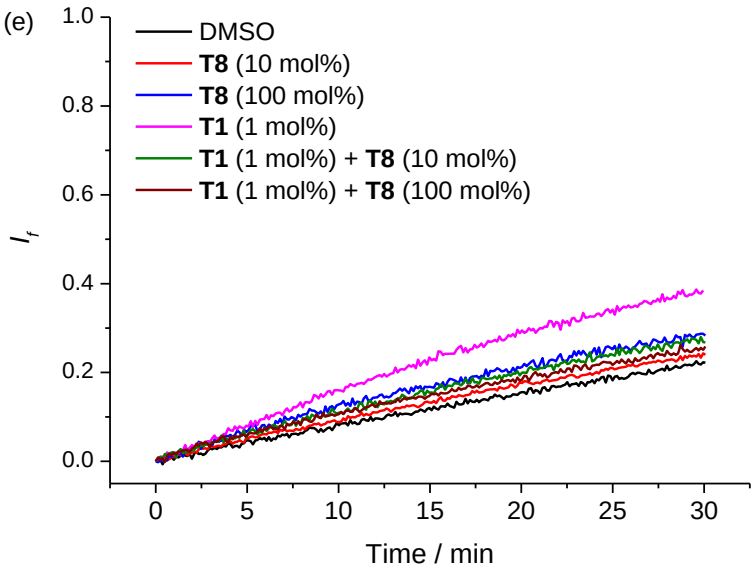
(e)
DMSO
T8 (10 mol%)
T8 (100 mol%)
T1 (1 mol%)
T1 (1 mol%) + T8 (10 mol%)
T1 (1 mol%) + T8 (100 mol%)
I_f
Time / min

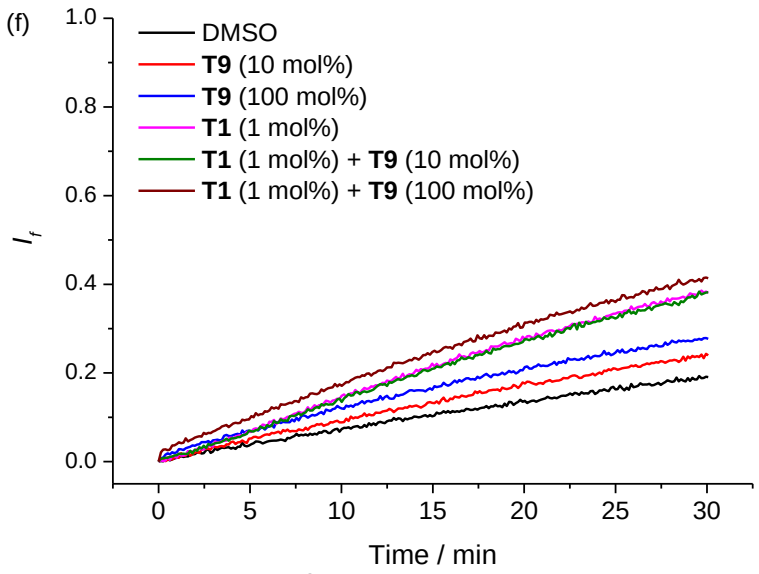

Figure 7.65 Gly influx (measured by the Cu^{2+}-Calcein assay) facilitated by **T4**-**T9** in the absence and presence of **T1**. POPC LUVs (mean diameter 200 nm) loaded with $CuSO_4$ (0.2 mM) and Calcein (0.2 mM) were suspended in an external solution containing Gly (30 mM) and $CuSO_4$ (0.2 mM). Both the internal and external solutions contained Na_2SO_4 (100 mM) and HEPES (20 mM) buffered at pH 7.4. At time 0, DMSO solutions of transporters or DMSO was added, and the fluorescence intensity (λ_{ex} = 495 nm, λ_{em} = 515 nm) was recorded. The fluorescence intensity was normalized to a fractional fluorescence intensity by saturation using a mixture of **T1** (1 mol%) and **T3** (50 mol%). Transporter loadings are shown as transporter to lipid molar ratios. Inset in (d) shows a possible mechanism for facilitated transport of Gly by the imine formed between the aldehyde and Gly, which was excluded as the model compound **T7** shows no Gly transport activity.

7.4.4.6 Effect of CCCP on Gly transport

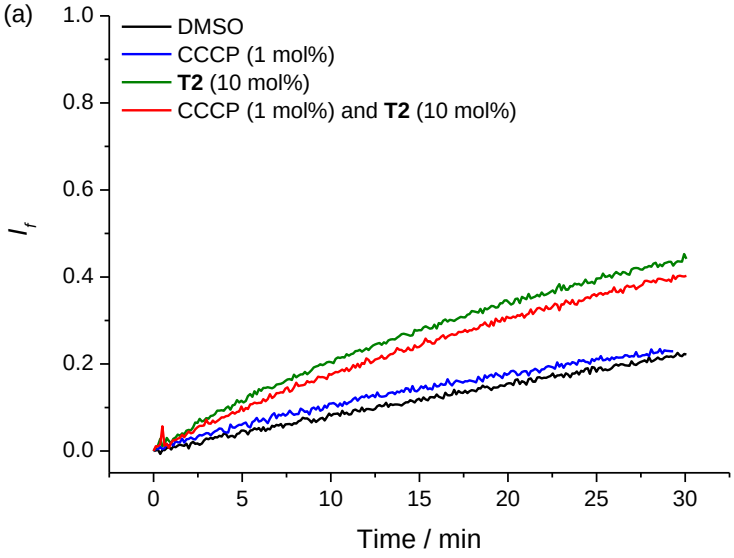

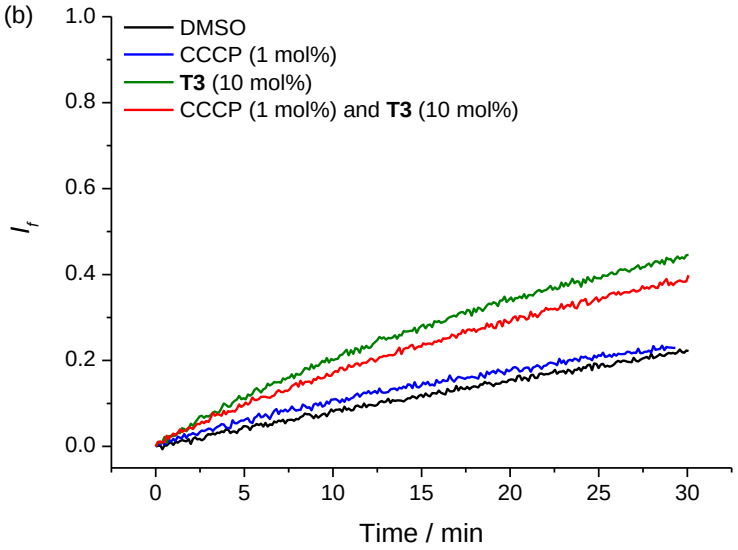

Figure 7.66 Effect of CCCP (1 mol%) on Gly influx (measured by the Cu^{2+}-Calcein assay). POPC LUVs (mean diameter 200 nm) loaded with $CuSO_4$ (0.2 mM) and Calcein (0.2 mM) were suspended in an external solution containing Gly (30 mM) and $CuSO_4$ (0.2 mM). Both the internal and external solutions contained Na_2SO_4 (100 mM) and HEPES (20 mM) buffered at pH 7.4. At time 0, DMSO solutions of transporters or DMSO was added, and the fluorescence intensity (λ_{ex} = 495 nm, λ_{em} = 515 nm) was recorded. The fluorescence intensity was normalized to a fractional fluorescence intensity by saturation using a mixture of **1** (1 mol%) and **3** (50 mol%). Transporter loadings are shown as transporter to lipid molar ratios.

7.4.4.7 Gly transport by T1 and aldehydes

The Gly transport kinetics of **T1** and aldehydes at different concentrations was measured by the Cu^{2+}-Calcein assay. The fractional fluorescence intensity I_f at 30 min was plotted as a function of the transporter loading. Hill coefficients and EC_{50} (30 min) values were calculated by fitting the curves to the following equation:

$$y = y_0 + (y_{max} - y_0)\frac{x^n}{K + x^n}$$

where y is I_f (30 min) value with the transporter loaded at concentration x, y_0 is I_f (30 min) value obtained without the transporter (in the cases of transporter pairs, y_0 is I_f (30 min) value obtained with the transporter with a fixed concentration throughout the Hill analysis), y_{max} is the maximum I_f value (which is set as 1), n is the Hill coefficient, and K is the EC_{50} (30 min) value.

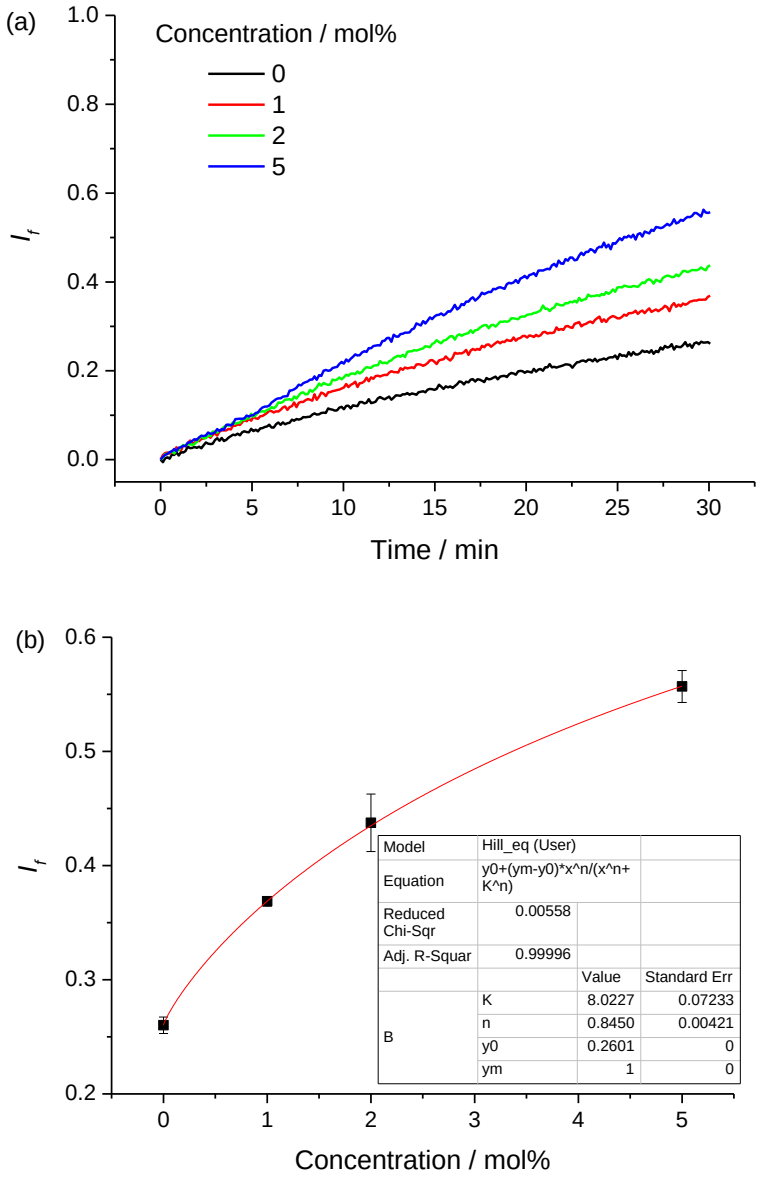

Figure 7.67 (a) Gly influx (measured by the Cu^{2+}-Calcein assay) facilitated by **T1**. POPC LUVs (mean diameter 200 nm) loaded with $CuSO_4$ (0.2 mM) and Calcein (0.2 mM) were suspended in an external solution containing Gly (30 mM) and $CuSO_4$ (0.2 mM). Both the internal and external solutions contained Na_2SO_4 (100 mM) and HEPES (20 mM) buffered at pH 7.4. At time 0, DMSO solutions of transporters or DMSO was added, and the fluorescence intensity (λ_{ex} = 495 nm, λ_{em} = 515 nm) was recorded. The fluorescence intensity was normalized to a fractional fluorescence intensity by saturation using a mixture of **T1** (1 mol%) and **T3** (50 mol%). Due to limited solubility of **T1** in DMSO, higher loadings were not tested. (b) Hill plot for Gly transport facilitated by **T1**. Transporter loadings are shown as transporter to lipid molar ratios. Error bars represent SD from two or three repeats.

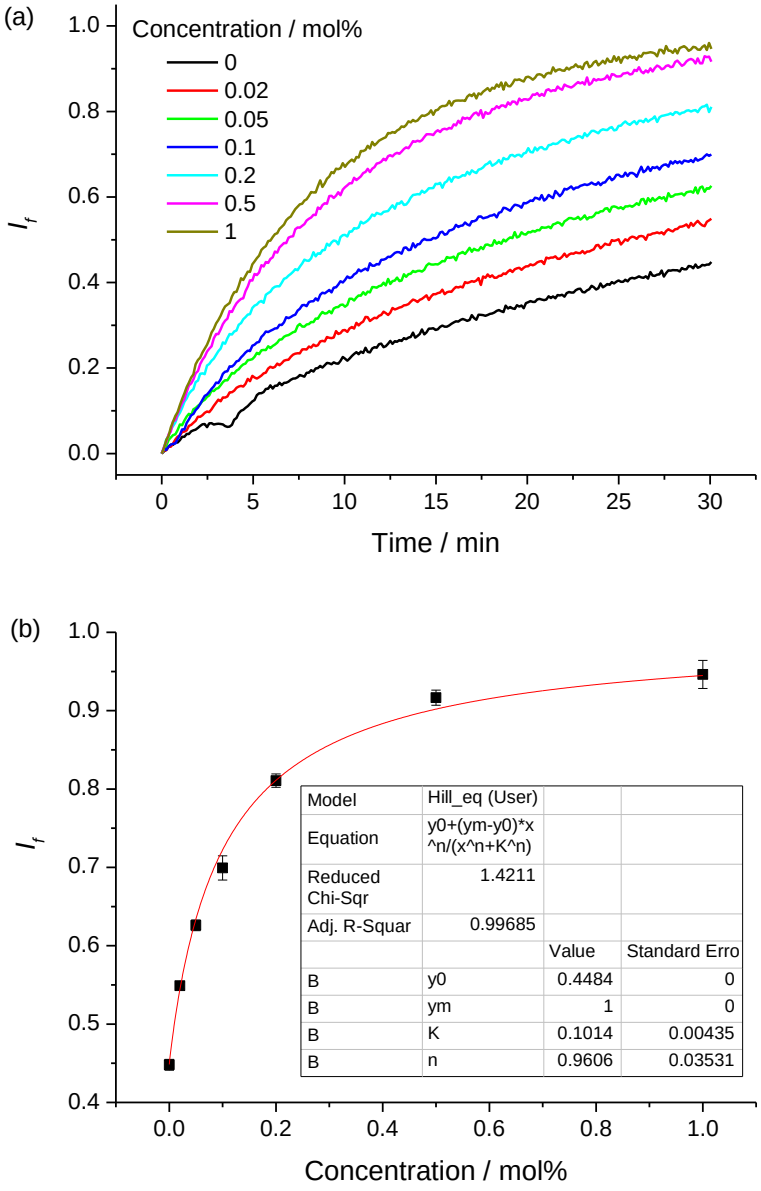

Figure 7.68 (a) Gly influx (measured by the Cu^{2+}-Calcein assay) facilitated by **T1** in the presence of **T2** (10 mol%). POPC LUVs (mean diameter 200 nm) loaded with $CuSO_4$ (0.2 mM) and Calcein (0.2 mM) were suspended in an external solution containing Gly (30 mM) and $CuSO_4$ (0.2 mM). Both the internal and external solutions contained Na_2SO_4 (100 mM) and HEPES (20 mM) buffered at pH 7.4. At time 0, DMSO solutions of transporters or DMSO was added, and the fluorescence intensity (λ_{ex} = 495 nm, λ_{em} = 515 nm) was recorded. The fluorescence intensity was normalized to a fractional fluorescence intensity by saturation using a mixture of **T1** (1 mol%) and **T3** (50 mol%). (b) Hill plot for Gly transport facilitated by **T1** in the presence of **T2** (10 mol%). Transporter loadings are shown as transporter to lipid molar ratios. Error bars represent SD from two or three repeats.

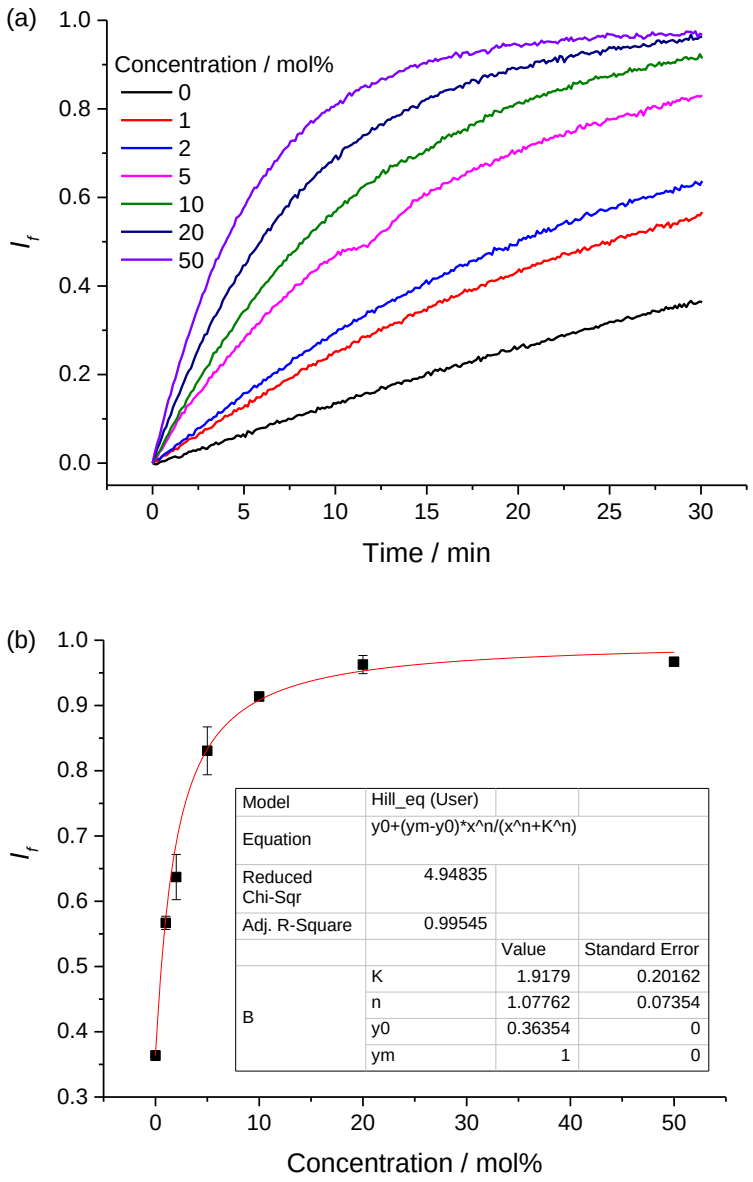

Figure 7.69 (a) Gly influx (measured by the Cu^{2+}-Calcein assay) facilitated by **T2** in the presence of **T1** (1 mol%). POPC LUVs (mean diameter 200 nm) loaded with $CuSO_4$ (0.2 mM) and Calcein (0.2 mM) were suspended in an external solution containing Gly (30 mM) and $CuSO_4$ (0.2 mM). Both the internal and external solutions contained Na_2SO_4 (100 mM) and HEPES (20 mM) buffered at pH 7.4. At time 0, DMSO solutions of transporters or DMSO was added, and the fluorescence intensity (λ_{ex} = 495 nm, λ_{em} = 515 nm) was recorded. The fluorescence intensity was normalized to a fractional fluorescence intensity by saturation using a mixture of **T1** (1 mol%) and **T3** (50 mol%). (b) Hill plot for Gly transport facilitated by **T2** in the presence of **T1** (1 mol%). Transporter loadings are shown as transporter to lipid molar ratios. Error bars represent SD from two or three repeats.

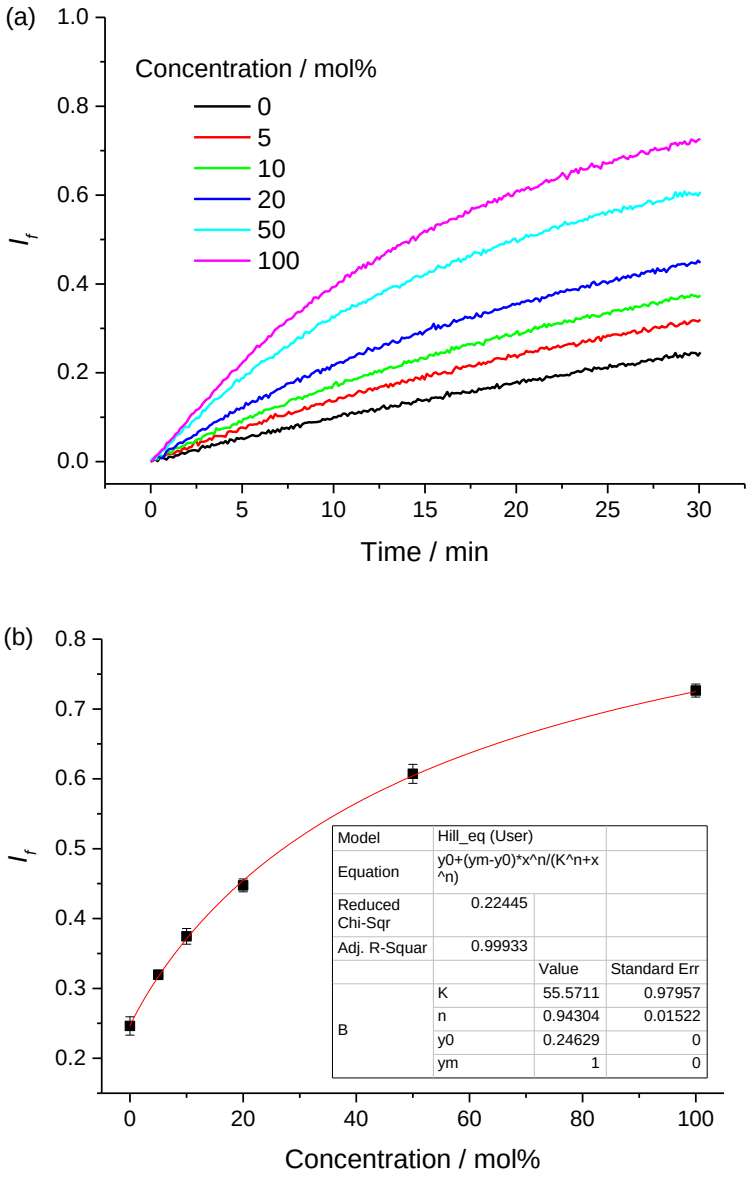

Figure 7.70 (a) Gly influx (measured by the Cu^{2+}-Calcein assay) facilitated by **T2**. POPC LUVs (mean diameter 200 nm) loaded with $CuSO_4$ (0.2 mM) and Calcein (0.2 mM) were suspended in an external solution containing Gly (30 mM) and $CuSO_4$ (0.2 mM). Both the internal and external solutions contained Na_2SO_4 (100 mM) and HEPES (20 mM) buffered at pH 7.4. At time 0, DMSO solutions of transporters or DMSO was added, and the fluorescence intensity (λ_{ex} = 495 nm, λ_{em} = 515 nm) was recorded. The fluorescence intensity was normalized to a fractional fluorescence intensity by saturation using a mixture of **T1** (1 mol%) and **T3** (50 mol%). (b) Hill plot for Gly transport facilitated by **T2**. Transporter loadings are shown as transporter to lipid molar ratios. Error bars represent SD from two or three repeats.

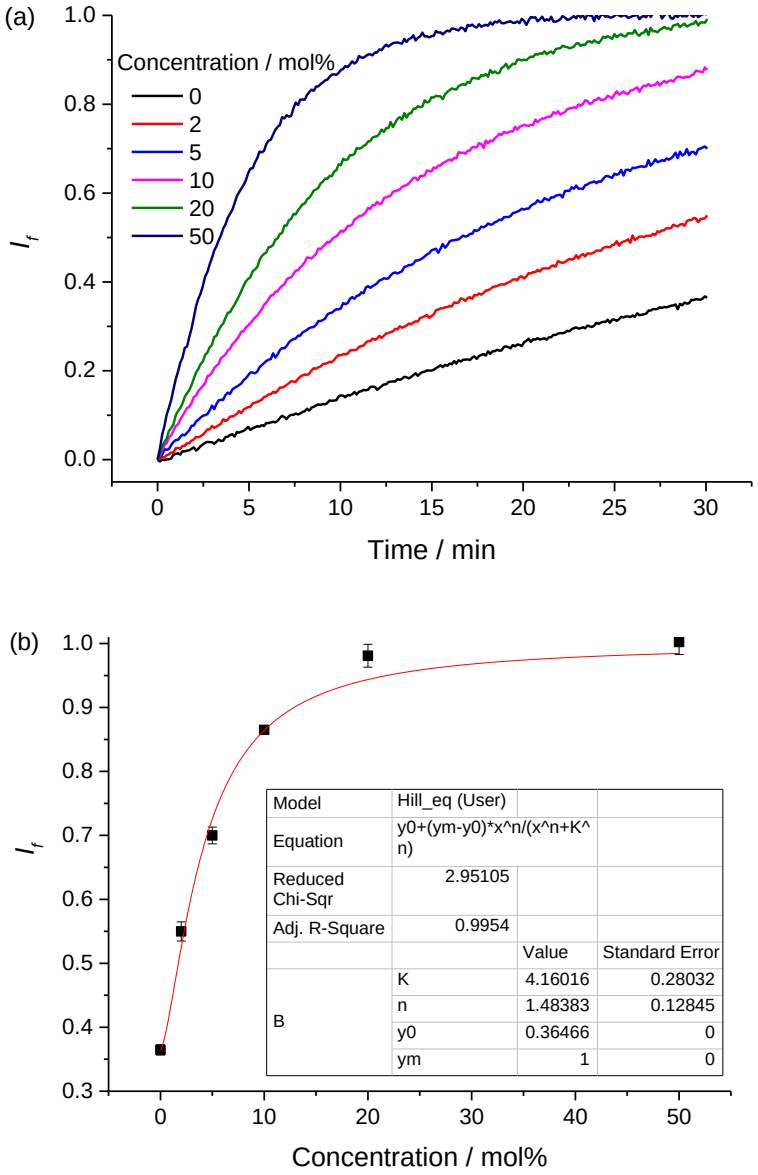

Figure 7.71 (a) Gly influx (measured by the Cu^{2+}-Calcein assay) facilitated by **T3** in the presence of **T1** (1 mol%). POPC LUVs (mean diameter 200 nm) loaded with $CuSO_4$ (0.2 mM) and Calcein (0.2 mM) were suspended in an external solution containing Gly (30 mM) and $CuSO_4$ (0.2 mM). Both the internal and external solutions contained Na_2SO_4 (100 mM) and HEPES (20 mM) buffered at pH 7.4. At time 0, DMSO solutions of transporters or DMSO was added, and the fluorescence intensity (λ_{ex} = 495 nm, λ_{em} = 515 nm) was recorded. The fluorescence intensity was normalized to a fractional fluorescence intensity by saturation using a mixture of **T1** (1 mol%) and **T3** (50 mol%). (b) Hill plot for Gly transport facilitated by **T3** in the presence of **T1** (1 mol%). Transporter loadings are shown as transporter to lipid molar ratios. Error bars represent SD from two or three repeats.

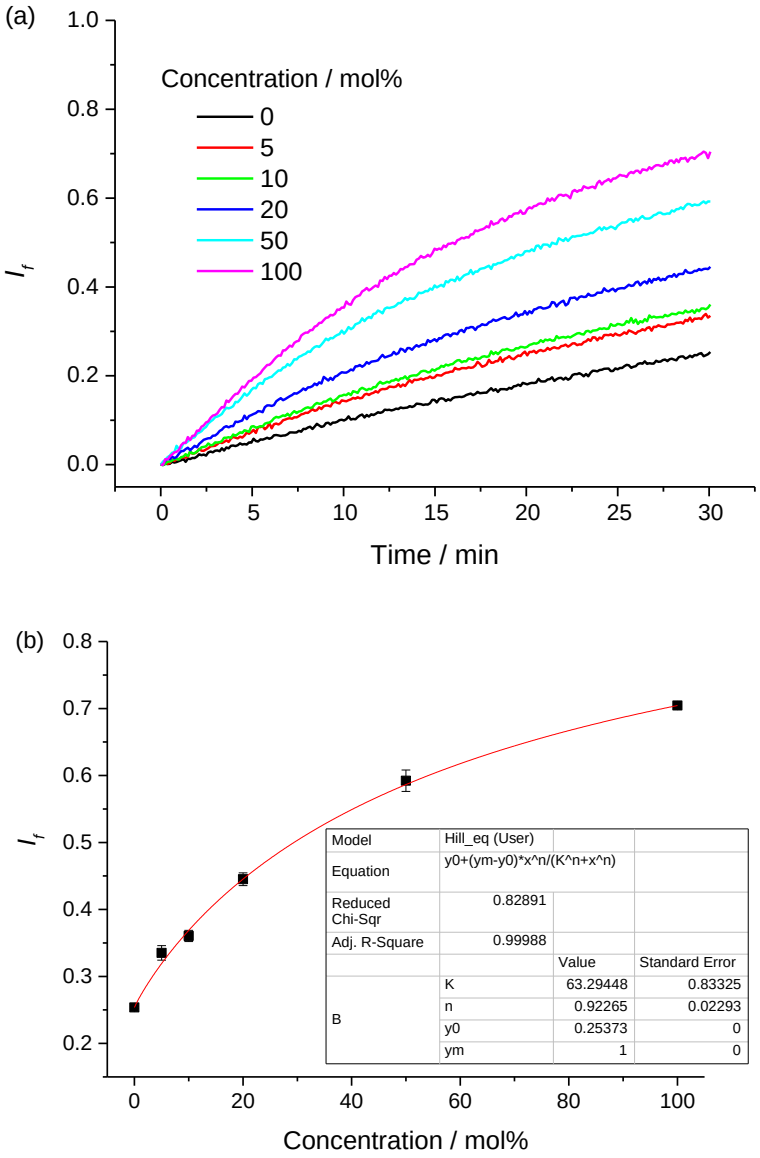

Figure 7.72 (a) Gly influx (measured by the Cu^{2+}-Calcein assay) facilitated by **T3**. POPC LUVs (mean diameter 200 nm) loaded with $CuSO_4$ (0.2 mM) and Calcein (0.2 mM) were suspended in an external solution containing Gly (30 mM) and $CuSO_4$ (0.2 mM). Both the internal and external solutions contained Na_2SO_4 (100 mM) and HEPES (20 mM) buffered at pH 7.4. At time 0, DMSO solutions of transporters or DMSO was added, and the fluorescence intensity (λ_{ex} = 495 nm, λ_{em} = 515 nm) was recorded. The fluorescence intensity was normalized to a fractional fluorescence intensity by saturation using a mixture of **T1** (1 mol%) and **T3** (50 mol%). (b) Hill plot for Gly transport facilitated by **T3**. Transporter loadings are shown as transporter to lipid molar ratios. Error bars represent SD from two or three repeats.

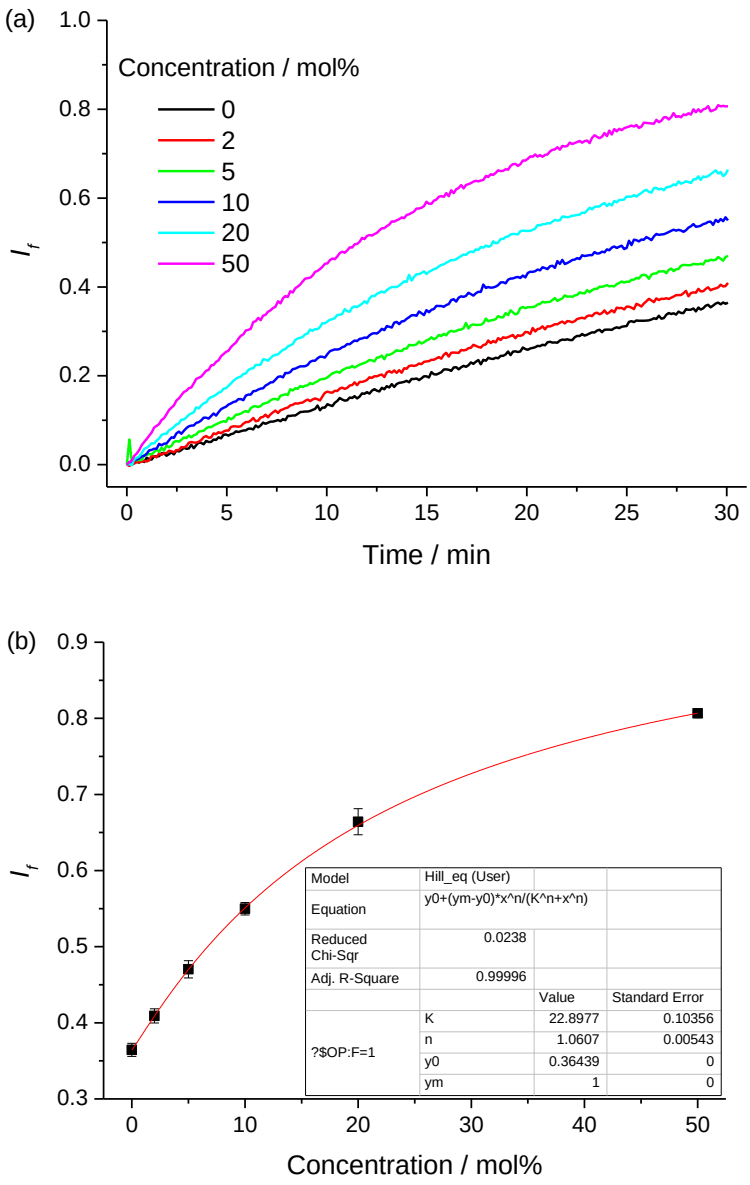

Figure 7.73 (a) Gly influx (measured by the Cu^{2+}-Calcein assay) facilitated by **T10** in the presence of **T1** (1 mol%). POPC LUVs (mean diameter 200 nm) loaded with $CuSO_4$ (0.2 mM) and Calcein (0.2 mM) were suspended in an external solution containing Gly (30 mM) and $CuSO_4$ (0.2 mM). Both the internal and external solutions contained Na_2SO_4 (100 mM) and HEPES (20 mM) buffered at pH 7.4. At time 0, DMSO solutions of transporters or DMSO was added, and the fluorescence intensity (λ_{ex} = 495 nm, λ_{em} = 515 nm) was recorded. The fluorescence intensity was normalized to a fractional fluorescence intensity by saturation using a mixture of **T1** (1 mol%) and **T3** (50 mol%). (b) Hill plot for Gly transport facilitated by **T10** in the presence of **T1** (1 mol%). Transporter loadings are shown as transporter to lipid molar ratios. Error bars represent SD from two or three repeats.

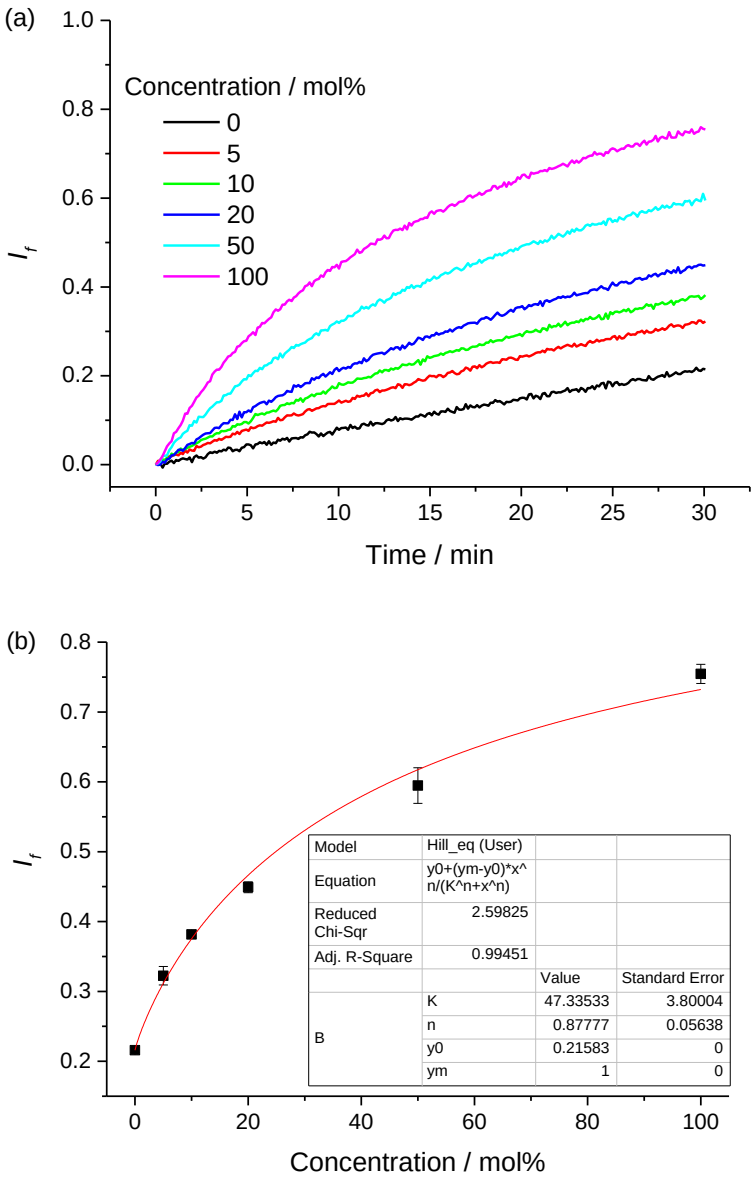

Figure 7.74 (a) Gly influx (measured by the Cu^{2+}-Calcein assay) facilitated by **T10**. POPC LUVs (mean diameter 200 nm) loaded with $CuSO_4$ (0.2 mM) and Calcein (0.2 mM) were suspended in an external solution containing Gly (30 mM) and $CuSO_4$ (0.2 mM). Both the internal and external solutions contained Na_2SO_4 (100 mM) and HEPES (20 mM) buffered at pH 7.4. At time 0, DMSO solutions of transporters or DMSO was added, and the fluorescence intensity (λ_{ex} = 495 nm, λ_{em} = 515 nm) was recorded. The fluorescence intensity was normalized to a fractional fluorescence intensity by saturation using a mixture of **T1** (1 mol%) and **T3** (50 mol%). (b) Hill plot for Gly transport facilitated by **T10**. Transporter loadings are shown as transporter to lipid molar ratios. Error bars represent SD from two or three repeats.

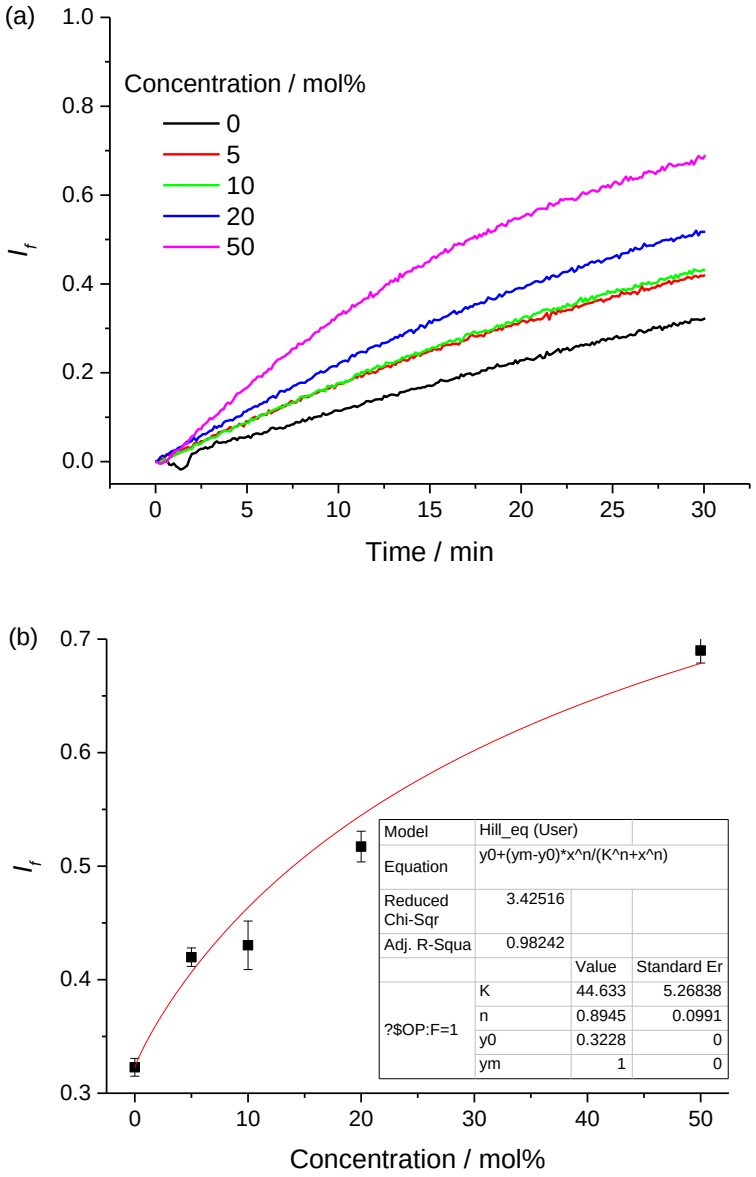

Figure 7.75 (a) Gly influx (measured by the Cu^{2+}-Calcein assay) facilitated by **T11** in the presence of **T1** (1 mol%). POPC LUVs (mean diameter 200 nm) loaded with $CuSO_4$ (0.2 mM) and Calcein (0.2 mM) were suspended in an external solution containing Gly (30 mM) and $CuSO_4$ (0.2 mM). Both the internal and external solutions contained Na_2SO_4 (100 mM) and HEPES (20 mM) buffered at pH 7.4. At time 0, DMSO solutions of transporters or DMSO was added, and the fluorescence intensity (λ_{ex} = 495 nm, λ_{em} = 515 nm) was recorded. The fluorescence intensity was normalized to a fractional fluorescence intensity by saturation using a mixture of **T1** (1 mol%) and **T3** (50 mol%). (b) Hill plot for Gly transport facilitated by **T11** in the presence of **T1** (1 mol%). Transporter loadings are shown as transporter to lipid molar ratios. Error bars represent SD from two or three repeats.

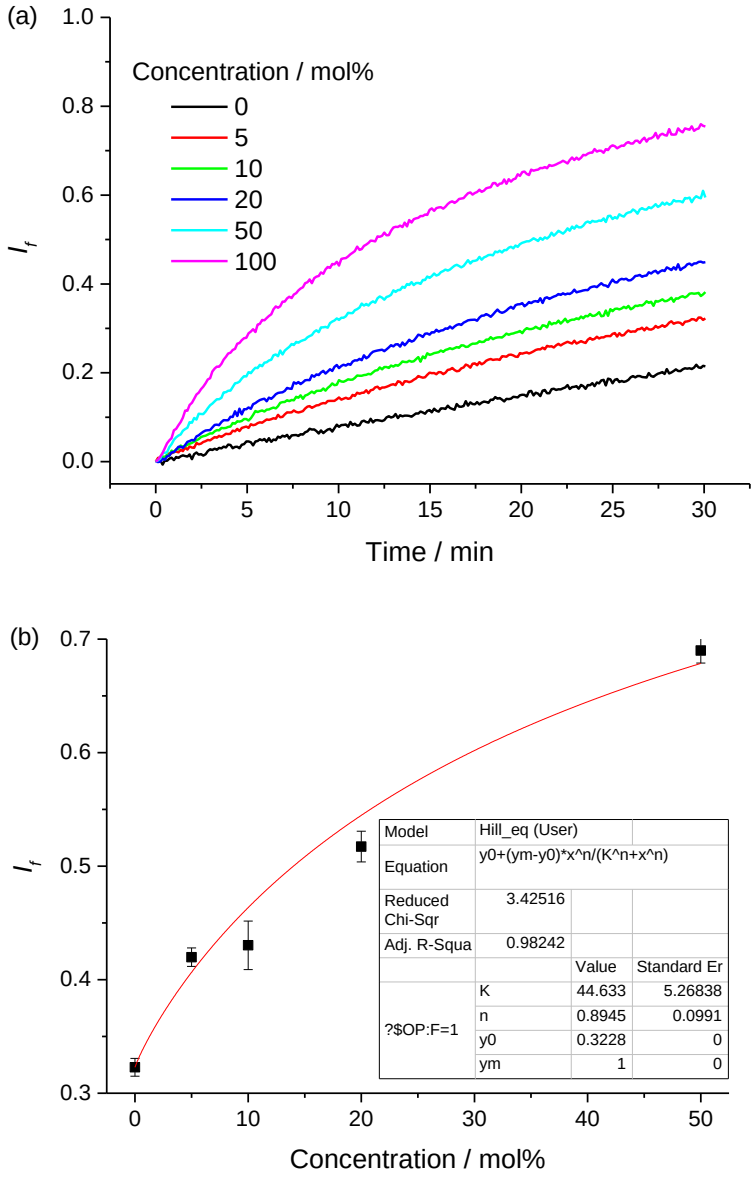

Figure 7.76 (a) Gly influx (measured by the Cu^{2+}-Calcein assay) facilitated by **T11**. POPC LUVs (mean diameter 200 nm) loaded with $CuSO_4$ (0.2 mM) and Calcein (0.2 mM) were suspended in an external solution containing Gly (30 mM) and $CuSO_4$ (0.2 mM). Both the internal and external solutions contained Na_2SO_4 (100 mM) and HEPES (20 mM) buffered at pH 7.4. At time 0, DMSO solutions of transporters or DMSO was added, and the fluorescence intensity (λ_{ex} = 495 nm, λ_{em} = 515 nm) was recorded. The fluorescence intensity was normalized to a fractional fluorescence intensity by saturation using a mixture of **T1** (1 mol%) and **T3** (50 mol%). (b) Hill plot for Gly transport facilitated by **T11**. Transporter loadings are shown as transporter to lipid molar ratios. Error bars represent SD from two or three repeats.

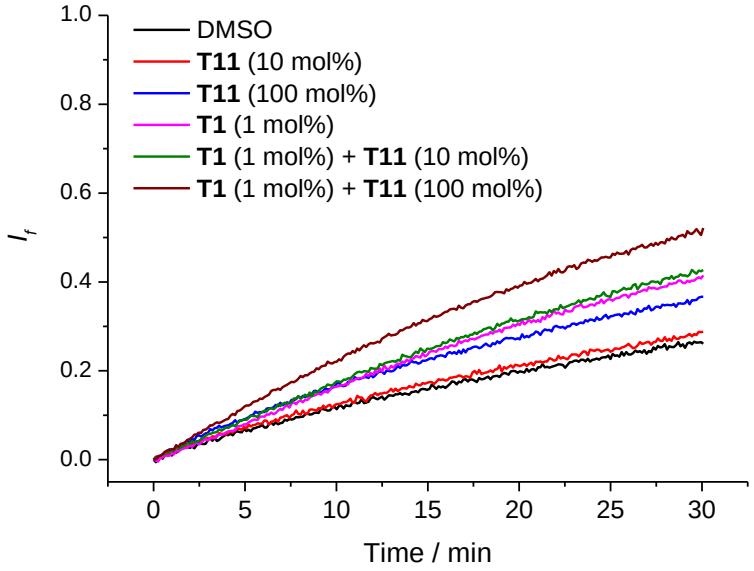

Figure 7.77 Gly influx (measured by the Cu^{2+}-Calcein assay) facilitated by **T12** in the absence and presence of **T1** (1 mol%). POPC LUVs (mean diameter 200 nm) loaded with $CuSO_4$ (0.2 mM) and Calcein (0.2 mM) were suspended in an external solution containing Gly (30 mM) and $CuSO_4$ (0.2 mM). Both the internal and external solutions contained Na_2SO_4 (100 mM) and HEPES (20 mM) buffered at pH 7.4. At time 0, DMSO solutions of transporters or DMSO was added, and the fluorescence intensity (λ_{ex} = 495 nm, λ_{em} = 515 nm) was recorded. The fluorescence intensity was normalized to a fractional fluorescence intensity by saturation using a mixture of **T1** (1 mol%) and **T3** (50 mol%). Transporter loadings are shown as transporter to lipid molar ratios. Hill analysis was not performed due to the low activity.

7.4.4.8 Effect of external Cu^{2+} on measurement of facilitated transport

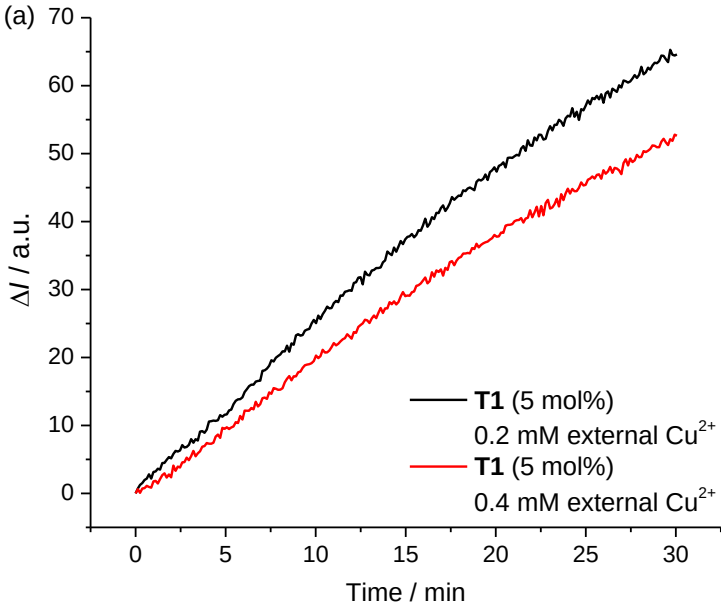

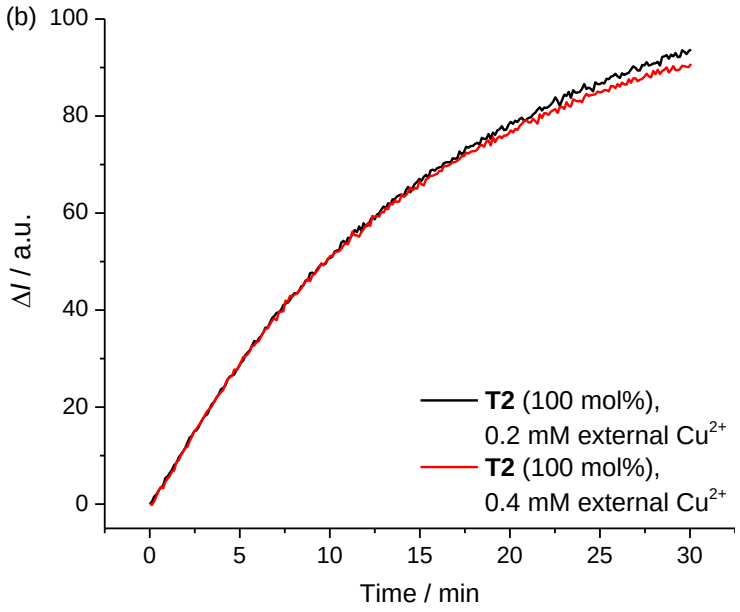
(b)
ΔI / a.u.
Time / min
T2 (100 mol%), 0.2 mM external Cu2+
T2 (100 mol%), 0.4 mM external Cu2+

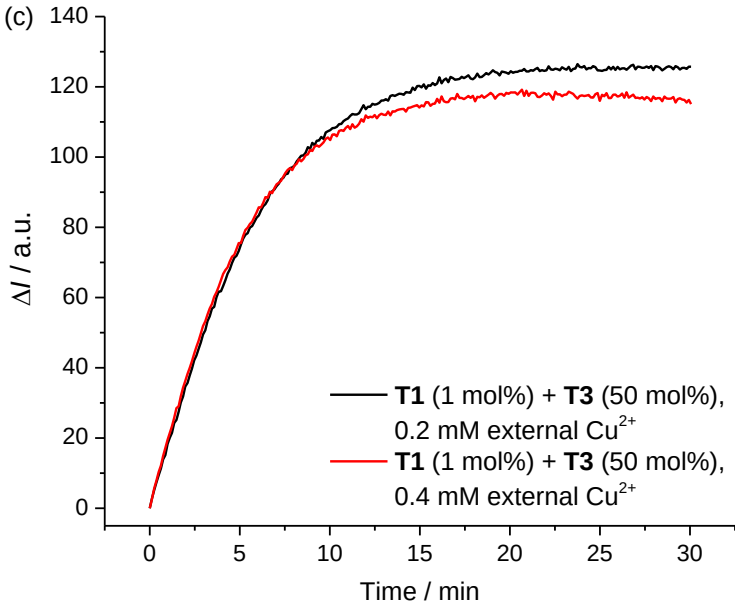
(c)
ΔI / a.u.
Time / min
T1 (1 mol%) + T3 (50 mol%), 0.2 mM external Cu2+
T1 (1 mol%) + T3 (50 mol%), 0.4 mM external Cu2+

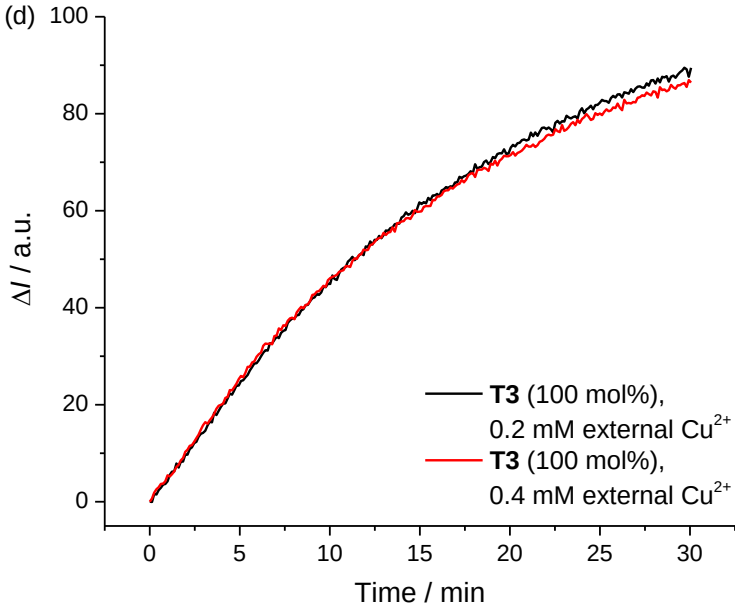
(d)
ΔI / a.u.
Time / min
T3 (100 mol%), 0.2 mM external Cu2+
T3 (100 mol%), 0.4 mM external Cu2+

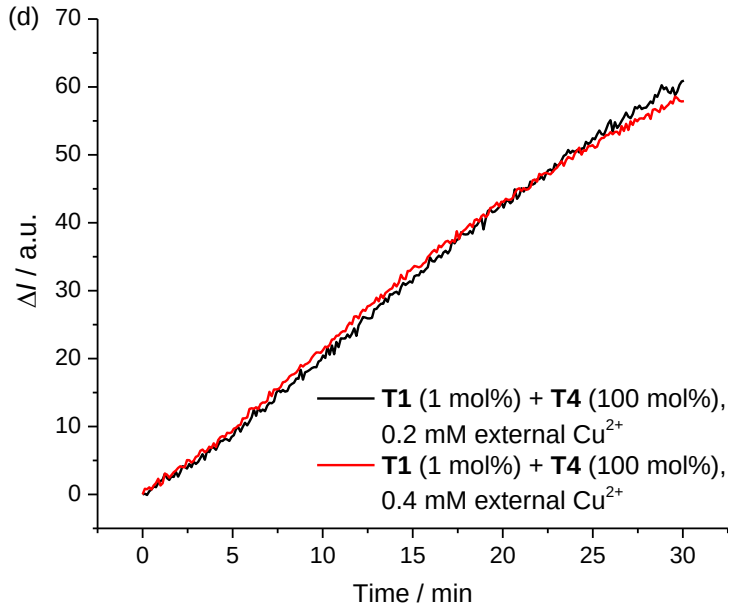
(d)
ΔI / a.u.
Time / min
T1 (1 mol%) + T4 (100 mol%), 0.2 mM external Cu2+
T1 (1 mol%) + T4 (100 mol%), 0.4 mM external Cu2+

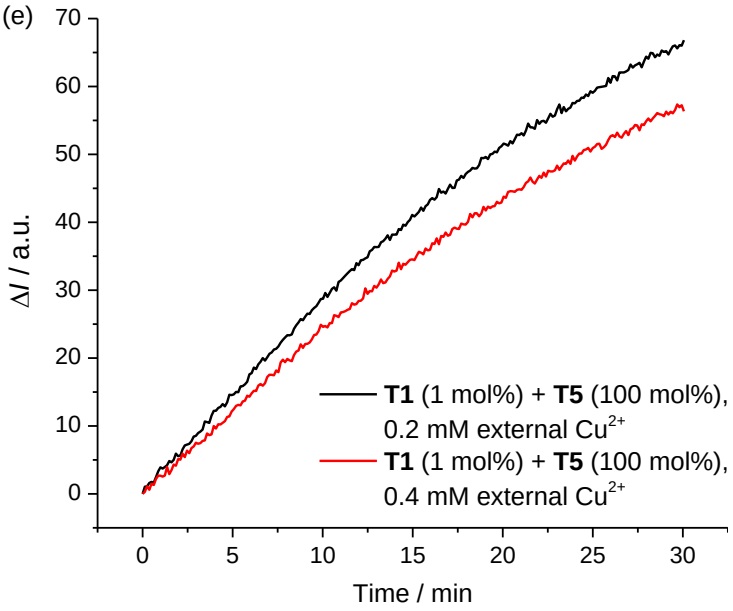
(e)
ΔI / a.u.
Time / min
T1 (1 mol%) + T5 (100 mol%), 0.2 mM external Cu2+
T1 (1 mol%) + T5 (100 mol%), 0.4 mM external Cu2+

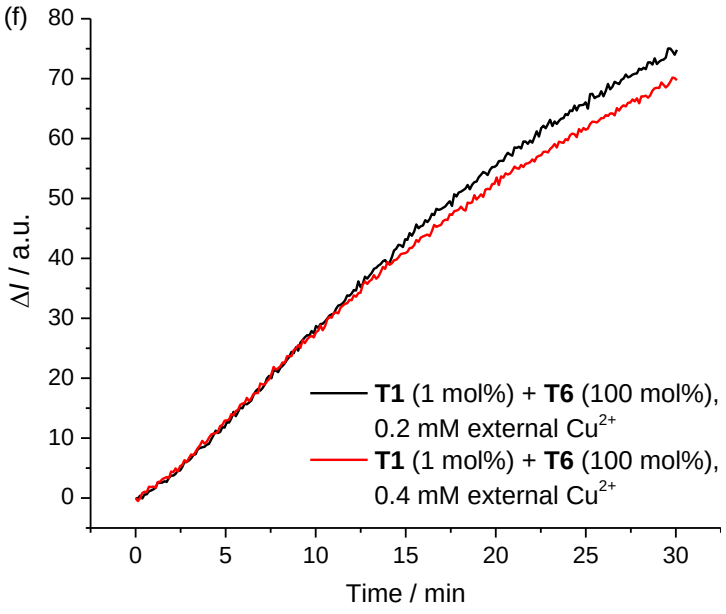
(f)
ΔI / a.u.
Time / min
T1 (1 mol%) + T6 (100 mol%), 0.2 mM external Cu2+
T1 (1 mol%) + T6 (100 mol%), 0.4 mM external Cu2+

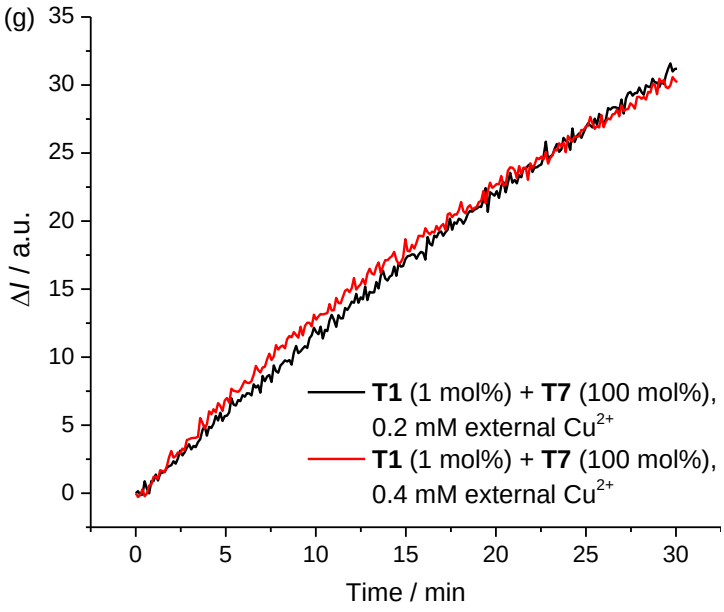
(g)
ΔI / a.u.
Time / min
T1 (1 mol%) + T7 (100 mol%), 0.2 mM external Cu2+
T1 (1 mol%) + T7 (100 mol%), 0.4 mM external Cu2+

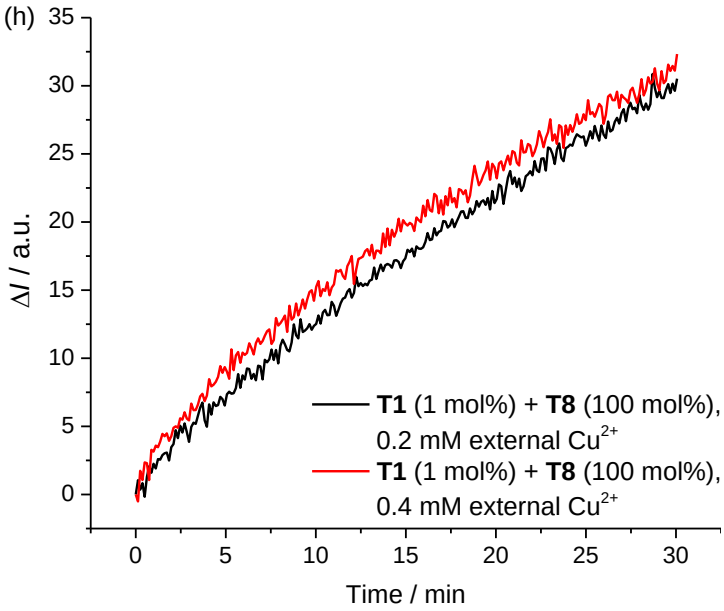
(h)
ΔI / a.u.
Time / min
T1 (1 mol%) + T8 (100 mol%), 0.2 mM external Cu2+
T1 (1 mol%) + T8 (100 mol%), 0.4 mM external Cu2+

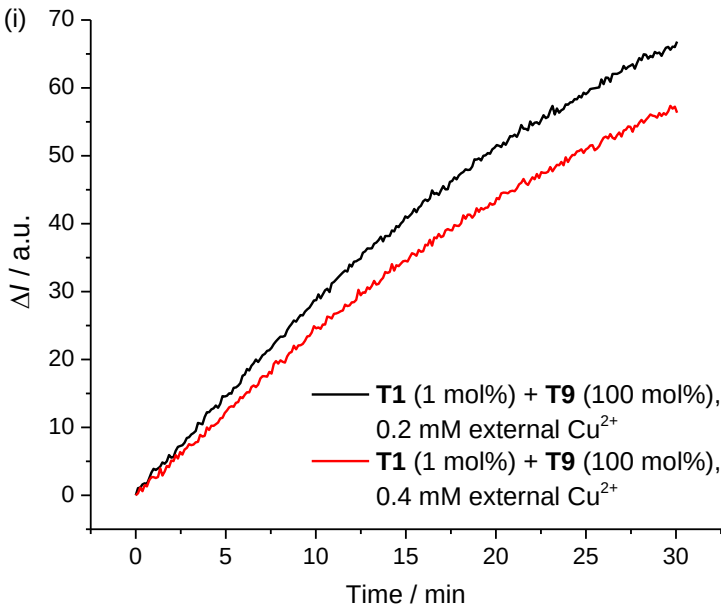
(i)
ΔI / a.u.
Time / min
T1 (1 mol%) + T9 (100 mol%), 0.2 mM external Cu2+
T1 (1 mol%) + T9 (100 mol%), 0.4 mM external Cu2+

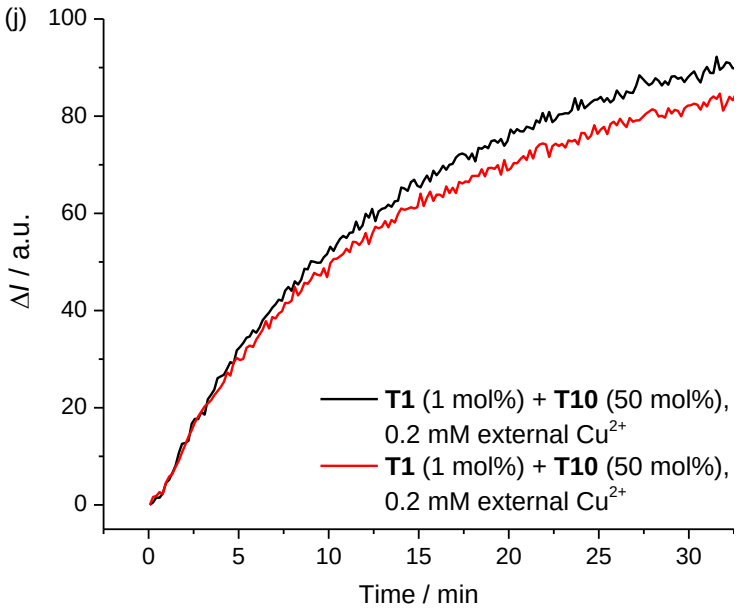
(j)
ΔI / a.u.
Time / min
T1 (1 mol%) + T10 (50 mol%), 0.2 mM external Cu2+
T1 (1 mol%) + T10 (50 mol%), 0.2 mM external Cu2+

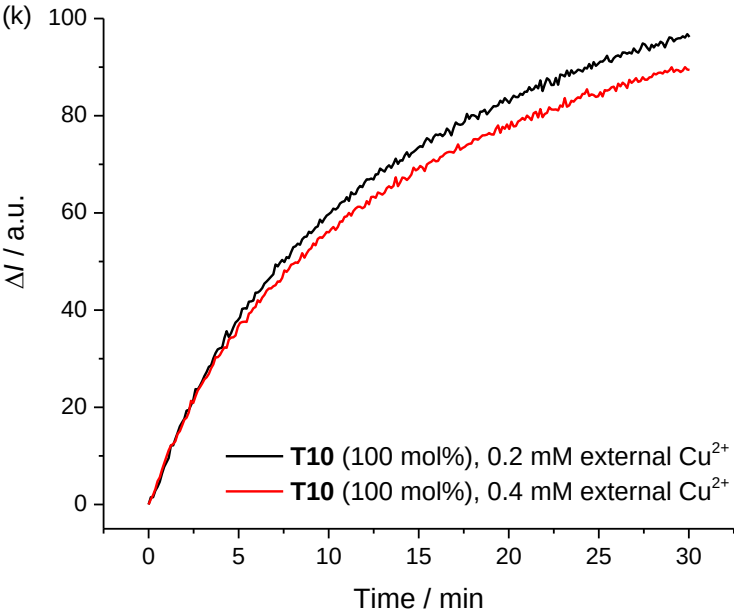
(k)
ΔI / a.u.
Time / min
T10 (100 mol%), 0.2 mM external Cu2+
T10 (100 mol%), 0.4 mM external Cu2+

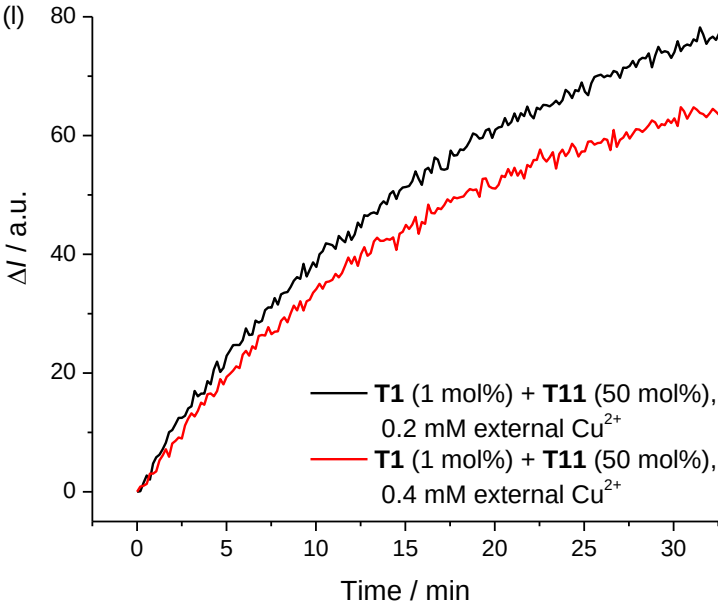
(l)
ΔI / a.u.
Time / min
T1 (1 mol%) + T11 (50 mol%), 0.2 mM external Cu2+
T1 (1 mol%) + T11 (50 mol%), 0.4 mM external Cu2+

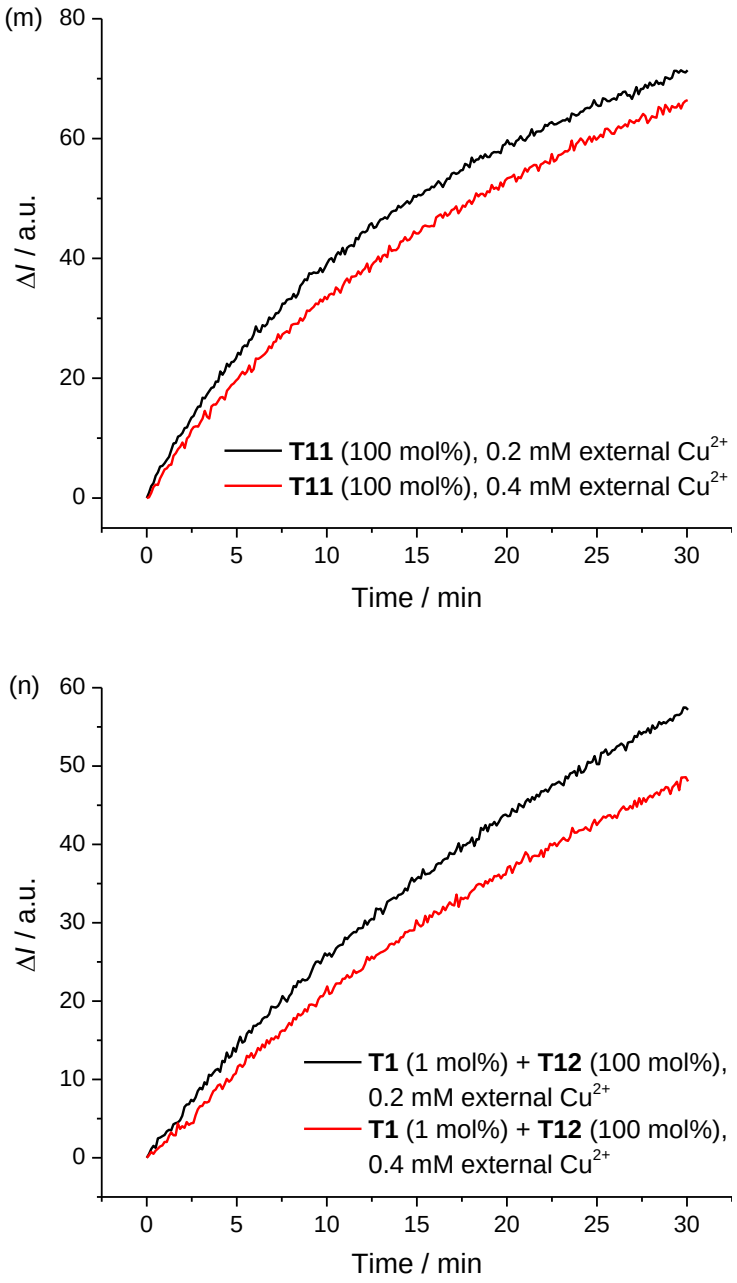

Figure 7.78 Effect of concentration of external Cu^{2+} on fluorescence intensity change (λ_{ex} = 495 nm, λ_{em} = 515 nm) with time. POPC LUVs (mean diameter 200 nm) loaded with $CuSO_4$ (0.2 mM) and Calcein (0.2 mM) were suspended in an external solution containing Gly (30 mM) and $CuSO_4$ (0.2 mM or 0.4 mM). Both the internal and external solutions contained Na_2SO_4 (100 mM) and HEPES (20 mM) buffered at pH 7.4. At time 0, DMSO solutions of various compounds were added. Transporter loadings are shown as transporter to lipid molar ratios.

7.4.4.9 Cholesterol test

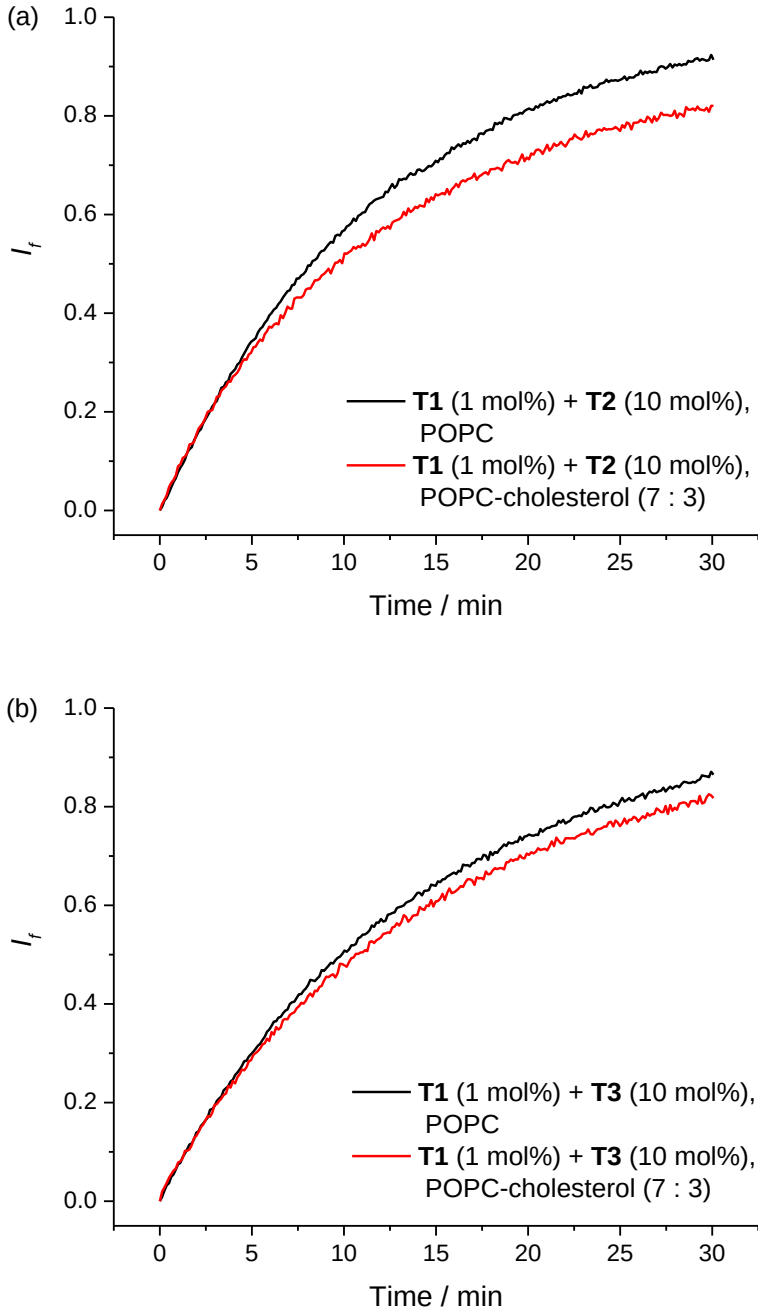

Figure 7.79 Comparison of Gly influx (measured by the Cu^{2+}-Calcein assay) into POPC and POPC-cholesterol (7 : 3, molar ratio) LUVs (mean diameter 200 nm). The vesicles were loaded with $CuSO_4$ (0.2 mM) and Calcein (0.2 mM) and suspended in an external solution containing Gly (30 mM) and $CuSO_4$ (0.2 mM). Both the internal and external solutions contained Na_2SO_4 (100 mM) and HEPES (20 mM) buffered at pH 7.4. At time 0, DMSO solutions of transporters were added, and the fluorescence intensity (λ_{ex} = 495 nm, λ_{em} = 515 nm) was recorded. The fluorescence intensity was normalized to a fractional fluorescence intensity by saturation using a mixture of **T1** (1 mol%) and **T3** (50 mol%). Transporter loadings are shown as transporter to lipid molar ratios.

7.4.4.10 DPPC test

DPPG LUVs (mean diameter 200 nm) were prepared as follows. A chloroform solution of lipids was evaporated in a round-bottle flask and the lipid film formed was dried under vacuum for at least 6 h. The lipid film was hydrated by vortexing with a buffered aqueous solution containing Cu^{2+} and Calcein (pH 7.4, 20 mM HEPES, 100 mM Na_2SO_4, 0.2 mM $CuSO_4$, 0.2 mM Calcein) at 50°C. The lipid solution was subjected to 25 freeze/thaw cycles (50°C water bath was used) and then extruded 25 times through a 200 nm polycarbonate membrane at 50°C. The unentrapped Cu^{2+} and Calcein were removed by size exclusion chromatography on a Sephadex G-25 column using a buffer solution as the eluent (pH 7.4, 20 mM HEPES, 100 mM Na_2SO_4).

For each run, the LUV stock solution prepared as stated above was added to an external solution containing Cu^{2+} and Gly (pH 7.4, 20 mM HEPES, 100 mM Na_2SO_4, 0.2 mM $CuSO_4$, 30 mM Gly) to a final lipid concentration of 1 mM and a final volume of 2 mL. The lipid solution was stirred and thermostated in a polystyrene cuvette at 37 °C or 45 °C. DMSO solutions of the transporters (DMSO volume ≤ 20 μL, in the cases of mixed transporters, the DMSO solutions of different transporters were added separately instead of being pre-mixed in DMSO) or DMSO (20 μL) was added to the lipid solution to start the measurement of Gly transport, and the fluorescence emission (λ_{ex} = 495 nm, λ_{em} = 515 nm) was recorded over 30 min. Each experiment was run in triplicate and the data were averaged over three runs. A maximum change of fluorescence intensity ($\Delta I_{max} = I_{max} - I_0$, where I_{max} is the maximum fluorescence intensity reached and I_0 is the fluorescence intensity before the addition of transporters) was obtained using a mixture of **T1** (1 mol%) and **T2** (10 mol%) for calibration. The fractional fluorescence intensity, which is an approximate of the percentage of Gly influx compared to the maximum transport, is calculated using the following equation:

$$I_f = \frac{I_t - I_0}{\Delta I_{\max}}$$

where I_t is the fluorescence intensity at time t, and I_0 is the fluorescence intensity at time 0.

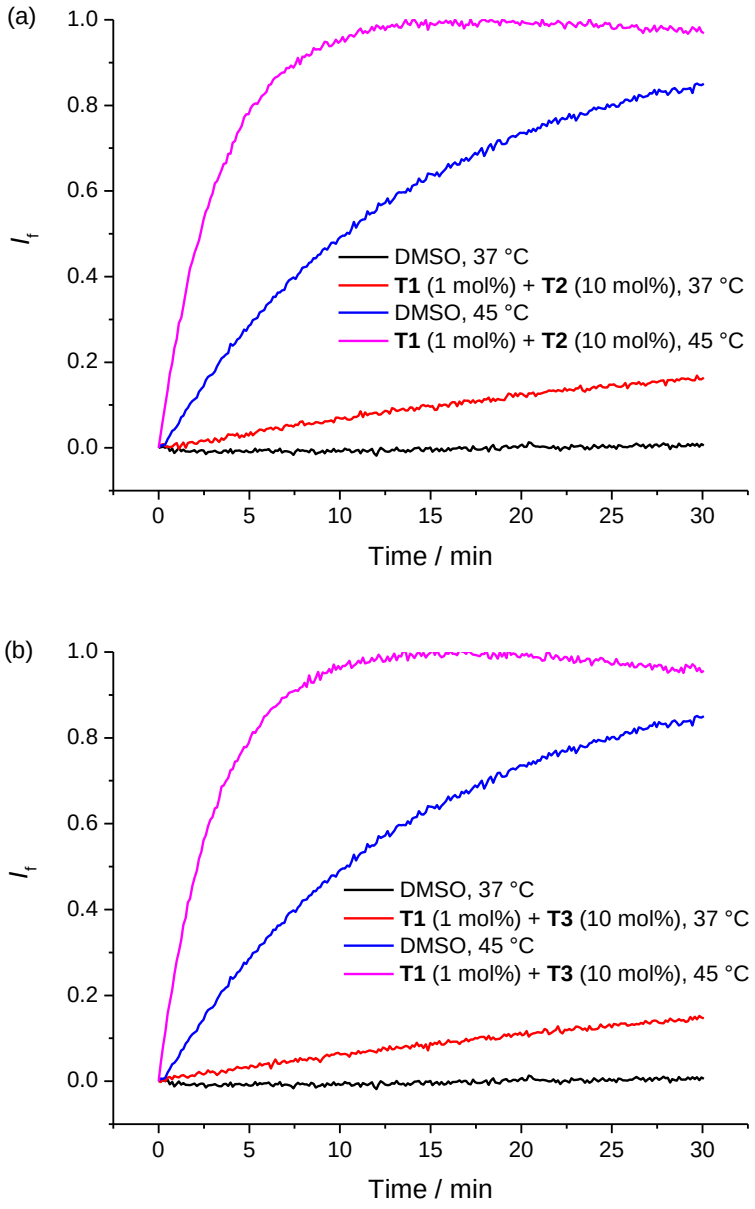

Figure 7.80 Comparison of Gly influx (measured by the Cu^{2+}-Calcein assay) into DPPC LUVs at 37 ℃ and 45 ℃. The LUVs (mean diameter 200 nm) were loaded with $CuSO_4$ (0.2 mM) and Calcein (0.2 mM) and suspended in an external solution containing Gly (30 mM) and $CuSO_4$ (0.2 mM). Both the internal and external solutions contained Na_2SO_4 (100 mM) and HEPES (20 mM) buffered at pH 7.4. At time 0, DMSO solutions of transporters or DMSO was added, and the fluorescence intensity (λ_{ex} = 495 nm, λ_{em} = 515 nm) was recorded. The fluorescence intensity was normalized to a fractional fluorescence intensity by saturation using a mixture of **T1** (1 mol%) and **T2** (10 mol%). Transporter loadings are shown as transporter to lipid molar ratios. Refer to Section 7.4.6 for an explanation for the slight decrease of fluorescence observed in magenta lines.

7.4.4.11 POPG test

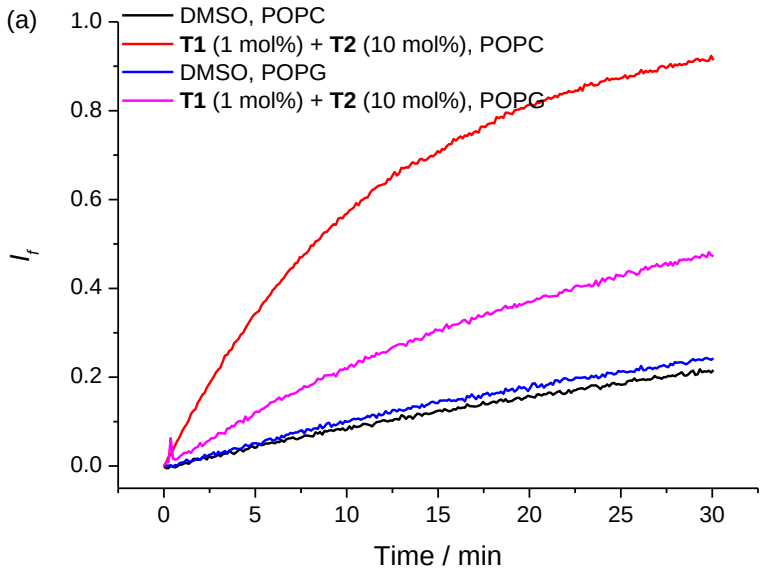

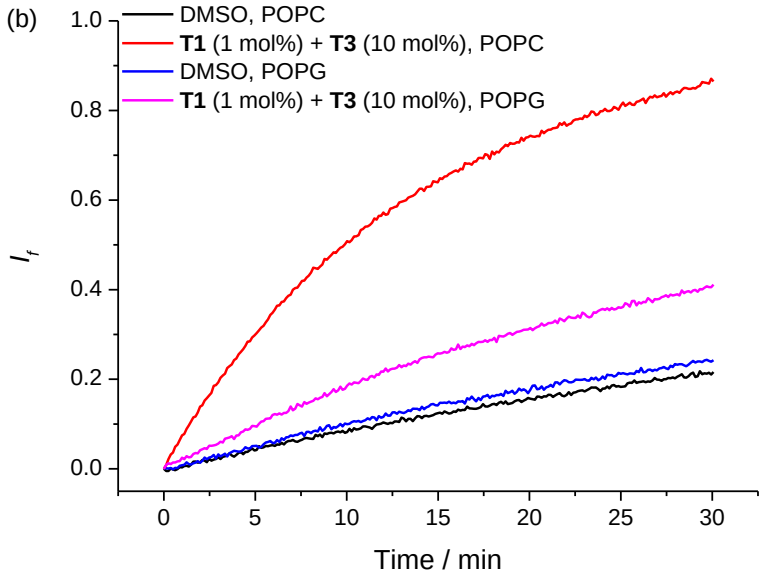

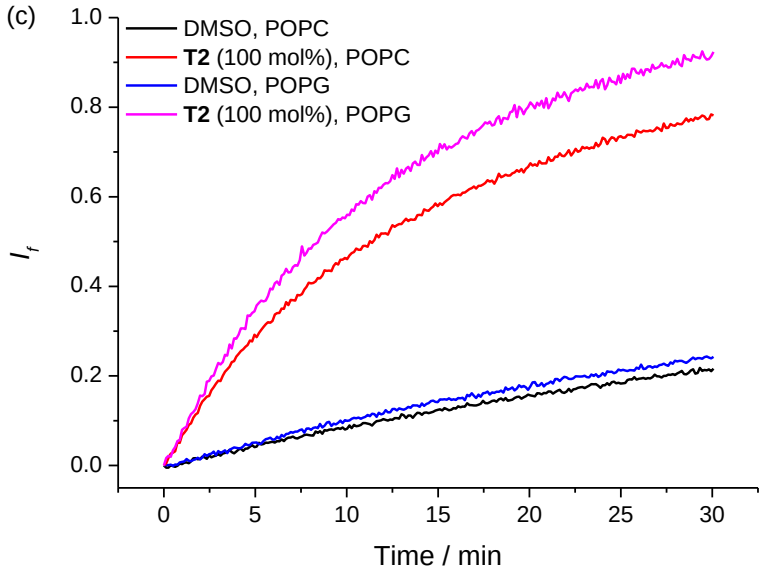

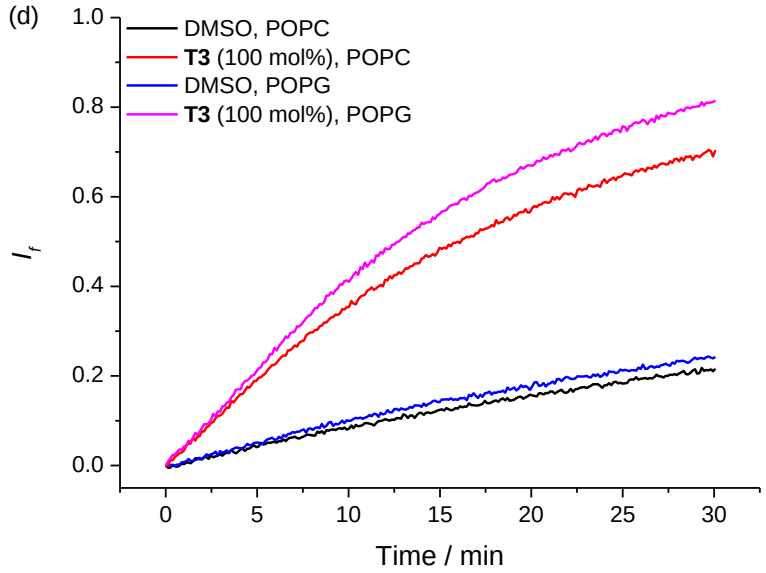

Figure 7.81 Comparison of Gly influx (measured by the Cu^{2+}-Calcein assay) into POPC and POPG LUVs (mean diameter 200 nm). The vesicles were loaded with $CuSO_4$ (0.2 mM) and Calcein (0.2 mM) and suspended in an external solution containing Gly (30 mM) and $CuSO_4$ (0.2 mM). Both the internal and external solutions contained Na_2SO_4 (100 mM) and HEPES (20 mM) buffered at pH 7.4. At time 0, DMSO solutions of transporters or DMSO was added, and the fluorescence intensity (λ_{ex} = 495 nm, λ_{em} = 515 nm) was recorded. The fluorescence intensity was normalized to a fractional fluorescence intensity by saturation using a mixture of **T1** (1 mol%) and **T3** (50 mol%). Transporter loadings are shown as transporter to lipid molar ratios.

7.4.5 Cu^{2+}-Calcein assay for transport of other substrates

7.4.5.1 Method

Similar to the general procedure described in 7.4.4.1. Gly was replaced by the substrate studied (30 mM). For *N*,*N*-dimethylglycine (DMG) transport, because the later Cu^{2+} influx observed in some cases reduces the fluorescence intensity over time, the maximum fluorescence intensity over the course of each run was used for calibration to a fractional fluorescence intensity (I_f) for the same run. For the transport of other substrates, the maximum fluorescence intensity change for calibration (ΔI_{max}) was obtained using a mixture of **T1** (1 mol%) and **T3** (50 mol%).

7.4.5.2 Sarcosine transport

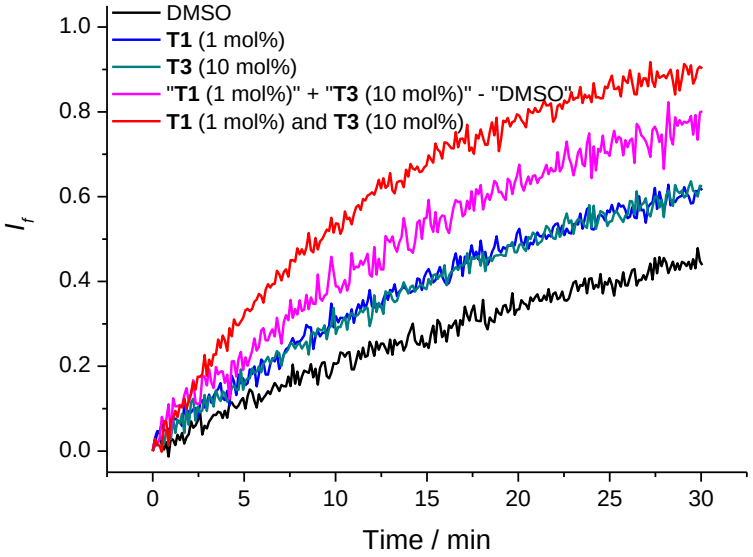

Figure 7.82 Sarcosine (Sar) transport kinetics measured by the Cu^{2+}-Calcein assay. POPC LUVs (mean diameter 200 nm) loaded with $CuSO_4$ (0.2 mM) and Calcein (0.2 mM) were suspended in an external solution containing Sar (30 mM) and $CuSO_4$ (0.2 mM). Both the internal and external solutions contained Na_2SO_4 (100 mM) and HEPES (20 mM) buffered at pH 7.4. At time 0, DMSO solutions of transporters or DMSO was added, and the fluorescence intensity (λ_{ex} = 495 nm, λ_{em} = 515 nm) was recorded. The fluorescence intensity was normalized by saturation using a mixture of **T1** (1 mol%) and **T3** (50 mol%). Transporter loadings are shown as transporter to lipid molar ratios.

7.4.5.3 Dimethylglycine transport

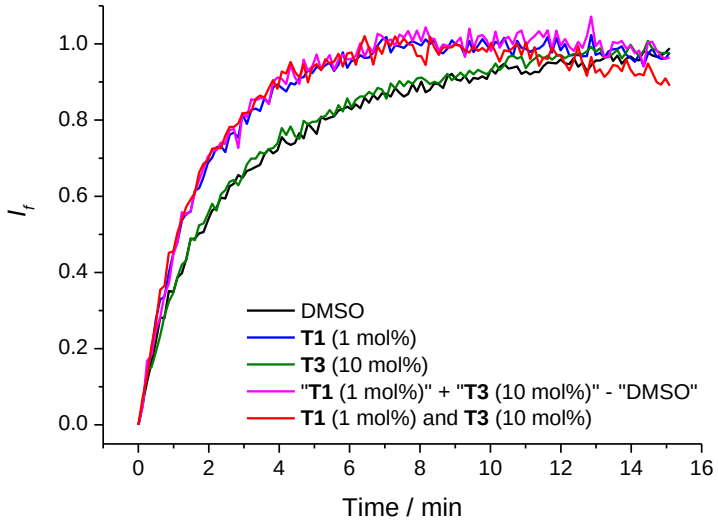

Figure 7.83 *N*,*N*-dimethylglycine (DMG) transport kinetics measured by the Cu^{2+}-Calcein assay. POPC LUVs (mean diameter 200 nm) loaded with $CuSO_4$ (0.2 mM) and Calcein (0.2 mM) were suspended in an external solution containing DMG (30 mM) and $CuSO_4$ (0.2 mM). Both the internal and external solutions contained Na_2SO_4 (100 mM) and HEPES (20 mM) buffered at pH 7.4. At time 0, DMSO solutions of transporters or DMSO was added, and the fluorescence intensity (λ_{ex} = 495 nm, λ_{em} = 515 nm) was recorded. The fluorescence intensity was normalized using the maximum fluorescence intensity over the course of each run. Transporter loadings are shown as transporter to lipid molar ratios.

7.4.5.4 Alanine transport

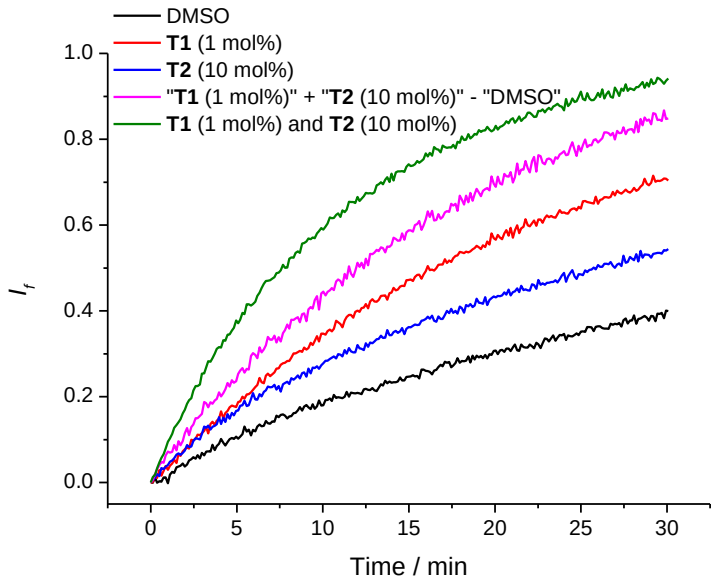

Figure 7.84 Alanine (Ala) transport kinetics measured by the Cu^{2+}-Calcein assay. POPC LUVs (mean diameter 200 nm) loaded with $CuSO_4$ (0.2 mM) and Calcein (0.2 mM) were suspended in an external solution containing Ala (30 mM) and $CuSO_4$ (0.2 mM). Both the internal and external solutions contained Na_2SO_4 (100 mM) and HEPES (20 mM) buffered at pH 7.4. At time 0, DMSO solutions of transporters or DMSO was added, and the fluorescence intensity (λ_{ex} = 495 nm, λ_{em} = 515 nm) was recorded. The fluorescence intensity was normalized to by saturation using a mixture of **T1** (1 mol%) and **T3** (50 mol%). Transporter loadings are shown as transporter to lipid molar ratios.

7.4.5.5 Serine transport

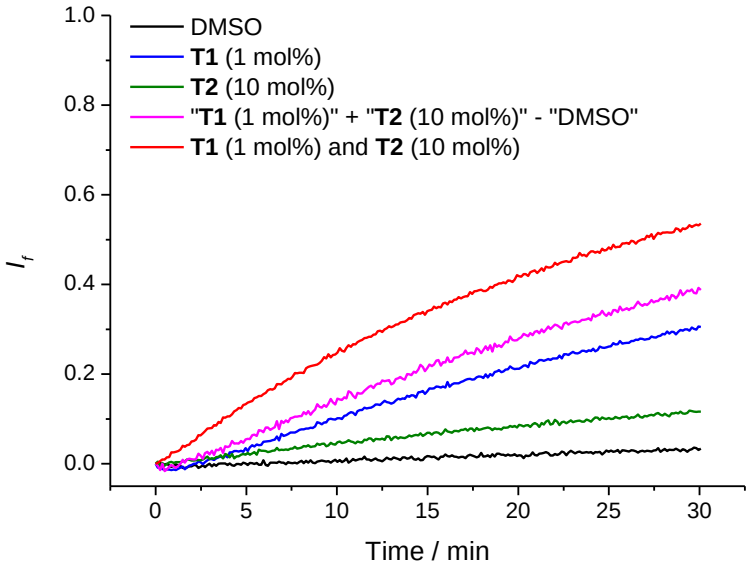

Figure 7.85 Serine (Ser) transport kinetics measured by the Cu^{2+}-Calcein assay. POPC LUVs (mean diameter 200 nm) loaded with $CuSO_4$ (0.2 mM) and Calcein (0.2 mM) were suspended in an external solution containing Ser (30 mM) and $CuSO_4$ (0.2 mM). Both the internal and external solutions contained Na_2SO_4 (100 mM) and HEPES (20 mM) buffered at pH 7.4. At time 0, DMSO solutions of transporters or DMSO was added, and the fluorescence intensity (λ_{ex} = 495 nm, λ_{em} = 515 nm) was recorded. The fluorescence intensity was normalized to by saturation using a mixture of **T1** (1 mol%) and **T3** (50 mol%). Transporter loadings are shown as transporter to lipid molar ratios.

7.4.6 Additional comments on the Cu^{2+}-Calcein assay

As discussed in Chapter 5, the feasibility of this assay depends on the rate of Cu^{2+} diffusion, which depends on the concentration difference of free Cu^{2+} (unbound to Calcein or amino acid) on opposite sides of the lipid bilayer (denoted here by $\Delta[Cu^{2+}]$) and whether a compound is present that facilitates Cu^{2+} transport. Little to no Cu^{2+} transport was observed using the described experimental conditions:

Before Gly influx: Inside: 0.2 mM Cu^{2+}, 0.2 mM Calcein; Outside: 0.2 mM Cu^{2+}, 30 mM Gly.

After completion of Gly influx: Inside: 0.2 mM Cu^{2+}, 0.2 mM Calcein, 30 mM Gly; Outside: 0.2 mM Cu^{2+}, 30 mM Gly).

Before significant Gly influx occurs, the presence of Calcein in the internal solution and Gly in the external solution balances $\Delta[Cu^{2+}]$ to the extent that no Cu^{2+} flux is observable from the time-dependent Calcein fluorescence intensity (Figure 7.62). After completion of Gly influx, there is a larger difference in between the internal and external free Cu^{2+} concentration (*i.e.*, a higher $\Delta[Cu^{2+}]$, in this case inside < outside) since the internal solution and the external solution now differs by the presence of Calcein (0.2 mM) which has a high affinity for Cu^{2+}. Therefore influx of Cu^{2+} might possibly occur that would lead to decrease of Calcein fluorescence after completion of Gly influx. This has not been observed, however, under standard conditions (25 °C, with 30 mM Gly, with 0.2 mM Cu^{2+} both inside and outside). In a few cases, influx of Cu^{2+} was observed in the presence of **T1** that can slightly facilitate Cu^{2+} transport (see Figure 7.78a). These include: (i) Figure 5.8b and Figure 7.83, when DMG (30 mM) was used in place of Gly. DMG has a lower affinity for Cu^{2+} because of the larger steric hindrance. Therefore the $\Delta[Cu^{2+}]$ due to the presence of internal 0.2 mM Calcein after completion of DMG transport is higher compared to the case of Gly transport; (ii) Figure 7.80 magenta, at a higher temperature (45 °C).

7.4.7 HPTS assay for Oxalic Acid/Oxalate transport

POPC LUVs (mean diameter 200 nm) were prepared as follows. A chloroform solution of POPC was evaporated in a round-bottle flask and the lipid film formed was dried under vacuum for at least 6 h. The lipid film was hydrated by vortexing with an aqueous solution containing pH sensitive dye HPTS and sodium oxalate (pH 7.0, 10 mM HEPES, 100 mM sodium oxalate, 1 mM HPTS). The lipid solution was subjected to nine freeze/thaw cycles and then extruded 25 times through a 200 nm polycarbonate membrane. The unentrapped HPTS was removed by size exclusion chromatography on a Sephadex G-25 column using a buffered sodium oxalate solution (pH 7.0, 10 mM HEPES, 100 mM sodium oxalate) as the eluent.

For each run, the LUV stock solution prepared as stated above was added to an external solution (pH 7.0, 10 mM HEPES, 100 mM sodium oxalate) to a final lipid concentration of 1 mM and a final

volume of 2 mL. The lipid solutions were stirred and thermostated in polystyrene cuvettes at 25 °C. The fluorescence ratio of HPTS (λ_{ex} = 460 nm, λ_{em} = 510 nm, base form vs λ_{ex} = 403 nm, λ_{em} = 510 nm, acid form) was recorded. DMSO solutions of the transporters (20 µL, in the cases of mixed transporters, the DMSO solutions of different transporters were added separately) or DMSO (20 µL) was added to the lipid solution. After the baseline stabilized, a pulse of NaOH (20 µL, 0.5 M in H_2O) was added to the lipid solution at time 0 to generate a transmembrane pH gradient. At 5 min, a detergent (20 µl of 0.232 mM octaethylene glycol monododecyl ether in 7 : 1 (v : v) H_2O-DMSO) was added to lyse the vesicles and destroy the pH gradient. Each experiment was run in triplicate and the data were averaged over three runs. The fractional fluorescence intensity is calculated using the following equation[182]:

$$I_f = \frac{R_t - R_0}{R_d - R_0}$$

where R_t is the fluorescence ratio at time t, R_0 is the fluorescence ratio at time 0, and R_d is the fluorescence ratio after detergent addition.

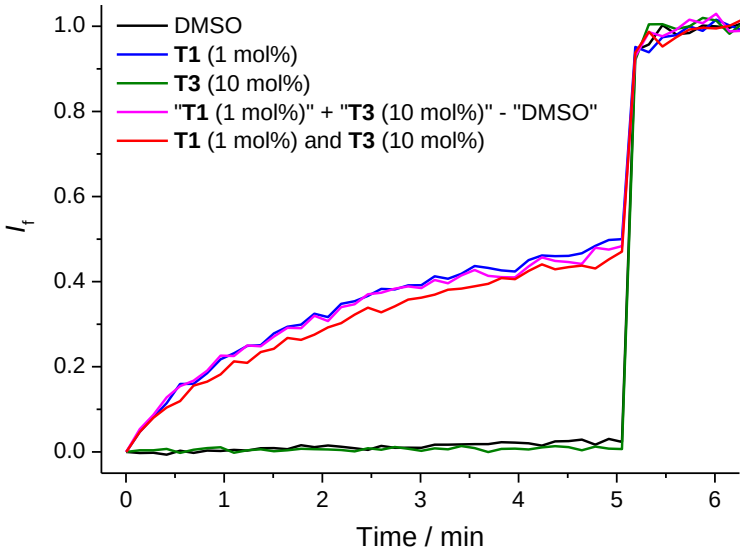

Figure 7.86 Oxalic acid/oxalate transport kinetics studied by a HPTS assay. POPC LUVs (mean diameter 200 nm) were loaded with HPTS (1 mM). Both the internal and external solutions contain sodium oxalate (100 mM) and HEPES (10 mM) buffered at pH 7.0. DMSO solutions of transporters or DMSO was added, followed by a pulse of NaOH (5 mM) at time 0, and the fluorescence ratio of HPTS (λ_{ex} = 460 nm, λ_{em} = 510 nm, base form vs λ_{ex} = 403 nm, λ_{em} = 510 nm, acid form) was recorded. The fluorescence ratio was normalized by calibration using a detergent to lyse the vesicles at 5 min.

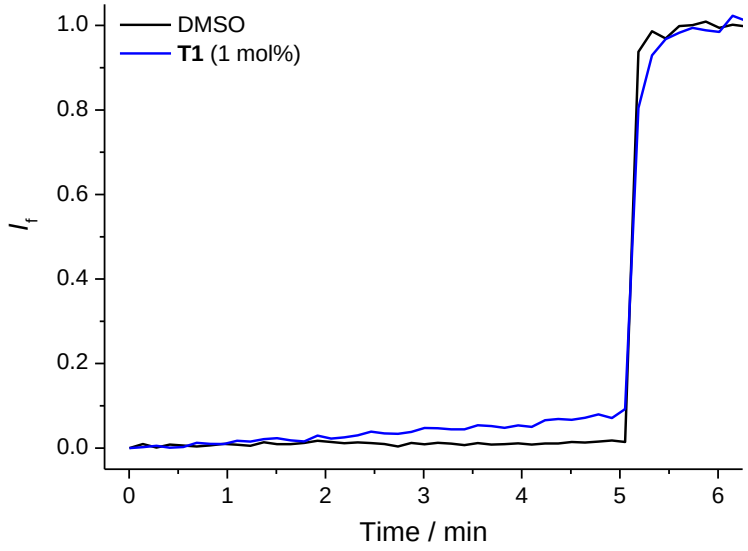

Figure 7.87 HPTS assay conducted with Na_2SO_4 vesicles. POPC LUVs (mean diameter 200 nm) were loaded with HPTS (1 mM). Both the internal and external solutions contain Na_2SO_4 (100 mM) and HEPES (10 mM) buffered at pH 7.0. DMSO solutions of transporters or DMSO was added, followed by a pulse of NaOH (5 mM) at time 0, and the fluorescence ratio of HPTS (λ_{ex} = 460 nm, λ_{em} = 510 nm, base form vs λ_{ex} = 403 nm, λ_{em} = 510 nm, acid form) was recorded. The fluorescence ratio was normalized by calibration using a detergent to lyse the vesicles at 5 min.

7.4.8 HPTS assay for studying Gly transport

POPC LUVs (mean diameter 200 nm) were prepared as follows. A chloroform solution of POPC was evaporated in a round-bottle flask and the lipid film formed was dried under vacuum for at least 6 h. The lipid film was hydrated by vortexing with a buffered aqueous solution containing pH sensitive dye HPTS (pH 7.4, 5 mM HEPES, 100 mM Na_2SO_4, 1 mM HPTS). The lipid solution was subjected to nine freeze/thaw cycles and then extruded 25 times through a 200 nm polycarbonate membrane. The unentrapped HPTS was removed by size exclusion chromatography on a Sephadex G-25 column using a buffer solution (pH 7.4, 5 mM HEPES, 100 mM Na_2SO_4) as the eluent.

For each run, the LUV stock solution prepared as stated above added to a buffer solution (pH 7.4, 5 mM HEPES, 100 mM Na_2SO_4) to a final lipid concentration of 1 mM and a final volume of 2 mL. The lipid solutions were stirred and thermostated in polystyrene cuvettes at 25 °C. The fluorescence intensity of HPTS (λ_{em} = 510 nm) at two excitation wavelengths (λ_{ex} = 460 nm, corresponding to the base form of HPTS and λ_{ex} = 403 nm, corresponding to the acid form of HPTS) was recorded. DMSO solutions of the transporters (DMSO volume ≤ 20 µL, in the cases of mixed transporters, the DMSO solutions of different transporters were added separately) or DMSO (20 µL) was added to the lipid solution within the first 2 min, followed by the addition of a solution of Gly (30 µL, 2 M Gly in pH 7.4 20 mM HEPES buffer containing 100 mM Na_2SO_4) if applicable. Each experiment was run in triplicate and the data were averaged over three runs.

Upon the addition of **1** (1 mol%), the $I_{460\ nm}$ / $I_{403\ nm}$ value underwent an initial increase followed by a slow relaxation (Figure 7.88a and Figure 7.88b). Upon the addition of **2** (100 mol%), the $I_{460\ nm}$ / $I_{403\ nm}$ value underwent a sudden decrease (Figure 7.88c). There changes are due to interference with the HPTS fluorescence, induced by **1** (1 mol%) and **2** (100 mol%), respectively, since they occur without a transmembrane pH gradient or any concentration gradient potentially able to generate a pH gradient. The effect of **2** in decreasing the $I_{460\ nm}$ / $I_{403\ nm}$ value is also observable in Figure 7.88a. Because of the interference, the HPTS fluorescence ratios were not converted to internal pH values. Nevertheless, by referring to a reported calibration equation,[143] the pH change induced by Gly is found always less than 0.05 pH unit. It should be mentioned that this minor change in HPTS fluorescence ratio induced by Gly may not indicate a real change in the intravesicular pH but may also result from the Gly-transporter interaction that changed the extent to which the transporters interfered with the HPTS fluorescence.

The initial increase of $I_{460\ nm}$ / $I_{403\ nm}$ value induced by **T1** is accompanied by a slow relaxation (Figure 7.88a and Figure 7.88b), which is not due to the later addition of **T2** or **T3** (Figure 7.89a black). The observed slow relaxation might result from **T1** slowly re-partitioning from the lipid bilayer into the aqueous solution since the relaxation was not observed after the vesicles were lysed by a detergent (Figure 7.89a red). It is likely that the HPTS fluorescence is perturbed most effectively by **T1** when **T1** partitions in the lipid bilayer, considering the high-surface-area-to-internal-volume ratio of the LUVs that would increase the "local concentration" of **T1** (here the concentration is calculated by the amount of **T1** present in one vesicle, divided by the volume of one vesicle including both the inner aqueous pool and the lipid bilayer), and also the possibility of HPTS absorption to the membrane exterior.[262] In contrast, if **T1** fully partitions in the aqueous phase, the interference would be much weaker, since the internal volume of POPC LUVs used (diameter 200 nm, lipid concentration 1 mM) is only ~0.67% that of the external volume[263] and therefore only a small portion of **T1** can interact with HPTS. Based on the above hypothesis, the percentage of **T1** that left the lipid bilayer at 30 min can be estimated by an exponential fit of the decay part of the curve assuming first-order kinetics and linear relationship between the $I_{460\ nm}$ / $I_{403\ nm}$ value and the percentage of **T1** that partitioned in the lipid bilayer. According to this calculation, there would be a 76% loss of **T1** in the lipid bilayer 30 min after the addition of **T1** to the lipid solution. Since the activity of **T1** is not affected seriously when the loading of **T1** is lowered from 1 mol% to 0.2 mol% (Figure 7.68), the kinetic studies using 1 mol% of **T1** over the course of 30 min should be valid.

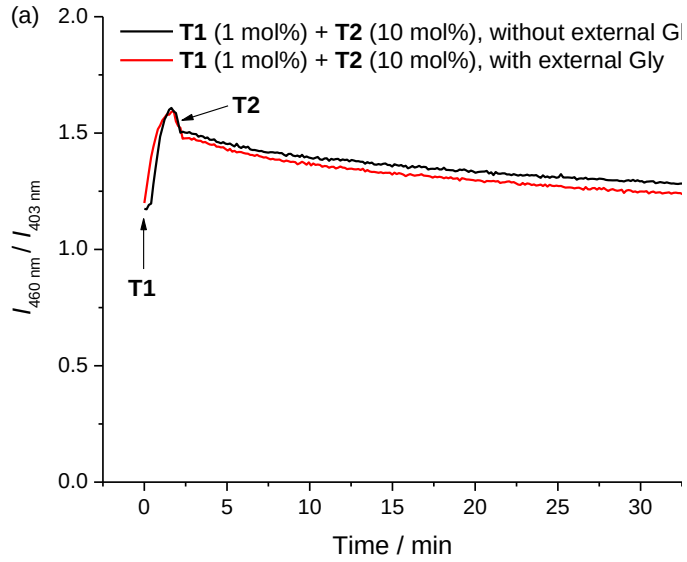
(a)
T1 (1 mol%) + T2 (10 mol%), without external Gl
T1 (1 mol%) + T2 (10 mol%), with external Gly
T2
T1
I460 nm / I403 nm
Time / min

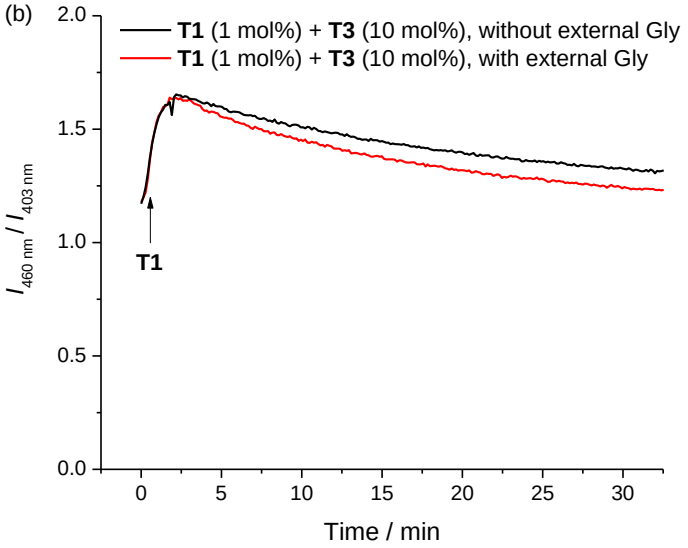
(b)
T1 (1 mol%) + T3 (10 mol%), without external Gly
T1 (1 mol%) + T3 (10 mol%), with external Gly
T1
I460 nm / I403 nm
Time / min

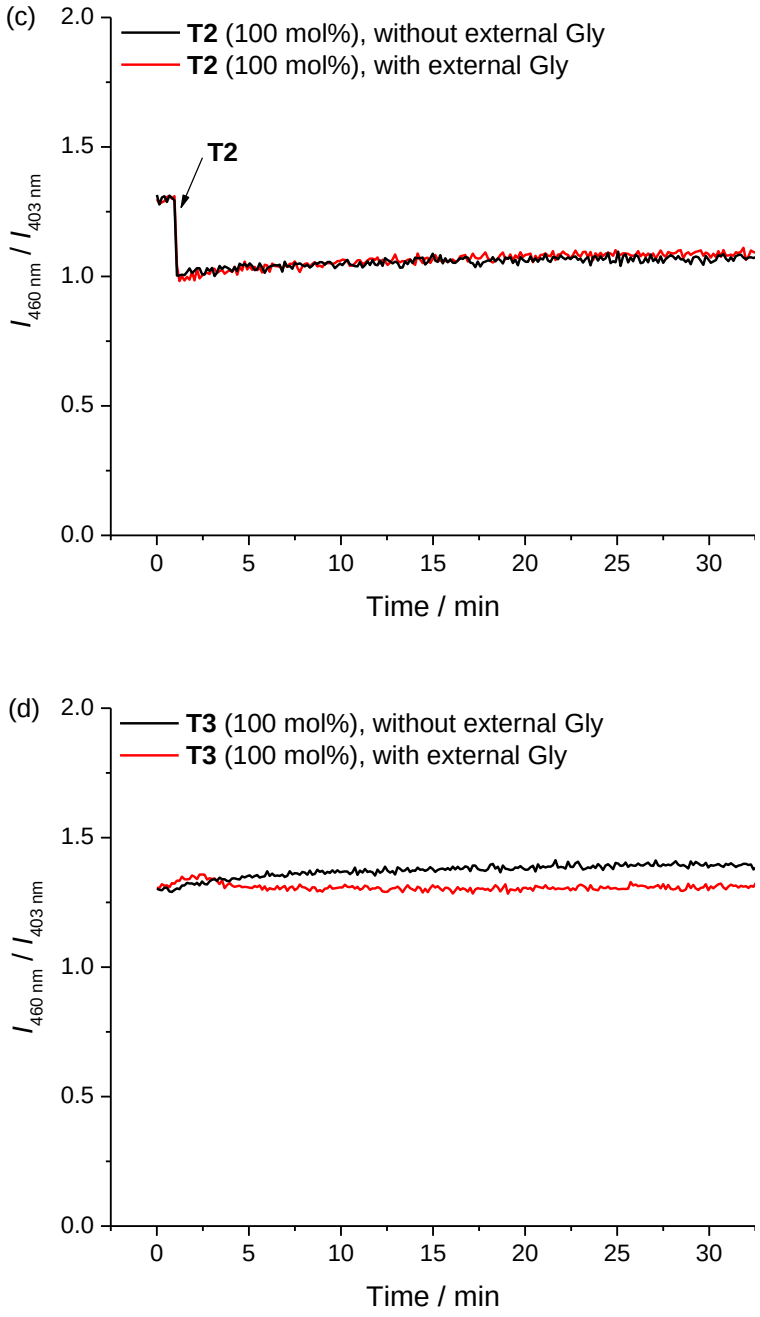

Figure 7.88 Fluorescence intensity ratio (λ_{ex} = 460 nm, λ_{em} = 510 nm, base form vs λ_{ex} = 403 nm, λ_{em} = 510 nm, acid form) of HPTS vs time. POPC LUVs (mean diameter 200 nm) were loaded with HPTS (1 mM) and suspended in an external buffer solution. Both the internal and external solutions contained Na_2SO_4 (100 mM) and HEPES (5 mM) buffered at pH 7.4. DMSO solutions of transporters were added to the lipid solution within the first 2 min, followed by the addition of Gly (30 mM) at t = 3 min. The changes in HPTS fluorescence ratio due to the addition of a transporter are shown with arrows. Transporter loadings are shown as transporter to lipid molar ratios.

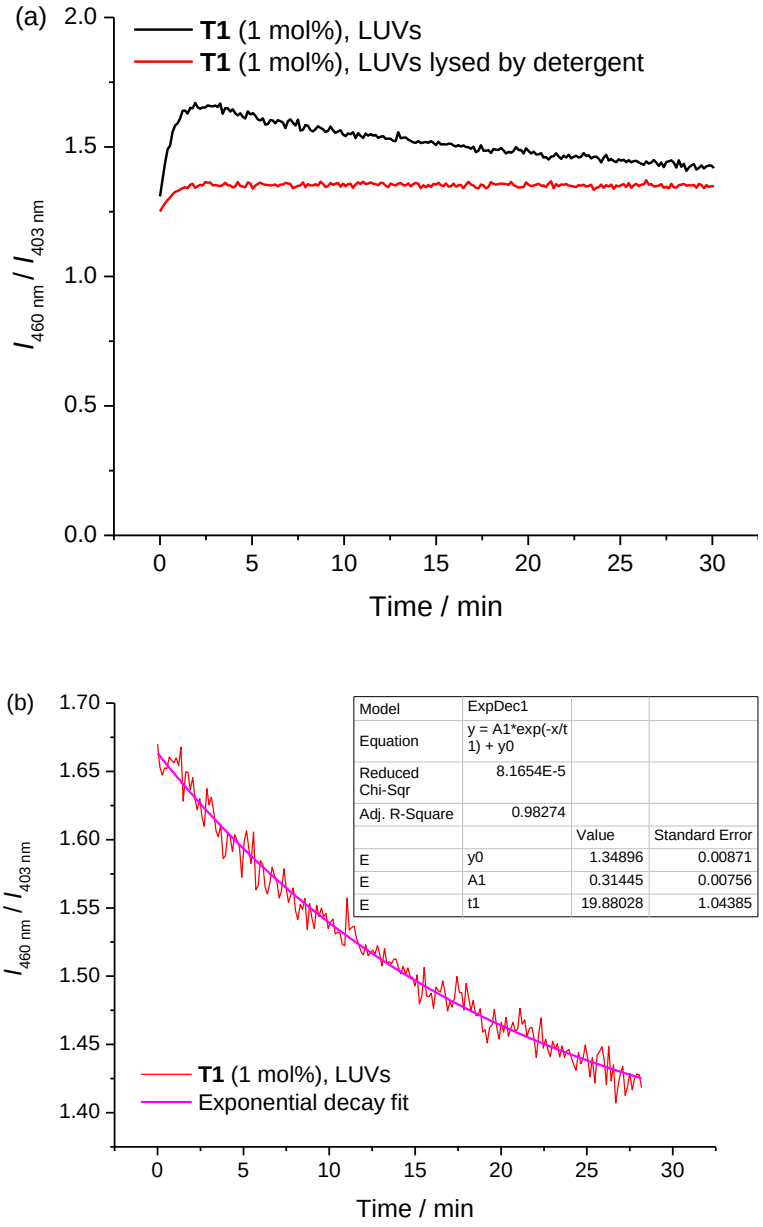

Figure 7.89 (a) Interference of **T1** with the HPTS fluorescence ratio (λ_{ex} = 460 nm, λ_{em} = 510 nm, base form vs λ_{ex} = 403 nm, λ_{em} = 510 nm, acid form) when HPTS was entrapped in vesicles (black) or dispersed in the solution (red, vesicles were lysed with a detergent before the start). POPC LUVs (mean diameter 200 nm) were loaded with HPTS (1 mM) and suspended in an external buffer solution. Both the internal and external solutions contained Na_2SO_4 (100 mM) and HEPES (5 mM) buffered at pH 7.4. At time 0, DMSO solutions of **T1** (10 μL, 2 mM) was added to the lipid solution. Transporter loadings are shown as transporter to lipid molar ratios. (b) First order exponential fit of the decay part of (a) black.

7.4.9 Calcein leakage assay

POPC LUVs (mean diameter 200 nm) were prepared as follows. A chloroform solution of POPC was evaporated in a round-bottle flask and the lipid film formed was dried under vacuum for at least 6 h. The lipid film was hydrated by vortexing with a concentrated Calcein solution (pH 7.4, 20 mM HEPES, 100 mM Na_2SO_4, 100 mM Calcein). The lipid solution was subjected to nine freeze/thaw cycles and then extruded 25 times through a 200 nm polycarbonate membrane. The unentrapped Calcein were removed by by size exclusion chromatography on a Sephadex G-25 column using a buffer solution as the eluent (pH 7.4, 20 mM HEPES, 150 mM Na_2SO_4).

For each run, the LUV stock solution prepared as stated above was added to an external solution (pH 7.4, 20 mM HEPES, 150 mM Na_2SO_4) to a final lipid concentration of 1 mM. The lipid solution was stirred and thermostated in a polystyrene cuvette at 25 °C. At 0 min, DMSO solutions of the transporters (DMSO volume ≤ 20 µL) or DMSO (20 µL) was added to the lipid solution to start the transport, and the fluorescence emission at time *t* (λ_{ex} = 495 nm, λ_{em} = 515 nm) was recorded over 30 min. At the end of each experiment, a detergent (20 µl of 0.232 mM octaethylene glycol monododecyl ether in 7 : 1 (v : v) H_2O/DMSO) was added to lyse the vesicles. Each experiment was run in triplicate and the data were averaged over three runs. The fractional fluorescence intensity I_f is calculated using the following equation:

$$I_f = \frac{I_t - I_0}{I_{\max} - I_0}$$

where I_t is the fluorescence intensity at time t, I_0 is the fluorescence intensity at time 0, and I_{max} is the fluorescence intensity after detergent addition.

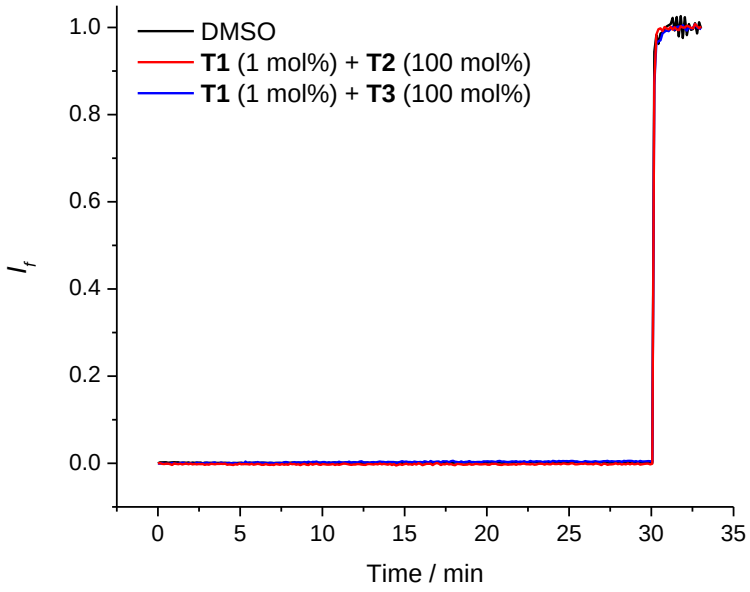

Figure 7.90 Fraction of Calcein leakage with time in the presence of various transporters. POPC LUVs (mean diameter 200 nm) loaded with an internal solution of Calcein (100 mM), Na_2SO_4 (100 mM) and HEPES (20 mM) buffered at pH 7.4 were suspended in an external solution of Na_2SO_4 (150 mM) and HEPES (20 mM) buffered at pH 7.4. At time 0, DMSO solutions of transporters or DMSO was added, and the fluorescence intensity (λ_{ex} = 495 nm, λ_{em} = 515 nm) was recorded. The fluorescence intensity was normalized to a fractional fluorescence intensity by adding a detergent to lyse the vesicles. Transporter loadings are shown as transporter to lipid molar ratios.

7.4.10 ^{1}H NMR study

A mixture of a $CDCl_3$ solution (0.6 mL) of **T2** (10 mM) and an aqueous solution (0.6 mL) of the indicated substrates was vortexed for 5 min and then left to stand until phase separation. The aqueous phase was removed, and the $CDCl_3$ phase was subject to ^{1}H NMR measurements.

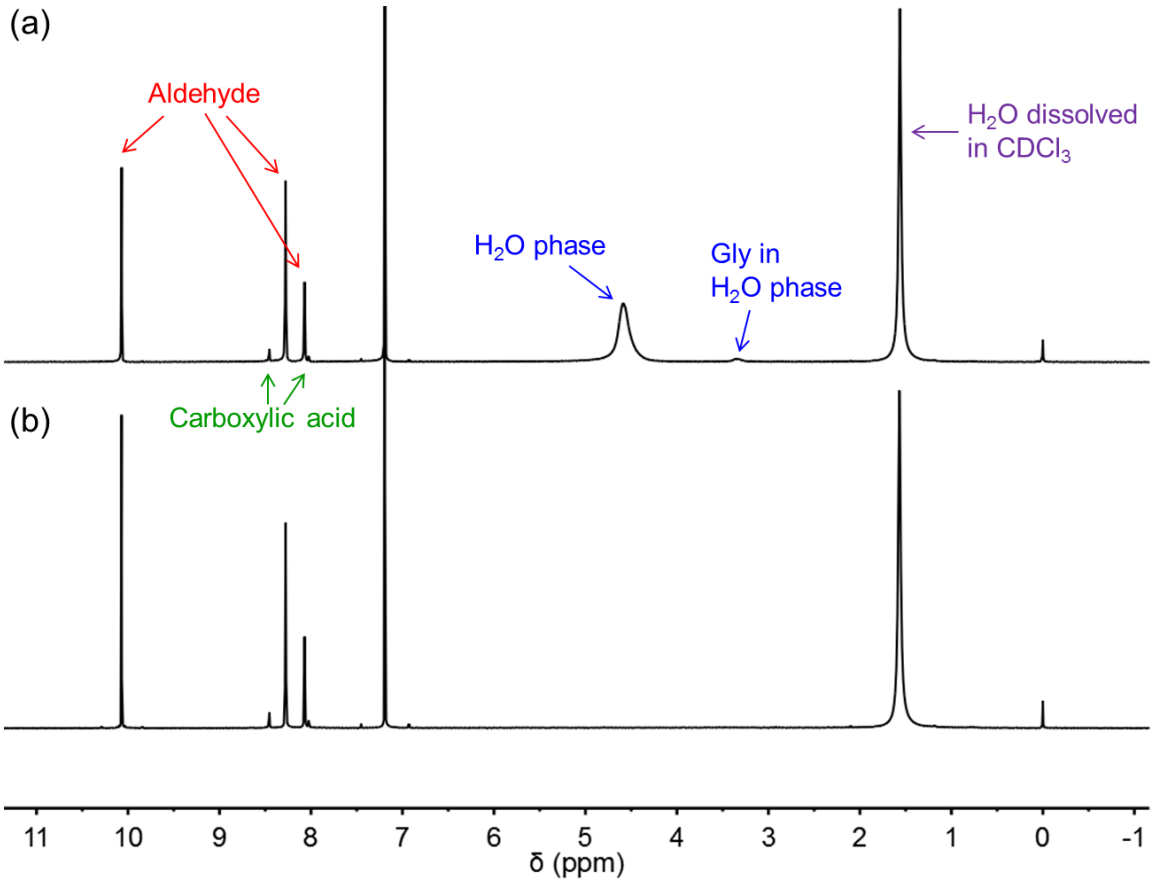

Figure 7.91 ^{1}H NMR spectra (400 MHz) of $CDCl_3$ solutions of **T2** (10 mM) after being treated with an aqueous solution of 2 M Gly (a) or 2 M Sar (b). Observed in the spectra are **2** and trace of 3,5-bis(trifluoromethyl)benzoic acid that results from oxidation of **T2**.

7.5 Supporting information for Chapter 6

7.5.1 General

POPC was purchased from Avanti Lipids. Other chemicals were purchased from Sigma-Aldrich, Alfa-Aesar, Apollo Scientific or Tokyo Chemical Industry, and used as received. ^{1}H NMR and ^{13}C NMR spectra were obtained on a Bruker AVII400 or a Bruker AVIII HD400 NMR spectrometer. High resolution mass spectra (HRMS) were were recorded on a Bruker Apex III Fourier Transform Mass Spectrometer. Infrared spectra were recorded on a Perkin Elmer Spectrum One FT-IR. Fluorescence measurements were performed using a Varian Cary Eclipse Fluorescence Spectrophotometer equipped with a stirrer plate and a temperature controller. Compounds **A1**[144] and **A4**[264] were synthesized by ILK, **A7**[259] and **A9**[227] by MW, **A8**[144] by NB, **A15**[265] by TL, **A16**[266] by AS, and **A17**[267] and **A18**[267] by LWJ. **A5**[144] **and A10**[268] were synthesized following reported procedures.

7.5.2 Compound synthesis and characterization

Synthesis of A2

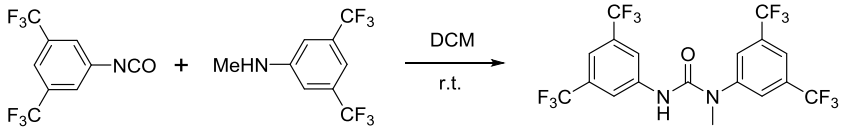

A2

A solution of 3,5-bis(trifluoromethyl)phenylisocyanate (0.60 g, 2.4 mmol) and 3,5-bis(trifluoromethyl)-*N*-methylaniline (0.57 g, 2.4 mmol, prepared according to a literature procedure[264]) in DCM (7 mL) was stirred overnight. The white precipitate formed was collected by filtration and washed with DCM. Yield: 0.79 g (65%); ^{1}H NMR (400 MHz, DMSO-d_6): δ = 9.22 (s, 1H), 8.20 (s, 2H), 8.15 (s, 2H), 7.97 (s, 1H), 7.67 (s, 1H), 3.43 (s, 3H); ^{13}C NMR (101 MHz, DMSO-d_6): δ = 154.08, 145.47, 142.00, 130.99 (q, *J* = 33.0 Hz), 130.38 (q, *J* = 32.6 Hz), 126.90, 123.34 (q, *J* = 272.5 Hz), 123.12 (q, *J* = 272.8 Hz), 119.52, 118.88, 114.79, 37.25; HRMS (ES+) *m/z*: $[M+H]^+$ calculated 499.0674, found 499.0669.

Synthesis of A3

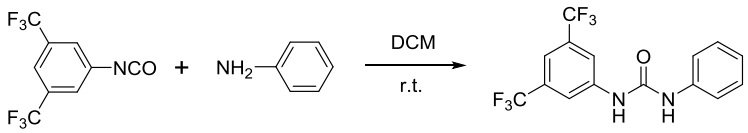

A3

3,5-Bis(trifluoromethyl)phenylisocyanate (0.49 g, 1.9 mmol) and aniline (0.18 g, 1.9 mmol) were mixed in DCM (20 mL) as a white precipitate formed immediately. The mixture was stirred for 10 min. The precipitate was collected by filtration and washed with DCM. Yield: 0.60 g (89%); ^{1}H NMR (400 MHz, DMSO-d_6): δ = 9.39 (s, 1H), 8.99 (s, 1H), 8.13 (s, 2H), 7.64 (s, 1H), 7.48 (dd, *J* = 8.6, 1.1 Hz, 2H), 7.30 (dd, *J* = 8.4, 7.5 Hz, 2H), 7.02 (tt, *J* = 7.4, 1.1 Hz, 1H). The ^{1}H NMR spectrum is consistent with literature data.[253]

Synthesis of A6

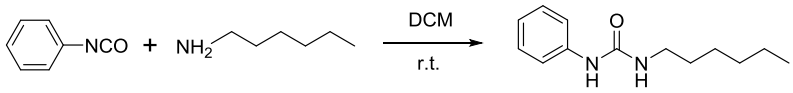

A6

Phenylisocyanate (0.36 g, 3.0 mmol) and *n*-hexylamine (0.30 g, 3.0 mmol) was stirred in DCM (5 mL) overnight. The solvent was evaporated. The white solid was recrystallized from hexane. Yield: 0.52 g (79%); ^{1}H NMR (400 MHz, DMSO-d_6): δ = 8.35 (s, 1H), 7.36 (d, *J* = 7.6 Hz, 2H), 7.20 (t, *J* = 7.9 Hz, 2H), 6.87 (t, *J* = 7.3 Hz, 1H), 6.09 (t, *J* = 5.5 Hz, 1H), 3.05 (td, *J* = 6.7, 5.9 Hz, 2H), 1.46 – 1.30 (m, 2H), 1.32 – 1.18 (m, 6H), 0.86 (t, *J* = 6.7 Hz, 3H). The ^{1}H NMR spectrum is consistent with literature data.

Synthesis of A11

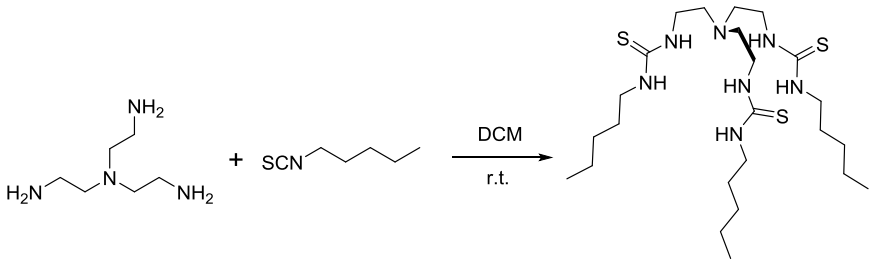

A11

A solution of tris(2-aminoethyl)amine (0.077 g, 0.53 mmol) and *n*-pentylisothiocyanate (0.21 g, 1.6 mmol) in DCM (3 mL) was stirred overnight. The solvent was evaporated, resulting in a light yellow oil. The residue was immersed in hexane for 24 h as it gradually became a white solid. The product was collected by filtration, washed with hexane, and dried under vacuum. Yield: 0.25 g (88%); ^{1}H NMR (400 MHz, DMSO-d_6): δ = 7.48 (s, 3H), 7.18 (s, 3H), 3.44 (s, 6H), 3.33 (s, 6H), 2.61 (t, *J* = 6.6 Hz, 6H), 1.52 – 1.38 (m, 6H), 1.33 – 1.19 (m, 12H), 0.86 (t, *J* = 6.9 Hz, 9H); ^{13}C NMR (101 MHz, DMSO-d_6): δ = 181.93, 52.60, 43.45, 41.51, 28.59, 28.39, 21.86, 13.87. HRMS (ES+) *m/z*: $[M+H]^+$ calculated 534.3441, found 534.3451.

Synthesis of A12

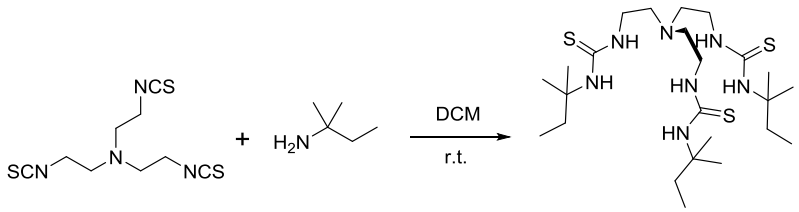

A12

A solution of tris(2-isothiocyanatoethyl)amine (0.34 g, 1.2 mmol, prepared according to a literature procedure[269]) and *tert*-pentylamine (0.33 g, 3.8 mmol) in DCM (3 mL) was stirred for 24 h. The solvent was evaporated. The residue was dissolved in DCM (1 mL) and then hexane (5 mL) was added as the product became a yellow sticky oil at the bottom of the flask. The mixture was left to stand till complete phase separation. The solvent was carefully poured and discarded. The oil was washed with hexane and dried under vacuum as it gradually became a yellow solid. The yellow solid was dissolved in hot DCM and left to stand overnight as white solid precipitated, which was collected by filtration. Yield: 0.30 g (45%); ^{1}H NMR (400 MHz, DMSO-d_6): δ = 7.10 (t, *J* = 4.8 Hz, 3H), 6.95 (s, 3H), 3.50 – 3.38 (m, 6H), 2.60 (t, *J* = 6.7 Hz, 6H), 1.85 (q, *J* = 7.3 Hz, 6H), 1.33 (s, 18H), 0.76 (t, *J* = 7.4 Hz, 9H); ^{13}C NMR (101 MHz, DMSO-d_6): δ = 181.27, 54.73, 52.50, 41.04, 32.02, 26.81, 8.27. HRMS (ES+) *m/z*: $[M+H]^+$ calculated 534.3441, found 534.3457.

Synthesis of A13

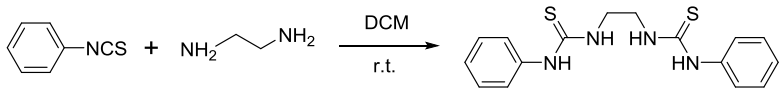

A13

Phenylisothiocyanate (0.98 g, 7.2 mmol) and ethylenediamine (0.22 g, 3.6 mmol) were mixed in DCM (15 mL) as a white precipitate formed immediately. The mixture was stirred for 2 h. The precipitate was collected by filtration and washed with DCM. Yield: 1.07 g (90%); ^{1}H NMR (400 MHz, DMSO): δ = 9.59 (s, 2H), 7.83 (s, 2H), 7.39 (d, *J* = 7.7 Hz, 4H), 7.32 (t, *J* = 7.8 Hz, 4H), 7.12 (t, *J* = 7.2 Hz, 2H), 3.69 (s, 4H). The ^{1}H NMR spectrum is consistent with literature data.[270]

Synthesis of A14

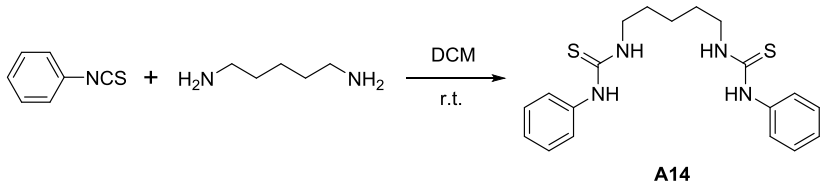

A14

A solution of phenylisothiocyanate (0.292 g, 2.16 mmol) and 1,5-diaminopentane (0.11 g, 1.08 mmol) in DCM (10 mL) was stirred overnight. The solvent was evaporated and the solid obtained was recrystallized from methanol. Yield: 0.14 g (35%); ^{1}H NMR (400 MHz, DMSO): δ = 9.46 (s, 2H), 7.75 (s, 2H), 7.39 (dd, *J* = 8.5, 1.1 Hz, 1H), 7.34 – 7.27 (m, 4H), 7.09 (tt, *J* = 7.3, 1.0 Hz, 2H), 3.46 (s, 4H), 1.64 – 1.46 (quint, *J* = 7.3 Hz, 4H), 1.39 – 1.22 (quint, *J* = 7.3 Hz, 2H). The ^{1}H NMR spectrum is consistent with literature data.[271]

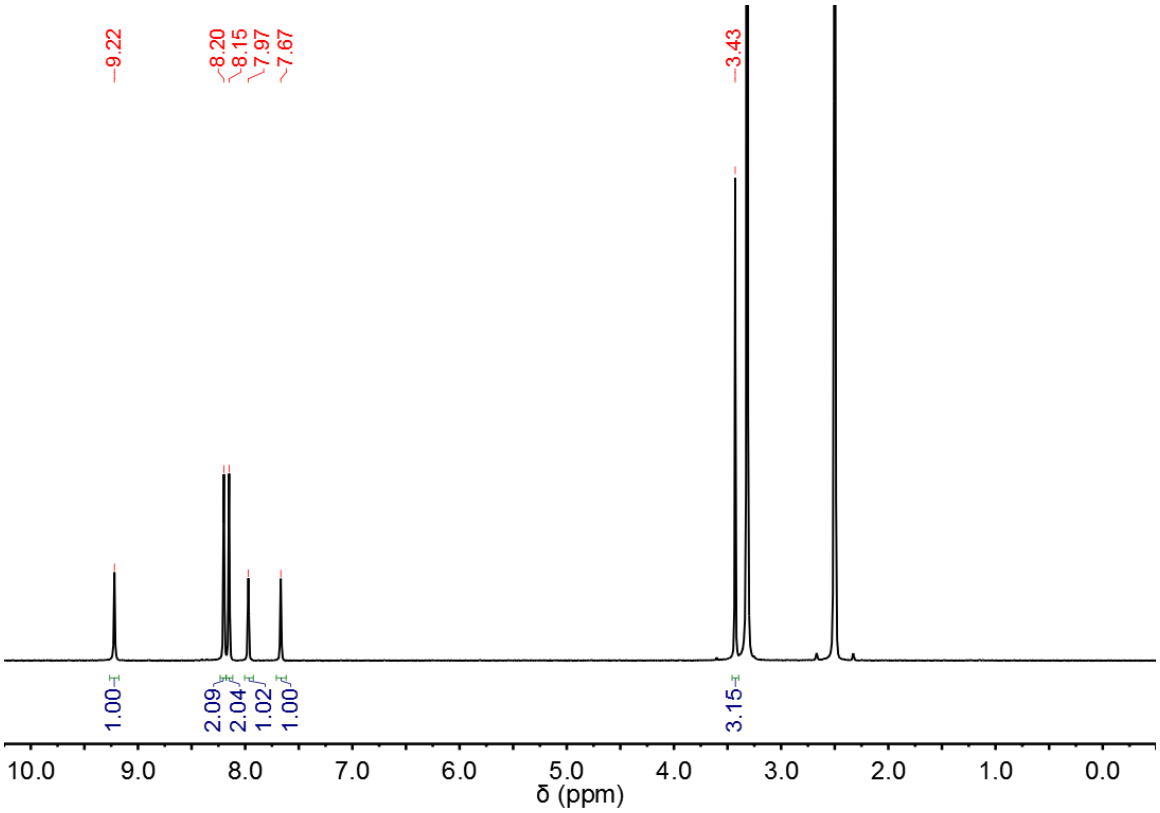

Figure 7.92 ^{1}H NMR spectra (400 MHz) of **A2** in DMSO-d_6.

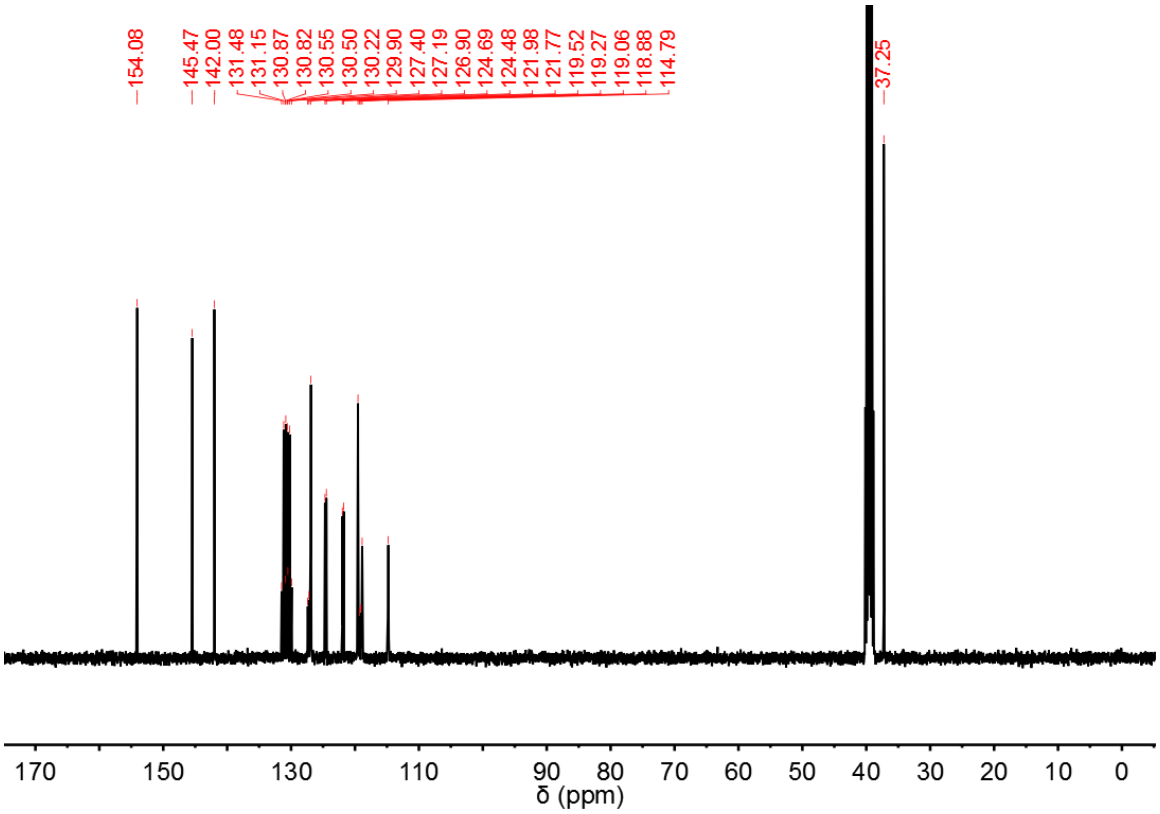

Figure 7.93 ^{13}C NMR spectra (101 MHz) of **A2** in DMSO-d_6.

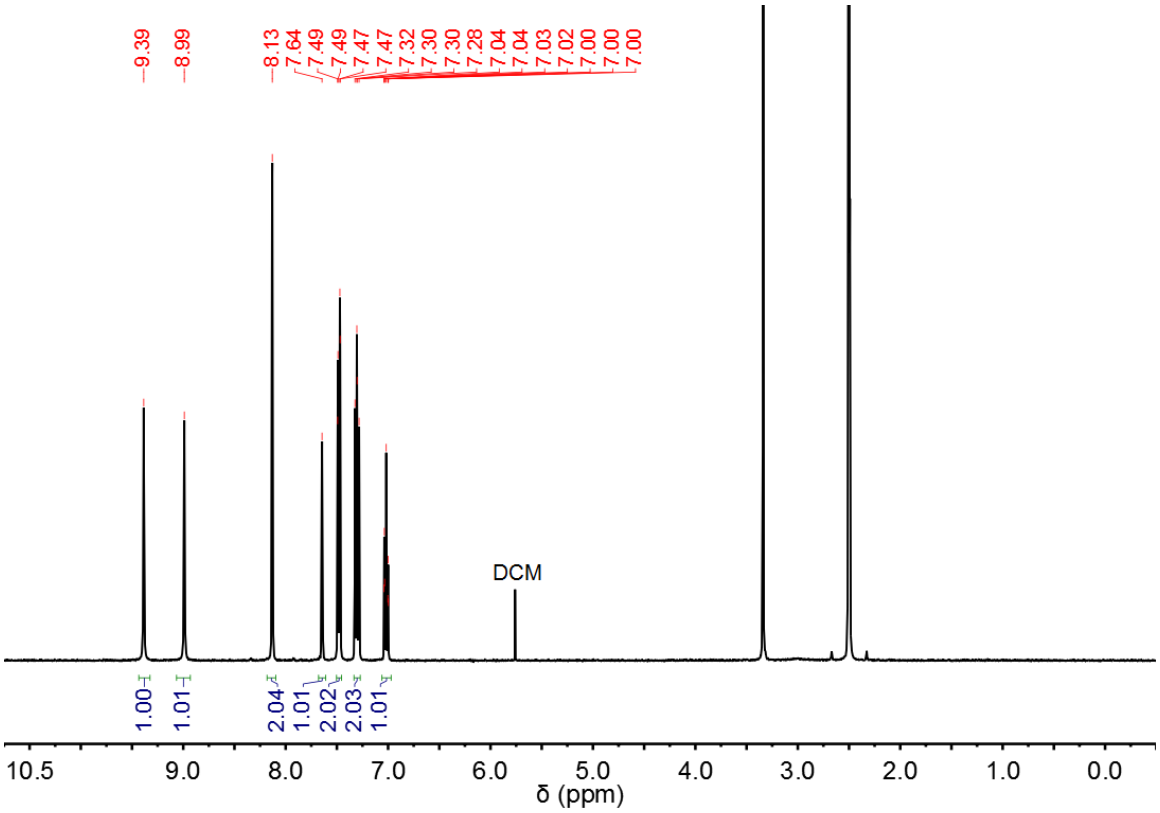

Figure 7.94 ^{1}H NMR spectra (400 MHz) of **A3** in DMSO-d_6.

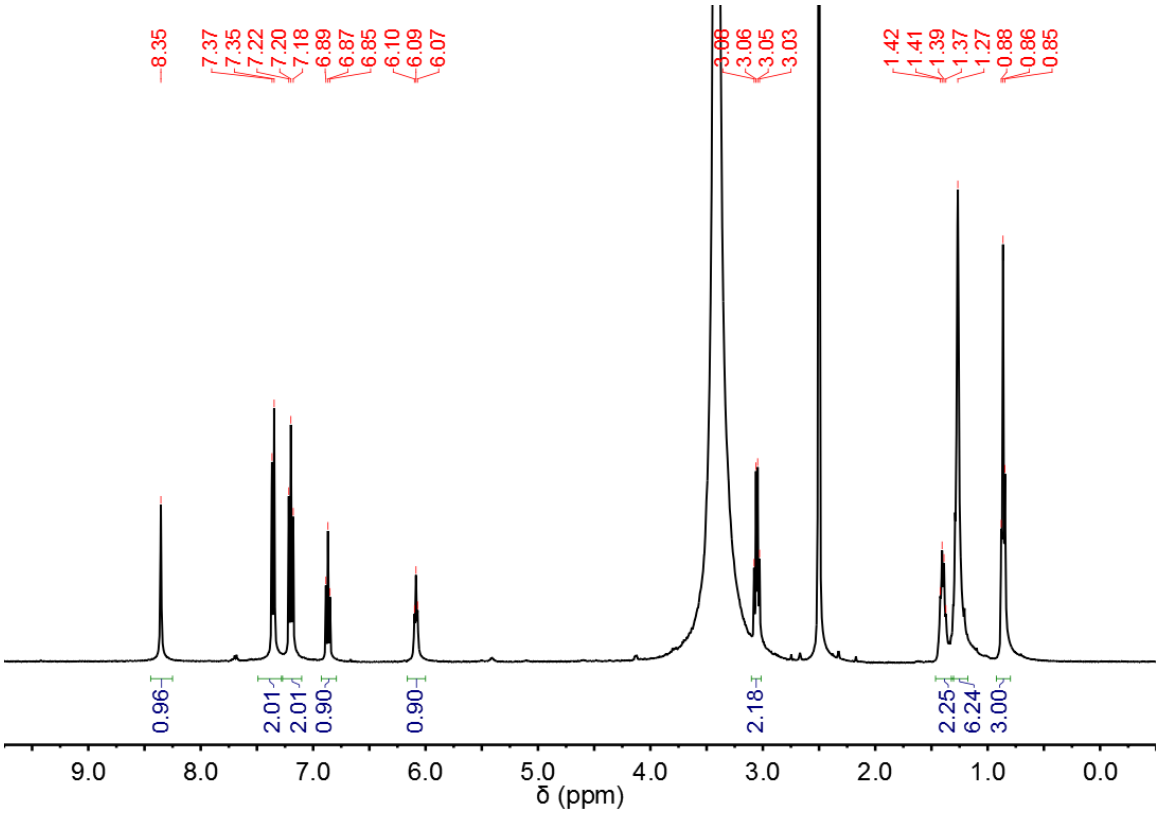

Figure 7.95 ^{1}H NMR spectra (400 MHz) of **A6** in DMSO-d_6.

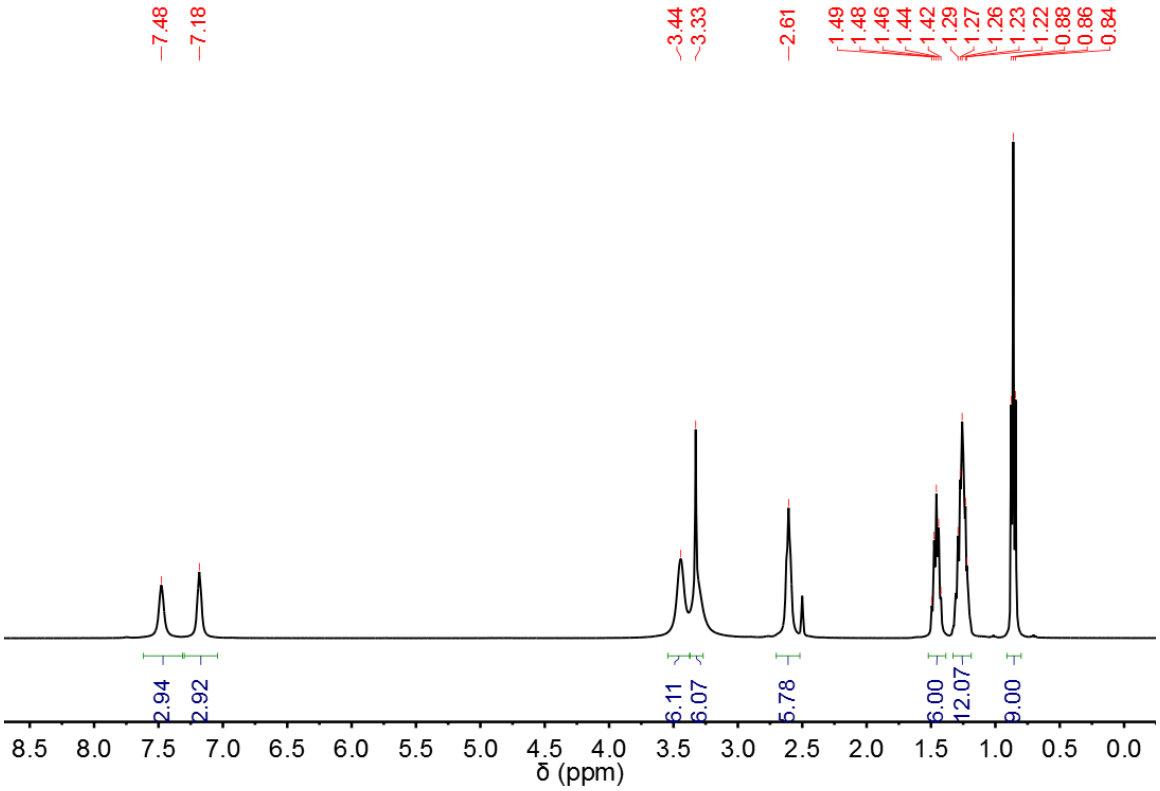

Figure 7.96 ^{1}H NMR spectra (400 MHz) of **A11** in DMSO-d_6.

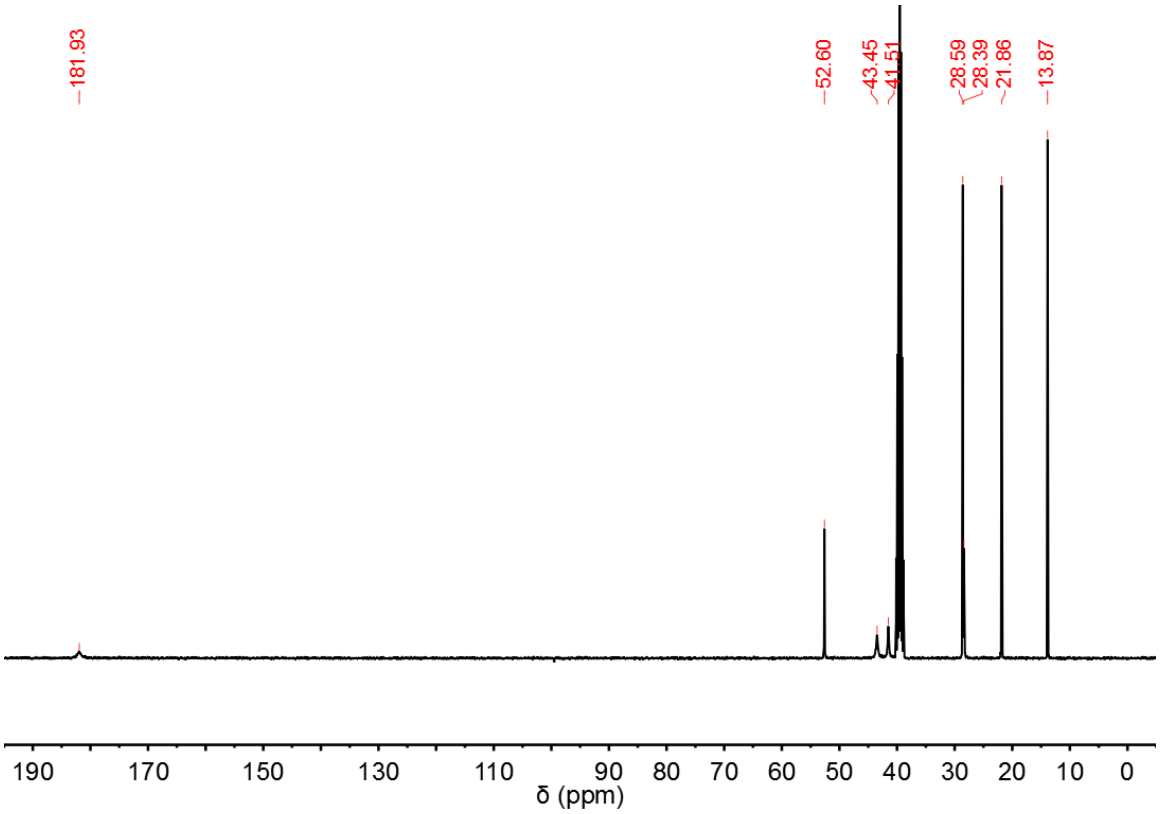

Figure 7.97 ^{13}C NMR spectra (101 MHz) of **A11** in DMSO-d_6.

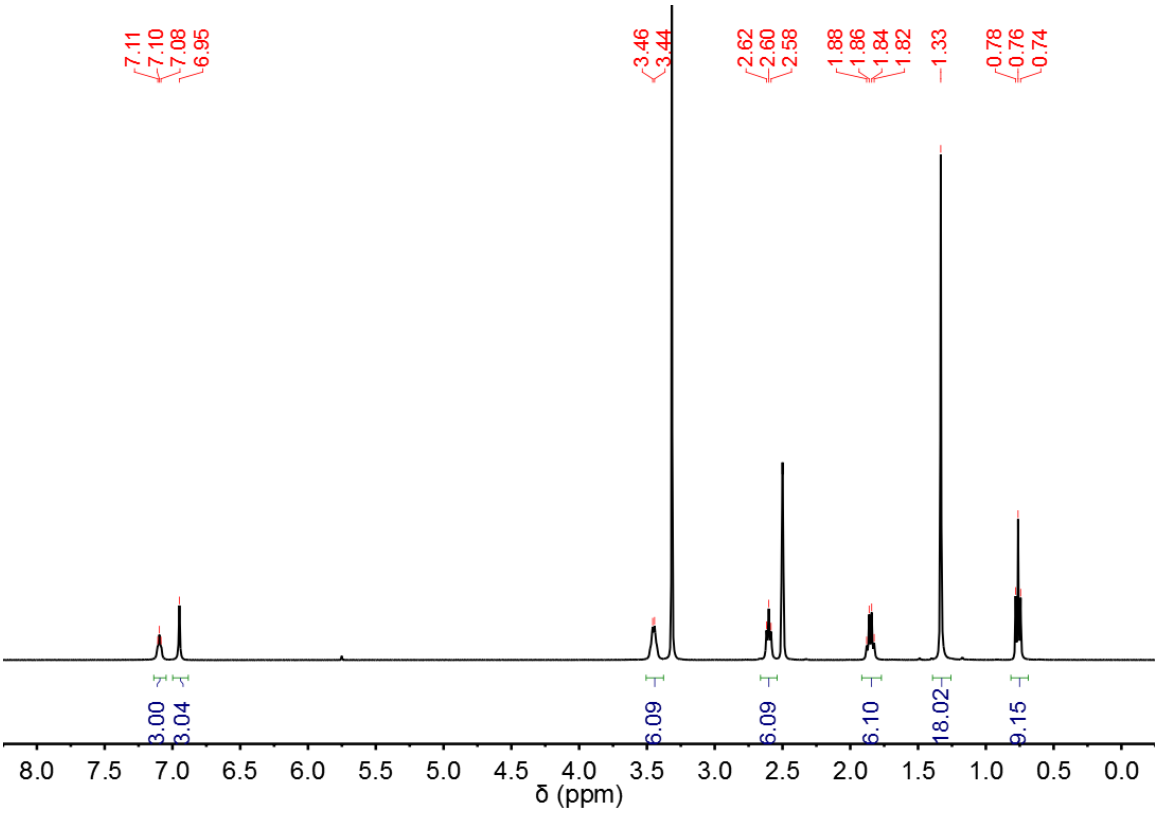

Figure 7.98 [1]H NMR spectra (400 MHz) of **A12** in DMSO-d_6.

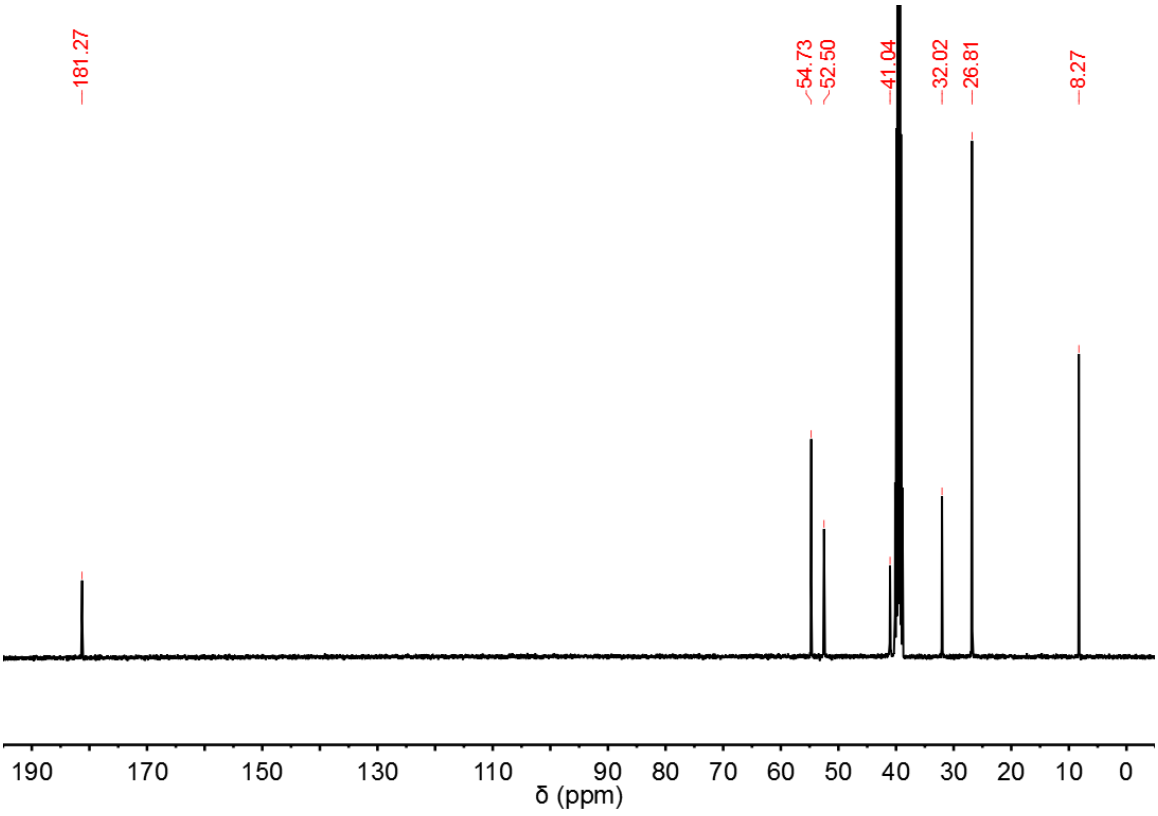

Figure 7.99 [13]C NMR spectra (101 MHz) of **A12** in DMSO-d_6.

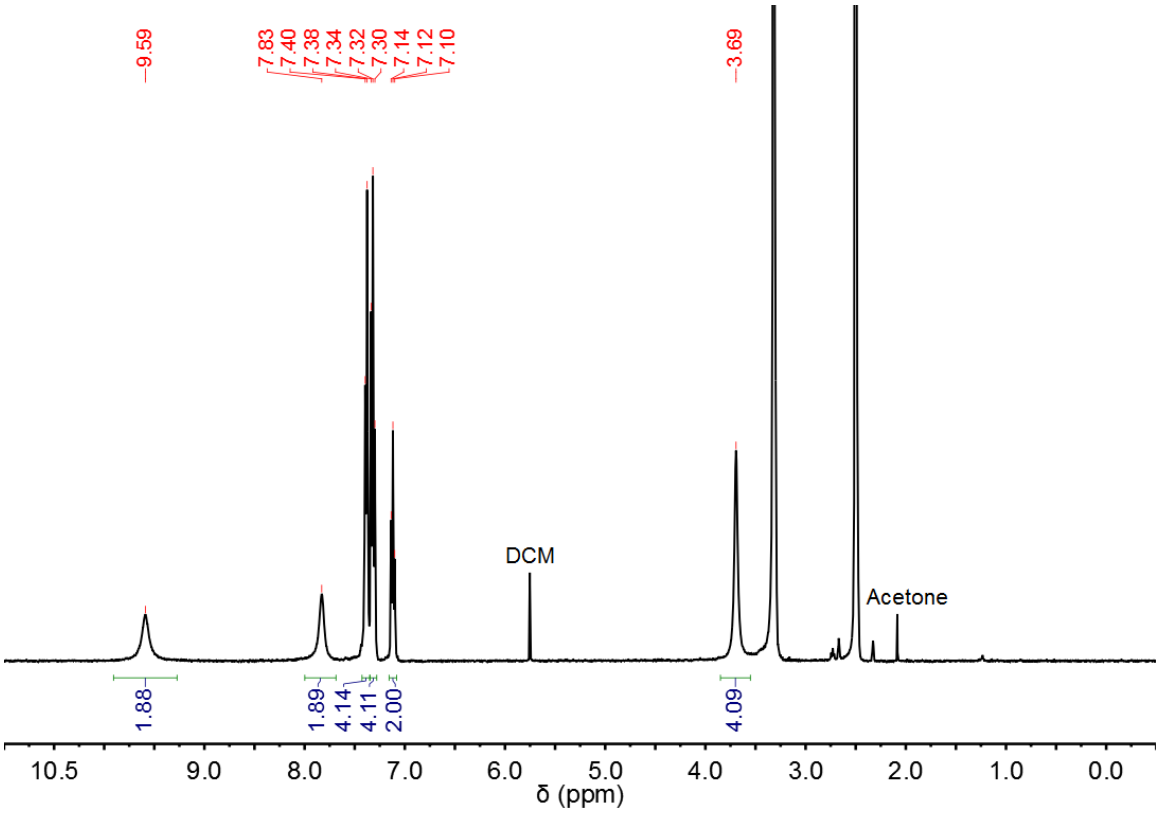

Figure 7.100 ^{1}H NMR spectra (400 MHz) of **A13** in DMSO-d_6.

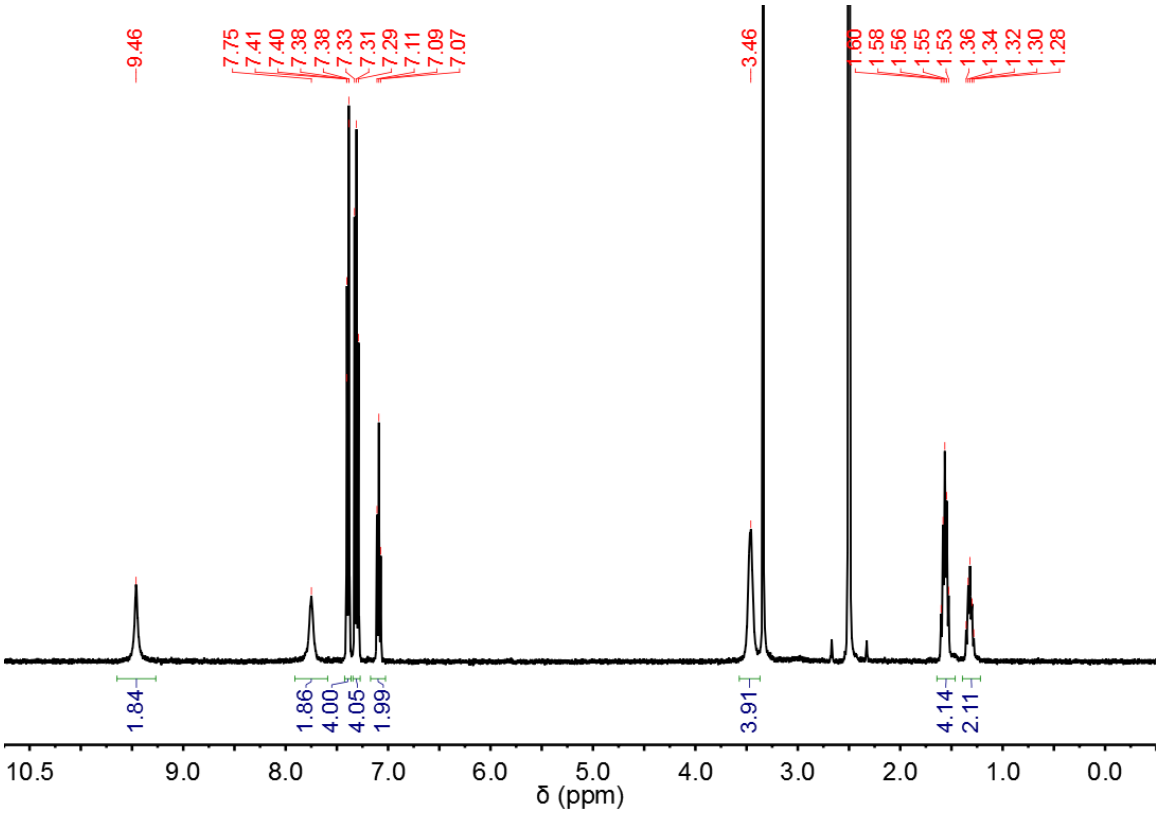

Figure 7.101 ^{1}H NMR spectra (400 MHz) of **A14** in DMSO-d_6.

7.5.3 NMR binding studies

7.5.3.1 Binding constant determination

1^1H NMR binding studies were conducted to evaluate the affinity of **A13** and **A14** for chloride. To a solution of the host (10 mM) in DMSO-d_6/0.5% H_2O were added aliquots of a solution containing TBACl (0.5 M) and the host (10 mM) in DMSO-d_6/0.5% H_2O, and ^{1}H NMR spectra were recorded, which show downfield shift of both thiourea NH proton resonances with increasing concentration of TBACl. Binding isotherms were obtained by plotting the chemical shift of two thiourea NH protons against concentration of TBACl. For both **A13** and **A14**, the addition of TBACl leads to initial sharpening of one of the thiourea NH proton peaks followed by broadening with higher concentration of TBACl (Figure 7.102 and Figure 7.104). This is indicative of stepwise binding of chloride.[272] The binding isotherms were therefore fitted according to the 1:2 (host to guest) binding model,[273] using global fitting with both NH proton signals. Data fit was performed using an online tool (www.supramolecular.org).

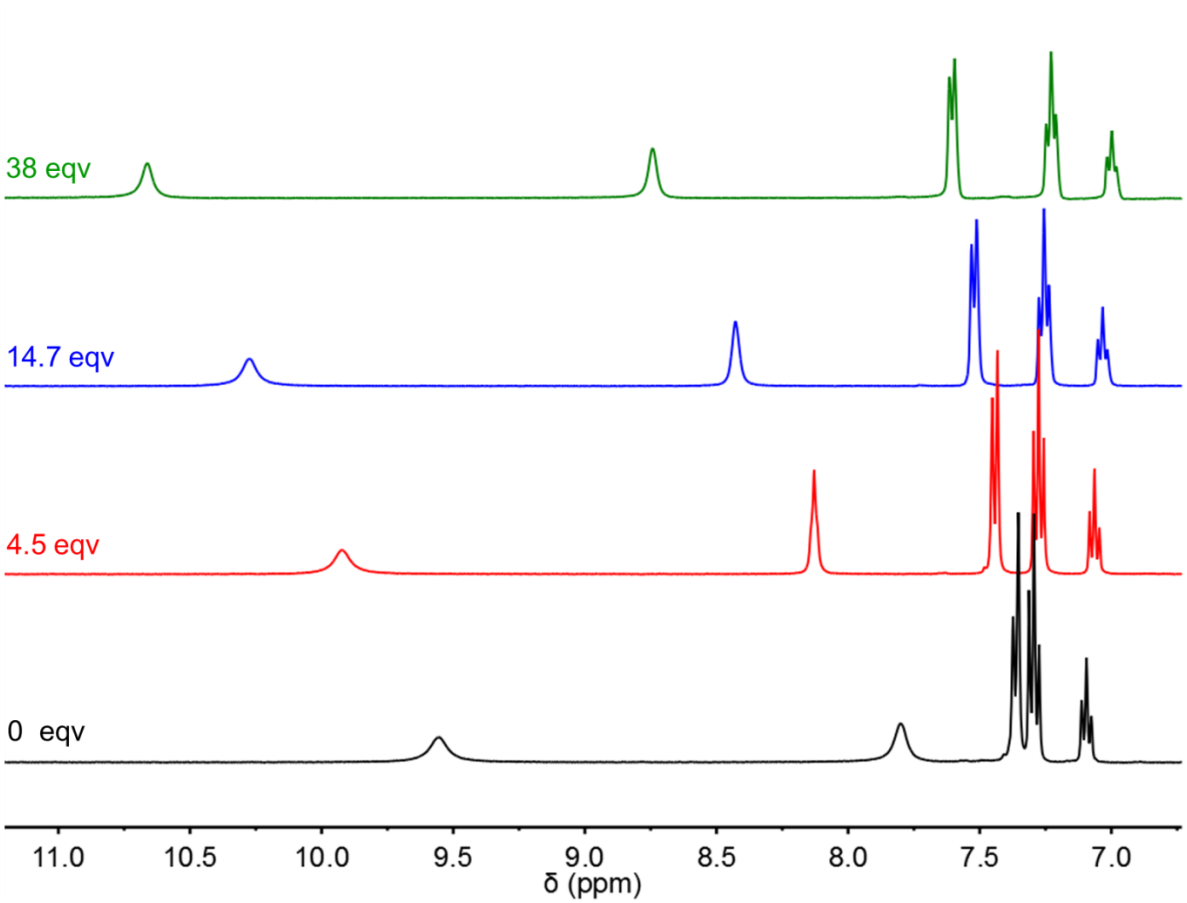

Figure 7.102 ^{1}H NMR spectra of **A13** (10 mM) with increasing concentration of TBACl in DMSO-d_6 containing 0.5% (v%) H_2O at 293 K.

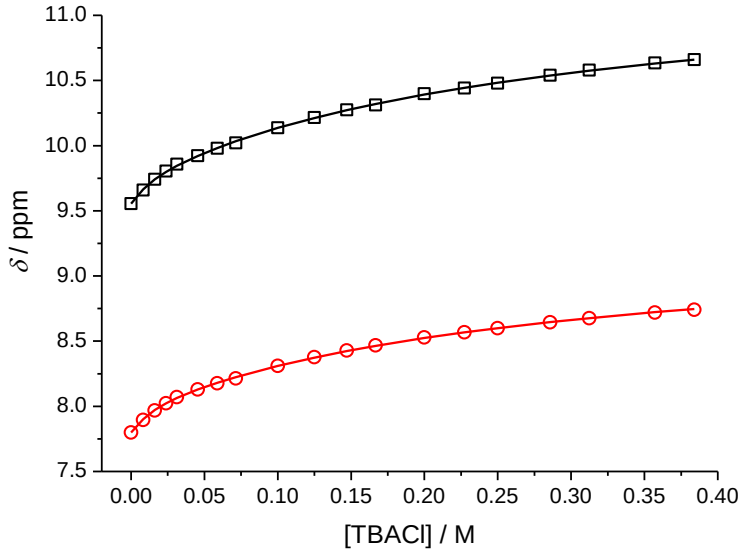

Figure 7.103 Chemical shifts of two thiourea NH protons of **A13** (10 mM) with increasing concentration of TBACl in DMSO-d_6 containing 0.5% (v%) H_2O at 293 K. The data were fitted to a 1:2 (host to guest) binding model, giving K_1 = 151 M^{-1}, and K_2 = 3.42 M^{-1}.

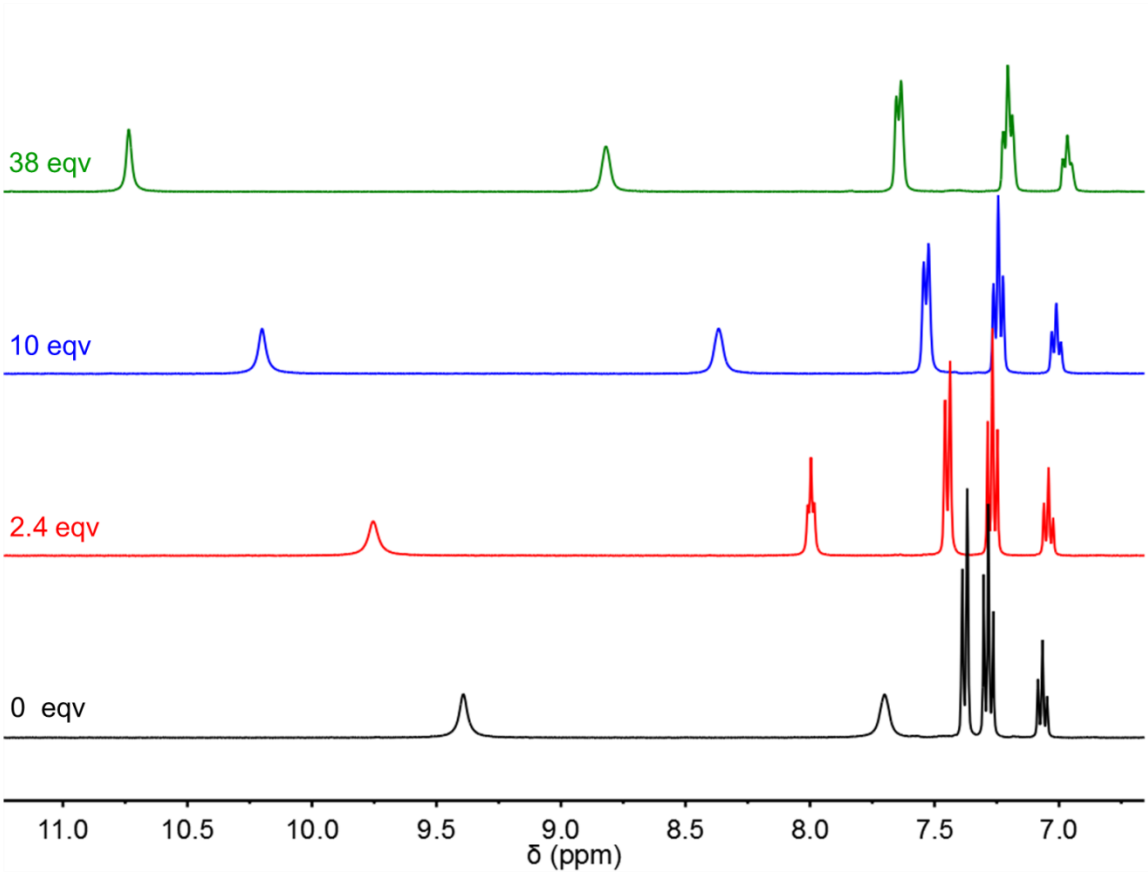

Figure 7.104 ^{1}H NMR spectra of **A14** (10 mM) with increasing concentration of TBACl in DMSO-d_6 containing 0.5% (v%) H_2O at 293 K.

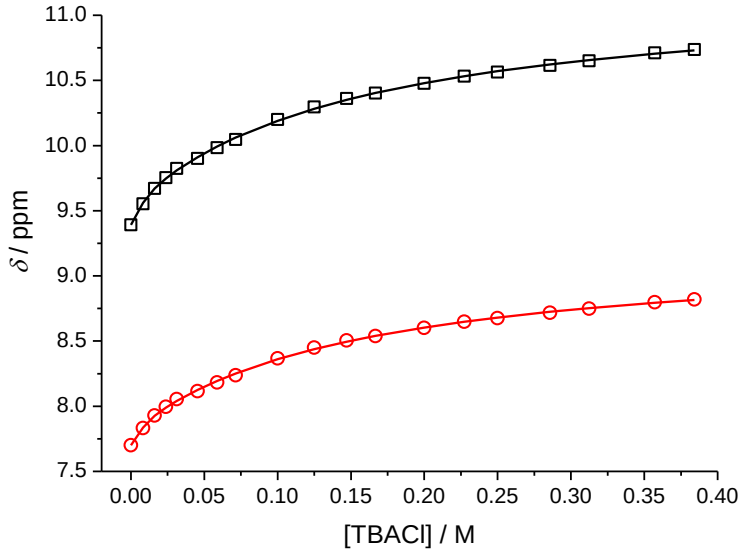

Figure 7.105 Chemical shifts of two thiourea NH protons of **A14** (10 mM) with increasing concentration of TBACl in DMSO-d_6 containing 0.5% (v%) H_2O at 293 K. The data were fitted to a 1:2 (host to guest) binding model, giving K_1 = 535 M^{-1}, and K_2 = 6.16 M^{-1}.

7.5.3.2 Interaction of A2 with TBACl

To investigate the existence of possible CH hydrogen bond between the *N*–CH_3 group of **A2** and chloride, the ^{1}H NMR spectra of **A2** (10 mM) in $CDCl_3$ were recorded in the absence and presence of TBACl (50 mM). Figure 7.106 shows the downfield shift of N–CH_3 resonance upon the addition of TBACl, supporting involvement of weak C–H···Cl^- hydrogen bonding.

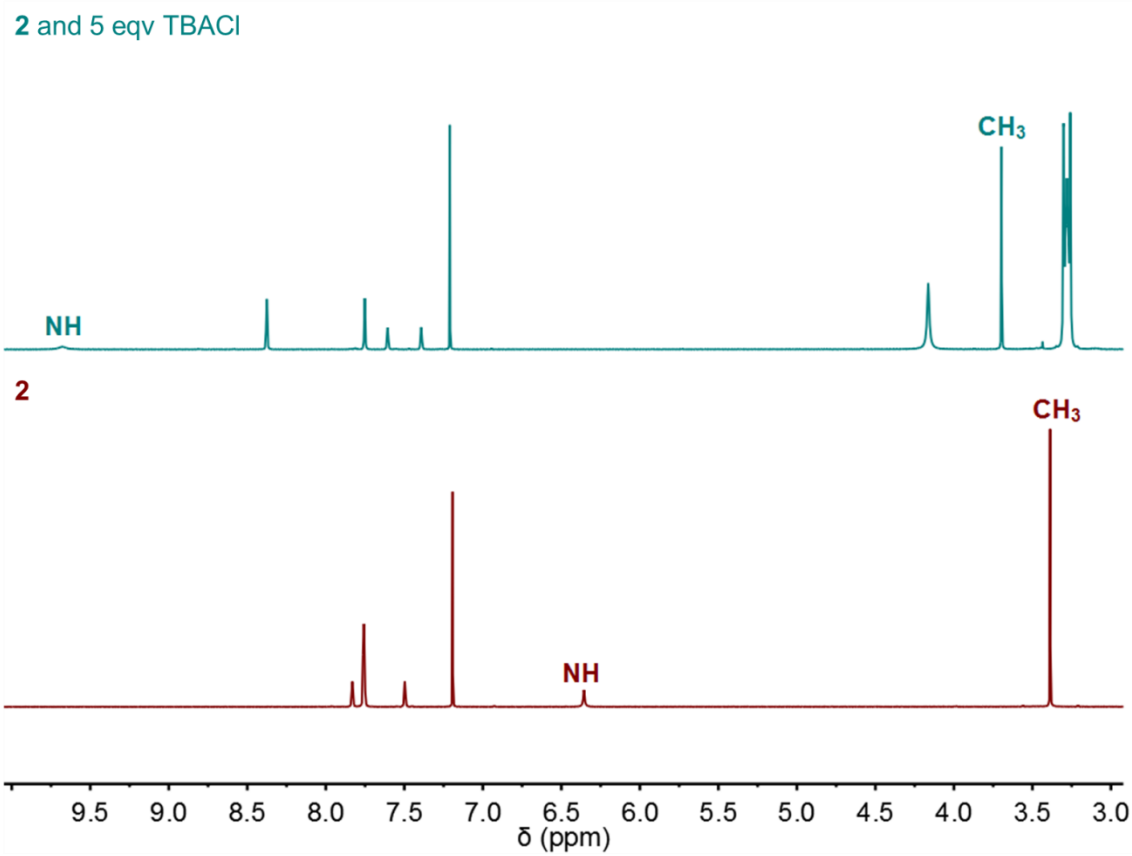

Figure 7.106 ^{1}H NMR spectra of **A2** (10 mM) in the absence and presence of TBACl (50 mM) in $CDCl_3$ at 293 K.

7.5.4 pK_a determination

Potentiometric titration methods were employed to determine pK_a values of **A4**, **A5** and **A10**. To a solution of the tested compound (~1 mM) in acetonitrile/H_2O (9:1, v:v, with 0.1 M $TBAPF_6$) was added increments of TBAOH (using a 0.125 M solution in the same solvent mixture), and the pH of the solution was recorded after each addition. The equivalence point (where the concentration of the compound tested equals that of TBAOH) was determined by finding the point where the second derivative of pH vs V_{TBAOH} passes through zero, and the pK_a value was the pH corresponding to the half-equivalence point.

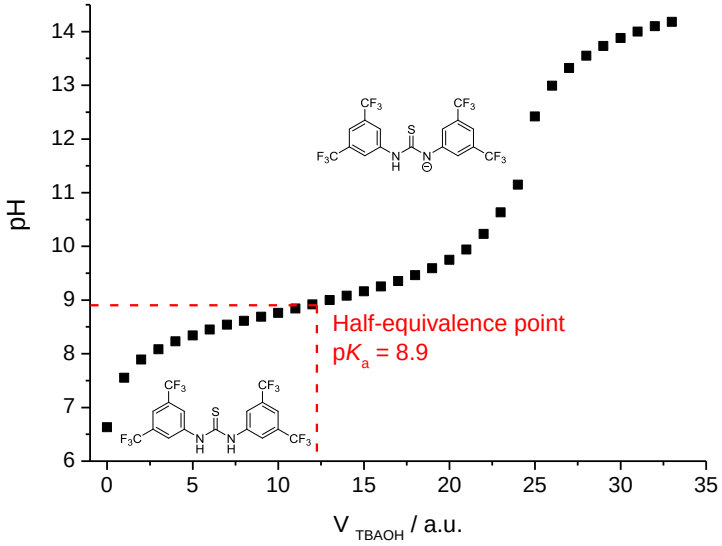

Figure 7.107 Determination of pK_a of **A4** by potentiometric titration in acetonitrile/H_2O (9:1, v:v, with 0.1 M $TBAPF_6$).

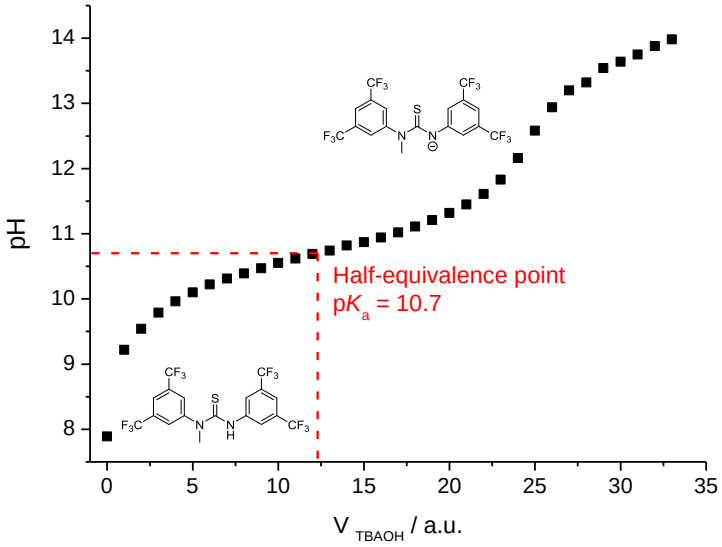

Figure 7.108 Determination of pK_a of **A5** by potentiometric titration in acetonitrile/H_2O (9:1, v:v, with 0.1 M $TBAPF_6$).

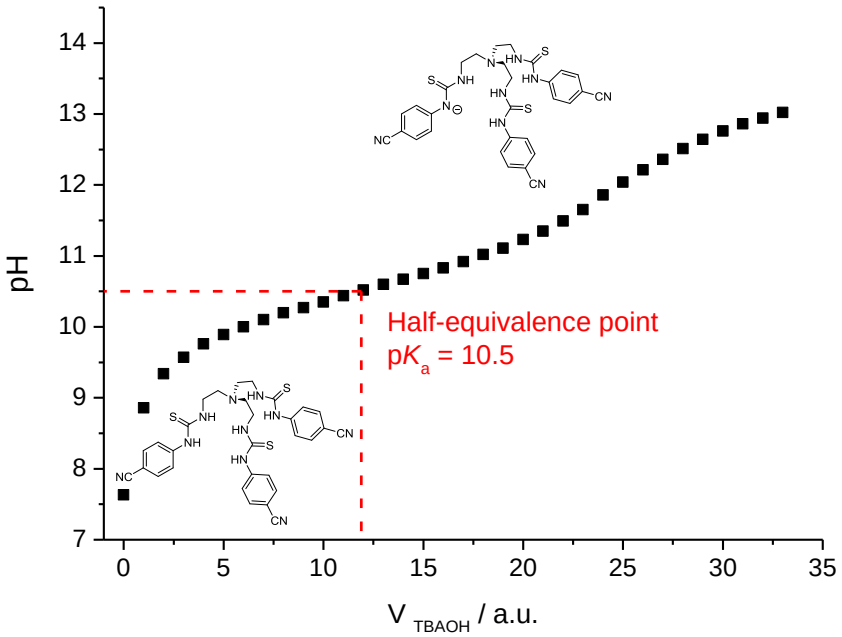

Figure 7.109 Determination of pK_a of **A10** by potentiometric titration in acetonitrile/H_2O (9:1, v:v, with 0.1 M $TBAPF_6$).

7.5.5 Computation studies

The electrostatic potential at nucleus R_A is given by the following equation:[255]

$$V_{R_A} = \sum_{i \neq A} \frac{Z_i}{|R_i - R_A|} - \int \frac{\rho(r)}{|r - R_A|} \mathrm{d}\tau$$

The structures of **A1**-**A6** were initially optimized by semi-empirical PM6 methods,[274] starting with the *syn* conformation. The EPN values were then calculated using DFT at the B3LYP/6-311++G(d,p)[275] level of theory with the SMD[276] water solvation model. All calculations were performed using the Gaussian 09 software package, revision B.01.[277]

The structures of chloride complexes of **A13** and **A14** were optimized with semi-empirical PM6 methods.[274]. All calculations were performed using the Gaussian 09 software package, revision B.01.[277]

7.5.6 X-ray crystallography

(This section was contributed by ENWH)

Single crystals of TEACl complex of **A12** were obtained by slow diffusion of diethyl ether into a DCM solution of **A12** in the presence of TEACl. The X-ray diffraction data was collected on a Rigaku AFC12 goniometer equipped with an enhanced sensitivity (HG) Saturn724+ detector mounted at the window of an FR-E+ Superbright MoKα (λ=0.71075 Å) rotating anode generator with HF Varimax optics, using the CrystalClear-SM Expert 3.1 b27 (Rigaku, 2013) software. Data set was collected at 100 K using an Oxford Cryostream low temperature device. Data reduction and cell refinement was carried out using CrysAlisPro (Version 1.171.37.31, Agilent Technologies). The structure was solved by direct methods as implemented in SHELXT[278] and refined by full-matrix least-squares refinements using SHELXL[279] to the final *R* value, carried out using the OLEX2 (Version 1.2.7) software[280]. All non-hydrogen atoms were refined with anisotropic displacement parameters. Most hydrogen atoms were added at calculated positions and refined using a riding model with isotropic displacement parameters based on the equivalent isotropic displacement parameters (U_{eq}) of the parent atom. The hydrogen atoms on the nitrogen atoms were assigned manually from the observed electron density peaks and refined with isotropic displacement parameters. C1, C9 and C17 are disordered over two positions; as such these atoms were refined with EADP constraint anisotropically, with occupancies of 0.78 and 0.22 respectively.

Crystal data for **A12**·TEACl complex: $C_{24}H_{51}N_7S_3 \cdot C_8H_{20}NCl$, crystal size = 0.06 × 0.05 × 0.04 mm^3, clear colourless block, monoclinic, space group: *P* $2_1/c$, *a* = 10.6344(3) Å, *b* = 35.5597(7) Å, *c* = 10.6467(3) Å, α = 90°, β = 106.039(3)°, γ = 90°, *V* = 3869.39 $Å^3$, *Z* = 4, R_1 = 4.03%. The CIF has been deposited in the Cambridge Crystallographic Database Centre (CCDC number 1431251).

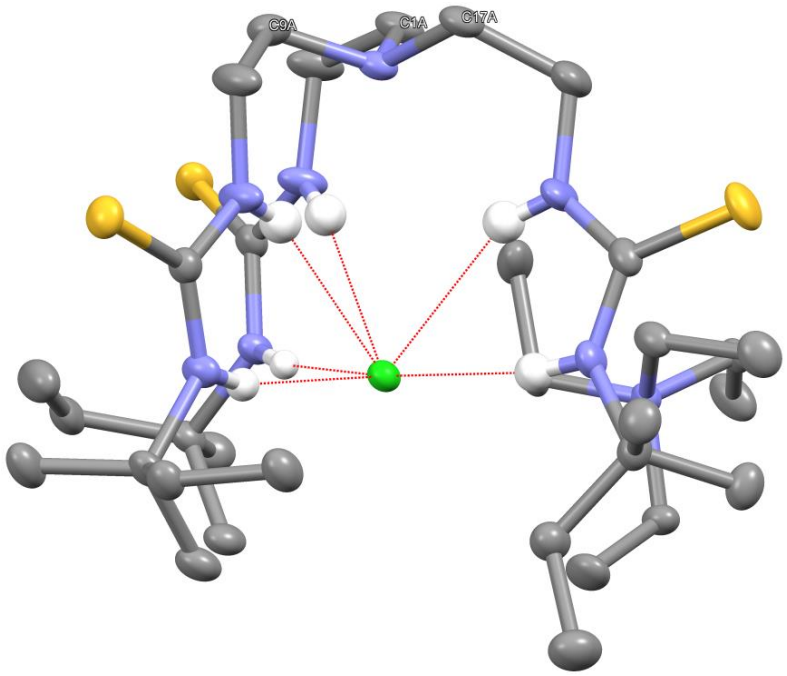

Figure 7.110 Crystal structure of **A12**·TEACl complex with thermal ellipsoids shown at 50% probability at 100 K. Non-hydrogen bonding hydrogen atoms are omitted for clarity. Atom colours: C (gray), H (white), N (blue), S (yellow), and Cl (green).

7.5.7 HPTS assays

7.5.7.1 General

Base-pulse HPTS assays[182] were conducted using POPC LUVs (mean diameter 200 nm) loaded with the pH sensitive fluorescence dye HPTS (1 mM). The HPTS-loaded POPC LUVs were prepared as follows. A chloroform solution of POPC was evaporated in a round-bottle flask and the lipid film formed was dried under vacuum for at least 6 h. The lipid film was hydrated by vortexing with a HPTS (1 mM) containing internal solution. The lipid solution was subjected to nine freeze/thaw cycles and then extruded 25 times through a 200 nm polycarbonate membrane. The unentrapped HPTS was removed by size exclusion chromatography on a Sephadex G-25 column using a HPTS-free external solution as the eluent.

The internal and external solutions used are identical salt solution (sodium gluconate, NMDG-Cl, $(NMDG)_2SO_4$, potassium gluconate or KCl, depending on the assay) buffered with 10 mM HEPES at pH 7.0 (except that the external solution does not contain HPTS). For each measurement, a concentrated vesicle stock solution (lipid concentration ~10 mM) was diluted using the external solution to obtain a 2 mL solution containing 0.1 mM of lipid. To this solution was added a base pulse (20 µL of 0.5 M TBAOH, NaOH, KOH or NMDG, depending on the assay, final base concentration 5 mM) to generate a transmembrane pH gradient. At the beginning of each measurement, 10 µL of a DMSO solution (except in the cases of trihexylamine and iodine where ethanol and acetonitrile solutions were used, respectively) of the tested carrier were added, and the ratiometric fluorescence of HPTS (λ_{ex} = 460 nm, λ_{em} = 510 nm, base form divided by λ_{ex} = 403 nm, λ_{em} = 510 nm, acid form) was recorded. In the cases when an assisting ionophore (gramicidin D, CCCP or valinomycin) was used, the assisting ionophore (as a 4 µL DMSO solution except in the case of experiments with iodine where a 4 µL acetonitrile solution was used) was added to the vesicle solution after the addition of base pulse and prior to the addition of the tested carrier. At 200 s, a detergent (20 µL of 11% (w%) Triton X-100 in 7 : 1 (v/v) H_2O-DMSO) was added to destroy the pH gradient for calibration. The results are the average over at least two repeats. The fractional fluorescence intensity (I_f) is calculated using the following equation:

$$I_f = \frac{R_\mathrm{t} - R_0}{R_\mathrm{d} - R_0}$$

where R_t is the fluorescence ratio at time t, R_0 is the fluorescence ratio at time 0, and R_d is the fluorescence ratio after detergent addition.

In some assays, Hill plot analyses were performed with the tested carrier loaded at different concentrations. The fractional fluorescence intensity I_f at 200s was plotted as a function of the compound concentration. Hill coefficients (n) and EC_{50} (200 s) values were calculated by fitting the curves to the following equation:

$$y = y_0 + (y_\mathrm{max} - y_0)\frac{x^n}{K + x^n}$$

where y is I_f (200 s) value with the carrier loaded at concentration x, y_0 is I_f (200 s) value obtained without the carrier, y_{max} is the maximum I_f value, n is the Hill coefficient, and K is the EC_{50} (200 s) value. The carrier concentration is expressed as carrier to lipid molar ratio.

7.5.7.2 TBAOH assay

7.5.7.2.1 Method

Conditions: Internal and external solutions (excluding HPTS): 100 mM sodium gluconate, buffered at pH 7.0 with 10 mM HEPES; Base pulse: 5 mM TBAOH.

Rationale: This assay is intended to evaluate the activity of the tested compound in facilitating *electrogenic* H^+/OH^- transport. In the presence of membrane permeable TBA^+ ion, the tested compound only needs to facilitate electrogenic H^+/OH^- transport to dissipate the pH gradient. As no Cl^- or other transportable anions are present, a carrier that cannot facilitate electrogenic transport of H^+/OH^- (but only facilitates electroneutral H^+/Cl^- symport or Cl^-/OH^- antiport) cannot couple to electrogenic diffusion of TBA^+ and therefore gives no response in this assay.

7.5.7.2.2 Hill plots

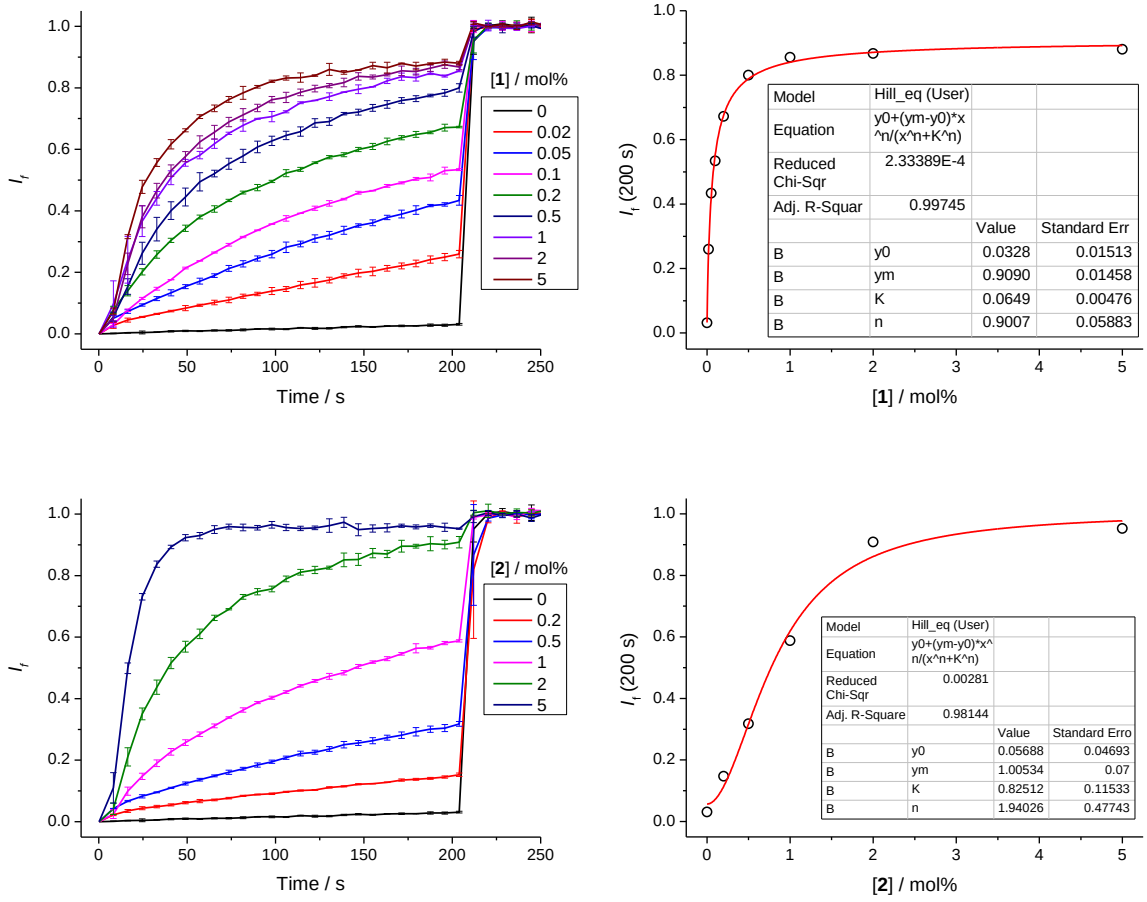

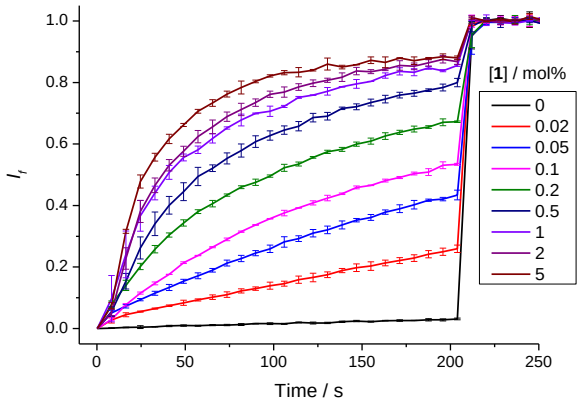

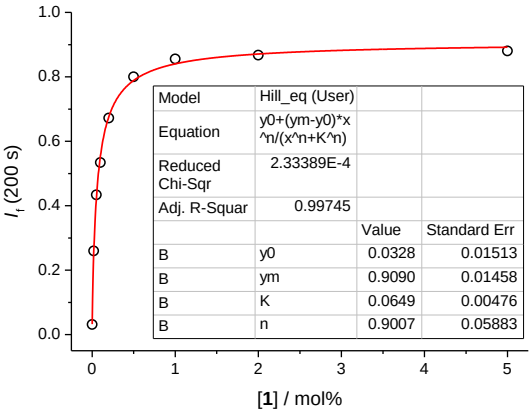

Model	Hill_eq (User)		
Equation	y0+(ym-y0)*x^n/(x^n+K^n)		
Reduced Chi-Sqr	2.33389E-4		
Adj. R-Squar	0.99745		
		Value	Standard Err
B	y0	0.0328	0.01513
B	ym	0.9090	0.01458
B	K	0.0649	0.00476
B	n	0.9007	0.05883

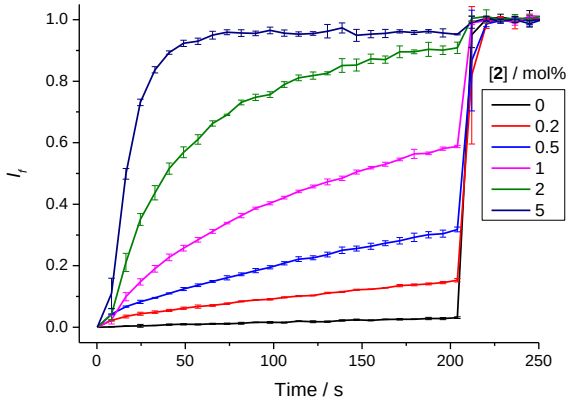

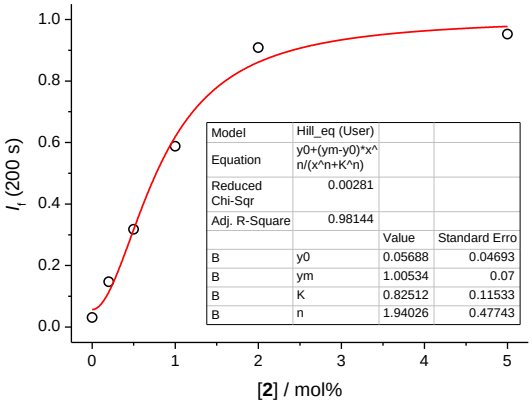

Model	Hill_eq (User)		
Equation	y0+(ym-y0)*x^n/(x^n+K^n)		
Reduced Chi-Sqr	0.00281		
Adj. R-Square	0.98144		
		Value	Standard Erro
B	y0	0.05688	0.04693
B	ym	1.00534	0.07
B	K	0.82512	0.11533
B	n	1.94026	0.47743

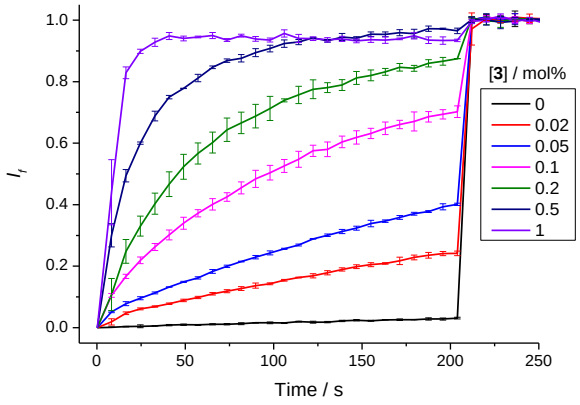

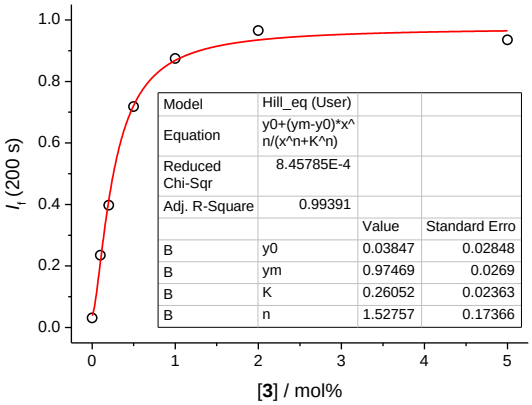

Model	Hill_eq (User)		
Equation	y0+(ym-y0)*x^n/(x^n+K^n)		
Reduced Chi-Sqr	8.45785E-4		
Adj. R-Square	0.99391		
		Value	Standard Erro
B	y0	0.03847	0.02848
B	ym	0.97469	0.0269
B	K	0.26052	0.02363
B	n	1.52757	0.17366

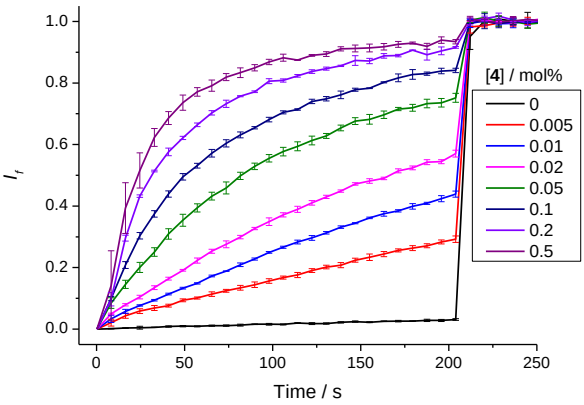

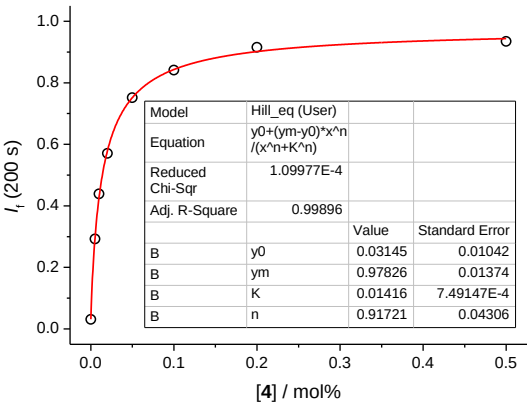

Model	Hill_eq (User)		
Equation	y0+(ym-y0)*x^n/(x^n+K^n)		
Reduced Chi-Sqr	1.09977E-4		
Adj. R-Square	0.99896		
		Value	Standard Error
B	y0	0.03145	0.01042
B	ym	0.97826	0.01374
B	K	0.01416	7.49147E-4
B	n	0.91721	0.04306

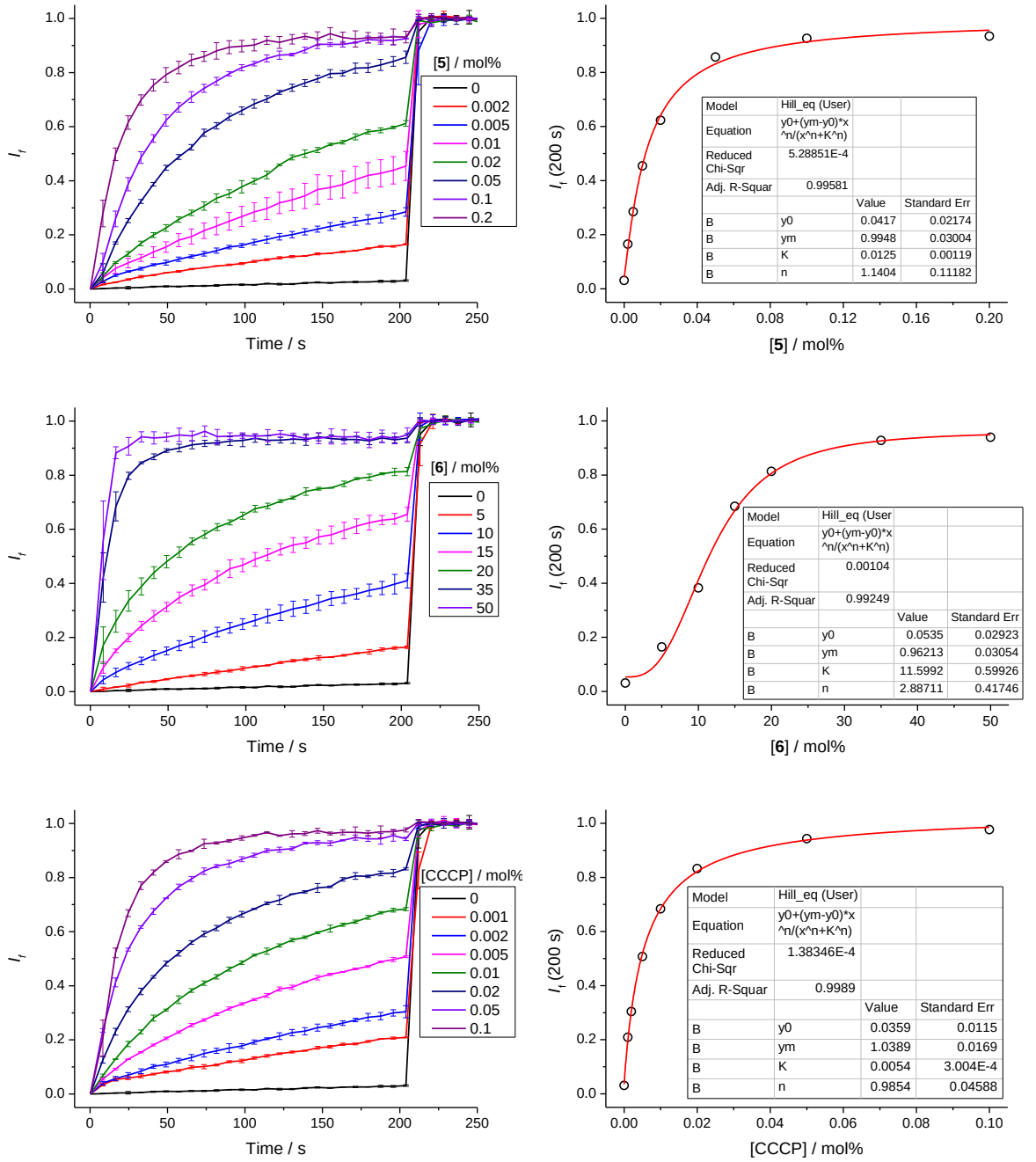

Figure 7.111 Hill plot analyses of electrogenic H^+/OH^- transport facilitated by compounds **A1-A6** and CCCP using TBAOH assay. Carrier concentrations are shown as carrier to lipid molar ratios. Error bars represent SD from two or three repeats.

Prodigiosin was found to significantly interfere with HPTS fluorescence above 1 mol%. Refer to Figure 7.112b in which an increase of I_{460}/I_{406} was observed even without the base pulse to generate a pH gradient, and therefore the prodigiosin-induced HPTS response observed in Figure 7.112a arises from interference instead of from ion transport. Since prodigiosin can facilitate H^+/Cl^- symport at lower loadings (EC_{50} = 0.000059 mol% in NMDG-Cl assay) while no electrogenic H^+/OH^- transport even at 1 mol% loading, its effect is hence confirmed to be electrically silent.

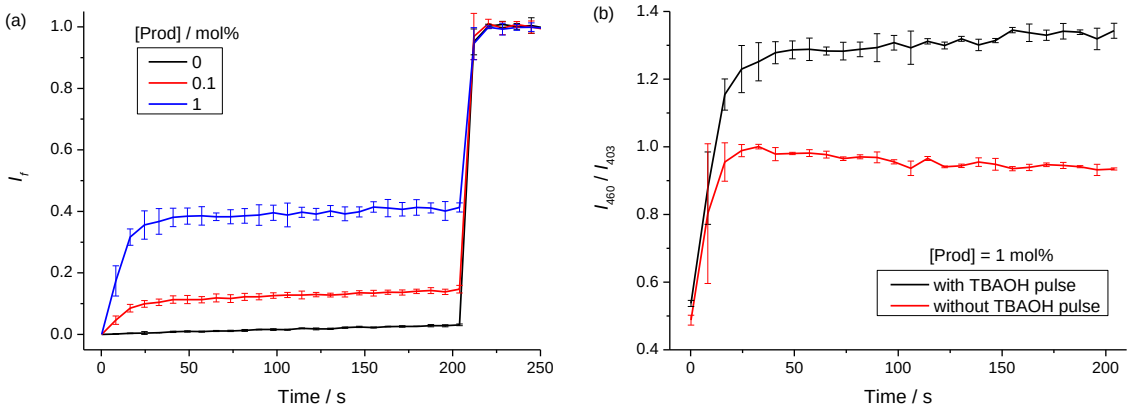

Figure 7.112 (a) Normalized HPTS response induced by prodigiosin in TBAOH assay. (b) Ratiometric HPTS response (λ_{em} = 510 nm, λ_{ex} = 460/403 nm) induced by prodigiosin (1 mol%) in the absence and presence of TBAOH (5 mM) pulse. Carrier concentrations are shown as carrier to lipid molar ratios. Error bars represent SD from two or three repeats.

Table 7.1 Hill plot analyses of anionophores **A1**-**A6**, prodigiosin (Prod), and CCCP in the TBAOH assay. Hill coefficients (*n*) and effective concentrations to reach 50% transport at 200 s (EC_{50}) were obtained by fitting the I_f (200 s) vs carrier concentration curve to the Hill equation. Carrier concentrations are shown as carrier to lipid molar ratios.

	n	EC_{50} (mol%)
A1	0.90 ± 0.06	0.065 ± 0.005
A2	1.9 ± 0.5	0.83 ± 0.11
A3	1.5 ± 0.2	0.26 ± 0.02
A4	0.92 ± 0.04	0.014 ± 0.001
A5	1.1 ± 0.1	0.013 ± 0.001
A6	2.9 ± 0.4	12 ± 0.6
Prodigiosin	-[a]	> 1[a]
CCCP	1.0 ± 0.0	0.0054 ± 0.0003

[a] No transport at 1 mol% loading. Higher loadings not tested due to interference with HPTS fluorescence.

7.5.7.2.3 Control experiments

NaOH pulse

To rule out other processes that may lead to HPTS response, including Na^+/H^+ antiport, Na^+/OH^- symport, gluconate/OH^- antiport, gluconate/H^+ symport, HPTS leakage, membrane instability and carrier interference with HPTS fluorescence, NaOH instead of TBAOH was used as the base pulse, and carrier-induced HPTS response was recorded, with the other conditions kept the same as in the TBAOH assay. The results show that in the absence of TBA^+, the HPTS response was negligible or minor compared to when TBA^+ was used, confirming that any of the abovementioned processes is negligible or insignificant.

Conditions: Internal and external solution (excluding HPTS): 100 mM sodium gluconate, buffered at pH 7.0 with 10 mM HEPES; Base pulse: 5 mM NaOH.

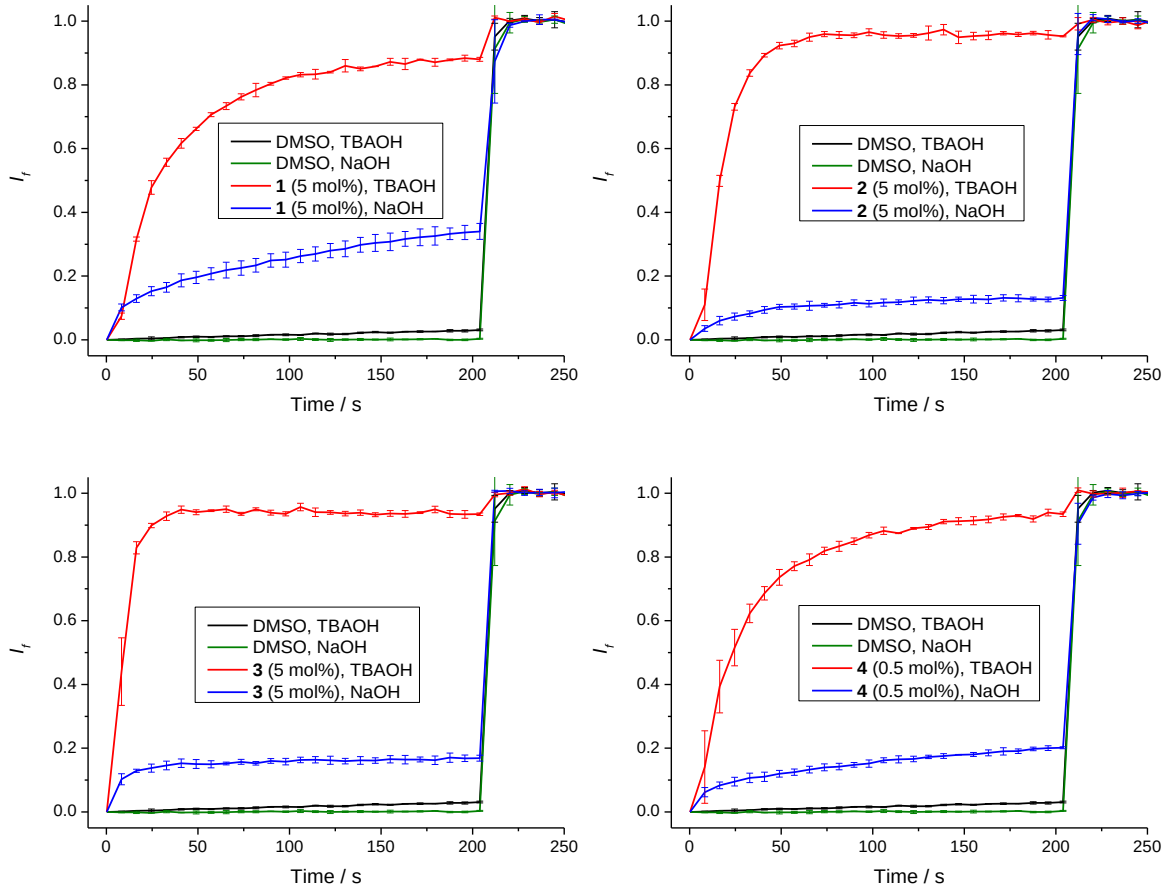

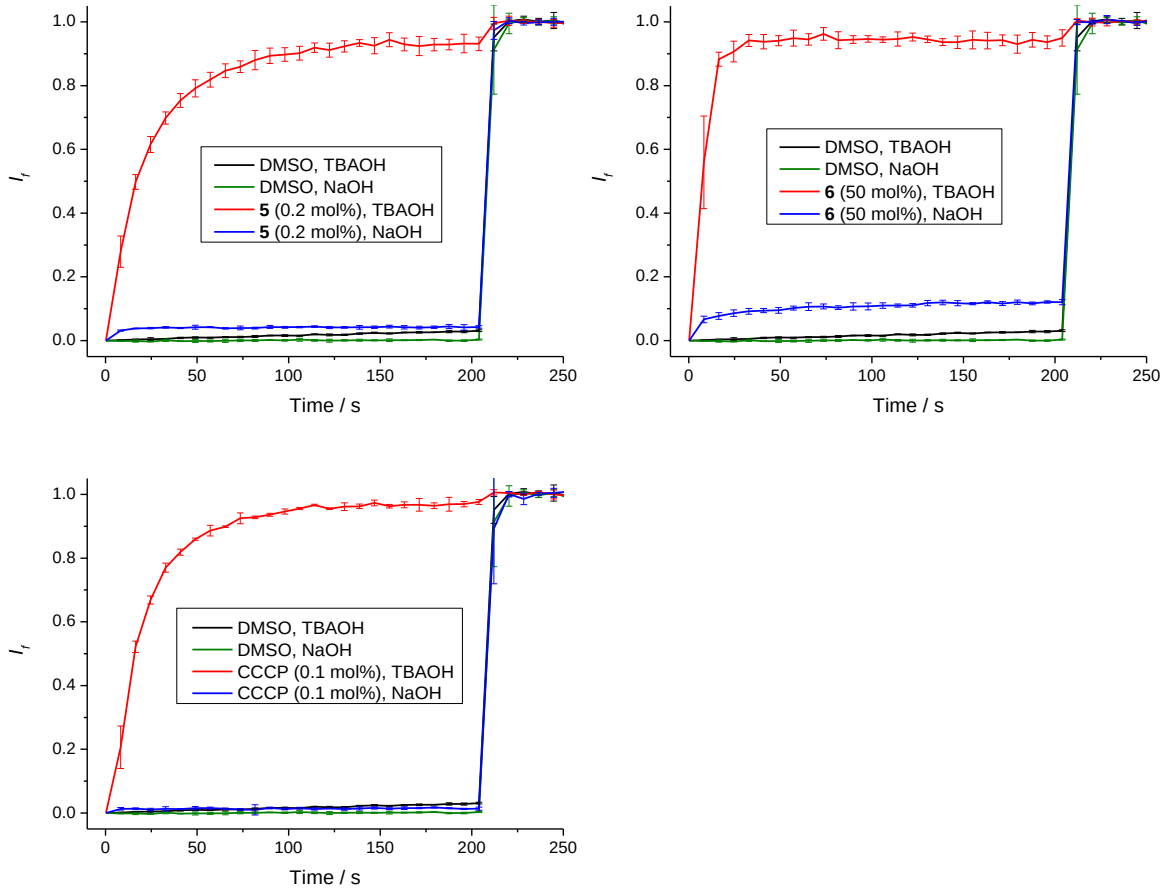

Figure 7.113 Control experiments for TBAOH assay. NaOH (5 mM) instead of TBAOH was used as the base pulse, and the results were compared to those obtained using TBAOH (5 mM) as the base pulse. Carrier concentrations are shown as carrier to lipid molar ratios. The same DMSO controls are used in all figures. Error bars represent SD from two or three repeats.

Effect of buffer agent

Another possibility that may lead to dissipation of the pH gradient in TBAOH assay is $TBA^+/HEPES^-$ symport. This cannot be excluded using the NaOH pulse control experiment described above. To examine this possibility, TBAOH assay was conducted with the external buffer agent changed to phosphate salts, with **A1** and **A6** tested as representative examples. In this case, apart from the assumed process TBA^+/H^+ antiport (or TBA^+/OH^- symport) and other processes that have already been ruled out, the only available pathways to dissipate the pH gradient are TBA^+/HPO_4^{2-} symport and TBA^+/PO_4^{3-} symport. Transport of basic phosphate species including HPO_4^{2-} and PO_4^{3-} is less likely than $HEPES^{--}$ transport due to their high hydrophilicity. If the dissipation of the pH gradient observed in the TBAOH assay is due to $TBA^+/HEPES^-$ symport, the rate of transport will decrease when the external buffer agent is changed from HEPES to phosphate. The results show no influence by change of the external buffer agent, indicating buffer agent transport unlikely. Refer to Section 7.5.9.1 for unambiguous evidence of H^+/OH^- transport that rules out buffer agent transport.

Conditions: Internal solution: 1 mM HPTS, 100 mM sodium gluconate, buffered at pH 7.0 with 10 mM HEPES; External solution: 100 mM sodium gluconate, buffered at pH 7.0 with 14 mM sodium phosphate salts; Base pulse: 5 mM TBAOH.

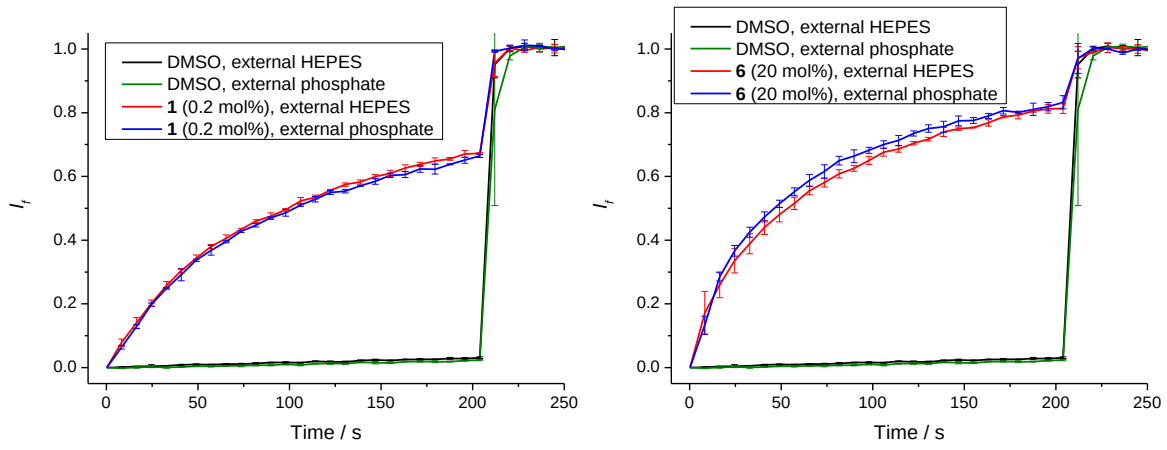

Figure 7.114 Effect of external buffer agent on HPTS response induced by **A1** (0.2 mol%) or **A6** (20 mol%) in TBAOH assay. Carrier concentrations are shown as carrier to lipid molar ratios. The same DMSO controls are used in both figures. Error bars represent SD from two or three repeats.

7.5.7.3 NMDG-Cl assay

7.5.7.3.1 Method

Conditions: Internal and external solutions (excluding HPTS): 100 mM NMDG-Cl, buffered at pH 7.0 with 10 mM HEPES; Base pulse: 5 mM NMDG.

Rationale: This assay is intended to evaluate the chloride transport activity and Cl^- > H^+/OH^- selectivity of the tested compound. The pH gradient after addition of NMDG (5 mM) can be dissipated by H^+/Cl^- symport or functionally equivalent Cl^-/OH^- antiport. The effect of proton channel gramicidin D (0.1 mol%) on the rate of pH gradient dissipation induced by the tested carrier is monitored. If H^+/OH^- transport is the rate-limiting process in H^+/Cl^- symport or Cl^-/OH^- antiport, *i.e.*, the carrier shows Cl^- > H^+/OH^- selectivity, the HPTS response will be accelerated by gramidicin that facilities electrogenic proton transport. Conversely, if H^+/OH^- transport is faster than Cl^- transport, the rate of HPTS response will be unaffected by gramidicin. The ratio between EC_{50} values obtained in the absence and presence of gramicidin (S-value shown in Table 7.2) is used to quantify the Cl^- > H^+/OH^- selectivity. The EC50 value obtained in the presence of gramicidin is used to evaluate chloride transport activity, as under this condition the tested carrier only needs to facilitate chloride transport to dissipate the pH gradient with proton permeation facilitated by gramicidin channel. Note that the background change in HPTS fluorescence is due to simple diffusion of neutral form of NMDG that slowly dissipates the pH gradient. Control experiments with $(NMDG)_2SO_4$ (Figure 7.116) show that none of the tested anionophores accelerated this process.

7.5.7.3.2 Hill plots

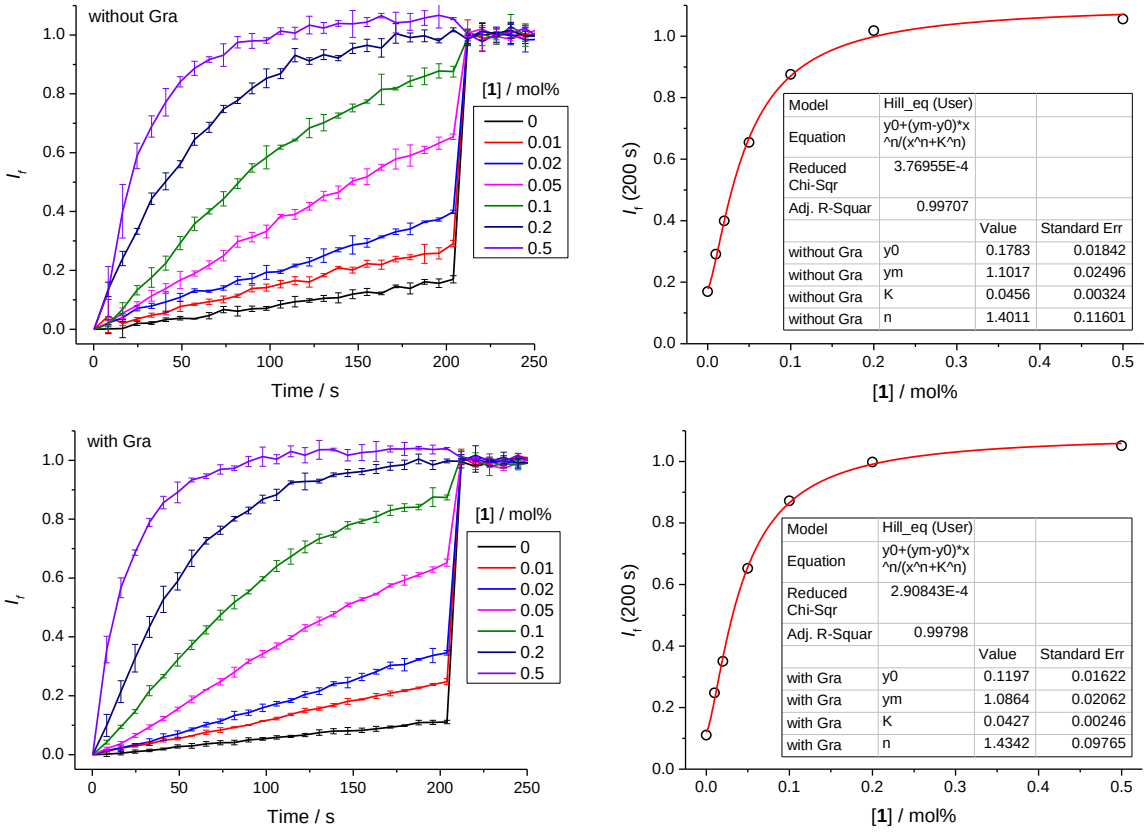

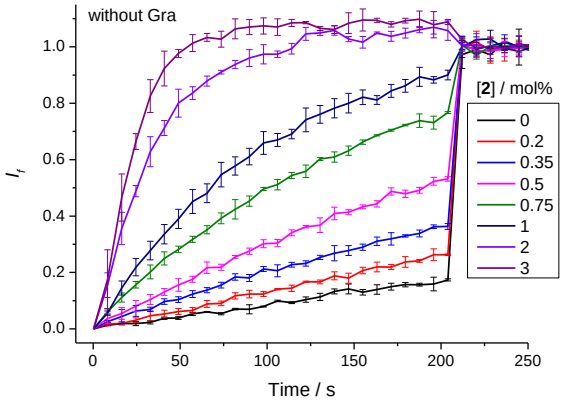
without Gra
[2] / mol%
0
0.2
0.35
0.5
0.75
1
2
3
I_f
Time / s

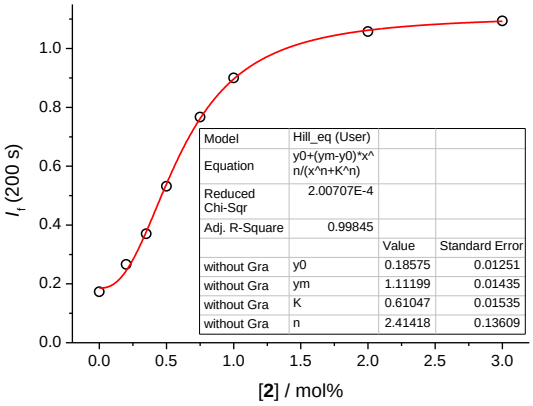
I_f (200 s)
[2] / mol%
Model Hill_eq (User)
Equation y0+(ym-y0)*x^n/(x^n+K^n)
Reduced Chi-Sqr 2.00707E-4
Adj. R-Square 0.99845
Value Standard Error
without Gra y0 0.18575 0.01251
without Gra ym 1.11199 0.01435
without Gra K 0.61047 0.01535
without Gra n 2.41418 0.13609

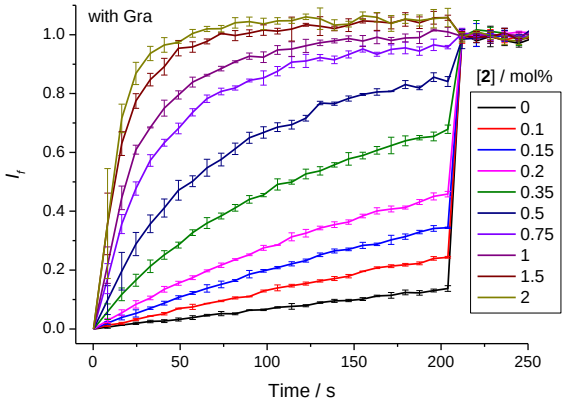
with Gra
[2] / mol%
0
0.1
0.15
0.2
0.35
0.5
0.75
1
1.5
2
I_f
Time / s

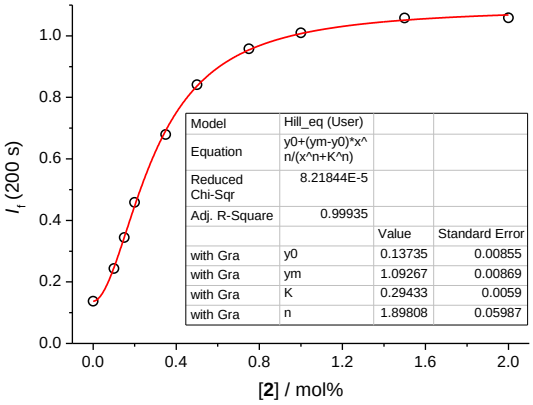
I_f (200 s)
[2] / mol%
Model Hill_eq (User)
Equation y0+(ym-y0)*x^n/(x^n+K^n)
Reduced Chi-Sqr 8.21844E-5
Adj. R-Square 0.99935
Value Standard Error
with Gra y0 0.13735 0.00855
with Gra ym 1.09267 0.00869
with Gra K 0.29433 0.0059
with Gra n 1.89808 0.05987

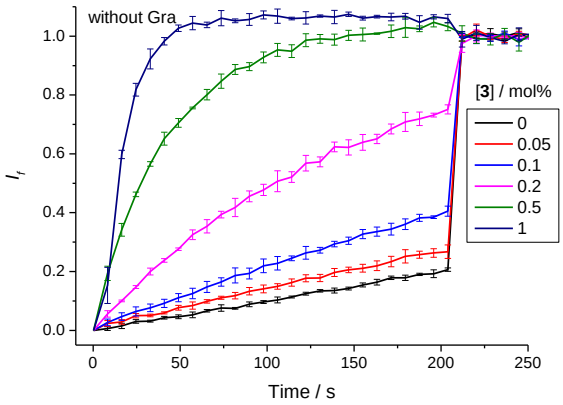
without Gra
[3] / mol%
0
0.05
0.1
0.2
0.5
1
I_f
Time / s

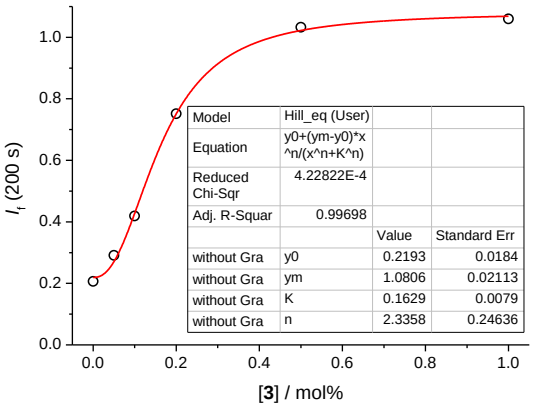
I_f (200 s)
[3] / mol%
Model Hill_eq (User)
Equation y0+(ym-y0)*x^n/(x^n+K^n)
Reduced Chi-Sqr 4.22822E-4
Adj. R-Squar 0.99698
Value Standard Err
without Gra y0 0.2193 0.0184
without Gra ym 1.0806 0.02113
without Gra K 0.1629 0.0079
without Gra n 2.3358 0.24636

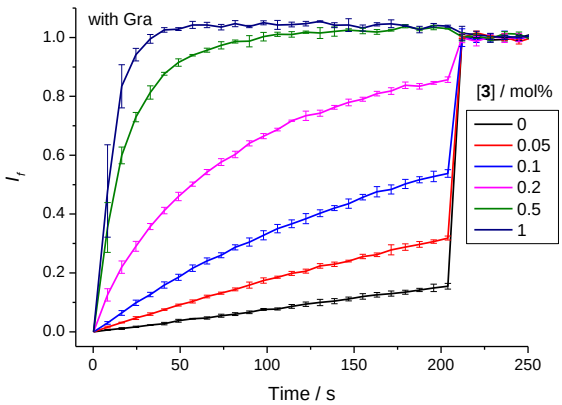
with Gra
[3] / mol%
0
0.05
0.1
0.2
0.5
1
I_f
Time / s

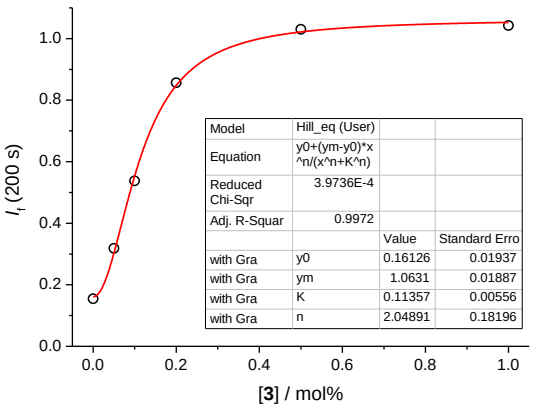
I_f (200 s)
[3] / mol%
Model Hill_eq (User)
Equation y0+(ym-y0)*x^n/(x^n+K^n)
Reduced Chi-Sqr 3.9736E-4
Adj. R-Squar 0.9972
Value Standard Erro
with Gra y0 0.16126 0.01937
with Gra ym 1.0631 0.01887
with Gra K 0.11357 0.00556
with Gra n 2.04891 0.18196

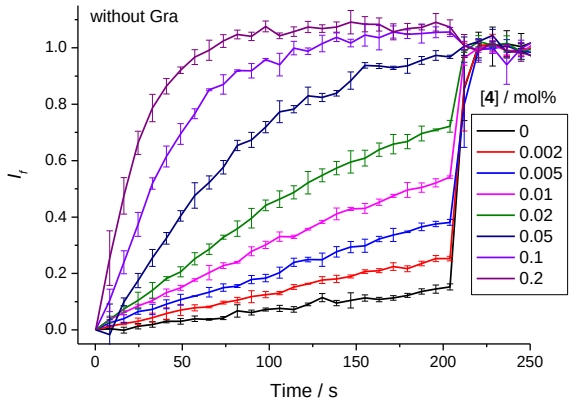

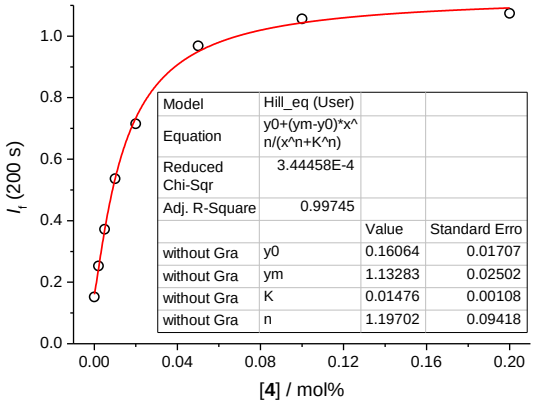

Model	Hill_eq (User)		
Equation	y0+(ym-y0)*x^n/(x^n+K^n)		
Reduced Chi-Sqr	3.44458E-4		
Adj. R-Square	0.99745		
		Value	Standard Erro
without Gra	y0	0.16064	0.01707
without Gra	ym	1.13283	0.02502
without Gra	K	0.01476	0.00108
without Gra	n	1.19702	0.09418

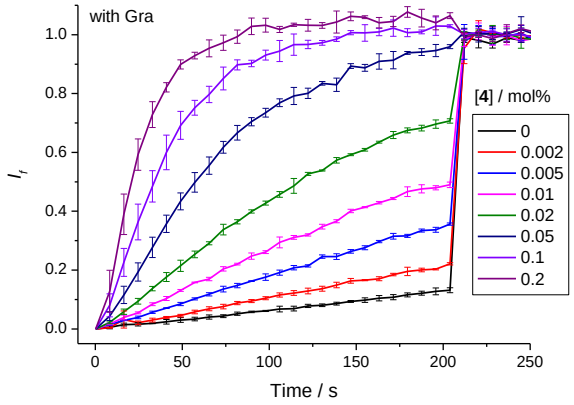

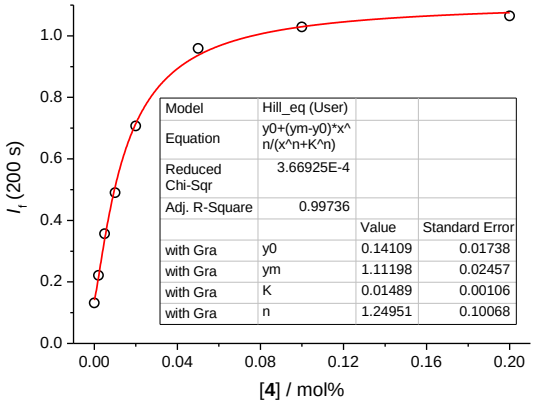

Model	Hill_eq (User)		
Equation	y0+(ym-y0)*x^n/(x^n+K^n)		
Reduced Chi-Sqr	3.66925E-4		
Adj. R-Square	0.99736		
		Value	Standard Error
with Gra	y0	0.14109	0.01738
with Gra	ym	1.11198	0.02457
with Gra	K	0.01489	0.00106
with Gra	n	1.24951	0.10068

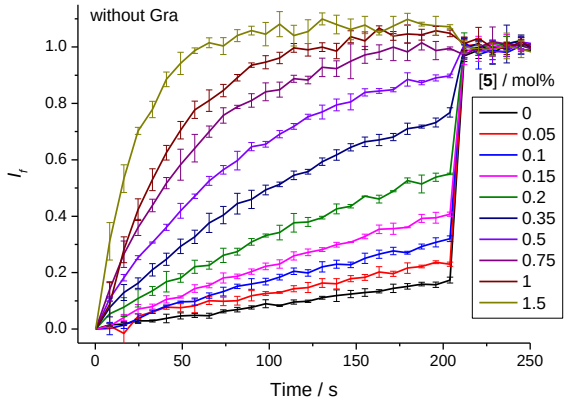

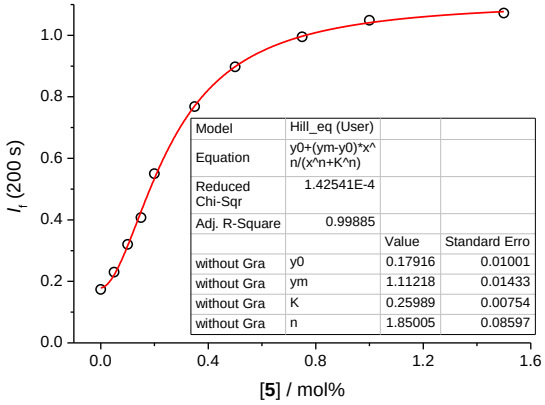

Model	Hill_eq (User)		
Equation	y0+(ym-y0)*x^n/(x^n+K^n)		
Reduced Chi-Sqr	1.42541E-4		
Adj. R-Square	0.99885		
		Value	Standard Erro
without Gra	y0	0.17916	0.01001
without Gra	ym	1.11218	0.01433
without Gra	K	0.25989	0.00754
without Gra	n	1.85005	0.08597

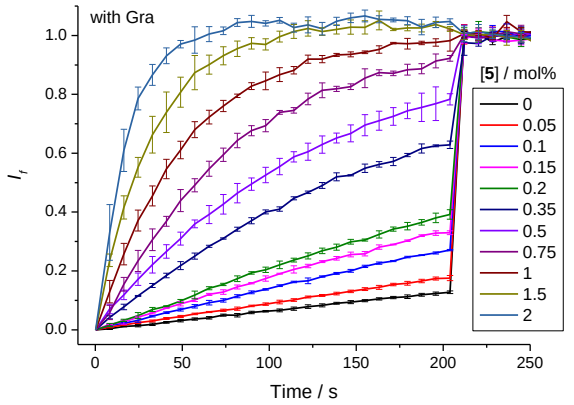

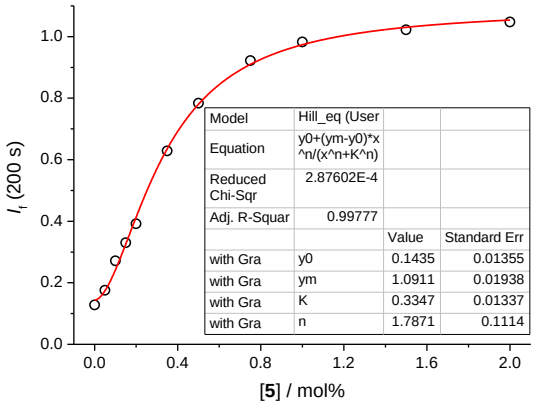

Model	Hill_eq (User		
Equation	y0+(ym-y0)*x^n/(x^n+K^n)		
Reduced Chi-Sqr	2.87602E-4		
Adj. R-Squar	0.99777		
		Value	Standard Err
with Gra	y0	0.1435	0.01355
with Gra	ym	1.0911	0.01938
with Gra	K	0.3347	0.01337
with Gra	n	1.7871	0.1114

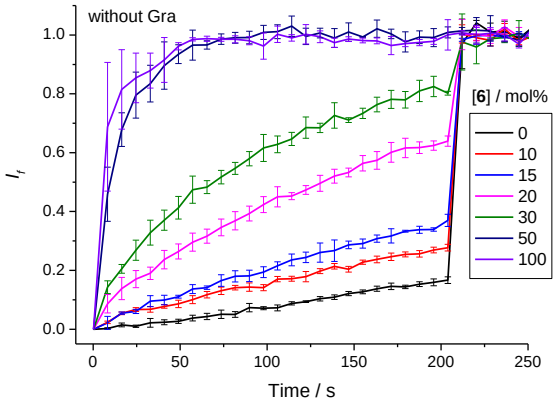
without Gra
[6] / mol%
0
10
15
20
30
50
100
I_f
Time / s

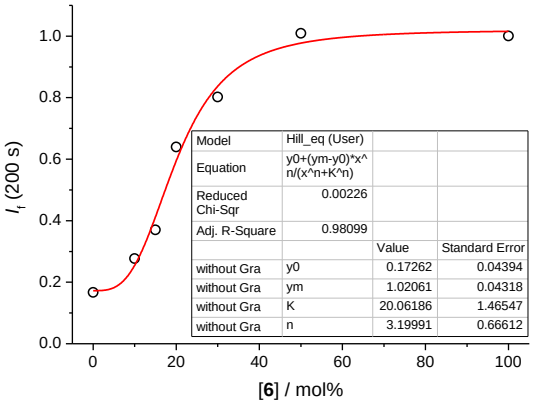
I_f (200 s)
[6] / mol%
Model Hill_eq (User)
Equation y0+(ym-y0)*x^n/(x^n+K^n)
Reduced Chi-Sqr 0.00226
Adj. R-Square 0.98099
Value Standard Error
without Gra y0 0.17262 0.04394
without Gra ym 1.02061 0.04318
without Gra K 20.06186 1.46547
without Gra n 3.19991 0.66612

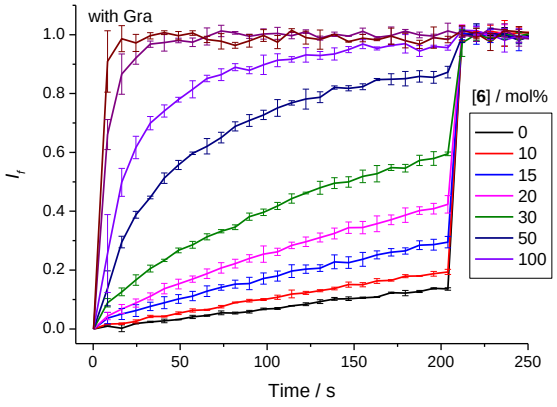
with Gra
[6] / mol%
0
10
15
20
30
50
100
I_f
Time / s

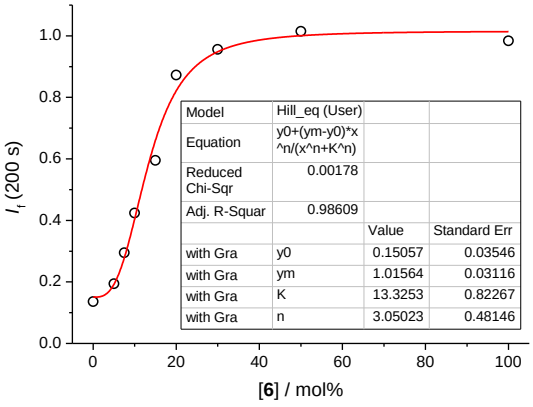
I_f (200 s)
[6] / mol%
Model Hill_eq (User)
Equation y0+(ym-y0)*x^n/(x^n+K^n)
Reduced Chi-Sqr 0.00178
Adj. R-Squar 0.98609
Value Standard Err
with Gra y0 0.15057 0.03546
with Gra ym 1.01564 0.03116
with Gra K 13.3253 0.82267
with Gra n 3.05023 0.48146

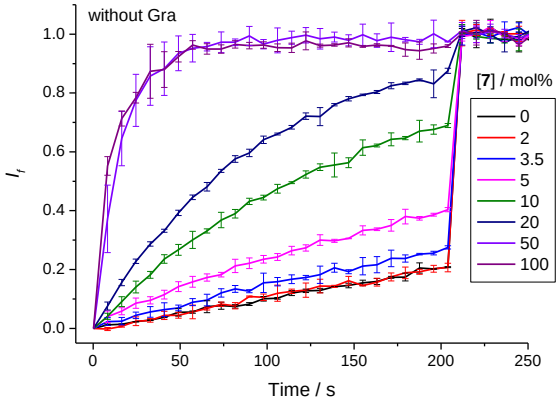
without Gra
[7] / mol%
0
2
3.5
5
10
20
50
100
I_f
Time / s

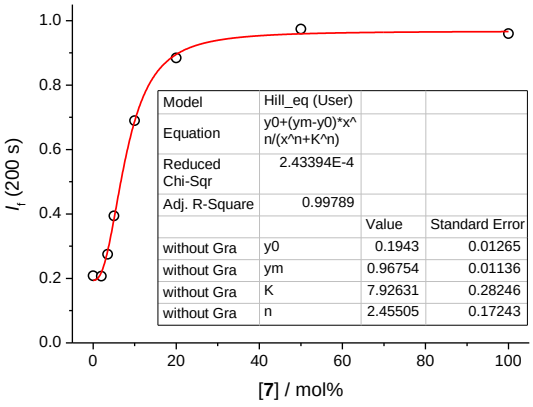
I_f (200 s)
[7] / mol%
Model Hill_eq (User)
Equation y0+(ym-y0)*x^n/(x^n+K^n)
Reduced Chi-Sqr 2.43394E-4
Adj. R-Square 0.99789
Value Standard Error
without Gra y0 0.1943 0.01265
without Gra ym 0.96754 0.01136
without Gra K 7.92631 0.28246
without Gra n 2.45505 0.17243

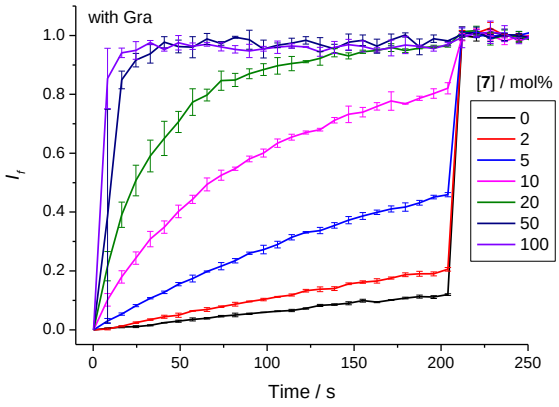
with Gra
[7] / mol%
0
2
5
10
20
50
100
I_f
Time / s

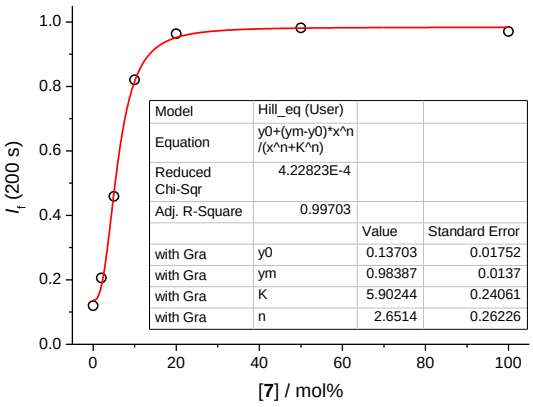
I_f (200 s)
[7] / mol%
Model Hill_eq (User)
Equation y0+(ym-y0)*x^n/(x^n+K^n)
Reduced Chi-Sqr 4.22823E-4
Adj. R-Square 0.99703
Value Standard Error
with Gra y0 0.13703 0.01752
with Gra ym 0.98387 0.0137
with Gra K 5.90244 0.24061
with Gra n 2.6514 0.26226

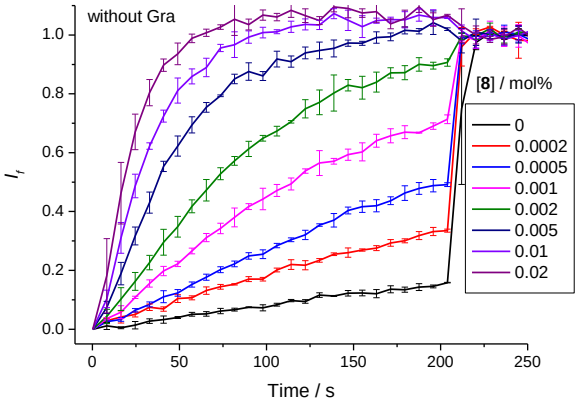

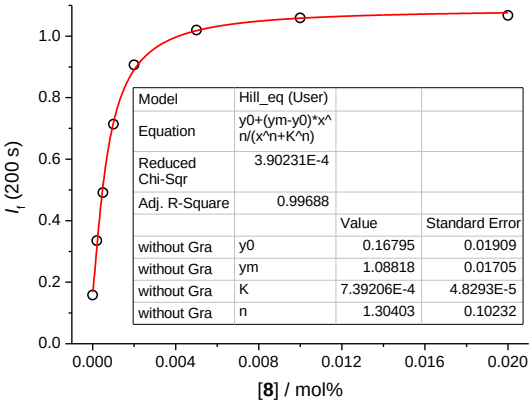

Model	Hill_eq (User)		
Equation	y0+(ym-y0)*x^n/(x^n+K^n)		
Reduced Chi-Sqr	3.90231E-4		
Adj. R-Square	0.99688		
		Value	Standard Error
without Gra	y0	0.16795	0.01909
without Gra	ym	1.08818	0.01705
without Gra	K	7.39206E-4	4.8293E-5
without Gra	n	1.30403	0.10232

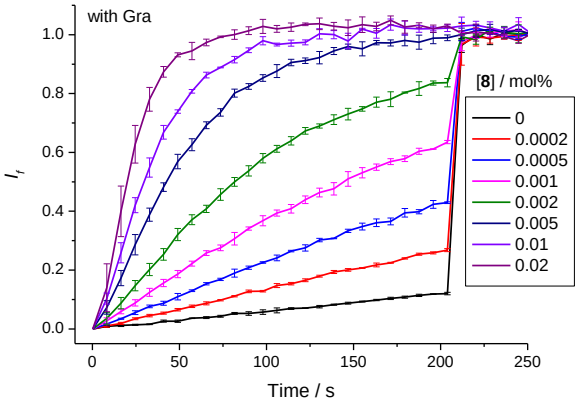

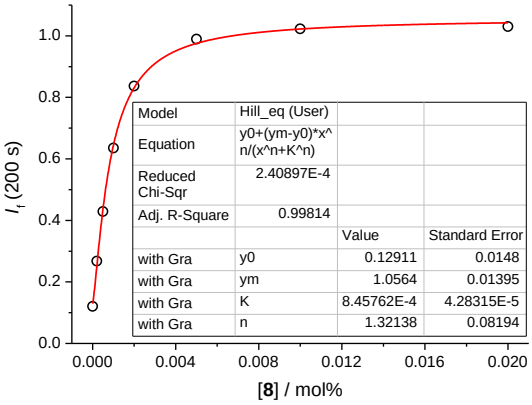

Model	Hill_eq (User)		
Equation	y0+(ym-y0)*x^n/(x^n+K^n)		
Reduced Chi-Sqr	2.40897E-4		
Adj. R-Square	0.99814		
		Value	Standard Error
with Gra	y0	0.12911	0.0148
with Gra	ym	1.0564	0.01395
with Gra	K	8.45762E-4	4.28315E-5
with Gra	n	1.32138	0.08194

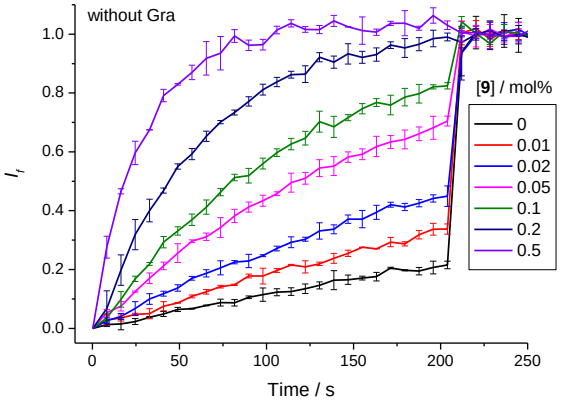

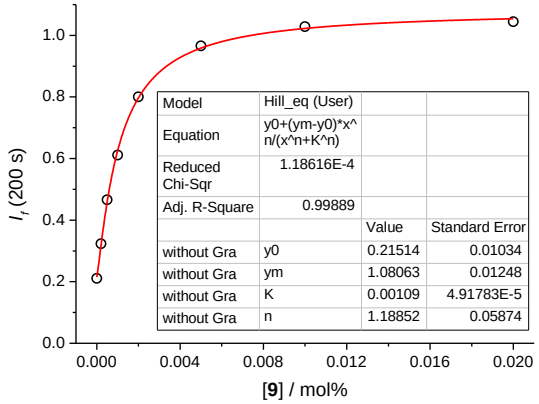

Model	Hill_eq (User)		
Equation	y0+(ym-y0)*x^n/(x^n+K^n)		
Reduced Chi-Sqr	1.18616E-4		
Adj. R-Square	0.99889		
		Value	Standard Error
without Gra	y0	0.21514	0.01034
without Gra	ym	1.08063	0.01248
without Gra	K	0.00109	4.91783E-5
without Gra	n	1.18852	0.05874

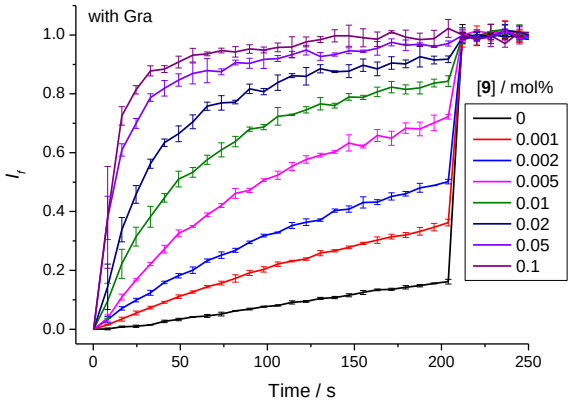

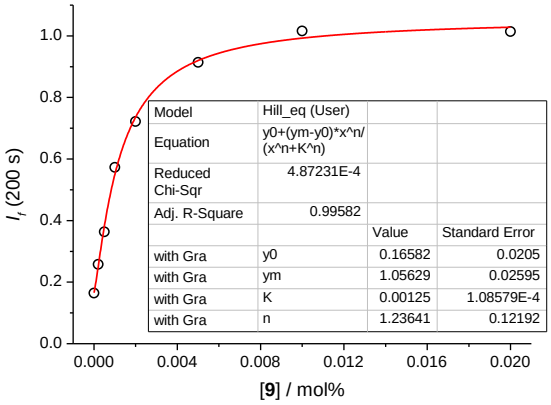

Model	Hill_eq (User)		
Equation	y0+(ym-y0)*x^n/(x^n+K^n)		
Reduced Chi-Sqr	4.87231E-4		
Adj. R-Square	0.99582		
		Value	Standard Error
with Gra	y0	0.16582	0.0205
with Gra	ym	1.05629	0.02595
with Gra	K	0.00125	1.08579E-4
with Gra	n	1.23641	0.12192

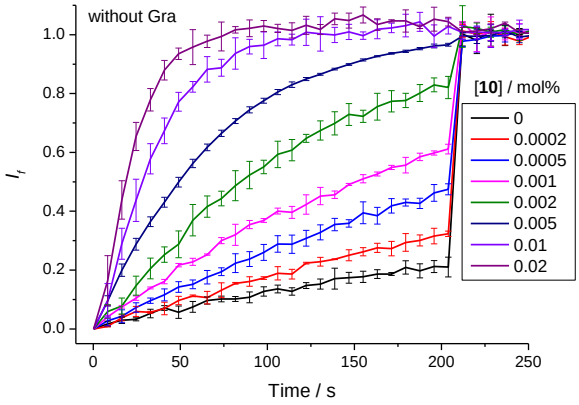

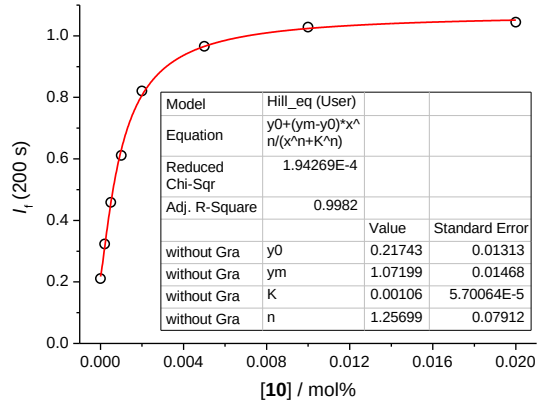

Model	Hill_eq (User)		
Equation	y0+(ym-y0)*x^n/(x^n+K^n)		
Reduced Chi-Sqr	1.94269E-4		
Adj. R-Square	0.9982		
		Value	Standard Error
without Gra	y0	0.21743	0.01313
without Gra	ym	1.07199	0.01468
without Gra	K	0.00106	5.70064E-5
without Gra	n	1.25699	0.07912

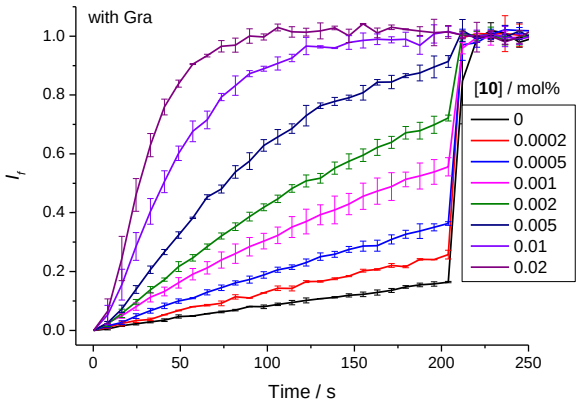

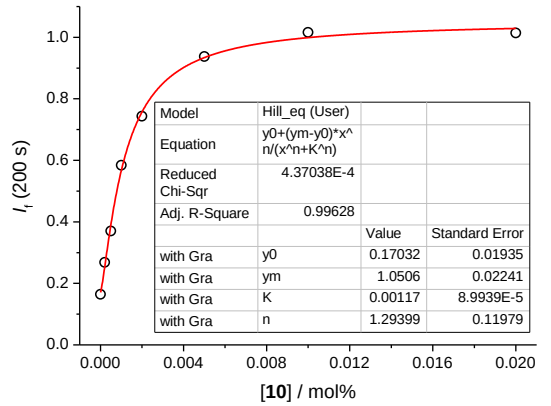

Model	Hill_eq (User)		
Equation	y0+(ym-y0)*x^n/(x^n+K^n)		
Reduced Chi-Sqr	4.37038E-4		
Adj. R-Square	0.99628		
		Value	Standard Error
with Gra	y0	0.17032	0.01935
with Gra	ym	1.0506	0.02241
with Gra	K	0.00117	8.9939E-5
with Gra	n	1.29399	0.11979

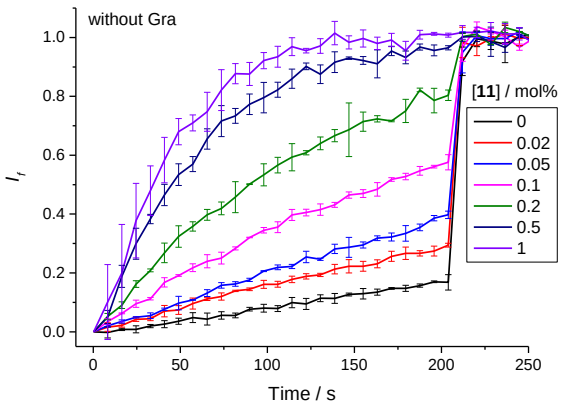

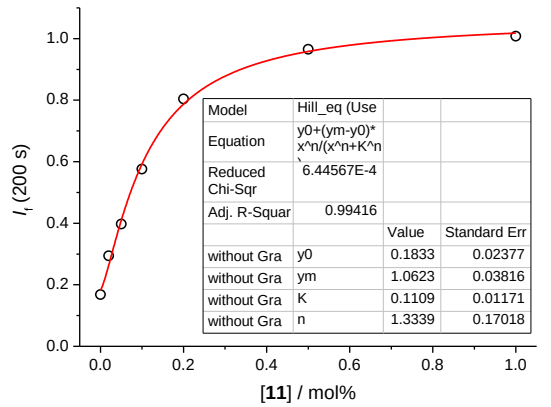

Model	Hill_eq (Use		
Equation	y0+(ym-y0)*x^n/(x^n+K^n		
Reduced Chi-Sqr	6.44567E-4		
Adj. R-Squar	0.99416		
		Value	Standard Err
without Gra	y0	0.1833	0.02377
without Gra	ym	1.0623	0.03816
without Gra	K	0.1109	0.01171
without Gra	n	1.3339	0.17018

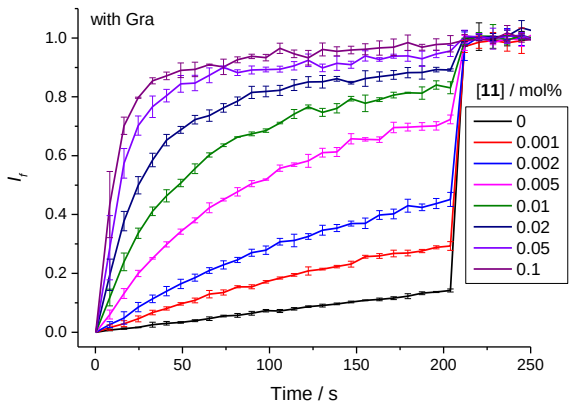

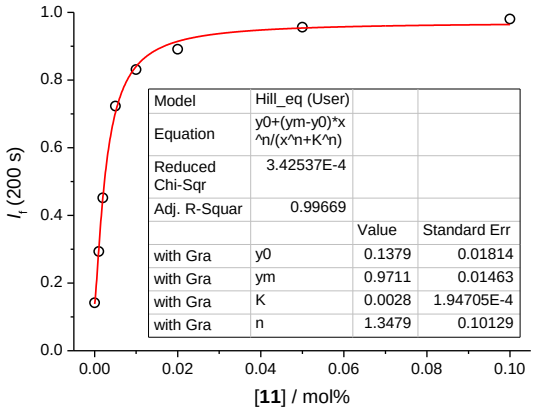

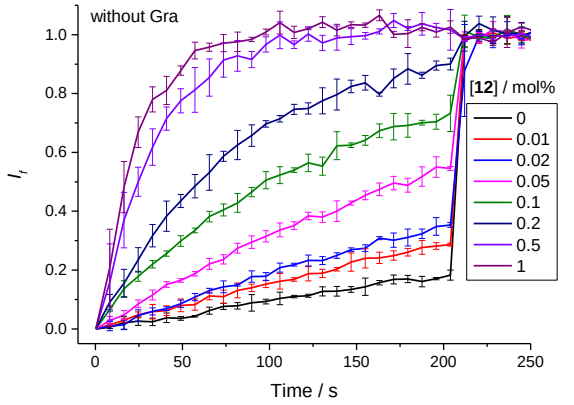

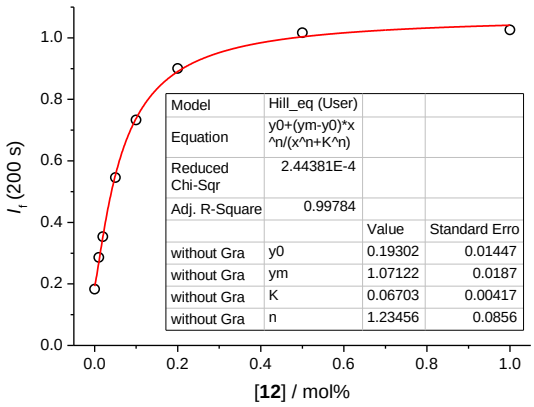

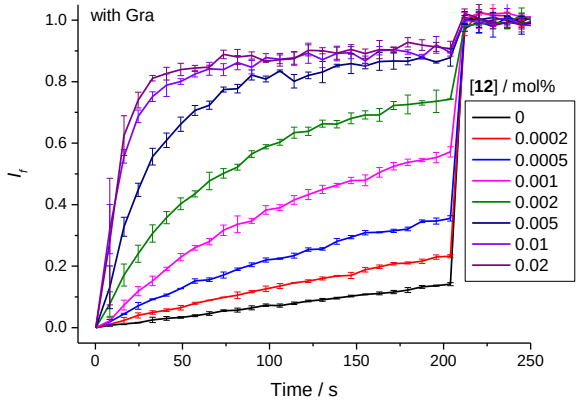

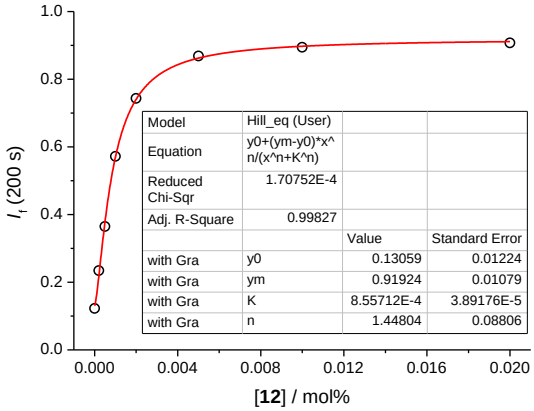

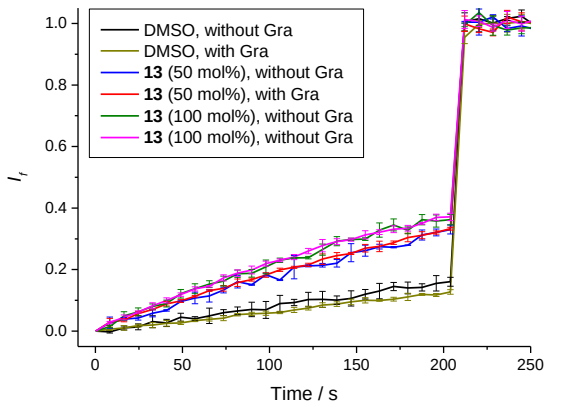

A13 was too inactive for performing Hill plot analysis. However the transport rates in the absence and presence of gramicidin are the same. Therefore **A13** shows no Cl^- > H^+/OH^- selectivity.

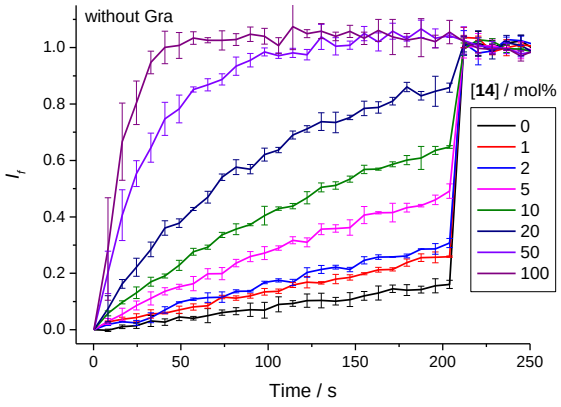

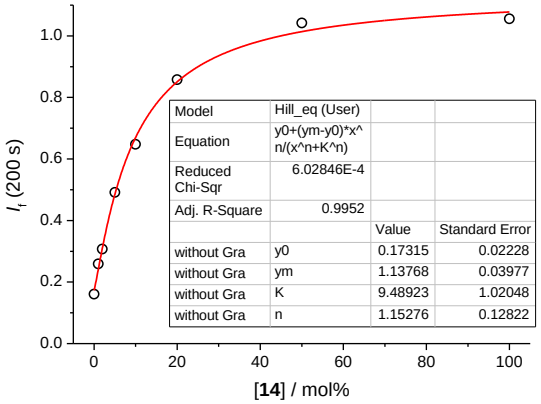

Model	Hill_eq (User)		
Equation	y0+(ym-y0)*x^n/(x^n+K^n)		
Reduced Chi-Sqr	6.02846E-4		
Adj. R-Square	0.9952		
		Value	Standard Error
without Gra	y0	0.17315	0.02228
without Gra	ym	1.13768	0.03977
without Gra	K	9.48923	1.02048
without Gra	n	1.15276	0.12822

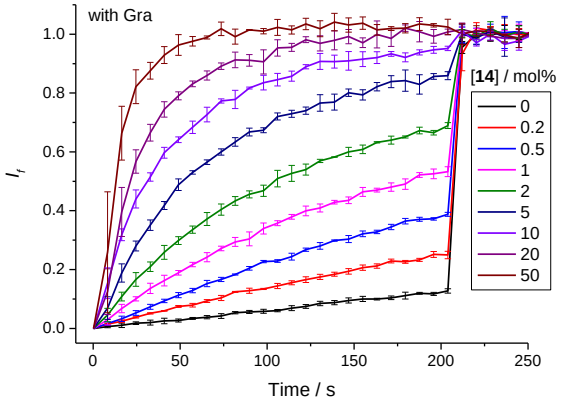

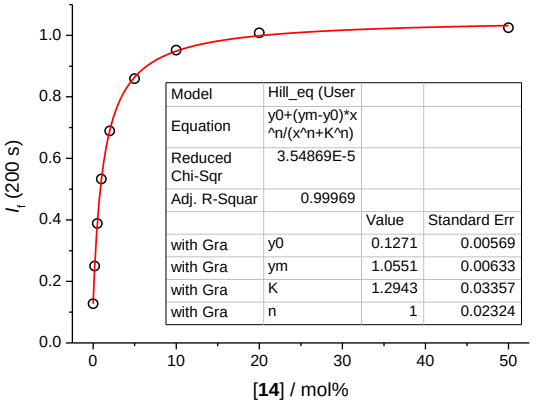

Model	Hill_eq (User		
Equation	y0+(ym-y0)*x^n/(x^n+K^n)		
Reduced Chi-Sqr	3.54869E-5		
Adj. R-Squar	0.99969		
		Value	Standard Err
with Gra	y0	0.1271	0.00569
with Gra	ym	1.0551	0.00633
with Gra	K	1.2943	0.03357
with Gra	n	1	0.02324

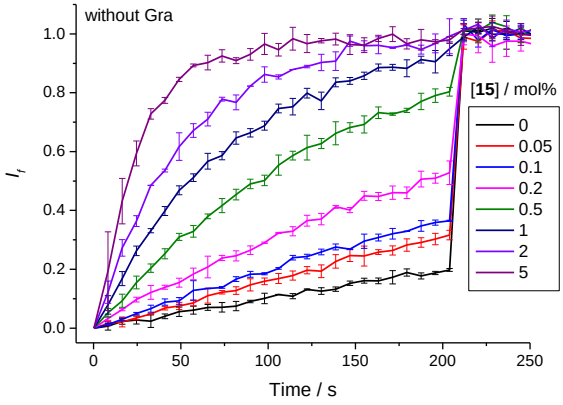

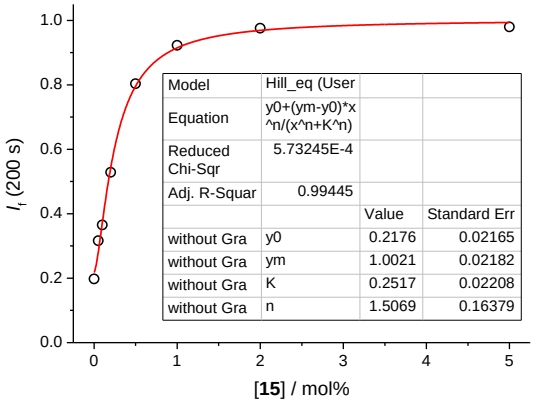

Model	Hill_eq (User		
Equation	y0+(ym-y0)*x^n/(x^n+K^n)		
Reduced Chi-Sqr	5.73245E-4		
Adj. R-Squar	0.99445		
		Value	Standard Err
without Gra	y0	0.2176	0.02165
without Gra	ym	1.0021	0.02182
without Gra	K	0.2517	0.02208
without Gra	n	1.5069	0.16379

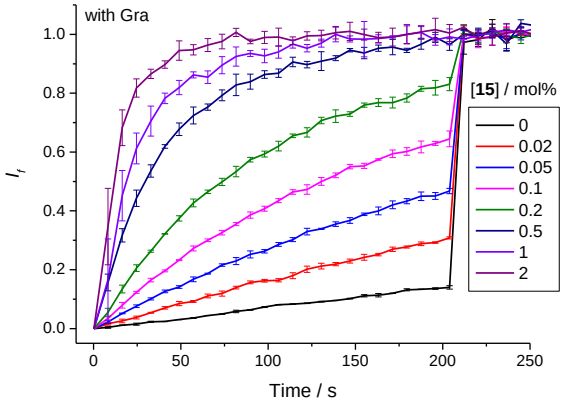

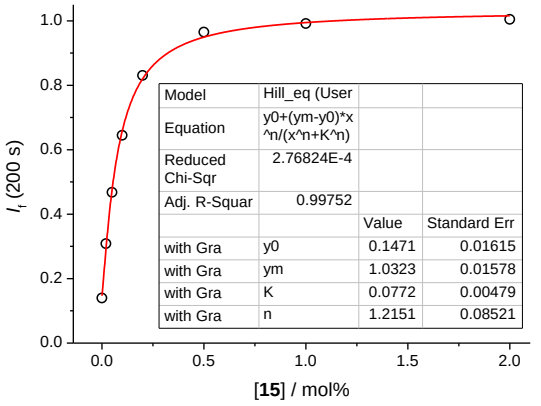

Model	Hill_eq (User		
Equation	y0+(ym-y0)*x^n/(x^n+K^n)		
Reduced Chi-Sqr	2.76824E-4		
Adj. R-Squar	0.99752		
		Value	Standard Err
with Gra	y0	0.1471	0.01615
with Gra	ym	1.0323	0.01578
with Gra	K	0.0772	0.00479
with Gra	n	1.2151	0.08521

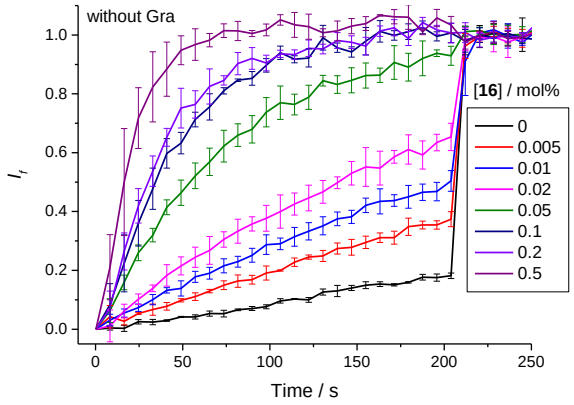

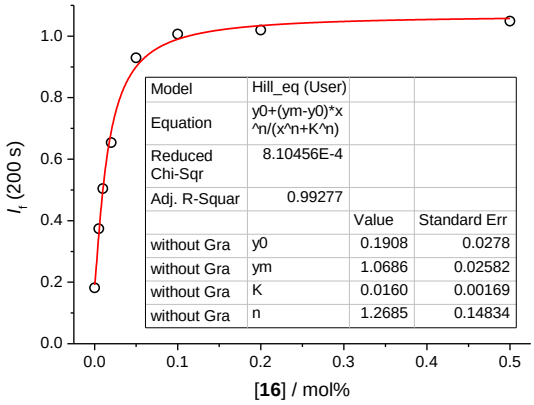

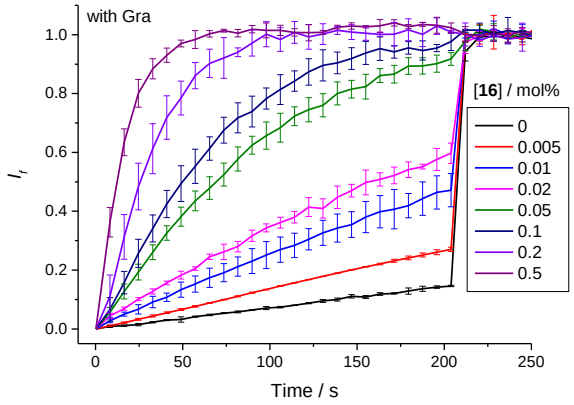

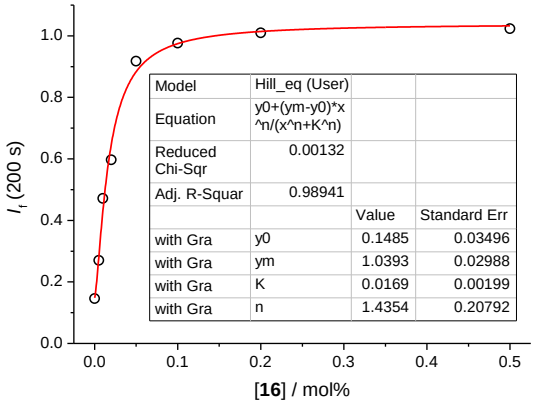

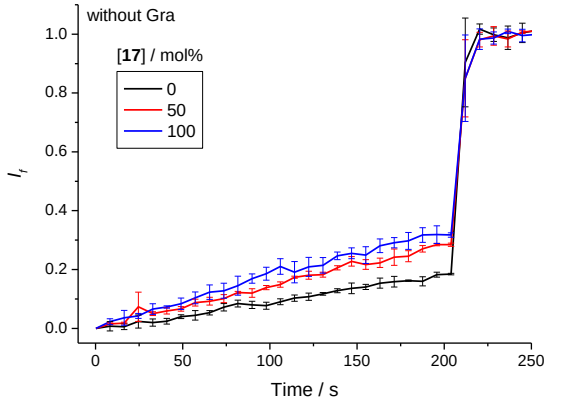

In the absence of gramidicin, **A17** was too inactive for performing Hill plot analysis in the NMDG-Cl assay.

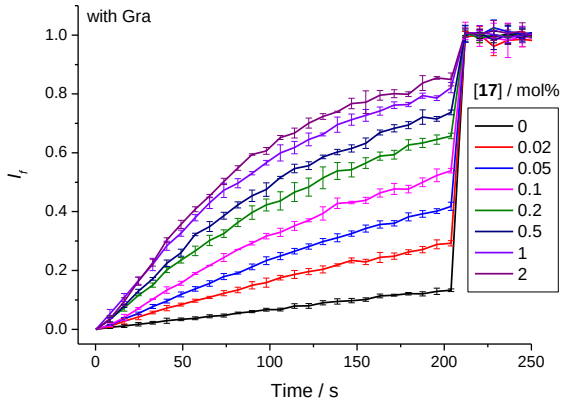

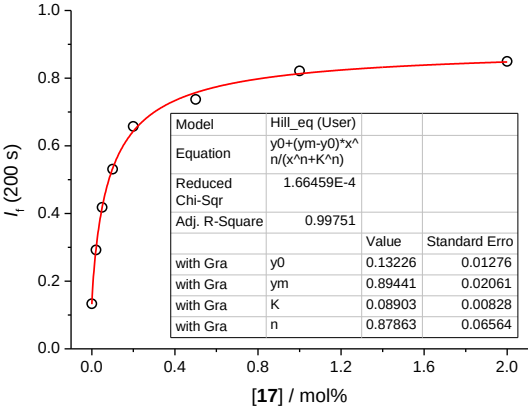

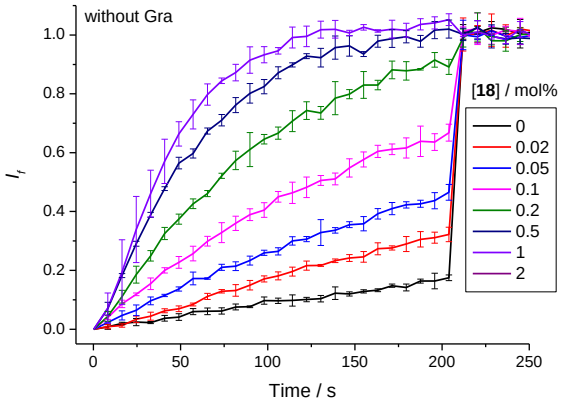
without Gra
[18] / mol%
0
0.02
0.05
0.1
0.2
0.5
1
2
I_f
Time / s

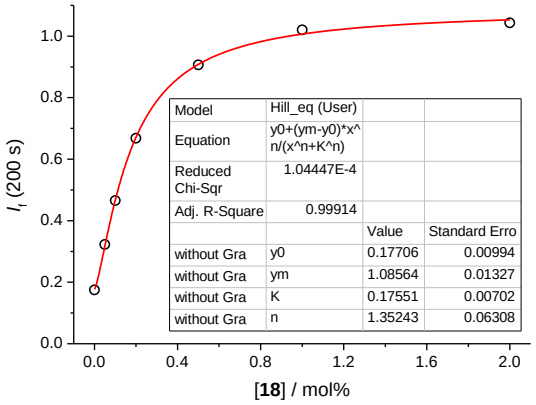
I_f (200 s)
[18] / mol%
Model Hill_eq (User)
Equation y0+(ym-y0)*x^n/(x^n+K^n)
Reduced Chi-Sqr 1.04447E-4
Adj. R-Square 0.99914
Value Standard Erro
without Gra y0 0.17706 0.00994
without Gra ym 1.08564 0.01327
without Gra K 0.17551 0.00702
without Gra n 1.35243 0.06308

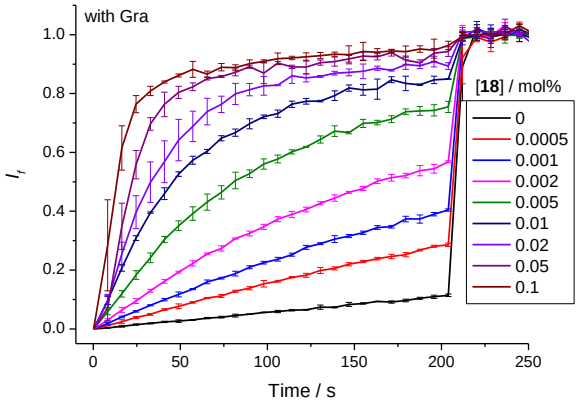
with Gra
[18] / mol%
0
0.0005
0.001
0.002
0.005
0.01
0.02
0.05
0.1
I_f
Time / s

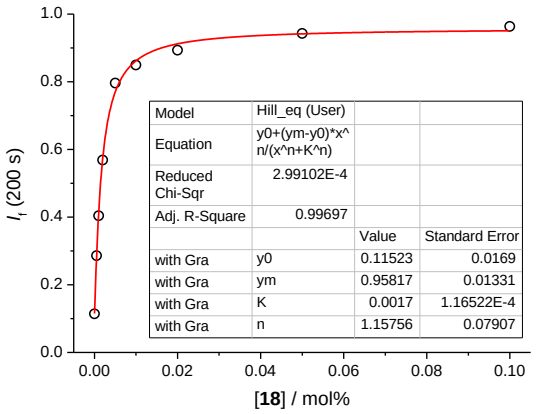
I_f (200 s)
[18] / mol%
Model Hill_eq (User)
Equation y0+(ym-y0)*x^n/(x^n+K^n)
Reduced Chi-Sqr 2.99102E-4
Adj. R-Square 0.99697
Value Standard Error
with Gra y0 0.11523 0.0169
with Gra ym 0.95817 0.01331
with Gra K 0.0017 1.16522E-4
with Gra n 1.15756 0.07907

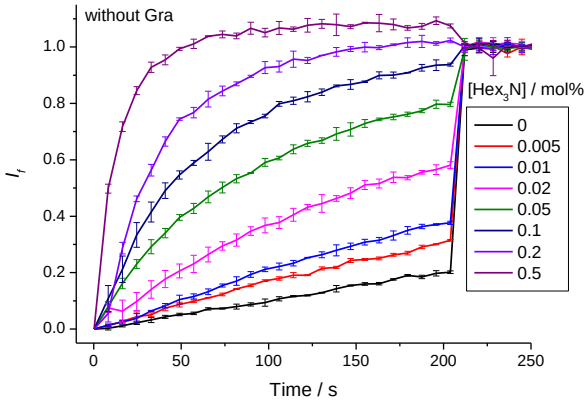
without Gra
[Hex$_3$N] / mol%
0
0.005
0.01
0.02
0.05
0.1
0.2
0.5
I_f
Time / s

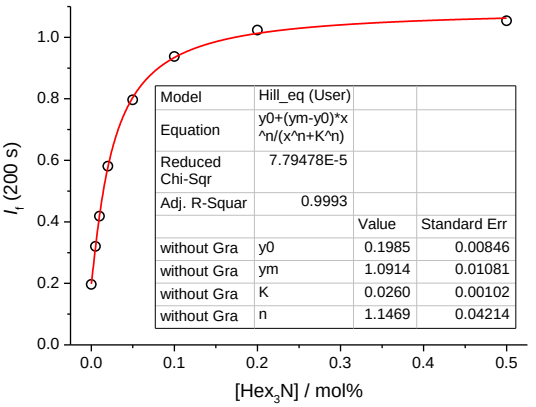
I_f (200 s)
[Hex$_3$N] / mol%
Model Hill_eq (User)
Equation y0+(ym-y0)*x^n/(x^n+K^n)
Reduced Chi-Sqr 7.79478E-5
Adj. R-Squar 0.9993
Value Standard Err
without Gra y0 0.1985 0.00846
without Gra ym 1.0914 0.01081
without Gra K 0.0260 0.00102
without Gra n 1.1469 0.04214

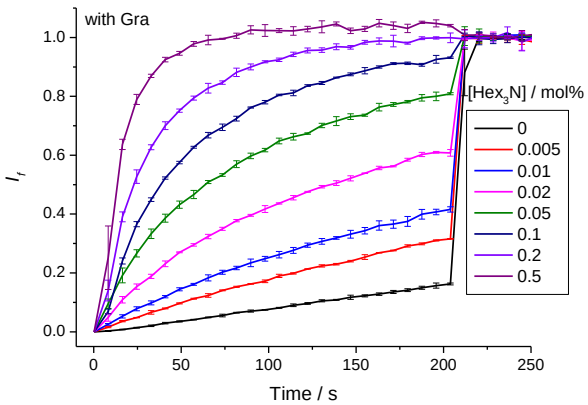
with Gra
[Hex$_3$N] / mol%
0
0.005
0.01
0.02
0.05
0.1
0.2
0.5
I_f
Time / s

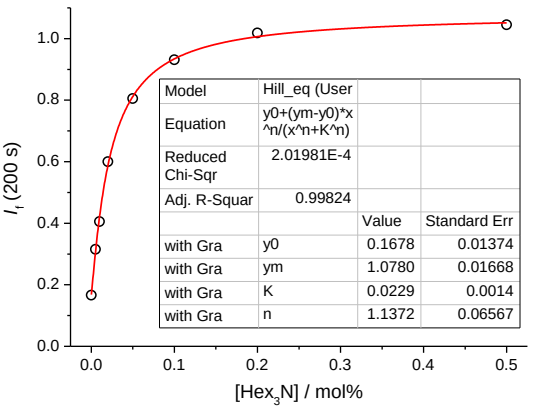
I_f (200 s)
[Hex$_3$N] / mol%
Model Hill_eq (User
Equation y0+(ym-y0)*x^n/(x^n+K^n)
Reduced Chi-Sqr 2.01981E-4
Adj. R-Squar 0.99824
Value Standard Err
with Gra y0 0.1678 0.01374
with Gra ym 1.0780 0.01668
with Gra K 0.0229 0.0014
with Gra n 1.1372 0.06567

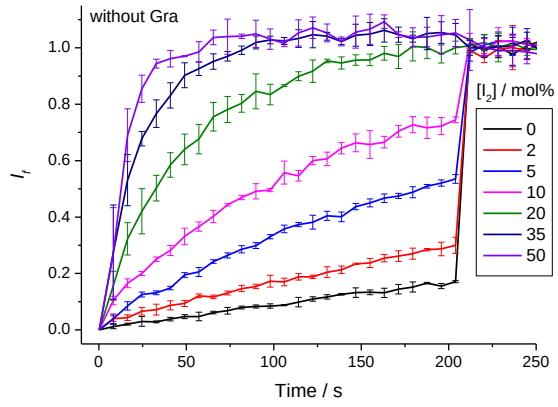

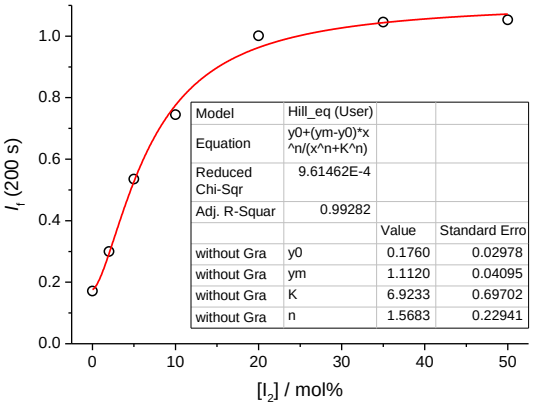

Model	Hill_eq (User)		
Equation	y0+(ym-y0)*x^n/(x^n+K^n)		
Reduced Chi-Sqr	9.61462E-4		
Adj. R-Squar	0.99282		
		Value	Standard Erro
without Gra	y0	0.1760	0.02978
without Gra	ym	1.1120	0.04095
without Gra	K	6.9233	0.69702
without Gra	n	1.5683	0.22941

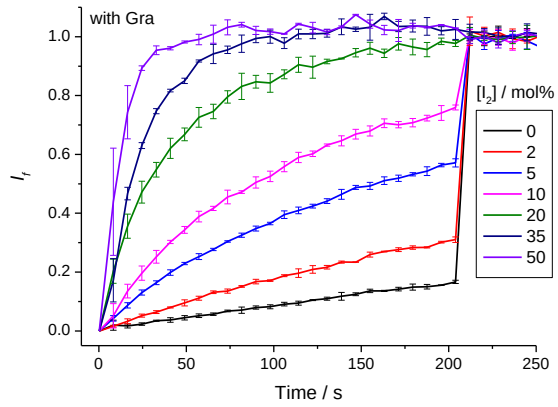

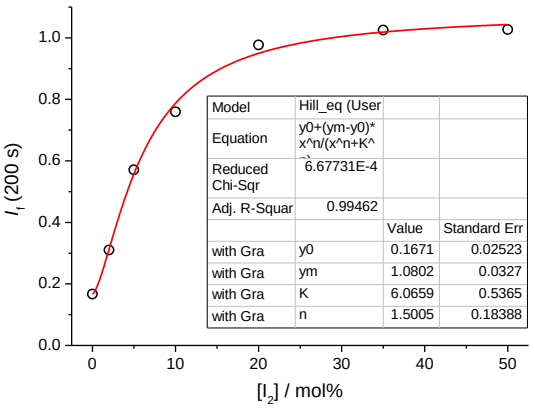

Model	Hill_eq (User		
Equation	y0+(ym-y0)*x^n/(x^n+K^		
Reduced Chi-Sqr	6.67731E-4		
Adj. R-Squar	0.99462		
		Value	Standard Err
with Gra	y0	0.1671	0.02523
with Gra	ym	1.0802	0.0327
with Gra	K	6.0659	0.5365
with Gra	n	1.5005	0.18388

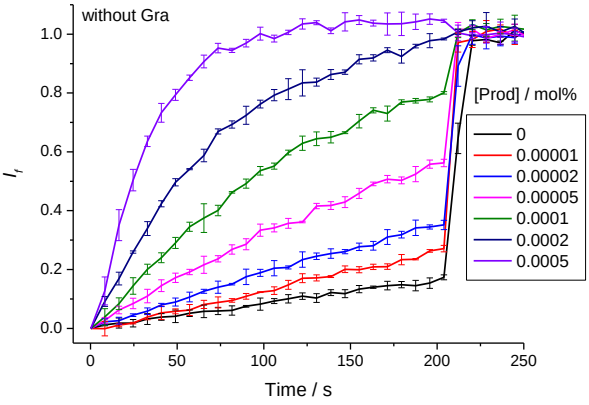

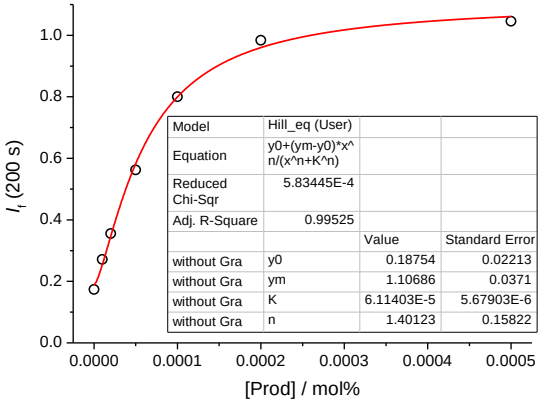

Model	Hill_eq (User)		
Equation	y0+(ym-y0)*x^n/(x^n+K^n)		
Reduced Chi-Sqr	5.83445E-4		
Adj. R-Square	0.99525		
		Value	Standard Error
without Gra	y0	0.18754	0.02213
without Gra	ym	1.10686	0.0371
without Gra	K	6.11403E-5	5.67903E-6
without Gra	n	1.40123	0.15822

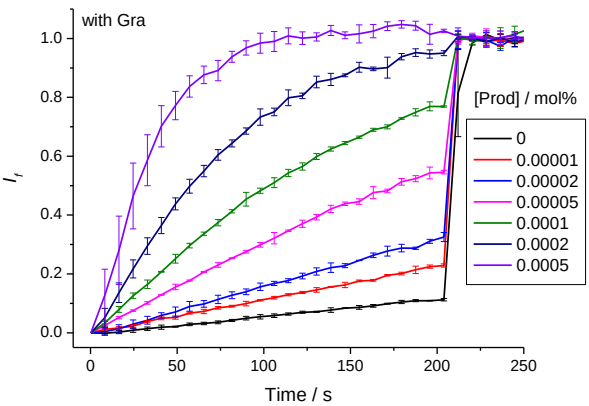

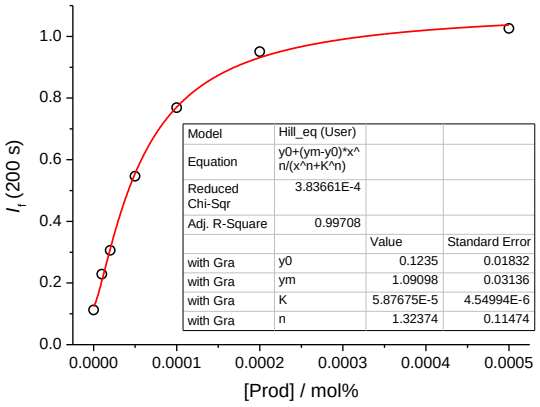

Model	Hill_eq (User)		
Equation	y0+(ym-y0)*x^n/(x^n+K^n)		
Reduced Chi-Sqr	3.83661E-4		
Adj. R-Square	0.99708		
		Value	Standard Error
with Gra	y0	0.1235	0.01832
with Gra	ym	1.09098	0.03136
with Gra	K	5.87675E-5	4.54994E-6
with Gra	n	1.32374	0.11474

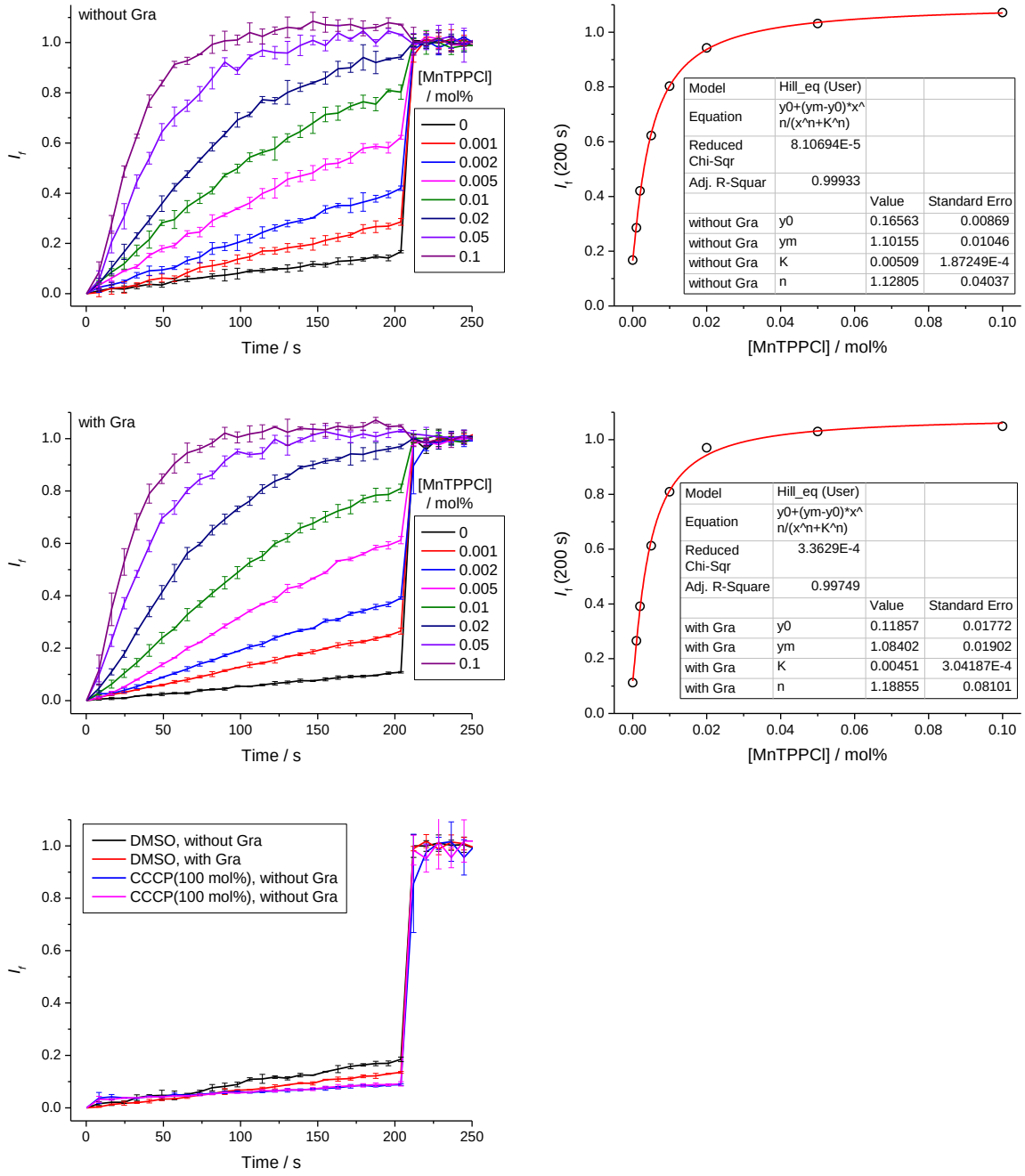

CCCP facilitates no observable chloride transport even at 100 mol% loading.

Figure 7.115 Hill plot analyses of H^+/Cl^- symport or Cl^-/OH^- antiport facilitated by compounds **A1-A18**, trihexylamine (Hex_3N), iodine (I_2), prodigiosin (Prod), MnTPPCl and CCCP in the absence and presence of proton channel gramicidin D (0.1 mol%). Carrier concentrations are shown as carrier to lipid molar ratios. Error bars represent SD from two or three repeats.

Table 7.2 Hill plot analyses of anionophores **A1**-**A18**, trihexylamine (Hex_3N), iodine (I_2), prodigiosin (Prod), and MnTPP in the NMDG-Cl assay in the absence and presence of proton channel gramicidin D (Gra). Hill coefficients (*n*) and effective concentrations to reach 50% transport at 200 s (EC_{50}) were obtained by fitting the I_f (200 s)-carrier concentration curve to the Hill equation. Cl^- > H^+/OH^- selectivity (S) is quantified by the EC_{50} in the absence of Gra divided by EC_{50} in the presence of Gra. An S-value of 1 indicates that H^+/OH^- transport is faster than Cl^- transport, *i.e.*, no selectivity. Carrier concentrations are shown as carrier to lipid molar ratios.

	without Gra		with Gra (0.1 mol%)		Selectivity (S)
	n	EC_{50} / mol%	*n*	EC_{50} / mol%	
1	1.4 ±0.1	0.046 ±0.003	1.4 ±0.1	0.043 ±0.002	1.1
2	2.4 ±0.1	0.61 ±0.02	1.9 ±0.1	0.29 ±0.01	2.1
3	2.3 ±0.2	0.16 ±0.01	2 ±0.2	0.11 ±0.01	1.4
4	1.2 ±0.1	0.015±0.001	1.2 ±0.1	0.015 ±0.001	1.0
5	1.9 ±0.1	0.26 ±0.01	1.8 ±0.1	0.33 ± 0.01	0.8
6	3.2 ±0.7	20 ±1	3.1 ±0.5	13 ±1	1.5
7	2.5 ±0.2	7.9 ±0.3	2.7 ±0.3	5.9 ±0.2	1.3
8	1.3 ±0.1	0.00074 ±0.00005	1.3 ±0.1	0.00085 ±0.00004	0.9
9	1.3 ±0.1	0.042 ±0.004	1.1 ±0.1	0.0030 ±0.0002	14
10	1.2 ±0.1	0.0011 ±0.0000	1.2 ±0.1	0.0012 ±0.0001	0.9
11	1.3 ±0.2	0.11 ±0.01	1.3 ±0.1	0.0029 ±0.0002	39
12	1.2 ±0.1	0.067 ±0.004	1.4 ±0.1	0.00086 ±0.00004	78
13	-	too inactive	-	too inactive	~1[a]
14	1.2 ±0.1	9.5 ±1.0	1.0 ±0.0	1.3 ±0.0	7.4
15	1.5 ±0.2	0.25 ±0.02	1.2 ±0.1	0.077 ±0.005	3.3
16	1.3 ±0.1	0.016 ±0.002	1.4 ±0.2	0.017 ±0.002	0.9
17	-	too inactive	0.88 ±0.07	0.089 ±0.008	-[b]
18	1.4 ±0.1	0.18 ±0.01	1.2 ±0.1	0.0017 ±0.0001	100
Hex_3N	1.1 ±0.0	0.026 ±0.001	1.1 ±0.1	0.023 ±0.001	1.1
I_2	1.6 ±0.2	6.9 ±0.7	1.5 ±0.2	6.1 ±0.5	1.1
Prod	1.4 ±0.2	0.000061 ±0.000006	1.3 ±0.1	0.000059 ±0.000005	1.0
MnTPPCl	1.1 ±0.0	0.0051 ±0.0002	1.2 ±0.1	0.0045 ±0.0003	1.1

[a] Too inactive for Hill plot analysis. A single-concentration comparison shows no selectivity.
[b] No S-value given because without gramicidin **17** was too inactive for Hill plot analysis. This indicates a very high Cl^- > H^+/OH^- selectivity that cannot be quantified by this method.

7.5.7.3.3 Control experiments

To rule out the tested carriers facilitating other processes that may lead to HPTS response, including $NMDG^+/H^+$ antiport, $NMDG^+/OH^-$ symport, transport of neutral NMDG, HPTS leakage, membrane instability and carrier interference with HPTS fluorescence, NMDG-Cl was replaced by $(NMDG)_2SO_4$, and carrier-induced HPTS response was recorded, with the other conditions kept the same as in the NMDG-Cl assay. Due to the hydrophilicity of sulfate, facilitation of sulfate transport is unlikely or would require a much higher carrier concentration[228], and therefore sulfate ion has been used by us as a negative control for chloride transport. The results show that

with $(NMDG)_2SO_4$ the HPTS response was negligible compared to when NMDG-Cl was used, confirming that the results obtained with the NMDG-Cl assay are due to chloride transport.

Conditions: Internal and external solution (excluding HPTS): 50 mM $(NMDG)_2SO_4$, buffered at pH 7.0 with 10 mM HEPES; Base pulse: 5 mM NMDG.

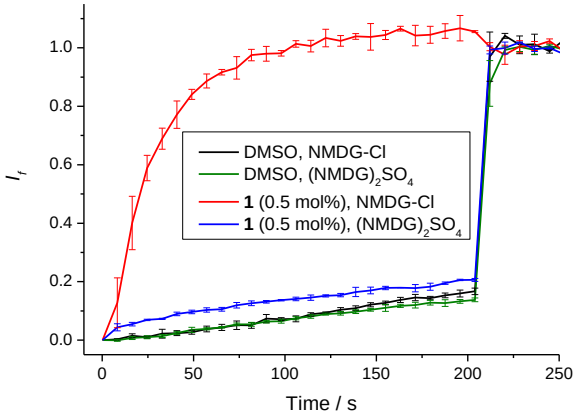

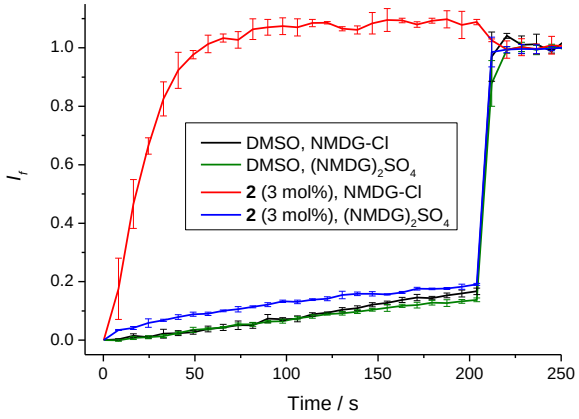

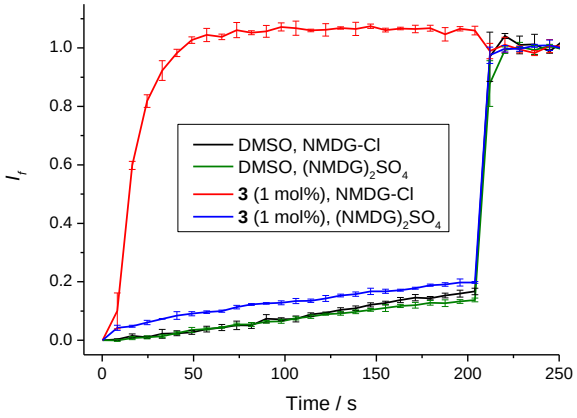

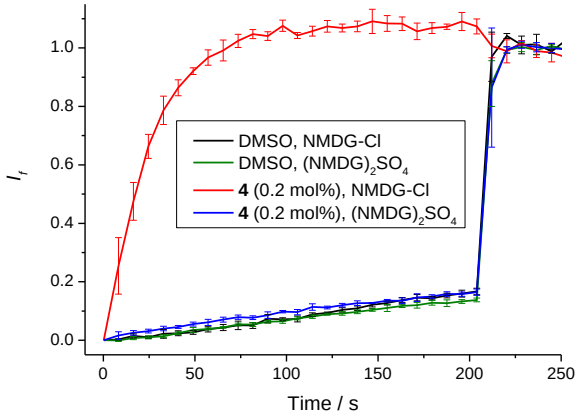

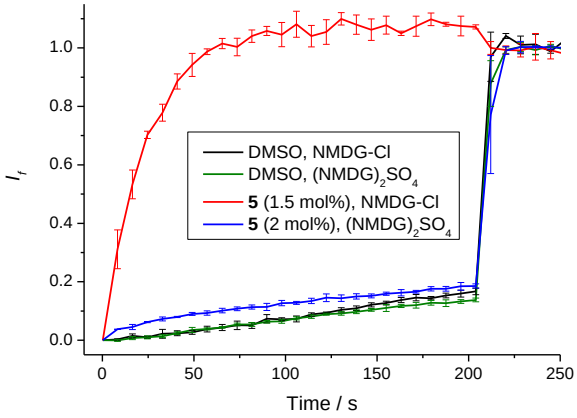

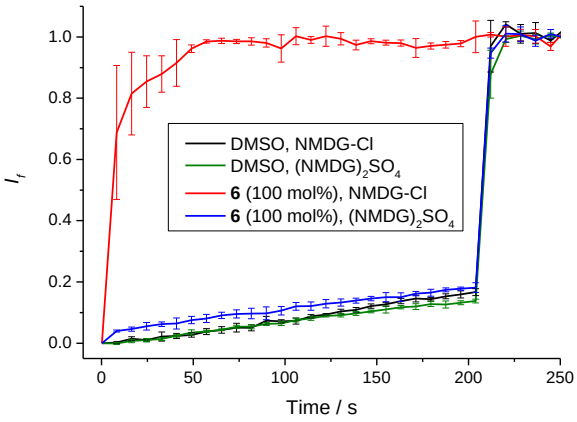

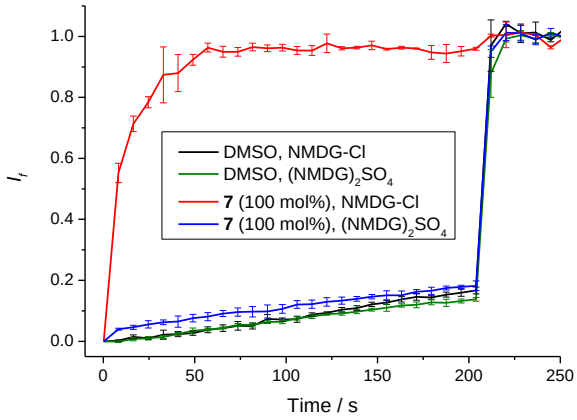
DMSO, NMDG-Cl
DMSO, (NMDG)2SO4
7 (100 mol%), NMDG-Cl
7 (100 mol%), (NMDG)2SO4
If
Time / s

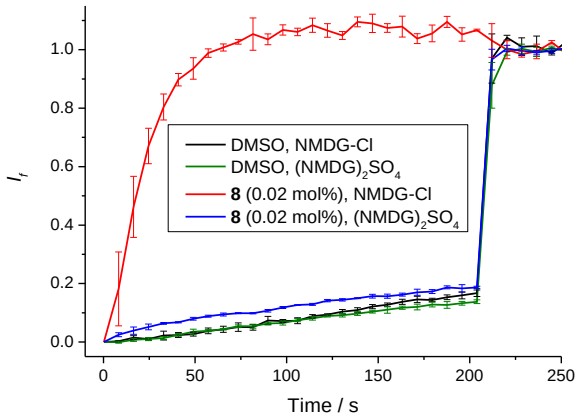
DMSO, NMDG-Cl
DMSO, (NMDG)2SO4
8 (0.02 mol%), NMDG-Cl
8 (0.02 mol%), (NMDG)2SO4
If
Time / s

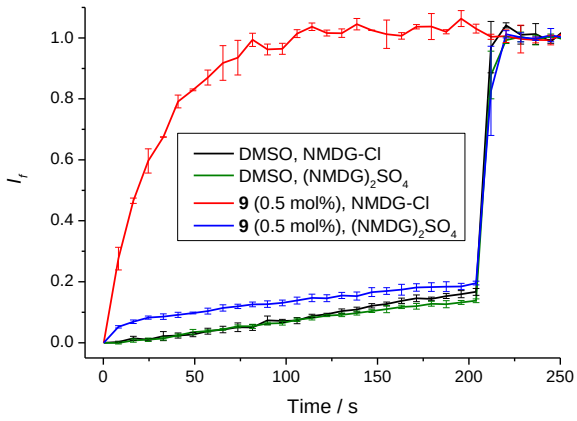
DMSO, NMDG-Cl
DMSO, (NMDG)2SO4
9 (0.5 mol%), NMDG-Cl
9 (0.5 mol%), (NMDG)2SO4
If
Time / s

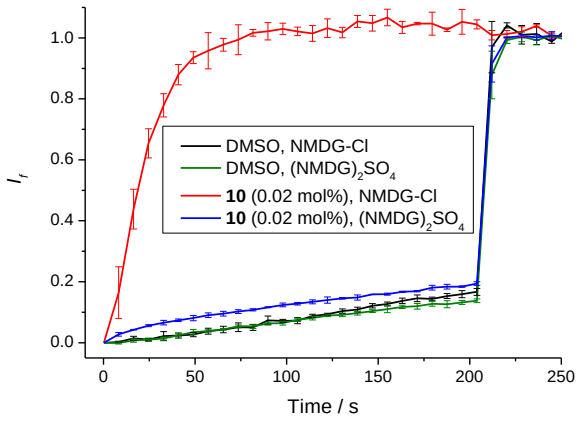
DMSO, NMDG-Cl
DMSO, (NMDG)2SO4
10 (0.02 mol%), NMDG-Cl
10 (0.02 mol%), (NMDG)2SO4
If
Time / s

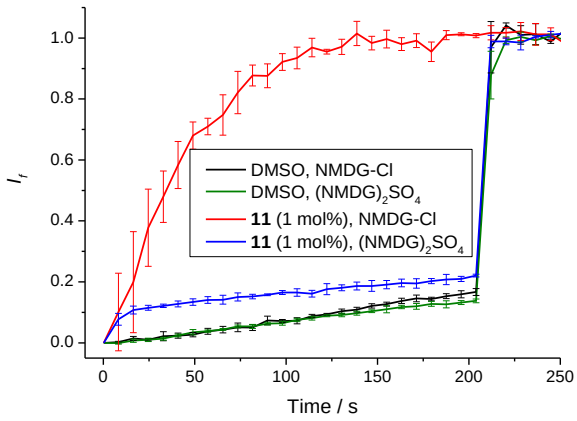
DMSO, NMDG-Cl
DMSO, (NMDG)2SO4
11 (1 mol%), NMDG-Cl
11 (1 mol%), (NMDG)2SO4
If
Time / s

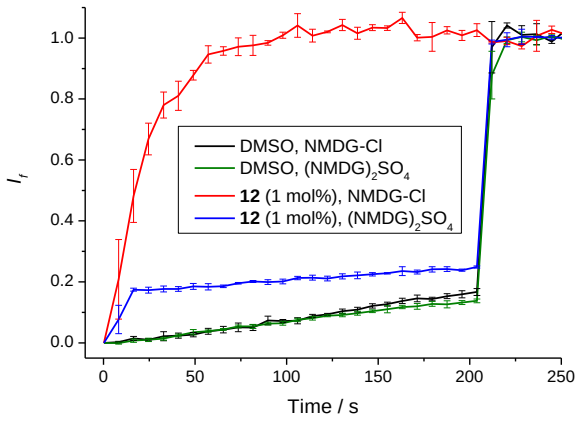
DMSO, NMDG-Cl
DMSO, (NMDG)2SO4
12 (1 mol%), NMDG-Cl
12 (1 mol%), (NMDG)2SO4
If
Time / s

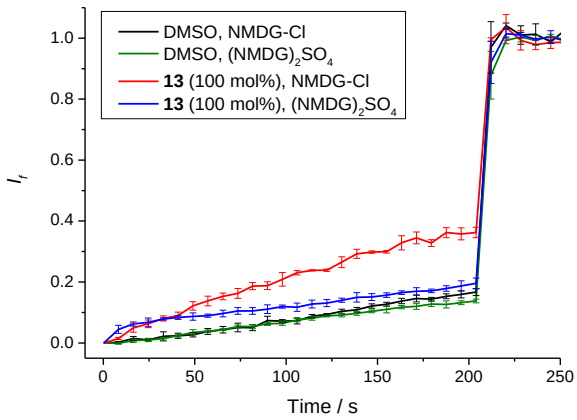
DMSO, NMDG-Cl
DMSO, (NMDG)2SO4
13 (100 mol%), NMDG-Cl
13 (100 mol%), (NMDG)2SO4
If
Time / s

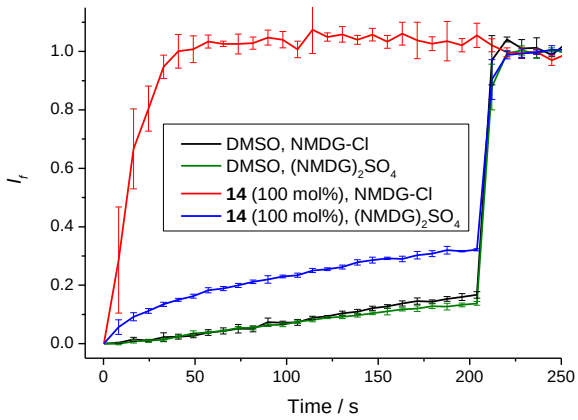
DMSO, NMDG-Cl
DMSO, (NMDG)2SO4
14 (100 mol%), NMDG-Cl
14 (100 mol%), (NMDG)2SO4
If
Time / s

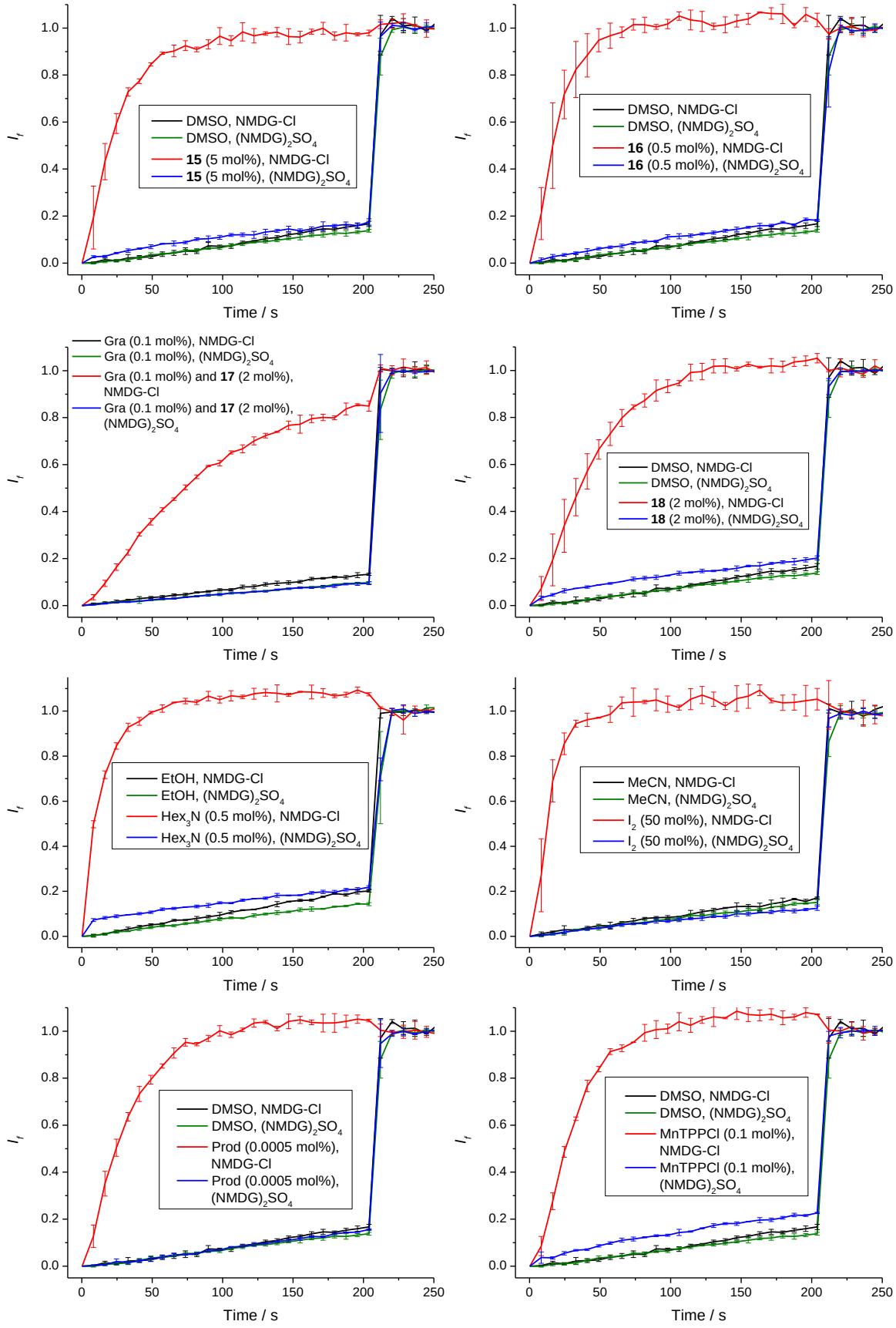

Figure 7.116 Control experiments for NMDG-Cl assay. $(NMDG)_2SO_4$ (50 mM) instead of NMDG-Cl was used as the salt component, and the results were compared with those obtained using NMDG-Cl (100 mM) as the salt component. Carrier concentrations are shown as carrier to lipid molar ratios. Error bars represent SD from two or three repeats.

7.5.8 ISE assays

7.5.8.1 Cl^-/NO_3^- exchange – pH dependence

POPC LUVs (mean diameter 200 nm) with internal NaCl and external $NaNO_3$ were prepared as follows. A chloroform solution of POPC was evaporated in a round-bottle flask and the lipid film formed was dried under vacuum for at least 6 h. The lipid film was hydrated by vortexing with a buffered internal solution containing NaCl. The lipid solution was subjected to nine freeze/thaw cycles and then extruded 25 times through a 200 nm polycarbonate membrane. The vesicles were dialysed against a buffered external solution containing $NaNO_3$ for at least 2 h to exchange external Cl^- for NO_3^-. The lipid solution obtained after dialysis was diluted to 10 mL with the external solution using a volumetric flask to obtain a lipid stock solution with known lipid concentration.

For each measurement, the lipid stock solution was diluted with the external solution to obtain a 5 mL solution containing 1 mM of lipid. At the beginning of each measurement, 25 µL of a DMSO solution (except in the case of trihexylamine where 25 µL of an ethanol solution was used) of the tested carrier was added to the vesicle solution, and the external chloride concentration was monitored by a chloride-selective electrode. At 5 min, a detergent (50 µL of 11% (w%) Triton X-100 in 7 : 1 (v/v) H_2O-DMSO) was added to lyse the vesicles and release all chloride to calibrate to 100% chloride efflux. The results were averaged over at least three repeats.

<u>Conditions for tests at different pH:</u>

pH 4.5: Internal solution: 488 mM NaCl, buffered at pH 4.5 with 5 mM citrate; External solution: 488 mM $NaNO_3$, buffered at pH 4.5 with 5 mM citrate.

pH 7.2: Internal solution: 487 mM NaCl, buffered at pH 7.2 with 5 mM phosphate; External solution: 487 mM $NaNO_3$, buffered at pH 7.2 with 5 mM phosphate.

pH 11.5: Internal solution: 497 mM NaCl, “buffered” at pH 11.5 with ~3 mM NaOH; External solution: 497 mM $NaNO_3$, “buffered” at pH 11.5 with ~3 mM NaOH.

7.5.8.2 NH_4Cl efflux

This is an independent assay for Cl^- > H^+/OH^- selectivity, used here to support the results of the HPTS-based NMDG-Cl-gramicidin assay (Section 7.5.7.3). Carrier-facilitated chloride efflux was measured from vesicles loaded with NH_4Cl (300 mM) and Na_2SO_4 (200 mM) suspended in an external Na_2SO_4 (200 mM) solution. This is an alternative assay for H^+/Cl^- symport or Cl^-/OH^- antiport, but measures a larger chloride flux (300 mM) compared to the chloride flux required in the HPTS assay (5 mM) to reach equilibrium. The pH gradient generated by carrier-facilitated H^+/Cl^- symport or Cl^-/OH^- antiport will be compensated by simple diffusion of basic neutral molecule NH_3 that exists in equilibrium with NH_4^+ ion, leading to formal NH_4Cl efflux and allowing chloride efflux to complete. Kinetics of chloride efflux induced by an anion carrier was recorded in the absence and presence of protonophore CCCP. Here gramicidin cannot be used due to its ability to facilitate NH_4^+ transport. Enhanced rate of NH_4Cl flux induced by CCCP can indicate Cl^- > H^+/OH^- selectivity, similarly to enhanced rate of pH gradient dissipation induced by gramicidin in the NMDG-Cl-gramicidin assay. The rationale of using NH_4Cl here is similar to the use of potassium acetate in studying swelling of mitochondria induced by cationophores and protonophores.[199]

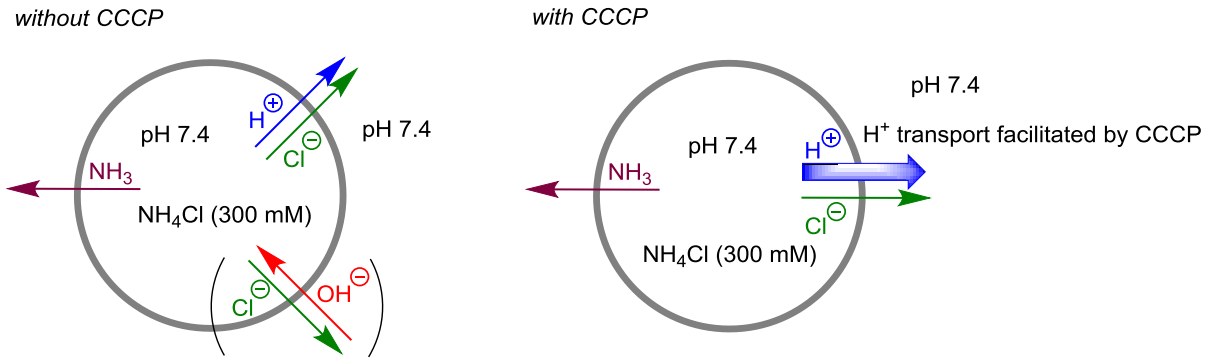

Figure 7.117 Schematic representation of NH_4Cl efflux assay for evaluating Cl^- > H^+/OH^- selectivity of anionophores. H^+/Cl^- symport or Cl^-/OH^- antiport (facilitated by ionophores) couples to simple diffusion of NH_3, leading to formal NH_4Cl flux. NH_4Cl efflux can be measured using a chloride selective electrode, or by monitoring light scattering intensity based on osmotic shrinkage of vesicles. In the absence of protonophore CCCP (left), the tested carrier needs to facilitate H^+/Cl^- symport or Cl^-/OH^- antiport to induce net NH_4Cl flux. In the presence of CCCP that facilitates H^+ transport, the tested carrier only needs to facilitate Cl^- transport to induce net NH_4Cl flux. If H^+/OH^- transport is rate-limiting with the tested carrier alone (*i.e.* if the tested carrier shows Cl^- > H^+/OH^- selectivity), CCCP will improve the rate-limiting step and thereby accelerate the rate of NH_4Cl efflux. Buffer agent (HEPES) and the salt (Na_2SO_4 in the ISE assay and NMDG-Glu in the osmotic response assay) used to balance the internal and external osmotic concentrations are omitted for clarity.

The results (Figure 7.118) show that chloride efflux facilitated by **A12** and **A18** was dramatically enhanced by CCCP, supporting the conclusion that **A12** and **A12** show Cl^- > H^+/OH^- selectivity.

Experimental details and results are given below:

POPC LUVs (mean diameter 200 nm) with internal NH_4Cl–Na_2SO_4 and external Na_2SO_4 were prepared as follows. A chloroform solution of POPC was evaporated in a round-bottle flask and the lipid film formed was dried under vacuum for at least 6 h. The lipid film was hydrated by vortexing with an internal solution containing NH_4Cl (300 mM) and Na_2SO_4 (200 mM), buffered at pH 7.4 with 5 mM HEPES. The lipid solution was subjected to nine freeze/thaw cycles and then extruded 25 times through a 200 nm polycarbonate membrane. The vesicles were dialysed against an isotonic solution of Na_2SO_4 (400 mM) buffered at pH 7.4 with 5 mM HEPES for at least 2 h to remove external Cl^- for SO_4^{2-}. The lipid solution obtained directly after dialysis was used as the stock solution, with the lipid concentration calculated after measuring the volume of the lipid solution.

For each measurement, the lipid stock solution was diluted with an external solution containing Na_2SO_4 (200 mM) buffered at pH 7.4 with 5 mM HEPES, to obtain a 5 mL solution containing 1 mM of lipid. At the beginning of each measurement, 25 µL of a DMSO solution of the tested carrier was added to the vesicle solution, and the external chloride concentration was monitored by a chloride-selective electrode. When CCCP was used, 10 µL of a 0.5 mM DMSO solution of CCCP was added to the vesicle solution prior to the addition of the tested carrier. At 5 min, a detergent (50 µL of 11% (w%) Triton X-100 in 7 : 1 (v/v) H_2O-DMSO) was added to lyse the vesicles and release all chloride to calibrate to 100% chloride efflux. The results were averaged over at least two repeats.

Conditions: Internal solution: 300 mM NH_4Cl, 200 mM Na_2SO_4, buffered at pH 7.4 with 5 mM HEPES; External solution: 200 mM Na_2SO_4, buffered at pH 7.4 with 5 mM HEPES.

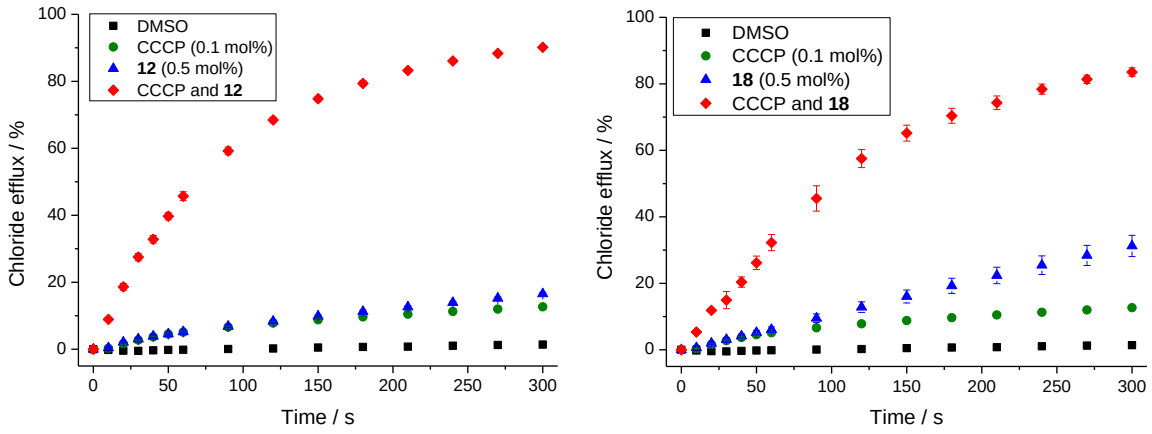

Figure 7.118 Effect of CCCP (0.1 mol%) on chloride efflux (measured using a chloride selective electrode) facilitated by **A12** (0.5 mol%) and **A18** (0.5 mol%) from POPC LUVs (mean diameter 200 nm) loaded with NH_4Cl (300 mM) and Na_2SO_4 (200 mM) suspended in a Na_2SO_4 (200 mM) solution buffered at pH 7.4 with 5 mM HEPES. Carrier concentrations are shown as carrier to lipid molar ratios. Error bars represent SD from two or three repeats.

7.5.8.3 KCl efflux – ionophore couplings

This is an independent assay that can evaluate Cl^- > H^+/OH^- selectivity under protonophore-free conditions and distinguish between electroneutral and electrogenic anionophores. Carrier-facilitated chloride efflux was measured from vesicles loaded with KCl (300 mM) and K_2SO_4 (200 mM) suspended in an external K_2SO_4 (200 mM) solution. Combinations of a cationophore and an anionophore were tested, in which valinomycin (an electrogenic K^+ carrier) or monensin (an electroneutral K^+/H^+ exchanger) was used as the cationophore component. The anionophore-facilitated chloride transport that couples to valinomycin-facilitated K^+ transport is electrogenic Cl^- transport, whereas the anionophore-facilitated chloride transport that couples to monensin-facilitated K^+/H^+ antiport is H^+/Cl^- symport or Cl^-/OH^- antiport, as discussed in the Chapter 6. The results are shown in Figures 6.16 and 6.24. Experimental details are given below:

POPC LUVs (mean diameter 200 nm) with internal KCl–K_2SO_4 and external K_2SO_4 were prepared as follows. A chloroform solution of POPC was evaporated in a round-bottle flask and the lipid film formed was dried under vacuum for at least 6 h. The lipid film was hydrated by vortexing with an internal solution containing KCl (300 mM) and K_2SO_4 (200 mM), buffered at pH 7.4 with 5 mM HEPES. The lipid solution was subjected to nine freeze/thaw cycles and then extruded 25 times through a 200 nm polycarbonate membrane. The vesicles were dialysed against an isotonic solution of K_2SO_4 (400 mM) buffered at pH 7.4 with 5 mM HEPES for at least 2 h to exchange external Cl^- for SO_4^{2-}. The lipid solution obtained directly after dialysis was used as the stock solution, with the lipid concentration calculated after measuring the volume of the lipid solution.

For each measurement, the lipid stock solution was diluted with an external solution containing K_2SO_4 (200 mM) buffered at pH 7.4 with 5 mM HEPES, to obtain a 5 mL solution containing 1 mM of lipid. At the beginning of each measurement, 25 µL of a DMSO solution of the tested anionophore was added to the vesicle solution, and the external chloride concentration was monitored by a chloride-selective electrode. When a cationophore (valinomycin or monensin) was used, 10 µL of a 0.5 mM DMSO solution of the cationophore was added to the vesicle solution prior to the addition of the tested anionophore. At 5 min, a detergent (50 µL of 11% (w%) Triton X-100 in 7 : 1 (v/v) H_2O-DMSO) was added to lyse the vesicles and release all chloride to calibrate to 100% chloride efflux. The results were averaged over at least two repeats.

<u>Conditions:</u>

Internal solution: 300 mM KCl, 200 mM K_2SO_4, buffered at pH 7.4 with 5 mM HEPES; External solution: 200 mM K_2SO_4, buffered at pH 7.4 with 5 mM HEPES.

7.5.9 Osmotic response assays

7.5.9.1 KCl efflux – evidence of H^+/OH^- transport

This assay (under buffer agent-free conditions) was conducted to provide unambiguous evidence that synthetic anionophores can facilitate H^+/OH^- transport. Carrier-facilitated KCl efflux was measured from vesicles loaded with KCl (300 mM) and suspended in an external potassium gluconate (300 mM) solution. KCl efflux is followed by water efflux due to the osmotic pressure, leading to vesicle shrinkage and an increase in 90° light scattering intensity which can be monitored using a fluorimeter.[177]

Anionophores were tested in combination with monensin. Anionophore-facilitated H^+/Cl^- symport or Cl^-/OH^- antiport couples to monensin-facilitated K^+/H^+ antiport, leading to formal KCl efflux. In this assay, buffer agent transport, which may contribute to pH gradient dissipation in HPTS assays, is excluded as no buffer agent is used. The results (Figure 7.120) show that all tested anionophores (**A1**, **A2** and **A3**) induced KCl efflux only in the presence of monensin. No KCl flux was observed without monensin, indicating that possible K^+/Cl^- symport facilitated by the tested anionophores is non-existing or negligible. These results confirm that synthetic aninophores do facilitate H^+/OH^- transport.

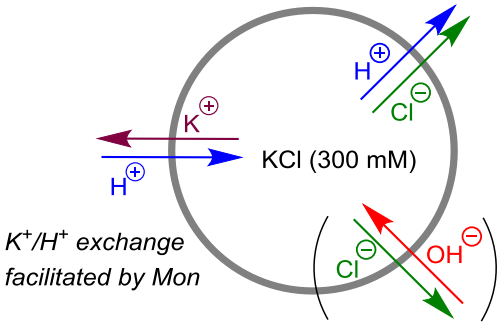

Figure 7.119 Anionophore-facilitated H^+/Cl^- symport or Cl^-/OH^- antiport coupling to monensin (Mon) facilitated K^+/H^+ antiport, leading to net KCl efflux. No buffer agent was used. Na_2SO_4 used to balance the internal and external osmotic concentrations is omitted for clarity.

Experimental details and results are given below:

POPC LUVs (mean diameter 400 nm) loaded with KCl were prepared as follows. A chloroform solution of POPC was evaporated in a round-bottle flask and the lipid film formed was dried under vacuum for at least 6 h. The lipid film was hydrated by vortexing with an internal solution of KCl (300 mM). The lipid solution was subjected to nine freeze/thaw cycles and then extruded 25 times through a 400 nm polycarbonate membrane to obtain a lipid stock solution. Removal of external KCl is not necessary.

For each measurement, the lipid stock solution was diluted with an isotonic external solution of potassium gluconate (300 mM) to obtain a 2 mL solution containing 0.4 mM of lipid. At the beginning of each measurement, 10 µL of a DMSO solution of the tested carrier was added to the

vesicle solution, and the 90° light scattering intensity at 600 nm was monitored by a fluorimeter. When monensin was used, 4 µL of a 0.2 mM DMSO solution of monensin was added to the vesicle solution prior to the addition of the tested carrier. At 10 min, prodigiosin (4 µL of a 2 mM DMSO solution) and monensin (if monensin was not added previously, 4 µL of a 2 mM DMSO solution) were added to calibrate the light scattering intensity to 100% KCl efflux. The results were averaged over at least three repeats. The fractional light scattering intensity (I_f) is calculated using the following equation[182]:

$$I_f = \frac{I_t - I_0}{I_p - I_0}$$

where I_t is the light scattering intensity at time t, I_0 is the light scattering intensity at time 0, and I_p is the light scattering intensity after the addition of prodigiosin (and monensin if monensin was not added previously).

Conditions: Internal solution: 300 mM KCl; External solution: 300 mM potassium gluconate.

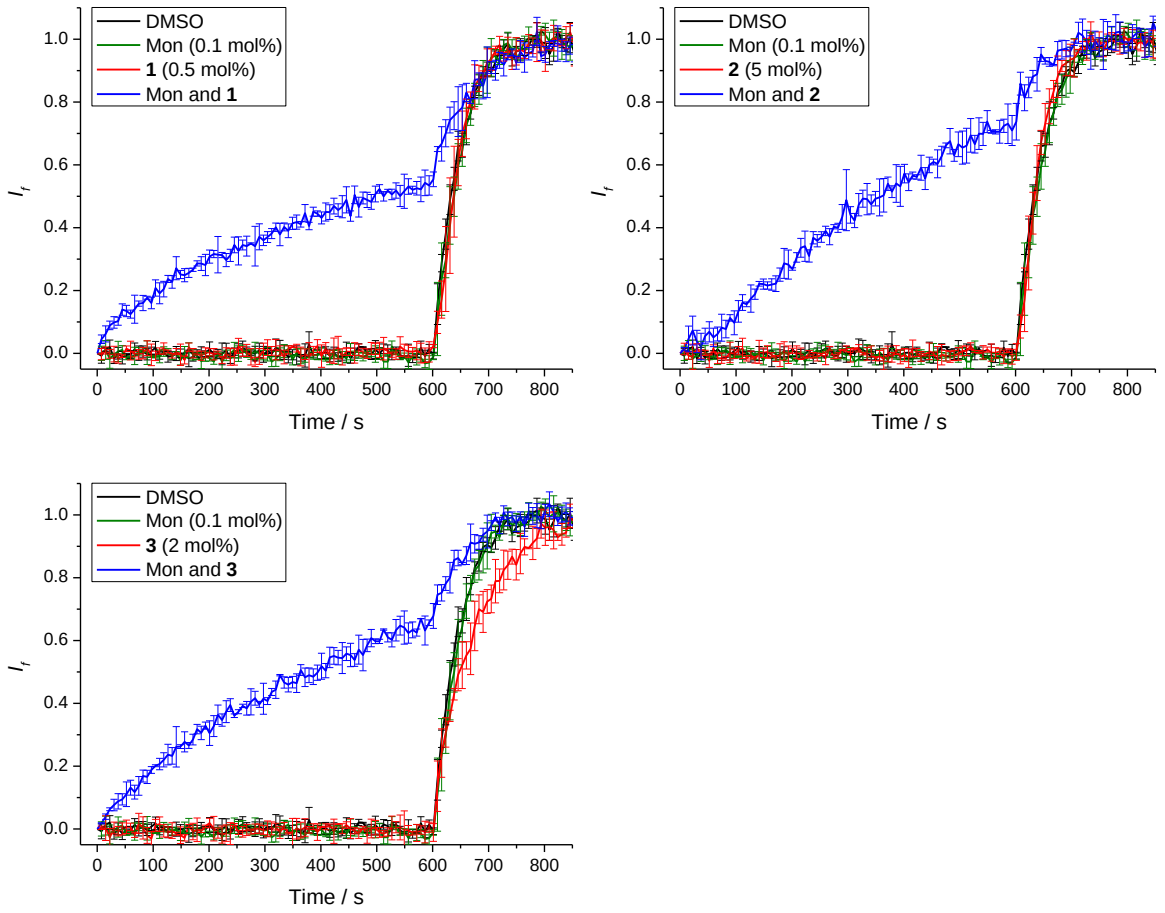

Figure 7.120 KCl efflux (indirectly measured by light scattering intensity) facilitated by monensin (0.1 mol%) and an anionophore (**A1**, **A2** or **A3**) from POPC LUVs (mean diameter 400 nm) loaded with KCl (300 mM) and suspended in a potassium gluconate (300 mM) solution. No buffer agent was used. Prodigiosin (1 mol%) (and monensin (0.1 mol%), if monensin was not added previously) was added at 600 s for calibration to 100% KCl efflux. Carrier concentrations are shown as carrier to lipid molar ratios. Error bars represent SD from two or three repeats.

7.5.9.2 NH_4Cl efflux

The chloride efflux measured in the ISE-based NH_4Cl efflux assay (Section 7.5.8.2) might contain contribution form Cl^-/SO_4^{2-} exchange.[228] To exclude this, an osmotic response assay was conducted in which an isosmotic NMDG-gluconate solution was used as the external media. NH_4Cl efflux was indirectly measured from the change in light scattering intensity due to water osmosis following NH_4Cl efflux. This assay does not respond to Cl^-/gluconate exchange since this process is osmotically silent. The results (Figure 7.121) are similar to those obtained using the ISE assay, confirming that CCCP enhances net NH_4Cl flux facilitated by **A12** and **A18**.

Experimental details and results are given below:

POPC LUVs (mean diameter 400 nm) loaded with NH_4Cl were prepared as follows. A chloroform solution of POPC was evaporated in a round-bottle flask and the lipid film formed was dried under vacuum for at least 6 h. The lipid film was hydrated by vortexing with an internal solution containing NH_4Cl (300 mM) buffered at pH 7.4 with 5 mM HEPES. The lipid solution was subjected to nine freeze/thaw cycles and then extruded 25 times through a 400 nm polycarbonate membrane to obtain a lipid stock solution. Removal of external NH_4Cl is not necessary.

For each measurement, the lipid stock solution was diluted with an isotonic external solution containing NMDG-gluconate (300 mM) buffered at pH 7.4 with 5 mM HEPES, to obtain a 2 mL solution containing 0.4 mM of lipid. At the beginning of each measurement, 10 µL of a DMSO solution of the tested carrier was added to the vesicle solution, and the 90° light scattering intensity at 600 nm was monitored by a fluorimeter. When CCCP was used, 4 µL of a 2 mM DMSO solution of CCCP was added to the vesicle solution prior to the addition of the tested carrier. At 10 min, prodigiosin (4 µL of a 2 mM DMSO solution) was added to calibrate the light scattering intensity to 100% NH_4Cl efflux. Each experiment was run in triplicate and the data were averaged over three runs. The fractional light scattering intensity (I_f) is calculated using the following equation:

$$I_f = \frac{I_\mathrm{t} - I_0}{I_\mathrm{p} - I_0}$$

where I_t is the light scattering intensity at time t, I_0 is the light scattering intensity at time 0, and I_p is the light scattering intensity after the addition of prodigiosin.

<u>Conditions:</u>

Internal solution: 300 mM NH_4Cl, buffered at pH 7.4 with 5 mM HEPES; External solution: 300 mM NMDG-gluconate, buffered at pH 7.4 with 5 mM HEPES.

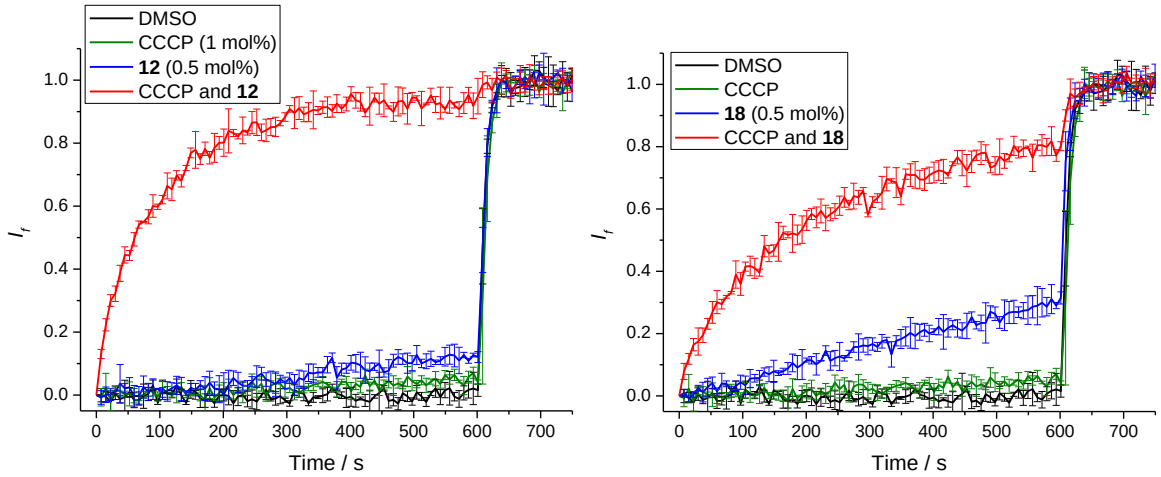

Figure 7.121 Effect of CCCP (1 mol%) on NH_4Cl efflux (indirectly measured by light scattering intensity) facilitated by **A12** (0.5 mol%) and **A18** (0.5 mol%) from POPC LUVs (mean diameter 400 nm) loaded with NH_4Cl (300 mM) and suspended in a NMDG-gluconate (300 mM) solution buffered at pH 7.4 with 5 mM HEPES. Prodigiosin (1 mol%) was added at 600 s for calibration to 100% NH_4Cl efflux. Carrier concentrations are shown as carrier to lipid molar ratios. Error bars represent SD from two or three repeats.

Appendix A Copyright permissions

Author reusing their own work published by the Royal Society of Chemistry

You do not need to request permission to reuse your own figures, diagrams, etc, that were originally published in a Royal Society of Chemistry publication. However, permission should be requested for use of the whole article or chapter except if reusing it in a thesis. If you are including an article or book chapter published by us in your thesis please ensure that your co-authors are aware of this.

Reuse of material that was published originally by the Royal Society of Chemistry must be accompanied by the appropriate acknowledgement of the publication. The form of the acknowledgement is dependent on the journal in which it was published originally, as detailed in 'Acknowledgements'.

http://www.rsc.org/journals-books-databases/journal-authors-reviewers/licences-copyright-permissions/#reuse-permission-requests

Title: Nuclear Magnetic Resonance Signaling of Molecular Chiral Information Using an Achiral Reagent

Author: Atsuomi Shundo, Jan Labuta, Jonathan P. Hill, et al

Publication: Journal of the American Chemical Society

Publisher: American Chemical Society

Date: Jul 1, 2009

PERMISSION/LICENSE IS GRANTED FOR YOUR ORDER AT NO CHARGE

This type of permission/license, instead of the standard Terms & Conditions, is sent to you because no fee is being charged for your order. Please note the following:

- Permission is granted for your request in both print and electronic formats, and translations.
- If figures and/or tables were requested, they may be adapted or used in part.
- Please print this page for your records and send a copy of it to your publisher/graduate school.
- Appropriate credit for the requested material should be given as follows: "Reprinted (adapted) with permission from (COMPLETE REFERENCE CITATION). Copyright (YEAR) American Chemical Society." Insert appropriate information in place of the capitalized words.
- One-time permission is granted only for the use specified in your request. No additional uses are granted (such as derivative works or other editions). For any other uses, please submit a new request.

If credit is given to another source for the material you requested, permission must be obtained from that source.

JOHN WILEY AND SONS LICENSE TERMS AND CONDITIONS

Jan 06, 2016

This Agreement between Xin Wu ("You") and John Wiley and Sons ("John Wiley and Sons") consists of your license details and the terms and conditions provided by John Wiley and Sons and Copyright Clearance Center.

License Number	3783120692488
License date	Jan 06, 2016
Licensed Content Publisher	John Wiley and Sons
Licensed Content Publication	Chemistry - A European Journal
Licensed Content Title	Induced Helical Chirality of Perylenebisimide Aggregates Allows for Enantiopurity Determination and Differentiation of α-Hydroxy Carboxylates by Using Circular Dichroism
Licensed Content Author	Xin Wu,Xuan-Xuan Chen,Bing-Nan Song,Yan-Jun Huang,Zhao Li,Zhan Chen,Tony D. James,Yun-Bao Jiang
Licensed Content Date	Jul 30, 2014
Pages	7
Type of use	Dissertation/Thesis
Requestor type	Author of this Wiley article
Format	Print and electronic
Portion	Full article
Will you be translating?	No
Title of your thesis / dissertation	Exploitation of Noncovalent/Dynamic Covalent Interactions in Sensing, Self-assembly and Membrane Transport
Expected completion date	Jan 2016
Expected size (number of pages)	300
Requestor Location	Xin Wu Chemistry University of Southampton Southampton, United Kingdom SO17 1BJ Attn: Xin Wu
Billing Type	Invoice
Billing Address	Xin Wu Chemistry University of Southampton Southampton, United Kingdom SO17 1BJ Attn: Xin Wu
Total	0.00 GBP
Terms and Conditions	

TERMS AND CONDITIONS

This copyrighted material is owned by or exclusively licensed to John Wiley & Sons, Inc. or one of its group companies (each a"Wiley Company") or handled on behalf of a society with

which a Wiley Company has exclusive publishing rights in relation to a particular work (collectively "WILEY"). By clicking "accept" in connection with completing this licensing transaction, you agree that the following terms and conditions apply to this transaction (along with the billing and payment terms and conditions established by the Copyright Clearance Center Inc., ("CCC's Billing and Payment terms and conditions"), at the time that you opened your RightsLink account (these are available at any time at http://myaccount.copyright.com).

Terms and Conditions

- The materials you have requested permission to reproduce or reuse (the "Wiley Materials") are protected by copyright.

- You are hereby granted a personal, non-exclusive, non-sub licensable (on a stand-alone basis), non-transferable, worldwide, limited license to reproduce the Wiley Materials for the purpose specified in the licensing process. This license, **and any CONTENT (PDF or image file) purchased as part of your order,** is for a one-time use only and limited to any maximum distribution number specified in the license. The first instance of republication or reuse granted by this license must be completed within two years of the date of the grant of this license (although copies prepared before the end date may be distributed thereafter). The Wiley Materials shall not be used in any other manner or for any other purpose, beyond what is granted in the license. Permission is granted subject to an appropriate acknowledgement given to the author, title of the material/book/journal and the publisher. You shall also duplicate the copyright notice that appears in the Wiley publication in your use of the Wiley Material. Permission is also granted on the understanding that nowhere in the text is a previously published source acknowledged for all or part of this Wiley Material. Any third party content is expressly excluded from this permission.

- With respect to the Wiley Materials, all rights are reserved. Except as expressly granted by the terms of the license, no part of the Wiley Materials may be copied, modified, adapted (except for minor reformatting required by the new Publication), translated, reproduced, transferred or distributed, in any form or by any means, and no derivative works may be made based on the Wiley Materials without the prior permission of the respective copyright owner.**For STM Signatory Publishers clearing permission under the terms of the STM Permissions Guidelines only, the terms of the license are extended to include subsequent editions and for editions in other languages, provided such editions are for the work as a whole in situ and does not involve the separate exploitation of the permitted figures or extracts,** You may not alter, remove or suppress in any manner any copyright, trademark or other notices displayed by the Wiley Materials. You may not license, rent, sell, loan, lease, pledge, offer as security, transfer or assign the Wiley Materials on a stand-alone basis, or any of the rights granted to you hereunder to any other person.

- The Wiley Materials and all of the intellectual property rights therein shall at all times remain the exclusive property of John Wiley & Sons Inc, the Wiley Companies, or their respective licensors, and your interest therein is only that of having possession of and the right to reproduce the Wiley Materials pursuant to Section 2 herein during the continuance of this Agreement. You agree that you own no right, title or interest in or to the Wiley Materials or any of the intellectual property rights therein. You shall have no rights hereunder other than the license as provided for above in Section 2. No right, license or interest to any trademark, trade name, service mark or other branding ("Marks") of WILEY or its licensors is granted hereunder, and you agree that you shall not assert any such right, license or interest with respect thereto

- NEITHER WILEY NOR ITS LICENSORS MAKES ANY WARRANTY OR REPRESENTATION OF ANY KIND TO YOU OR ANY THIRD PARTY, EXPRESS, IMPLIED OR STATUTORY, WITH RESPECT TO THE MATERIALS OR THE ACCURACY OF ANY INFORMATION CONTAINED IN THE MATERIALS, INCLUDING, WITHOUT LIMITATION, ANY IMPLIED WARRANTY OF MERCHANTABILITY, ACCURACY, SATISFACTORY QUALITY, FITNESS FOR A PARTICULAR PURPOSE, USABILITY, INTEGRATION OR NON-INFRINGEMENT AND ALL SUCH WARRANTIES ARE HEREBY EXCLUDED BY WILEY AND ITS LICENSORS AND WAIVED BY YOU.

- WILEY shall have the right to terminate this Agreement immediately upon breach of this Agreement by you.

- You shall indemnify, defend and hold harmless WILEY, its Licensors and their respective directors, officers, agents and employees, from and against any actual or threatened claims, demands, causes of action or proceedings arising from any breach of this Agreement by you.

- IN NO EVENT SHALL WILEY OR ITS LICENSORS BE LIABLE TO YOU OR ANY OTHER PARTY OR ANY OTHER PERSON OR ENTITY FOR ANY SPECIAL, CONSEQUENTIAL, INCIDENTAL, INDIRECT, EXEMPLARY OR PUNITIVE DAMAGES, HOWEVER CAUSED, ARISING OUT OF OR IN CONNECTION WITH THE DOWNLOADING, PROVISIONING, VIEWING OR USE OF THE MATERIALS REGARDLESS OF THE FORM OF ACTION, WHETHER FOR BREACH OF CONTRACT, BREACH OF WARRANTY, TORT, NEGLIGENCE, INFRINGEMENT OR OTHERWISE (INCLUDING, WITHOUT LIMITATION, DAMAGES BASED ON LOSS OF PROFITS, DATA, FILES, USE, BUSINESS OPPORTUNITY OR CLAIMS OF THIRD PARTIES), AND WHETHER OR NOT THE PARTY HAS BEEN ADVISED OF THE POSSIBILITY OF SUCH DAMAGES. THIS LIMITATION SHALL APPLY NOTWITHSTANDING ANY FAILURE OF ESSENTIAL PURPOSE OF ANY LIMITED REMEDY PROVIDED HEREIN.

- Should any provision of this Agreement be held by a court of competent jurisdiction to be illegal, invalid, or unenforceable, that provision shall be deemed amended to achieve as nearly as possible the same economic effect as the original provision, and the legality, validity and enforceability of the remaining provisions of this Agreement shall not be affected or impaired thereby.

- The failure of either party to enforce any term or condition of this Agreement shall not constitute a waiver of either party's right to enforce each and every term and condition of this Agreement. No breach under this agreement shall be deemed waived or excused by either party unless such waiver or consent is in writing signed by the party granting such waiver or consent. The waiver by or consent of a party to a breach of any provision of this Agreement shall not operate or be construed as a waiver of or consent to any other or subsequent breach by such other party.

- This Agreement may not be assigned (including by operation of law or otherwise) by you without WILEY's prior written consent.

- Any fee required for this permission shall be non-refundable after thirty (30) days from receipt by the CCC.

- These terms and conditions together with CCC's Billing and Payment terms and conditions (which are incorporated herein) form the entire agreement between you and WILEY concerning this licensing transaction and (in the absence of fraud) supersedes all prior agreements and representations of the parties, oral or written. This Agreement may not be amended except in writing signed by both parties. This Agreement shall be binding upon and inure to the benefit of the parties' successors, legal representatives, and authorized assigns.

- In the event of any conflict between your obligations established by these terms and conditions and those established by CCC's Billing and Payment terms and conditions, these terms and conditions shall prevail.

- WILEY expressly reserves all rights not specifically granted in the combination of (i) the license details provided by you and accepted in the course of this licensing transaction, (ii) these terms and conditions and (iii) CCC's Billing and Payment terms and conditions.

- This Agreement will be void if the Type of Use, Format, Circulation, or Requestor Type was misrepresented during the licensing process.

- This Agreement shall be governed by and construed in accordance with the laws of the State of New York, USA, without regards to such state's conflict of law rules. Any legal action, suit or proceeding arising out of or relating to these Terms and Conditions or the breach thereof shall be instituted in a court of competent jurisdiction in New York County in the State of New York in the United States of America and each party hereby consents and submits to the personal jurisdiction of such court, waives any objection to venue in such court and consents to service of process by registered or certified mail, return receipt requested, at the last known address of such party.

WILEY OPEN ACCESS TERMS AND CONDITIONS

Wiley Publishes Open Access Articles in fully Open Access Journals and in Subscription journals offering Online Open. Although most of the fully Open Access journals publish open access articles under the terms of the Creative Commons Attribution (CC BY) License only, the subscription journals and a few of the Open Access Journals offer a choice of Creative Commons Licenses. The license type is clearly identified on the article.

The Creative Commons Attribution License

The Creative Commons Attribution License (CC-BY) allows users to copy, distribute and transmit an article, adapt the article and make commercial use of the article. The CC-BY license permits commercial and non-

Creative Commons Attribution Non-Commercial License

The Creative Commons Attribution Non-Commercial (CC-BY-NC)License permits use, distribution and reproduction in any medium, provided the original work is properly cited and is not used for commercial purposes.(see below)

Creative Commons Attribution-Non-Commercial-NoDerivs License

The Creative Commons Attribution Non-Commercial-NoDerivs License (CC-BY-NC-ND) permits use, distribution and reproduction in any medium, provided the original work is properly cited, is not used for commercial purposes and no modifications or adaptations are made. (see below)

Use by commercial "for-profit" organizations

Use of Wiley Open Access articles for commercial, promotional, or marketing purposes

requires further explicit permission from Wiley and will be subject to a fee.
Further details can be found on Wiley Online Library
http://olabout.wiley.com/WileyCDA/Section/id-410895.html

Other Terms and Conditions:

v1.10 Last updated September 2015

Questions? customercare@copyright.com or +1-855-239-3415 (toll free in the US) or +1-978-646-2777.

ROYAL SOCIETY OF CHEMISTRY LICENSE TERMS AND CONDITIONS

May 25, 2016

This Agreement between Xin Wu ("You") and Royal Society of Chemistry ("Royal Society of Chemistry") consists of your license details and the terms and conditions provided by Royal Society of Chemistry and Copyright Clearance Center.

License Number	3875961034558
License date	May 25, 2016
Licensed Content Publisher	Royal Society of Chemistry
Licensed Content Publication	Chemical Communications (Cambridge)
Licensed Content Title	Bis(zinc porphyrin) as a CD-sensitive bidentate host molecule: direct determination of absolute configuration of mono-alcohols
Licensed Content Author	Satoshi Hayashi,Miku Yotsukura,Masahiro Noji,Toshikatsu Takanami
Licensed Content Date	May 28, 2015
Licensed Content Volume Number	51
Licensed Content Issue Number	55
Type of Use	Thesis/Dissertation
Requestor type	academic/educational
Portion	figures/tables/images
Number of figures/tables/images	1
Format	print and electronic
Distribution quantity	10
Will you be translating?	no
Order reference number	None
Title of the thesis/dissertation	Exploitation of Noncovalent/Dynamic Covalent Interactions in Sensing, Self-assembly and Membrane Transport
Expected completion date	Jan 2016
Estimated size	300
Requestor Location	Xin Wu Chemistry University of Southampton Southampton, United Kingdom SO17 1BJ Attn: Xin Wu
Billing Type	Invoice
Billing Address	Xin Wu Chemistry University of Southampton Southampton, United Kingdom SO17 1BJ Attn: Xin Wu
Total	0.00 GBP

Terms and Conditions

This License Agreement is between {Requestor Name} ("You") and The Royal Society of Chemistry ("RSC") provided by the Copyright Clearance Center ("CCC"). The license consists of your order details, the terms and conditions provided by the Royal Society of Chemistry, and the payment terms and conditions.

RSC / TERMS AND CONDITIONS

INTRODUCTION

The publisher for this copyrighted material is The Royal Society of Chemistry. By clicking "accept" in connection with completing this licensing transaction, you agree that the following terms and conditions apply to this transaction (along with the Billing and Payment terms and conditions established by CCC, at the time that you opened your RightsLink account and that are available at any time at .

LICENSE GRANTED

The RSC hereby grants you a non-exclusive license to use the aforementioned material anywhere in the world subject to the terms and conditions indicated herein. Reproduction of the material is confined to the purpose and/or media for which permission is hereby given.

RESERVATION OF RIGHTS

The RSC reserves all rights not specifically granted in the combination of (i) the license details provided by your and accepted in the course of this licensing transaction; (ii) these terms and conditions; and (iii) CCC's Billing and Payment terms and conditions.

REVOCATION

The RSC reserves the right to revoke this license for any reason, including, but not limited to, advertising and promotional uses of RSC content, third party usage, and incorrect source figure attribution.

THIRD-PARTY MATERIAL DISCLAIMER

If part of the material to be used (for example, a figure) has appeared in the RSC publication with credit to another source, permission must also be sought from that source. If the other source is another RSC publication these details should be included in your RightsLink request. If the other source is a third party, permission must be obtained from the third party. The RSC disclaims any responsibility for the reproduction you make of items owned by a third party.

PAYMENT OF FEE

If the permission fee for the requested material is waived in this instance, please be advised that any future requests for the reproduction of RSC materials may attract a fee.

ACKNOWLEDGEMENT

The reproduction of the licensed material must be accompanied by the following acknowledgement:

Reproduced ("Adapted" or "in part") from {Reference Citation} (or Ref XX) with permission of The Royal Society of Chemistry.

If the licensed material is being reproduced from New Journal of Chemistry (NJC), Photochemical & Photobiological Sciences (PPS) or Physical Chemistry Chemical Physics (PCCP) you must include one of the following acknowledgements:

For figures originally published in NJC:

Reproduced ("Adapted" or "in part") from {Reference Citation} (or Ref XX) with permission of The Royal Society of Chemistry (RSC) on behalf of the European Society for Photobiology, the European Photochemistry Association and the RSC.

For figures originally published in PPS:

Reproduced ("Adapted" or "in part") from {Reference Citation} (or Ref XX) with permission of The Royal Society of Chemistry (RSC) on behalf of the Centre National de la Recherche Scientifique (CNRS) and the RSC.

For figures originally published in PCCP:

Reproduced ("Adapted" or "in part") from {Reference Citation} (or Ref XX) with permission of the PCCP Owner Societies.

HYPERTEXT LINKS

With any material which is being reproduced in electronic form, you must include a hypertext link to the original RSC article on the RSC's website. The recommended form for the hyperlink is http://dx.doi.org/10.1039/DOI suffix, for example in the link http://dx.doi.org/10.1039/b110420a the DOI suffix is 'b110420a'. To find the relevant DOI suffix for the RSC article in question, go to the Journals section of the website and locate the article in the list of papers for the volume and issue of your specific journal. You will find the DOI suffix quoted there.

LICENSE CONTINGENT ON PAYMENT

While you may exercise the rights licensed immediately upon issuance of the license at the end of the licensing process for the transaction, provided that you have disclosed complete and accurate details of your proposed use, no license is finally effective unless and until full payment is received from you (by CCC) as provided in CCC's Billing and Payment terms and conditions. If full payment is not received on a timely basis, then any license preliminarily granted shall be deemed automatically revoked and shall be void as if never granted. Further, in the event that you breach any of these terms and conditions or any of CCC's Billing and Payment terms and conditions, the license is automatically revoked and shall be void as if never granted. Use of materials as described in a revoked license, as well as any use of the materials beyond the scope of an unrevoked license, may constitute copyright infringement and the RSC reserves the right to take any and all action to protect its copyright in the materials.

WARRANTIES

The RSC makes no representations or warranties with respect to the licensed material.

INDEMNITY

You hereby indemnify and agree to hold harmless the RSC and the CCC, and their respective officers, directors, trustees, employees and agents, from and against any and all claims arising out of your use of the licensed material other than as specifically authorized pursuant to this licence.

NO TRANSFER OF LICENSE

This license is personal to you or your publisher and may not be sublicensed, assigned, or transferred by you to any other person without the RSC's written permission.

NO AMENDMENT EXCEPT IN WRITING

This license may not be amended except in a writing signed by both parties (or, in the case of "Other Conditions, v1.2", by CCC on the RSC's behalf).

OBJECTION TO CONTRARY TERMS

You hereby acknowledge and agree that these terms and conditions, together with CCC's Billing and Payment terms and conditions (which are incorporated herein), comprise the entire agreement between you and the RSC (and CCC) concerning this licensing transaction, to the exclusion of all other terms and conditions, written or verbal, express or implied (including any terms contained in any purchase order, acknowledgment, check endorsement or other writing prepared by you). In the event of any conflict between your obligations established by these terms and conditions and those established by CCC's Billing and Payment terms and conditions, these terms and conditions shall control.

JURISDICTION

This license transaction shall be governed by and construed in accordance with the laws of the District of Columbia. You hereby agree to submit to the jurisdiction of the courts located in the District of Columbia for purposes of resolving any disputes that may arise in connection with this licensing transaction.

LIMITED LICENSE

The following terms and conditions apply to specific license types:

Translation

This permission is granted for non-exclusive world English rights only unless your license was granted for translation rights. If you licensed translation rights you may only translate this content into the languages you requested. A professional translator must perform all translations and reproduce the content word for word preserving the integrity of the article.

Intranet
If the licensed material is being posted on an Intranet, the Intranet is to be password-protected and made available only to bona fide students or employees only. All content posted to the Intranet must maintain the copyright information line on the bottom of each image. You must also fully reference the material and include a hypertext link as specified above.
Copies of Whole Articles
All copies of whole articles must maintain, if available, the copyright information line on the bottom of each page.
Other Conditions
v1.2
Gratis licenses (referencing $0 in the Total field) are free. Please retain this printable license for your reference. No payment is required.
If you would like to pay for this license now, please remit this license along with yourpayment made payable to "COPYRIGHT CLEARANCE CENTER" otherwise you will be invoiced within 48 hours of the license date. Payment should be in the form of a check or money order referencing your account number and this invoice number {Invoice Number}.
Once you receive your invoice for this order, you may pay your invoice by credit card.
Please follow instructions provided at that time.
Make Payment To:
Copyright Clearance Center
Dept 001
P.O. Box 843006
Boston, MA 02284-3006
For suggestions or comments regarding this order, contact Rightslink Customer Support:
customercare@copyright.com or +1-855-239-3415 (toll free in the US) or +1-978-646-2777.

Questions? customercare@copyright.com or +1-855-239-3415 (toll free in the US) or +1-978-646-2777.

JOHN WILEY AND SONS LICENSE
TERMS AND CONDITIONS

May 25, 2016

This Agreement between Xin Wu ("You") and John Wiley and Sons ("John Wiley and Sons") consists of your license details and the terms and conditions provided by John Wiley and Sons and Copyright Clearance Center.

License Number	3875970897133
License date	May 25, 2016
Licensed Content Publisher	John Wiley and Sons
Licensed Content Publication	Chemistry - A European Journal
Licensed Content Title	Supramolecular Tandem Enzyme Assays for Multiparameter Sensor Arrays and Enantiomeric Excess Determination of Amino Acids
Licensed Content Author	David M. Bailey,Andreas Hennig,Vanya D. Uzunova,Werner M. Nau
Licensed Content Date	May 28, 2008
Pages	9
Type of use	Dissertation/Thesis
Requestor type	University/Academic
Format	Print and electronic
Portion	Figure/table
Number of figures/tables	1
Original Wiley figure/table number(s)	Scheme 1
Will you be translating?	No
Title of your thesis / dissertation	Exploitation of Noncovalent/Dynamic Covalent Interactions in Sensing, Self-assembly and Membrane Transport
Expected completion date	Jan 2016
Expected size (number of pages)	300
Requestor Location	Xin Wu Chemistry University of Southampton Southampton, United Kingdom SO17 1BJ Attn: Xin Wu
Billing Type	Invoice
Billing Address	Xin Wu Chemistry University of Southampton Southampton, United Kingdom SO17 1BJ Attn: Xin Wu
Total	0.00 GBP
Terms and Conditions	

TERMS AND CONDITIONS

This copyrighted material is owned by or exclusively licensed to John Wiley & Sons, Inc. or

one of its group companies (each a"Wiley Company") or handled on behalf of a society with which a Wiley Company has exclusive publishing rights in relation to a particular work (collectively "WILEY"). By clicking "accept" in connection with completing this licensing transaction, you agree that the following terms and conditions apply to this transaction (along with the billing and payment terms and conditions established by the Copyright Clearance Center Inc., ("CCC's Billing and Payment terms and conditions"), at the time that you opened your RightsLink account (these are available at any time at http://myaccount.copyright.com).

Terms and Conditions

- The materials you have requested permission to reproduce or reuse (the "Wiley Materials") are protected by copyright.

- You are hereby granted a personal, non-exclusive, non-sub licensable (on a stand-alone basis), non-transferable, worldwide, limited license to reproduce the Wiley Materials for the purpose specified in the licensing process. This license, **and any CONTENT (PDF or image file) purchased as part of your order,** is for a one-time use only and limited to any maximum distribution number specified in the license. The first instance of republication or reuse granted by this license must be completed within two years of the date of the grant of this license (although copies prepared before the end date may be distributed thereafter). The Wiley Materials shall not be used in any other manner or for any other purpose, beyond what is granted in the license. Permission is granted subject to an appropriate acknowledgement given to the author, title of the material/book/journal and the publisher. You shall also duplicate the copyright notice that appears in the Wiley publication in your use of the Wiley Material. Permission is also granted on the understanding that nowhere in the text is a previously published source acknowledged for all or part of this Wiley Material. Any third party content is expressly excluded from this permission.

- With respect to the Wiley Materials, all rights are reserved. Except as expressly granted by the terms of the license, no part of the Wiley Materials may be copied, modified, adapted (except for minor reformatting required by the new Publication), translated, reproduced, transferred or distributed, in any form or by any means, and no derivative works may be made based on the Wiley Materials without the prior permission of the respective copyright owner.**For STM Signatory Publishers clearing permission under the terms of the STM Permissions Guidelines only, the terms of the license are extended to include subsequent editions and for editions in other languages, provided such editions are for the work as a whole in situ and does not involve the separate exploitation of the permitted figures or extracts,** You may not alter, remove or suppress in any manner any copyright, trademark or other notices displayed by the Wiley Materials. You may not license, rent, sell, loan, lease, pledge, offer as security, transfer or assign the Wiley Materials on a stand-alone basis, or any of the rights granted to you hereunder to any other person.

- The Wiley Materials and all of the intellectual property rights therein shall at all times remain the exclusive property of John Wiley & Sons Inc, the Wiley Companies, or their respective licensors, and your interest therein is only that of having possession of and the right to reproduce the Wiley Materials pursuant to Section 2 herein during the continuance of this Agreement. You agree that you own no right, title or interest in or to the Wiley Materials or any of the intellectual property rights therein. You shall have no rights hereunder other than the license as provided for above in Section 2. No right, license or interest to any trademark, trade name, service mark or other branding ("Marks") of WILEY or its licensors is granted hereunder, and you agree that you

shall not assert any such right, license or interest with respect thereto

- NEITHER WILEY NOR ITS LICENSORS MAKES ANY WARRANTY OR REPRESENTATION OF ANY KIND TO YOU OR ANY THIRD PARTY, EXPRESS, IMPLIED OR STATUTORY, WITH RESPECT TO THE MATERIALS OR THE ACCURACY OF ANY INFORMATION CONTAINED IN THE MATERIALS, INCLUDING, WITHOUT LIMITATION, ANY IMPLIED WARRANTY OF MERCHANTABILITY, ACCURACY, SATISFACTORY QUALITY, FITNESS FOR A PARTICULAR PURPOSE, USABILITY, INTEGRATION OR NON-INFRINGEMENT AND ALL SUCH WARRANTIES ARE HEREBY EXCLUDED BY WILEY AND ITS LICENSORS AND WAIVED BY YOU.

- WILEY shall have the right to terminate this Agreement immediately upon breach of this Agreement by you.

- You shall indemnify, defend and hold harmless WILEY, its Licensors and their respective directors, officers, agents and employees, from and against any actual or threatened claims, demands, causes of action or proceedings arising from any breach of this Agreement by you.

- IN NO EVENT SHALL WILEY OR ITS LICENSORS BE LIABLE TO YOU OR ANY OTHER PARTY OR ANY OTHER PERSON OR ENTITY FOR ANY SPECIAL, CONSEQUENTIAL, INCIDENTAL, INDIRECT, EXEMPLARY OR PUNITIVE DAMAGES, HOWEVER CAUSED, ARISING OUT OF OR IN CONNECTION WITH THE DOWNLOADING, PROVISIONING, VIEWING OR USE OF THE MATERIALS REGARDLESS OF THE FORM OF ACTION, WHETHER FOR BREACH OF CONTRACT, BREACH OF WARRANTY, TORT, NEGLIGENCE, INFRINGEMENT OR OTHERWISE (INCLUDING, WITHOUT LIMITATION, DAMAGES BASED ON LOSS OF PROFITS, DATA, FILES, USE, BUSINESS OPPORTUNITY OR CLAIMS OF THIRD PARTIES), AND WHETHER OR NOT THE PARTY HAS BEEN ADVISED OF THE POSSIBILITY OF SUCH DAMAGES. THIS LIMITATION SHALL APPLY NOTWITHSTANDING ANY FAILURE OF ESSENTIAL PURPOSE OF ANY LIMITED REMEDY PROVIDED HEREIN.

- Should any provision of this Agreement be held by a court of competent jurisdiction to be illegal, invalid, or unenforceable, that provision shall be deemed amended to achieve as nearly as possible the same economic effect as the original provision, and the legality, validity and enforceability of the remaining provisions of this Agreement shall not be affected or impaired thereby.

- The failure of either party to enforce any term or condition of this Agreement shall not constitute a waiver of either party's right to enforce each and every term and condition of this Agreement. No breach under this agreement shall be deemed waived or excused by either party unless such waiver or consent is in writing signed by the party granting such waiver or consent. The waiver by or consent of a party to a breach of any provision of this Agreement shall not operate or be construed as a waiver of or consent to any other or subsequent breach by such other party.

- This Agreement may not be assigned (including by operation of law or otherwise) by you without WILEY's prior written consent.

- Any fee required for this permission shall be non-refundable after thirty (30) days

from receipt by the CCC.

- These terms and conditions together with CCC's Billing and Payment terms and conditions (which are incorporated herein) form the entire agreement between you and WILEY concerning this licensing transaction and (in the absence of fraud) supersedes all prior agreements and representations of the parties, oral or written. This Agreement may not be amended except in writing signed by both parties. This Agreement shall be binding upon and inure to the benefit of the parties' successors, legal representatives, and authorized assigns.

- In the event of any conflict between your obligations established by these terms and conditions and those established by CCC's Billing and Payment terms and conditions, these terms and conditions shall prevail.

- WILEY expressly reserves all rights not specifically granted in the combination of (i) the license details provided by you and accepted in the course of this licensing transaction, (ii) these terms and conditions and (iii) CCC's Billing and Payment terms and conditions.

- This Agreement will be void if the Type of Use, Format, Circulation, or Requestor Type was misrepresented during the licensing process.

- This Agreement shall be governed by and construed in accordance with the laws of the State of New York, USA, without regards to such state's conflict of law rules. Any legal action, suit or proceeding arising out of or relating to these Terms and Conditions or the breach thereof shall be instituted in a court of competent jurisdiction in New York County in the State of New York in the United States of America and each party hereby consents and submits to the personal jurisdiction of such court, waives any objection to venue in such court and consents to service of process by registered or certified mail, return receipt requested, at the last known address of such party.

WILEY OPEN ACCESS TERMS AND CONDITIONS

Wiley Publishes Open Access Articles in fully Open Access Journals and in Subscription journals offering Online Open. Although most of the fully Open Access journals publish open access articles under the terms of the Creative Commons Attribution (CC BY) License only, the subscription journals and a few of the Open Access Journals offer a choice of Creative Commons Licenses. The license type is clearly identified on the article.

The Creative Commons Attribution License

The Creative Commons Attribution License (CC-BY) allows users to copy, distribute and transmit an article, adapt the article and make commercial use of the article. The CC-BY license permits commercial and non-

Creative Commons Attribution Non-Commercial License

The Creative Commons Attribution Non-Commercial (CC-BY-NC)License permits use, distribution and reproduction in any medium, provided the original work is properly cited and is not used for commercial purposes.(see below)

Creative Commons Attribution-Non-Commercial-NoDerivs License

The Creative Commons Attribution Non-Commercial-NoDerivs License (CC-BY-NC-ND) permits use, distribution and reproduction in any medium, provided the original work is properly cited, is not used for commercial purposes and no modifications or adaptations are made. (see below)

Use by commercial "for-profit" organizations

Use of Wiley Open Access articles for commercial, promotional, or marketing purposes

requires further explicit permission from Wiley and will be subject to a fee.
Further details can be found on Wiley Online Library
http://olabout.wiley.com/WileyCDA/Section/id-410895.html

Other Terms and Conditions:

v1.10 Last updated September 2015

Questions? customercare@copyright.com or +1-855-239-3415 (toll free in the US) or +1-978-646-2777.

JOHN WILEY AND SONS LICENSE TERMS AND CONDITIONS

May 25, 2016

This Agreement between Xin Wu ("You") and John Wiley and Sons ("John Wiley and Sons") consists of your license details and the terms and conditions provided by John Wiley and Sons and Copyright Clearance Center.

License Number	3876010063846
License date	May 25, 2016
Licensed Content Publisher	John Wiley and Sons
Licensed Content Publication	Angewandte Chemie International Edition
Licensed Content Title	Noncovalent Chirality Sensing Ensembles for the Detection and Reaction Monitoring of Amino Acids, Peptides, Proteins, and Aromatic Drugs
Licensed Content Author	Frank Biedermann,Werner M. Nau
Licensed Content Date	Apr 9, 2014
Pages	6
Type of use	Dissertation/Thesis
Requestor type	University/Academic
Format	Print and electronic
Portion	Figure/table
Number of figures/tables	2
Original Wiley figure/table number(s)	Figure 1 and Figure 2
Will you be translating?	No
Title of your thesis / dissertation	Exploitation of Noncovalent/Dynamic Covalent Interactions in Sensing, Self-assembly and Membrane Transport
Expected completion date	Jan 2016
Expected size (number of pages)	300
Requestor Location	Xin Wu Chemistry University of Southampton Southampton, United Kingdom SO17 1BJ Attn: Xin Wu
Billing Type	Invoice
Billing Address	Xin Wu Chemistry University of Southampton Southampton, United Kingdom SO17 1BJ Attn: Xin Wu
Total	0.00 GBP
Terms and Conditions	

TERMS AND CONDITIONS

("Marks") of WILEY or its licensors is granted hereunder, and you agree that you shall not assert any such right, license or interest with respect thereto

- NEITHER WILEY NOR ITS LICENSORS MAKES ANY WARRANTY OR REPRESENTATION OF ANY KIND TO YOU OR ANY THIRD PARTY, EXPRESS, IMPLIED OR STATUTORY, WITH RESPECT TO THE MATERIALS OR THE ACCURACY OF ANY INFORMATION CONTAINED IN THE MATERIALS, INCLUDING, WITHOUT LIMITATION, ANY IMPLIED WARRANTY OF MERCHANTABILITY, ACCURACY, SATISFACTORY QUALITY, FITNESS FOR A PARTICULAR PURPOSE, USABILITY, INTEGRATION OR NON-INFRINGEMENT AND ALL SUCH WARRANTIES ARE HEREBY EXCLUDED BY WILEY AND ITS LICENSORS AND WAIVED BY YOU.

- WILEY shall have the right to terminate this Agreement immediately upon breach of this Agreement by you.

- You shall indemnify, defend and hold harmless WILEY, its Licensors and their respective directors, officers, agents and employees, from and against any actual or threatened claims, demands, causes of action or proceedings arising from any breach of this Agreement by you.

- IN NO EVENT SHALL WILEY OR ITS LICENSORS BE LIABLE TO YOU OR ANY OTHER PARTY OR ANY OTHER PERSON OR ENTITY FOR ANY SPECIAL, CONSEQUENTIAL, INCIDENTAL, INDIRECT, EXEMPLARY OR PUNITIVE DAMAGES, HOWEVER CAUSED, ARISING OUT OF OR IN CONNECTION WITH THE DOWNLOADING, PROVISIONING, VIEWING OR USE OF THE MATERIALS REGARDLESS OF THE FORM OF ACTION, WHETHER FOR BREACH OF CONTRACT, BREACH OF WARRANTY, TORT, NEGLIGENCE, INFRINGEMENT OR OTHERWISE (INCLUDING, WITHOUT LIMITATION, DAMAGES BASED ON LOSS OF PROFITS, DATA, FILES, USE, BUSINESS OPPORTUNITY OR CLAIMS OF THIRD PARTIES), AND WHETHER OR NOT THE PARTY HAS BEEN ADVISED OF THE POSSIBILITY OF SUCH DAMAGES. THIS LIMITATION SHALL APPLY NOTWITHSTANDING ANY FAILURE OF ESSENTIAL PURPOSE OF ANY LIMITED REMEDY PROVIDED HEREIN.

- Should any provision of this Agreement be held by a court of competent jurisdiction to be illegal, invalid, or unenforceable, that provision shall be deemed amended to achieve as nearly as possible the same economic effect as the original provision, and the legality, validity and enforceability of the remaining provisions of this Agreement shall not be affected or impaired thereby.

- The failure of either party to enforce any term or condition of this Agreement shall not constitute a waiver of either party's right to enforce each and every term and condition of this Agreement. No breach under this agreement shall be deemed waived or excused by either party unless such waiver or consent is in writing signed by the party granting such waiver or consent. The waiver by or consent of a party to a breach of any provision of this Agreement shall not operate or be construed as a waiver of or consent to any other or subsequent breach by such other party.

- This Agreement may not be assigned (including by operation of law or otherwise) by you without WILEY's prior written consent.

- Any fee required for this permission shall be non-refundable after thirty (30) days from receipt by the CCC.

- These terms and conditions together with CCC's Billing and Payment terms and conditions (which are incorporated herein) form the entire agreement between you and WILEY concerning this licensing transaction and (in the absence of fraud) supersedes all prior agreements and representations of the parties, oral or written. This Agreement may not be amended except in writing signed by both parties. This Agreement shall be binding upon and inure to the benefit of the parties' successors, legal representatives, and authorized assigns.

- In the event of any conflict between your obligations established by these terms and conditions and those established by CCC's Billing and Payment terms and conditions, these terms and conditions shall prevail.

- WILEY expressly reserves all rights not specifically granted in the combination of (i) the license details provided by you and accepted in the course of this licensing transaction, (ii) these terms and conditions and (iii) CCC's Billing and Payment terms and conditions.

- This Agreement will be void if the Type of Use, Format, Circulation, or Requestor Type was misrepresented during the licensing process.

- This Agreement shall be governed by and construed in accordance with the laws of the State of New York, USA, without regards to such state's conflict of law rules. Any legal action, suit or proceeding arising out of or relating to these Terms and Conditions or the breach thereof shall be instituted in a court of competent jurisdiction in New York County in the State of New York in the United States of America and each party hereby consents and submits to the personal jurisdiction of such court, waives any objection to venue in such court and consents to service of process by registered or certified mail, return receipt requested, at the last known address of such party.

WILEY OPEN ACCESS TERMS AND CONDITIONS

Wiley Publishes Open Access Articles in fully Open Access Journals and in Subscription journals offering Online Open. Although most of the fully Open Access journals publish open access articles under the terms of the Creative Commons Attribution (CC BY) License only, the subscription journals and a few of the Open Access Journals offer a choice of Creative Commons Licenses. The license type is clearly identified on the article.

The Creative Commons Attribution License

The Creative Commons Attribution License (CC-BY) allows users to copy, distribute and transmit an article, adapt the article and make commercial use of the article. The CC-BY license permits commercial and non-

Creative Commons Attribution Non-Commercial License

The Creative Commons Attribution Non-Commercial (CC-BY-NC)License permits use, distribution and reproduction in any medium, provided the original work is properly cited and is not used for commercial purposes.(see below)

Creative Commons Attribution-Non-Commercial-NoDerivs License

The Creative Commons Attribution Non-Commercial-NoDerivs License (CC-BY-NC-ND) permits use, distribution and reproduction in any medium, provided the original work is properly cited, is not used for commercial purposes and no modifications or adaptations are made. (see below)

Use by commercial "for-profit" organizations

List of References

1. S. J. Rowan, S. J. Cantrill, G. R. L. Cousins, J. K. M. Sanders, J. F. Stoddart, *Angew. Chem., Int. Ed.* **2002**, *41*, 898-952.
2. T. M. Beale, M. G. Chudzinski, M. G. Sarwar, M. S. Taylor, *Chem. Soc. Rev.* **2013**, *42*, 1667-1680.
3. B. L. Schottel, H. T. Chifotides, K. R. Dunbar, *Chem. Soc. Rev.* **2008**, *37*, 68-83.
4. S. D. Bull, M. G. Davidson, J. M. H. van den Elsen, J. S. Fossey, A. T. A. Jenkins, Y.-B. Jiang, Y. Kubo, F. Marken, K. Sakurai, J. Zhao, T. D. James, *Acc. Chem. Res.* **2012**, *46*, 312-326.
5. S. P. Black, J. K. M. Sanders, A. R. Stefankiewicz, *Chem. Soc. Rev.* **2014**, *43*, 1861-1872.
6. M. E. Belowich, J. F. Stoddart, *Chem. Soc. Rev.* **2012**, *41*, 2003-2024.
7. L. You, S. R. Long, V. M. Lynch, E. V. Anslyn, *Chem. Eur. J.* **2011**, *17*, 11017-11023.
8. M. Matsui, K. Yamada, K. Funabiki, *Tetrahedron* **2005**, *61*, 4671-4677.
9. Y. Ura, J. M. Beierle, L. J. Leman, L. E. Orgel, M. R. Ghadiri, *Science* **2009**, *325*, 73-77.
10. J. Mosquera, S. Zarra, J. R. Nitschke, *Angew. Chem., Int. Ed.* **2013**, *53*, 1556-1559.
11. P. T. Corbett, J. Leclaire, L. Vial, K. R. West, J.-L. Wietor, J. K. M. Sanders, S. Otto, *Chem. Rev.* **2006**, *106*, 3652-3711.
12. J.-F. Ayme, J. E. Beves, D. A. Leigh, R. T. McBurney, K. Rissanen, D. Schultz, *Nat. Chem.* **2012**, *4*, 15-20.
13. S. Mura, J. Nicolas, P. Couvreur, *Nat. Mater.* **2013**, *12*, 991-1003.
14. S. Kassem, A. T. L. Lee, D. A. Leigh, A. Markevicius, J. Solà, *Nat. Chem.* **2015**, *8*, 138-143.
15. E. V. Anslyn, *J. Org. Chem.* **2007**, *72*, 687-699.
16. X. Wu, X.-X. Chen, B.-N. Song, Y.-J. Huang, Z. Li, Z. Chen, T. D. James, Y.-B. Jiang, *Chem. Eur. J.* **2014**, *20*, 11793-11799.
17. X. Wu, X.-X. Chen, B.-N. Song, Y.-J. Huang, W.-J. Ouyang, Z. Li, T. D. James, Y.-B. Jiang, *Chem. Commun.* **2014**, *50*, 13987-13989.
18. X. Wu, N. Busschaert, N. J. Wells, Y.-B. Jiang, P. A. Gale, *J. Am. Chem. Soc.* **2015**, *137*, 1476-1484.
19. X. Zhang, J. Yin, J. Yoon, *Chem. Rev.* **2014**, *114*, 4918-4959.
20. H. H. Jo, C.-Y. Lin, E. V. Anslyn, *Acc. Chem. Res.* **2014**, *47*, 2212-2221.
21. C. Wolf, K. W. Bentley, *Chem. Soc. Rev.* **2013**, *42*, 5408-5424.
22. J. Labuta, S. Ishihara, T. Šikorský, Z. Futera, A. Shundo, L. Hanyková, J. V. Burda, K. Ariga, J. P. Hill, *Nat. Commun.* **2013**, *4*, 2188.
23. J. Labuta, S. Ishihara, A. Shundo, S. Arai, S. Takeoka, K. Ariga, J. P. Hill, *Chem. Eur. J.* **2011**, *17*, 3558-3561.

24. A. Shundo, J. Labuta, J. P. Hill, S. Ishihara, K. Ariga, *J. Am. Chem. Soc.* **2009**, *131*, 9494-9495.

25. Z. Chen, Q. Wang, X. Wu, Z. Li, Y.-B. Jiang, *Chem. Soc. Rev.* **2015**, *44*, 4249-4263.

26. S. Superchi, D. Casarini, A. Laurita, A. Bavoso, C. Rosini, *Angew. Chem., Int. Ed.* **2001**, *40*, 451-454.

27. N. Berova, G. Pescitelli, A. G. Petrovic, G. Proni, *Chem. Commun.* **2009**, 5958-5980.

28. X. Li, M. Tanasova, C. Vasileiou, B. Borhan, *J. Am. Chem. Soc.* **2008**, *130*, 1885-1893.

29. X. Huang, N. Fujioka, G. Pescitelli, F. E. Koehn, R. T. Williamson, K. Nakanishi, N. Berova, *J. Am. Chem. Soc.* **2002**, *124*, 10320-10335.

30. H. Yoon, C.-H. Lee, W.-D. Jang, *Chem. Eur. J.* **2012**, *18*, 12479-12486.

31. S. Hayashi, M. Yotsukura, M. Noji, T. Takanami, *Chem. Commun.* **2015**, *51*, 11068-11071.

32. L. A. Joyce, M. S. Maynor, J. M. Dragna, G. M. da Cruz, V. M. Lynch, J. W. Canary, E. V. Anslyn, *J. Am. Chem. Soc.* **2011**, *133*, 13746-13752.

33. L. A. Joyce, J. W. Canary, E. V. Anslyn, *Chem. Eur. J.* **2012**, *18*, 8064-8069.

34. L. You, G. Pescitelli, E. V. Anslyn, L. Di Bari, *J. Am. Chem. Soc.* **2012**, *134*, 7117-7125.

35. L. You, J. S. Berman, E. V. Anslyn, *Nat. Chem.* **2011**, *3*, 943-948.

36. D. P. Iwaniuk, C. Wolf, *J. Am. Chem. Soc.* **2011**, *133*, 2414-2417.

37. D. P. Iwaniuk, C. Wolf, *Org. Lett.* **2011**, *13*, 2602-2605.

38. M. W. Ghosn, C. Wolf, *J. Am. Chem. Soc.* **2009**, *131*, 16360-16361.

39. M. W. Ghosn, C. Wolf, *Tetrahedron* **2010**, *66*, 3989-3994.

40. L. Pu, *Acc. Chem. Res.* **2011**, *45*, 150-163.

41. H.-L. Liu, Q. Peng, Y.-D. Wu, D. Chen, X.-L. Hou, M. Sabat, L. Pu, *Angew. Chem., Int. Ed.* **2010**, *49*, 602-606.

42. Y. Perez-Fuertes, A. M. Kelly, J. S. Fossey, M. E. Powell, S. D. Bull, T. D. James, *Nat. Protocols* **2008**, *3*, 210-214.

43. P. Metola, E. V. Anslyn, T. D. James, S. D. Bull, *Chem. Sci.* **2012**, *3*, 156-161.

44. E. G. Shcherbakova, T. Minami, V. Brega, T. D. James, P. Anzenbacher, *Angew. Chem., Int. Ed.* **2015**, *54*, 7130-7133.

45. A. Shundo, J. Labuta, J. P. Hill, S. Ishihara, K. Ariga, *Journal of the American Chemical Society* **2009**, *131*, 9494-9495.

46. J. Labuta, S. Ishihara, A. Shundo, S. Arai, S. Takeoka, K. Ariga, J. P. Hill, *Chemistry--A European Journal* **2011**, *17*, 3558-3561.

47. D. M. Bailey, A. Hennig, V. D. Uzunova, W. M. Nau, *Chem. Eur. J.* **2008**, *14*, 6069-6077.

48. F. Biedermann, W. M. Nau, *Angew. Chem. Int. Ed.* **2014**, *53*, 5694-5699.

49. E. Yashima, K. Maeda, T. Nishimura, *Chem. Eur. J.* **2004**, *10*, 42-51.

50. A. R. A. Palmans, E. W. Meijer, *Angew. Chem., Int. Ed.* **2007**, *46*, 8948-8968.

51. J. van Gestel, A. R. A. Palmans, B. Titulaer, J. A. J. M. Vekemans, E. W. Meijer, *J. Am. Chem. Soc.* **2005**, *127*, 5490-5494.

52. M. M. Green, B. A. Garetz, B. Munoz, H. Chang, S. Hoke, R. G. Cooks, *J. Am. Chem. Soc.* **1995**, *117*, 4181-4182.

53. R. Nonokawa, E. Yashima, *J. Am. Chem. Soc.* **2002**, *125*, 1278-1283.

54. H. M. Seifert, Y.-B. Jiang, E. V. Anslyn, *Chem. Commun.* **2014**, *50*, 15330-15332.

55. J. H. K. K. Hirschberg, L. Brunsveld, A. Ramzi, J. A. J. M. Vekemans, R. P. Sijbesma, E. W. Meijer, *Nature* **2000**, *407*, 167-170.

56. A. R. A. Palmans, J. A. J. M. Vekemans, E. E. Havinga, E. W. Meijer, *Angew. Chem., Int. Ed. Engl.* **1997**, *36*, 2648-2651.

57. J.-S. Zhao, J.-H. Wang, W.-B. He, Y.-B. Ruan, Y.-B. Jiang, *Chem. Eur. J.* **2012**, 3631-3636.

58. L. Zhang, M. Liu, *J. Phy. Chem. B* **2009**, *113*, 14015-14020.

59. R. A. Garoff, E. A. Litzinger, R. E. Connor, I. Fishman, B. A. Armitage, *Langmuir* **2002**, *18*, 6330-6337.

60. J.-S. Zhao, Y.-B. Ruan, R. Zhou, Y.-B. Jiang, *Chem. Sci.* **2011**, *2*, 937-944.

61. T. Ma, C. Li, G. Shi, *Langmuir* **2007**, *24*, 43-48.

62. D. Franke, M. Vos, M. Antonietti, N. A. J. M. Sommerdijk, C. F. J. Faul, *Chem. Mater.* **2006**, *18*, 1839-1847.

63. H. Fenniri, B.-L. Deng, A. E. Ribbe, *J. Am. Chem. Soc.* **2002**, *124*, 11064-11072.

64. S. Arimori, M. Takeuchi, S. Shinkai, *J. Am. Chem. Soc.* **1996**, *118*, 245-246.

65. A. D'Urso, R. Randazzo, L. Lo Faro, R. Purrello, *Angew. Chem., Int. Ed.* **2010**, *49*, 108-112.

66. J. M. Ribó, J. Crusats, F. Sagués, J. Claret, R. Rubires, *Science* **2001**, *292*, 2063-2066.

67. N. Micali, H. Engelkamp, P. G. van Rhee, P. C. M. Christianen, L. M. Scolaro, J. C. Maan, *Nat. Chem.* **2012**, *4*, 201-207.

68. F. Riobe, A. P. H. J. Schenning, D. B. Amabilino, *Org, Biomol. Chem.* **2012**, *10*, 9152-9157.

69. S. J. George, Ž. Tomović, M. M. J. Smulders, T. F. A. de Greef, P. E. L. G. Leclère, E. W. Meijer, A. P. H. J. Schenning, *Angew. Chem., Int. Ed.* **2007**, *46*, 8206-8211.

70. R. F. Fink, J. Seibt, V. Engel, M. Renz, M. Kaupp, S. Lochbrunner, H.-M. Zhao, J. Pfister, F. Würthner, B. Engels, *J. Am. Chem. Soc.* **2008**, *130*, 12858-12859.

71. D. Görl, X. Zhang, F. Würthner, *Angew. Chem., Int. Ed.* **2012**, *51*, 6328-6348.

72. F. Würthner, *Chem. Commun.* **2004**, 1564-1579.

73. N. Katif, R. Harries, A. Kelly, J. Fossey, T. James, F. Marken, *J. Solid State Electrochem.* **2009**, *13*, 1475-1482.

74. Y. Yang, P. T. Lewis, J. O. Escobedo, N. N. St. Luce, W. D. Trealeaven, R. L. Cooks, R. M. Strongin, *Collect. Czech. Chem. Commun.* **2004**, *69*, 1282.

75. S. L. Wiskur, J. J. Lavigne, A. Metzger, S. L. Tobey, V. Lynch, E. V. Anslyn, *Chem. Eur. J.* **2004**, *10*, 3792-3804.

76. G. M. Coppola, H. F. Schuster, *α-Hydroxyl Acids in Enantioselective Synthesis*, Wiley-VCH, Weinheim, Germany, **1997**.

77. L. Guo, X. Zhang, D. Zhou, A. L. Okunade, X. Su, *J. Lipid. Res.* **2012**, *53*, 1327-1335.

78. K. Djanashvili, L. Frullano, J. A. Peters, *Chem. Eur. J.* **2005**, *11*, 4010-4018.

79. R. O. Marcon, J. G. dos Santos, K. M. Figueiredo, S. Brochsztain, *Langmuir* **2006**, *22*, 1680-1687.

80. T. van der Boom, G. Evmenenko, P. Dutta, M. R. Wasielewski, *Chem. Mater.* **2003**, *15*, 4068-4074.

81. H. Langhals, R. Ismael, *Eur. J. Org. Chem.* **1998**, *1998*, 1915-1917.

82. W. E. Ford, *J. Photochem.* **1987**, *37*, 189-204.

83. M. Kasha, H. R. Rawls, M. A. El Bayoumi, *Pure Appl. Chem.* **1965**, *11*, 371.

84. W. Wang, L.-S. Li, G. Helms, H.-H. Zhou, A. D. Q. Li, *J. Am. Chem. Soc.* **2003**, *125*, 1120-1121.

85. C. Fasting, C. A. Schalley, M. Weber, O. Seitz, S. Hecht, B. Koksch, J. Dernedde, C. Graf, E.-W. Knapp, R. Haag, *Angew. Chem., Int. Ed.* **2012**, *51*, 10472-10498.

86. X. Wu, Z. Li, X.-X. Chen, J. S. Fossey, T. D. James, Y.-B. Jiang, *Chem. Soc. Rev.* **2013**, 8032-8048.

87. P. Schreier, A. Bernreuther, M. Huffer, *Analysis of Chiral Organic Molecules: Methodology and Applications*, De Gruyter, Würzburg, **1995**.

88. D. Leung, S. O. Kang, E. V. Anslyn, *Chem. Soc. Rev.* **2012**, *41*, 448.

89. S. Yang, Y. Liu, G. Feng, *RSC Adv.* **2013**, *3*, 20171-20178.

90. D. W. Smith, *J. Chem. Educ.* **1977**, *54*, 540.

91. M. Cametti, K. Rissanen, *Chem. Soc. Rev.* **2013**, *42*, 2016-2038.

92. C. A. Ilioudis, D. A. Tocher, J. W. Steed, *J. Am. Chem. Soc.* **2004**, *126*, 12395-12402.

93. P. Ashokkumar, H. Weißhoff, W. Kraus, K. Rurack, *Angew. Chem., Int. Ed.* **2014**, *53*, 2225-2229.

94. S. Guha, S. Saha, *J. Am. Chem. Soc.* **2010**, *132*, 17674-17677.

95. I.-S. Ke, M. Myahkostupov, F. N. Castellano, F. P. Gabbaï, *J. Am. Chem. Soc.* **2012**, *134*, 15309-15311.

96. T. Hayashita, T. Onodera, R. Kato, S. Nishizawa, N. Teramae, *Chem. Commun.* **2000**, 755-756.

97. A. B. Descalzo, D. Jimenez, J. E. Haskouri, D. Beltran, P. Amoros, M. D. Marcos, R. Martinez-Manez, J. Soto, *Chem. Commun.* **2002**, 562-563.

98. R. Hu, J. Feng, D. Hu, S. Wang, S. Li, Y. Li, G. Yang, *Angew. Chem., Int. Ed.* **2010**, *49*, 4915-4918.

99. C. R. Wade, A. E. J. Broomsgrove, S. Aldridge, F. o. P. Gabbaï, *Chem. Rev.* **2010**, *110*, 3958-3984.

100. C. R. Cooper, N. Spencer, T. D. James, *Chem. Commun.* **1998**, 1365-1366.

101. T. Nishimura, S.-Y. Xu, Y.-B. Jiang, J. S. Fossey, K. Sakurai, S. D. Bull, T. D. James, *Chem. Commun.* **2013**, *49*, 478-480.

102. Y. Kim, F. o. P. Gabbaï, *J. Am. Chem. Soc.* **2009**, *131*, 3363-3369.

103. D. Janeliunas, P. van Rijn, J. Boekhoven, C. B. Minkenberg, J. H. van Esch, R. Eelkema, *Angew. Chem., Int. Ed.* **2013**, *52*, 1998-2001.

104. C. B. Minkenberg, F. Li, P. van Rijn, L. Florusse, J. Boekhoven, M. C. A. Stuart, G. J. M. Koper, R. Eelkema, J. H. van Esch, *Angew. Chem., Int. Ed.* **2011**, *50*, 3421-3424.

105. S. Chen, Y. Ruan, J. D. Brown, J. Gallucci, V. Maslak, C. M. Hadad, J. D. Badjić, *J. Am. Chem. Soc.* **2013**, *135*, 14964-14967.

106. Y.-J. Huang, W.-J. Ouyang, X. Wu, Z. Li, J. S. Fossey, T. D. James, Y.-B. Jiang, *J. Am. Chem. Soc.* **2013**, *135*, 1700-1703.

107. J. Yan, G. Springsteen, S. Deeter, B. Wang, *Tetrahedron* **2004**, *60*, 11205-11209.

108. L. I. Bosch, T. M. Fyles, T. D. James, *Tetrahedron* **2004**, *60*, 11175-11190.

109. N. Sakai, T. Takeuchi, S. Futaki, S. Matile, *Chembiochem* **2005**, *6*, 114-122.

110. W.-M. Yau, W. C. Wimley, K. Gawrisch, S. H. White, *Biochemistry-us.* **1998**, *37*, 14713-14718.

111. Y. Kubo, T. Ishida, A. Kobayashi, T. D. James, *J. Mater. Chem.* **2005**, *15*, 2889-2895.

112. P. Agarwal, J. van der Weijden, E. M. Sletten, D. Rabuka, C. R. Bertozzi, *Proc. Natl. Acad. Sci. USA* **2013**, *110*, 46-51.

113. C. Ke, H. Destecroix, M. P. Crump, A. P. Davis, *Nat. Chem.* **2012**, *4*, 718-723.

114. T. D. James, M. D. Phillips, S. Shinkai, *Boronic Acids in Saccharide Recognition*, The Royal Society of Chemistry, Cambridge, UK, **2006**.

115. S. J. Angyal, *Adv. Carbohydr. Chem. Biochem.* **1984**, *42*, 15-68.

116. S. J. Angyal, *Adv. Carbohydr. Chem. Biochem.* **1991**, *49*, 19-35.

117. J. P. Lorand, J. O. Edwards, *J. Org. Chem.* **1959**, *24*, 769-774.

118. T. D. James, K. R. A. S. Sandanayake, S. Shinkai, *Angew. Chem., Int. Ed. Engl.* **1994**, *33*, 2207-2209.

119. M. Bielecki, H. Eggert, J. C. Norrild, *J. Chem. Soc., Perkin Trans. 2* **1999**, 449-456.

120. J. D. Larkin, K. A. Frimat, T. M. Fyles, S. E. Flower, T. D. James, *New J. Chem.* **2010**, *34*, 2922-2931.

121. W. Yang, H. He, D. G. Drueckhammer, *Angew. Chem., Int. Ed.* **2001**, *40*, 1714-1718.

122. Y. Hong, J. W. Y. Lam, B. Z. Tang, *Chem. Commun.* **2009**, 4332-4353.

123. Y. Liu, C. Deng, L. Tang, A. Qin, R. Hu, J. Z. Sun, B. Z. Tang, *J. Am. Chem. Soc.* **2010**, *133*, 660-663.

124. T. F. A. De Greef, M. M. J. Smulders, M. Wolffs, A. P. H. J. Schenning, R. P. Sijbesma, E. W. Meijer, *Chem. Rev.* **2009**, *109*, 5687-5754.

125. C. W. Hoerr, M. R. McCorkle, A. W. Ralston, *J. Am. Chem. Soc.* **1943**, *65*, 328-329.

126. N. J. Gutierrez-Moreno, F. Medrano, A. K. Yatsimirsky, *Org, Biomol. Chem.* **2012**, *10*, 6960-6972.

127. C. B. Minkenberg, L. Florusse, R. Eelkema, G. J. M. Koper, J. H. van Esch, *J. Am. Chem. Soc.* **2009**, *131*, 11274-11275.

128. A. Sorrenti, O. Illa, R. M. Ortuno, *Chem. Soc. Rev.* **2013**, *42*, 8200-8219.

129. R. Quesada, in *Supramolecular Chemistry: From Molecules to Nanomaterials* (Eds.: P. A. Gale, J. W. Steed), John Wiley & Sons, Ltd, Chichester, **2012**.

130. S. Matile, A. Vargas Jentzsch, J. Montenegro, A. Fin, *Chem. Soc. Rev.* **2011**, *40*, 2453-2474.

131. B. A. McNally, W. M. Leevy, B. D. Smith, *Supramol. Chem.* **2007**, *19*, 29-37.

132. G. W. Gokel, S. Negin, *Acc. Chem. Res.* **2013**, *46*, 2824-2833.

133. J. K. W. Chui, T. M. Fyles, *Chem. Soc. Rev.* **2012**, *41*, 148-175.

134. P. A. Gale, R. Perez-Tomas, R. Quesada, *Acc Chem Res* **2013**, *46*, 2801-2813.

135. H. Valkenier, A. P. Davis, *Acc. Chem. Res.* **2013**, *46*, 2898-2909.

136. S.-K. Ko, S. K. Kim, A. Share, V. M. Lynch, J. Park, W. Namkung, W. Van Rossom, N. Busschaert, P. A. Gale, J. L. Sessler, I. Shin, *Nat. Chem.* **2014**, *6*, 885-892.

137. B. Shen, X. Li, F. Wang, X. Yao, D. Yang, *PLoS ONE* **2012**, *7*, e34694.

138. N. Busschaert, M. Wenzel, M. E. Light, P. Iglesias-Hernández, R. Pérez-Tomás, P. A. Gale, *J. Am. Chem. Soc.* **2011**, *133*, 14136-14148.

139. A. V. Koulov, J. M. Mahoney, B. D. Smith, *Org, Biomol. Chem.* **2003**, *1*, 27-29.

140. C. C. Tong, R. Quesada, J. L. Sessler, P. A. Gale, *Chem. Commun.* **2008**, 6321-6323.

141. T. Sato, H. Konno, Y. Tanaka, T. Kataoka, K. Nagai, H. H. Wasserman, S. Ohkuma, *J. Biol. Chem.* **1998**, *273*, 21455-21462.

142. H. Valkenier, L. W. Judd, H. Li, S. Hussain, D. N. Sheppard, A. P. Davis, *J. Am. Chem. Soc.* **2014**, *136*, 12507-12512.

143. N. Busschaert, R. B. P. Elmes, D. D. Czech, X. Wu, I. L. Kirby, E. M. Peck, K. D. Hendzel, S. K. Shaw, B. Chan, B. D. Smith, K. A. Jolliffe, P. A. Gale, *Chem. Sci.* **2014**, *5*, 3617-3626.

144. N. Busschaert, I. L. Kirby, S. Young, S. J. Coles, P. N. Horton, M. E. Light, P. A. Gale, *Angew. Chem., Int. Ed.* **2012**, *51*, 4426-4430.

145. P. V. Santacroce, J. T. Davis, M. E. Light, P. A. Gale, J. C. Iglesias-Sánchez, P. Prados, R. Quesada, *J. Am. Chem. Soc.* **2007**, *129*, 1886-1887.

146. A. V. Koulov, T. N. Lambert, R. Shukla, M. Jain, J. M. Boon, B. D. Smith, H. Li, D. N. Sheppard, J.-B. Joos, J. P. Clare, A. P. Davis, *Angew. Chem., Int. Ed.* **2003**, *42*, 4931-4933.

147. A. Vargas Jentzsch, S. Matile, *J. Am. Chem. Soc.* **2013**, *135*, 5302-5303.

148. A. Vargas Jentzsch, D. Emery, J. Mareda, S. K. Nayak, P. Metrangolo, G. Resnati, N. Sakai, S. Matile, *Nat. Commun.* **2012**, *3*, 905.

149. M. El-Etri, J. Cuppoletti, *Am. J. Physiol.* **1996**, *270*, L386-L392.

150. D. Milano, B. Benedetti, M. Boccalon, A. Brugnara, E. Iengo, P. Tecilla, *Chem. Commun.* **2014**, *50*, 9157-9160.

151. D. A. Doyle, J. M. Cabral, R. A. Pfuetzner, A. Kuo, J. M. Gulbis, S. L. Cohen, B. T. Chait, R. MacKinnon, *Science* **1998**, *280*, 69-77.

152. M. M. Tedesco, B. Ghebremariam, N. Sakai, S. Matile, *Angew. Chem., Int. Ed.* **1999**, *38*, 540-543.

153. R. Kumpf, D. Dougherty, *Science* **1993**, *261*, 1708-1710.

154. R. E. Dawson, A. Hennig, D. P. Weimann, D. Emery, V. Ravikumar, J. Montenegro, T. Takeuchi, S. Gabutti, M. Mayor, J. Mareda, C. A. Schalley, S. Matile, *Nat. Chem.* **2010**, *2*, 533-538.

155. A. Vargas Jentzsch, D. Emery, J. Mareda, P. Metrangolo, G. Resnati, S. Matile, *Angew. Chem., Int. Ed.* **2011**, *50*, 11675-11678.

156. A. Wilson, G. Gasparini, S. Matile, *Chem. Soc. Rev.* **2014**, *43*, 1948-1962.

157. A. Herrmann, *Chem. Soc. Rev.* **2014**, *43*, 1899-1933.

158. P. R. Westmark, S. J. Gardiner, B. D. Smith, *J. Am. Chem. Soc.* **1996**, *118*, 11093-11100.

159. P. R. Westmark, B. D. Smith, *J. Am. Chem. Soc.* **1994**, *116*, 9343-9344.

160. P. R. Westmark, B. D. Smith, *J. Pharm. Sci.* **1996**, *85*, 266-269.

161. W. Stillwell, *Biosystems.* **1976**, *8*, 111-117.

162. E.-K. Bang, G. Gasparini, G. Molinard, A. Roux, N. Sakai, S. Matile, *J. Am. Chem. Soc.* **2013**, *135*, 2088-2091.

163. E. Mertz, J. B. Beil, S. C. Zimmerman, *Org. Lett.* **2003**, *5*, 3127-3130.

164. D. A. Evans, G. Borg, K. A. Scheidt, *Angew. Chem., Int. Ed.* **2002**, *41*, 3188-3191.

165. C. D. Ritchie, *J. Am. Chem. Soc.* **1984**, *106*, 7187-7194.

166. T. Iwasawa, R. J. Hooley, J. Rebek, *Science* **2007**, *317*, 493-496.

167. R. Shi, L. McDonald, Q. Cui, A. Matte, M. Cygler, I. Ekiel, *Proc. Natl. Acad. Sci. USA* **2011**, *108*, 1302-1307.

168. C. Siebold, L. F. García-Alles, B. Erni, U. Baumann, *Proc. Natl. Acad. Sci. USA* **2003**, *100*, 8188-8192.

169. J. T. Davis, P. A. Gale, O. A. Okunola, P. Prados, J. C. Iglesias-Sánchez, T. Torroba, R. Quesada, *Nat. Chem.* **2009**, *1*, 138-144.

170. P. D. McNamara, B. Ozegović, L. M. Pepe, S. Segal, *Proc. Natl. Acad. Sci. USA* **1976**, *73*, 4521-4525.

171. A. C. Chakrabarti, D. W. Deamer, *Biochim. Biophys. Acta* **1992**, *1111*, 171-177.

172. D. F. H. Wallach, T. L. Steck, *Anal. Chem.* **1963**, *35*, 1035-1044.

173. K. E. S. Dean, G. Klein, O. Renaudet, J.-L. Reymond, *Bioorg. Med. Chem. Lett* **2003**, *13*, 1653-1656.

174. S. M. Kaiser, B. I. Escher, *Environ. Sci. Technol.* **2006**, *40*, 1784-1791.

175. S. Li, K. D. Smith, J. H. Davis, P. B. Gordon, R. R. Breaker, S. A. Strobel, *Proc. Natl. Acad. Sci. USA* **2013**, *110*, 19018-19023.

176. F. Castelli, A. Raudino, M. Fresta, *J. Colloid Interf. Sci* **2005**, *285*, 110-117.

177. R. B. Stockbridge, H.-H. Lim, R. Otten, C. Williams, T. Shane, Z. Weinberg, C. Miller, *Proc. Natl. Acad. Sci. USA* **2012**, *109*, 15289-15294.

178. P. G. Heytler, W. W. Prichard, *Biochem. Biophys. Res. Commun.* **1962**, *7*, 272-275.

179. S. Bhosale, S. Matile, *Chirality* **2006**, *18*, 849-856.

180. A. V. Hill, *Biochem. J.* **1913**, *7*, 471-470.

181. A. J. Kirby, I. V. Komarov, V. A. Bilenko, J. E. Davies, J. M. Rawson, *Chem. Commun.* **2002**, 2106-2107.

182. S. Matile, N. Sakai, in *Analytical Methods in Supramolecular Chemistry* (Ed.: C. A. Schalley), 2 ed., Wiley-VCH, Weinheim, **2012**, pp. 711-742.

183. N. R. Clement, J. M. Gould, *Biochemistry-us.* **1981**, *20*, 1534-1538.

184. N. K. Subbarao, R. C. MacDonald, *Biochim. Biophys. Acta* **1994**, *1189*, 101-107.

185. E. H. Cordes, W. P. Jencks, *J. Am. Chem. Soc.* **1962**, *84*, 832-837.

186. J. Crugeiras, A. Rios, E. Riveiros, J. P. Richard, *J. Am. Chem. Soc.* **2009**, *131*, 15815-15824.

187. C. Kirby, J. Clarke, G. Gregoriadis, *Biochem. J.* **1980**, *186*, 591-598.

188. A. C. Chakrabarti, *Amino Acids* **1994**, *6*, 213-229.

189. B. C. Pressman, *Annu. Rev. Biochem.* **1976**, *45*, 501-530.

190. Q. Xie, G. Gokel, J. Hernandez, L. Echegoyen, Y. Li, *J. Am. Chem. Soc.* **1994**, *116*, 690-696.

191. J. T. Davis, O. Okunola, R. Quesada, *Chem. Soc. Rev.* **2010**, *39*, 3843-3862.

192. A. P. Davis, D. N. Sheppard, B. D. Smith, *Chem. Soc. Rev.* **2007**, *36*, 348-357.

193. J. H. Lee, J. H. Lee, Y. R. Choi, P. Kang, M.-G. Choi, K.-S. Jeong, *J. Org. Chem.* **2014**, *79*, 6403-6409.

194. S. G. McLaughlin, J. P. Dilger, *Physiol. Rev.* **1980**, *60*, 825-863.

195. H. Lodish, *Molecular Cell Biology*, W. H. Freeman, **2008**.

196. M. M. Shemyakin, Y. A. Ovchinnikov, V. T. Ivanov, V. K. Antonov, E. I. Vinogradova, A. M. Shkrob, G. G. Malenkov, A. V. Evstratov, I. A. Laine, E. I. Melnik, I. D. Ryabova, *J. Membr. Biol.* **1969**, *1*, 402-430.

197. W. C. McMurray, R. W. Begg, *Arch. Biochem. Biophys.* **1959**, *84*, 546-548.

198. P. Läuger, *Science* **1972**, *178*, 24-30.

199. P. J. F. Henderson, J. D. McGivan, J. B. Chappell, *Biochem. J.* **1969**, *111*, 521-535.

200. R. Sandeaux, J. Sandeaux, C. Gavach, B. Brun, *Biochim. Biophys. Acta* **1982**, *684*, 127-132.

201. V. S. Markin, V. S. Sokolov, L. I. Boguslavsky, L. S. Jaguzhinsky, *J. Membr. Biol.* **1975**, *25*, 23-45.

202. E. Carafoli, C. S. Rossi, *Biochem. Biophys. Res. Commun.* **1967**, *29*, 153-157.

203. P. Mitchell, *Biol. Rev.* **1966**, *41*, 445-501.

204. T. Kataoka, M. Muroi, S. Ohkuma, T. Waritani, J. Magae, A. Takatsuki, S. Kondo, M. Yamasaki, K. Nagai, *FEBS Lett.* **1995**, *359*, 53-59.

205. S. Ohkuma, T. Sato, M. Okamoto, H. Matsuya, K. Arai, T. Kataoka, K. Nagai, H. H. Wasserman, *Biochem. J.* **1998**, *334*, 731-741.

206. A. R. Graves, P. K. Curran, C. L. Smith, J. A. Mindell, *Nature* **2008**, *453*, 788-792.

207. Y. Ishida, S. Nayak, J. A. Mindell, M. Grabe, *J. Gen. Physiol* **2013**, *141*, 705-720.

208. H. H. Mollenhauer, D. James Morré, L. D. Rowe, *Biochim. Biophys. Acta Rev. Biomembr.* **1990**, *1031*, 225-246.

209. J. L. Seganish, J. T. Davis, *Chem. Commun.* **2005**, 5781-5783.

210. A. G. Cioffi, J. Hou, A. S. Grillo, K. A. Diaz, M. D. Burke, *J. Am. Chem. Soc.* **2015**, *137*, 10096-10099.

211. S. J. Moore, M. G. Fisher, M. Yano, C. C. Tong, P. A. Gale, *Chem. Commun.* **2011**, *47*, 689-691.

212. J. Biwersi, B. Tulk, A. S. Verkman, *Anal. Biochem.* **1994**, *219*, 139-143.

213. B. A. McNally, A. V. Koulov, B. D. Smith, J.-B. Joos, A. P. Davis, *Chem. Commun.* **2005**, 1087-1089.

214. S. K. Berezin, J. T. Davis, *J. Am. Chem. Soc.* **2009**, *131*, 2458-2459.

215. H. T. Tien, A. Ottova-Leitmannova, *Planar Lipid Bilayers (BLMs) and Their Applications*, Elsevier Science, **2003**.

216. R. C. Bean, W. C. Shepherd, H. Chan, J. Eichner, *J. Gen. Physiol* **1969**, *53*, 741-757.

217. P. Bühlmann, E. Pretsch, E. Bakker, *Chem. Rev.* **1998**, *98*, 1593-1688.

218. A. P. Singh, P. Nicholls, *Biochemistry and Cell Biology* **1986**, *64*, 647-655.

219. N. J. Andrews, C. J. E. Haynes, M. E. Light, S. J. Moore, C. C. Tong, J. T. Davis, W. A. Harrell Jr, P. A. Gale, *Chem. Sci.* **2011**, *2*, 256-260.

220. P. A. Gale, C. C. Tong, C. J. E. Haynes, O. Adeosun, D. E. Gross, E. Karnas, E. M. Sedenberg, R. Quesada, J. L. Sessler, *J. Am. Chem. Soc.* **2010**, *132*, 3240-3241.

221. S. Bahmanjah, N. Zhang, J. T. Davis, *Chem. Commun.* **2012**, *48*, 4432-4434.

222. H. Valkenier, C. J. E. Haynes, J. Herniman, P. A. Gale, A. P. Davis, *Chem. Sci.* **2014**.

223. S. Hussain, P. R. Brotherhood, L. W. Judd, A. P. Davis, *J. Am. Chem. Soc.* **2011**, *133*, 1614-1617.

224. L. W. Judd, A. P. Davis, *Chem. Commun.* **2010**, *46*, 2227-2229.

225. S. J. Edwards, H. Valkenier, N. Busschaert, P. A. Gale, A. P. Davis, *Angew. Chem., Int. Ed.* **2015**, *127*, 4675-4679.

226. J. A. Cooper, S. T. G. Street, A. P. Davis, *Angew. Chem., Int. Ed.* **2014**, 5609-5613.

227. N. Busschaert, P. A. Gale, C. J. E. Haynes, M. E. Light, S. J. Moore, C. C. Tong, J. T. Davis, J. W. A. Harrell, *Chem. Commun.* **2010**, *46*, 6252-6254.

228. N. Busschaert, L. E. Karagiannidis, M. Wenzel, C. J. E. Haynes, N. J. Wells, P. G. Young, D. Makuc, J. Plavec, K. A. Jolliffe, P. A. Gale, *Chem. Sci.* **2014**, *5*, 1118-1127.

229. L. E. Karagiannidis, C. J. E. Haynes, K. J. Holder, I. L. Kirby, S. J. Moore, N. J. Wells, P. A. Gale, *Chem. Commun.* **2014**, *50*, 12050-12053.

230. S. J. Moore, C. J. E. Haynes, J. González, J. L. Sutton, S. J. Brooks, M. E. Light, J. Herniman, G. J. Langley, V. Soto-Cerrato, R. Pérez-Tomás, I. Marques, P. J. Costa, V. Felix, P. A. Gale, *Chem. Sci.* **2013**, *4*, 103-117.

231. B. A. McNally, A. V. Koulov, T. N. Lambert, B. D. Smith, J.-B. Joos, A. L. Sisson, J. P. Clare, V. Sgarlata, L. W. Judd, G. Magro, A. P. Davis, *Chem. Eur. J.* **2008**, *14*, 9599-9606.

232. J. Shang, W. Si, W. Zhao, Y. Che, J.-L. Hou, H. Jiang, *Org. Lett.* **2014**, *16*, 4008-4011.

233. M. Lisbjerg, H. Valkenier, B. M. Jessen, H. Al-Kerdi, A. P. Davis, M. Pittelkow, *J. Am. Chem. Soc.* **2015**, *137*, 4948-4951.

234. K. H. Klotz, R. Benz, *Biophys. J.* **1993**, *65*, 2661-2672.

235. M. G. Sarwar, B. Dragisic, S. Sagoo, M. S. Taylor, *Angew. Chem., Int. Ed.* **2010**, *49*, 1674-1677.

236. B. P. O'Sullivan, S. D. Freedman, *The Lancet* **2009**, *373*, 1891-1904.

237. A. Fürstner, *Angew. Chem., Int. Ed.* **2003**, *42*, 3582-3603.

238. J. L. Sessler, L. R. Eller, W.-S. Cho, S. Nicolaou, A. Aguilar, J. T. Lee, V. M. Lynch, D. J. Magda, *Angew. Chem., Int. Ed.* **2005**, *44*, 5989-5992.

239. P. I. Hernandez, D. Moreno, A. A. Javier, T. Torroba, R. Pérez-Tomás, R. Quesada, *Chem. Commun.* **2012**, *48*, 1556-1558.

240. H. Li, H. Valkenier, L. W. Judd, P. R. Brotherhood, S. Hussain, J. A. Cooper, O. Jurček, H. A. Sparkes, D. N. Sheppard, A. P. Davis, *Nat. Chem.* **2016**, *8*, 24-32.

241. D. N. Sheppard, M. J. Welsh, *Physiol. Rev.* **1999**, *79*, S23-S45.

242. F. Hofmeister, *Arch. Exp. Pathol. Pharmakol.* **1888**, *24*, 247-260.

243. B. A. Moyer, *Ion Exchange and Solvent Extraction: Volume 21, Supramolecular Aspects of Solvent Extraction*, Taylor & Francis, **2013**.

244. S. K. Berezin, *J. Membr. Biol.* **2014**, *247*, 651-665.

245. K. P. Xiao, P. Bühlmann, S. Nishizawa, S. Amemiya, Y. Umezawa, *Anal. Chem.* **1997**, *69*, 1038-1044.

246. M. J. Berrocal, A. Cruz, I. H. A. Badr, L. G. Bachas, *Anal. Chem.* **2000**, *72*, 5295-5299.

247. B. Roux, S. Bernèche, B. Egwolf, B. Lev, S. Y. Noskov, C. N. Rowley, H. Yu, *J. Gen. Physiol* **2011**, *137*, 415-426.

248. S. K. Berezin, *Supramol. Chem.* **2013**, *25*, 323-334.

249. N. Demaurex, *Physiology* **2002**, *17*, 1-5.

250. D. A. Kelkar, A. Chattopadhyay, *Biochim. Biophys. Acta* **2007**, *1768*, 2011-2025.

251. M. Denda, S. Fuziwara, K. Inoue, *J. Investig. Dermatol.* **2003**, *121*, 362-367.

252. E. Šturdík, E. Ďurčová, V. Mikeš, V. Dadák, Š. Baláž, P. Sulo, M. Antalík, *Collect. Czech. Chem. Commun.* **1987**, *52*, 2819 - 2825.

253. G. Jakab, C. Tancon, Z. Zhang, K. M. Lippert, P. R. Schreiner, *Org. Lett.* **2012**, *14*, 1724-1727.

254. Y. Marcus, *J. Chem. Soc. Faraday Trans.* **1991**, *87*, 2995-2999.

255. S. Liu, L. G. Pedersen, *J. Phys. Chem. A* **2009**, *113*, 3648-3655.

256. C. A. Hunter, H. L. Anderson, *Angew. Chem., Int. Ed.* **2009**, *48*, 7488-7499.

257. L. A. Weiss, N. Sakai, B. Ghebremariam, C. Ni, S. Matile, *J. Am. Chem. Soc.* **1997**, *119*, 12142-12149.

258. N. Sakai, K. C. Brennan, L. A. Weiss, S. Matile, *J. Am. Chem. Soc.* **1997**, *119*, 8726-8727.

259. N. Busschaert, S. J. Bradberry, M. Wenzel, C. J. E. Haynes, J. R. Hiscock, I. L. Kirby, L. E. Karagiannidis, S. J. Moore, N. J. Wells, J. Herniman, G. J. Langley, P. N. Horton, M. E. Light, I. Marques, P. J. Costa, V. Felix, J. G. Frey, P. A. Gale, *Chem. Sci.* **2013**, *4*, 3036-3045.

260. J. C. Norrild, H. Eggert, *J. Am. Chem. Soc.* **1995**, *117*, 1479-1484.

261. J. C. Norrild, H. Eggert, *J. Chem. Soc., Perkin Trans. 2* **1996**, 2583-2588.

262. M. Merritt, M. Lanier, G. Deng, S. L. Regen, *J. Am. Chem. Soc.* **1998**, *120*, 8494-8501.

263. P. L. Luisi, *The Emergence of Life: From Chemical Origins to Synthetic Biology*, Cambridge University Press, New York, **2006**.

264. G. Jakab, A. Hosseini, H. Hausmann, P. R. Schreiner, *Synthesis* **2013**, *45*, 1635-1640.

265. T. N. Lambert, J. M. Boon, B. D. Smith, M. N. Pérez-Payán, A. P. Davis, *J. Am. Chem. Soc.* **2002**, *124*, 5276-5277.

266. A. L. Sisson, V. del Amo Sanchez, G. Magro, A. M. E. Griffin, S. Shah, J. P. H. Charmant, A. P. Davis, *Angew. Chem., Int. Ed.* **2005**, *44*, 6878-6881.

267. L. W. Judd, *Cholapods and cholaphanes : steroid based receptors for anion transport*, University of Bristol, **2010**.

268. P. Bose, R. Dutta, S. Santra, B. Chowdhury, P. Ghosh, *Eur. J. Inorg. Chem.* **2012**, *2012*, 5791-5801.

269. X.-a. Zhang, W.-D. Woggon, *J. Am. Chem. Soc.* **2005**, *127*, 14138-14139.

270. M. Lipowska, B. L. Hayes, L. Hansen, A. Taylor, L. G. Marzilli, *Inorg. Chem.* **1996**, *35*, 4227-4231.

271. J. Rana, D. J. Robins, *J. Chem. Soc., Perkin Trans. 1* **1986**, 1133-1137.

272. E. N. W. Howe, M. Bhadbhade, P. Thordarson, *J. Am. Chem. Soc.* **2014**, *136*, 7505-7516.

273. P. Thordarson, in *Supramolecular Chemistry: From Molecules to Nanomaterials* (Eds.: P. Gale, J. Steed), John Wiley & Sons, Ltd, **2012**.

274. J. P. Stewart, *J. Mol. Model.* **2007**, *13*, 1173-1213.

275. A. D. Becke, *J. Chem. Phys.* **1993**, *98*, 5648-5652.

276. A. V. Marenich, C. J. Cramer, D. G. Truhlar, *J. Phy. Chem. B* **2009**, *113*, 6378-6396.

277. M. J. Frisch, G. W. Trucks, H. B. Schlegel, G. E. Scuseria, M. A. Robb, J. R. Cheeseman, G. Scalmani, V. Barone, B. Mennucci, G. A. Petersson, H. Nakatsuji, M. Caricato, X. Li, H. P. Hratchian, A. F. Izmaylov, J. Bloino, G. Zheng, J. L. Sonnenberg, M. Hada, M. Ehara, K. Toyota, R. Fukuda, J. Hasegawa, M. Ishida, T. Nakajima, Y. Honda, O. Kitao, H. Nakai, T. Vreven, J. A. Montgomery Jr., J. E. Peralta, F. Ogliaro, M. J. Bearpark, J. Heyd, E. N. Brothers, K. N. Kudin, V. N. Staroverov, R. Kobayashi, J. Normand, K. Raghavachari, A. P. Rendell, J. C. Burant, S. S. Iyengar, J. Tomasi, M. Cossi, N. Rega, N. J. Millam, M. Klene, J. E. Knox, J. B. Cross, V. Bakken, C. Adamo, J. Jaramillo, R. Gomperts, R. E. Stratmann, O. Yazyev, A. J. Austin, R. Cammi, C. Pomelli, J. W. Ochterski, R. L. Martin, K. Morokuma, V. G. Zakrzewski, G. A. Voth, P. Salvador, J. J. Dannenberg, S. Dapprich, A. D. Daniels, Ö. Farkas, J. B. Foresman, J. V. Ortiz, J. Cioslowski, D. J. Fox, Gaussian, Inc., Wallingford, CT, USA, **2009**.

278. G. Sheldrick, *Acta Crystallogr. A* **2015**, *71*, 3-8.

279. G. Sheldrick, *Acta Crystallogr. A* **2008**, *64*, 112-122.

280. O. V. Dolomanov, L. J. Bourhis, R. J. Gildea, J. A. K. Howard, H. Puschmann, *J. Appl. Crystallogr.* **2009**, *42*, 339-341.